Institute of Low Temperature and Structure Research

Polish Academy of Sciences

Doctoral dissertation

The investigation of the influence of the chemical composition of the host material on the probability of thermally induced depopulation processes of the excited levels of the transition metal ions of 3d^3 electronic configuration in inorganic oxide materials for applications in luminescence thermometry

In the form of thematically coherent series of articles published in scientific journals

mgr inż. Wojciech Piotrowski

Supervisor: Prof. dr hab. Łukasz Marciniak

Wrocław, 2023

Table of content

1. The aim of the thesis

The aim of this PhD thesis is to investigate the influence of the composition and the resulting material parameters of the host material, such as local crystal symmetry, crystal field strength, phonon energy, etc., on the spectroscopic properties and sensitivity of luminescence thermometers based on the luminescence of lanthanide and transition metal ions with particular emphasis on Mn^{4+} and Cr^{3+} ions of $3d^3$ electronic configuration. The two promising strategies for luminescence thermometry, i.e. based on the ratio of transition metal and lanthanide ions emission band intensities and transition metal ion luminescence lifetimes, were analyzed. Furthermore, the role of phosphor stoichiometry in the thermally dependent probability of energy transfer between Mn^{4+} or Cr^{3+} ions and lanthanide ions was investigated in order to improve the thermometric performance of thermometers based on the ratio of lanthanide ion emission intensities. Conducted studies allow an understanding and the modelling of the luminescent thermal quenching mechanism and therefore facilitate the design of on-demand highly sensitive luminescent thermometers operating in the ratiometric and lifetime-based approaches.

2. Abstract (in English)

Luminescence thermometry is an experimental method of remote temperature determination using analysis of temperature dependence of the spectroscopic properties of phosphors. Its great popularity, observed in recent years, is mainly caused by the possibility of fast and accurate temperature readout in an electrically passive manner. The main requirement for a luminescent thermometer is its high accuracy of temperature determination, which mainly depends on the brightness of the material and its sensitivity to temperature changes. Therefore, increasing interest in this context is devoted to the phosphors doped with transition metal ions (TM), especially with the ions with $3d^3$ electron configuration (i.e. mainly Mn^{4+} and Cr^{3+}) due to their high luminescence brightness and the ease of optimizing their thermometric properties by modifying the chemical composition of the host material. Although the influence of host material stoichiometry on the thermal stability of Mn^{4+} and Cr^{3+} luminescence intensities has already been partially investigated, the lack of systematic studies enabling the selection of material parameters as well as the determination of their role in the thermal quenching of Mn^{4+} and Cr^{3+} emissions significantly hinders the design of highly sensitive luminescent thermometers. On the other hand, Mn^{4+} and Cr^{3+} ions can act as sensitizers for luminescent thermometers based on emission of other optically active ions - lanthanides (Ln^{3+}), what means that TM ions can increase the relative sensitivity of luminescent thermometer. For this purpose, it is necessary to select such a host-TM-Ln^{3+} system, which will enable an effective energy transfer from TM ions to Ln^{3+} ions. The use of TM ions as sensitizers of Ln^{3+} emission is particularly

beneficial because of much higher absorption cross-section of TM ions in respect to the Ln^{3+}, which enables significant enhancement of the emission brightness of this type of phosphors. Such use of TM ions in luminescence thermometry has not been investigated systematically so far.

To sum up, the aim of this doctoral dissertation is to investigate the influence of the chemical composition and material parameters, such as the local symmetry of the crystals, the crystal field strength, the phonon energy etc., on the sensitivity of luminescent thermometers based on the ratio of the intensity of the emission bands of TM and Ln^{3+} ions and their luminescence lifetimes for transition metal ions with the $3d^3$ electronic configuration with special emphasis on Mn^{4+} and Cr^{3+} ions. Furthermore, the role of phosphor stoichiometry in the thermally dependent probability of the energy transfer between Mn^{4+} or Cr^{3+} ions and Ln^{3+} ions was investigated to improve the thermometric performance of thermometers based on the emission band ratio of lanthanide ions.

3. Streszczenie (w języku polskim)

Termometria luminescencyjna jest eksperymentalną metodą zdalnego wyznaczania temperatury, wykorzystującą analizę wpływu temperatury na właściwości spektroskopowe luminoforu. Jej duża popularność, obserwowana w ostatnich latach, wynika głównie z możliwości szybkiego i precyzyjnego odczytu temperatury w sposób elektrycznie pasywny. Głównym wymogiem, który musi spełniać termometr luminescencyjny jest jego duża dokładność wyznaczenia temperatury, która przede wszystkim zależy od jasności materiału (ang. brightness) oraz jego czułości na zmiany temperatury (ang. sensitivity). Dlatego też coraz większe zainteresowanie poświęcane jest, w tym kontekście, grupie jonów metali przejściowych (TM), a zwłaszcza jonów o konfiguracji elektronowej $3d^3$ (tj. przede wszystkim Mn^{4+} i Cr^{3+}) ze względu na wysoką jasność luminescencji oraz łatwość optymalizacji ich właściwości termometrycznych poprzez modyfikację składu chemicznego materiału matrycy. Pomimo, iż donoszono już o wpływie stechiometrii matrycy na stabilność termiczną intensywności luminescencji Mn^{4+} i Cr^{3+}, brak systematycznych badań umożliwiających dobór parametrów materiałowych, a także określenie ich roli w wygaszaniu temperaturowym emisji jonów Mn^{4+} i Cr^{3+} znacząco utrudnia świadome projektowanie wysokoczułych termometrów luminescencyjnych. Co więcej, inną rolą jonów Mn^{4+} i Cr^{3+} może być wzmocnienie luminescencji termometrów bazujących na emisji innych jonów luminescencyjnych – lantanowców (Ln^{3+}), przyczyniając się do zwiększenia ich czułości wyznaczania temperatury. Do tego celu należy dobrać taki układ matryca-TM-Ln^{3+}, który umożliwi efektywny transfer energii od metalu przejściowego do lantanowca. Wykorzystanie jonów metali przejściowych jako uczulaczy emisji jonów Ln^{3+} jest szczególnie korzystne, ponieważ metale przejściowe charakteryzują się znacznie wyższym przekrojem czynnym na absorpcję niż

lantanowce, co umożliwia istotne zwiększanie jasności emisji tego typu luminoforów. Takie wykorzystanie jonów metali przejściowych w termometrii luminescencyjnej nie zostało jednak dotychczas zbadane w sposób systematyczny.

Podsumowując, celem niniejszej pracy doktorskiej jest zbadanie wpływu składu i wynikających z niego parametrów materiałowych matrycy, takich jak lokalna symetria kryształu, siła pola krystalicznego, energia fononów itp., na czułość termometrów luminescencyjnych bazujących na stosunku intensywności pasm emisyjnych jonów TM i Ln^{3+} oraz ich czasach zaniku luminescencji dla jonów metali przejściowych w konfiguracji elektronicznej $3d^3$ ze szczególnym uwzględnieniem jonów Mn^{4+} i Cr^{3+}. Ponadto, w ramach niniejszej pracy zbadano rolę stechiometrii luminoforu w termicznie zależnym prawdopodobieństwie transferu energii pomiędzy jonami Mn^{4+} i Cr^{3+} a jonami lantanowców w celu poprawiania parametrów termometrycznych termometrów bazujących na stosunku intensywności emisji jonów lantanowców.

4. Scientific resume of the author

Wojciech Piotrowski, MSc Eng.

Total number of citations (by Google Scholar on 15.12.23): 355

Total number of citations (by Scopus on 15.12.23): 305

h-index: 11

Education

01/2020 - present	**PhD Student of Wrocław Doctoral School of Institutes of Polish Academy of Sciences** **Discipline:** Chemical sciences
02/2018 – 09/2019	**Wroclaw University of Science and Technology** **Field of study:** Materials Engineering **Specialty:** Advanced Functional Materials **Education level:** Master of Science
10/2014 - 02/2018	**Wroclaw University of Science and Technology** **Field of study:** Materials Engineering **Education level:** Engineer

Projects

01/2020 – 05/2023	**NCN Beethoven Classic 3 - 2018/31/G/ST5/03258** Sensitization of lanthanide-based phosphors by transition metals for high-brightness tunable thermometers **PhD Scholarship- Investigator**
04/2022 – 07/2022	**NAWA Bekker - BPN/BEK/2021/1/00029** The Cr^{3+} ions luminescence-based in vitro and ex vivo thermal sensing and imaging **Internship – Principal Investigator**
01/2022 – present (12/2023)	**NAWA Canaletto - PPN/BIT/2021/1/00012** Fe^{3+}, Bi^{3+} co-doped phosphors for novel efficient Near-Infrared LEDs **Investigator**
01/2023 – present (01/2025)	**NCN Preludium 21 - 2022/45/N/ST5/01457** Investigation of the influence of chemical composition of the $LnAlO_3$ host material on spectroscopic properties of luminescent nanothermometers based on Ti^{3+} lifetimes **Principal Investigator**
07/2023 – present (12/2023)	**NCN OPUS - 2020/37/B/ST5/00164** Nanocrystalline luminescent manometers based on transition metal ions emission **Investigator**

List of publications included in the doctoral dissertation

[P1] W. M. Piotrowski, V. Kinzhybalo, L. Marciniak, *Revisiting $Y_3Al_{5-x}Ga_xO_{12}$ Solid Solutions Doped with Chromium Ions: Effect of Local Symmetry on Thermal Quenching of Cr^{3+} and Cr^{4+} Ions*, ECS J Solid State Sci Technol, 12, (2023), 066003.

[P2] W. M. Piotrowski, M. Szymczak, E. Martín Rodríguez, R. Marin, M. Henklewska, B. Poźniak, M. Dramićanin, Ł. Marciniak; *Step by step optimization of luminescence thermometry in $MgTiO_3:Cr^{3+}$, $Nd^{3+}@SiO_2$ nanoparticles towards bioapplications*, Mater. Chem. Phys., 312, (2023), 128623.

[P3] W. Piotrowski, K. Kniec, L. Marciniak, *Enhancement of the Ln^{3+} ratiometric nanothermometers by sensitization with transition metal ions*, J. Alloys Compd., 870, (2021), 159386.

[P4] W. Piotrowski, L. Dalipi, R. Szukiewicz, B. Fond, M. Dramićanin, L. Marciniak, *The role of Cr^{3+} and Cr^{4+} in emission brightness enhancement and sensitivity improvements of NIR-emitting Nd^{3+}/Er^{3+} ratiometric luminescence thermometers*, J. Mater. Chem. C, 9, (2021), 12671-12680.

[P5] W. M. Piotrowski, K. Maciejewska, L. Dalipi, B. Fond, L. Marciniak, *Cr^{3+} ions as an efficient antenna for the sensitization and brightness enhancement of Nd^{3+}, Er^{3+}-based ratiometric thermometer in $GdScO_3$ perovskite lattice*, J. Alloys Compd. 923, (2022), 166343.

[P6] W. M. Piotrowski, K. Maciejewska, L. Marciniak, *Boosting the thermometric performance of the Nd^{3+}, Er^{3+} based luminescence thermometers by sensitization via Cr^{3+} ions: the role of the host material*, Mater. Today Chem. 30, (2023), 101591.

[P7] W. M. Piotrowski, K. Kniec-Stec, M. Suta, B. Bogielski, B. Pozniak, L. Marciniak, *Positive luminescence thermal coefficient of Mn^{2+} ions for highly sensitive luminescence thermometry*, Chem. Eng. J. 464, (2023), 142492.

[P8] W. Piotrowski, K. Trejgis, K. Maciejewska, K. Ledwa, B. Fond, L. Marciniak, *Thermochromic luminescent nanomaterials based on Mn^{4+}/Tb^{3+} codoping for temperature imaging with digital cameras*, ACS Appl. Mater. Interfaces, 12, 39, (2020), 44039-44048.

[P9] W. M. Piotrowski, P. Bolek, M. Brik, E. Zych, L. Marciniak, *Frontiers of deep-red emission of Mn^{4+} ions with Ruddlesden-Popper perovskites*, Inorg. Chem. (2024), accepted, DOI: https://doi.org/10.1021/acs.inorgchem.3c03113

[P10] W. M. Piotrowski, K. Trejgis, M. Dramićanin, L. Marciniak, *Strong sensitivity enhancement in lifetime-based luminescence thermometry by co-doping of $SrTiO_3:Mn^{4+}$ nanocrystals with trivalent lanthanide ions*, J. Mater. Chem. C, 9, (2021), 32, 10309-10316.

List of remaining publications

[P11] Miniewicz, A. Sobolewska, <u>W. Piotrowski,</u> P. Karpinski, S. Bartkiewicz, E. Schab-Balcerzak, *Thermocapillary Marangoni Flows in Azopolymers*, Materials 13, 11, (2020), 2464.

[P12] K. Kniec, <u>W. Piotrowski</u>, K. Ledwa, L. D. Carlos, L. Marciniak, *Spectral and thermometric properties altering through crystal field strength modification and host material composition in luminescent thermometers based on Fe^{3+} doped AB_2O_4 type nanocrystals (A = Mg, Ca; B = Al, Ga)*, J. Mater. Chem. C, 9, (2021), 517-527.

[P13] K. Kniec, <u>W. Piotrowski</u>, K. Ledwa, M. Suta, L. D. Carlos, L. Marciniak, *From quencher to potent activator – Multimodal luminescence thermometry with Fe^{3+} in the oxides MAl_4O_7 (M = Ca, Sr, Ba)*, J. Mater. Chem. C, 9, (2021), 6268-6276.

[P14] J. Periša, Z. Ristić, <u>W. Piotrowski</u>, Ž. Antić, L. Marciniak, M. D. Dramićanin, *All near-infrared multiparametric luminescence thermometry using Er^{3+}, Yb^{3+}-doped YAG nanoparticles*, RSC Advances, 11, (2021), 15933-15942.

[P15] <u>W. Piotrowski</u>, M. Kuchowicz, M. Dramićanin, L. Marciniak, *Lanthanide dopant stabilized Ti^{3+} state and supersensitive Ti^{3+}-based multiparametric luminescent thermometer in $SrTiO_3:Ln^{3+}$ ($Ln^{3+} = Lu^{3+}$, La^{3+}, Tb^{3+}) nanocrystals*, Chem. Eng. J., 428, (2021), 131165.

[P16] <u>W. Piotrowski</u>, L. Dalipi, K. Elzbieciak-Piecka, A. Bednarkiewicz, B. Fond, L. Marciniak, *Self-referenced temperature imaging with dual LED excitation and single band emission of $AVO_4:Eu^{3+}$ (A = Y, La, Lu, Gd) nanophosphors*, Adv. Photonics Research, 3 (2021), 6, 2100139.

[P17] L. Marciniak, <u>W. Piotrowski</u>, M. Szalkowski, V. Kinzhybalo, M. Drozd, M. Dramicanin, A. Bednarkiewicz, *Highly sensitive luminescence nanothermometry and thermal imaging facilitated by phase transition*, Chem. Eng. J., 427, (2021), 131941.

[P18] Z. Ristić, <u>W. Piotrowski</u>, M. Medić, J. Periša, Ž. M. Antić, L. Marciniak, M. D. Dramićanin, *Near-Infrared Luminescent Lifetime-Based Thermometry with Mn^{5+}-Activated $Sr_3(PO_4)_2$ and $Ba_3(PO_4)_2$ Phosphors*, ACS Appl. Electron. Mater. 4, (2022), 3, 1057-1062.

[P19] L. Marciniak, <u>W. M. Piotrowski</u>, M. Drozd, V. Kinzhybalo, A. Bednarkiewicz, M. Dramicanin, *Phase Transition-Driven Highly Sensitive, NIR–NIR Band-Shape Luminescent Thermometer Based on $LiYO_2:Nd^{3+}$*, Adv. Opt. Mater. 10 (2022), 9, 2102856.

[P20] <u>W. M. Piotrowski</u>, Z. Ristic, M. D. Dramićanin, Ł. Marciniak, *Modification of the thermometric performance of the lifetime-based luminescent thermometer exploiting Ti^{3+} emission in $SrTiO_3$ and $CaTiO_3$ by doping with lanthanide ions*, J. Alloys Compd. 906 (2022), 164398.

[P21] M. D. Dramićanin, Ł. Marciniak, S. Kuzman, <u>W. Piotrowski</u>, Z. Ristić, J. Periša, I. Evans, J. Mitrić, V. Đorđević, N. Romčević, M. G. Brik, C.-G. Ma, *Mn^{5+}-activated $Ca_6Ba(PO_4)_4O$ near-infrared phosphor and its application in luminescence thermometry*, Light Sci. Appl. 11 (2022), 1, 1-13.

[P22] <u>W. M. Piotrowski</u>, R. Marin, M. Szymczak, E. Martín Rodríguez, D. H. Ortgies, P. Rodríguez-Sevilla, M. D. Dramićanin, D. Jaque, L. Marciniak, *Mn^{5+} lifetime-based thermal imaging in the optical transparency windows through skin-mimicking tissue phantom*, Adv. Opt. Mater. 11 (2022), 3, 2202366.

[P23] <u>W. M. Piotrowski</u>, M. Kardach, P. Sobierajska, A. Watras, J. M. Reeks, V. Kinzhybalo, L. Marciniak, R. J. Wiglusz, *Tunable luminescence thermal stability in $YV_xAs_{1-x}O_4:Eu^{3+}$ through the introduction of As^{5+} ions for remote temperature sensing applications*, J. Mater. Chem. C, (2023), 11, 1418-1428.

[P24] K. Elzbieciak-Piecka, <u>W. M. Piotrowski</u>, M. D. Dramicanin, L. Marciniak, *Understanding the Power of Luminescence Ratiometric Thermal History Indicators driven by Phase Transitions: The case of Eu^{3+} doped $LaVO_4$*, Dalton Trans. 52 (2023), 6077-6084.

[P25] <u>W. M. Piotrowski</u>, R. Marin, M. Szymczak, E. Martín Rodríguez, D. Ortgies, P. Rodriguez, P. Bolek, M. Dramićanin, D. Jaque, L. Marciniak, *Critical Evaluation of the Thermometric Performance of Ratiometric Luminescence Thermometers based on $Ba_3(VO_4)_2:Mn^{5+}$, Nd^{3+} for Deep-Tissue Thermal Imaging*, J. Mater. Chem. C, 11, (2023), 6713-6723

[P26] M. Pieprz, <u>W. Piotrowski</u>, P. Woźny, M. Runowski, L. Marciniak, *Highly sensitive lifetime-based luminescent manometer on Mn^{4+} luminescence in $Sr_4Al_{14}O_{25}:Mn^{4+}$*, Adv. Opt. Mater. (2023), 2301316.

[P27] G. Ouertani, K. Maciejewska, <u>W. Piotrowski</u>, K. Horchani-Naifer, L. Marciniak, M. Ferhi, *High thermal stability of warm white emitting single phase $GdPO_4:Dy^{3+}/Sm^{3+}$ phosphor for UV excited wLEDs*, J. Lumin. 265, (2024), 120228.

[P28] M. Sojka, <u>W. Piotrowski</u>, L. Marciniak, E. Zych, *Co-doping to extend the operating range of luminescence thermometers. The case of $Y_2SiO_5:Pr^{3+}$, Tb^{3+}*, J Alloys and Compd, 970, (2024), 172662.

Conferences

1) **2nd International Conference on Phosphor Thermometry (ICP),** July 27-29th 2020, Magdeburg, Germany, (online), „$Sr_4Al_{14}O_{25}$ doped with Mn^{4+} and Tb^{3+} ions as a highly sensitive thermographic phosphor" – oral presentation

2) **Phobia Annual Nanophotonics International Conference 2020 (PANIC),** October 12-14th 2020, Wrocław, Poland (online), "Temperature imaging with Mn^{4+} and Tb^{3+} codoped ratiometric phosphor" – oral presentation

3) **International Conference on the Physics of Optical Materials and Devices (ICOM-Asia),** December 11-12th 2020, Chongqing, China (online), "The sensitization of the Tb^{3+}, Eu^{3+}-co-doped luminescent thermometer by the transition metal ions" – oral presentation

4) **V Ogólnopolska Studencka Fizyczno-Optyczna Konferencja (FOKA 2020),** December 11-13th 2020, Wrocław, Poland (online), "Uczulanie termometrów luminescencyjnych bazujących na emisji jonów lantanowców przez jony metali przejściowych" – oral presentation

5) **19th International Conference on Luminescence (ICL 2020),** 26-30th July 2021, Changchun, China (online), "Investigation of thermochromic properties of $Sr_4Al_{14}O_{25}$:Mn^{4+}/Tb^{3+} for temperature imaging" – poster

6) **4th International Conference on Optics, Photonics and Lasers (OPAL'2021)**, 13-15th October 2021, Corfu, Greece (in person), „Beneficial influence of transition metal ions on the Ln^{3+}-based ratiometric thermometers" – oral presentation

7) **ACers 14th Pacific Rim Conference on Ceramic and Glass Technology (PACRIM 14),** 12-17th December 2021, Vancouver, Canada (online), „Sensitization of the Ln^{3+}-based thermometers operating in NIR spectral region through Cr^{3+} ions" – oral presentation

8) **"Spectral sHapIng For biomedical and energy applicaTions" International Conference (SHIFT 2022),** October 2022, Canary Islands, Spain (in person), „The influence of vanadate host material on the relative sensitivity and brightness in the single band ratiometric thermometry – poster

9) **11th International Conference on f-elements (ICFE-11),** 22-26th August 2023, Strasburg, France (in person), "Influence of Ln^{3+} ions on Ti^{3+} lifetime for luminescence thermometry" – poster

10) **20th International Conference on Luminescence (ICL 20),** 27th August-1st September 2023, Paris, France, "Ti^{3+} lifetime based luminescent thermometry in $LnAlO_3$ (Ln = La^{3+}, Gd^{3+}, Lu^{3+})" – poster

Research stays and courses

12/2021	Otto-von-Guericke-Universität in Magdeburg, Germany (2 weeks)
01/2022	University of Tartu, Estonia – within the framework of Dora Plus programme funded by European Regional Development Fund and Republic of Estonia (1 month)
04/2022-06/2022	Universidad Autónoma de Madrid, Spain – within the framework of NAWA Bekker programme (Polish National Agency for Academic Exchange) (3 months)
05/2023	Ca' Foscari University of Venice - within the framework of NAWA Canaletto programme (Polish National Agency for Academic Exchange) and MAECI PO22MO12 project of the bilateral Executive Protocol (Ministry of Foreign Affairs and International Cooperation, Italy) (1 week)
01/2021-06/2021	Training and mentoring programme TopMinds 2021

Awards and scholarships

| 05/2023 | 3rd place in 1st China-CEEC Youth Innovation and Entrepreneurship Competition (Ningo, China) |
| 05/2023 | Scholarship START 2023 of Foundation for Polish Science (FNP) |

5. List of used abbreviations

BET – back energy transfer
CF – crystal field
CFT – crystal field theory
CT – charge transfer
CCD – charge-coupled device
DAC – diamond anvil cell
EIR – effective ionic radii
ESA – excited state absorption
ET – phonon-assisted energy transfer
ICP-EOS – inductively coupled plasma optical emission spectroscopy
LED/LEDs – light emitting diodes
LFT – ligand field theory
LIR – luminescence intensity ratio
Ln^{3+} – trivalent lanthanide (ions)
IR/NIR – infrared/near infrared
MOF – metal-organic framework
NTE – negative thermal expansion
pc-LED – phosphor-converted light emitting diodes
PEG – poly(ethylene glycol)
PTE – positive thermal expansion
QE – quantum efficiency
QY – quantum yield
SEM – scanning electron microscopy
TEM – transmission electron microscopy
TM – transition metal (ions)
T-S – Tanabe-Sugano (diagram)
UV – ultraviolet
XPS – X-ray photoelectron spectroscopy
XRPD – X-ray powder diffraction
YAG – $Y_3Al_5O_{12}$
YGG – $Y_3Ga_5O_{12}$
ZPL – zero-phonon line

6. Descriptive introduction

6.1. Selected processes in materials doped with luminescent centers

Luminescence is defined as the emission of light by the matter, unrelated to heat[1]. There are several types of luminescence, which are categorized by the energy source that leads to the luminescence phenomenon with prefixes such as: chemo- (including bio-), electro- (including cathodo-), thermo-, mechano- or photo- luminescence[2,3]. This dissertation focuses on photoluminescence, which is observed following the absorption of photon by the material. Many groups of materials are known to exhibit photoluminescence of which the most popular should be mentioned: Ln^{3+} and TM doped inorganic crystals, metal-organic frameworks (MOFs), quantum dots, carbon dots, fluorescent diamonds, luminescent polymers, organic dyes[4–6]. These materials are referred as phosphors. Inorganic crystals doped with luminescent centers have been of particular interest in recent years[2,7–9]. In their case, the crystal structure allows the spectroscopic properties of the phosphor to be understood and then modified in a controlled manner. In general, the properties and thus the potential applications of the materials are determined by the appropriate choice of host material[10–13]. Of these, an important role is played by oxides, which are characterized by high mechanical, chemical, photochemical, and thermal properties and can be synthesized by a variety of techniques allowing both nanoscopic, microscopic and macroscopic ('bulk') crystals to be obtained[14–17]. As mentioned, one group of luminescent centers that can locate as impurities in inorganic crystals are transition metal ions, among others, with a $3d^3$ electron configuration. Their spectroscopic properties are particularly susceptible to the host material in which they are located, and will therefore be discussed in detail in section 6.3. Beforehand, however, the fundamental processes occurring in materials doped with luminescent centers will be presented.

6.1.1. Absorption and emission in phosphors

To observe the phenomenon of photoluminescence (hereinafter referred to as luminescence), the absorption of energy in the form of electromagnetic radiation passing through the material is required. If it is taken into account that the material is partially transparent, this means that only part of the radiation has been absorbed. Using the Bouguer-Lambert-Beer law, it is possible to determine the intensity I of radiation that passes through a material[7,18,19]:

$$I = I_0 e^{(-\alpha l)} \tag{1}$$

where: I_0 is the intensity of the initial radiation before the material, α is the absorption coefficient and l is the thickness of the sample or the distance the radiation will travel in the medium.

However, it should be mentioned that Eq. 1 remains true if low intensities of the radiation are used. Nevertheless, this is a particularly useful correlation for identifying materials, since α is a characteristic property of materials. Moreover, the value of α depends on the wavelength, as indirectly indicated by the different colours of the materials.

To discuss the subsequent processes including luminescence, it may be helpful to graphically represent the energy absorption by the material as a result of the electron transition from the ground state (denoted as *"0"*) with energy E_0 to the excited state (*"1"*) with energy E_1, where $E_1 > E_0$ (Figure 1a)[20]. This is possible if the difference between these levels is equal to the energy of the photon:

$$h\nu = E_1 - E_0 = \Delta E_{10} \tag{2}$$

where: h is the Planck constant and ν is photon's electromagnetic frequency. On the other hand, if the electron is energetically in the excited state *1*, the reverse process may be induced by a photon, i.e., an electronic transition from *1* to *0* with the release of energy in the form of other photon (Figure 1b). This process is the so-called induced emission. In this case, the energy of the photon will also be equal to the difference in energy of the levels between which the transition occurs and the energy of the inducing photon, according to Eq. 2. Moreover, both photons will be characterized by the same energy, polarization, phase and direction.

Finally, there is a third process, so-called spontaneous emission, which requires, like induced emission, an electron in the excited state, but does not require a photon induction (Figure 1c). It can be considered as the most important of the three processes mentioned for this doctoral dissertation since the process of spontaneous emission is equivalent to luminescence[7]. After a specific time called as the lifetime of the excited state, the luminescence intensity decreases by an order of magnitude.
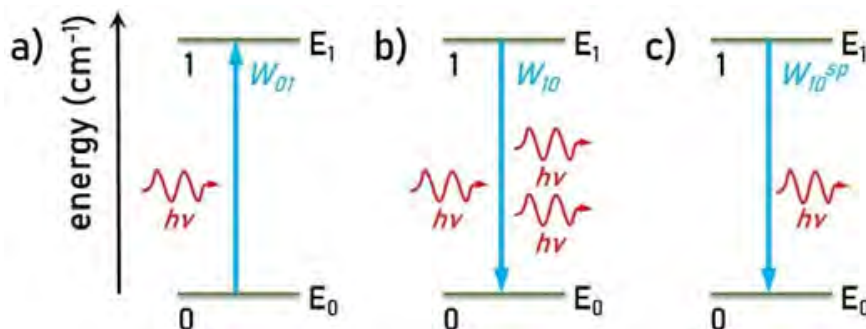
Figure 1. Possible radiative processes in a two level system: the absorption – a), the induced emission – b) and spontaneous emission – c).

To describe the probability of absorption, induced emission and spontaneous emission per time unit, they are defined as W_{01}, W_{10} and W_{10}^{sp}, respectively[18,21]:

$$W_{01} = -B_{01}N_0\rho_v \ , \tag{3}$$

$$W_{10} = -B_{10}N_1\rho_v \ , \tag{4}$$

$$W_{10}^{sp} = -A_{10}N_1 \ , \tag{5}$$

where: B_{01}, B_{10} and A_{10} are the Einstein coefficients for the absorption, induced emission and spontaneous emission, respectively, N_0 and N_1 are the population of the ground and excited states, respectively and ρ_v is the spectral volume density of the electromagnetic field energy[20]. When comparing the three equations, it is worth noting that spontaneous emission is not dependent on ρ_v compared to induced emission. Moreover, A_{10} is the inverse of radiative lifetime (τ_R) of excited state:

$$A_{10} = \frac{1}{\tau_R} \ . \tag{6}$$

6.1.2. Mechanisms of radiative and nonradiative transitions

Up to now, for simplicity, a simple two-level system is shown in Figure 1, for which the energy required for absorption and the energy produced during spontaneous emission (luminescence) were equal. Under experimental conditions, i.e. in materials, such a situation is only partially true at very low temperatures (in general <40K). However, even in this range, it can be observed experimentally that the emission band (on the emission spectrum) is shifted towards lower energies in respect to the absorption band (on the absorption spectrum) (Figure 2a). It is known as the Stokes shift. This phenomenon is most easily explained using the example of the optical centre in a crystal. It is known that all ions in crystals oscillate around equilibrium positions, resulting in different distances between the optical centre and the ions that surround it. Both the presence of the optical centre in the vicinity of other ions and the distance between them affect the formation of the energy states (this topic will be described in more detail in section 6.3.1). For this reason, a shift of energy states in the wavevector domain Q is presented, and due to the harmonic motion of the optical centre and surrounding ions, the energy states take the shape close to parabolas (Figure 2b). On this basis, it is possible to represent the energy difference between absorption and emission. At first, the absorption of the photon leads to the transition of the electron from the ground state to the excited state. Note that this occurs without any change in Q, remaining in Q_0 (the equilibrium position in the ground state),

which is graphically represented as a vertical arrow. It stays in line with Frank-Condon principles, which assume that electron transition processes are much faster than crystal lattice vibrations[19,20]. Subsequently, a relaxation of electron to the minimum of the excited state parabola occurs, and therefore the electron is located in the equilibrium position of the excited state – Q_1. Such relaxation is a nonradiative process and is associated with the emission of phonon, i.e. the vibrational energy quantum of the crystal lattice. From the bottom of the parabola, an electron transition from the excited state to the ground state takes place, resulting in luminescence, which, similar to absorption, happens without any change in Q, i.e. it remains with Q_1. Finally, the electron is relaxed to the ground state minimum with Q_0. The Stokes shift is measured as an energy difference as follows:

$$E_{Stokes} = E_{abs} - E_{em} = h\nu_{abs} - h\nu_{em} \qquad (7)$$

where: E_{abs}, E_{em}, ν_{abs} and ν_{em} are energies and frequencies of absorption and emission transitions, respectively.
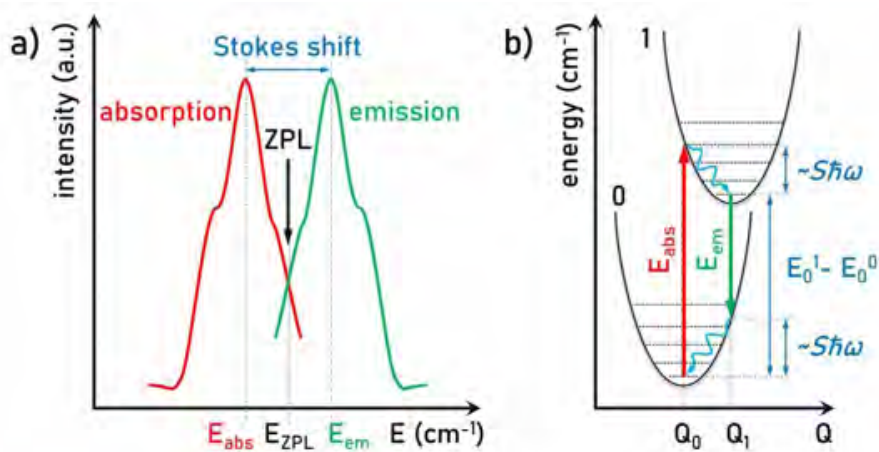
Figure 2. Representative comparison of absorption and emission band – a); schematic visualization of absorption and emission processes on the configurational coordinate diagram of two levels – b).

It should be mentioned that particularly useful in the correct determination of E_{Stokes} is the so-called zero-phonon line (ZPL), which corresponds to the transition between ground and excited state without phonon participation and therefore its presence on the absorption and emission spectra overlap spectrally[22]. In this case, it should be expected that at sub-zero temperatures the absorption and emission bands will be their mirror image and the ZPL will be their mirror plane (see Figure 2a)[23]. For this reason, the relation $E_{Stokes} = 2(E_{ZPL} - E_{max})$, where E_{max} is the maximum of absorption or emission band, should be true[7].

To more accurately graphically reflect the experimental results on the configurational coordinate diagram, the correlation between the Stokes shift and ΔQ_e, where $\Delta Q_e = Q_1 - Q_0$ refers to the equilibrium position offset, should be determined. In this case, the Huang-Rhys parameter S was proposed, defined as follows:

$$S = \frac{1}{2}\frac{M\omega}{\hbar}(\Delta Q_e)^2 \qquad (8)$$

where: M is the reduced mass of the vibrating system, ω is the characteristic vibrational frequency and $\hbar$ is the reduced Planck constant ($\hbar = \frac{h}{2\pi}$) [7,19,23]. A dimensionless parameter S serves to determine the difference in the electron-phonon coupling, and thus represents the offset between ground and excited parabolas in wavevector domain. Therefore, according to theoretical calculations, the relation between E_{Stokes} and S presents itself as:

$$E_{Stokes} = (2S-1)\hbar\omega \ [24] \qquad (9)$$

or

$$E_{Stokes} = 2S\hbar\omega \ [25]. \qquad (10)$$

As can be seen, the commonly used formula is not unambiguous and depends on the parameters taken into account when deriving it. However, Jong et al.[23] presented that Eq. 9 and Eq. 10 represent only a theoretical approximation, while the experimental relation becomes correct for:

$$S = (\frac{1}{2}\frac{E_{Stokes}}{\hbar\omega} + \frac{1}{4}) \pm \frac{1}{4} \ . \qquad (11)$$

6.1.3. Quantum yield of luminescence and brightness

Having introduced the concept of Stokes shift, it is possible to define quantum yield of luminescence (QY) in the terms of absorption and emission as follows[1,26]:

$$\Phi(\lambda) = \frac{number \ of \ photons \ emitted}{number \ of \ photons \ absorbed} \qquad (12)$$

This is a well-known parameter that is determined with the help of the integrating sphere. It is noteworthy that this parameter, although usually determined at room temperature, is strongly temperature dependent, according to[25]:

$$\Phi(T) = \frac{\Phi(0)}{1 + A\exp\left(\frac{-E_a}{kT}\right)} \qquad (13)$$

where: $\Phi(0)$ is the quantum yield at T=0K, A is dimensionless constant and E_a is the activation energy. However, please note that it is a popular problem in the literature to use quantum yield and quantum efficiency interchangeably. However, based on the work of Wong, Bünzli and Tanner[26], quantum efficiency (QE) is defined in terms of optical energy (not photons, specified in [W]) as:

$$\eta = \frac{energy\ output}{energy\ input} \quad . \tag{14}$$

This work systematizes both definitions and emphasizes that, despite the apparent similarity of Eq. 12 and Eq. 14, it should be noted that equality $\Phi(\lambda) = \eta$ is only true for two-level systems, such as shown in Figure 1. In most cases where there are energy losses, the number of emitted and absorbed photons may be the same, but the values of the incoming and outgoing energies will differ ($\Phi(\lambda) > \eta$). Therefore, it is theoretically possible to obtain a system for which $\Phi(\lambda) = 1$, but according to the Stokes shift the energy of the emitted photons will be less than the energy of the absorbed photons (Figure 2b). Part of this energy will be transferred in the form of phonons to the crystal lattice (as heat).

On the other hand, gaining popularity in recent years is the brightness parameter B. Its definition according to [1] coincides with the following formula:

$$B = \Phi(\lambda) \times \varepsilon(\lambda) \tag{15}$$

where: $\varepsilon(\lambda)$ is the molar absorption coefficient which is also dependent on the excitation wavelength. According to Ref. [26] this definition is particularly suited to solutions since measuring $\varepsilon(\lambda)$ is easy and relatively precise for them compared to solid samples. On the other hand, the alternative formula is presented as:

$$B = \Phi(\lambda) \times \xi_{abs} \tag{16}$$

where: ξ_{abs} is the absorption efficiency and is defined as the ratio of the number of absorbed photons and incident photons. According to this definition, the determination of ξ_{abs} is possible with the help of the integrating sphere and can be used for both solutions and solid samples.

When comparing the usefulness of determining QY and B values, we find that it depends on the range of applications. High QY is desirable for the design of phosphors for light emitting diodes (LEDs). On the other hand, a high molar absorption coefficient can compensate for low QY values and also provide high brightness, which is particularly considered for biomedical applications. Nevertheless, in both cases it should be emphasized that QY and B values

depend on a number of experimental parameters, such as excitation wavelength or temperature, which should be highlighted when reporting these parameters[26].

6.1.4. Boltzmann thermal equilibrium and Mott-Seitz model

So far, it was shown that the emission intensity depends on the excitation wavelength. However, the dependence of luminescence as a function of temperature should be also considered. To further discuss the emission intensity, the phosphor should be treated as a multi-electron system operating in the time domain. At first, the emission intensity from the excited state i to the ground state 0 should generally be described as:

$$I_{i0}(T) = p_i N_i(T) \tag{17}$$

where: p_i is transition probability and N_i is the population of i state[27]. This equation highlights that only the second factor is temperature-dependent. More specifically, Collins et al.[28] described the proportionality of emission intensity from the following parameters:

$$I_{i0} \propto \hbar \omega_{i0} A_{i0} N_i \tag{18}$$

where: ω_{i0} and A_{i0} are the angular frequency of the $i \rightarrow 0$ transition and the total spontaneous emission rate, respectively. The first formula taking up the correlation between the level population (according to Eq. 17 indirectly the emission intensity) and temperature, requires the consideration of two excited states from which emission can occur. If the energy difference ΔE_{21} between them is small (roughly from 200 to 2000 cm^{-1}), they can be treated as "thermally coupled" according to Boltzmann law (Figure 3a). Then their thermodynamic equilibrium is expressed with the formula[6,20,21]:

$$N_2 = N_2 \cdot \left(\frac{g_2}{g_1} \right) \cdot \exp\left(\frac{-\Delta E_{21}}{kT} \right), \tag{19}$$

where: g_2 and g_1 are the degeneracies of 2 and 1 states when k is Boltzmann constant. This means that if the thermodynamic equilibrium in the two level system is not changed in the time interval then the number of absorption transitions is equal to the emission transitions. This is a particularly useful equation for thermally coupled levels, which will be described in more detail in section 6.5.1.
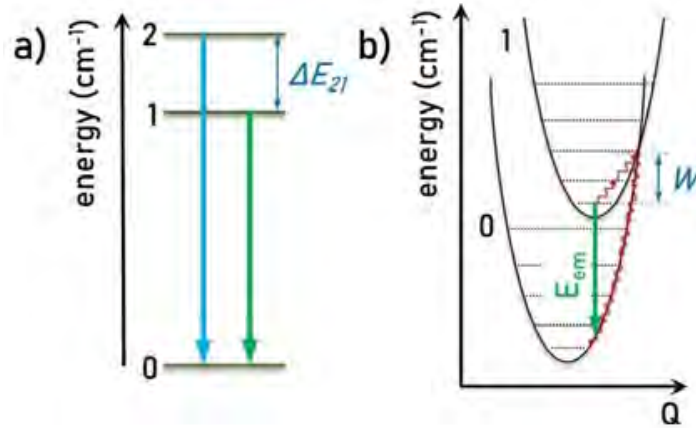
Figure 3. Visualization of thermally coupled excited states – a); schematic presentation of radiative and nonradiative depopulation of the excited state on the configurational coordinate diagram of two levels – b).

On the other hand, for an optical center with a noticeable shift in wavevector domain Q (such as the transition metal ions), it is possible to describe the temperature dependence of the emission intensity by using the configurational coordinate diagram consisting of two parabolas (Figure 3b). Based on this, Nevill Mott and Frederick Seitz[29,30] proposed that the relaxation of the excited electron to the ground state can occur through two competing transitions. These include (1) the previously mentioned direct radiative transition resulting in emission (see Figure 1c) and (2) an indirect nonradiative transition, which must be thermally assisted[31]. Therefore, the Mott-Seitz model assumes that the total transition probability is the sum of the probability of radiative (A_R) and nonradiative (A_{NR}) transitions. Using Eq. 6, this sum can be written as the inverse of the τ lifetime as follows[32]:

$$\frac{1}{\tau} = \frac{1}{\tau_R} + \frac{1}{\tau_{NR}} \ , \tag{20}$$

where: τ_R and τ_{NR} are the radiative and nonradiative lifetimes, respectively. It is assumed that τ_R is independent of temperature and therefore equal to $\tau_R(0)$ and thus τ_0 (the lifetime τ at T=0K), while τ_{NR} is described by the Arrhenius dependence:

$$\tau_{NR} = \tau_{NR}(0) \cdot \exp\left(\frac{-W}{kT}\right) \tag{21}$$

where: $\tau_{NR}(0)$ is nonradiative lifetime at T=0K and W is the activation energy of the thermal quenching process (here the original symbol from the Mott-Seitz model was used instead of ΔE in order to distinguish this parameter from the energy difference between the two thermally

coupled states). By combining the equations of Eq. 18 and Eq. 19 the Mott-Seitz equation is obtained[6]:

$$\tau = \frac{\tau_0}{1 + \dfrac{A_{NR}}{A_R} \cdot \exp\left(\dfrac{-W}{kT}\right)} = \frac{\tau_0}{1 + \alpha \cdot \exp\left(\dfrac{-W}{kT}\right)} \tag{22}$$

where: $\alpha = \dfrac{A_{NR}}{A_R}$ is usually used as the dimensionless parameter. Importantly, since the correlation between the emission intensity and lifetime presents as follows[32,33]:

$$\frac{1}{\Gamma_0} = \frac{\tau}{\tau_0} \tag{23}$$

where: Γ_0 is the emission intensity at T=0K, it is also possible to determine Eq. 22 in the intensity regime as follows:

$$I = \frac{\Gamma_0}{1 + \alpha \cdot \exp\left(\dfrac{-W}{kT}\right)} . \tag{24}$$

Finally, if there is more than one thermal quenching process, the above equations can be extended to the form[6]:

$$\tau = \frac{\tau_0}{1 + \sum_i \left(\alpha_i \cdot \exp\left(\dfrac{-W_i}{kT}\right) \right)} \tag{25}$$

and

$$I = \frac{\Gamma_0}{1 + \sum_i \left(\alpha_i \cdot \exp\left(\dfrac{-W_i}{kT}\right) \right)} . \tag{26}$$

Therefore, the Mott-Seitz model is also true when describing energy transfers between two optical centers. It is a particularly useful tool when analyzing thermally dependent mechanisms, which are fundamental to the design and development of luminescent thermometers, as will be discussed in more detail in section 6.5.1.

6.2. Importance of Cr^{3+} and Mn^{4+} ions

As already mentioned, the inorganic phosphors doped with TM ions with the electronic configuration of d^n ($1 \leq n \leq 9$) are one of a group of materials that are of broad interest in the scientific research community. This is due to their high photo- and thermochemical

stability suitable for many different applications[34]. In general, TM ions provide high absorption cross-section in a wide spectral range and intense emission. Additionally, the spectral location of their excitation and emission bands is dependent on the host material in which they are incorporated. This stands in contrast to the other popular luminescent centers group of Ln^{3+} ions, whose excitation and emission bands are barely susceptible to host material, and which the absorption capacity is weaker than TM ions[35,36]. Among the TM ions, the best known are those with $3d^3$ electronic configuration including V^{2+}, Cr^{3+}, Mn^{4+}, and Fe^{5+} ions[22]. They generally offer red or near infrared (NIR) emission (~600-1000 nm), which can be effectually excited over a wide spectral range from ultraviolet (UV) through blue to even reddish (from below 250 nm to even ~650 nm), providing a wide range of application possibilities[22,37,38]. This is due to the unique combination of the spin-doublet and spin-quartet states of their electronic shell, which allows to obtain both sharp and broadband emission depending on the host material composition[39]. It should also be noted that for this reason theoretical models (like crystal field and ligand field theory, which will be mentioned below) were developed based on materials with $3d^3$ ions[2,8,40].

When considering the four representatives of $3d^3$ ions, it is noticeable in the literature that the dominant contribution is from works devoted to Cr^{3+} and Mn^{4+}, over V^{2+} and Fe^{5+} ions[41–43]. This is due to several characteristic features of these ions. Firstly, Cr^{3+} and Mn^{4+} ions are the most stable representatives in terms of their electronic charge among the available options, i.e. $Cr^{2+/3+/4+/5+/6+}$ and $Mn^{2+/3+/4+/5+/6+}$. In contrast, for vanadium and iron ions, the emission of V^{3+}, V^{4+}, V^{5+} and Fe^{3+} ions were usually observed. Moreover, in the case of vanadium ions, often the ions at two or more oxidation states occurred in a single material[44–50]. Indeed, V^{2+} emission has been already reported in a few materials to date, including one oxide (MgO), but Fe^{5+} emission has not been reported to date[51–55]. Such a trend may adversely affect the reproducibility of syntheses of phosphors doped with V^{2+} and Fe^{5+} ions, as well as their scaling up for industrial production. Moreover, from a practical point of view, it has been noted that the energy levels of Cr^{3+} and Mn^{4+} located in the crystal field are optimal in terms of excitation and expected emission[56]. This is well illustrated by Brik and Srivastava on the energy diagram for free $3d^3$ ions, where the V^{2+} levels are located in the lower energy range in respect to Cr^{3+} and Mn^{4+} ions (suggesting the emission in the NIR spectra range), and the Fe^{5+} levels in the higher range (with emission located preferentially in the UV range)[41]. The above arguments encourage the scientific community to focus their attention on Cr^{3+} and Mn^{4+} ions as representatives of TM ions with $3d^3$ electronic configuration, in order to both have a good understanding of the processes that affect their luminescence, but also to select suitable materials for potential applications. For this reason, a number of review papers have been presented on both of these topics for both Cr^{3+} and Mn^{4+} ions[11,25,41–43,56,57].

Although Cr^{3+} and Mn^{4+} belong to the same group of $3d^3$ ions, their luminescence characteristics differ. Mn^{4+} ions are characterized always by narrow emission associated with the $^2E \rightarrow {}^4A_2$ transition occurring in the red spectral range, whereas Cr^{3+} can emit in both the red and NIR ranges with narrow or broad band, corresponding to $^2E \rightarrow {}^4A_2$ and $^4T_2 \rightarrow {}^4A_2$ transitions, respectively. Due to these differences between spectroscopic properties, Cr^{3+} and Mn^{4+} cover a wide spectrum of applications. At first, both of these ions are historically known as luminescent centers in the solid-state lasers[19,58–60]. Furthermore, the possibility of using phosphors based on Cr^{3+} and Mn^{4+} luminescence for temperature sensing[61–64], but also as sensors controlling changes of pressure[65–68], gas[69–72], humidity[73–75], pH[76–79] or glucose[80–82], has been demonstrated in many works. Moreover, they can be used for anti-counterfeiting[83–85] or fingerprint detection[86–88]. In terms of persistent luminescence, extensive applications have been presented for in vivo imaging for tumor targeting therapy[89–91]. Among biological applications, increasing potential has been also presented for Cr^{3+} doped materials as nanoheaters for the photothermal therapy[92–94]. On the other hand, particularly popular concepts are presented for Cr^{3+} doped phosphors for the night vision with phosphor-converted LED (pc-LED) [95–97], while Mn^{4+} ions find application as part of the white light generating LED devices[98–100] or as red light for the efficient plant growth[101–104]. The potential has also been reported in the use of $YAlO_3$ and $Y_3Al_5O_{12}$ doped with Mn^{4+} for the optical data storage[105,106] and thermoluminescence dosimetry of γ-radiation[107]. The listed examples are among the most effectively developed approaches for the practical application of phosphors doped with $3d^3$ ions, but do not cover all the possibilities, which will certainly be further investigated and developed. Additionally, it should be emphasized that the study of the influence of the host material composition on the spectroscopic and thermometric properties of Mn^{4+} and Cr^{3+} ions may not only find practical application for luminescence thermometry, but also give information necessary for other applications, e.g. about temperature stability of the intensity of NIR-emitting LED coated with Cr^{3+} doped phosphor. Therefore, it is important to recognize that investigating the influence of host material on the thermal performance of the Cr^{3+} and Mn^{4+} luminescence is a topical issue and relevant to many scientific and industrial fields.

6.3. Fundamentals of 3d³ ions spectroscopy

6.3.1. Basic postulates of the crystal field theory and ligand field theory

A commonly used theory to relate the spectroscopic properties of TM ions and the structure in which they are located is the crystal field theory (CFT) proposed in 1925 by H. Bethe and J. van Vleck. It assumes that chemical bonds are the result of electrostatic attraction between a positively charged metal ion, known as the central ion, and the so-called ligands,

surrounding it[108,109]. The ligands can be negative ions (e.g. O^{2-}, F^-, OH^-), small molecules directed negatively towards the central ion (e.g. H_2O, NH_3) or larger molecules (e.g. ethylenediamine)[110]. In all cases, CFT treats the central ion and the ligands as point charges. It allows to determine the number of unpaired electrons and then construct energy level diagrams for a given configuration and a given symmetry (in the case of TM ions, these will be the Tanabe-Sugano (T-S) diagrams described in the next section). It enables a good assignment of the different bands in the electron spectrum to the corresponding electron transitions. Therefore, CFT determines the effect of the ligand field on the shape of the d orbitals. If the metal ion was isolated or in a spherical ligand field, its five d orbitals would correspond to the same energy, i.e. it would be five times degenerate[36,111]. These orbitals are d_{xy}, d_{yz}, d_{xz}, $d_{x^2-y^2}$ and d_{z^2}. However, among the ligand fields that occur in reality, octahedral and tetrahedral can be distinguished. The more common type of complex is the octahedral, in which in the highest symmetry (point group O_h) the central ion and ligand are located at the center and vertices of the regular octahedron, respectively. In this case, the contours of the d_{xy}, d_{yz}, d_{xz} orbitals are directed between the ligands in different planes, but their distance from the ligands is the same[42]. Therefore, their energy increase by the same amount, so they remain threefold degenerate (Figure 4). Therefore, their energy level is the triplet state and named t_{2g} [112,113]. On the other hand, the $d_{x^2-y^2}$ and d_{z^2} orbitals are oriented in direct contact with ligands, so ligands will interact with them to the same extent, but with stronger repulsion interactions than the previous three orbitals[114]. For this reason, these orbitals are doubly degenerate and their energy state is called the doublet state and denoted as e_g.
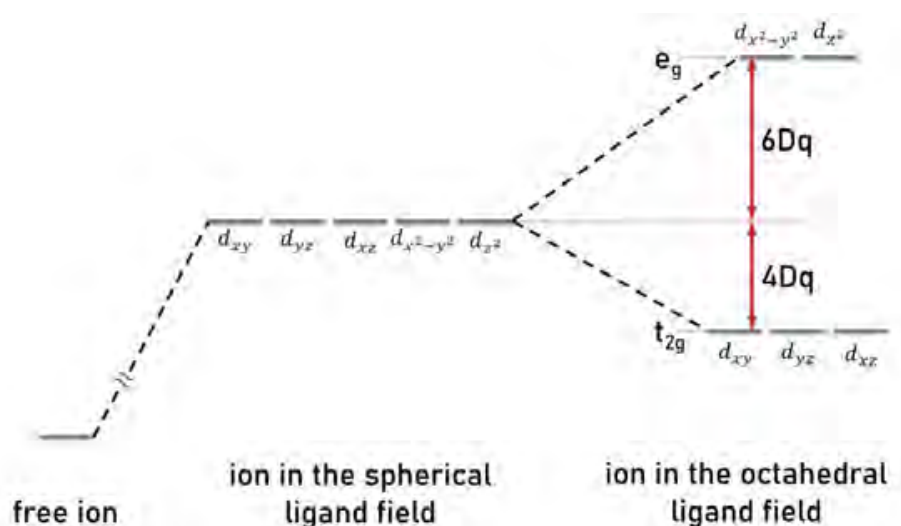
Figure 4. The splitting of 3d energy levels of ion in the spherical and octahedral ligand field.

Due to the simplified assumptions of CFT involving a point charge model of central ion and ligands, it is possible to determine the energy difference between e_g and t_{2g} levels,

which is referred as *10Dq*. A tenth of this value (*Dq*) is called as crystal field strength and is a combined parameter consisting of the properties of the central ion (*D*) and the ligands (*q*), which are included in formulae 27 and 28, respectively[18]:

$$D = \frac{35 \cdot Z \cdot e^2}{4 \cdot R^5} \,, \tag{27}$$

$$q = \frac{2}{105} \cdot \left\langle r^4 \right\rangle_{32} \,, \quad \left\langle r^k \right\rangle_{32} = \int \left| R_{32}(r) \right|^2 r^{k+2} dr \tag{28}$$

where: *Z* – anion valence, *e* – the elementary charge, *R* – the distance between the central ion and ligands, $R_{32}(r)$ – the radial part of five wavefunctions of the d orbitals, *r* – the electron coordinate, *k* – integer which takes only *k = 0, 2, 4* in the case of *d* electrons. Therefore, it can be found that *Dq* parameter is reduced to the following form[18,36,111]:

$$Dq = \frac{Z \cdot e^2 \cdot \left\langle r^4 \right\rangle_{32}}{6} \cdot \frac{1}{R^5} \,. \tag{29}$$

However, it should be noted that the power at *R* takes on a value of 5 due to the point charge model used and can range from 3.5 to 7.3 when a more realistic exchange charge model is employed[8,38,115]. Nevertheless, it can be seen from the above formula that the value of *Dq* decreases as the distance between the central ion and ligands increases.

The use of an exchange charge over point charge model is related to the characterization of the bonds in the complexes as ionic-covalent, which is one of the main assumptions of ligand field theory (LFT) (in comparison to the ionic bonds described in CFT). Therefore, CFT contains some simplifications that do not allow to precisely explain all experimental observations. LFT is one of the more complex theories, which combines CFT with the molecular orbital theory[116–118]. As mentioned, the main simplification of CFT, corrected by LFT, is the neglect of the covalent nature of the bonds, i.e. the sharing of electrons between the central ion and the ligand. Confirmation of the presence of such bonds is provided by the so-called nephelauxetic effect, which involves a weakening of the repulsion between the electrons of the metal ion located in a complex in respect to the free metal ion[110]. This is due to the substitution of the atomic orbitals hosting the electrons by larger molecular orbitals, formed by the superposition of the atomic orbitals of the metal (central ion) with those of the ligands. This allows the electrons in such an orbital to be further apart and therefore the repulsion between them is weaker. When considering the spectroscopic properties of TM ions, the nephelauxetic effect leads to a reduction in the difference between their levels and thus in the energy corresponding to excitation and emission transitions. However, since the *d-d* transitions in TM ions or the *f-f* transitions in Ln^{3+} ions take place within one orbital,

for them the nephelauxetic effect is less pronounced than in the case of the *f-d* transition, occurring for example, in Ce^{3+} or Eu^{2+} ions[36,42].

Nevertheless, it is possible to quantitatively calculate the effect of ligand electrons on the *d* electrons of a metal ion, which was calculated by Racah based on the theory of Slater, Condon and Shortley[119–121]. Racah's calculations assume that the electrons of the *d* ion repel each other to a lesser extent when the surrounding ligand electrons are present than if they exist as a part of free ion. On this basis, parameters *A, B* and *C* were proposed, called the Racah parameters. For further discussion, it is worth mentioning that *B* and *C* can be determined experimentally and represent the strength of Coulomb repulsion between electrons. Subsequently, Jörgensen developed Racah's theory and defined a parameter of the degree of bond covalency, so-called the nephelauxetic parameter, as[122–124]:

$$\beta = \frac{B}{B_0}$$

(30)

where: *B* and *B$_0$* (under the topic of dissertation, the values of $B_0 = 918$ cm^{-1} and 1160 cm^{-1} for Cr^{3+} and Mn^{4+} ions, respectively can be mentioned) are Racah parameter of ion in the crystal field and in a free state, respectively. By design, β was intended to quantitatively represent the expansion of the electron density cloud of the metal in the complex. It means the more covalent the bond, the smaller the value of β. However, Brik et al. noted that the Racah parameter *C* was ignored in the β parameter[56,125]. This may be related with the long-held belief that the *C/B* ratio is almost constant whether the ion is in the complex or in the free state. Over time, this has proven to be untrue for many materials. Therefore, Brik proposed a new nephelauxetic ratio parameter defined as follows[18,125,126]:

$$\beta_1 = \sqrt{\left(\frac{B}{B_0}\right)^2 + \left(\frac{C}{C_0}\right)^2}$$

(31)

where by analogy to the previous equation: *C* and *C$_0$* ($C_0 = 3850$ cm^{-1} and 4303 cm^{-1} for Cr^{3+} and Mn^{4+} ions, respectively) are Racah parameter of ion in the crystal field and in a free state. It is noted that the parameter defined in this way allows a linear correlation of β_1 and the energy of spin-forbidden transitions to be found[18,38,56].

Another element that cannot be explained by CFT is the so-called spectrochemical series[110,127]. Based on experimental data, it orders the influence of both ligands (for the same central ion) and central ions (for the same ligands) on the increasing *10Dq* value. Among the ligands, it is worth mentioning that the lowest *10Dq* value is to be expected for I$^-$ and Br$^-$, while it may be relevant from the point of view of phosphors that F$^-$ provides

lower energy splitting values than O^{2-} and OH^-. On the other hand, for one type of ligand the *10Dq* value for Cr^{3+} should be lower than for Mn^{4+}. This is related to the general principle that *10Dq* increases with increasing charge and an atomic number of d-block metals[110,127]. This will be confirmed later in the section 6.3.2.

In summary, the addition of covalency parameters to the CFT, such as the Racah and β and β_1 parameters, brings the theory significantly closer to the results obtained experimentally. However, many different models, including CFT and LFT, are still used depending on the specific problem.

6.3.2. Tanabe-Sugano diagram for 3d^3 ions

When an ion with a single *d* electron (i.e. d^1) is considered in the crystal field, the aforementioned energy dependence between its split levels and the *10Dq* parameter is true[18,22,128]. However, this is the simplest model and there are many ions with the higher number of *d* electrons. Examples include Mn^{4+} and Cr^{3+} ions with *3d^3* electronic configuration. Based on the parameters included in the CFT and LFT, i.e. *10Dq*, *B* and *C*, it is possible to include the Coulomb and crystal field interactions to describe the energy levels for ions with d^n configuration ($n \in <1,9>$)[18,110]. However, the combination of the above three parameters and *E* (as the energy of different states on which electrons can be located) in the form of a 2D diagram, to facilitate their interpretation, would not be possible. Therefore, in 1954, Yukito Tanabe and Satoru Sugano presented plots of *E/B* ratio with *Dq/B* ratio for a fixed *C/B* ratio, which are known as Tanabe-Sugano (T-S) diagrams[18,42,129]. As an example, a T-S diagram for *3d^3* electronic configuration in an octahedral crystal field (point group O_h) for *C/B*=4.5 is shown in Figure 5.
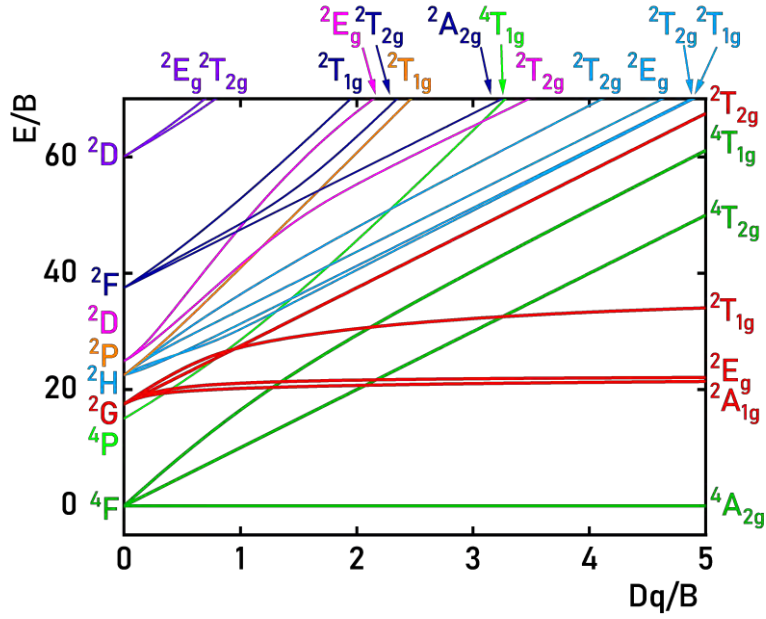
Figure 5. Tanabe-Sugano diagram for TM ions of $3d^3$ electronic configuration.

To correctly understand such a diagram, firstly the situation of three $3d$ electrons in a free state ions should be considered, which corresponds to Dq/B=0[2,3]. In this case, there are specific energy states of the electrons, which depend on the coupling of the spin moments and orbital moments of all the electrons in the ion and are called terms[18,110]. For $3d^3$ ions in free state, there are 8 terms, given in Table 1. The names of the terms are denoted by ^{2S+1}L, where S is the total spin quantum number when L is the total orbital angular momentum and are denoted in the form of letters: S, P, D, F, G etc. for L=0, 1, 2, 3, 4, respectively. In this case, according to Hund's rule, the ^{4}F term is the ground state[2,3]. The energy of the atomic terms was calculated and given in terms of Slater-Condon-Shortley integrals, which were then simplified to a combination of Racah parameters A, B, C[110,119,120]. Since the T-S diagrams are presented in relative form to the energy of the ground state, ^{4}F takes the 0 value, while the subsequent terms are defined only by the Racah parameters B and C (excluding A). This is a practical tool because the difference between the ^{4}P and ^{4}F levels depends only on B, which is experimentally determinable[18,119,129].

Table 1. Energies of terms of $3d^3$ ions defined by Racah parameters[18,22].

atomic terms	relative energies determined with Racah parameters
^4F	0
^4P	$15B$
^2P	$9B+3C$
$^2D_{1,2}$	$20B+3C\pm\sqrt{193B^2+8BC+4C^2}$
^2F	$24B+3C$
^2G	$4B+3C$
^2H	$9B+3C$

For $Dq/B>0$, metal ions located in a crystal field are considered[8,22,38]. As presented earlier for atomic orbitals, the atomic terms undergo analogous splitting in the crystal field and new terms are formed. With reference to the previously mentioned the total orbital angular momentum L, the degeneracy of the level is $2L+1$ which states as the maximal number of levels that may be split by the crystal field. In this case, energy levels in crystals are named as ^{2S+1}X, where X may be A/B, E or T, which means no degeneracy, two-fold and three-fold degeneracy, respectively[2,3,18,110]. Thus, ^4F is split into three energy levels, namely $^4A_2$, $^4T_2$ and $^4T_1$, while ^2G is split into four energy levels, namely ^2E, $^2T_1$, $^2T_2$ and $^2A_1$. For part of the ^2G term originating levels, it can be seen that ^2E, $^2T_1$ and $^2T_2$ are almost parallel to the ground state $^4A_2$ over a wide range of Dq/B. This is due to their origin from the same electron configuration of three electrons, namely t_{2g}^3. On the other hand, both $^4T_2(^4F)$ and $^4T_1(^4F)$ are characterized by a significant effect of Dq/B on their energy, which is related to their formation from $t_{2g}^2e_g$ orbitals, when the $^4T_1(^4P)$ state has an even greater increase with Dq/B value because it is formed from $t_{2g}e_g^2$ orbitals[8,22,130]. This is important from a spectroscopic point of view since transitions between levels originating from different orbitals will be spin-allowed transitions (e.g. $^4T_{2g}\rightarrow^4A_{2g}$), when originating from the same orbitals will be spin-forbidden transitions (e.g. $^2E_g\rightarrow^4A_{2g}$)[18,22,131].

An important aspect of T-S diagram for $3d^3$ electronic configuration is the influence of Dq/B value on the determination of the first excited state. It can be found the intersection of $^4T_2$ and ^2E energy levels occurs for $Dq/B\approx2.2$. This value should not be taken rigidly as a rule, since depending on the C/B ratio, the energy course of excited state levels may vary slightly[38,125]. Nevertheless, this T-S diagram is divided into three regions: the weak crystal field (CF) when $Dq/B<2.2$, the intermediate CF when $Dq/B\approx2.2$ and the strong CF with $Dq/B>2.2$[18,36,132,133]. This classification will be crucial in the shape of the emission spectrum, as described in the next section. Among $3d^3$ ions it is known that

the weak CF can be found for V^{2+} and sometimes Cr^{3+} whereas the strong CF may affect Fe^{5+}, Mn^{4+} and sometimes Cr^{3+}. Therefore, although Mn^{4+} and Cr^{3+} are isoelectronic, Mn^{4+} with a higher electronic charge has always strong CF with ^2E as first excited state when Cr^{3+} may be located in weak, intermediate or strong CF depending on the host material[36,43,134].

6.3.3. Mechanisms of electronic transitions in $3d^3$ ions

Although the T-S diagram presented in Figure 5 contains many energy levels, only a few are relevant for optical spectroscopy. The following electronic transitions may occur between these energy levels: (1) an electronic transition involving the excitation of an electron from the ground to the excited level by a photon delivered to the phosphor or (2) an electronic transition from the excited to the ground level, which involves the occurrence of luminescence from the phosphor. In (1), when absorption is considered, three spin-allowed transitions are possible: $^4A_2 \rightarrow {}^4T_2$, $^4A_2 \rightarrow {}^4T_1$ (^4F), and $^4A_2 \rightarrow {}^4T_1$ (^4P). These are reflected in the absorption or excitation spectra by broad bands with high absorption cross-section, often covering a wide range from the UV spectral range to even 700 nm. At this point, it can be mentioned that interionic charge transfer absorption resulting from charge transfer between O^{2-} and metal ions. Its position is dependent on the host material (it may be located energetically around the other excitation bands or in the UV spectral range) but the mechanism of absorbing the photon remains the same as for the energy levels of $3d^3$ ions. On the other hand, in the case of (2), emission follows nonradiative relaxation of electrons to the lowest excited state. As previously mentioned, the lowest excited state is determined by the CF strength. Figure 6 shows three possibilities for the configurational coordinate scheme of $3d^3$ ions, i.e. for the strong, intermediate and weak CF.
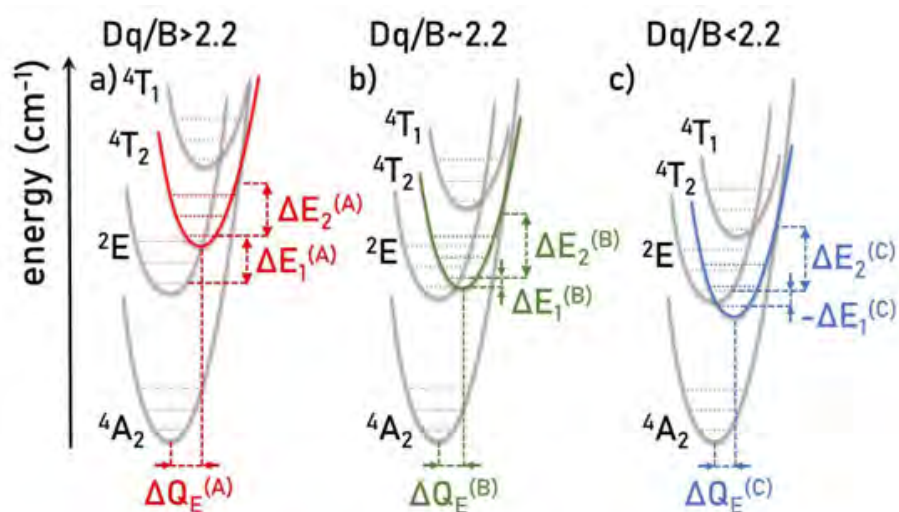
Figure 6. Configurational coordinate diagram of $3d^3$ ions located in the strong – a), intermediate – b) and weak crystal field – c).

In the case of strong CF (Figure 6a), the ^{2}E spin-doublet becomes the first excited state resulting in spin-forbidden ^{2}E→^{4}A$_2$ transition, which results in a narrow emission band. Due to the same degeneracy of ^{2}E and ^{4}A$_2$ energy states, the position of this emission band is barely dependent on the *Dq/B* value, but its maximum can occur in the range of 620-734 nm in the case of Mn^{4+} ions and ~680-780 nm for Cr^{3+} ions. The parity selection rule and the spin selection rule ensure that the lifetime of the ^{2}E excited state will take values of a few milliseconds. In the case of intermediate CF (*Dq/B~2.2*), the energy difference between ^{4}T$_2$ and ^{2}E states is relatively small as manifested by the simultaneous emission associated with ^{2}E→^{4}A$_2$ and T$_2$→^{4}A$_2$ transitions (Figure 6b). In this situation, the emission spectrum consists of a narrow band and a broad band, which usually partially overlap. In the third option, narrow emission is no longer observed since ^{4}T$_2$ is the first excited state (Figure 6c). In this case, a broadband emission related to the ^{4}T$_2$→^{4}A$_2$ transition occurs. It can be mentioned that the lifetime of ^{4}T$_2$ excited state is shorter than ^{2}E and is of the order of tens of microseconds. Moreover, the position of the ^{4}T$_2$→^{4}A$_2$ band is strongly dependent on the *Dq/B* parameter and can fall in the range of ~700-1100 nm. Among the presented scenarios, it should be emphasized that Mn^{4+} ions, due to their high positive charge, can only locate in sites with strong CF, while Cr^{3+} can locate in both strong and intermediate or weak CF[22,39,135].

However, to facilitate the above classification of the crystallographic sites offered by the host materials, the determination of *Dq/B* would be useful. As mentioned earlier, both *Dq* and the Racah parameters *B* can be calculated from experimental data using the semi-empirical formulae below[18,136]:

$$Dq = \frac{E\left(^4A_2 \rightarrow {}^4T_2\right)}{10} \, , \tag{32}$$

$$x = \frac{E\left(^4A_2 \rightarrow {}^4T_1\right) - E\left(^4A_2 \rightarrow {}^4T_2\right)}{Dq} \, , \tag{33}$$

$$\frac{B}{Dq} = \frac{x^2 - 10x}{15(x-8)} \, , \tag{34}$$

where: $E\left(^4A_2 \rightarrow {}^4T_1\right)$ and $E\left(^4A_2 \rightarrow {}^4T_2\right)$ corresponds with the energy of the barycentre of the ^{4}A$_2$→^{4}T$_1$ and ^{4}A$_2$→^{4}T$_2$ excitation bands. In addition, with the knowledge of the position of the zero-phonon line (ZPL) of the emission band associated with the ^{2}E→^{4}A$_2$ transition, the Racah C parameter can be calculated, which is necessary to calculate the nephelauxetic parameter β_1. The formula taking into account the C parameter is as follows:

$$\frac{E\left(^2E \rightarrow\ ^4A_2\right)}{B} = 3.05\frac{C}{B} + 7.90 - 1.80\frac{B}{Dq} \tag{35}$$

where: $E\left(^2E \rightarrow\ ^4A_2\right)$ is the energy of ZPL of $^2E \rightarrow ^4A_2$ emission band.

6.4. Correlation between the composition of the host material and spectroscopic properties of 3d^3 ions

The research results that have been published so far allow to select the ions which are most frequently substituted by Mn^{4+} and Cr^{3+}. As is well known, the preferential crystallographic site for $3d^3$ ions is the 6-fold coordinated octahedral site. Among the ions that can be found with this coordination are: B^{3+}, Al^{3+}, Ga^{3+}, In^{3+}, Si^{4+}, Ge^{4+}, Sn^{4+}, Mg^{2+}, Sc^{3+}, Ti^{3+}, Ti^{4+}, Zr^{4+} and Hf^{4+}. As shown in Figures 5 and 6, the main factor determining the spectroscopic properties of $3d^3$ ions is the crystal field. A comparison of the effective ionic radii (*EIR*)[137] allows one to predict that Al^{3+} with *EIR*=53.5 pm in the host material will generally determine stronger CF than Ga^{3+} with *EIR*=62 pm, since host material with Al^{3+} should more effectively compress the dopant of $3d^3$ ions. Furthermore, the system and space group in which the host material crystallizes plays a crucial role. Therefore, the comparison of *EIR* values should be considered as a practical tool at the initial stage of material design and used mainly when considering host material with the same symmetry. Then, the distance between the metal ion located in the octahedral site and the surrounding ligands (denoted *R(M-L)* or simply *R*) is considered as a more universal structural parameter that can lead to the determination of a correlation with luminescence properties. Firstly, according to the work of Grinberg et al.[57], if the a_{1g} one-dimensional symmetrical mode is assumed as the only considered local vibration mode in $3d^3$ ions, then the configurational coordinate $Q_{a_{1g}}$ will be equal to the average distance between the metal ion and ligands:

$$Q_{a_{1g}} = \frac{1}{6}\left(\sum_{i=1}^6 R_i\right) = R \ . \tag{36}$$

This is due to the large impact of crystal field Dq, which is a source of the electron-lattice coupling to the a_{1g} mode, according to Eq. 29. This assumption makes it possible to determine approximately ΔQ_e and subsequently the Huang-Rhys parameter S according to Eq. 8. So far, Brik et al. have presented that there is no direct correlation of R with energy of $^2E \rightarrow ^4A_2$ transition and with B parameter in some Mn^{4+}-doped host materials[138]. However, the relation $Dq \propto R^{-5}$ from Eq. 29 presents great potential for determining the relationship of a structural parameter with many optical parameters. The average distance R is a parameter available for all structures recorded in the crystallographic databases. On the other hand, the parameter Dq allows a theoretical determination of the position of the $^4T_2$ energy state.

Nevertheless, no dataset with a good fit of this relationship has been presented so far. This is probably due to the relatively small number of host materials doped with Mn^{4+} or Cr^{3+} ions for which low-temperature excitation and emission spectra have been measured (temperatures of ~10K or lower are preferred, but ~80K could also be considered). The low-temperature measurement reduces the influence of nonradiative processes that may interfere with the correct interpretation of the energies that correspond to vibronic modes and ZPL of excitation and emission bands.

6.5. Luminescence thermometry

The purpose of luminescence thermometry is to measure temperature. Temperature, according to the Oxford dictionary - a measure of the heat content of an object or substance[139], is one of the most important thermodynamic parameters that affects our daily lives at every turn. There are a number of devices and methods that make it possible to measure temperature. However, luminescence thermometry techniques allow the temperature to be determined using optical methods in a remote manner. Of the known methods, the thermographic infrared (IR) camera offers similar possibilities. However, its application is limited to the surface of the first object. Moreover, a correct temperature readout with an IR camera requires knowledge of the target's emissivity, which is usually difficult to verify, especially in the case of biological tissues. On the other hand, to obtain the spatial resolution which is available for digital cameras, much more expensive IR cameras should be considered. Luminescent thermometry overcomes these limitations, making it potentially applicable for in vivo temperature imaging and may be combined with the photothermal therapy in biomedicine[140–142]. Furthermore, it transcends IR camera applications and can serve as temperature measurement for fluid or gas flows by using thermographic tracer particles in the automotive and aerospace industry[143–145]. Therefore, it is a technique around which the scientific interest is growing and many novel strategies and approaches are developed. The main categories within which different luminescent thermometers are distinguished are (1) the material from which it is made and its application; (2) the temperature-dependent parameter that determines their mode of operation and (3) the temperature range in which the phosphor material finds its practical use. In the case of materials, all luminescent materials listed in the Introduction of section 6.1 show an influence of temperature on their optical properties and therefore are the subject of research. The numerous temperature-dependent parameters that have been proposed so far in the literature can be divided into two main groups: steady-state methods, which include: emission intensity, band position, bandwidth, spectral shape with representative luminescence intensity ratio (LIR), dual-excited single emission band and polarization and time-resolved methods: emission decay time, emission rise time,

time-resolved single emission and polarization lifetime[146]. LIR and lifetime approaches as the most promising temperature-dependent parameters will be discussed in detail in subsection 6.5.2. Among the temperature ranges which find great interest in luminescent thermometry, the physiological range (298-318 K) can be mentioned first and foremost, due to its potential for medical applications. However, in addition to this, the temperature ranges relevant to industry and fundamental studies should also be mentioned: the cryogenic range and temperatures above physiological temperatures (high-temperature engineering, metallurgy, aerospace engineering). The aforementioned possibilities outline a number of variables that can be considered in the design of materials for luminescence thermometry, which states why increasing commitment is put into the development of this technique.

6.5.1. Thermally dependent mechanisms for luminescent thermometers

As shown above in Eqs. 13, 17, 19, 21-22, 24-26 luminescent processes are susceptible on temperature. So far, it was mentioned that thermally dependent mechanisms occur within a ion (intraionic) or require interactions between a pair of ions (interionic) but also can result from structural changes in the host material. The popularly occurring term $\exp(\frac{\Delta E}{kT})$ in these formulae generally indicates an effect of thermal quenching on the emission and lifetime of excited state of luminescent centers. Such mechanisms comprise thermal quenching. However, it has also been reported that there are several processes that, with increasing temperature, have a positive effect on luminescence[5,146,147]. Moreover, there is also the possibility that there are two competing processes that negate each other or that all temperature-dependent processes are not activated in a certain range of low temperatures, in which case the terms of 'zero thermal quenching' is sometimes used. The most relevant of both types of processes are presented below.

The very first process that have been already mentioned is the energy transfer between thermally coupled states of one ion. The probability of its occurrence depends on the energy difference between two states, according to the Boltzmann distribution (Eq. 19). It is typically observed in Ln^{3+} ions such as: Er^{3+}, Nd^{3+}, Pr^{3+}, Dy^{3+}[148]. On the other hand, energy transfer between the two excited states of the dopant ion is also one of the processes consisting of thermal quenching in TM ions. According to the configurational coordinate diagram for $3d^3$ ion located in strong CF (Figure 6a), two processes can be considered as participating in the thermal quenching of $^2E \rightarrow \,^4A_2$ luminescence. This is (1) the energy transfer between the ^2E and $^4T_2$ levels, for which the energy difference, i.e. the activation energy ΔE_1,

is determined in terms of a Boltzmann distribution. On the other hand, this process is followed by (2) energy transfer from $^4T_2$ to $^4A_2$, which leads to nonradiative depopulation of excited states and therefore thermal quenching of luminescence. In this case, the activation energy ΔE_2 is determined according to the Mott-Seitz equation (Eq. 22), where $\Delta E_2 = W$. In this case, if $\Delta E_1 > \Delta E_2$ these processes will be activated in the order as listed[5,6]. Then it should resulted in a lower thermal quenching rate after exceeding ΔE_1 and a much steeper rate above ΔE_2. However, if $\Delta E_1 < \Delta E_2$, then both processes should be activated at once, when the phonon energy equals ΔE_2 is reached. Due to the greater variability of the position of the $^4T_2$ parabola as a function of Dq/B in respect to ^2E, the $\Delta E_1 < \Delta E_2$ relationship is expected to be more likely for values of Dq/B values closer to ~2.2. In the case of the intermediate CF (Figure 6b), the energy transfer between ^2E and $^4T_2$ mainly determine the thermal quenching of $^2E\rightarrow^4A_2$ transition, since the additional pumping of the $^4T_2$ level can be followed independently of temperature by the radiative $^4T_2\rightarrow^4A_2$ transition. Therefore, the emission from the ^2E level should quench thermally faster than $^4T_2$, while the thermalization corresponding to ΔE_2 will directly affect the quenching of the broadband emission corresponding to the $^4T_2\rightarrow^4A_2$ transition[130,149]. In the third option, when weak CF is considered (Figure 6c), energy transfer corresponding with ΔE_2 is the only possible intraionic energy transfer process of $3d^3$ ions. In addition, depending on the host material, one should keep in mind the different energetical position of the ligand$\rightarrow$TM charge transfer (CT) state, which can affect the thermal quenching of TM emission by crossing the CT state with TM ground state. Actually, a correlation between the quenching temperature and the energy of the $F^-\rightarrow Mn^{4+}$ CT state was found by Dorenbos[150], while several other works have confirmed the influence of the CT state on thermal quenching in Mn^{4+}-doped oxides[2,43,151,152].

Additional temperature-dependent processes may take place when two different luminescent centers in the host material are considered. Therefore, if there is a relatively small energy mismatch between the energy levels of two dopants, the phonon-assisted energy transfer occurs between them as the temperature increases[153,154]. In such a system, the ion from which the energy is transferred is called the sensitizer (or donor) and the ion receiving the energy is the activator (acceptor). This process associated with host vibrations has been described theoretically by the Miyakawa-Dexter model[154,155]:

$$W_{PAT}(\varepsilon_0) = W_{PAT}(0)e^{-\beta\varepsilon_0} \tag{37}$$

where: $W_{PAT}(0)$ - transfer probability excluding the energy mismatch ε_0 between the excited states of ions and β - electron–phonon coupling parameter. Energy transfers can play the role of an additional depopulation or pumping channel. In the former case, the higher-energy excited state of the activator provides an additional depopulation channel of the excited state of the sensitizer, which is activated when the temperature necessary to provide phonon energy equal to the energy mismatch ε_0 is reached. Therefore, it is expected from both the lifetime of excited state and emission intensity to have a faster thermal quenching rate in respect to the system without activator, thus improving their thermometric performance[156,157]. On the other hand, energy transfer can have a positive effect on activator luminescence. This effect is called sensitization a representative example of which may be the TM→Ln³⁺ system as sensitizer→activator[147]. TM ions are used to improve the brightness of Ln³⁺ emission due to the higher absorption cross section of TM ions, which contributes to more efficient absorption of the excitation radiation. Furthermore, the phonon-assisted TM→Ln³⁺ energy transfer is susceptible to temperature changes, which also leads to the improvement of thermometric properties of Ln³⁺-based luminescent thermometers. Nevertheless, in both cases it is important to bear in mind the possibility of a parasitic process, the so-called back energy transfer. This can have a negative or positive impact on the experimental results. Defining whether the observed luminescence changes as a function of temperature are associated with the energy transfer or back energy transfer is possible with analysis of the lifetimes of excited states of sensitizer and activator.

Additionally, it can be mentioned that thermally dependent mechanisms that are not related to luminescent processes, but have a direct impact on them. A representative example of such a mechanism is the structural phase transition. The luminescence properties of dopants are susceptible to the host material including chemical composition and crystal symmetry. Therefore, if an increase in temperature leads to a phase change, this can lead to a symmetry breaking that affects the spectroscopic properties of the dopant. This effect has so far been applied to Ln³⁺ ions, whose crystal field splitting determines the number of Stark sublevels, as well as the probabilities of radiative transitions, which clearly affects the shape of the luminescence spectrum. Among the phase transitions, one should mention first order phase transitions, which are characterized by the reversibility of the process, and second order phase transitions, which are not reversible. The first group can find applications as high-sensitivity luminescent thermometers, while in the second case thermal history markers are sought[147,158–160].

As mentioned at the beginning of this chapter, thermally dependent mechanisms are not always synonymous with thermal quenching since temperature can also activate or enhance

processes that positively influence spectroscopic properties. One such example is the thermally induced mixing of the wavefunctions of excited states reported i.e. for Mn^{4+} and Cr^{3+} ions[57,161,162]. It results from a relaxation of the selection rules, usually occurring in the low temperature range (below 200K). The other mechanism is described as excited state absorption (ESA)[147]. ESA involves the selection of an excitation wavelength that is not energetically matched to the effective excitation of electrons located on the ground state. Instead, excitation is matched to effective absorption from the higher state which is thermally coupled with the ground state. Therefore, to occur the ESA process, thermalization of the higher state is necessary. As a result, in contrast to the conventional absorption, the emission signal increases at higher temperature, while in low temperature the signal is at noise level. This approach was presented for e.g.: Eu^{3+}, Tb^{3+}, Nd^{3+}, Pr^{3+}[163–166]. At the end, another mechanism related to the change in structure that affects the spectroscopic properties of phosphors can be mentioned. In most materials the interionic distance increases at elevated temperatures, which is so-called as positive thermal expansion (PTE). However, there is a group of materials for which the opposite effect of negative thermal expansion (NTE) is observed[147,167]. This means that host lattice shrinkage occurs with the increase of temperature. In such a case, by using two dopants, i.e. a sensitizer and an activator, it is possible to reduce the distance between them as the temperature increases. As a result, the efficiency of energy transfer between them improves and the intensity signal is improved. Among the ion pairs for which this mechanism has been confirmed are Yb^{3+}-Er^{3+}, Yb^{3+}-Tm^{3+} and Yb^{3+}-Ho^{3+}[168–170].

To sum up, there are many optical and structural processes that are susceptible to temperature and can be used for thermometry. It is particularly important to consider all of the above-mentioned possibilities in the characterization of materials in order to correctly attribute the mechanisms that are responsible for changes in luminescence with temperature. It is worth noting that measurements in the function of temperature can also be a powerful tool in understanding the nature of a given process, since they convey additional information not manifested when measured at a given temperature. Finally, the intentional employment of several combined processes in a function of temperature can lead to improvements in the thermometric properties of a material, with the aim of creating a more accurate luminescence thermometer.

6.5.2. Thermometric parameters in luminescent thermometry

Temperature dependent parameters

There are actually many spectroscopic parameters that are temperature-dependent as mentioned in the Introduction of this section. However, few of these can find real application in temperature determination as a thermometer. It is affected by a requirement that a thermometer does not demand recalibration after a change in excitation and detection setup. Therefore, for example, the simplest approach of detecting the intensity of a single emission band with temperature changes is not a recommended route to designing luminescent thermometers. So far, strategies that found the greatest potential are the ones based on the luminescence intensity ratio (LIR) and lifetime of the excited state (τ). In the first case, a simple formula for the LIR parameter should be given:

$$LIR = \frac{I_2}{I_1} \ .$$
(38)

where: I_1 and I_2 are integral intensities of two spectral ranges (usually emission bands). Using the ratio takes the advantage of its independence from the emission signal, which limits the use of the single emission intensity. It was found that such a ratio can be determined theoretically when the emission originating from two thermally coupled excited states is considered. One can use the representation of the band intensity according to the Boltzmann distribution (Eq. 19) to determine a parameter as follows:

$$LIR = \frac{I_2}{I_1} = \frac{\hbar\omega_{20}A_{20}g_2}{\hbar\omega_{10}A_{10}g_1} = \frac{\hbar\omega_{20}A_{20}}{\hbar\omega_{10}A_{10}} \cdot \exp\left(\frac{-\Delta E_{21}}{kT}\right) ,$$
(39)

which can be simplified to:

$$LIR = B \cdot \exp\left(\frac{-\Delta E_{21}}{kT}\right) ,$$
(40)

where:

$$B = \frac{\hbar\omega_{20}A_{20}N_2}{\hbar\omega_{10}A_{10}N_1} \ .$$
(41)

Therefore, by transforming the equation Eq. 40, the temperature T can be determined[6]:

$$T = \frac{-\Delta E_{21}}{k} \frac{1}{\ln\left(\dfrac{B}{LIR}\right)} \ .$$
(42)

The parameters used in Eq. 39-42 refers to: ω_{20} and ω_{10} – the angular frequency of the $2 \to 0$ and $1 \to 0$ transitions, respectively, A_{20} and A_{10} – the total spontaneous emission rates, g_2 and g_1 – the degeneracies of 2 and 1 states, k – Boltzmann constant and ΔE_{21} – activation energy. Such a temperature determination applies to primary luminescent thermometers, for which recurrent interest is observed currently[148]. However, it should be borne in mind that the requirement to consider two energy states, from which the radiative electronic transitions come, as thermally coupled is an energy difference ΔE_{21} between them ranging from 200 to 2000 cm^{-1}. The advantage of thermometers based on the emission originating from such states is that they do not need to be calibrated experimentally, but due to the limitation of ΔE_{21}, their thermal resolution will be limited to some maximum. However, it should be noted that another approach is to determine the LIR value for two emission bands that are not thermally coupled with simply Eq. 38. This approach is used for phosphors doped and co-doped with TM ions. In this case, the thermal performance of emission intensity of two bands should be describable by Eq. 24 or Eq. 26, depending on the number of processes affecting the luminescence. Therefore, Eq. 26 for the LIR can be extended as follows:

$$LIR = \frac{I_2}{I_1} = \frac{\Gamma_{02}}{\Gamma_{01}} \cdot \frac{1 + \sum_i \left(\alpha_{i1} \cdot \exp\left(\frac{-W_{i1}}{kT} \right) \right)}{1 + \sum_i \left(\alpha_{i2} \cdot \exp\left(\frac{-W_{i2}}{kT} \right) \right)} = LIR_0 \cdot \frac{1 + \sum_i \left(\alpha_{i1} \cdot \exp\left(\frac{-W_{i1}}{kT} \right) \right)}{1 + \sum_i \left(\alpha_{i2} \cdot \exp\left(\frac{-W_{i2}}{kT} \right) \right)} \ .$$

(43)

On the other hand, among the time-resolved methods, the most common is the measurement of emission decay time. According to the theory given in section 6.1.4., the lifetime τ consists of the components derived from the radiative τ_R and nonradiative transition τ_{NR}. They are combined in the form of Eq. 22. However, to facilitate the interpretation of experimental data of luminescent decay profiles of emission from the excited state, it is necessary to calculate lifetime values. The single exponential equation takes the following form:

$$I(t) = I_0 \cdot \exp\left(-\frac{t}{\tau} \right) ,$$

(44)

where: I_0 is the initial intensity at time t = 0. However, due to the frequent occurrence of two or more intra- and interionic processes in phosphors, the single exponential equation may not reflect well the resulting luminescence decay curve. For this reason, other models

have been proposed that take into account the impact of multi-exponential decays. One example is the stretched exponential function, also known as the Kohlrausch–Williams–Watts function[171–174]:

$$I(t) = I_0 \cdot \exp\left(-\left(\frac{t}{\tau}\right)^{\beta}\right) , \tag{45}$$

where: τ - the characteristic time constant, and β - the heterogeneity parameter ($0 < \beta < 1$). However, since materials with up to two optical centres are most often analysed, the use of a bi-exponential function is a popular solution:

$$I(t) = I_0 + A_1 \cdot \exp\left(-\frac{t}{\tau_1}\right) + A_2 \cdot \exp\left(-\frac{t}{\tau_2}\right) , \tag{46}$$

where: τ_1, τ_2 are the decay parameters and A_1, A_2 are amplitudes. Using these parameters, the average lifetime is determined as:

$$\tau_{avr} = \frac{A_1\tau_1^2 + A_2\tau_2^2}{A_1\tau_1 + A_2\tau_2} . \tag{47}$$

Parameters evaluating thermometric performance of luminescence thermometer

The determination of the dependence of the parameters listed above on temperature is intended to verify their applicative potential in luminescence thermometry[6,146,175]. To check the temperature range over which a given parameter varies most, absolute thermal sensitivity is used:

$$S_A = \frac{d\Omega}{dT} , \tag{48}$$

where: Ω - a temperature-dependent parameter. However, it should be noted that the unit of such a parameter depends on Ω, making it impossible to compare S_A values for thermometers of different nature. The parameter that allows this is the widely used relative thermal sensitivity:

$$S_R = \frac{1}{\Omega} \cdot \frac{d\Omega}{dT} \cdot 100\% . \tag{49}$$

A popular practice in articles is to present the highest S_R value (denoted e.g. as $S_{R\max}$) and the temperature at which it was obtained ($T(S_{R\max})$). However, it is assumed that temperature readout is reliable when $S_R > 1\% K^{-1}$ [176]. This is one of the criteria that define the temperature range within which the thermometer can be used, the so-called temperature

operating range[176,177]. The second parameter is the temperature determination uncertainty (or temperature resolution), defined as follows:

$$\delta T = \frac{1}{S_R} \cdot \frac{d\Omega}{\Omega} \quad .$$

(50)

Satisfactory thermal uncertainty was considered to be $\delta T < 0.1K$ [176]. However, it should be mentioned that δT is a parameter dependent on measurement conditions and experimental setup and thus should not be considered as a feature of the luminescence thermometer as shown by van Swieten et al.[178]. Nevertheless, δT is a useful qualitative tool since its minimum value corresponds to the highest S_R value and a strong luminescence signal[148]. Therefore, it allows the estimation of the temperature range in which the thermometric properties of the phosphor will be most promising.

Other parameters assessing the applicability of the thermometer

The above-mentioned formulae are considered to be a part of standard analysis in fundamental studies for luminescence thermometry, as a consequence of the continuous development of a field. However, there are also other parameters used for comparing thermometric materials that are dedicated to verify their performance in the form of a proof-of-concept experiment, approaching a specified application. For example, accuracy describes how close the measurement result is to the actual temperature value. It is usually defined as mean signed or unsigned (absolute) deviation[148]. This parameter is mainly determined for fluorescent polymers, quantum dots and nanodiamonds, since their size is included in the calculations[6].

In order to make the improvement from temperature sensing to temperature imaging (or temperature mapping), temperature measurement takes place with a change in a spatial position (at least one variable direction). This is an important step toward the applicability of the thermometer for dynamic temperature measurements. The spatial resolution is defined as the minimum distance between points, which present a change of temperature larger than δT with the formula of [6,146]:

$$\delta x = \frac{\delta T}{|\nabla_x T|}$$

(51)

where: $\nabla_x T$ is the maximum temperature gradient. Furthermore, the dynamic character of temperature measurements should take into account the change as a function of time. The temporal resolution is a similar parameter to δx referring to the minimal time interval instead of minimum distance. It is defined as:

$$\delta t = \frac{\delta T}{|\partial T / \partial t|} \qquad (52)$$

where: $\partial T / \partial t$ is a maximum change of temperature per unit of time. By combining the two parameters in spatiotemporal resolution, it is important to emphasize that photoluminescent thermometry is a competitive method to currently known techniques for determining temperature in a noncontact way. As presented by Brites et al.[6,179] thermometric phosphors can show better ∂t than the examples from the scanning thermal microscopy and Raman spectroscopy, and better ∂x than thermoreflectance.

Repeatability and reproducibility are apparently similar parameters. However, repeatability refers to the ability of the phosphor to repeat the result under the same experimental conditions and is defined by the formula[5]:

$$R = 1 - \frac{\max\left(\Omega_c - \Omega(T)\right)}{\Omega_c} \qquad (53)$$

where: Ω_c and $\Omega(T)$ is the mean value of Ω and Ω measured at each temperature, respectively. Reproducibility, on the other hand, refers to obtaining the same calibration curve, but under different conditions (different measuring system, different location, different operator)[146].

6.5.3. The general correlation between the structural and thermometric parameters

The search for a correlation of the structural properties with thermometric properties of $3d^3$-doped phosphors is even more difficult than with spectroscopic ones (section 6.4.). Although determining the relationship between the S_R or δT of luminescent thermometers and the structural parameters would directly allow the design of a phosphor tailored to an on-demand application, this is not possible due to the multitude of processes that affect their values. However, a few general rules can be identified that can serve as a guide with material design. Firstly, a promising parameter is the activation energy - both that of the Boltzmann distribution (ΔE_{21} from Eq. 19) and the Mott-Seitz model (W from Eq. 22). From these, it is possible to estimate in which host material the greater splitting of energy levels occurs. When considering $3d^3$ ions, the activation energy denoted as W in the Mott-Seitz model responsible for the thermal quenching process is particularly relevant. When defining the difference between the $^4T_2$ and ^2E state, it should be related to CF in the form of the Dq/B parameter, which is already in general correlation with the metal-ligand distance R ($Dq \propto R^{-5}$). However, the correct determination of W could be difficult for many host materials that belong to different crystallographic systems, and also when $3d^3$ ions locate

in more than one crystallographic site. Another parameter determining thermometric properties that is often determined is the quenching temperature $T_{1/2}$, defined as the temperature at which τ or emission intensity reaches 50% of its initial value. So far, Senden et al.[43] have noted a promising correlation between $T_{1/2}$ and the $^4A_2 \rightarrow \,^4T_2$ band energy for Mn^{4+}. In this case, Mn^{4+} ions in different host materials provide results that are easier to interpret in respect to Cr^{3+} since it is always in a strong CF, i.e. the ^2E parabola is always located above $^4T_2$. The correlation can be justified within the activation energy W, i.e. if parabola ^2E is barely susceptible to a change in Dq/B, then mainly the position of parabola $^4T_2$ should determine the thermal quenching rate. In such a case, however, it must be assumed that the differences between the phonon energies for different matrices are negligible, which is not true in general. In addition, to obtain such a relationship it was necessary to take into account the energetic position of CT, which in some host materials (more precisely $F^- \rightarrow Mn^{4+}$ CT in fluorides) determined lower values of the $T_{1/2}$ parameter than expected. This is indeed a promising result, which encourages the search for further correlations. Unfortunately, in the abovementioned work a correlation between $T_{1/2}$ and metal-ligand distance R was not obtained. Particularly problematic may be the determination of the desired correlation for oxides, which, despite the great interest of the scientific community, are characterized by a smaller change in R value with a large scatter in $T_{1/2}$ value, which may result in an increased risk of misinterpretation. Finally, as in section 6.4, it should be mentioned that the creation of a reliable database is hampered by the relatively small number of papers reporting the temperature dependence of Mn^{4+} luminescence on low temperatures (<100K, and even less starting at ~10K). Unfortunately, it prevents correct interpretation since $T_{1/2}$ should be determined from either the thermal evolution of τ value or the emission intensity, which values are stable over a certain temperature range. In spite of this, the high interest in Mn^{4+}-based phosphors may provide in next years an adequate database to precisely define all the processes responsible for the thermal quenching of Mn^{4+} luminescence and then define the correlation between the structural and thermometric parameters.

6.5.4. Application of luminescent thermometers based on $3d^3$ ions luminescence

Due to the wide range of luminescent materials being investigated for luminescence thermometry applications, inorganic crystals doped with $3d^3$ ions represent only a fraction of the potential possibilities. Despite this, a few of the most attractive solutions can be mentioned. The first application of luminescent thermometry based on $3d^3$ ions was reported by Weinstein in 1986 for an Al_2O_3:Cr^{3+} crystal known as ruby[180]. Even then, ruby was a well-known pressure indicator used in manometry. However, using the ratio of the intensities of R_1 and R_2 lines for the ratiometric approach, the temperature can also be determined according

to the Arrhenius equation (Eq. 19). This fact was used to control the temperature change in the cryobaric diamond anvil cell (DAC) while varying the set pressure. It was observed that in the range of 10-100K, it is possible to determine the temperature accurately, working in the pressure range from 0 to 120 kbar.

On another note, $3d^3$ ions were found to be attractive for temperature determination using lifetime-based methods. Fernicola et al. presented an optical-electrical setup for temperature determination, at the end of which a fiber optic temperature probe with the $Y_3Al_5O_{12}:Cr^{3+}$ crystal as a temperature sensor was placed[181]. Using it, ^2E excited-state lifetimes were measured, which, after calibration, allowed to determine the temperature in the range of 273-573K (0-300°C) with a readout error not exceeding 0.5 K and a repeatability in the range of 0.04-0.12 K. In other work, the luminescence decay profiles of the ^2E excited state of Cr^{3+} in $YAl_3(BO_3)_4$ served as a thermographic parameter for temperature imaging[182]. Microcrystalline powder was dispersed in hydrogel and laid down as a homogeneous layer. Subsequently, imaging with a time-gated charge-coupled device (CCD) camera showed a clear reduction in lifetime in the range of 298-323K (5-50°C). An interesting solution was also presented for the $Mg_4FGeO_6:Mn^{4+}$ phosphor, for which the figure of merit was the rise time measured after a long excitation pulse (> 1 ms) instead of the conventional approach of luminescence decay profiles measured after a short excitation pulse (roughly < 10 ns)[61]. On this basis, it was observed that the time at which signal saturation occurs, resulting from the excitation of all electrons in the sample to the ^2E level, increases when the temperature elevates. This is expected since, with increasing temperature, the ^2E level is depopulated faster and faster, and consequently more time is required to fully occupy the excited state. To confirm the applicability of the proposed method, the authors mixed phosphor powder with hydroxypropyl cellulose binder and sprayed it on the copper plate, followed by a demonstration with the jet impingement cooling. With the change in temperature as a function of time, they were able to determine the temperature gradient based on the rise time of Mn^{4+} ions.

A third approach confirming the applicability of $3d^3$ ions in temperature determination, finding wider interest after the publication of the article **[P8]** forming part of this doctoral dissertation, is the use of the phenomenon of luminescence thermochromism. Luminescence thermochromism manifests itself by changing the colour of the material as a function of temperature. To make this phenomenon possible, $3d^3$ doped phosphors use the intense red luminescence of $3d^3$ ions (Mn^{4+} so far), which is highly susceptible to temperature changes, and the luminescence from Ln^{3+} ions, which should change slightly with temperature. As a result, at lower temperature the color of the phosphor is red due to the dominant influence of Mn^{4+} emission, while with increasing temperature the intensity of Mn^{4+} band quenches when the luminescence of Ln^{3+} ions remains. So far, the most significant color changes

have been observed for Mn^{4+}, Tb^{3+} co-doped systems providing green luminescence after complete thermal quenching of Mn^{4+} emission. This has been confirmed in $CaGdAlO_4$:Mn^{4+}, Tb^{3+} between 298 and 473K[63] and $Na_4Mg(WO_4)_3$:Mn^{4+}, Tb^{3+} phosphor between 350 and 450K[62]. In contrast, Sm^{3+} ions used as a co-dopant in $LaGaO_3$:Mn^{4+}, Sm^{3+} phosphor provided a color change in luminescence from deep red at 293K to bright orange at 573K[64]. Nevertheless, for this powder, mixing with polydimethylsiloxane (PDMS) led to the formation of a transparent elastomer film. The use of powders exhibiting luminescence thermochromism could find practical and simple applications in everyday life, as proposed by Ramalho et al.[183], who summarized so far presented research on determining temperature with a smartphone camera. They suggested that with thermochromic phosphors embedded in a polymer composite or coated onto surface, it would be possible to create a mobile application with an uploaded calibration curve that converts the detected color to temperature. Therefore, designing materials whose colour change occurs at different temperature ranges would allow such a method to be universally applicable. Interest in luminescent thermometers based on $3d^3$ ions luminescence continues to grow, so further work confirming their practical application should be expected in the coming years.

7. Experimental methods used in the doctoral dissertation

7.1. Synthesis

The significant influence of the host material on the spectroscopic and thermometric parameters of materials doped with TM ions of $3d^3$ configuration makes it easy to obtain phosphors exhibiting different properties tailored to different applications. Therefore, it was desirable to design and produce materials belonging to different families, with different compositions and stoichiometry. All the obtained materials used in a doctoral dissertation are summarized in Table 2.

Table 2. Materials used in doctoral dissertation.

Publication number	Samples composition
P1	$Y_3Al_{5-x}Ga_xO_{12}$:1% $Cr^{3+/4+}$ (x=0, 1, 2, 3, 4, 5)
P2	$MgTiO_3$:x% Cr^{3+} (x=0.1, 0.2, 0.5, 1, 2, 5)
P2	$MgTiO_3$:0.1% Cr^{3+}, y% Nd^{3+} (y = 0.1, 0.5, 1, 2, 5)
P3	$Y_3Al_5O_{12}$:1% Tb^{3+}, 1% Eu^{3+}, x% Cr^{3+} (x= 0, 0.1, 0.5, 1, 2, 3, 5, 10)
P3	$Y_3Al_5O_{12}$:1% Tb^{3+}, 1% Eu^{3+}, x% Mn^{4+} (x= 0.1, 0.5, 1, 5, 10, 20)
P4, P6	$Y_3Al_5O_{12}$:1% Nd^{3+}, 1% Er^{3+}, x% $Cr^{3+/4+}$ (x= 0, 1, 2, 5, 10, 15, 20)
P5, P6	$GdScO_3$:1% Nd^{3+}, 1% Er^{3+}, x% Cr^{3+} (x = 0, 0.5, 1, 2, 5, 10, 15, 20)
P6	$Y_3Al_2Ga_3O_{12}$:1% Nd^{3+}, 1% Er^{3+}, x% Cr^{3+} (x=0, 15)
P6	$LaScO_3$:1% Nd^{3+}, 1% Er^{3+}, x% Cr^{3+} (x=0, 15)
P6	$LaGaO_3$:1% Nd^{3+}, 1% Er^{3+}, x% Cr^{3+} (x=0, 15)
P7	$CaGa_4O_7$:0.01% Mn^{2+}, y% Cr^{3+} (y=0.01, 0.05, 0.1, 0.5)
P8	$Sr_4Al_{14}O_{25}$:0.1% Mn^{4+}, x% Tb^{3+} (x=1, 5, 10, 20)
P9, P10	$SrTiO_3$:0.1% Mn^{4+}
P9	Sr_2TiO_4:0.1% Mn^{4+}
P9	$Sr_3Ti_2O_7$:0.1% Mn^{4+}
P10	$SrTiO_3$:0.1% Mn^{4+}, 1% Ln^{3+} (Ln^{3+} = Lu^{3+}, Tm^{3+}, Er^{3+}, Ho^{3+}, Dy^{3+}, Eu^{3+}, La^{3+})

Oxide materials from different groups was prepared with solid state **[P1, P4, P5]**[184,185] and modified Pechini method **[P2, P3, P6-P10]**[186,187]. These are well-known methods for the synthesis of inorganic oxide materials, which provides the nano- and microcrystalline powder phosphors, convenient to analyze their properties and search for correlation in the field of fundamental studies. The universal steps of the phosphors preparation procedure are shown in Figure 7. The methods differ in the preparation of the precursor mixture prior

to annealing. For the solid state method, stoichiometric amounts of precursors (irrespective of the initial form of oxides or salts) were mixed in n-hexane and ground well in an agate mortar three times until the n-hexane evaporated (Figure 7a). Then, the mixture was pre-annealed in air at 1273K for 24 h and the grounding step was repeated, ensuring a more homogeneous ion distribution of host material[188]. It was followed by a final annealing process at 1873K for 24 h in air. Finally, the resulting material was well ground in an agate mortar. For the Pechini method, on the other hand, these steps are replaced by mixing the precursors in water (Figure 7b). For this purpose, all precursors soluble in water (except Ln^{3+} oxides) were used and mixed in a stoichiometric ratio. Ln^{3+} oxides were diluted in a water solution of ultrapure nitric acid. After recrystallization three times, water-soluble lanthanide nitrates were obtained and added to an aqueous solution of the remaining salts. Then, the solution was mixed with a 6-fold excess of citric acid in respect to the metal ions. Afterwards, the poly(ethylene glycol) (PEG-200) was added to the solution and mixed together. Finally, the obtained solution was dried at 363K for 1 week to form a resin. Citric acid plays the role of a carboxylic acid chelating agent to complex metal ions, when the presence of PEG-200 allows the chelates to start polymerization to form a resin when the mixture is heated[189,190]. A special case worth singling out for the Pechini method is the synthesis of titanates (Figure 7c). In this case, it was necessary to mix of 2,4-pentanedione with titanium(IV) n-butoxide $Ti(OC_4H_9)_4$ solution in ratio of 1:1 in a separate beaker to stabilize Ti precursor. Then the mixture was added to the remaining aqueous solutions last. The synthesis was then continued by successively adding citric acid and PEG-200. After this, it was dried to remove excess water. Finally, resin was annealed in air with different conditions and created powder was ground well in an agate mortar.
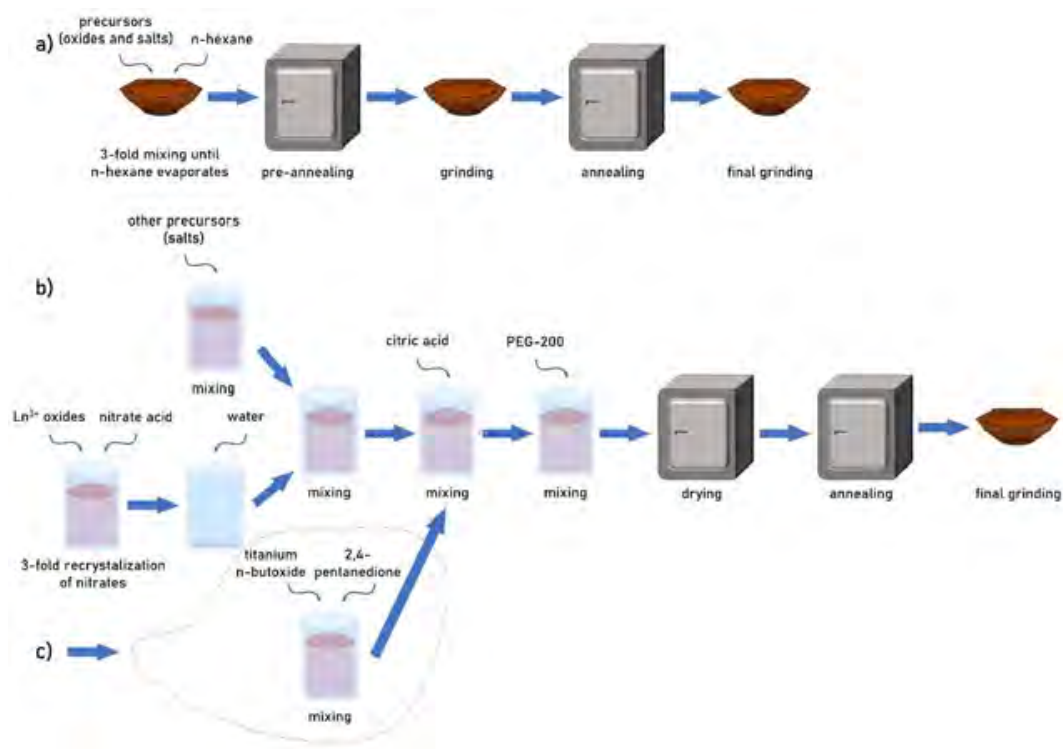
Figure 7. Schematic route of synthesis: solid-state method – a); modified Pechini method – b) and additional step for Ti^{3+}/Ti^{4+} precursors – c).

[P2] To obtain silica coated $MgTiO_3:Cr^{3+}$, Nd^{3+} nanoparticles, a modified ultrasound-assisted Stöber method was used [191,192]. The following starting materials were used as reagents: $NH_3 \cdot H_2O$ (28% solution, CHEMPUR), tetraethyl orthosilicate (TEOS; ≥99.0%, Sigma-Aldrich), ethanol (EtOH; 96% solution; POL-AURA). Specifically, an ethanolic suspension of $MgTiO_3:Cr^{3+}$, Nd^{3+} nanoparticles (30 mg of powder in 23 cm^3 of EtOH) was placed in an ultrasound bath for 2 h, to obtain well-dispersed nanoparticles, without aggregates. After this time, an ammonia solution (0.55 cm^3/7 cm^3 of distilled H_2O) was added to the dispersed nanoparticles and left for 15 min under continuous stirring. Meanwhile, a solution of TEOS in ethanol (0.75 cm^3/7.5 cm^3 EtOH) was prepared and added dropwise. The mixture prepared in this way was again placed in an ultrasound bath for 90 minutes. After this time, the obtained $MgTiO_3:Cr^{3+}$, Nd^{3+} @SiO_2 were collected by centrifugation (12000 rpm, 5 min) and washed with ethanol 3 times. The purified NPs were redispersed in ethanol or dried, for further analysis.

[P7] To prepare a flexible film with thermometric phosphor, the $CaGa_4O_7$ powder doped with 0.01% Mn^{2+} and 0.1% Cr^{3+} ions was selected. In the first step, 500.0 mg of crystalline powder was mixed with 5 ml of chloroform (pure P.A., POCH SA, Poland) and left for 15 minutes in an ultrasonic bath. Then, 10.000 g of colourless silicone (Ceresit CS 20, 100% neutral, alkoxy type sanitary silicone) was added gradually under vigorous stirring of the solution.

The solution was stirred for additional 30 minutes after complete addition of the silicone. Finally, the resulting mixture was poured into a gingerbread cookie-shaped mould attached to a glass surface and left to cure for 24 h at room temperature in air. After this time, the composite film was separated from the glass surface using a bookbinding cutter and used for the proof-of-concept experiment without further processing. The resulting gingerbread cookie-shaped film had dimensions of 64 mm x 49 mm x 1 mm. The film was stored in air at room temperature and covered to prevent dust deposition.

7.2. Characterization and proof-of-concept setup

Structural and morphological characterization

[P1-P10] All of the synthesized materials were examined by XRPD measurements carried out on PANalitycal X'Pert diffractometer, equipped with an Anton Paar TCU 1000 N temperature control unit, using Ni-filtered Cu-K$_\alpha$ radiation (V = 40 kV, I = 30 mA).

[P8] The ICP-EOS measurements were taken using a Thermo Scientific ICAP 7000 spectrometer with a charge injection device detector.

[P3, P8, P9, P10] TEM images were taken using FEI TITAN Cubed G2 60–300 microscope equipped with two spherical aberration correction devices, a monochromator and a set of four EDS detectors. The samples were applied to a lacey copper mesh in a mechanical manner. Studies were performed in a conventional TEM procedure with 300 keV parallel beam electron energy. Images were digitally recorded using the Gatan Ultrascan 1000XP. The microstructure and morphology of the samples were tested using a Philips CM-20 SuperTwin TEM microscope operating at 160kV. The sizes were determined manually using ImageJ software by measuring the longest linear size (Feret diameter) of each particle.

[P4, P5] SEM images were taken with a Field Emission Scanning Electron Microscope (FEI Nova NanoSEM 230) equipped with an energy-dispersive spectrometer (EDAX Genesis XM4). The sample was ground in a mortar and dispersed in methanol and then a drop of the suspension was placed on the carbon stub and dried.

[P4] XPS has been used for surface chemical composition analysis. The non-monochromatized X-ray Mg Ka excitation source was used. All measurements have been performed using an AES/XPS system EA10 (Leybold-Heraeus GmbH, Cologne, Germany). The overall resolution of the spectrometer during the measurements was 0.96 eV as a full width of half maximum (FWHM) of the Ag 3d$_{5/2}$ line. During measurements the pressure was kept in the 10^{-9} mbar range. All acquired spectra were calibrated to adventitious carbon C1s at 285 eV. After subtraction of the Shirley-type background, the core-level spectra

were decomposed into main components with mixed Gaussian–Lorentzian lines (70% G + 30% L for majority of photo-peaks) by a non-linear least squares curve-fitting procedure, using CasaXPS software. The atomic concentration was determined based on XPS spectra analysis, taking into account the presence of individual elements O, C, Y, Al, N and Cr.

Spectroscopic characterization

[P1-P10] The temperature of the sample was controlled using a THMS 600 heating-cooling stage from Linkam (0.1 K temperature stability and 0.1 K set point resolution).

[P1-P8, P10] The emission spectra were measured using different laser diodes as an excitation source (266 nm, 445 nm, 668 nm, 808 nm) and a Silver-Nova Super Range TEC spectrometer from Stellarnet (1 nm spectral resolution), a NIRQUEST spectrometer from Ocean Optics (1.5 nm spectral resolution) or the FLS1000 Fluorescence spectrometer with a R928P side window photomultiplier tube from Hamamatsu and R5509-72 photomultiplier tube from Hamamatsu in nitrogen-flow cooled housing as a detector. Thermal dependencies of the integral intensities of the emission bands to calculate LIR were fitted using the Mott–Seitz model (Eq. 22).

[P1-P8, P10] The excitation spectra were recorded using the FLS1000 Fluorescence spectrometer with a R928P side window photomultiplier tube from Hamamatsu and R5509-72 photomultiplier tube from Hamamatsu in nitrogen-flow cooled housing as a detector for visible and near infrared range detection, respectively with a 450 W Xenon lamp.

[P2-P5, P8, P10] The luminescence decay profiles were recorded using the FLS1000 Fluorescence spectrometer with a R928P side window photomultiplier tube from Hamamatsu and R5509-72 photomultiplier tube from Hamamatsu in nitrogen-flow cooled housing as a detector for visible and near infrared range detection, respectively with a Xenon μFlash lamp or different pulsed work laser diodes (445 nm, 668 nm, 808 nm) as excitation sources. The average lifetimes of the excited states were calculated with the use of double exponential function according to the procedure described in Eq. 46-47.

[P9] The excitation and emission spectra were measured using a double-grating FLS1000 spectrometer from Edinburg Instruments Ltd equipped with a 450 W Xenon lamp and a 60 W Xenon flash lamp as excitation sources for continuous and pulse excitation, respectively, and a Hamamatsu R928P high-gain photomultiplier detector cooled to 253K with a Peltier plate. The sample was mounted on the copper holder of a closed-cycle helium cryostat (Lake Shore Cryotronics, Inc.) using Silver Adhesive 503 glue from Electron Microscopy Sciences.

[P7] The Raman spectra were recorded at room temperature using an InVia confocal microscope from Renishaw supplied with a silicon CCD camera as a detector, employing the 488 nm excitation line and under a 20x objective with a spatial resolution below 1 mm.

[P8] The luminescence quantum yield of the synthesized nanocrystalline powders was measured using a FLS980 Fluorescence spectrometer from Edinburgh Instruments equipped with an integrating sphere, with a 450 W xenon lamp as an excitation source and a R928P side window photomultiplier tube from Hamamatsu as a detector. The luminescence QY of the synthesized nanocrystalline powders was measured using the abovementioned system equipped with an integrating sphere and Al_2O_3 powder as a reference.

[P4] To quantify the enhancement in Nd^{3+} emission offered by Cr^{3+} sensitization, the luminescence emission was quantified from suspensions of particles in water. For each sample, 10 mg of the phosphor powder was dispersed in 20 mL deionized water, yielding a standard dispersion with a concentration of 500 mg L^{-1}. An ultrasonic homogenizer (Bandelin Sonopuls HD 2200) was used to disperse and break agglomerated particles. The stirred suspensions were illuminated by a white LED (Thorlabs MCWHL5), focused using a 85 mm objective lens (Zeiss 85 mm f/1.4) and a f = +75 mm plano-convex lens to yield an intensity of 930 mW cm^{-2} in the measurement region. A visible 315–710 nm band-pass filter (Schott KG3) was positioned between the LED and the beaker to block any IR light. For visualization, images of 1064 nm emission were captured using a CMOS camera (Basler acA1300–200 mm), equipped with a 50 mm objective lens (Nikon 50 mm f/1.4) and an IR long-pass filter (Schott RG 1000) to block the scattered light from the LED beam. For quantitative spectroscopic measurements, the luminescence was collected from the dispersions using a 50 mm objective lens (Nikon 50 mm f/4) and focused onto the entrance slit of a monochromator (Spectrapro: HRS-300, Princeton Instruments), and detected using a non-amplified silicon photodiode (Thorlabs DET1002A). The grating (100 grooves per mm blazed at 450 nm) was centered at 1065 nm with the entrance and exit slit set to provide a bandwidth (FWHM) of 60 nm. For low-noise interference-free detection, the LED was modulated at 8 Hz and the current from the photodiode amplified using a lock-in amplifier (Stanford Research Systems SR510) and temporally filtered. To account for potential differences in dispersion stability, prior to luminescence measurements, the particle suspensions were illuminated by a 375 nm diode laser (PhoxX-Omicron Lasers), and the scattered light from the particles recorded using the monochromator at 375 nm and the photodiode. The amplitude of the scattered light was read from the lock-in amplifier. Variations in particle scattering between the dispersions of various samples were within a factor of 2.6, and to compare luminescence signals for the same amount of particles in the probe volume, the measured luminescence emission

was corrected by dividing by its normalized scattering intensity. To convert measured amplifier voltage to photons per s per mg, the various components of the systems were taken into consideration following the procedure from Ref. [193].

[P5] To verify the increase of the emission brightness of $GdScO_3:Nd^{3+}$, Er^{3+} when co-doping with Cr^{3+}, a spectroscopic study of liquid dispersions of the particles was performed. The experimental approach is similar to that outlined in **[P4]**. The particles were dispersed in deionized water at a concentration of 500 mg L^{-1} and placed in a borosilicate beaker. These dispersions were probed with two different light sources, namely a white LED (Thorlabs MCWHL5), with an emission spectrum which consisted of two bands: a narrow band with a center wavelength around 460 nm and a 20 nm full width at half maximum (FWHM) and a broad band with a center wavelength of 580 nm with a FWHM of 130 nm; and a blue LED (Thorlabs M455L3) centered at 455 nm with a 20 nm FWHM. The LED emission was focused by an 85mm objective lens (Zeiss 85mmf/1.4) and a f = +75mm plano-convex lens onto the center of the beaker, with a power density of 860 and 960 W/cm^2, for the blue and white LED respectively. The difference between the two LEDs do not allow IR radiation from the white LED was blocked by a visible band pass filter (Schott KG3). The luminescence from the stirred dispersions was collected by a 50mm objective lens (Nikon 50mmf/4) and imaged onto the entrance slit of a monochromator (Spectrapro: HRS-300, Princeton Instruments) with a grating (100 grooves per mm blazed at 450 nm). To reject the LED illumination, a an IR long-pass filter (Schott RG 1000) was used. A non-amplified silicon photodiode (Thorlabs DET1002A) was placed at the exit slit of the monochromator to collect the 1064 nm emission with a 60 nm bandwidth (FWHM). The photodiode current was further amplified using a lock-in amplifier (Stanford Research Systems SR510) referenced at 8 Hz, at the same modulation frequency of the excitation source. To account for difference in dispersion stability, Mie scattering measurements were also performed before and after the luminescence measurements. For this, the particles were illuminated with a 375 nm diode laser (PhoxX-Omicron Lasers), and the scattered intensity was recorded with the same system for a monochromator center wavelength of 375 nm. For these measurements, both filters were removed and the LED were turned off. The comparison of brightness of the luminescent thermometers was performed based on the ratio of collected luminescence signal and Mie scattering signal for each dispersion. To evaluate possible signal leakage between the excitation source and the detection and luminescence from the beaker to the nonluminescent Al_2O_3 particles (Phosphor Technology) with 3 μm average particle size were dispersed in water and illuminated with the white and blue LED, while the emission at 1064 nm was recorded. The signal detected at 1064 nm for aluminium oxide particles was used as a background for luminescence intensities

and subtracted. To account for the contribution of the beaker wall to the scattering signal when illuminated at 375 nm, a background signal was also recorded with the beaker filled with deionized water in the absence of phosphor particles.

Cytotoxicity characterization

[P2] The cell lines used in the study included murine fibroblasts 3T3 Swiss Albino, murine macrophages RAW 264.7 (ATCC, Rockville, MD, USA) and canine kidney epithelium line MDCK (Sigma-Aldrich, Steinheim, Germany). All cell lines were cultured in RPMI-1640 medium (Institute of Immunology and Experimental Therapy, Wrocław, Poland) supplemented with 10% foetal bovine serum (FBS, Sigma, USA), L-glutamine (Sigma, UK) and antibiotics (streptomycin and penicillin, Sigma, Germany). For the cytotoxicity assessment, cells were seeded in 96-well-plates (TTP, Switzerland) at a density of 3×10^3 (3T3 , Swiss Albino), 10×10^3 (RAW 264.7) or 2×10^3 (MDCK) cells per well and pre-incubated at 310K (37°C) overnight in a humidified atmosphere of 5% CO_2. After that, dispersions of silica-coated and uncoated $MgTiO_3:Cr^{3+}$, Nd^{3+} were added. Nanoparticles were suspended in 80% ethanol and bath-sonicated at room temperature for up to 5 min. Next, the stock dispersions were further diluted in sterile 80% ethanol and dispersions in complete culture medium were prepared so that the concentration of ethanol was 1% for all nanoparticle dilutions (this concentration was found to be well-tolerated by cells in preliminary experiments). In parallel, the highest nanoparticle concentrations were centrifuged at 30 000 g for 1 h and the particle-free supernatants were used as a diluent control (to exclude any possible particle-unrelated effects due to the presence of soluble compounds). Cells were exposed to increasing concentrations (1, 5, 10, 20, 40 µg/ml) of the dispersions for 48 h (5% CO_2, 310K). After that, the MTT assay was carried out. The test is based on the enzymatic reduction of the tetrazolium salt MTT [3-(4,5-dimethylthiazol-2-yl)-2,5-diphenyl-tetrazoliumbromide] in living, metabolically active cells. The metabolite, purple-coloured formazan is measured colourimetrically. Preliminary experiment showed no interference of the nanoparticles with MTT in a cell-free system at concentrations used in this study. After 3.5 h of incubation, cells were lysed with a dedicated buffer (225 mL dimethylformamide, 67.5 g sodium dodecyl sulphate, 275 mL distilled water) and optical density (OD) was measured after further 24 hours using a spectrophotometric microplate reader (Tecan Spark 10M, Switzerland) at the wavelength of 570 nm (reference 630 nm). The OD of control cells was taken as 100%. The results were obtained from at least 3 independent experiments and viability values were compared between the control and nanoparticle-exposed cells as well as between both types of nanoparticles using Student's t test ($P\leq0.05$ was considered statistically significant).

Additionally, shortly before MTT addition, pictures were taken using an inverted light microscope coupled with a dedicated camera (Axiovert, Zeiss, Germany).

[P7] Cytotoxicity tests were carried out on murine fibroblast (3T3/Swiss Albino) and macrophage (J774.E) cell lines. The choice of the *in vitro* model was based on the fact that 3T3 cells are a standard model to screen for cytotoxicity of biomaterials as fibroblasts are the main cellular component of connective tissues [194,195]. On the other hand, under *in vivo* conditions, macrophages form the primary line of defence to foreign bodies e.g. implants or biomaterials [196,197]. Thus they are responsible for the distribution and clearance of nanoparticles and their agglomerates. Cells were cultured in RPMI-1640 medium (Institute of Immunology and Experimental Therapy, Wrocław, Poland) supplemented with 10% fetal bovine serum (FBS, Sigma, USA), L-glutamine (Sigma, UK) and antibiotic (streptomycin and penicillin, Sigma, Germany). For the cytotoxicity assessment, cells were seeded in 96-well-plates (TTP, Switzerland) at a density of 6×10^3 (3T3) or 8×10^3 (J774.E) cells per well and pre-incubated at 37°C overnight in a humidified atmosphere of 5% CO_2. After that, nanoparticle dispersions were added. Nanoparticles were suspended in 0.05% BSA water solution and bath-sonicated at room temperature for up to 5 min. Next, the stock solutions were further diluted in 0.05% BSA and dispersions in complete culture medium were prepared. In parallel, the highest nanoparticle concentrations were centrifuged at 30 000×g for 2 h and the particle-free supernatants were used as a diluent control (to exclude any possible particle-unrelated effects due to the presence of soluble compounds). Cells were exposed to the dispersions for 48 h (5% CO_2, 37°C). After that, the MTT assay was carried out. The test is based on the enzymatic reduction of the tetrazolium salt MTT [3-(4,5-dimethylthiazol-2-yl)-2,5-diphenyl-tetrazoliumbromide] in living, metabolically active cells. The metabolite, purple-coloured formazan is measured colourimetrically, using a multiwell plate reader. Preliminary experiment showed no interference of the nanoparticles with MTT or formazan in a cell-free system at concentrations used in this study. After 4 h of incubation, cells were lysed and optical density (OD) was measured after 24 hours using a spectrophotometric microplate reader (Tecan Spark 10M, Switzerland) at the wavelength of 570 nm (reference 630 nm). The OD of control cells was taken as 100%. Cell viability was determined as follows: % viability = (mean OD in the test wells/mean OD for control wells)×100. The results were obtained from at least 3 independent experiments.

58

Proof-of-concept setups

[P7] In the thermal imaging experiment involving luminescence thermometry the $CaGa_4O_7:Mn^{2+}$, Cr^{3+}/silicone composite film was placed on a heating plate with a centrally located single heater and excited with 254 nm excitation light of a Hg lamp. Digital images were taken with a Canon EOS 400D camera with an EFS 60 mm macro lens with an integration time of 20 s, a spatial resolution of 14.3 lp/mm. The pairs of colour images of the composite film were taken with one of two optical filters placed in front of macro lens of digital camera: 1) a long pass filter at 650 nm (Thorlabs FELH650); 2) a short pass filter at 650 nm (Thorlabs FESH650). In addition, a long pass filter at 550 nm (Thorlabs FELH650) was used in both cases to exclude the effect of excitation light scattering on the blue channel of the colour images. The RGB images were converted to 32-bit type emission maps in the ImageJ 1.8.0 software. Then, the resulting images were divided by each other using OriginLab 2022 software to obtain the LIR images ($LIR = \dfrac{FESH\,650}{FELH\,650}$). No smoothing was applied to the images. The 2-dimensional LIR maps were converted to 8 temperature maps using a calibration curve. The calibration curve was obtained by placing a small 5x8 cm rectangle of 1 mm in thickness film in the centre of the heating plate and taking a series of optical images as a function of temperature. The image pairs were processed according to the procedure described above, while the temperature of the film was controlled by a FLIR T590 thermal camera. The emissivity of the composite film was evaluated by comparing the temperature of the powder placed on a fixed-temperature heating plate (313K monitored by the IR camera) with that of a Scotch 130C tape with a standardised emissivity (0.95).

[P8] The digital images were taken using a Canon EOS 400D camera with a EFS 60 mm macro lens using a 1s integration time, 14.3 lp/mm spatial resolution. After capturing colour images of the quartz cuvette filled with $Sr_4Al_{14}O_{25}:Mn^{4+},Tb^{3+}$ powder the emission maps for red and green channels (RGB) were extracted using IrfanView 64 4.51 software. After that obtained pictures were divided by each other using OriginLab 2019 Software in order to obtain LIR profiles along the quartz tube. No smoothing was applied to the image. LIR profiles were converted into temperature profiles using the calibration curve. To obtain this calibration curve, the $Sr_4Al_{14}O_{25}:Mn^{4+},Tb^{3+}$ powder was placed on the heating plate and LIR was calculated using the above-described procedure as a function of temperature. The temperature of the powder was controlled by the thermovision camera. The emissivity of the $Sr_4Al_{14}O_{25}:Mn^{4+},Tb^{3+}$ powder was estimated by the comparison of the temperature of the powder placed on the heating plate of constant temperature (40°C monitored by IR camera) with the temperature of the Scotch 130C tape of standardized emissivity (0.95). The emissivity of the quartz tube has been estimated using the same procedure.

8. Results and discussion

8.1. Influence of the structure of the host material on the Cr^{3+} ions luminescence with different roles

8.1.1. Cr^{3+} for ratiometric approach [P1, P2]

In **[P1]**, the effect of Al^{3+}/Ga^{3+} ions ratio in $Y_3Al_{5-x}Ga_xO_{12}$ on the spectroscopic properties of chromium ions was investigated. Other authors have reported the occurrence of Cr^{3+} and/or Cr^{4+} in garnet structures, which preferentially locate in octahedral and tetrahedral sites. The presence of Cr^{3+} in garnets is by far the more widely known, due to the fact its ionic charge match with Al^{3+}/Ga^{3+} ions. Nevertheless, stabilization of Cr^{4+} is also possible, most often using a charge compensation strategy or doping with high concentration of chromium ions, which results in saturation of the octahedral site with Cr^{3+} ions and the appearance of co-existing Cr^{4+} ions (the latter approach was presented in **[P4]**). However, **[P1]** presents the stabilization of both Cr^{3+} and Cr^{4+} at a total dopant concentration of 1% by annealing at high temperature (1873K) as an oxidizing conditions.

Moreover, when considering the solid-solution series of $Y_3Al_{5-x}Ga_xO_{12}$, several dependencies of the spectroscopic and structural properties were observed. Firstly, the position of the $^2E \rightarrow ^4A_2$ emission band maximum of Cr^{3+} shifts sublinearly with increasing Ga^{3+} content from 687.4 nm to 690.2 nm. A similar correlation was observed for the excitation bands, i.e. the position of bands corresponding to $^4A_2 \rightarrow ^4T_1(^4F)$ and $^4A_2 \rightarrow ^4T_2$ electronic transitions shifts from 429.2 nm (23300 cm^{-1}) to 437.2 nm (22870 cm^{-1}) and from 593.5 nm (16850 cm^{-1}) to nm 608.2 (16440 cm^{-1}), respectively, when Ga^{3+} ions gradually replace Al^{3+} ions. Using empirical equations taking into account the spectral position of the excitation bands, it was calculated that Dq/B slightly decreases from 2.649 for $Y_3Al_5O_{12}$ to 2.578 for $Y_3Ga_5O_{12}$. This is expected since the larger ionic radii of Ga^{3+} ions in respect to Al^{3+} ions lead to a weakening of the crystal field strength. On the other hand, the spin-allowed $^3B_2 \rightarrow ^3B_1$ emission band of Cr^{4+} ions was found to have a shift from 1330 nm to 1384 nm as the Ga^{3+} content increases. This gives a shift of ~54 nm in respect to the 2.8 nm observed for the emission band of the $^2E \rightarrow ^4A_2$ transition. Nevertheless, it should be mentioned that the λ_{exc}=445 nm popularly used for excitation of Cr^{3+} ions, is suitable for simultaneous excitation of Cr^{4+} ions. This is particularly beneficial for the LIR-based thermometry approach. Two strategies were proposed for the ratiometric approach: (I) LIR$_1$ defined as the ratio of two spectral bands comprising the vibronic bands $^3B_2 \rightarrow ^3B_1$ emission band of Cr^{4+} ions and (II) LIR$_2$ defined as the ratio of $^2E \rightarrow ^4A_2$ emission band of Cr^{3+} ions and $^3B_2 \rightarrow ^3B_1$ emission band of Cr^{4+} ions. In the first case, it should be mentioned that a luminescence thermometer based

on the ratio of vibronic bands of Cr^{4+} ions has been proposed for the first time. The advantage of such a thermometer is that it significantly reduces the influence of the dispersive character of the photon extinction by the environment in which the phosphor could be found (like glass or biological tissue) on wavelength, thus ensuring a small deviation of the temperature readout from the calibration curve determined under laboratory conditions. For LIR_1 approach, the maximal obtained S_R value was $0.64\%\,K^{-1}$ at 283K for $Y_3Al_3Ga_2O_{12}$. On the other hand, for LIR_2, the emission bands are well separated, but a detector operating over a wide spectral range is required. In this case, $|S_{Rmax}|=2.04\%\,K^{-1}$ at 373K for $Y_3AlGa_4O_{12}:Cr^{3+}$, Cr^{4+} phosphor was achieved. It follows that the approach using both Cr^{3+} and Cr^{4+} (LIR_2) is more favorable than the approach with vibronic states of Cr^{4+} (LIR_1). Moreover, in the case of LIR_2 the host material composition (Al^{3+}/Ga^{3+} ratio) played an important role in determining the temperature range in which $S_R>1\%\,K^{-1}$ (between 230-460K). An important aspect when analyzing the thermometric properties is the determination of the activation energy $\varDelta E$. For Cr^{3+} ions in $Y_3Al_{5-x}Ga_xO_{12}$ series, $\varDelta E$ was found to decrease quasi-linearly from $\varDelta E=\sim730$ cm^{-1} to $\varDelta E=\sim430$ cm^{-1} as Ga^{3+} increases from $Y_3Al_5O_{12}$ to $Y_3Ga_5O_{12}$. This is in agreement with the weakening of the crystal field, as it determines the energy mismatch between the ^2E and $^4T_2$ states. However, the correlation between Dq/B and $\varDelta E$ was not found to be linear, what is correlated with the fact the shift in the wavevector coefficient domain was not taken into account. On the other hand, $\varDelta E=\sim400$ cm^{-1} was determined for Cr^{4+} in most of the materials with a prominent slightly higher ~460 cm^{-1} for $Y_3Al_3Ga_2O_{12}$. Nevertheless, in both cases of Cr^{3+} and Cr^{4+}, the $\varDelta E$ values do not find a correlation with the obtained values of the $T_{1/2}$ parameter. When considering Cr^{3+} ions, the highest $T_{1/2}=309$ K and 259 K were observed for $Y_3Al_5O_{12}$ and $Y_3Ga_5O_{12}$, respectively. In contrast, the $T_{1/2}$ values for the solid solutions range from 246 to 198 K as the Ga^{3+} content increases from 1/5 to 4/5. This may suggest a correlation with the point symmetry of the octahedral Cr^{3+} site. In this case, the local symmetry of the octahedra should depend on the first coordination zone, which consists of Al^{3+}/Ga^{3+} tetrahedra. Therefore, when 100% of Al^{3+} or Ga^{3+} is in tetrahedra, the symmetry should be highest. However, the lowest symmetry should be achieved for only one other ion in six tetrahedra. Therefore, the lowest $T_{1/2}$ was obtained for x=4, for which an Al^{3+} site content of 16.1 % was calculated based on Rietveld refinement. This value is close to the 16.(6)% corresponding to the statistical distribution of Al^{3+} and Ga^{3+} ions in a ratio of $\frac{1}{6}:\frac{5}{6}$. The analogous situation corresponds to the $T_{1/2}$ obtained for Cr^{4+} ions at $\lambda_{exc}=668$ nm. The highest $T_{1/2}$ values were obtained for $Y_3Al_5O_{12}$ and $Y_3Ga_5O_{12}$, while among the mixed solid solutions, the lowest $T_{1/2}$ was achieved for x=2. In order to obtain the lowest tetrahedral symmetry where Cr^{4+} ions are located, it is necessary that statistically only one of the surrounding octahedra differs, which is 25% of all octahedra ($\frac{1}{4}$).

Such a situation was calculated for x=2.1, which is the closest value to x=2. On this basis, it has been confirmed that the host material has a significant influence on the spectroscopic and thermometric properties of luminescent centers, but a number of mechanisms often allow only for determination of the closest correlation. Therefore, only a thorough analysis will allow an understanding of all the overlapping processes separately.

As noted, relative sensitivity can be improved when the thermometric parameter changes more rapidly. To achieve this, the activation of additional temperature-dependent processes, such as energy transfers, is beneficial. The $Cr^{3+} \rightarrow Cr^{4+}$ ET was indeed observed in $Y_3Al_{5-x}Ga_xO_{12}$ structures. However, in these materials, the control of ET efficiency was hampered by the shared concentration value of Cr^{3+} and Cr^{4+} ions. Therefore, the influence of Cr^{3+} and Nd^{3+} concentrations on thermometric performance of Cr^{3+} luminescence was studied in $MgTiO_3$ host material in [P2]. In contrast to $Y_3Al_{5-x}Ga_xO_{12}$ structures, which provide strong CF for Cr^{3+} ions, Cr^{3+} ions are located in intermediate CF when are a dopant of $MgTiO_3$ structure. This allows simultaneous detection of emission from $^2E \rightarrow ^4A_2$ and $^4T_2 \rightarrow ^4A_2$ transitions. In $MgTiO_3$:Cr^{3+} it is represented by a sharp emission band with the maximum at 733.5 nm and a broad emission band centered around 835 nm, respectively. Interestingly, a sharp emission band around 697 nm is additionally observed in the emission spectrum of $MgTiO_3$:Cr^{3+}, which has been attributed to the $^2E \rightarrow ^2T_2$ electronic transition of Ti^{3+} ions. This is a result of the stabilization of Ti^{3+} ions in the $X^{2+}Ti^{4+}O_3$ structure by doping with Cr^{3+} ions, which locally form Cr^{3+}-Ti^{3+} pairs. This is possible since Cr^{3+} ions substitute positions of Mg^{2+} ions, and Mg^{2+} and Ti^{4+} octahedra form alternating layers in the $MgTiO_3$ structure. Confirmation of this hypothesis is provided by the similar shape of emission band observed for $MgTiO_3$ doped with optically inactive La^{3+} ions. In addition, by comparing the excitation spectra monitored at λ_{em}=697 nm and λ_{em}=835 nm it can be found that the broad band around 340 nm consists of two overlapped bands corresponding with $^4A_2 \rightarrow ^4T_1$ transition of Cr^{3+} ions and $O^{2-} \rightarrow Ti^{4+}$ charge transfer, respectively. Apart from this band, no other excitation band is observed for Ti^{3+} emission, whereas for Cr^{3+} ions a second characteristic band corresponding to $^4A_2 \rightarrow ^4T_2$ was detected. Using the position of Cr^{3+} excitation bands, the Dq/B=1.86 parameter was determined for 0.1% of Cr^{3+} ions. Once the origin of the emission bands was correctly identified, their thermal evolution was investigated. In the case of the Cr^{3+} $^2E \rightarrow ^4A_2$ emission band, the intensity decreases starting at 83K. It can be generally assumed that the shape of the intensity-temperature curve is weakly dependent on the Cr^{3+} concentration. Therefore, $T_{1/2}$ covers the range of 243-263K, when ~12% of the initial value was found at ~403K. On the other hand, the emission intensity of $^4T_2 \rightarrow ^4A_2$ band remains almost constant between 83 and 143K. Above 143K, the signal decreases and the quenching rate is faster when Cr^{3+} increases. Therefore, $T_{1/2}$ equals 331 K, 295 K and 213K for 0.1%, 0.2% and 0.5% Cr^{3+}, respectively. For spectral ranges including $^4T_2 \rightarrow ^4A_2$ and $^2E \rightarrow ^4A_2$,

$$LIR_1 = \frac{\int_{790nm}^{899nm} I(^4T_2 \rightarrow {}^4A_2)[Cr^{3+}]d\lambda}{\int_{731nm}^{736nm} I(^2E \rightarrow {}^4A_2)[Cr^{3+}]d\lambda}$$ was determined. The highest $|S_R|$ values were $0.97\%\,\mathrm{K}^{-1}$

at 450K, $0.65\%\,\mathrm{K}^{-1}$ at 490K and $0.77\%\,\mathrm{K}^{-1}$ at 218 K for 0.1%, 0.2% and 0.5% Cr^{3+}, respectively. For this reason, 0.1% of Cr^{3+} concentration was chosen as the most promising for further investigation. Subsequently, co-doping with Nd^{3+} ions was proposed to improve the thermometric properties of $MgTiO_3$:Cr^{3+} phosphors. It is worth noting that in $MgTiO_3$ it is impossible to separate Stark components of Nd^{3+} bands and the bands are extraordinarily broad in respect to Nd^{3+} in other host materials. This is due to the low local symmetry of polyhedra occupied by Nd^{3+} ions. The Nd^{3+} emission bands overlap spectrally with the Cr^{3+} broad band, but are more pronounced for Nd^{3+} concentrations higher than 0.5%. In addition, they are better detectable above 463K, when Cr^{3+} emission decreases significantly. By comparing different spectral ranges with the complex spectra of $MgTiO_3$:Cr^{3+}, Nd^{3+} phosphors, two ranges were

selected, based on which $LIR_2 = \dfrac{\int_{950nm}^{967nm} I\big((^4T_2 \rightarrow {}^4A_2)[Cr^{3+}] + (^2F_{9/2} \rightarrow {}^4I_{9/2})[Nd^{3+}]\big)d\lambda}{\int_{710nm}^{717nm} I(^2E \rightarrow {}^2T_2)[Ti^{3+}]d\lambda}$

was proposed. In this case, it can be clearly seen that an increase in Nd^{3+} concentration leads to a shift in temperature of the thermal quenching of the spectral range from denominator toward lower temperatures. Meanwhile, thermal quenching of Ti^{3+} band is roughly similar for all Nd^{3+} concentrations. Therefore, the temperature at which the LIR assumes its highest values also shifts to lower temperatures as the Nd^{3+} concentration increases. It resulted in two temperature ranges in which the highest LIR changes with inverse monotonicities. Thus a two local S_R maxima with the positive and negative sign could be determined. In the first regime, the $S_{Rmax}=1.00\%\,\mathrm{K}^{-1}$ at 203K was obtained for $MgTiO_3$:0.1% Cr^{3+}, 0.1% Nd^{3+} phosphors. On the other hand, $S_R=0.87\%\,\mathrm{K}^{-1}$ at 483K was achieved for 2% Nd^{3+}. It follows that Nd^{3+} ions have a positive effect on the thermometric performance of LIR-based thermometer. Moreover, Cr^{3+}, Nd^{3+} doped materials can cover a wide temperature range with satisfactory relative sensitivity, but require selection of appropriate dopant concentration depending on the applicative temperature range.

Contribution of the author's work in [P1]:

the conceptualization, synthesis of microcrystalline phosphors, structural characterization of materials, conduction of spectroscopic measurements: the excitation spectra and thermal evolution of the emission spectra, analysis and interpretation of data, preparation of original draft of paper

8.1.2. Cr^{3+} for lifetime based approach [P2]

In order to determine the optimal temperature-dependent parameter in **[P2]** in $MgTiO_3$:Cr^{3+}, Nd^{3+} phosphors, the effect of co-dopants concentration on the thermal evolution of lifetime of $^4T_2$ excited state of Cr^{3+} ions was also investigated. The lifetime of $^4T_2$ excited state of Cr^{3+} ions was chosen as a figure of merit because of higher intensity of $^4T_2 \rightarrow {}^4A_2$ band in respect to $^2E \rightarrow {}^4A_2$ band. Moreover, the broad band related to $^4T_2 \rightarrow {}^4A_2$ transition enables the selection of a spectral range that is not overlapped with other emission bands. In a first step, the effect of Cr^{3+} concentration on τ_{avr} values in $MgTiO_3$:Cr^{3+} materials was investigated. In the case of 0.1% Cr^{3+}, it was found that τ_{avr}=23.8 μs remains at the same value in the range from 83K to 183K. Above this temperature, thermal quenching occurs resulting in reaching τ_{avr}=6.67 μs at 383K. On the other hand, thermal evolution of τ_{avr} in both 0.2% and 0.5% contrast with 0.1% Cr^{3+} concentration. Initially, an increase in lifetime to τ_{avr}=34.9 μs at 83K was detected for 0.2% Cr^{3+} ions. In this case, the lifetime shortening starts above ~123K. However, it is important to highlight the change in quenching rate in the range of 243-283K, which indicates the occurrence of an additional depopulation channel. This would imply that the elongation of lifetimes below 200K is the effect of $Cr^{3+} \rightarrow Ti^{3+}$ ET. For 0.5% Cr^{3+} ions, the value of τ_{avr}=23.8 μs at 83K is similar to 0.1% Cr^{3+}, but the shape of its thermal evolution is the same as that of the $MgTiO_3$:0.2% Cr^{3+} phosphor. This maintains the occurrence of $Cr^{3+} \rightarrow Ti^{3+}$ ET, but the simultaneous increase in Cr^{3+} and Ti^{3+} concentration may result in a shortening of lifetimes of the ^2E state of the Ti^{3+} ions, and thus $^4T_2$ of the Cr^{3+} ions. Nevertheless, by comparing the thermal evolution of S_R values for materials solely doped with Cr^{3+}, one process occurring for 0.1% Cr^{3+} results in a single maximum in the S_R vs temperature plot, i.e. S_{Rmax}=1.13%K^{-1} at 323K. However, it was found that the two depopulation processes for the 0.2% and 0.5% Cr^{3+} ions resulted in two local maxima of S_R values. Therefore, S_R=0.93%K^{-1} at 183K and S_{Rmax}=1.55%K^{-1} at 383K were found for $MgTiO_3$:0.2% Cr^{3+} while S_R=0.50%K^{-1} at 203K and S_{Rmax}=1.67%K^{-1} at 403K were noted for 0.5% Cr^{3+} ion concentration. Due to the bias of the presented studies towards bioapplication, despite the higher S_R values for 0.5% Cr^{3+} concentration, the 0.1% Cr^{3+} was chosen for further optimization due to the highest S_R achieved in the physiological temperature range. When co-doping $MgTiO_3$:0.1% Cr^{3+} with 0.1% Nd^{3+} ions, the lifetime of Ti^{3+} ions was found to increase from τ_{avr}=2.31 ms to 3.05 ms. This is a similar observation to that for increasing Cr^{3+} concentration from 0.1% to 0.2%. However, for concentrations of Nd^{3+} higher than 0.1% (with 0.1% Cr^{3+}), a gradual shortening of the Ti^{3+} lifetime was observed. Considering the lifetimes of the $^4T_2$ state of Cr^{3+} ions, for Nd^{3+} concentrations in the range of 0.1%-2%, a general increase in the lifetime value was obtained. The highest values at 83K equal to τ_{avr}=38.3 μs were noticed for 0.1% Nd^{3+} content. However, as the temperature increased to 183K, an even higher value

of τ_{avr}=50.9 μs was reached. Above this value, a gradual shortening was observed up to τ_{avr}=23.4 μs at 363K. For 0.5% and 1% Nd^{3+} ions, the increase in lifetime in the range of 183K was not observed. For 2% of Nd^{3+} ions, the increase in Cr^{3+} lifetimes occurs similarly to that for 0.1% Nd^{3+}. This may indicate the greatest lattice distortion at 2% Nd^{3+} doping in respect to lower Nd^{3+} concentrations, which affects the rise of Cr^{3+} lifetime values. Nevertheless, this effect did not have a beneficial effect on the thermometric performance of τ_{avr}-based luminescence thermometer. Therefore, the highest values were achieved for 0.5% and 1% Nd^{3+} ions, namely S_{Rmax}=1.75%K^{-1} at 413K and 1.90%K^{-1} at 543K, respectively. On the other hand, the 2% Nd^{3+} concentration showed the best S_R values in the physiological temperature range achieving 0.85-1.18%K^{-1} over 303-343K. For this reason, the $MgTiO_3$:0.1% Cr^{3+}, 2% Nd^{3+} phosphor was selected as the most promising for bioapplications. Finally, among LIR_1, LIR_2 and τ_{avr} as potential thermometric parameters of $MgTiO_3$:Cr^{3+}, Nd^{3+} phosphor it was found that the latter has the greatest application potential due to its highest relative sensitivity, as well as it does not require to match appropriate filters to the extract selected spectral ranges of ratiometric approach.

Contribution of the author's work in [P2]:

the conceptualization, synthesis of nanocrystalline phosphors, structural and morphological characterization of materials, conduction of spectroscopic measurements: the excitation spectra, thermal evolution of the emission spectra and thermal evolution of the luminescent decay profiles, analysis and interpretation of data, preparation of original draft of paper

8.1.3. Cr^{3+} as a sensitizer in Ln^{3+}-based luminescent thermometers [P3, P4, P5, P6]

In addition to above mentioned conventional approaches using Cr^{3+} ion luminescence as a temperature-dependent parameter, Cr^{3+} can play the role of a sensitizer for luminescent thermometers. This is motivated by the desire to improve the sensitivity and brightness of thermometers based on Ln^{3+} luminescence, which possess well-defined and spectrally separated emission bands. It is known that TM ions like Cr^{3+} ions have a higher and broader absorption cross section and their luminescence exhibits stronger dependence on temperature in respect to Ln^{3+} ions. In addition, the occurrence of sensitizer-to-Ln^{3+} energy transfer can occur with the assistance of phonon and therefore this process is also dependent on temperature. For the first time the confirmation of that strategy was presented in **[P3]** for the pair of Tb^{3+} and Eu^{3+} ions in $Y_3Al_5O_{12}$ (YAG) structure. In the case of Tb^{3+} and Eu^{3+} ions, emission bands are associated with the $^5D_4 \rightarrow {}^7F_J$ and $^5D_0 \rightarrow {}^7F_J$ transitions, respectively. They are thermally stable over a wide temperature range due to the high energy separation between $^5D_4$/$^5D_0$ states and the closest lower excited states (14700 cm^{-1} and 12200 cm^{-1} for Tb^{3+} and Eu^{3+}, respectively), making it difficult

to activate the multiphonon depopulation process. Therefore, the phonon assisted energy transfer between $^5D_4$ state of Tb^{3+} and $^5D_0$ of Eu^{3+} ions may be the only thermally dependent process occurring in YAG:Tb^{3+}, Eu^{3+} over wide temperature range. The occurrence of $Eu^{3+} \rightarrow Tb^{3+}$ energy transfer was confirmed by the presence of excitation bands from Eu^{3+} ions on the excitation spectra of Tb^{3+} ions. To confirm low sensitivity to temperature changes, a calculation

of $LIR = \dfrac{\int I(^5D_0 \rightarrow {}^7F_1)[Eu^{3+}]d\lambda}{\int I(^5D_4 \rightarrow {}^7F_5)[Tb^{3+}]d\lambda}$ was proposed. Indeed, LIR variation as a function

of temperature led to S_{Rmax}=0.09%K^{-1} at 193K.

To improve the thermometric performance of YAG:Tb^{3+}, Eu^{3+} phosphor, co-doping with different concentrations of Cr^{3+} ions has been proposed. Firstly, by analyzing the excitation spectra for the Cr^{3+} ion emission, a $O^{2-} \rightarrow Eu^{3+}$ charge transfer band can be detected, indicating the presence of $Eu^{3+} \rightarrow Cr^{3+}$ energy transfer (ET). Furthermore, several narrow excitation bands were assigned to the electron transitions: $^7F_0 \rightarrow {}^5H_7$, $^7F_0 \rightarrow {}^5G_5$ and $^7F_0 \rightarrow {}^5D_3$ of the Tb^{3+} ions, confirming the $Tb^{3+} \rightarrow Cr^{3+}$ ET. On the other hand, a broad band associated with the $^4A_2 \rightarrow {}^4T_1$ transition of Cr^{3+} ions was found, which contribution increases with increasing temperature, suggesting that the probability of the $Cr^{3+} \rightarrow Eu^{3+}$ ET process occurrence is temperature-dependent. Moreover, the average lifetimes of both $^5D_4$ (Tb^{3+}) and $^5D_0$ (Eu^{3+}) decrease with increasing Cr^{3+} concentration, similarly as the ^2E (Cr^{3+}) lifetimes, which may indicate $Cr^{3+} \rightarrow Ln^{3+}$ and $Ln^{3+} \rightarrow Cr^{3+}$ ET. Next, the thermal evolution of the Tb^{3+} and Eu^{3+} emission intensities was analyzed as a function of Cr^{3+} concentration. Due to the numerous energy transfer processes occurring in the investigated system, their comparison is complex. However, it can be assumed that the comparison of LIR values determined within the same spectral ranges provides an opportunity to highlight new processes which probability of occurrence increases with Cr^{3+} concentration. Therefore, it was found that the shape of LIR vs temperature plot remains similar in the range of 0-2% of Cr^{3+} concentration. Further changes are observed for 3% and 5% Cr^{3+} ions, resulting in improved relative sensitivity. As a result, S_{Rmax}=0.16%K^{-1} at 373K is achieved for YAG:1% Tb^{3+}, 1% Eu^{3+}, 5% Cr^{3+} phosphor. This represents an enhancement of S_R value by 200% compared to S_R=0.0075%K^{-1} obtained for unco-doped with Cr^{3+} ions counterpart. In summary, above the critical concentration of Cr^{3+} ions, the higher Cr^{3+} content the more spectacular sensitization. However, at the same time, an increase in Cr^{3+} ions concentration is associated with an increase in the probability of the back $Ln^{3+} \rightarrow Cr^{3+}$ energy transfer, which manifests itself in the reduction of the Ln^{3+} emission intensity. In turn, it does not have a favorable effect on the temperature determination uncertainty δT, which, despite being reduced with an improvement in S_R value, increases with a decrease in signal intensity. Therefore, δT=~3K was obtained for both 3% and 5% of Cr^{3+} ions. Higher concentrations of Cr^{3+} ions in YAG:Tb^{3+}, Eu^{3+} were not analyzed due to the increasing

contribution of Cr^{3+} absorption overlapping spectrally with Tb^{3+} and Eu^{3+} emission. Therefore, a pair of other Ln^{3+} ions which emission is shifted towards the NIR spectral range, i.e. Nd^{3+} and Er^{3+}, were proposed in a subsequent paper.

In **[P4]**, the YAG structure was retained, which has Al^{3+} and Y^{3+} crystallographic sites suitable for Cr^{3+} and Ln^{3+} ions, respectively, as well as provides good physicochemical parameters. However, in **[P4]** a solid state method with high annealing temperature (second annealing at 1873K, 24h, the same route as in **[P1]**) was used in respect to Pechini method used in **[P3]** (annealing at 1373K, 12h). This arrangement was aimed at obtaining microcrystals with a smaller surface-to-volume ratio than in the case of the nanosized particles. It reduced the influence of defects on the surface, which would decrease the brightness of samples. However, it should be borne in mind that brightness still may be limited by structural changes resulting from high concentrations of dopants. More importantly, due to the larger grain size, the difference in luminescence resulting from additional energy transfers should be more pronounced than in nanoparticles, due to the higher quantitative content of dopants in one extracted grain.

In contrast to the Tb^{3+}-Eu^{3+} pair, the Nd^{3+}-Er^{3+} system (undoped with Cr^{3+}) can be excited directly through λ_{exc}=445 nm, due to the weak absorption band associated with the $^4I_{9/2} \rightarrow (^2P_{1/2}, {}^2D_{5/2})$ electronic transition of Nd^{3+} ions. In the case of Nd^{3+}, nonradiative transitions to the $^4F_{3/2}$ metastable state are followed by radiative depopulations of $^4F_{3/2} \rightarrow {}^4I_{9/2}$, $^4F_{3/2} \rightarrow {}^4I_{11/2}$ and $^4F_{3/2} \rightarrow {}^4I_{13/2}$, resulting in the generation of three characteristic emission bands at 880 nm, 1064 nm and 1350 nm. Due to the relatively small energy mismatch between the $^4F_{3/2}$ state of Nd^{3+} and the $^4I_{11/2}$ state of Er^{3+}, an $Nd^{3+} \rightarrow Er^{3+}$ energy transfer can occur, which also allows the detection of an emission band at 1550 nm associated with the $^4I_{13/2} \rightarrow {}^4I_{15/2}$ electronic transition of Er^{3+} ions. $Nd^{3+} \rightarrow Er^{3+}$ ET is a temperature-dependent process, which guarantees that the intensity of Nd^{3+} emission gradually decreases with temperature, reducing the initial intensity observed at 123K to 40% at 573K. On the contrary, Er^{3+} emission is less temperature-dependent, reaching at 573K 66% of its initial intensity at 123K. However, when Cr^{3+} ions are used as a co-dopant in the YAG:Nd^{3+}, Er^{3+} phosphor, several beneficial effects are observed from a spectroscopic and thermometric point of view. When comparing the excitation spectra monitored at Nd^{3+} emission, among the numerous Nd^{3+} excitation bands, some narrow bands corresponding to electron transitions of Er^{3+} were found, i.e. $^4I_{15/2} \rightarrow {}^4F_{7/2}$, $^4I_{15/2} \rightarrow {}^2H_{11/2}$, $^4I_{15/2} \rightarrow {}^4S_{3/2}$ and $^4I_{15/2} \rightarrow {}^4I_{9/2}$. This suggests the $Er^{3+} \rightarrow Nd^{3+}$ ET. In addition, two broad bands of $^4A_2 \rightarrow {}^4T_1$ and $^4A_2 \rightarrow {}^4T_2$ electronic transitions were found when doping with Cr^{3+} ions, confirming $Cr^{3+} \rightarrow Nd^{3+}$ ET. Similar Cr^{3+} bands, with increasing contribution when the Cr^{3+} concentration increases, were detected in the excitation spectra detected for Er^{3+} emission, indicating the occurrence of $Cr^{3+} \rightarrow Er^{3+}$ ET. Therefore, it can be concluded

that a significantly higher absorption cross section of Cr^{3+} ions at λ_{exc}=445 nm leads to an enhancement of the Nd^{3+} and Er^{3+} emission signal. To estimate an enhancement, a contribution parameter was calculated that represents the intensity of signal integrated in the spectral range in which the $^4A_2 \rightarrow {}^4T_1$ excitation band of Cr^{3+} ions can be found. In this case the $^4I_{9/2} \rightarrow {}^4F_{7/2}$ excitation band of Nd^{3+} ions was used as reference. Thus, it was confirmed that, for co-doping with 20% Cr^{3+} ions, the $^4A_2 \rightarrow {}^4T_1$ band provides almost 50 times higher absorption at 445 nm with respect to the $^4I_{9/2} \rightarrow ({}^2P_{1/2}, {}^2D_{5/2})$ band of Nd^{3+} ions. Furthermore, a comparison of the absolute emission intensity of the 1064 nm band ($^4F_{3/2} \rightarrow {}^4I_{11/2}$ transition of Nd^{3+} ions) in dilute particle dispersions upon excitation with a white LED was presented in collaboration with prof. B. Fond (Otto-von-Guericke University Magdeburg). The brightness was found to increase quasi-linearly with Cr^{3+} concentration, reaching a ~30-fold increase in intensity for 20% Cr^{3+} with respect to the undoped with Cr^{3+} ions counterpart. It confirms the positive effect of Cr^{3+} ions on Ln^{3+} luminescence, which is one of the assumptions of the sensitization mechanism. On the other hand, in order to verify if the occurring ETs have a significant effect on the improvement of S_R values, the thermal evolution of the emission intensity of Nd^{3+} and Er^{3+} was investigated. For both Nd^{3+} and Er^{3+} ions, an inhibition of thermal quenching was observed for Cr^{3+} concentrations in the 1-5% range. This suggests an influence of $Cr^{3+} \rightarrow Nd^{3+}/Er^{3+}$ ETs which counteract thermal quenching of Ln^{3+} emission. However, for 10% and 20% Cr^{3+} ions, the Nd^{3+} emission bands thermally quench even more efficiently than for the counterpart undoped with Cr^{3+} ions. In the same temperature range the intensity of Er^{3+} increases, reaching almost 3 times the intensity at 573K with respect to the value at 123K. Such a drastic change between the thermal performance of Nd^{3+} and Er^{3+} emission when Cr^{3+} doping increases from 5% to 10% suggests the activation of new processes. With reference to **[P1]**, the occurrence of Cr^{4+} ions in tetrahedral sites available in the YAG structure should be considered. Therefore, it can be concluded that when a concentration of $Cr^{3+/4+}$ ions is higher than 5%, the ET processes involving Cr^{4+} starts to be noticeable. Therefore, the $Nd^{3+} \rightarrow Cr^{4+} \rightarrow Er^{3+}$ ET should be highlighted, which, due to the favorable energy position of the $^3B_2$ state, acts as the energy bridge between Nd^{3+} and Er^{3+} ions improving the efficiency of the phonon assisted energy transfer hitherto observed between Ln^{3+} ions. The occurrence of such a process is most probable since the sharp decrease in the intensity of Nd^{3+} emission in 10% and 20% Cr^{3+} co-doped samples occurs in a similar temperature range as the enhancement of $^4I_{13/2} \rightarrow {}^4I_{15/2}$ emission of Er^{3+} ions. The effective thermal quenching of Nd^{3+} emission band could also be explained by $Nd^{3+} \rightarrow Cr^{3+}$ BET. However, the enhancement of the emission intensity of Er^{3+} ions cannot be explained in any other way than through the crucial importance of Cr^{4+} ions. Using the inverse monotonicity of Nd^{3+} and Er^{3+} emission intensities as a function of temperature,

$$LIR = \frac{\int I(^4F_{3/2} \rightarrow {}^4I_{11/2})[Nd^{3+}]d\lambda}{\int I(^4I_{13/2} \rightarrow {}^4I_{15/2})[Er^{3+}]d\lambda}$$ was determined. Consistent with the thermal evolution

of two bands discussed above, the shape of the LIR vs temperature was similar for $Cr^{3+/4+}$ concentration in the 0-2% range. Above this value it improved progressively, reaching the best results for 20% of $Cr^{3+/4+}$ ions. These results translated into the S_R values. For Nd^{3+}/Er^{3+} ratiometric thermometer co-doped with 20% of $Cr^{3+/4+}$ ions, $S_{Rmax}=1.67\% K^{-1}$ at 300K was achieved, which in comparison to $S_{Rmax}=0.25\% K^{-1}$ at 468 K obtained without $Cr^{3+/4+}$ ions co-doping indicates sensitivity enhancement of ~670%.

The aim of the work **[P5]** was to prove that Cr^{4+} ions correspond with the occurrence of additional ET processes favoring the sensitization process in YAG:Nd^{3+}, Er^{3+}, $Cr^{3+/4+}$, however, doping with Cr^{3+} is sufficient to observe the sensitization mechanism and this approach can be used universally for many host materials. For this reason, the GdScO$_3$:Nd^{3+}, Er^{3+}, Cr^{3+} system was chosen, in which, due to the lack of tetrahedral sites, there is no possibility of the occurrence of Cr^{4+} ions. Due to the small effect of the crystal field on the position of Ln^{3+} energy states, as in the YAG host material, the interionic $Nd^{3+} \rightarrow Er^{3+}$ and $Er^{3+} \rightarrow Nd^{3+}$ ETs were confirmed in GdScO$_3$ unco-doped with Cr^{3+} ions by comparing excitation spectra. Next, the possibility of $Cr^{3+} \rightarrow Ln^{3+}$ ETs was verified. It was confirmed by the effective excitation of both Nd^{3+} and Er^{3+} emission at λ_{exc}=445 nm, which corresponds well with $^4A_2 \rightarrow {}^4T_1(^4F)$ electronic transition of Cr^{3+} ions. Furthermore, bands associated with $^4A_2 \rightarrow {}^4T_1(^4P)$, $^4A_2 \rightarrow {}^4T_1(^4F)$, $^4A_2 \rightarrow {}^4T_2(^4F)$ and $^4A_2 \rightarrow {}^2E$ electronic transitions of Cr^{3+} ions were observed in excitation spectra monitored for Nd^{3+} and Er^{3+} emission in samples with Cr^{3+} concentrations of 0.5% to 20%. In analogy to **[P4]**, the contribution parameter was used to perform the increasing influence of the Cr^{3+} absorption bands in the excitation spectra of Nd^{3+} and Er^{3+} ions. At 2% Cr^{3+} concentration, the $^4A_2 \rightarrow {}^4T_1$ band of Cr^{3+} ions was found to be 31 and 23 times more intense than the excitation bands corresponding to the $^4I_{9/2} \rightarrow {}^4G_{7/2}$ transition of Nd^{3+} ions and $^4I_{15/2} \rightarrow {}^2H_{11/2}$ of Er^{3+} ions, respectively. These values increased to 64 and 41 times for phosphor doped with 20% Cr^{3+}. The following step was to evaluate the brightness enhancement factor. In contrast to YAG:Nd^{3+}, Er^{3+}, $Cr^{3+/4+}$ phosphors the absolute emission intensity of Nd^{3+} ions (1064 nm) did not appear to increase linearly with the concentration of Cr^{3+} in the GdScO$_3$ host material. The best result was obtained for 15% of Cr^{3+} concentration, which corresponds to ~12 and ~25 times improvement of the brightness with white and blue LED excitation, respectively. The highest concentration of 20% Cr^{3+} presented similar absolute intensity values as 2% and 5% of Cr^{3+}. The decrease in brightness from 15% to 20% Cr^{3+} concentration may be related to the increasing contributions of $Cr^{3+} \rightarrow Cr^{3+}$, $Cr^{3+} \rightarrow Nd^{3+}$, $Cr^{3+} \rightarrow$ defects ETs and $Nd^{3+} \rightarrow Cr^{3+}$ BET, which, despite a higher absorption cross section, adversely affect the quantum efficiency for the Nd^{3+} emission.

Besides brightness, thermometric parameters of $GdScO_3$:Nd^{3+}, Er^{3+}, Cr^{3+} were also evaluated. In the case of Cr^{3+} unco-doped counterpart, Nd^{3+} emission intensity decreases gradually with increasing temperature, which is expected due to $Nd^{3+} \rightarrow Er^{3+}$ ET. However, Er^{3+} intensity increases, reaching at 463K 3 times higher intensity than at 83K. This demonstrates the greater efficiency of the $Nd^{3+} \rightarrow Er^{3+}$ ET than that found in YAG:Nd^{3+}, Er^{3+}, where the introduction of Cr^{4+} with $^3B_2$ excited state as an energy bridge between Ln^{3+} excited states was necessary to achieve the increase in Er^{3+} emission intensity. However, despite the inverse monotonicity, which is beneficial from a thermometric point of view, this provides a quasi-linear reduction of the LIR value as a function of temperature. Therefore, the resulting S_R remains almost constant at ~0.30%K^{-1} over a wide range of 83-483K. However, even co-doping with 0.5% Cr^{3+} ions affects the thermal evolution of Ln^{3+} bands. Both Nd^{3+} and Er^{3+} emission remains almost constant up to ~350K, resulting disadvantageously in a decline of S_R over the entire temperature range. However, with increasing Cr^{3+} concentration the contribution of energy transfers related with Cr^{3+} ions gains in importance. Therefore, the most favorable LIR changes were obtained for more than 10% of Cr^{3+} ions, where both Nd^{3+} and Er^{3+} emission signals were intensively decreasing starting at 83K. As a result, for 15% of Cr^{3+} the S_R value exceeded 0.5%K^{-1} in the range of 225-380K with S_{Rmax}=0.96%K^{-1} at 300K. On the other hand, the S_{Rmax} for 20% Cr^{3+} was slightly lower (0.87%K^{-1} at 295K), but the S_R>0.5%K^{-1} was maintained over a wider range of 195-390K. In summary, for 15% Cr^{3+} an improvement in sensitivity by ~280% was obtained. Therefore, it can be concluded that the presence of Cr^{3+} ions has a beneficial effect on Ln^{3+}-based luminescent thermometers and no co-existence of Cr^{4+} ions is required to effectively implement a sensitization mechanism. Nevertheless, comparing the S_{Rmax} values and the percentage improvement in sensitivity in respect to Cr^{3+} unco-doped counterpart, it has to be acknowledged that Cr^{4+} ions may have had a significant role in achieving better results for the YAG structure than $GdScO_3$.

The final step in investigating the mechanism of sensitization was to compare five representative host materials doped with fixed ions concentrations of 1%Nd^{3+}, 1% Er^{3+} and 0%/15% Cr^{3+} as presented in **[P6]**. The aim was to find correlations between spectroscopic or even structural properties that improve sensitivity in different host materials. For this purpose, YAG, $GdScO_3$, $Y_3Al_2Ga_3O_{12}$ (YAGG), $LaGaO_3$ and $LaScO_3$ host materials were used. At first, it was determined that, according to the average distance between the metal ion, in which position Cr^{3+} ions may locate and their ligands R_{avr}(Cr^{3+}-O^{2-}), the investigated host materials are arranged in the following order: YAG<YAGG<$LaGaO_3$<$GdScO_3$<$LaScO_3$. Therefore, a fine correlation between Dq/B and R_{avr}^{-5} was determined, since it was found that both $^4A_2 \rightarrow ^4T_1$ and $^4A_2 \rightarrow ^4T_2$ excitation bands shift towards shorter energies with increasing R_{avr} value. Investigated host materials are characterized by Dq/B>2.4 values, which allows them to be classified as intermediate

or strong CF. Furthermore, the position of the ^2E excited state was determined for the investigated host materials from literature. This was not possible directly for the 15% Cr^{3+} concentration due to concentration quenching. Nevertheless, despite less pronounced changes in the position of the ^2E state in respect to $^4T_1$ and $^4T_2$, it was found that as R_{avr} increases, the energy of the ^2E state decreases progressively. This is the expected effect, according to the T-S diagram for $3d^3$ electronic configuration. Significantly, due to the small effect of CF on the emission of Ln^{3+} ions in respect to Cr^{3+} ions, it can be assumed that the position of the Cr^{3+} bands affects the energy mismatch between Cr^{3+} and Ln^{3+} ions, which is directly related with the probability of $Cr^{3+} \rightarrow Ln^{3+}$ ET. Due to the much shorter time of the intraionic nonradiative transition than the interionic ET, it is expected that the lowest excited state of Cr^{3+} ions is responsible for the transfer to Ln^{3+} ions. In the case of intermediate and strong CF, the lowest excited state is ^2E state. On the other hand, comparing the position of energy states of Nd^{3+} and Er^{3+} ions, it is noted that the first closest Ln^{3+} level underneath ^2E state is overlapping Stark components of the $^4F_{7/2}$, $^4S_{3/2}$ levels of Nd^{3+} ions. Therefore, the ^2E and $^4F_{7/2}$, $^4S_{3/2}$ levels are expected to play a dominant role in the ETs between Cr^{3+} and Ln^{3+} ions. Therefore, the energy difference (denoted simply as ΔE) between them was determined for the investigated host materials. Based on this, it was estimated that the ΔE for YAG and YAGG would be in the range of ~850-950 cm^{-1}, for $LaGaO_3$ it would be ~450 cm^{-1}, while for $GdScO_3$ and $LaScO_3$ in the order of ~40 cm^{-1}. The order presented in such way is consistent with the increasing value of R_{avr}.

Subsequently, by investigating the thermal evolution of emission spectra, it was confirmed that in all host materials doping with 15% Cr^{3+} leads to a faster rate of thermal quenching of Nd^{3+} and Er^{3+} bands in respect to solely Nd^{3+}, Er^{3+} doped counterparts. However, the abundance of nonradiative processes occurring in doubly and triply doped systems and their different contribution to the thermal evolution of emission spectra depending on the considered host material makes it significantly difficult to find a correlation between spectroscopic and structural parameters. For this reason, the determination of $LIR = \dfrac{\int I(^4F_{3/2} \rightarrow {}^4I_{11/2})[Nd^{3+}]d\lambda}{\int I(^4I_{13/2} \rightarrow {}^4I_{15/2})[Er^{3+}]d\lambda}$

was proposed. Thus, it was assumed that using thermal evolution of LIR, it is possible to include all processes occurring in $Nd^{3+}+Er^{3+}$ system. Thus, a comparison of LIR vs temperature plots in materials undoped and co-doped with Cr^{3+} should represent the influence of processes related only to $Cr^{3+} \leftrightarrow Ln^{3+}$ interaction. However, sorting the host materials into Nd^{3+}, Er^{3+}-co-doped and Nd^{3+}, Er^{3+}, Cr^{3+}-co-doped groups, no correlation was found. Therefore, it was assumed that when the LIR value reaches 50% of its initial value (at 123K), all nonradiative processes are already taken into account. Therefore, the $\Delta T_{1/2}$ parameter was defined as the difference between $T_{1/2}(LIR)$ for 0% Cr^{3+} and 15% Cr^{3+}. Indeed, it was found that $\Delta T_{1/2}$ decreases with $R_{avr}(Cr^{3+}-O^{2-})$ value. These parameters are not directly related, but such a correlation is justified due to the shifting

position of the ^2E states of Cr^{3+} ions. Moreover, to confirm that the host material directly affects the dynamics of the LIR change, the correlation of $\Delta T_{1/2}$ with Dq/B was noticed. However, the most accurate correlation is presented for $\Delta T_{1/2}$ and ΔE, since ΔE takes into account both the effect of host material on Cr^{3+} ions, but also Ln^{3+} ions. This result confirms that it is possible to predict the influence of host material on thermometric properties related to such a complex mechanism as sensitization of Ln^{3+}-based thermometers by Cr^{3+} ions. Finally, S_R values were calculated for the obtained LIR values. As expected, both S_{Rmax} and temperature at which it occurs do not fit into a correlation with any of the parameters mentioned above. Nevertheless, for all investigated host materials an improvement in sensitivity was obtained after co-doping with 15% Cr^{3+} ions. The highest $S_{Rmax}=1.11\% K^{-1}$ was obtained for YAG:Nd^{3+}, Er^{3+}, Cr^{3+}. On the other hand, the most spectacular sensitivity enhancement of 543% was obtained for the $LaGaO_3$ host material. In this case, it should be noted that the processes in the solely Nd^{3+}-Er^{3+} system play an important role in the determination of the relative sensitivity before sensitization. Nevertheless, the proposed mechanism can be considered universal for host materials that have crystallographic sites suitable for Cr^{3+} ions and related research should be further developed to lead to even better thermometric properties.

Contribution of the author's work in [P3]:

synthesis of nanocrystalline phosphors, structural and morphological characterization of materials, conduction of spectroscopic measurements: the excitation spectra, thermal evolution of the emission spectra and thermal evolution of the luminescent decay profiles, analysis and interpretation of data, preparation of original draft of paper

Contribution of the author's work in [P4]:

synthesis of microcrystalline phosphors, structural and morphological characterization of materials, conduction of spectroscopic measurements: the excitation spectra, thermal evolution of the emission spectra and thermal evolution of the luminescent decay profiles, analysis and interpretation of data, preparation of original draft of paper

8.1.4. Cr^{3+} as a luminescent reference [P7]

As presented above, the emission bands of Cr^{3+} ions show pronounced susceptibility to temperature. For this reason, they are widely known as temperature probe for ratiometric thermometry when temperature insensitive emission bands originating from other centers (usually Ln^{3+} ions) play the role of luminescent reference. Such a system provides relatively good relative sensitivity. However, in **[P7]** a particular $CaGa_4O_7$:Mn^{2+} phosphor was presented, which luminescence is enhanced with increasing temperature in the range from 83 to ~583K. Therefore, for this system the Cr^{3+} ions band was chosen as a luminescent reference since its inverse monotonicity of emission signal in a function of temperature with respect to the Mn^{2+} band is advantageous from a thermometric point of view. The unique spectral characteristic features of Mn^{2+} ions in $CaGa_4O_7$ are a result of the structural properties of the host material. In this case, it was found that the localization of Mn^{2+} ions in the 5-fold coordinated trigonal bipyramid of Ca^{2+} ions is more probable than in the tetrahedral sites of Ga^{3+} ions. This is supported by both the electronic charge match between Mn^{2+} and Ca^{2+} ions, as well as the smaller difference between their effective ionic radii compared to Mn^{2+}/Ga^{3+} ions. Despite substitution of 5-fold coordinated Ca^{2+} ions, Mn^{2+} ions form distorted octahedra, and thus may manifest luminescence. Such an interpretation is in agreement with previous reports from literature, according to which the emission of $CaGa_4O_7$:Mn^{2+} with a maximum at 578 nm is spectrally closer to the reported >600 nm range in octahedral coordination than the green emission range for tetrahedral coordination of Mn^{2+} sites. Additionally, as a curiosity, it is worth mentioning that in $CaGa_4O_7$ doped with 0.01% to 2% of Mn^{2+} ions, a narrow band at 652 nm with side band at 665 nm corresponding with Mn^{4+} ions was observed. This may indicate that a small fraction of the manganese ions stabilizes on the 4+ oxidation state substituting Ca^{2+} ions in a 1:2 ratio to compensate the electrical charge. Nevertheless, the aforementioned intriguing thermal performance of $^4T_1 \rightarrow {}^6A_1$ emission band of Mn^{2+} ions should be highlighted. The thermally induced

enhancement of its intensity is observed for Mn^{2+} concentration in the range of 0.01% to 5%. However, the increase in intensity by factor of 14.0 at 550K for 0.05% Mn^{2+} is reduced gradually to a factor of 7.5 for 5% of dopant. To understand the mechanism of emission enhancement as a function of temperature, the thermal evolution of the excited state lifetimes of Mn^{2+} was analyzed. It was found that the average decay time remains almost constant in the range of 123-323K. It increases slightly up to 363K and then gradually shortens to 543K. The simultaneous increase in intensity up to 503K and the shortening of lifetimes above 363K suggests a thermally activated population of a higher emissive state from which the radiative transition becomes symmetry-allowed. However, further studies with the electron paramagnetic resonance (EPR) method should be conducted to confirm this interpretation. Given the beneficial thermometric properties of the thermal enhancement of the Mn^{2+} emission intensity, the need to find an internal reference was noted. For this purpose, Ln^{3+} ions are usually used, which emission intensity remains barely temperature dependent over a wide temperature range, and the spectral position of their emission bands is well known. However, in the case of $CaGa_4O_7:Mn^{2+}$ phosphor, thermally induced quenching of Cr^{3+} emission allowed the use of the opposite trend with increasing temperature to obtain the highest relative sensitivity. The emission spectra of $CaGa_4O_7:Mn^{2+}$, Cr^{3+} were enriched by a broad band in the range of 680-900 nm with local maxima at 691.0 nm and 696.5 nm. These can be attributed to $^2E\rightarrow^4A_2$ (narrow bands) and $^4T_2\rightarrow^4A_2$ (broad band) electronic transitions of Cr^{3+} ions. The occurrence of emission from both transitions indicates intermediate CF of Cr^{3+} octahedra, what was also confirmed by Dq/B calculation. Subsequently, the effect of Cr^{3+} co-doping on the average lifetime of Mn^{2+} ions was investigated. The shortening of $\tau_{avr}(Mn^{2+})$ value indicates process of $Mn^{2+}\rightarrow Cr^{3+}$ ET. Considering two emission bands of Cr^{3+} ions, two LIR values defined

as: $LIR_1 = \dfrac{\int I(^4T_1 \rightarrow {}^6A_1)[Mn^{2+}]d\lambda}{\int I(^2E \rightarrow {}^4A_2)[Cr^{3+}]d\lambda}$ and $LIR_2 = \dfrac{\int I(^4T_1 \rightarrow {}^6A_1)[Mn^{2+}]d\lambda}{\int I(^4T_2 \rightarrow {}^4A_2)[Cr^{3+}]d\lambda}$. For LIR_1, a similar

decrease to 52-56% of initial value at 243K was observed for 0.01%, 0.05% and 0.5% of Cr^{3+} ions, when for 0.1% the almost constant value was found in range of 123-223K. Above 243K a sharp increase was noted for all concentrations, with maximal LIR_1=15.7, 23.1, 49.6 and 14.3 at 583K, respectively, which is associated with an increase in the intensity of Mn^{2+} emission. Above 583K, there is a decrease in LIR_1, which is the effect of thermal quenching of both Mn^{2+} and Cr^{3+} emission. On the other hand, it was found that thermal changes of LIR_2 are less rapid than LIR_1 and thus the maximal values of LIR_2 are lower than LIR_1. This suggests worse temperature uncertainty than for LIR_1. Such a result is caused by the shift of the highest signal intensity of $^4T_2\rightarrow^4A_2$ emission towards higher temperatures of 603K versus 563K for the $^2E\rightarrow^4A_2$ counterpart. It stays in the same temperature range in which the greatest thermal enhancement of Mn^{2+} emission occurs, which inhibits the steeper increase in LIR_2 value. For this reason,

LIR$_1$ was selected as a more representative thermally dependent parameter and the relative sensitivities were determined for it. The highest values of S$_{Rmax}$=2.08%K^{-1} at 403K were obtained for 0.05% Cr^{3+}. However, for 0.01% and 0.05% Cr^{3+} ions S$_R$>1%K^{-1} maintained in the range of 283-523K. For Cr^{3+} concentration in the range 0.01%-0.5%, δT<0.16 K was obtained in the range of 303-503K, and the lowest value of δT=~0.08K was obtained for 0.01% and 0.05% Cr^{3+} ions. Due to the opposite temperature evolution of LIR$_1$ above 583K, the useful temperature range for CaGa$_4$O$_7$:0.01 % Mn^{2+}, 0.05 % Cr^{3+} should be limited to 263-543K. Due to the promising thermal properties of the CaGa$_4$O$_7$:Mn^{2+}, Cr^{3+} phosphor, a 1 mm thick composite film was prepared from the phosphor powder and colorless sanitary silicone for the thermal imaging experiment. Confirming the possibility to cut and form any shape of such material, the film was cut to the shape of a gingerbread man. The experiment involved placing the composite film on a heating plate to induce a temperature gradient along its length and excite it with λ$_{exc}$=254 nm. For each set, two images of the luminescence of Mn^{2+} and Cr^{3+} emissions were taken using optical filters: short-pass at 650 nm and long-pass at 650 nm, respectively, in front of the camera. Excitation light scattering was excluded by an additional long-pass filter at 550 nm. Dividing the two images by each other, the LIR parameter was determined. The LIR calibration curve as a function of temperature was determined using a thermal imaging camera. Its shape in the range between 300 and 500K was found to be similar to that of LIR$_1$. The obtained results can be quantitatively compared by comparing the 2D thermal map prepared with luminescence thermometry and the image from the IR camera. The selectivity of the luminescence thermometry technique should be emphasized, as thermal imaging with the CaGa$_4$O$_7$:Mn^{2+}, Cr^{3+} phosphor is limited only to the spatial region in which the film is placed. In addition, taking two images with a digital camera provides higher resolution in respect to an IR camera. Fundamental studies on CaGa$_4$O$_7$:Mn^{2+}, Cr^{3+} phosphors, supported by proof-of-concept temperature imaging experiment, confirm their applicative potential in luminescence thermometry.

Contribution of the author's work in [P7]:

synthesis of microcrystalline phosphors for proof-of-concept experiment, structural and morphological characterization of materials, preparation of a composite film for proof-of-concept experiment, preparation of proof-of-concept experiment setup and conduction of measurements on it, analysis and interpretation of data, preparation of original draft of paper

8.2. Influence of the structure of the host material on the Mn^{4+} ions luminescence with different roles

8.2.1. Mn^{4+} for ratiometric approach [P8, P9]

Belonging to the same $3d^3$ electronic configuration as Cr^{3+} ions, Mn^{4+} ions also show a significant temperature dependence of luminescence. For this reason, this subchapter describes Mn^{4+} ions as luminescent centers for ratiometric approaches in four different host materials. Firstly, in **[P8]** $Sr_4Al_{14}O_{25}$ phosphor doped with Mn^{4+} and Tb^{3+} ions was investigated. $Sr_4Al_{14}O_{25}$ is an interesting host material for Mn^{4+} doping due to the three octahedral sites (Al_4, Al_5, and Al_6) into which Mn^{4+} ions can locate. Based on the literature, it is known that the more covalent Al_4 and Al_5 sites, rather than the Al_6 sites, are the more preferred by Mn^{4+} ions. Moreover, previous works reported that a constant Mn^{4+} dopant concentration of 0.1% should provide the most intense emission of Mn^{4+} ions in $Sr_4Al_{14}O_{25}$. Therefore, this concentration was adopted in **[P8]**. Nevertheless, the effect of annealing temperature on the luminescent properties of $Sr_4Al_{14}O_{25}$:Mn^{4+} phosphor was verified. It was found that for annealing temperature above 1273K, it is possible to obtain well-crystallized particles with the absence of an amorphous phase. Thus for this annealing temperature, the emission spectra had the characteristic shape for Mn^{4+} ions, i.e. a narrow emission band at 652 nm with broad sideband around 664 nm, both corresponding with $^2E\rightarrow^4A_2$ electronic transition. Due to the preference of Mn^{4+} ions to locate in the two crystallographic sites in $Sr_4Al_{14}O_{25}$, the *Dq/B* parameter was calculated to be 3.06 and 3.23 for Mn^{4+} located in two sites. In addition, an activation energy of ΔE=~2470 cm^{-1} was determined. Subsequently, Tb^{3+} ions was selected as co-dopant due to emission bands that are not spectrally overlapped with Mn^{4+} $^2E\rightarrow^4A_2$ band. The most intense band of Tb^{3+} ions at 545 nm originates from $^5D_4\rightarrow^7F_5$, providing a green luminescence color. Excitation spectra performed for both Tb^{3+} and Mn^{4+} ions in co-doped system did not show the presence of additional excitation bands, indicating the absence of $Mn^{4+}\rightarrow Tb^{3+}$ and $Tb^{3+}\rightarrow Mn^{4+}$ ETs. It indicates that both Mn^{4+} and Tb^{3+} ions are excited directly with λ_{exc}=266 nm. On the other hand, it was observed that Tb^{3+} concentration affects the contribution of Tb^{3+} and Mn^{4+} luminescence in the emission spectra of $Sr_4Al_{14}O_{25}$:Mn^{4+}, Tb^{3+} phosphor. At room temperature, an increase in the intensity of Tb^{3+} emission occurs from 1% to 10% Tb^{3+}. For 20% Tb^{3+} a decrease in their intensity occurred in respect to Mn^{4+}, which may be related to concentration quenching explained in the terms of structural changes in the host material or by energy migration towards the surface quenchers.

When considering the thermal evolution of the emission spectra of Mn^{4+}, Tb^{3+} doped materials, it can be seen that the $^2E\rightarrow^4A_2$ emission band is gradually quenched up to about 483K. However, for 10% and 20% Tb^{3+} concentrations, the thermal quenching rate of the Mn^{4+} band

increases above 423K in respect to lower Tb^{3+} concentrations. Meanwhile, the Tb^{3+} emission intensity remains almost temperature-independent in the range of 123-573K due to the large energy difference between the $^5D_4$ and $^7F_0$ excited states (>14000 cm^{-1}), which hinders the multiphonon

relaxation in this temperature range. For further analysis, $LIR = \dfrac{\int I(^5D_4 \rightarrow ^7F_5)[Tb^{3+}]d\lambda}{\int I(^2E \rightarrow ^4A_2)[Mn^{4+}]d\lambda}$

was defined as thermometric parameter. Irrespective of Tb^{3+} concentration, the LIR value changed only slightly from 123K to 323K. Above 323K, a sharp decrease in LIR value was noticed associated with thermal quenching of Mn^{4+} ions. It stays in agreement with the obtained S_R values, which below 323K do not exceed $S_R=0.5\%\,K^{-1}$. However for 5% of Tb^{3+} concentration, $S_R>2\%\,K^{-1}$ maintained in the range of 353-503K with $S_{Rmax}=2.8\%\,K^{-1}$ at 423K. Moreover, in addition to the satisfactory relative sensitivity, it should be noted that, emission color shifts from bright red at 273K to green at 573K. This aspect was used to verify the applicative potential of $Sr_4Al_{14}O_{25}$:Mn^{4+}, Tb^{3+} phosphor as thermochromic luminescent material. For this purpose, a quartz tube was filled with powder and its bottom was placed on a heating plate. When the heating was turned on, the temperature gradient along the quartz tube deepened as a function of time, which was represented as a change in luminescence color from red to green. Digital camera images were taken at 5s intervals. After experiment, the intensities of red and green channels from RGB images were divided by each other. In this way, 2D LIR maps were created from which LIR profiles were extracted. With the help of the calibration curve, calculated by determining the LIR at different controlled temperatures, it was possible to convert the LIR profiles into temperature profiles. This experiment confirms the feasibility of using Mn^{4+}, Tb^{3+}-doped phosphor for noncontact temperature imaging with a simple digital camera.

In contrast to $Sr_4Al_{14}O_{25}$ host material representing one of the higher Dq/B noted for Mn^{4+} ions, a strategy proposed in **[P9]** leads to lower CF obtained in $SrTiO_3$:Mn^{4+} by modifying its perovskite structure. $SrTiO_3$ has so far been recognized as the host material in which the lowest Dq/B was obtained among Mn^{4+} doped phosphors, and consequently the most shifted emission band towards longer wavelengths (with a maximum at 724 nm). Therefore it was found that among the perovskite structures, there are also other host materials, the so-called Ruddlesden-Popper structures, which general formula is as follows: $Sr_{n+1}Ti_nO_{3n+1}$. Among these, Sr_2TiO_4, $Sr_3Ti_2O_7$ are the two representatives with the lowest n value (*1* and *2*, respectively) and were possible to be synthesized in powder form. In general, the n number refers to the number of layers of Ti-O surrounded by Sr-O double layers. For $SrTiO_3$, $n=\infty$ is assumed due to the lack of the Sr-O double layered slabs. Due to the same electronic charge and similar effective ionic radii, Mn^{4+} ions are expected to locate in 6-fold coordinated Ti^{4+} sites. For this reason, it was assumed that the average Ti-O distance (R_{avr}) should be crucial for changes in the optical properties of R-P structures doped with Mn^{4+} ions. The R_{avr} values were found

in the following order: 1.9556 Å, 1.9517 Å and 1.9271 Å for Sr_2TiO_4, $SrTiO_3$ and $Sr_3Ti_2O_7$, respectively. Moreover, excitation and emission spectra performed at 13K for three host materials were compared at first among experimental studies. The emission bands corresponding with $^2E \rightarrow ^4A_2$ transition adopted maxima at 728.5 nm (~13727 cm^{-1}), 733.2 nm (~13639 cm^{-1}) and 733.6 nm (~13631 cm^{-1}) for Sr_2TiO_4, $SrTiO_3$ and $Sr_3Ti_2O_7$, respectively, which stays in agreement with the order of decreasing R_{avr} value. The barycenters of $^4A_2 \rightarrow ^4T_1$ and $^4A_2 \rightarrow ^4T_2$ excitation bands are arranged in the same order. In addition, it should be emphasized that the experimental data were supported by theoretical studies, which confirm the energies of $^4T_1$, $^4T_2$ and ^2E levels. When describing the emission spectrum of $Sr_3Ti_2O_7$:Mn^{4+} phosphor, an additional broad band observed around 850 nm should be mentioned, which has been attributed to the $^2E \rightarrow ^2T_2$ transition of Ti^{3+} ions. Its presence results from the oxygen vacancies occurring in the structure.

Nevertheless, in fact the spectral position of the maximum of $^2E \rightarrow ^4A_2$ band of Mn^{4+} ions in $Sr_3Ti_2O_7$ host material is the most redshifted position reported so far. To highlight this, the nephelauxetic parameter β_1 was calculated using Racah parameters of R-P materials. Subsequently, a quasi-linear correlation with the energy of ^2E state was presented for R-P materials and other representative host materials from literature. Indeed, Sr_2TiO_4, $SrTiO_3$ and $Sr_3Ti_2O_7$ host materials present the lowest β_1 and $E(^2E)$ values reported so far for Mn^{4+} doped phosphors. On the other hand, it can be noted that so far in the literature the maximum of emission band of $SrTiO_3$:Mn^{4+} was determined at ~724 nm. This is related to the higher measurement temperature, i.e. 80K compared to 13K. Indeed, in the case of the three R-P materials, the maximum of $^2E \rightarrow ^4A_2$ band shifts when the temperature elevates. This is the related with taking the highest impact on the emission band shape by the emission from the higher vibronic levels of $^4A_2$ state in accordance with their thermal promotion. Therefore, for $Sr_3Ti_2O_7$:Mn^{4+} the record emission band maximum reaches values of 733.7-734.2 nm in 13-110K range, which is associated with the vibronic v_3 state. In the range of 120-180K the greatest influence is adopted by the v_4 state with a value of ~728.9 nm, and above 190K shifts to 724.6 nm associated with the v_6 vibronic state. Due to the variable maximum, the thermal evolution of the emission band covering the broad spectral range 670-760 nm was first investigated. In Sr_2TiO_4 and $SrTiO_3$ materials, thermal quenching was found to occur above 250 and 230K, respectively. In the case of $Sr_3Ti_2O_7$:Mn^{4+} phosphor, the same process started above 120K, but correct interpretation may be hampered by overlap with the broad band emission of Ti^{3+} and the occurrence of $Ti^{3+} \rightarrow Mn^{4+}$ ET. Nevertheless, the determined ΔE=2362 cm^{-1}, 2041 cm^{-1} and 1867 cm^{-1}, for Sr_2TiO_4, $SrTiO_3$ and $Sr_3Ti_2O_7$ doped with Mn^{4+} ions, respectively, suggest that the energy difference between the bottom of the ^2E parabola and its intersection with the $^4T_2$ parabola corresponds to the R_{avr} value. It can also be noted that the obtained values are lower than for $Sr_4Al_{14}O_{25}$:Mn^{4+}.

As shown above, the thermal changes of the different spectral regions of the Mn^{4+} emission band can vary considerably between them. On this basis, the 730-745 nm spectral range was selected, where the Mn^{4+} band was quenched most rapidly. On the other hand, it was found that in the range located energetically above the ZPL of Mn^{4+} emission, i.e. 690-705 nm, the intensity increases significantly with increasing temperature. Using two spectral bands with opposite thermal evolution of intensity, the LIR was determined

as follows: $LIR = \dfrac{\int_{690nm}^{705nm} I(^2E \rightarrow {}^4A_2)[Mn^{4+}]d\lambda}{\int_{730nm}^{745nm} I(^2E \rightarrow {}^4A_2)[Mn^{4+}]d\lambda}$. Due to the intense increase in signal intensity

in the 690-705 nm range, LIR values reached an increase to the value in the range of 48-92 at 100K depending on the host material. However, the largest changes were obtained for $Sr_3Ti_2O_7$, which finally reached LIR=977 at 300K. Therefore, the S_{Rmax} calculated for the LIR for $Sr_3Ti_2O_7$:Mn^{4+} phosphor was 10.37% K^{-1} at 40K and did not decline below 3.73% K^{-1} in the range 13-100K. As a result, δT takes values in the range of 0.05-0.12 K between 13 and 200K. However, such large changes in LIR values below 100K result in a flattening of the LIR vs temperature plot above 100K and at 290K the S_R value was less than 0.1% K^{-1}. Therefore, the useful range of a thermometer should be limited to 13-200K. A comparison of the results obtained for different host materials in **[P8]** and **[P9]** confirms the important influence of the composition of host material on the spectroscopic and thermometric properties of the luminescent thermometer. Moreover, the selection of a suitable approach makes it possible to create a promising luminescent thermometer that can operate in really different temperature ranges.

Contribution of the author's work in [P8]:

synthesis of nanocrystalline phosphors, structural and morphological characterization of materials, conduction of spectroscopic measurements: luminescence quantum yields, the excitation spectra, thermal evolution of the emission spectra and thermal evolution of the luminescent decay profiles, preparation of proof-of-concept experiment setup and conduction of measurements on it, analysis and interpretation of data, preparation of original draft of paper

8.2.2. Mn^{4+} for lifetime based approach [P9, P10]

Previous literature has reported that a relatively small ΔE in the $SrTiO_3$:Mn^{4+} phosphor results in an abrupt change in the lifetime of the ^2E state of Mn^{4+} ions and thus good S_R of lifetime-based luminescent thermometer. In papers **[P9]** and **[P10]**, two strategies were proposed to improve the sensitivity of this thermometer. Following the discussion carried out in **[P9]** on the influence of host material composition on the thermal evolution of emission spectra of $SrTiO_3$:Mn^{4+}, Sr_2TiO_4:Mn^{4+} and $Sr_3Ti_2O_7$:Mn^{4+}, it was proposed to analyze the change

in ^2E excited state lifetime as a function of temperature. Similar to the LIR approach, it was found that τ_{avr} do not form a correlation with R_{avr} values of host materials, which is related, among other things, to additional depopulation channels such as ETs or spectral overlap of Mn^{4+} and Ti^{3+} emission bands. In $Sr_2TiO_4:Mn^{4+}$, an almost linear shortening of τ_{avr} from 1.30 ms was recorded in the 13-240K range, while above 240K the quenching rate increased to 340K. For $SrTiO_3$ ^2E state lifetime was $\tau_{avr}=0.54$ ms at 13K and was almost doubled to 80K reaching 1.02 ms. Thereafter, it started to slowly quench, and in the 140-340K range its values were similar to $Sr_2TiO_4:Mn^{4+}$. In contrast, in $Sr_3Ti_2O_7$ a slight elongation from 0.69 ms to 0.75 ms was noted in the range of 13-40K, followed by shortening to 0.54 ms at 140K. Another elongation was obtained in the range of 140-180K, to become progressively quenched from 180 to 300K, similar to the other R-P materials. The elongation of τ_{avr} above 140K may be related to the increasing contribution of lifetime of ^2E state originating from Ti^{3+} ions, which emission band overlaps spectrally with the Mn^{4+} band. This was experimentally confirmed by performing the thermal evolution of lifetimes with increasing wavelength from 724.5 nm to 850.0 nm, shifting from the Mn^{4+} band maximum to the Ti^{3+} counterpart. Nevertheless, τ_{avr} of Mn^{4+} excited state was treated as a thermometric parameter and S_R was determined for them. For $SrTiO_3$, Sr_2TiO_4 and $Sr_3Ti_2O_7$, $S_{Rmax}=3.04\%\,K^{-1}$, $3.70\%\,K^{-1}$ and $4.68\%\,K^{-1}$ were obtained in the range of 280-290K, respectively. However, it should be emphasized that the sharp reduction in lifetimes and the significant reduction in Mn^{4+} intensity will prevent the determination of lifetimes above 320K. According to S_{Rmax}, δT_{min} reaches ~0.10K for $SrTiO_3:Mn^{4+}$ and $Sr_2TiO_4:Mn^{4+}$ around 270-280K, while the lowest $\delta T=0.013$K at 280K was obtained for the $Sr_3Ti_2O_7:Mn^{4+}$ phosphor.

The aim of **[P10]** was to investigate the effect of selected Ln^{3+} (Ln = Lu, Tm, Er, Ho, Dy, Eu, La) on the rate of thermal quenching of lifetime of $^2E(Mn^{4+})$ excited state in $SrTiO_3$. As mentioned, the $^2E\rightarrow^4A_2$ band maximum in $SrTiO_3:Mn^{4+}$ is at ~724 nm above 80K. The higher vibrational states of ^2E parabola are gradually occupied with increasing temperature, until the temperature at which thermal energy exceeds ΔE and nonradiative process becomes the second depopulation channel of the ^2E level (after radiative one). However, when Ln^{3+} ions are present as co-dopants in the host material, two additional processes may occur. First is the $Mn^{4+}\rightarrow Ln^{3+}$ ET, which can occur with the assistance of phonon. However, similar to what was presented for the $MgTiO_3:Cr^{3+}$, Nd^{3+} phosphor in **[P2]**, the presence of Ln^{3+} ions in the $SrTiO_3$ structure leads to the stabilization of Ti^{3+} ions that are optically active. For this reason, another process to be considered is $Mn^{4+}\rightarrow Ti^{3+}$ ET. The occurrence of this process was confirmed by the difference between thermal evolution of emission spectra of $SrTiO_3$ doped with Mn^{4+} ions and co-doped with Mn^{4+} and optically inactive La^{3+}/Lu^{3+} ions. Moreover, this was confirmed by the similar shortening of the ^2E state lifetime of Mn^{4+} at 123K when doping

with both La^{3+}/Lu^{3+} and other optically active Ln^{3+} ions. As a representative example, the shortening from τ_{avr}=1.72 ms at 123K for $SrTiO_3$:Mn^{4+} to 0.53 ms for $SrTiO_3$:Mn^{4+}, Tm^{3+} phosphor can be pointed.

Comparing the effect of different Ln^{3+} ions on the thermal evolution of ^2E lifetimes may be too complex due to the similar shape of the curves. However, the calculation of S_A and S_R values allows a quantitative comparison of Mn^{4+}, Ln^{3+} doped phosphors. In the first case, the highest S_{Amax}=14.93 μsK^{-1} at 273K was obtained for $SrTiO_3$ doped singly with Mn^{4+} ions. This is related to the fact that shorter τ_{avr} values for co-doped materials result in lower S_A values. On the other hand, the S_R confirm an improvement in the variability of τ_{avr} as a thermometric parameter. The best S_{Rmax}=5.19%K^{-1} at 298K was achieved for $SrTiO_3$:Mn^{4+},Tm^{3+}, resulting in a 145% improvement in sensitivity in respect to S_R=3.57%K^{-1} at 318K for singly Mn^{4+} doped counterpart. Improvements in sensitivity were also obtained when $SrTiO_3$:Mn^{4+} was doped with Er^{3+}, Eu^{3+}, Dy^{3+}, Ho^{3+} and Lu^{3+} ions. Only for the La^{3+} co-doped system a lower S_R value was obtained, which is related to the lower slope of the $\tau_{avr}(T)$ dependence. However, due to the improved sensitivity, a lower δT_{min}=0.020K for $SrTiO_3$:Mn^{4+}, Tm^{3+} in respect to δT=0.034 K for $SrTiO_3$:Mn^{4+} phosphor was also achieved. The approach presented in **[P10]** confirms that $Mn^{4+} \rightarrow Ln^{3+}$ ET can significantly improve thermometric properties in Mn^{4+} lifetime-based strategy.

Contribution of the author's work in [P9]:

the conceptualization, synthesis of nano-/microcrystalline phosphors, structural and morphological characterization of materials, conduction of spectroscopic measurements: the excitation and emission spectra, analysis and interpretation of data, preparation of original draft of paper

Contribution of the author's work in [P10]:

synthesis of nanocrystalline phosphors, structural and morphological characterization of materials, conduction of spectroscopic measurements: the excitation spectra, thermal evolution of the emission spectra and thermal evolution of the luminescent decay profiles, analysis and interpretation of data, preparation of original draft of paper

8.2.3. Mn^{4+} as a sensitizer in Ln^{3+}-based luminescent thermometers [P3]

In the case of Mn^{4+} ions, as for Cr^{3+} ions, it has also been proposed that the higher absorption cross section and higher temperature susceptibility of the luminescence with respect to Ln^{3+} ions may be beneficial for Ln^{3+}-based ratiometric thermometry. Therefore, the effect of Mn^{4+} concentration on the thermometric performance of $Y_3Al_5O_{12}$:Tb^{3+}, Eu^{3+} phosphors was investigated in **[P3]**. Comparing the emission spectra of phosphors, it can be seen

that the $^2E \rightarrow ^4A_2$ emission band of Mn^{4+} ions is no longer detectable above 2% of Mn^{4+} concentration, suggesting the occurrence of the $Mn^{4+} \rightarrow Ln^{3+}$ ET. Excitation spectra detected for Mn^{4+} emission consist of, among others, the narrow bands originating from $^7F_0 \rightarrow ^5L_7$, $^7F_0 \rightarrow ^5L_6$, $^7F_0 \rightarrow ^5D_3$ electronic transitions of Eu^{3+}, confirming the $Mn^{4+} \rightarrow Eu^{3+}$ ET. The probability of this process is increasing effectively, since above 5% Mn^{4+} additional Eu^{3+} excitation bands ($^7F_0 \rightarrow ^5D_2$) appear on the Mn^{4+} excitation spectra. Moreover, the shortening of lifetimes of $^2E(Mn^{4+})$ excited state when Mn^{4+} increases suggests an increase in the probability of $Mn^{4+} \rightarrow Ln^{3+}$ ET. On the other hand, lifetimes of Tb^{3+} and Eu^{3+} also shorten with increasing Mn^{4+} concentration. This may be related to a $Ln^{3+} \rightarrow Mn^{4+}$ back energy transfer, which further affects thermometric performance on the YAG:Tb^{3+}, Eu^{3+}, Mn^{4+} phosphors. The increasing impact of the coexisting ETs and BETs between Mn^{4+} and Tb^{3+}/Eu^{3+} ions resulted in a gradual increase in S_R value with increase of Mn^{4+} concentration, until reaching $S_{Rmax}=0.28\%\,K^{-1}$ at 268K. This represents an improvement in S_R value by over 300% in respect to counterpart unco-doped with Mn^{4+} ions. Nevertheless, $\delta T_{min}=4K$ was obtained due to the relatively small S_R.

When comparing the potential of Mn^{4+} and Cr^{3+} ions for the sensitization approach, it was noted that Cr^{3+} ions are generally characterized by a higher absorption cross section in respect to Mn^{4+} ions. More importantly, since Cr^{3+} may be located in both strong, intermediate and weak CF depending on the host material provides a wider energy range in which excited states of Cr^{3+} can be found in respect to Mn^{4+} ions. This allows a more flexible design of the energy mismatch between excited states of Cr^{3+} and Ln^{3+} ions and thus temperature at which ET activates. For the above reasons, Cr^{3+} ions are a more versatile representative of TM ions for developing a sensitization strategy.

9. Conclusions

The main objective of the doctoral dissertation was to investigate the effect of host material on the spectroscopic and thermometric properties of phosphors doped with $3d^3$ ions, i.e. Mn^{4+} and Cr^{3+}. For this purpose, a series of materials that are suitable for doping with Cr^{3+} and Mn^{4+} ions were selected (Table 3). The selected materials were synthesized using solid state and Pechini methods, resulting in micro- and nanoscopic size of particles. Considering the *Dq/B* parameter, it is known that Mn^{4+} ions are always situated in strong CF. However, in the case of Cr^{3+} ions the selected host materials provided both strong and intermediate CF. The above-mentioned variables highlight the wide range of structural and spectroscopic properties (two optical centers located in the different host materials with different CF) that were taken into account within the doctoral dissertation.

At first, it should be emphasized that fundamental studies devoted to the study of the luminescence of $3d^3$ and Ln^{3+} ions as a function of temperature have proved to be a useful tool in the analysis of the structure of host material. In **[P1]**, it was confirmed that high annealing temperature is a sufficient factor to achieve stabilization of Cr^{3+} and Cr^{4+} in $Y_3Al_{5-x}Ga_xO_{12}$ garnets, without additional electrical charge compensation. Furthermore, by analyzing the distribution of Al^{3+} and Ga^{3+} ions in octahedral and tetrahedral sites as a function of Ga^{3+} content, it was suggested that the lowest symmetry should be expected for x=4 ($Y_3AlGa_4O_{12}$) and x=2 ($Y_3Al_3Ga_2O_{12}$) in the case of octahedra and tetrahedra, respectively. This is related to the presence of only one other ion in the first coordination sphere. This phenomenon was correlated with the $T_{1/2}$ value of Cr^{3+} and Cr^{4+} emission, which was the lowest for x=4 and x=2, respectively. In **[P2]** and **[P10]** confronting the difference between effective ionic radii led to the finding that Cr^{3+} ions in $MgTiO_3$ locate in crystallographic positions of Mg^{2+}, while Mn^{4+} ions in $SrTiO_3$ locate in positions of Ti^{4+} ions. Additionally, in $MgTiO_3$ the exceptionally low symmetry of the Mg^{2+} site led to the observation of broad emission bands of Nd^{3+} ions, which is in contrast to most host materials, including $SrTiO_3$, where the shape of emission bands of Ln^{3+} typically consisted in numerous Stark compounds. On the other hand, both works confirmed the stabilization of Ti^{3+} ions located near Ln^{3+} or Cr^{3+} ions in $X^{2+}Ti^{4+}O_3$ perovskites. This has important implications for the thermometric performance of phosphors since ^2E excited state of Ti^{3+} ions can provide an additional depopulation channel for the excited state of Cr^{3+}, Mn^{4+} or Ln^{3+} ions. In **[P7]** in $CaGa_4O_7$ spectroscopic studies confirmed the formation of Cr^{3+} distorted octahedra at the 5-fold coordinated sites of Ca^{2+} cations. Furthermore, in addition to the dominant presence of Mn^{2+} ions in $CaGa_4O_7$ doped with manganese ions, luminescence of Mn^{4+} ions was observed. This suggests that a small fraction of Mn^{4+} ions substitutes Ca^{2+} in a 1:2 ratio to compensate for the electrical charge and forms even stronger distorted octahedra. This is another example, after Ti^{3+} in $MgTiO_3:Cr^{3+}$, $MgTiO_3:Ln^{3+}$ and $SrTiO_3:Ln^{3+}$, confirming the occurrence of an additional unintentional luminescent centers that affects the spectroscopic properties of the remaining dopants.

Furthermore, to demonstrate the versatility of TM ions with $3d^3$ electronic configuration, their potential in luminescence thermometry based on three strategies was analyzed: (1) ratiometric and (2) lifetime-based approaches considering the luminescence of $3d^3$ ions as a figure of merit, but also (3) the sensitization of Ln^{3+} ratiometric-based thermometers by $3d^3$ ions. These three approaches are summarized within Table 4, 5 and 6, respectively. The ratiometric approach considered emission bands of $3d^3$ ions associated with both $^2E \rightarrow ^4A_2$ **[P1, P8, P9]** and $^4T_2 \rightarrow ^4A_2$ **[P2, P7]** (Table 4). The emission maximum for Mn^{4+} ions in the selected host materials is reached between 652.5 and 734.2 nm, while for Cr^{3+} the emission from the ^2E level was detected in the range from 687.4 nm to 733.5 nm, and from $^4T_2$ in the range

from 716 to 835 nm. For this approach, the highest $|S_{Rmax}|=10.37\%\,K^{-1}$ at 43K and the associated lowest $\delta T_{min}=0.05K$ were obtained for $Sr_3Ti_2O_7$:0.1% Mn^{4+} (Figure 8a). However, it is also worth noting the $|S_{Rmax}|=1.98\%\,K^{-1}$ at 303K calculated for $Y_3Ga_5O_{12}$:1% $Cr^{3+/4+}$, as well as $|S_{Rmax}|=2.80\%\,K^{-1}$ at 423K for $Sr_4Al_{14}O_{25}$:0.1% Mn^{4+}, 5% Tb^{3+}. This indicates the wide temperature range over which the proposed luminescent thermometers can operate. This is an expected effect due to the broad values range of $T_{1/2}$ reaching from 60 to 488K. Satisfactory S_{Rmax} values exceeding $1.00\%\,K^{-1}$ obtained for most materials are the result of enhanced thermal quenching of $3d^3$ ions through additional phonon assisted energy transfers.

A strategy using the lifetime of $3d^3$ ions excited state as a figure of merit has mostly focused on the ^2E level of Mn^{4+} [P9, P10], but in [P2] the lifetime of $^4T_2$ of Cr^{3+} ions was also used (Table 5). This is related to the greater application potential of luminescence decay profiles of ^2E, which are in general two orders of magnitude longer than those of $^4T_2$ state (for example 1.30 ms for Sr_2TiO_4:0.1% Mn^{4+} in respect to 23.8 μs for $MgTiO_3$:0.1% Cr^{3+}). Longer lifetimes also encourage the inclusion of additional processes of ETs, which will provide more rapid changes in lifetimes as a function of temperature and thus greater S_R values. On the other hand, the use of the $^4T_2$ state allows a spectral shift of both excitation and emission towards shorter wavelengths, more suitable for bioapplications. This concept has been proposed for Cr^{3+} in $MgTiO_3$ host material. However, $S_{Rmax}>1.00\%\,K^{-1}$ was achieved for both lifetimes of ^2E and $^4T_2$. The highest result obtained for $SrTiO_3$:0.1% Mn^{4+}, 1% Tm^{3+} equal to $5.19\%\,K^{-1}$ at 298K (Figure 8b). Furthermore, all maximum S_R values were achieved close to the physiological temperature range, i.e. from 280 to 383K. Therefore, $S_R(300K)$ even reached $5.16\%\,K^{-1}$.

Finally, Table 6 summarizes the phosphors used to demonstrate the sensitization strategy of Ln^{3+} ratiometric thermometers by $3d^3$ ions. Using phonon assisted energy transfers occurring between TM and Ln^{3+} ions, it has been demonstrated that enhancement of relative sensitivity in Tb^{3+}-Eu^{3+} pair as well as Nd^{3+}-Er^{3+} is possible. For the first pair of ions it was demonstrated in YAG using Cr^{3+} and Mn^{4+} ions achieving 180% and 310% improvement in sensitivity, respectively. Additionally, co-doping with Cr^{3+} allowed the excitation wavelength to be shifted from 266 nm to 445 nm for simultaneous effective detection of Tb^{3+} and Eu^{3+} emission, which is beneficial from an application point of view. Further studies on the sensitization mechanism were continued with Cr^{3+} ions as a sensitizer, which generally show a higher absorption cross-section than Mn^{4+}, as well as a greater effect of the sensitization process on the host material since their absorption bands can shift more as the CF changes from strong to weak. For the Nd^{3+}-Er^{3+} pair, YAG:1% Nd^{3+}, 1% Er^{3+}, 20% $Cr^{3+/4+}$ proved to be the representative material, which $S_{Rmax}=1.67\%\,K^{-1}$ at 300K in respect to $0.25\%\,K^{-1}$ for counterpart without sensitizer (Figure 8c). This results in a sensitivity improvement of more than 660%. In this case, Cr^{4+} ions played an important role as an energy bridge between Nd^{3+} and Er^{3+} ions. However, an even higher

value of 540% was achieved for $LaGaO_3$:1% Nd^{3+}, 1% Er^{3+}, 15% Cr^{3+}, in which Cr^{4+} ions could not be located due to the lack of tetragonal sites. This confirms the exclusive beneficial effect of Cr^{3+} ions as a sensitizer. On the other hand, in YAG:Nd^{3+}, Er^{3+}, $Cr^{3+/4+}$ phosphor it was confirmed that a much higher absorption cross-section of Cr^{3+} ions in respect to Ln^{3+} ions leads to an enhancement of brightness of the phosphor. The factor of ~30 for the brightness improvement was achieved for YAG:1% Nd^{3+}, 1% Er^{3+}, 20% $Cr^{3+/4+}$ in respect to the $Cr^{3+/4+}$ unco-doped counterpart. This is particularly significant since brightness is a parameter that, at the same time as relative sensitivity S_R, is responsible for improving temperature determination uncertainty. It can be said that improving brightness plays as important a role in sensitization approach as improving S_R. Finally, a comparison of thermal evolution of LIR=Nd^{3+}/Er^{3+} in five host materials co-doped and unco-doped with Cr^{3+} ions allowed us to determine the dependence of $\Delta T_{1/2}$ on the energy difference occurring between the first excited state of Cr^{3+} ions and the nearest excited state of Nd^{3+} ions, i.e. $^4F_{7/2}$, $^4S_{3/2}$ levels. This suggests that there is a dominant thermally induced energy transfer between these levels. This also allows a preliminary prediction of the performance of this process in the new host materials, since the trend between $\Delta T_{1/2}$ and *Dq/B* has also been determined.
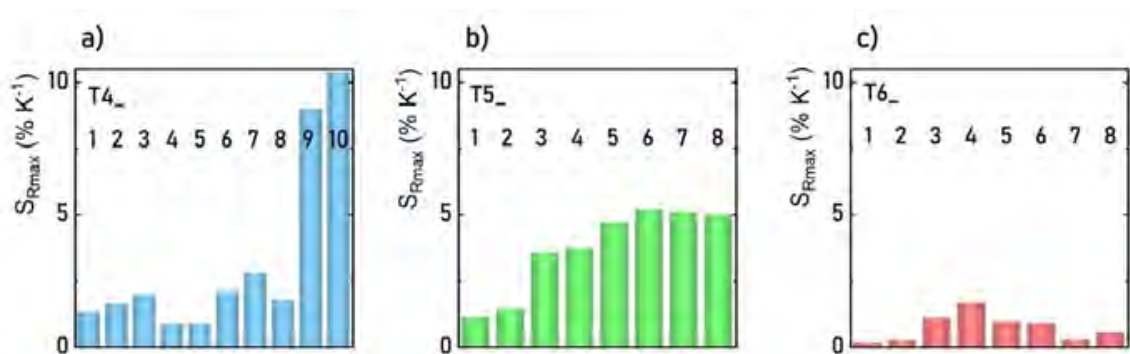
Figure 8. Comparison of S_{Rmax} values obtained for representative thermometers
for ratiometric –a), lifetime – b) and sensitization approaches – c).

The presented approaches demonstrate the versatility of *3d³* ions as optically active centers in phosphors but also find their role in many strategies used in luminescence thermometry. The highest S_R value among the presented materials is presented by the $Sr_3Ti_2O_7$:0.1% Mn^{4+} based LIR-based approach with S_R=10.37% K^{-1}. On the other hand, the lifetime based strategy in $SrTiO_3$:0.1% Mn^{4+}, 1% Tm^{3+} phosphor provided the highest S_R=5.19% K^{-1} in the around-room temperature range (298K). In this case, however, it should be remembered that the applicability of the luminescent thermometer depends on many factors, i.e. temperature operating range, but also excitation and emission spectral range, spatial and temporal resolution, the size and shape of particles, stability in different solutions, toxicity, etc. From this point of view,

it is worth mentioning that the studies carried out in **[P7]** were supported by cytotoxicity assessments, which confirmed that $CaGa_4O_7:Mn^{2+}$, Cr^{3+} shows no toxicity issues in the analyzed concentration of the particle range. Moreover, in **[P2]** a positive effect of silica coating on the reduction of toxicity of $MgTiO_3:Cr^{3+}$, Nd^{3+} nanoparticles on MDCK and 3T3 cells was found. Such conducted studies serve as a step forward towards food related or biological applications of investigated phosphors. On the other hand, proof-of-concept experiments performed in **[P9]** and **[P7]** confirm that Mn^{4+} and Cr^{3+} co-doped materials have high application potential in thermal imaging. In both cases, a major advantage of the presented applications is the possibility to perform them with a simple digital camera.

In conclusion, the dependence of the luminescent and thermometric properties of TM ions with $3d^3$ electronic configuration on the chemical composition of host materials is undoubtedly a unique feature that ensures that materials doped with Mn^{4+} and Cr^{3+} ions have a wide application potential in luminescent thermometry. The knowledge accumulated in the present form allows for the design of luminescent thermometers on demand, but studies should be continued in order to have a good understanding of all the processes occurring in Mn^{4+}/Cr^{3+} doped systems so that direct correlations between luminescent and structural properties can be determined.

Table 3. Comparison of general characterization of representative samples included in a doctoral dissertation.

publication No.	sample composition	dopants localization	average particle size (nm)	R(M-O)$_{avr}$ (Å)	β_1	Dq/B
	$Y_3Al_5O_{12}$:1% $Cr^{3+/4+}$	$Cr^{3+} \to (Al/Ga)^{3+}_{octa}$; $Cr^{4+} \to (Al/Ga)^{3+}_{tetra}$	-	1.924	-	2.649
P1	$Y_3Al_3Ga_2O_{12}$:1% $Cr^{3+/4+}$	$Cr^{3+} \to (Al/Ga)^{3+}_{octa}$; $Cr^{4+} \to (Al/Ga)^{3+}_{tetra}$	-	1.936	-	2.597
	$Y_3Ga_5O_{12}$:1% $Cr^{3+/4+}$	$Cr^{3+} \to (Al/Ga)^{3+}_{octa}$; $Cr^{4+} \to (Al/Ga)^{3+}_{tetra}$	-	2.038	-	2.578
P2	$MgTiO_3$:0.1% Cr^{3+}	$Cr^{3+} \to Mg^{2+}$; -	40	2.024	-	**1.86**
	$MgTiO_3$:0.1% Cr^{3+}, 2% Nd^{3+}	$Cr^{3+} \to Mg^{2+}$; $Nd^{3+} \to Mg^{2+}$	26	2.024	-	-
P3	$Y_3Al_5O_{12}$:1% Tb^{3+}, 1% Eu^{3+}, 5% Cr^{3+}	$Cr^{3+} \to Al^{3+}_{octa}$; $(Tb/Eu)^{3+} \to Y^{3+}$	90	1.924	-	-
	$Y_3Al_5O_{12}$:1% Tb^{3+}, 1% Eu^{3+}, 10% Mn^{4+}	$Mn^{4+} \to Al^{3+}_{octa}$	90	1.924	-	-
P4, P6	$Y_3Al_5O_{12}$:1% Nd^{3+}, 1% Er^{3+}, 15% $Cr^{3+/4+}$	$Cr^{3+} \to Al^{3+}_{octa}$; $(Nd/Er)^{3+} \to Y^{3+}$	-	1.924	-	**3.10**
P5, P6	$GdScO_3$:1% Nd^{3+}, 1% Er^{3+}, 15% Cr^{3+}	$Cr^{3+} \to Sc^{3+}$; $(Nd/Er)^{3+} \to Gd^{3+}$	-	2.098	-	2.47
	$Y_3Al_2Ga_3O_{12}$:1% Nd^{3+}, 1% Er^{3+}, 15% Cr^{3+}	$Cr^{3+} \to (Al/Ga)^{3+}_{octa}$; $(Nd/Er)^{3+} \to Y^{3+}$	-	1.936	-	2.96
P6	$LaScO_3$:1% Nd^{3+}, 1% Er^{3+}, 15% Cr^{3+}	$Cr^{3+} \to Sc^{3+}$; $(Nd/Er)^{3+} \to La^{3+}$	-	2.102	-	2.46
	$LaGaO_3$:1% Nd^{3+}, 1% Er^{3+}, 15% Cr^{3+}	$Cr^{3+} \to Ga^{3+}$; $(Nd/Er)^{3+} \to La^{3+}$	-	1.977	-	2.83
P7	$CaGa_4O_7$:0.01% Mn^{2+}, 0.05% Cr^{3+}	$Cr^{3+} \to Ca^{2+}$; $Mn^{2+} \to Ca^{2+}$	228	2.300	-	2.06
P8	$Sr_4Al_{14}O_{25}$:0.1% Mn^{4+}	$Cr^{3+} \to Al^{3+}_{octa}$; $Tb^{3+} \to Sr^{2+}$	90	1.906	-	3.01/3.23
P9, P10	$SrTiO_3$:0.1% Mn^{4+}	-	27/29	1.952	0.902	2.47
P9	Sr_2TiO_4:0.1% Mn^{4+}	$Mn^{4+} \to Ti^{4+}$	62	1.956	0.922	-
P9	$Sr_3Ti_2O_7$:0.1% Mn^{4+}	-	133	1.927	0.904	-
P10	$SrTiO_3$:0.1% Mn^{4+}, 1% Tm^{3+}	$Ln^{3+} \to Sr^{2+}$	25	1.952	-	2.47

Table 4. Comparison of luminescent properties of ratiometric-based luminescent thermometers included in a doctoral dissertation.

sample No.	publication No.	sample composition	λ^{em}_{max} (nm)	3d³ electronic transition	LIR definition	$|S_{Rmax}|$ (%K^{-1})	$T(S_{Rmax})$ (K)	$|S_R(300K)|$ (%K^{-1})	δT_{min} (K)	$T_{1/2}$ (3d³) (K)	confirmed ETs
T4_1		Y$_3$Al$_5$O$_{12}$: 1% Cr$^{3+/4+}$	687.4		$\dfrac{\int_{686nm}^{691nm} I(^2E \to {}^4A_2)[Cr^{3+}]d\lambda}{\int_{1260nm}^{1500nm} I(^3B_2 \to {}^3B_1)[Cr^{4+}]d\lambda}$	1.3	323	1.06	-	308.8	
T4_2	P1	Y$_3$Al$_3$Ga$_2$O$_{12}$: 1% Cr$^{3+/4+}$	688.2	$^2E \to {}^4A_2$		1.64	463	0.32	-	224.6	Cr$^{3+}\to$Cr^{4+}; Cr$^{4+}\to$Cr^{3+}
T4_3		Y$_3$Ga$_5$O$_{12}$: 1% Cr$^{3+/4+}$	690.2			1.98	303	**1.98**	-	258.9	
T4_4		MgTiO$_3$: 0.1% Cr^{3+}	733.5; 835		$\int_{950nm}^{967nm} I\left(\begin{array}{c}(^4T_2 \to {}^4A_2)[Cr^{3+}]+\\(^2F_{9/2} \to {}^4I_{9/2})[Nd^{3+}]\end{array}\right)d\lambda$	0.85	223	<0.01	-	223	Cr$^{3+}\to$Ti^{3+}
T4_5	P2	MgTiO$_3$: 0.1% Cr^{3+}, 2% Nd^{3+}	733.5; **835**	$^2E \to {}^4A_2$ and $^4T_2 \to {}^4A_2$	$\int_{710nm}^{717nm} I(^2E \to {}^2T_2)[Ti^{3+}]d\lambda$	0.87	483	0.21	-	203	Cr$^{3+}\to$Ti^{3+}; Nd$^{3+}\to$Ti^{3+}
T4_6	P7	CaGa$_2$O$_7$: 0.01% Mn^{2+}, 0.05% Cr^{3+}	696.5; 716		$\dfrac{\int_{542nm}^{617nm} I(^4T_1 \to {}^6A_1)[Mn^{2+}]d\lambda}{\int_{732nm}^{802nm} I(^4T_2 \to {}^4A_2)[Cr^{3+}]d\lambda}$	2.08	403	1.35	0.09	**488**	Mn$^{2+}\to$Cr^{3+}
T4_7	P8	Sr$_4$Al$_{14}$O$_{25}$: 0.1% Mn^{4+}, 5% Tb^{3+}	**652.5**		$\dfrac{\int_{541nm}^{554nm} I(^5D_4 \to {}^7F_5)[Tb^{3+}]d\lambda}{\int_{650nm}^{658nm} I(^2E \to {}^4A_2)[Mn^{4+}]d\lambda}$	2.80	423	0.59	0.42	363	-
T4_8	P9	SrTiO$_3$: 0.1% Mn^{4+}	733.2@13K; 723.7@83K	$^2E \to {}^4A_2$		1.76	13	1.45	0.12	**60**	Mn$^{4+}\to$Ti^{3+}
T4_9		Sr$_2$TiO$_4$: 0.1% Mn^{4+}	728.5@13K; 723.4@83K		$\int_{690nm}^{705nm} I(^2E \to {}^4A_2)[Mn^{4+}]d\lambda$	8.99	43	0.08	0.06	273	Mn$^{4+}\to$Ti^{3+}
T4_10	P9	Sr$_3$Ti$_2$O$_7$: 0.1% Mn^{4+}	733.6@13K; **734.2@83K**		$\int_{730nm}^{745nm} I(^2E \to {}^4A_2)[Mn^{4+}]d\lambda$	**10.37**	43	-	**0.05**	140	Mn$^{4+}\to$Ti^{3+}; Ti$^{3+}\to$CT; Mn$^{4+}\to$CT

* The $T_{1/2}$ parameter was determined for comparison purposes, despite the knowledge that it may be subject to error (overestimation) due to the lack of stability of the intensity signal in the low temperature range.

Table 5. Comparison of luminescent and thermometric properties of lifetime-based luminescent thermometers included in a doctoral dissertation.

sample No.	publication No.	sample composition	λ^{em}_{max} (nm)	excited state	initial τ (ms)	τ@300K (ms)	$\|S_{Rmax}\|$ (%K^{-1})	T(S_{Rmax}) (K)	$\|S_R(300K)\|$ (%K^{-1})	δT_{min} (K)	T$_{1/2}$ (K)	confirmed ETs
T5_1		MgTiO$_3$: 0.1% Cr^{3+}	835	^{4}T$_2$	**23.8·10^{-3}** @83K	**13.4·10^{-3}**	1.13	323	1.11	-	313	Cr^{3+}→Ti^{3+}
T5_2	P2	MgTiO$_3$:0.1% Cr^{3+}, 2% Nd^{3+}	835	^{4}T$_2$	38.3·10^{-3} @83K	30.3·10^{-3}	1.41	**383**	0.86	-	353 *	Cr^{3+}→Ti^{3+}; Nd^{3+}→Ti^{3+}
T5_3	P9, P10	SrTiO$_3$: 0.1% Mn^{4+}	733.2@13K; 723.7@83K	^{2}E	0.54@13K; 0.93@123K	**0.16**	3.57	318	3.45	0.10	253 (in respect to τ@83K); 283 (in respect to τ@13K) *	Mn^{4+}→Ti^{3+}
T5_4		Sr$_2$TiO$_4$: 0.1% Mn^{4+}	728.5@13K; 723.4@83K	^{2}E	**1.30@13K**; 0.98@123K	0.11	3.71	290	3.68	0.10	253 (in respect to τ@13K) *	Mn^{4+}→Ti^{3+}
T5_5	P9	Sr$_3$Ti$_2$O$_7$: 0.1% Mn^{4+}	733.6@13K; 734.2@83K	^{2}E	0.69@13K; 0.55@123K	0.05	4.68	280	4.43	**0.013**	**233** (in respect to τ@13K) *	Mn^{4+}→Ti^{3+}; Ti^{3+}→CT and Mn^{4+}→CT
T5_6		SrTiO$_3$:0.1% Mn^{4+}, 1% Tm^{3+}	723.7@83K	^{2}E	0.54@123K	0.033	**5.19**	298	**5.16**	0.02	253 *	
T5_7	P10	SrTiO$_3$:0.1% Mn^{4+}, 1% Er^{3+}	723.7@83K	^{2}E	0.78@123K	0.033	5.10	290	5.03	<0.05	243 *	Mn^{4+}→Ln^{3+}; Mn^{4+}→Ti^{3+}
T5_8		SrTiO$_3$:0.1% Mn^{4+}, 1% Eu^{3+}	723.7@83K	^{2}E	0.91@123K	0.059	5.00	301	4.99	<0.05	243	

* The T$_{1/2}$ parameter was determined for comparison purposes, despite the knowledge that it may be subject to error (overestimation) due to the lack of stability of the lifetimes in the low temperature range.

Table 6. Comparison of thermometric properties of Ln^{3+}-based luminescent thermometers sensitized by Cr^{3+}/Mn^{4+} ions included in a doctoral dissertation.

sample No.	publication No.	sample composition	LIR definition	confirmed ETs	$\|S_{Rmax}\|$ (%K^{-1})	T(S$_{Rmax}$) (K)	$\|S_R(300K)\|$ (%K^{-1})	$\|S_R\|$ without sensitizer (%K^{-1})	sensitivity enhancement
T6_1		Y$_3$Al$_5$O$_{12}$:1% Tb^{3+}, 1% Eu^{3+}, 5% Cr^{3+}	$\int_{576nm}^{603nm} I(^5D_0 \to {}^7F_1)[Eu^{3+}]d\lambda$	Cr^{3+}→(Tb/Eu)$^{3+}$; (Tb/Eu)$^{3+}$→Cr^{3+}; Tb^{3+}→Eu^{3+}	0.16	483	0.15	0.09	180%
T6_2	P3	Y$_3$Al$_5$O$_{12}$:1% Tb^{3+}, 1% Eu^{3+}, 20% Mn^{4+}	$\int_{535nm}^{572nm} I(^5D_4 \to {}^7F_5)[Tb^{3+}]d\lambda$	Mn^{4+}→(Tb/Eu)$^{3+}$; (Tb/Eu)$^{3+}$→Mn^{4+}; Tb^{3+}→Eu^{3+}	0.28	263	0.26	0.09	310%
T6_3	P6	Y$_3$Al$_5$O$_{12}$:1% Nd^{3+}, 1% Er^{3+}, 15% Cr$^{3+/4+}$	$\dfrac{\int_{1063nm}^{1089nm} I(^4F_{3/2} \to {}^4I_{11/2})[Nd^{3+}]d\lambda}{\int_{1514nm}^{1569nm} I(^4I_{13/2} \to {}^4I_{15/2})[Er^{3+}]d\lambda}$	Cr^{3+}→(Nd/Er)$^{3+}$; (Nd/Er)$^{3+}$→Cr^{3+}; Nd^{3+}→Cr^{4+}→Er^{3+}; Cr^{3+}→Cr^{4+}	1.11	384	0.71	0.25	444%
T6_4	P4	Y$_3$Al$_5$O$_{12}$:1% Nd^{3+}, 1% Er^{3+}, 20% Cr$^{3+/4+}$			**1.67**	300	**1.67**	0.25	668%
T6_5	P5, P6	GdScO$_3$:1% Nd^{3+}, 1% Er^{3+}, 15% Cr^{3+}			0.96	301	**0.96**	0.34	285%
T6_6		Y$_3$Al$_2$Ga$_3$O$_{12}$:1% Nd^{3+}, 1% Er^{3+}, 15% Cr^{3+}		Cr^{3+}→(Nd/Er)$^{3+}$; (Nd/Er)$^{3+}$→Cr^{3+}; Nd^{3+}→Er^{3+}	0.90	340	0.86	0.18	499%
T6_7	P6	LaScO$_3$:1% Nd^{3+}, 1% Er^{3+}, 15% Cr^{3+}			0.29	203	0.14	0.14	209%
T6_8		LaGaO$_3$:1% Nd^{3+}, 1% Er^{3+}, 15% Cr^{3+}			0.54	239	0.59	0.10	**543%**

10. Copies of publications constituting the cycle of the doctoral dissertation

Revisiting $Y_3Al_{5-x}Ga_xO_{12}$ Solid Solutions Doped with Chromium Ions: Effect of Local Symmetry on Thermal Quenching of Cr^{3+} and Cr^{4+} Ions

W. M. Piotrowski,[z] [iD] **V. Kinzhybalo, and L. Marciniak[z]** [iD]

Institute of Low Temperature and Structure Research, Polish Academy of Sciences, 50–422 Wroclaw, Poland

The oxidation of chromium ions to the 4+ state in phosphors doped with Cr^{3+} ions is often considered negative due to the activation of the parasitic $Cr^{3+} \rightarrow Cr^{4+}$ luminescence quenching channel. However, in this paper, a systematic study of the effect of host material stoichiometry on the spectroscopic properties of Cr^{4+} in $Y_3Al_{5-x}Ga_xO_{12}$ is investigated to develop ratiometric luminescence thermometers. Correlations between the structural properties of the host and the luminescence thermal quenching process of Cr^{4+} ions emission associated with the $^3B_2 \rightarrow ^3B_1$ electronic transition enabled the development of a luminescence thermometer exploiting the ratio of Cr^{3+} to Cr^{4+} emissions with a relative sensitivity of $2.04\%K^{-1}$. The studies carried out enabled a better understanding of the formation processes of Cr^{4+} ions.
© 2023 The Electrochemical Society ("ECS"). Published on behalf of ECS by IOP Publishing Limited. [DOI: 10.1149/2162-8777/acd80e]

Supplementary material for this article is available online

The crystallographic position occupied by a dopant ion in inorganic host materials can determine both spectroscopic properties and oxidation state of the ion. This effect is particularly evident for transition metal (TM) ions known for the susceptibility of their spectroscopic properties to changes in the local ions environment.[1–4] Therefore predicting the crystallographic site, that will be occupied by dopant ions and enforced by it oxidation state of dopant, is one of the key steps during the design of inorganic phosphors. Existing theoretical knowledge including theoretical calculations is helpful, but results obtained during simulations are not always reproducible under experimental conditions. The multitude of possible variants in the case of TM is particularly large.[2,5–9] As an example, Fe^{3+} ions show luminescence both from octahedral (surrounded by 6 oxygen ions) and tetrahedral sites (surrounded by 4 oxygen ions).[10–14] A summary of both cases is presented for the following host materials: $MgAl_2O_4:Fe^{3+}$ and $CaGa_2O_4:Fe^{3+}$.[15] It was found that the occupation of the octahedral site of Al^{3+} ions by Fe^{3+} ions results in emission with a maximum at 719 nm, while the Fe^{3+} in the tetrahedral site of Ga^{3+} ions emit with a maximum at 809 nm. On the other hand, Zhu et al. proposed interesting approaches to design materials co-doped with Mn^{2+} and Mn^{4+} ions.[16] They found that manganese in $BaAl_{12}O_{19}$ forms stable Mn^{2+} ions substituting for Ba^{2+} ions, while in $SrAl_{12}O_{19}$, emission of Mn^{4+} ions located in Al^{3+} octahedral sites was observed. On this basis, authors proposed a strategy to produce a solid solution in which Sr^{2+} and Ba^{2+} ions are present in a 1:1 ratio ($Sr_{0.5}Ba_{0.5}Al_{12}O_{19}$), resulting in a material in which emission from both Mn^{2+} and Mn^{4+} ions was observed. It is also worth noting that in the case of $SrAl_{12}O_{19}$ host material, Mn^{4+} ions locate in the Al^{3+} site despite the electric charge mismatch. This is a well-known behavior that results from the higher thermodynamical stability of Mn^{4+} ions compared to Mn^{3+} ions. A major risk in designing phosphors with charge mismatch is the formation of defects, which can lead to a reduction in emission intensity. To prevent this, charge compensation by stoichiometric or non-stoichiometric doping with alkali metals or alkaline Earth metal ions (most commonly Li^+ or Na^+ and Mg^{2+} or Ca^{2+}, respectively) is used. A good example is the work of Wang et al. who investigated the effect of Li^+ ions on the spectroscopic properties of the $Mg_4Ta_2O_9:Cr^{3+}$ phosphor.[17] They found that although in the $Mg_4Ta_2O_9$ structure both Mg^{2+} and Ta^{5+} are octahedrally surrounded by 6 oxygen ions, Cr^{3+} ions locate in Mg^{2+} sites. Therefore

by using a charge compensation mechanism, that can be written in the form: $Cr^{3+} + Li^+ \rightarrow 2\ Mg^{2+}$, the number of defects was significantly reduced. As a result external luminescence quantum efficiency as high as 61.25% was achieved. In addition, the authors pointed out that charge compensation with Li^+ ions inhibits the formation of Cr^{4+}. This is important in terms of the occurrence of additional optical centers, which can affect the spectroscopic properties of the material through unresolved energy transfer. In the case of Cr^{4+} ions, the risk is reasonable since its absorption bands may cover a broad range corresponding to the emission spectral range of Cr^{3+} ions. A key example of a family of host materials in which it is possible to stabilize both 3+ and 4+ chromium ions are garnets. Their best-known representative is $Y_3Al_5O_{12}$.[4,18–21] So far, it was found that Cr^{3+} ions preferentially occupy Al^{3+} octahedral sites with efficient emission with a maximum at 688 nm.[22] However, there are some reports confirming the presence of Cr^{4+} ions stabilized in $Y_3Al_5O_{12}$ and describing their broad emission at ~1350 nm associated with the $^3B_2 \rightarrow ^3B_1$ electronic transition.[23–27] The stable Cr^{4+} oxidation state can be achieved using several strategies: (1) due to charge mismatch, a strategy of compensating the Cr^{4+} charge with Ca^{2+} ions is employed; (2) when doped with a high concentration of chromium ions, saturation of the octahedral site with Cr^{3+} ions and the appearance of co-existing Cr^{4+} ions was observed; (3) or at a high annealing temperature, which is an oxidizing agent and allows sufficient energy to be supplied to form Cr^{4+} ions.[26,28–31] Given that the spectral range of Cr^{4+} ion emission is potentially relevant from the perspective of near infrared (NIR) related phosphors, systematic studies on the spectroscopic properties of Cr^{4+} in $Y_3Al_{5-x}Ga_xO_{12}$ are necessary. One such application is luminescence thermometry.

In this work, we report the coexistence of Cr^{3+} and Cr^{4+} ions in solid solutions of $Y_3Al_{5-x}Ga_xO_{12}$ obtained without charge compensation, from a high-temperature synthesis. Furthermore, the temperature dependence of the emission of Cr^{3+} and Cr^{4+} bands was investigated and, for the first time, the design of a ratiometric luminescent thermometer based on vibronic levels of Cr^{4+} ions was proposed. The influence of the composition of the host solid solution materials on the spectral position of the emission bands of Cr^{4+} and the temperature quenching rate of the materials was also analyzed.

Experimental

The powders of the solid solution $Y_3Al_{5-x}Ga_xO_{12}$: 1% $Cr^{3+/4+}$ microcrystals were synthesised by the use of the solid-state method. $Al(NO_3)_3 \cdot 9H_2O$ (99.999% purity, Alfa Aesar), $Ga(NO_3)_3 \cdot 9H_2O$ (99.999% purity, Alfa Aesar), Y_2O_3 (99.999% purity, Stanford

[z]E-mail: w.piotrowski@intibs.pl; l.marciniak@intibs.pl

Materials Corporation) and $Cr(NO_3)_3 \cdot 9H_2O$ (99.99% purity, Alfa Aesar) were used as starting materials. The stoichiometric amounts of compounds were mixed in n-hexane and ground well in an agate mortar three times until the n-hexane evaporated. Next, the powders were first calcined in porcelain crucibles at 1273 K in air for 24 h. The pre-annealed powders with 1% molar $Cr^{3+/4+}$ concentration with respect to Al^{3+} and Ga^{3+} ions were subsequently ground again with the same procedure and sintered in corundum crucibles in air at 1873 K for 24 h.

All of the synthesized materials were examined by X-ray powder diffraction (XRPD) measurements carried out on PANalitycal X'Pert diffractometer using Ni-filtered Cu-K$_\alpha$ radiation (V = 40 kV, I = 30 mA).

The emission spectra were measured using a FLS1000 Fluorescence spectrometer from Edinburgh Instruments with a R928P side window photomultiplier tube from Hamamatsu and R5509–72 photomultiplier tube from Hamamatsu in nitrogen-flow cooled housing as a detector for visible and near infrared range detection, respectively and the 445 nm and 668 nm laser diode as excitation sources. The excitation spectra were also recorded using the FLS1000 Fluorescence spectrometer with the same detectors and a 450 W Xenon lamp. The temperature of the sample was controlled using a THMS 600 heating-cooling stage from Linkam (0.1 K temperature stability and 0.1 K set point resolution).

In order to obtain the results of relative sensitivity with lower uncertainty, all luminescent intensity ratio (LIR) values were fitted according to the Mott-Seitz equation (Eq. S1).

Results and Discussion

Structural and morphological characterization.— $Y_3Al_{5-x}Ga_xO_{12}$ materials belong to the garnets family and crystallize in the cubic structure of $Ia\bar{3}d$ (No. 230) space group.[3,4,19–21,32] Their well-studied chemical composition is described with a general chemical formula of $C_3A_2D_3O_{12}$, where the Y^{3+} ions occupy the dodecahedral "C" site and Al^{3+}/Ga^{3+} ions occupy both the octahedral "A" and tetrahedral "D" sites (Fig. 1a). It should be noted that (Al^{3+}/Ga^{3+})–O^{2-} bonds are bridged between (Al^{3+}/Ga^{3+}) ions in octahedral and tetrahedral sites. This means that each octahedron is vertex-bridged by 6 tetrahedra, and each tetrahedron is bridged by 4 octahedra. When considering the doping of garnets with chromium ions, it is expected that Cr^{3+} ions will locate in octahedral sites due to the ionic charge match with Al^{3+}/Ga^{3+} ions, which has been repeatedly reported.[18,33–36] On the other hand, the stabilization of Cr^{4+} ions in $Y_3Al_5O_{12}$ and $Y_3Ga_5O_{12}$ has also been reported.[23,24] In this case, Cr^{4+} ions could occupy both octahedral and tetrahedral sites. However, Eilers et al. defined that the spectroscopic properties of Cr^{4+} ions in $Y_3Al_5O_{12}$ should be attributed mainly to the tetrahedral site.[37] To verify the purity of the materials, their X-ray powder diffraction (XRPD) patterns were compared with the reference data ($Y_3Al_5O_{12}$ - ICSD 280104 and $Y_3Ga_5O_{12}$ − 14343) (Fig. 1b). A gradual shift of all reflections towards smaller 2θ angles was observed as the content of Ga^{3+} ions in the material increased, without the appearance of separate additional reflections, suggesting the formation of a single crystalline phase as a solid solution, independently of the ratio of Al^{3+} and Ga^{3+} ions. The gradual shift is clearly illustrated by the position of most intense reflection (420), which changes from 33.5° to 32.7° for a change of the chemical composition from $Y_3Al_5O_{12}$ to $Y_3Ga_5O_{12}$. In addition, as the content of Ga^{3+} ions increases, a decrease in the intensity of the reflections characteristic for the $Y_3Al_5O_{12}$ structure is evident in respect to the main peak, e.g. at 21° (220) and 27.8° (321), but are still distinguishable for x = 3 (i.e. $Y_3Al_2Ga_3O_{12}$ structure). In order to ensure greater accuracy when comparing materials, the Rietveld refinement of the XRD patterns was performed (Fig. S1). The reference numbers corresponding with the ICSD database can be found in Table SI. It was determined that the cell volume gradually increases from 1733.47 Å^3 for $Y_3Al_5O_{12}$ to 1851.02 Å^3 for $Y_3Ga_5O_{12}$ and perfectly obeys the Vegard's law

(Fig. S2, Table SII). Furthermore, the average metal-oxygen distances R($(Al/Ga)^{3+}$−O^{2-}) for the octahedral and tetrahedral sites were determined (Fig. 1c). In the case of tetrahedral sites, a quasi-linear bond elongation of R($(Al/Ga)^{3+}$−O^{2-}) was observed with increasing Ga^{3+} ion content, i.e. from 1.767 to 1.837 Å for $Y_3Al_5O_{12}$ and $Y_3Ga_5O_{12}$, respectively. This effect is expected since ionic radius of Ga^{3+} ions is larger than the one of Al^{3+}. On the other hand, a slight shortening of the metal-oxygen distance for x = 1 ($Y_3Al_4GaO_{12}$) was observed in the octahedral coordination. This phenomenon may be related to the preferential localization of larger Ga^{3+} ions in the tetrahedral site,[38] leading to a contraction of the octahedra, for which Al^{3+}/Ga^{3+} ratio is greater than for tetrahedra in $Y_3Al_4GaO_{12}$. A gradual increase in $(Al/Ga)^{3+}$−O^{2-} distance from 1.924 to 2.038 Å was also observed for octahedral site. Both metal-oxygen distances show two-slope broken-line dependence on x with breakpoint at $x \approx 2$. With increasing Ga^{3+} content from $x = 0$ to 2 the metal-oxygen distance in tetrahedral site increases with a higher gradient than in octahedral site. At the breakpoint the gradients switch places and octahedral site metal-oxygen distance grows faster than tetrahedral one (Fig. 1c). This observation correlates well with the Rietveld-refined occupancies of Al^{3+} and Ga^{3+} in tetrahedral and octahedral sites (Figs. 1d and 1e). Particularly noteworthy is the content of Ga^{3+} ions for both sites for x = 1. Indeed, it can be clearly seen that the content of Ga^{3+} ions in the tetrahedral site in $Y_3Al_4GaO_{12}$ is as high as 27.5% compared to 10.4% for the octahedral site. It stays with great agreement with Nakatsuka et al. and Marezio et al.[38,39] In addition, the difference between the content of Ga^{3+} ions for which the distribution of Al^{3+} and Ga^{3+} ions is 50% in both sites is clearly outlined. In the case of octahedral site this value falls at $x = \sim 3.4$ in respect to $x = \sim 1.9$ for the tetrahedral site. Due to the different occupancy of the first coordination zone around octahedra and tetrahedra depending on the composition of the solid solutions, it is possible to predict the effect of surrounding tetrahedra or octahedra on the local point symmetry of octahedra and tetrahedra, respectively. This is particularly relevant in the case of doping, when a third ion appears in the solid solution substituting into the same crystallographic position (Cr^{3+} in octahedral and Cr^{4+} in tetrahedral in this case). Therefore, when there are 6 tetrahedra of $(AlO_4)^{5-}$ or 6 tetrahedra of $(GaO_4)^{5-}$ around the octahedron, the highest possible point symmetry is expected. In the case of Cr^{3+} in $Y_3Al_5O_{12}$, this is C_{3i}. However, for mixed solid solutions, when statistically both tetrahedra of $(AlO_4)^{5-}$ and $(GaO_4)^{5-}$ around the octahedron can be found, a decrease in the local point symmetry of octahedra should be expected. Interestingly, the lowest symmetry should be reached when only one tetrahedron out of six (1/6 of all tetrahedra) around the octahedron differs from the others. Such a case, according to the percentage of Al^{3+} and Ga^{3+} ions can be observed in Fig. 1e, where it falls for x = ~4.0. An analogous case can be made for a Cr^{4+} ions in a tetrahedron with D_{2d} local symmetry. When it is surrounded by 4 octahedra and only one is different from the others (1/4 of all octahedra), the lowest local symmetry is expected. Such a case in $Y_3Al_{5-x}Ga_xO_{12}$, according to Fig. 1d should occur for x = ~2.1.

Comparison of luminescent properties.— The emission of Cr^{3+} ions in octahedral site in $Y_3Al_5O_{12}$ and $Y_3Ga_5O_{12}$ garnets has already been reported many times in the literature.[18,33–36] An important contribution to this research was made by professor di Bartolo.[18,20,36] However, to facilitate the discussion of the spectroscopic properties, a diagram of Cr^{3+} ions will be briefly described (Fig. 2a). The commonly used for Cr^{3+} ions excitation λ_{exc} = 445 nm populates the $^4T_1$ excited level, which is followed by nonradiative depopulation to the ^2E excited state. Its radiative depopulation to the $^4A_2$ ground level results in the occurrence of the narrow emission band ($^2E \rightarrow ^4A_2$ electronic transition). The position of the emission band maximum shifts sublinearly with increasing Ga^{3+} content in $Y_3Al_{5-x}Ga_xO_{12}$ from 687.4 nm to 690.2 nm (Figs. 2b and S3). In addition to the narrow band with the highest intensity, the emission spectra also contain further broad
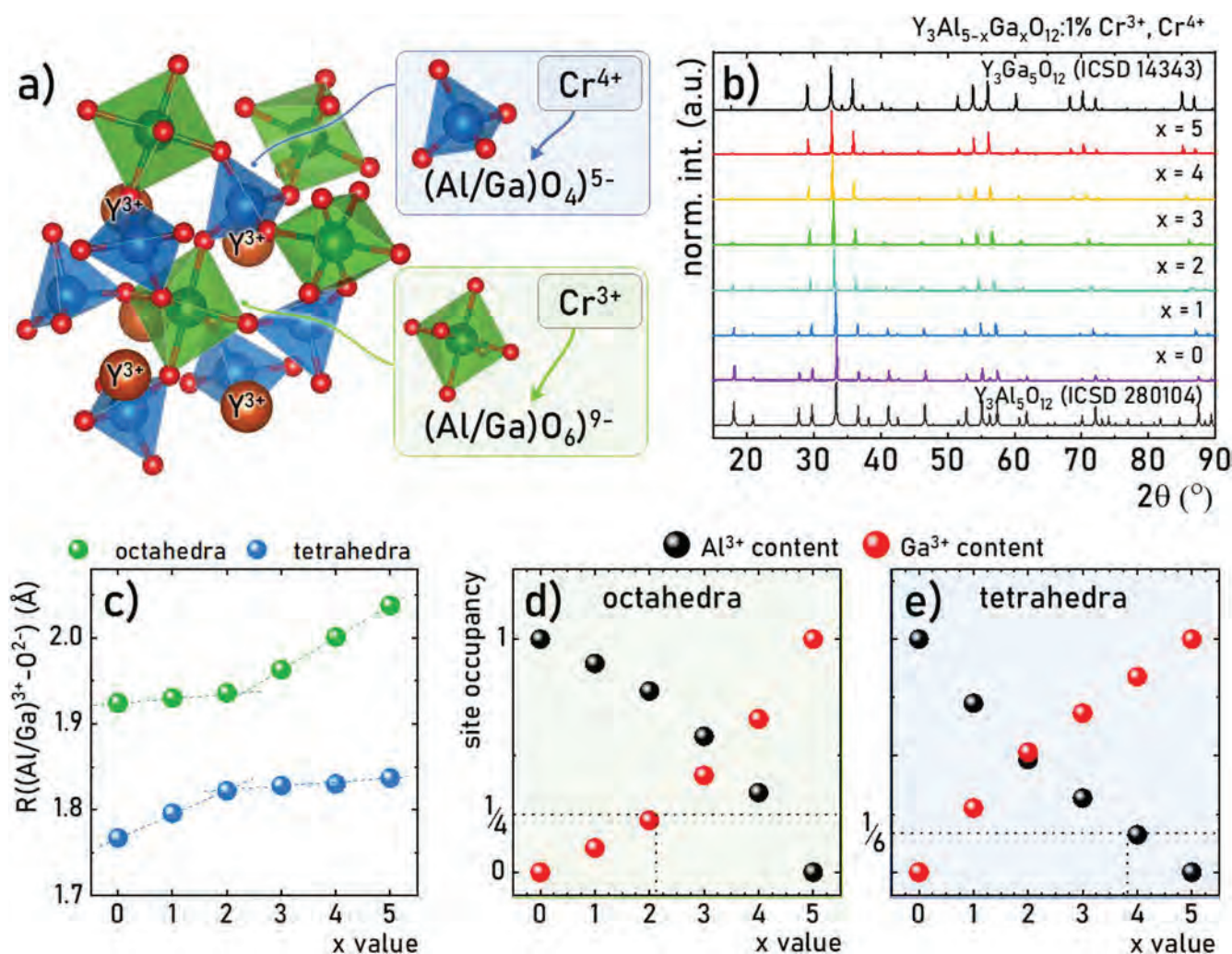
Figure 1. Schematic crystal structure of $Y_3Al_{5-x}Ga_xO_{12}$: $Cr^{3+/4+}$ garnets—(a); X-ray diffraction patterns of $Y_3Al_{5-x}Ga_xO_{12}$: $Cr^{3+/4+}$ with different Al^{3+}/Ga^{3+} ratio—(b); influence of overall Al^{3+}/Ga^{3+} content in $Y_3Al_{5-x}Ga_xO_{12}$ materials on metal-oxygen distance $R((Al/Ga)^{3+}-O^{2-})$ in octahedral and tetrahedral sites —(c); Al^{3+}/Ga^{3+} ions content in $Y_3Al_{5-x}Ga_xO_{12}$ materials in octahedral—(d) and tetrahedral sites—(e).

bands between 700 and 740 nm, which are associated with vibronic levels of $^2E \rightarrow ^4A_2$ transition overlapping with the $^4T_2 \rightarrow ^4A_2$ emission band (Fig. S4). For all materials, the excitation spectra consist of three broad bands with maxima at around 280, 435 and 600 nm, corresponding to $^4A_2 \rightarrow ^4T_1(^4P)$, $^4A_2 \rightarrow ^4T_1(^4F)$ and $^4A_2 \rightarrow ^4T_2$ electronic transitions, respectively (Fig. 2c). The position of the excitation band maxima shifts gradually towards lower energies (longer wavelengths) when Ga^{3+} ions content increases, from $23,300 \, cm^{-1}$ to $22,870 \, cm^{-1}$ in the case of $^4A_2 \rightarrow ^4T_1$ and from $16,850 \, cm^{-1}$ to $16,440 \, cm^{-1}$ in the case of $^4A_2 \rightarrow ^4T_2$ (Fig. S5). Using the empirical equations of Eqs. S2–4, the crystal field parameters were determined and summarized in Table SIII. It was found that the crystal field strength parameter Dq/B slightly decreases from 2.649 for $Y_3Al_5O_{12}$ to 2.578 for $Y_3Ga_5O_{12}$, which, based on Tanabe-Sugano diagrams, allows the crystal field surrounding Cr^{3+} ions to be classified as strong. On the other hand, due to the occurrence of tetrahedral crystallographic sites in the investigated garnet structures, the presence of Cr^{4+} ions was also considered. So far, Cr^{4+} ions emission has been reported only in the weak crystal field, located in the tetrahedral site.[23,24] For this reason, it can be assumed that in the energy diagram the $^3B_1(^3A_2)$ will be its ground level, while the $^3B_2(^3T_2)$ will be its first excited state (Fig. 2d). Hence using the 668 nm excitation, it is also possible to transfer the electrons to the $^1A_2$ and $^3E(^3T_1(^3F))$ levels, which is then nonradiatively relaxed to the $^3B_2(^3T_2)$ level, from which a radiative

transition to the $^3B_1(^3A_2)$ ground level occurs. Hence, as a consequence of the $^3B_2 \rightarrow ^3B_1$ transition, it is possible to observe an emission band at $\sim$1400 nm (Fig. 2e). Apparently, similarly to Cr^{3+} ions, the maximum of the Cr^{4+} emission band shifts towards longer wavelengths with increasing Ga^{3+} content in $Y_3Al_{5-x}Ga_xO_{12}$:$Cr^{3+/4+}$ materials (Fig. S6). It is worth noting that this shift is larger, i.e. by $\sim$54 nm from 1330 nm to 1384 nm, in respect to 2.8 nm observed for the $^2E \rightarrow ^4A_2$ band. This is related to the different nature of the transitions, i.e. for Cr^{3+} ions $^2E \rightarrow ^4A_2$ is a spin-forbidden, while for Cr^{4+} ions $^3B_2 \rightarrow ^3B_1$ is a spin-allowed transition. At the same time, the absence of a narrow emission band of Cr^{4+} ions in the emission spectrum leads to the conclusion that the observed emission band originates only from Cr^{4+} ions located in tetrahedral sites and there is no obvious confirmation for the presence of Cr^{4+} ions in octahedral sites. In contrast to the emission spectra, the excitation spectra measured for Cr^{4+} emission show a less pronounced shift of bands positions (Fig. 2f). The spectra show four broad bands with maxima at about $35,500 \, cm^{-1}$ (280 nm), $22,500 \, cm^{-1}$ (440 nm) and partially overlapping $16,000 \, cm^{-1}$ (625 nm) and $15,000 \, cm^{-1}$ (660 nm), which correspond with $^3B_1 \rightarrow ^1A_1(^1E) + ^1E(^1T_2)$, $^3B_1 \rightarrow ^3E(^3T_1(^3P))$, $^3B_1 \rightarrow ^1A_2$ and $^3B_1 \rightarrow ^3E(^3T_1(^3F))$ electronic transitions. It can be found that these values correspond well with theoretical calculations presented by Kück and Brik.[40] A shift of the band maxima as a function of Ga^{3+} content was observed (Fig. S7). By performing a deconvolution of
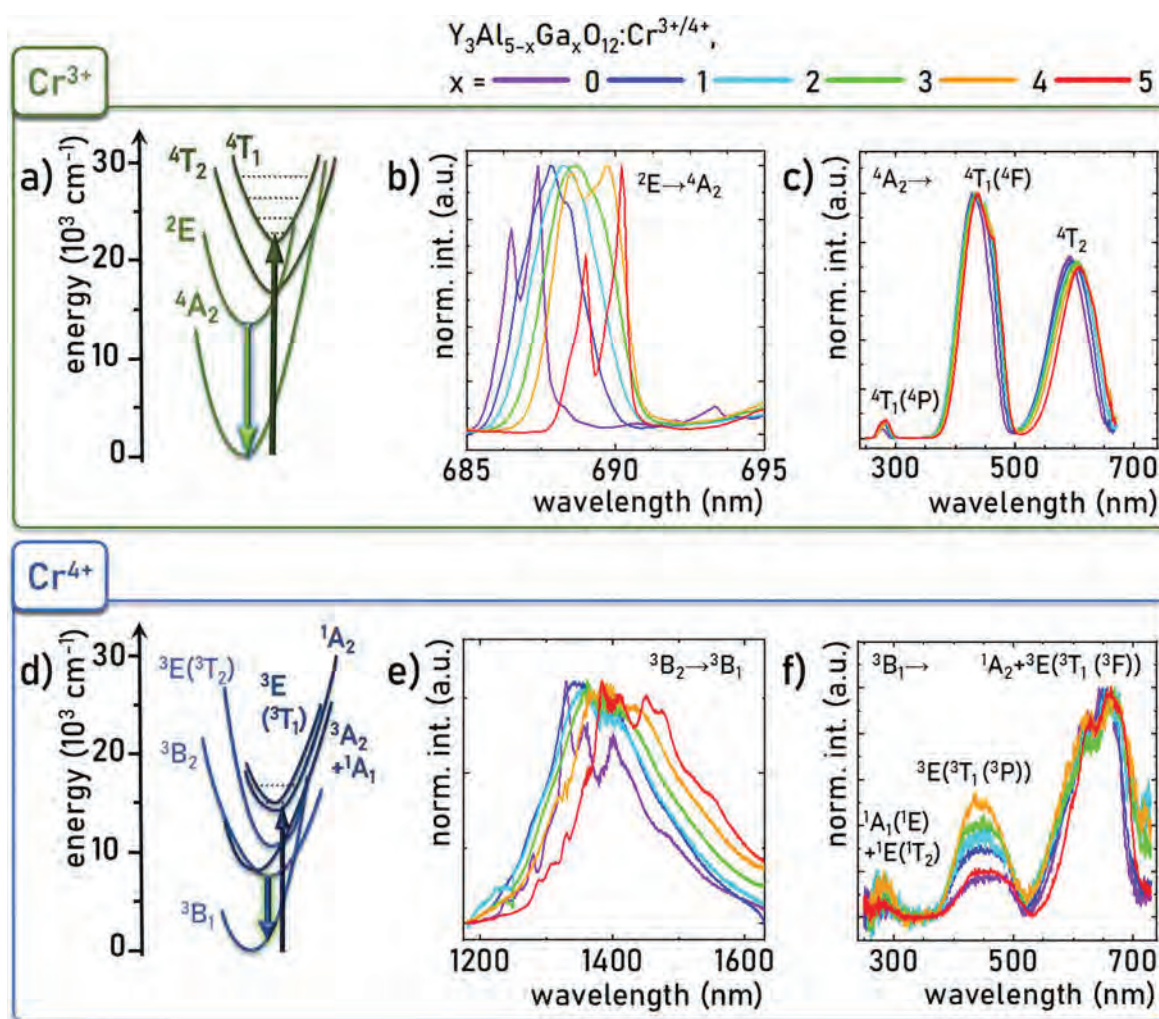
Figure 2. Schematic configurational coordinate diagram for Cr^{3+}—(a) and Cr^{4+} ions—(d); comparison of low temperature (83 K) emission ($\lambda_{exc} = 445$ nm—(b), $\lambda_{exc} = 668$ nm—(e)) and excitation spectra ($\lambda_{em} = \sim690$ nm—c, $\lambda_{em} = \sim1330$ nm (λ_{em} corresponds to the maximum intensity of the emission band of Cr^{3+} and Cr^{4+} ions, respectively)– (f)) measured for Cr^{3+} (b), (c) and Cr^{4+} ions (e), (f) for $Y_3Al_{5-x}Ga_xO_{12}$:1% $Cr^{3+/4+}$ materials.

the overlapping bands $^3B_1 \rightarrow {}^1A_2$ and $^3B_1 \rightarrow {}^3E(^3T_1(^3F))$, a gradual shift of the maxima of both bands towards lower energies with increasing Ga^{3+} content from 16,110 cm^{-1} to 15,810 cm^{-1} and from 15,100 cm^{-1} to 14,820 cm^{-1} was noted, respectively. This is expected, due to the weakening of the crystal field with the increasing amount of Ga^{3+} ions of larger ionic radii in respect to Al^{3+} ions. In contrast, the position of the $^3B_1 \rightarrow {}^3E(^3T_1(^3P))$ band for $Y_3Al_5O_{12}$ and $Y_3Ga_5O_{12}$ does not differ significantly, i.e. 22,240 and 22,170 cm^{-1}, but the mixed solid solutions (x = <1, 4>) present a slight blueshift of this band, reaching values from 22,530 to 22,610 cm^{-1}. Moreover, considering the $^3T_1(^3P)$ excitation band in the Cr^{4+} spectra, it can be found that it is possible to excite Cr^{3+} and Cr^{4+} ions simultaneously using $\lambda_{exc} = 445$ nm excitation (Fig. S8). This can be particularly beneficial when analyzing the intensity ratio of two bands. However, the Cr^{4+} ions emission intensity is at most $\sim0.2\%$ of the Cr^{3+} ion emission intensity for $Y_3Al_5O_{12}$ and $Y_3Ga_5O_{12}$, and is even lower for mixed solid solutions. The lower emission intensity of Cr^{4+} with respect to the Cr^{3+} ions in for the x <1,4> in comparison to the $Y_3Al_5O_{12}$ and $Y_3Ga_5O_{12}$ can be related with the two effects: 1) an enhancement in the Cr^{3+} ion emission intensity resulting from a decrease in the point symmetry of octahedral sites or 2) a deterioration in the Cr^{4+} ion emission intensity resulting from a decrease in the point symmetry of tetrahedral sites.

Comparison of thermometric properties.—Subsequently, the thermal evolution of $^3B_2 \rightarrow {}^3B_1$ emission band of Cr^{4+} ions in the NIR spectral range upon $\lambda_{exc} = 668$ nm excitation was investigated (Figs. 3a and S9). It can be clearly observed that its intensity is completely quenched at relatively low temperatures. Previously, a rapid temperature quenching of the emission band of Cr^{4+} ions in aluminate glass has already been reported in the literature, with the emission maximum located at ~1350 nm.[41] Figure S10 compares the $T_{1/2}$ parameter, defined as the temperature at which the emission intensity reaches 50% of the intensity read at 83 K. All values are below 220 K, which suggests relatively low thermal energy necessary to activate nonradiative depopulation process. Nevertheless, it is worth noting that the lowest $T_{1/2} = 191$ K was obtained for x = 2 ($Y_3Al_3Ga_2O_{12}$) in respect to $T_{1/2} = 212$ K for $Y_3Al_5O_{12}$ and $T_{1/2} = 207$ K for $Y_3Ga_5O_{12}$. To define what energy is needed to activate the temperature quenching, the Arrhenius equation was used (Eq. S5). The obtained values of the activation energy depending on the structure composition are summarized in Fig. S11. Indeed, the values obtained are small, for x = 0, 1, 3, 4 and 5 ΔE value equals ~400 cm^{-1}. Only for $Y_3Al_3Ga_2O_{12}$ the value of ΔE is slightly higher, reaching ~460 cm^{-1}. Due to the similar ΔE values obtained, other factors affecting $T_{1/2}$ values were considered. It is worth noting that the lowest $T_{1/2}$ value for Cr^{4+} ions occupying the tetrahedral site is for x = 2, for which it was previously determined that the octahedral site is occupied by single Ga^{3+} ion, generating the lowest local symmetry of tetrahedral site. In comparison, the materials
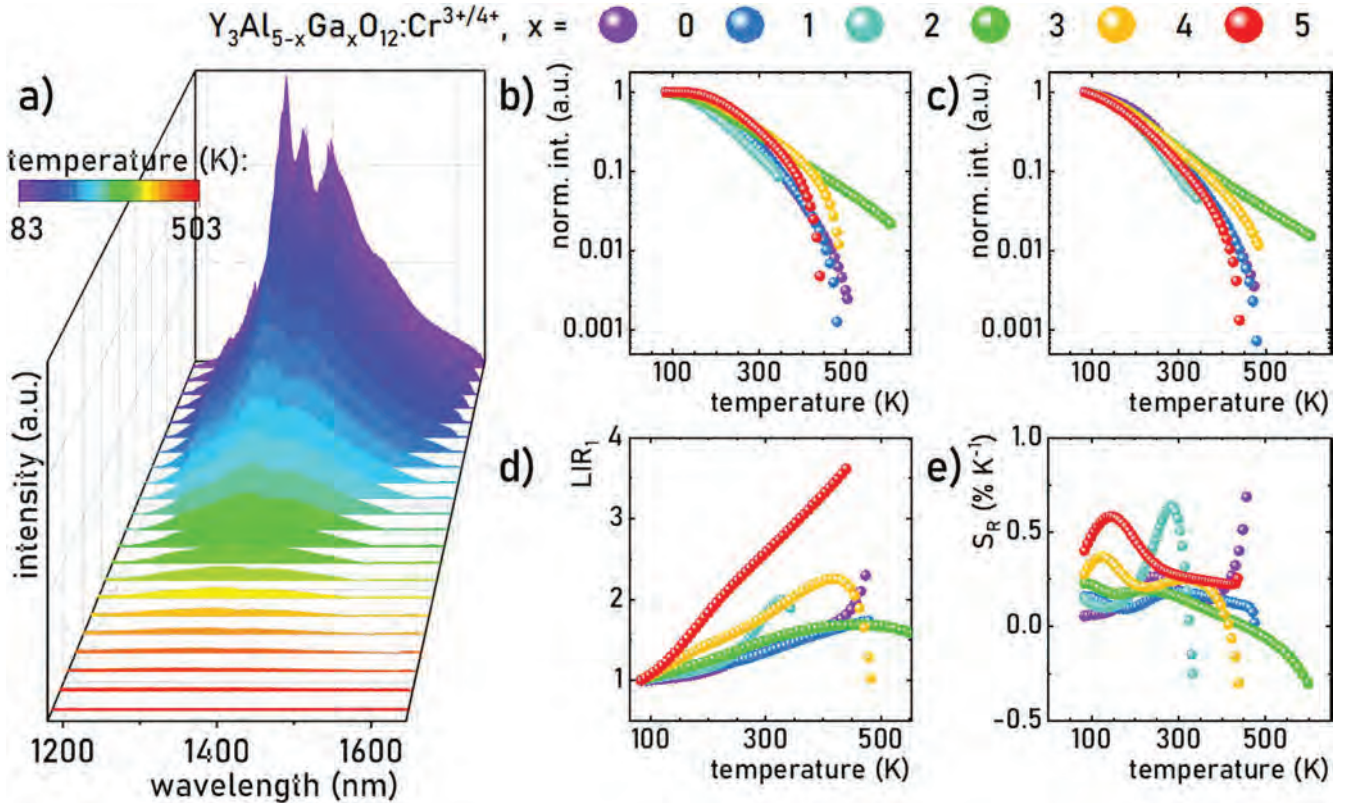
Figure 3. Thermal evolution of Cr^{4+} emission band in $Y_3Al_5O_{12}:Cr^{3+/4+}$ phosphor ($\lambda_{exc} = 668$ nm)—(a); thermal evolution of the integrated intensity of $^3B_2 \rightarrow ^3B_1$ vibronic band at 1280 nm—(b) and 1385 nm—(c), their ratio LIR_1—(d) and corresponding relative sensitivity—(e) for $Y_3Al_{5-x}Ga_xO_{12}:Cr^{3+/4+}$ materials.

$Y_3Al_5O_{12}$ and $Y_3Ga_5O_{12}$ (for which the tetrahedra site content will obviously be 100% of Al^{3+} and Ga^{3+}, respectively) represent the highest $T_{1/2}$ values. In these materials, it can be assumed that the highest local symmetry among $Y_3Al_{5-x}Ga_xO_{12}$ solid solutions has been achieved. Therefore, a comparison of $T_{1/2}$ for Al^{3+} content in the octahedra site is proposed (Fig. S12). As mentioned, the lowest $T_{1/2}$ value was obtained for x = 2, for which the Al^{3+} content in octahedral site is ~77.7%. This is the closest value to 75%, or 3/4 part, statistically suggesting the presence of 3 octahedra with Al^{3+} in the center and 1 tetrahedra with Ga^{3+} around the tetrahedra, which would generate the largest distortion of tetrahedra. It is noted that this relationship only occurs when Ga^{3+} are in the minority, whereas for 25% of Al^{3+} such a situation is not observed.

In all $Y_3Al_{5-x}Ga_xO_{12}$ materials it was noted that thermal quenching rates of the luminescence from the vibronic depends on the chemical composition of the phosphor. Therefore, two wavelengths were selected for which the thermal evolution of emission intensity was analyzed (Figs. 3b and 3c). Firstly, for $\lambda_{em} = 1280$ nm for $Y_3Al_5O_{12}:Cr^{3+/4+}$, gradual luminescence thermal quenching was observed already from the lowest temperature of 83 K, reaching $T_{1/2} = 230$ K, and the emission was almost completely quenched above 400 K. Subsequently, as the x value (Ga^{3+} content) increases through 1 to 2, an enhancement in the rate of emission quenching was observed. The most rapid quenching with $T_{1/2} = 198$ K was found for x = 2 ($Y_3Al_3Ga_2O_{12}$). Surprisingly, above x = 3 the opposite trend was observed. For x = 3 ($Y_3Al_2Ga_3O_{12}$), the course of emission intensity as a function of temperature is similar to that obtained for $Y_3Al_5O_{12}$. In contrast, for x = 4 and x = 5, the emission intensity of Cr^{4+} ions remains almost constant (>98% of the initial value) up to 123 and 143 K, respectively. This results in a $T_{1/2}$ of 257 K for $Y_3Ga_5O_{12}$. Nevertheless, for all analyzed $Y_3Al_{5-x}Ga_xO_{12}$ solid solutions, the emission is very low above 400 K. In contrast, Fig. 3c shows the temperature quenching of emission intensity at 1385 nm. In this case, independently on the host material, the

emission intensity starts to be quenched already at 83 K. For $Y_3Al_5O_{12}$, the quenching rate is the smallest with $T_{1/2} = 213$ K, when it is the largest for $Y_3Ga_5O_{12}$ with $T_{1/2} = 183$ K. Nevertheless, the emission intensity is at the noise level at about 340 K. Taking advantage of the different temperature quenching of chosen vibronic bands, the luminescent intensity ratio (LIR_1) was defined as:

$$LIR_1 = \frac{\int_{280\text{ nm}}^{1281\text{ nm}} I(^3B_2 \rightarrow ^3B_1)[Cr^{4+}]d\lambda}{\int_{1385\text{ nm}}^{1386\text{ nm}} I(^3B_2 \rightarrow ^3B_1)[Cr^{4+}]d\lambda} \quad [1]$$

The thermal evolution of LIR_1 is shown in Fig. 3d. LIR_1 for $Y_3Al_{5-x}Ga_xO_{12}$ materials with Ga^{3+} content between 0 and 3 in the range of 83–213 K slowly increases without exceeding 120% of the initial value. In the case of x = 0, x = 1 and x = 3, such a slow increase is observed over the entire temperature range up to ~453 K and does not increase more than twice in this range. To verify the influence on thermal changes of LIR values in a quantitative way, the relative sensitivity S_R was calculated according to the following formula (Eq. 2):

$$S_R = \frac{1}{LIR}\frac{\Delta LIR}{\Delta T} \times 100\% \quad [2]$$

where ΔLIR represents the change of LIR for the ΔT change of temperature. Figure 3e summarises the effect of Al^{3+}/Ga^{3+} ratio on relative sensitivity. It is worth highlighting the values of $S_R = 0.36\%K^{-1}$ at 123 K and $0.58\%K^{-1}$ at 153 K for x = 4 and x = 5, associated with a higher rate of increase in the LIR_1 value in respect to the other host materials. Moreover, the sharp increase in the LIR_1 value for x = 2 ($Y_3Al_3Ga_2O_{12}$) results in the highest value of $S_R = 0.64\%K^{-1}$ at 283 K.

The simultaneous co-existence of the emission bands of Cr^{3+} and Cr^{4+} in the emission spectrum obtained upon $\lambda_{exc} = 445$ nm excitation may be encouraging to consider their ratio as a thermometric parameter. For this purpose, the thermal evolution of emission spectra in the visible spectral range was performed at first (Fig. S13). It can be seen that the thermal quenching rates of vibronic levels of Cr^{3+} ions is dependent on the Al^{3+}/Ga^{3+} ratio. However, the R line of the $^2E{\rightarrow}^4A_2$ at the shortest wavelengths appears to be the most favorable from a thermometric point of view due to the highest quenching rate at low temperatures range (below 300 K). The comparison of the thermal evolution of that emission band for different host materials is shown in Fig. 4a. In the range from 83–183 K it can be found that the emission intensity of $^2E{\rightarrow}^4A_2$ for $Y_3Al_5O_{12}$ does not fall below 90% of the initial value. As the content of Ga^{3+} ions increases, the quenching rate increases, up to $Y_3Ga_5O_{12}$, for which at 183 K the emission intensity reached 65% of initial value. A similar quenching rate is maintained up to 283–-323 K independently of the host material. Above this temperature, the quenching rate slows down. For $Y_3Al_5O_{12}$ at 823 K, 10% of initial intensity was observed. For the mixed solid solution (x equal to 1–4), 10% of initial intensity was reached at the lower temperature between 663–703 K. For $Y_3Ga_5O_{12}$, this value was also reached at 703 K, but in the wide range from 283–583 K the emission intensity is between 46% and 28%, which is about twice higher intensity than for the mixed solid solutions. For $^2E{\rightarrow}^4A_2$ band intensity, the absolute sensitivity S_A was calculated according to the following formula (Eq. 3):

$$S_A = \frac{\Delta I}{\Delta T} \qquad [3]$$

Thermal evolution of S_A values at temperature range below 400 K shows a clear correlation with the host material composition (Fig. 4b). Firstly, the temperature at which the maximum S_A value was obtained for $^2E{\rightarrow}^4A_2$ emission decreases monotonically from 243 K for $Y_3Al_5O_{12}$ to 153 K for $Y_3Ga_5O_{12}$. In addition, the value of S_{Amax} increases from $4.28\cdot10^{-3}$ K^{-1} to $5.81\cdot10^{-3}$ K^{-1} as the Ga^{3+} content increases from x = 0 to x = 4. In contrast, for $Y_3Ga_5O_{12}$ S_{Amax} takes on a value similar to $Y_3Al_5O_{12}$, namely $4.43\cdot10^{-3}$ K^{-1}. To understand the reduction of $T(S_{Amax})$ with Al^{3+} content, the activation energy ΔE for Cr^{3+} ions emission was calculated according to Eq. S5 and plotted in the function of Al/Ga^{3+} ratio in Fig. S14a. It can be found that ΔE decreases quasi-linearly from $\Delta E = {\sim}730$ cm^{-1} for $Y_3Al_5O_{12}$ to $\Delta E = {\sim}430$ cm^{-1} for $Y_3Ga_5O_{12}$. Therefore, it is to be expected that the lower energy is sufficient to activate the nonradiative depopulation of ^2E excited state, the lower $T(S_{Amax})$. Moreover, ΔE decreases with the weakening of the crystal field strength expressed as Dq/B, which is expected since ΔE is determined as an energy mismatch between ^2E and $^4T_2$ state (Fig. S14b). Nevertheless, the correlation is not linear, since the shift in the wavefactor domain has not been taken into account.

Due to the possibility of simultaneous excitation of Cr^{3+} and Cr^{4+} ions by $\lambda_{exc} = 445$ nm, it was considered that the effect of temperature on the emission intensity of Cr^{4+} ions might differ from that obtained at $\lambda_{exc} = 668$ nm. For this reason, the thermal evolution of emission band of $Y_3Al_{5-x}Ga_xO_{12}$ upon excitation through $\lambda_{exc} = 445$ nm was performed (Fig. S15). The integral emission intensity of Cr^{4+}ions calculated in the 1260–1500 nm spectral range was analyzed (Fig. 4c). Firstly, it can be seen that the rate of thermal quenching of Cr^{4+} ions is more rapid than that of Cr^{3+} ions, as manifested by the narrower temperature range over which emission was observed. The lowest quenching rate was observed for x = 1 ($Y_3Al_4GaO_{12}$), for which 10% of the initial
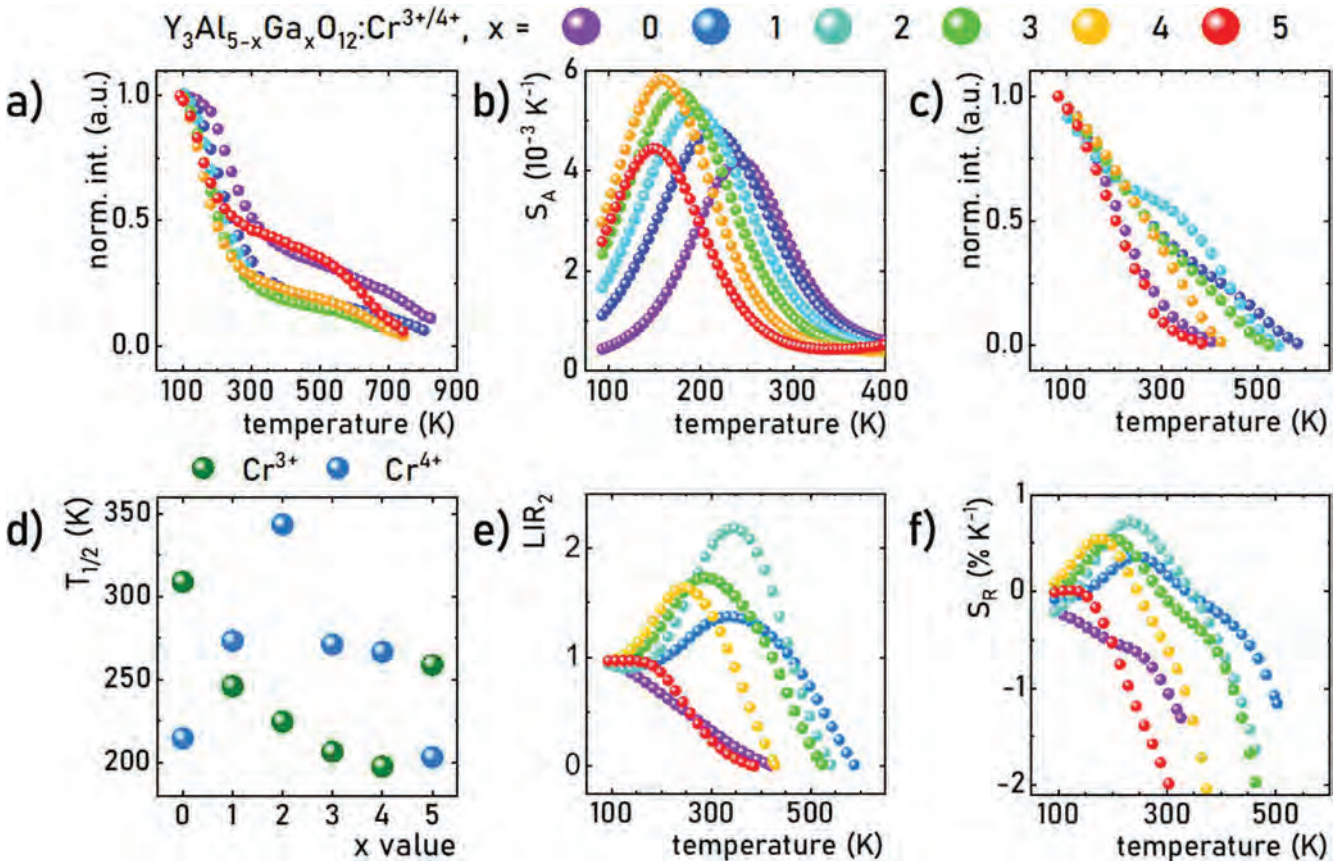
Figure 4. Thermal evolution of $^2E{\rightarrow}^4A_2$ emission band of Cr^{3+} ions ($\lambda_{exc} = 445$ nm)—(a) and S_A for this band—(b); thermal evolution of $^3B_2{\rightarrow}^3B_1$ emission band of Cr^{4+} ions—(c); influence of Al^{3+}/Ga^{3+} content on $T_{1/2}$ of Cr^{3+} and Cr^{4+} emission bands in $Y_3Al_{5-x}Ga_xO_{12}:Cr^{3+/4+}$ materials—(d); thermal evolution of LIR—(e) and relative sensitivity—(f).

intensity was detected at 523 K, whereas the fastest in $Y_3Al_5O_{12}$ and $Y_3Ga_5O_{12}$, reaching 10% of the intensity from 83 K at 323 K and 303 K, respectively. It is worth noting the different profile of the integrated emission intensity of Cr^{4+} as a function of temperature in $Y_3Al_3Ga_2O_{12}$ (x = 2), for which, above 223 K, a clear reduction in the temperature quenching rate is observed, which can also be identified for other mixed solid solutions (x = 1, 3 and 4), but is not as pronounced. This observation can be explained as reduction of local symmetry associated with the presence of non-equivalent centres in octahedra surrounding tetrahedra, where Cr^{4+} ions are located. The quenching rate of the emission intensity translates directly into the $T_{1/2}$ values (Fig. 4d). For Cr^{3+} ions in the octahedral site, the highest $T_{1/2} = 309$ K was observed for $Y_3Al_5O_{12}$ and a slightly lower $T_{1/2} = 259$ K for $Y_3Ga_5O_{12}$. These values contrast with the $T_{1/2}$ values for the mixed solid solutions, which reach lower values of 246 to 198 K in the order from x = 1 to x = 4. This may suggest a correlation with the point symmetry of the octahedral site, which depends on the ratio of Al^{3+}/Ga^{3+} ions forming tetrahedra in the first coordination zone. As in the case of Cr^{4+} ions in the tetrahedral site excited by $\lambda_{exc} = 668$ nm, a dependence on the Al^{3+} ions content in tetrahedral site was also determined (Fig. S16). In this case, it can be seen that the lowest $T_{1/2}$ values were achieved for x = 2, for which an Al^{3+} sites content of 16.1% was calculated, which is close to the 16.(6)% value corresponding to the statistical distribution of Al^{3+} and Ga^{3+} ions in a 1:5 ratio. In contrast to the octahedral site, for Cr^{4+} ions the $T_{1/2}$ values clearly divided into three groups. These are 1) the lowest values of ~210 K obtained for $Y_3Al_5O_{12}$ and $Y_3Ga_5O_{12}$, 2) those with $T_{1/2} = $ ~270 K for x = 1, x = 3 and x = 4, and the clear outlier 3) $T_{1/2} = 343$ K for x = 2. These values, as with $\lambda_{exc} = 668$ nm, can be arranged in correlation with $\Delta(Al^{3+}/Ga^{3+})$ at the tetrahedral site. However, a decisive difference is the inverse monotonicity of the results obtained. For x = 2, with excitation through $\lambda_{exc} = 668$ nm $T_{1/2}$ was lowest, while with excitation through $\lambda_{exc} = 445$ nm it is highest compared to other host materials. This effect can be attributed to the gradual reduction of local point symmetry around Cr^{4+} ions. It is expected that for 1) the symmetry will be the highest of investigated solid solutions, since all the octahedra surrounding the tetrahedra have the same centre. For 2) there will be a different ratio of centres surrounding the tetrahedra, leading to a lower symmetry. The lowest possible symmetry is likely to be achieved for a system 3) where statistically only one of the surrounding centres will differ (25% of all octahedra), for which indeed the highest probability exists for x = ~2.

Due to the encouraging possibility of simultaneous excitation of Cr^{3+} and Cr^{4+} ions via $\lambda_{exc} = 445$ nm, a second thermometric parameter was proposed as LIR_2 as follows:

$$LIR_2 = \frac{\int_{686\,nm}^{691\,nm} I(^2E \rightarrow {}^4A_2)[Cr^{3+}]d\lambda}{\int_{1260\,nm}^{1500\,nm} I(^3B_2 \rightarrow {}^3B_1)[Cr^{4+}]d\lambda} \qquad [4]$$

For $Y_3Al_5O_{12}$ and $Y_3Ga_5O_{12}$, LIR_2 decreases in temperature, reaching less than $LIR_2 = 0.1$ at 403 and 363 K, respectively (Fig. 4e). This is the effect of the rapid thermal quenching of Cr^{4+} emission combined with a relatively slow decrease in Cr^{3+} ion intensity in the range 83–283 K. In contrast, for x = 1 lIR_2 does not change from 83 K to 213 K, but above this value its value increases to 1.37 at 348 K and then gradually decreases to ~0.1 at 573 K. A more favorable increase in the LIR_2 value was achieved for x = 2 ($Y_3Al_3Ga_2O_{12}$), where, at the same temperature of 348 K, $LIR_2 = 2.18$. Then, for x = 3 and x = 4, both a shift in the maximal LIR value to lower temperatures and a decrease in LIR values were observed, namely $LIR_2 = 1.73$ at 288 K and 1.63 at 243 K, respectively. In order to quantitatively compare the luminescence thermometers based on the LIR_2 with those calculated for the LIR_1, the relative sensitivity was calculated again, according to Eq. 2

(Fig. 4f). In this case, at low temperatures the most promising S_R values were obtained for x = 2, with $S_{Rmax} = 0.72\%K^{-1}$ at 228 K. It is also worth noting the shift in the temperature at which S_{Rmax} was achieved for x in the range of 1–4, towards lower values, i.e. 243 K, 228 K, 198 and 168 K. This demonstrates the negative impact of Ga^{3+} ions on the application potential of these phosphors in luminescence thermometry. On the other hand, negative S_R values are worth noting. They are the result of a reversal of the monotonicity of LIR_2, i.e. when its values start to decrease. This is possible in the temperature range where the signal intensity of Cr^{4+} ions is higher than that of Cr^{3+} ions. Therefore, it is possible to achieve negative S_R values that exceed $|S_{Rmax}| = 0.72\%K^{-1}$. In the case of $Y_3Ga_5O_{12}$, the S_R is less than $-1\%K^{-1}$ in the range from 228 to 303 K, while for $Y_3Al_2Ga_3O_{12}$ these values were noted in the range 423–463 K. It should be noticed that the calculated S_R values have been limited to temperature ranges in which it is possible to accurately detect the intensity of both bands. This is limited by the rapidly quenching Cr^{4+} ion band and therefore the S_R was determined for temperatures where the emission intensity of the Cr^{4+} ion exceeds 10% of the initial signal intensity. It can be clearly noticed that the chemical composition of the host material affects the operating range of the Cr^{3+}/Cr^{4+} luminescence thermometer. Considering that in many applications the 300–350 K temperature range is important, $Y_3AlGa_4O_{12}$:Cr^{3+}, Cr^{4+} material should be considered as the most promising, whose S_R equals $-0.62\%K^{-1}$ at 303 K, but is more than doubled at 348 K, i.e. $S_R = -1.33\%K^{-1}$, and reaches its maximum at 373 K with a value of $S_R = -2.04\%K^{-1}$. In summary, a luminescence thermometer based on the ratio of Cr^{3+} and Cr^{4+} bands (LIR_2) guarantees better relative sensitivities than the ratio of vibronic bands of Cr^{4+} (LIR_1). In addition, the possibility to control the temperature range over which the thermometer can operate by the chemical composition of host material is an important advantage. The only requirement that may hinder application is the need to detect a signal coming from two optical ranges (visible and NIR), however it unquestionably provides good separation of the signal coming from both bands.

Conclusions

In this work, the group of the solid solution $Y_3Al_{5-x}Ga_xO_{12}$ garnets was doped with chromium ions, which locate in both the octahedral and tetrahedral position Al^{3+}/Ga^{3+} ions as Cr^{3+} and Cr^{4+}, respectively. The stabilization of the Cr^{4+} ions is the result of high annealing temperatures. No charge compensators (e.g. in the form of bivalent ions) or a high concentration of dopant ions (1%) were used. Based on the Rietveld refinement, the percentage content of Al^{3+} and Ga^{3+} ions at octahedral and tetrahedral sites in solid solutions was determined. Due to the corner-sharing character of polyhedra connections, it was noted that the local symmetry of octahedral and tetrahedral sites is determined by their surroundings in the second coordination sphere, i.e. 6 tetrahedra around the octahedra and 4 octahedra around the tetrahedra. The highest local symmetry was obtained for $Y_3Al_5O_{12}$ and $Y_3Ga_5O_{12}$, while the lowest for x = 4 ($Y_3AlGa_4O_{12}$) in the case of octahedra and x = 2 ($Y_3Al_3Ga_2O_{12}$) in the case of tetrahedra, which is statistically related to the presence of only one other ion in the first coordination sphere. This phenomenon was correlated with the $T_{1/2}$ value, which was highest at the highest symmetry and lowest at the lowest symmetry. Finally, two temperature-dependent LIR parameters based on 1) the ratio of vibronic levels of $^3B_2 \rightarrow {}^3B_1$ band of Cr^{4+} ions and 2) the ratio between $^2E \rightarrow {}^4A_2$ emission of Cr^{3+} ions and $^3B_2 \rightarrow {}^3B_1$ emission of Cr^{4+} ions were proposed and compared with each other. Better results were obtained in the second case, with a representative value of $|S_R| = 2.04\%K^{-1}$ at 373 K for $Y_3AlGa_4O_{12}$:Cr^{3+}, Cr^{4+} phosphor. However, it should be noted the significant influence of host material composition (Al^{3+}/Ga^{3+} ratio) on both thermometric parameters results in the fact that by appropriate material selection, $S_R > 1\%K^{-1}$ can be achieved in the range 230–460 K.

ORCID

W. M. Piotrowski https://orcid.org/0000-0002-8155-2688
L. Marciniak https://orcid.org/0000-0001-5181-5865

References

1. R. C. Powell and B. Dibartolo, "Optical properties of heavily doped ruby." *Phys. Status Solidi*, **10**, 315 (1972).
2. G. Fuxi and L. Huimin, "Spectroscopy of transition metal ions in inorganic glasses." *J. Non. Cryst. Solids.*, **80**, 20 (1986).
3. G. Armagan and B. D. Bartolo, "Mechanism for the thermal dependence of the Cr to Nd energy transfer in garnets." *IEEE J. Quantum Electron.*, **24**, 974 (1988).
4. G. Armagan, B. Di Bartolo, and A. M. Buonchristiani, "Spectroscopic investigation of Cr to Tm energy transfer in yttrium aluminum garnet crystals." *J. Lumin.*, **44**, 129 (1989).
5. L. Marciniak, K. Kniec, K. Elżbieciak-Piecka, K. Trejgis, J. Stefanska, and M. Dramićanin, "Luminescence thermometry with transition metal ions. A review." *Coord. Chem. Rev.*, **469**, 214671 (2022).
6. M. G. Brik and C.-G. Ma, *Theoretical Spectroscopy of Transition Metal and Rare Earth Ions* (New York)(Jenny Stanford Publishing) 1st edn ed. (2019).
7. M. Dramićanin, "Lanthanide and transition metal ion doped materials for luminescence temperature sensing." *Luminescence Thermometry*, ed. M. B. T.-L. T. Dramićanin (Amsterdam)(Woodhead Publishing)p 113 (2018).
8. H. H. Kung, *Review of Spectroscopy of Transition Metal Ions on Surfaces* (Leuven) (Leuven University Press) (2001).
9. J. G. Solé, L. E. Bausá, and D. Jaque, "Applications: rare earth and transition metal ions, and color centers." *An Introd. to Opt. Spectrosc. Inorg. Solids.*, 199 (2005).
10. M. W. Gaultois and A. P. Grosvenor, "Coordination-induced shifts of absorption and binding energies in the $SrFe_{1-x}Zn_xO_{3-\Delta}$." *system, J. Phys. Chem. C*, **114**, 19822 (2010).
11. D. Plessers, M. L. Bols, H. M. Rhoda, A. J. Heyer, E. I. Solomon, B. F. Sels, and R. A. Schoonheydt, "Single site spectroscopy of transition metal ions and reactive oxygen complexes in zeolites." *Ref. Modul. Chem. Mol. Sci. Chem. Eng.* (Amsterdam)(Elsevier) (2021).
12. I. Fontana, A. Lauria, and G. Spinolo, "Optical absorption spectra of Fe^{2+} and Fe^{3+} in aqueous solutions and hydrated crystals." *Phys. Status Solidi*, **244**, 4669 (2007).
13. K. Kniec, M. Tikhomirov, B. Pozniak, K. Ledwa, and L. Marciniak, "$LiLa_5O_8:Fe^{3+}$ and $LiAl_5O_8:Fe^{3+}$, Nd^{3+} as a new luminescent nanothermometer operating in 1st biological optical window." *Nanomaterials.*, **10**, 189 (2020).
14. K. Kniec, K. Ledwa, K. MacIejewska, and L. Marciniak, "Intentional modification of the optical spectral response and relative sensitivity of luminescent thermometers based on Fe^{3+},Cr^{3+},Nd^{3+}co-doped garnet nanocrystals by crystal field strength optimization." *Mater. Chem. Front.*, **4**, 1697 (2020).
15. K. Kniec, W. Piotrowski, K. Ledwa, L. D. Carlos, and L. Marciniak, "Spectral and thermometric properties altering through crystal field strength modification and host material composition in luminescence thermometers based on Fe^{3+} doped AB_2O_4 type nanocrystals (A = Mg, Ca; B = Al, Ga)." *J. Mater. Chem. C.*, **9**, 517 (2021).
16. Y. Zhu, C. Li, D. Deng, B. Chen, H. Yu, H. Li, L. Wang, C. Shen, X. Jing, and S. Xu, "A high-sensitivity dual-mode optical thermometry based on one-step synthesis of $Mn^{2+}:BaAl_{12}O_{19}$–$Mn^{4+}:SrAl_{12}O_{19}$ solid solution phosphors." *J. Alloys Compd.*, **853**, 157262 (2021).
17. S. Wang, R. Pang, T. Tan, H. Wu, Q. Wang, C. Li, S. Zhang, T. Tan, H. You, and H. Zhang, "Achieving high quantum efficiency broadband NIR $Mg_4Ta_2O_9:Cr^{3+}$ phosphor through lithium-ion compensation." *Adv. Mater.*, 2300124 (2023), n/a.
18. M. Erdem, G. Ozen, U. Yahsi, and B. Di Bartolo, "Thermal and size effect on the R lines luminescence in $YAG:Cr^{3+}$." *J. Lumin.*, **158**, 464 (2015).
19. H. Örücü, G. Özen, B. Di Bartolo, and J. Collins, "Site-selective spectroscopy of garnet crystals doped with chromium ions." *J. Phys. Chem. A*, **116**, 8815 (2012).
20. G. Ozen, J. Collins, M. Bettinelli, and B. Di Bartolo, "Luminescence of $Y_3Al_5O_{12}$ nano-particles doped with praseodymium ions." *Opt. Mater. (Amst).*, **35**, 1360 (2013).
21. P. Hong, X. X. Zhang, C. W. Struck, and B. Di Bartolo, "Luminescence of Cr^{3+} and energy transfer between Cr^{3+} and Nd^{3+} ions in yttrium aluminum garnet,." *J. Appl. Phys.*, **78**, 4659 (1995).
22. P. Głuchowski, R. Pązik, D. Hreniak, and W. Stręk, "Luminescence properties of $Cr^{3+}:Y_3Al_5O_{12}$ nanocrystals." *J. Lumin.*, **129**, 548 (2009).
23. H. Eilers, U. Hömmerich, S. M. Jacobsen, W. M. Yen, and M. Kokta, "Spectroscopic properties of $Cr^{4+}:Lu_3Al_5O_{12}$." *Opt. Lett.*, **18**, 1928 (1993).
24. K.-Y. Huang, K.-Y. Hsu, and S.-L. Huang, "Analysis of ultra-broadband amplified spontaneous emissions generated by Cr^{4+}: YAG single and glass-clad crystal fibers." *J. Light. Technol.*, **26**, 1632 (2008).
25. M. A. Chaika et al., "The role of Ca^{2+} ions in the formation of high optical quality $Cr^{4+},Ca:YAG$ ceramics." *J. Eur. Ceram. Soc.*, **39**, 3344 (2019).
26. M. A. Chaika et al., "Kinetics of Cr^{3+} to Cr^{4+} ion valence transformations and intra-lattice cation exchange of Cr^{4+} in Cr,Ca:YAG ceramics used as laser gain and passive Q-switching media." *J. Chem. Phys.*, **151**, 134708 (2019).
27. M. Chaika, R. Lisiecki, K. Lesniewska-Matys, and O. M. Vovk, "A new approach for measurement of Cr^{4+} concentration in $Cr^{4+}:YAG$ transparent materials: Some conceptual difficulties and possible solutions." *Opt. Mater. (Amst).*, **126**, 112126 (2022).
28. S. A. Markgraf, M. F. Pangborn, and R. Dieckmann, "Influence of different divalent co-dopants on the Cr^{4+} content of Cr-doped $Y_3Al_5O_{12}$." *J. Cryst. Growth*, **180**, 81 (1997).
29. M. Chaika et al., "Influence of Cr doping on the phase composition of Cr,Ca:YAG ceramics by solid state reaction sintering." *J. Am. Ceram. Soc.*, **102**, 2104 (2019).
30. X. Chen, Z. Lu, M. Hu, H. Chang, Y. Duan, J. Fang, T. Lu, N. Wei, Y. Wu, and W. Guo, "Investigation of the structure, optical properties and Cr^{4+} conversion level of Yb^{3+} and Cr^{3+} codoped YAG transparent ceramics." *Opt. Mater. (Amst).*, **109**, 110406 (2020).
31. W. Piotrowski, L. Dalipi, R. Szukiewicz, B. Fond, M. Dramicanin, and L. Marciniak, "The role of Cr^{3+} and Cr^{4+} in emission brightness enhancement and sensitivity improvement of NIR-emitting Nd^{3+}/Er^{3+} ratiometric luminescent thermometers." *J. Mater. Chem. C*, **9**, 12671 (2021).
32. G. Özen, O. Forte, B. Di Bartolo, and J. M. Collins, "Upconversion as a discriminating tool in site-selective spectroscopy of the praseodymium ion in $Y_3Al_5O_{12}$." *J. Appl. Phys.*, **102**, 23110 (2007).
33. W. Xu, F. Bai, L. Zheng, C. Hu, Z. Zhang, Y. Zhang, and Z. Sun, "Thermally enhanced upconversion luminescence of Cr^{3+} in $Er^{3+}-Yb^{3+}-Cr^{3+}$ tri-doped garnet phosphors for sensitive optical thermometry." *Ceram. Int.* (2023).
34. H. Yang, W. Zhao, X. Lin, Z. Liao, Z. Nie, L. Luo, W. Zhang, Z. Hu, and J. Zhong, "Hundreds of times of photo-stimulation with low energy light as a new reused bio-imaging phosphor from Cr^{3+}, Si^{4+}-doped $Y_3Ga_5O_{12}$." *J. Lumin.*, **219**, 116871 (2020).
35. J. Periša, Z. Ristić, V. Đorđević, M. Sekulić, T. Dramićanin, Ž. Antić, and M. D. Dramićanin, "Multiparametric luminescence thermometry from Dy^{3+}, Cr^{3+} double luminophore." *J. Lumin.*, **238**, 118306 (2021).
36. J. P. Hehir, M. O. Henry, J. P. Larkin, and G. F. Imbusch, "Nature of the luminescence from YAG:Cr^{3+}." *J. Phys. C: Solid State Phys.*, **7**, 2241 (1974).
37. H. Eilers, U. Hömmerich, S. M. Jacobsen, W. M. Yen, K. R. Hoffman, and W. Jia, "Spectroscopy and dynamics of $Cr^{4+}:Y_3Al_5O_{12}$." *Phys. Rev. B*, **49**, 15505 (1994).
38. A. Nakatsuka, A. Yoshiasa, and T. Yamanaka, "Cation distribution and crystal chemistry of $Y_3Al_{5-x}Ga_xO_{12}$ garnet solid solutions." *Acta Crystallogr. Sect. B.*, **55**, 266 (1999).
39. M. Marezio, J. P. Remeika, and P. D. Dernier, "Cation distribution in $Y_3Al_{5-x}Ga_xO_{12}$ garnet." *Acta Crystallogr. Sect. B.*, **24**, 1670 (1968).
40. M. G. Brik, N. M. Avram, C. N. Avram, N. M. Avram, and M. G. Brik, "Exchange charge model of crystal field for 3d ions." *Opt. Prop. 3d-Ions Cryst. Spectrosc. Cryst. F. Anal.* (Berlin, Heidelberg)(Springer)p. 29 (2013).
41. S. Tanabe and X. Feng, "Temperature variation of near-infrared emission from Cr^{4+} in aluminate glass for broadband telecommunication." *Appl. Phys. Lett.*, **77**, 818 (2000).

Supporting Information

Revisiting $Y_3Al_{5-x}Ga_xO_{12}$ solid solutions doped with chromium ions: effect of local symmetry on thermal quenching of Cr^{3+} and Cr^{4+} ions

W. M. Piotrowski[1]*, V. Kinzhybalo[1], L. Marciniak[1]*

[1]Institute of Low Temperature and Structure Research, Polish Academy of Sciences, Okólna 2, 50-422 Wroclaw,

Poland

* corresponding author: w.piotrowski@intibs.pl, l.marciniak@intibs.pl

KEYWORDS luminescent thermometry, transition metal ions, chromium, $Y_3Al_5O_{12}$, $Y_3Ga_5O_{12}$

The integral intensities of the Cr^{3+} and Cr^{4+} bands to calculate LIR values were fitted with Mott-Seitz equation (Eq. S1):

$$I = \frac{I_0}{C \cdot \exp(-\frac{W}{k \cdot T}) + 1} \qquad \text{(Eq. S1)}$$

where: I – the intensity in temperature T, I_0 – the intensity in the initial temperature,

W - the activation energy, k – Boltzmann constant, C – the dimensionless constant

Table S1. Reference patterns used for Rietveld refinement.

x	host	ICSD number
0	YAG	280104
1	$Y_3Al_4GaO_{12}$	280105
2	$Y_3Al_3Ga_2O_{12}$	280106
3	$Y_3Al_2Ga_3O_{12}$	280107

4		$Y_3AlGa_4O_{12}$	280108
5		YGG	14343
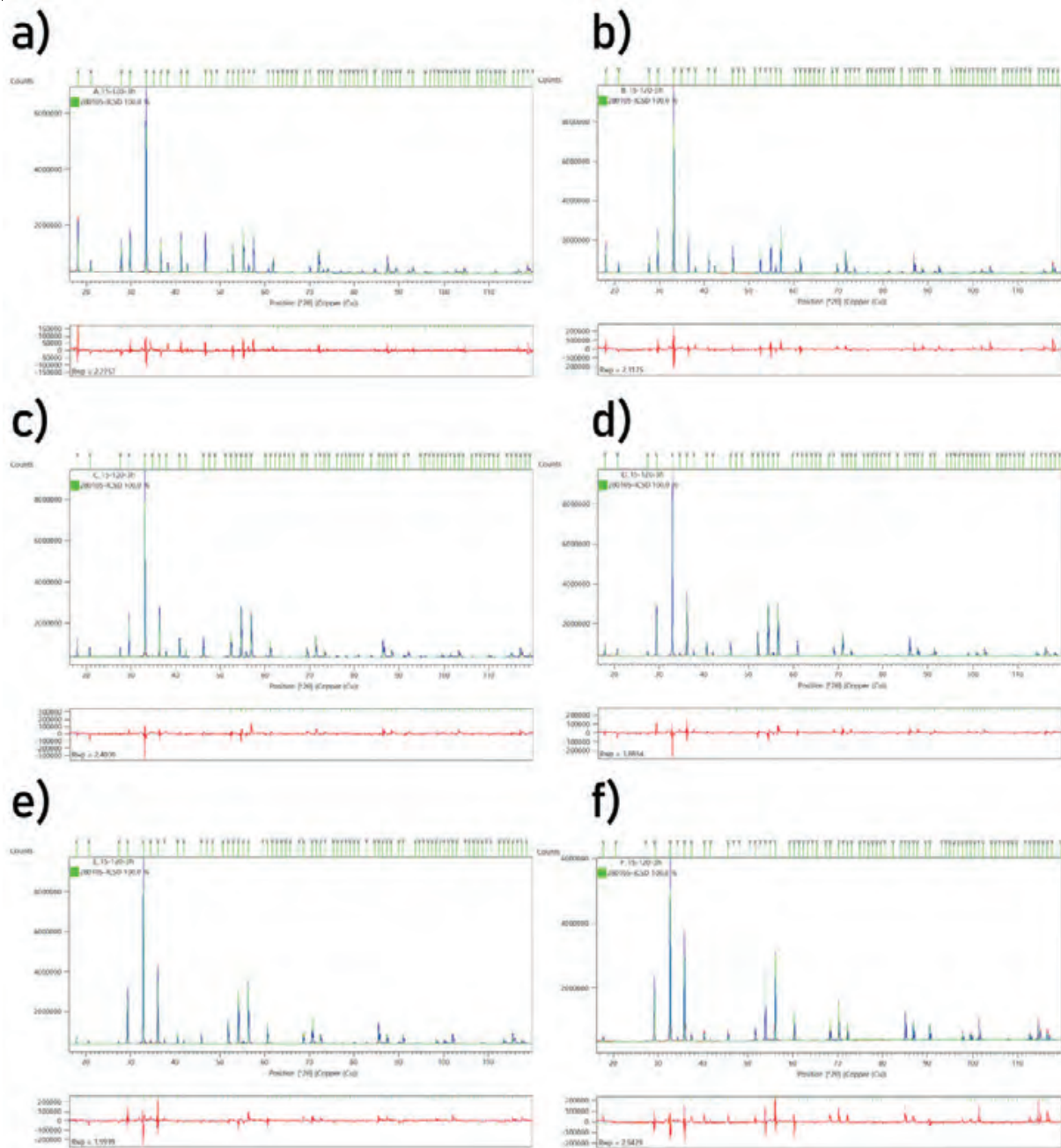
Figure S1. Rietveld refinement of $Y_3Al_{5-x}Ga_xO_{12}$:1% $Cr^{3+/4+}$ materials.

Table S2. Unit cell parameters calculated with Rietveld refinement for $Y_3Al_{5-x}Ga_xO_{12}$:1% $Cr^{3+/4+}$ materials.

x	host	a (Å)	V (Å^3)	R profile	weighted R profile	goodness of fit
0	YAG	12.0126	1733.5	1.52	2.28	3.05
1	$Y_3Al_4GaO_{12}$	12.0642	1755.9	1.54	2.32	3.28
2	$Y_3Al_3Ga_2O_{12}$	12.1144	1777.9	1.62	2.40	3.52
3	$Y_3Al_2Ga_3O_{12}$	12.1689	1802.0	1.31	1.89	2.84
4	$Y_3AlGa_4O_{12}$	12.2254	1827.2	1.37	2.00	3.07
5	YGG	12.2783	1851.0	1.69	2.94	4.19
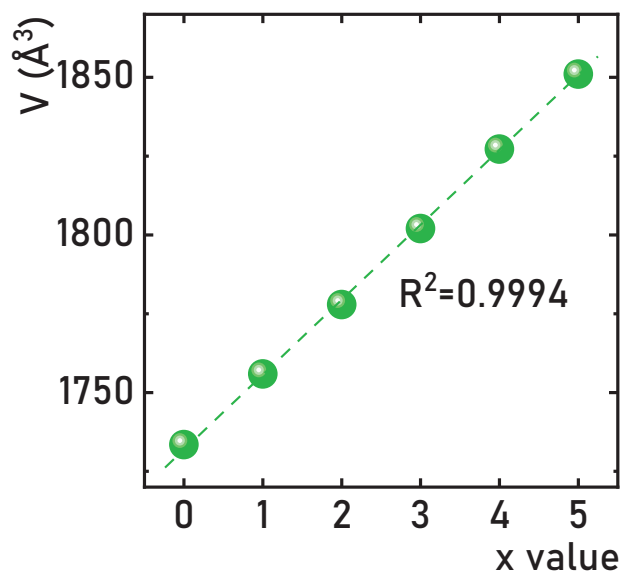
Figure S2. Influence of Al^{3+}/Ga^{3+} ratio on cell volume of $Y_3Al_{5-x}Ga_xO_{12}$:1% $Cr^{3+/4+}$ materials.
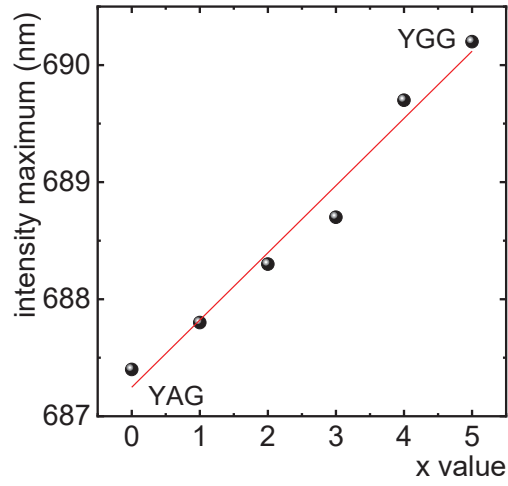
Figure S3. Influence of Al/Ga^{3+} content on the $^2E \rightarrow ^4A_2$ emission maximum of Cr^{3+} ions in Y$_3$Al$_{5-x}$Ga$_x$O$_{12}$:Cr$^{3+/4+}$ materials.
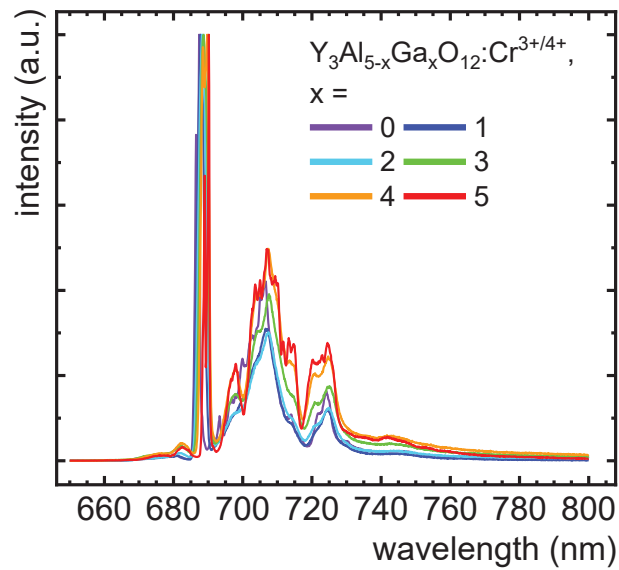
Figure S4. Comparison of emission spectra in visible spectral range measured for λ_{exc} = 445 nm for Y$_3$Al$_{5-x}$Ga$_x$O$_{12}$:Cr$^{3+/4+}$ materials.
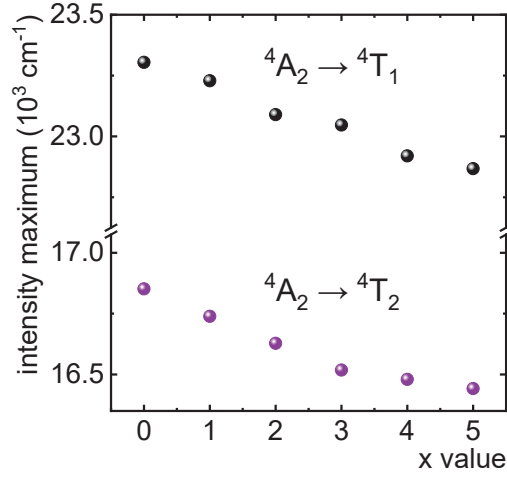
Figure S5. Influence of Al/Ga^{3+} content on the $^4A_2{\rightarrow}^4T_1$ and $^4A_2{\rightarrow}^4T_2$ excitation maxima of Cr^{3+} ions in Y$_3$Al$_{5-x}$Ga$_x$O$_{12}$:Cr$^{3+/4+}$ materials.

The crystal field parameter Dq and Racah parameter B for Cr^{3+} ions were defined based on the energies of $^4A_2 \rightarrow {}^4T_1$ and $^4A_2 \rightarrow {}^4T_2$ bands obtained from excitation spectra. The empirical equations take the following form:

$$E(\,{}^4A_2 \rightarrow \,{}^4T_2) = 10Dq \qquad\qquad \text{(Eq. S2)}$$

$$\frac{Dq}{B} = \frac{15\left(\frac{\Delta E}{Dq}-8\right)}{\left(\frac{\Delta E}{Dq}\right)^2-10\cdot\frac{\Delta E}{Dq}} \qquad\qquad \text{(Eq. S3)}$$

where ΔE was predefined as:

$$\Delta E = E(\,{}^4A_2 \rightarrow \,{}^4T_1) - E(\,{}^4A_2 \rightarrow \,{}^4T_2) \qquad\qquad \text{(Eq. S4)}$$

Table S3. Comparison of crystal field parameters of Cr^{3+} ions for Y$_3$Al$_{5-x}$Ga$_x$O$_{12}$:1% Cr$^{3+/4+}$ materials.

Host	Dq [cm^{-1}]	B [cm^{-1}]	Dq/B [-]
YAG	1685.2	636.4	2.649

$Y_3Al_4GaO_{12}$	1673.9	642.5	2.605
$Y_3Al_3Ga_2O_{12}$	1662.8	640.2	2.597
$Y_3Al_2Ga_3O_{12}$	1655.9	641.7	2.580
$Y_3AlGa_4O_{12}$	1648.0	639.2	2.578
YGG	1644.2	637.8	2.578
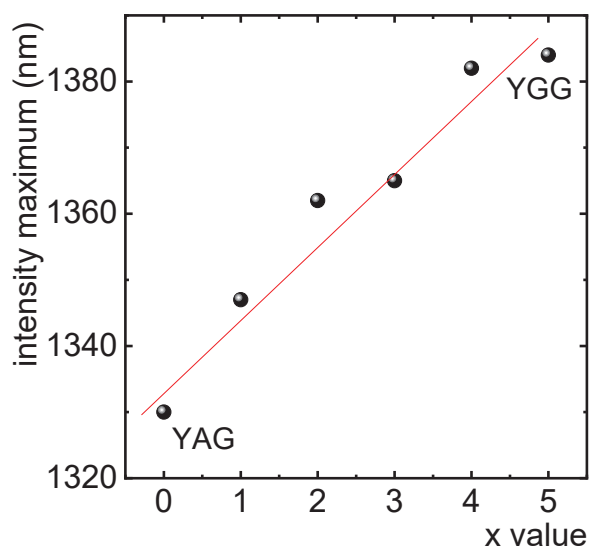
Figure S6. Influence of Al/Ga^{3+} content on the $^3B_2(^3T_2)\rightarrow {}^3B_1(^3A_2)$ emission maximum of Cr^{4+} ions in $Y_3Al_{5-x}Ga_xO_{12}:Cr^{3+/4+}$ materials.
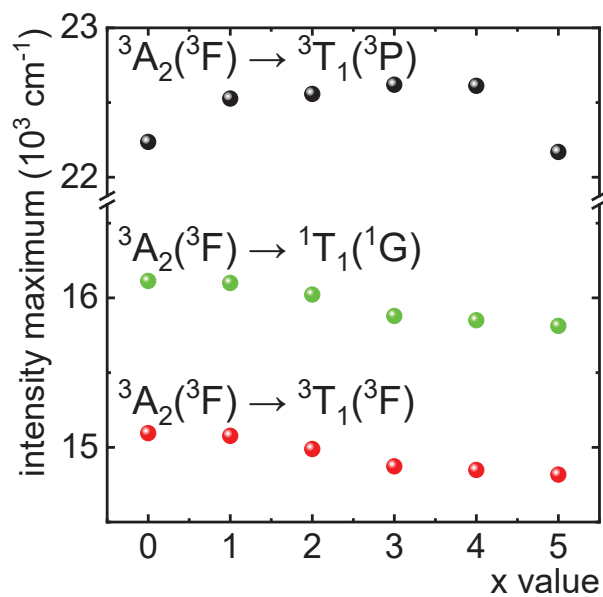
Figure S7. Influence of Al/Ga^{3+} content on the $^3A_2(^3F) \rightarrow ^3T_1(^3P)$, $^3A_2(^3F) \rightarrow ^1T_1(^1G)$ and $^3A_2(^3F) \rightarrow ^3T_1(^3F)$ excitation maxima of Cr^{4+} ions in Y$_3$Al$_{5-x}$Ga$_x$O$_{12}$:Cr$^{3+/4+}$ materials.
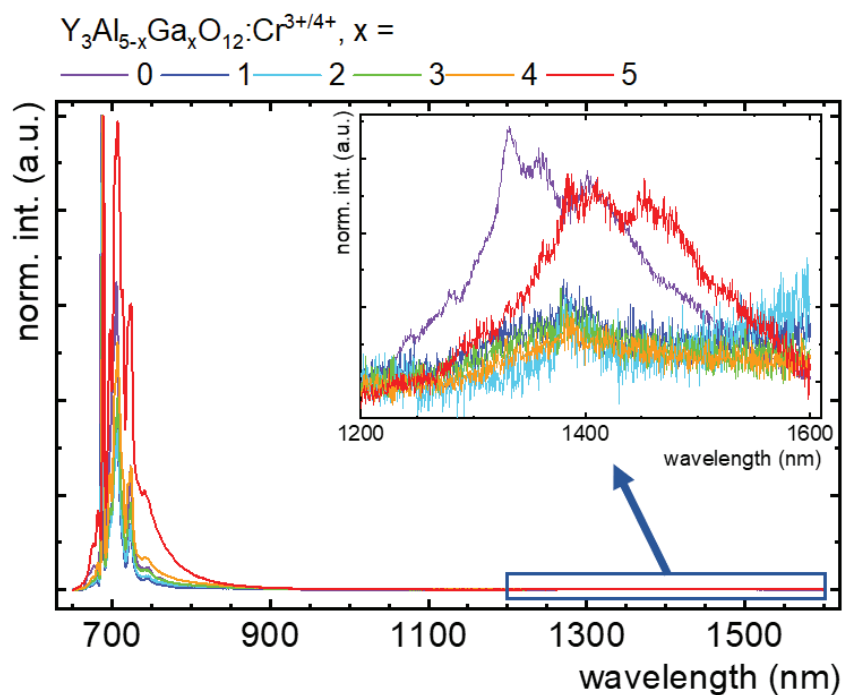
Figure S8. Comparison of emission spectra in visible and IR spectral ranges measured for λ_{exc} = 445 nm for Y$_3$Al$_{5-x}$Ga$_x$O$_{12}$:Cr$^{3+/4+}$ materials with zoom in on the Cr^{4+} ions emission.
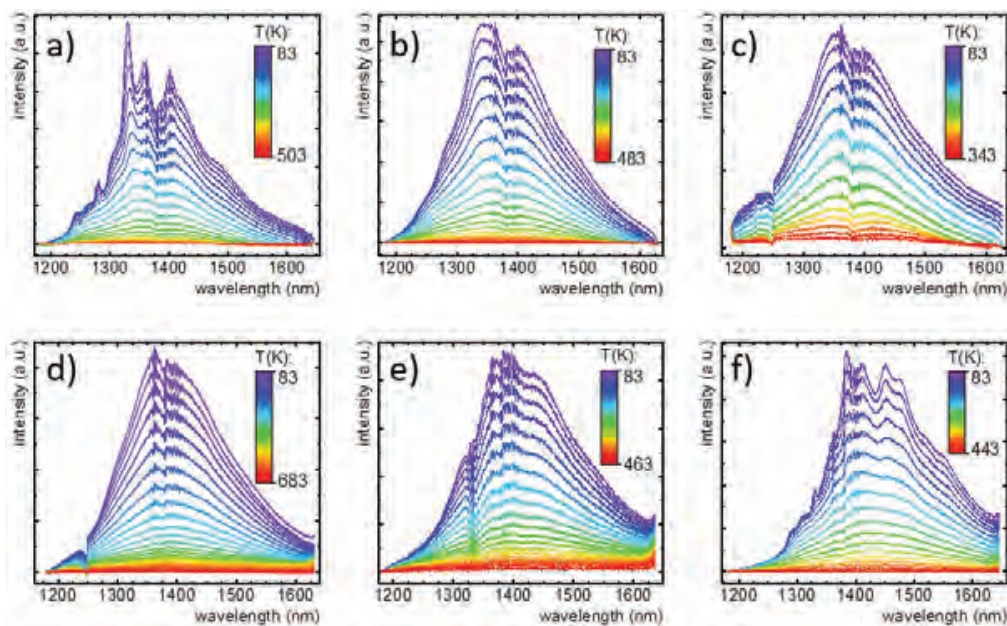
Figure S9. Thermal evolution of emission spectra of Cr^{4+} ions excited by λ_{exc} = 668 nm performed for $Y_3Al_{5-x}Ga_xO_{12}:Cr^{3+/4+}$ materials, where x = 0 – a); 1 – b); 2 – c); 3 – d); 4 – e); 5 – f).
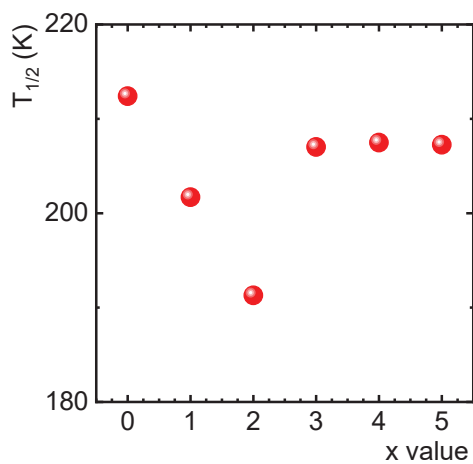
Figure S10. Influence of Al/Ga^{3+} content on $T_{1/2}$ value for Cr^{4+} ions emission excited by λ_{exc} = 668 nm in $Y_3Al_{5-x}Ga_xO_{12}:Cr^{3+/4+}$ materials.

The activation energy ΔE of Cr^{3+} and Cr^{4+} ions was calculated with the Arrhenius equation:

$$\frac{-\Delta E}{k} \cdot \frac{1}{T} = \ln\left(\frac{I_0}{I_{em}} - 1\right)$$ (Eq. S5)

where I_{em} is the emission intensity at T temperature, I_0 is the initial emission intensity (at $T =$ 83 K) and k is Boltzmann constant.
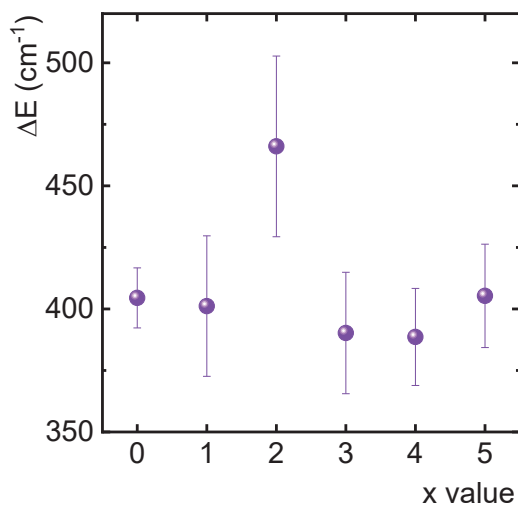
Figure S11. Influence of Al/Ga^{3+} content on ΔE value for Cr^{4+} ions emission in $Y_3Al_{5-x}Ga_xO_{12}$:$Cr^{3+/4+}$ materials.
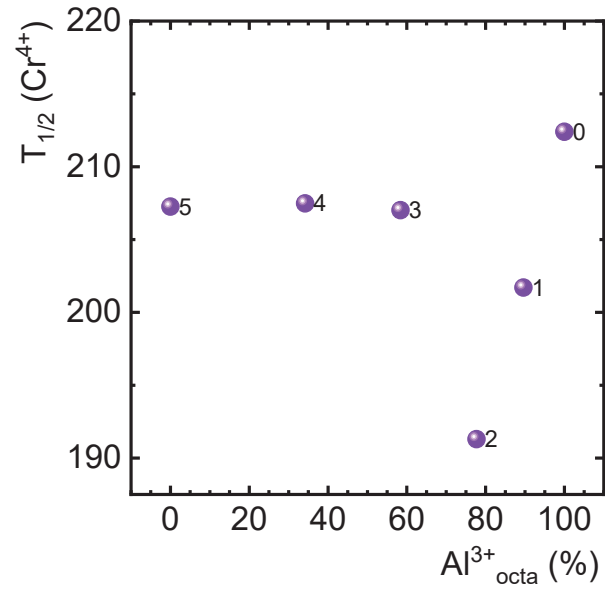
Figure S12. Influence of Al^{3+} ions content in octahedral site on $T_{1/2}$ value for Cr^{4+} ions emission $(^3B_2(^3T_2) \rightarrow {}^3B_1(^3A_2))$ excited by $\lambda_{exc} = 668$ nm in $Y_3Al_{5-x}Ga_xO_{12}:Cr^{3+/4+}$ materials.

Figure S13. Thermal evolution of emission spectra of Cr^{3+} ions excited by $\lambda_{exc} = 445$ nm performed for $Y_3Al_{5-x}Ga_xO_{12}:Cr^{3+/4+}$ materials, where x = 0 – a); 1 – b); 2 – c); 3 – d); 4 – e); 5 – f).

Figure S14. Influence of Al/Ga^{3+} content on ΔE value for Cr^{3+} ions emission in Y$_3$Al$_{5-x}$Ga$_x$O$_{12}$:Cr$^{3+/4+}$ materials.

Figure S15. Thermal evolution of emission spectra of Cr^{4+} ions excited by λ_{exc} = 445 nm performed for Y$_3$Al$_{5-x}$Ga$_x$O$_{12}$:Cr$^{3+/4+}$ materials, where x = 0 – a); 1 – b); 2 – c); 3 – d); 4 – e); 5 – f).
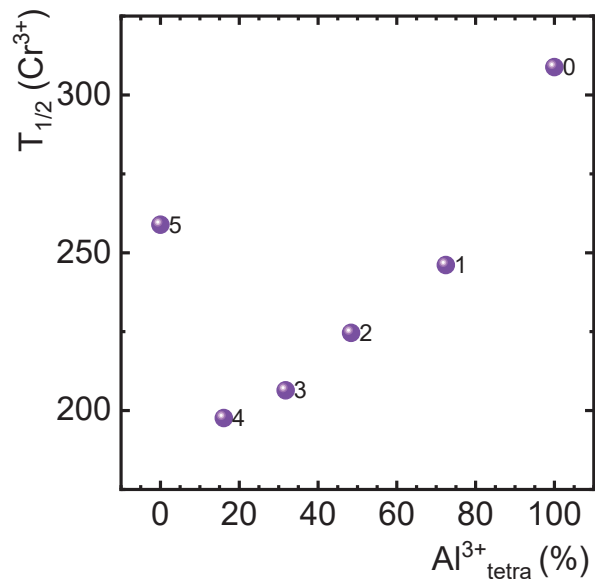
Figure S16. Influence of Al^{3+} ions content in tetrahedral site on $T_{1/2}$ value for Cr^{3+} ions emission ($^2E \rightarrow ^4A_2$)

excited by $\lambda_{exc} = 445$ nm in $Y_3Al_{5-x}Ga_xO_{12}:Cr^{3+/4+}$ materials.
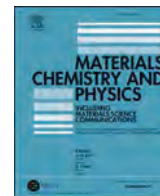
Step by step optimization of luminescence thermometry in MgTiO$_3$:Cr^{3+}, Nd^{3+}@SiO$_2$ nanoparticles towards bioapplications

Wojciech M. Piotrowski [a],[**], Maja Szymczak [a], Emma Martín Rodríguez [b], Riccardo Marin [c], Marta Henklewska [d], Błażej Poźniak [d], Miroslav Dramićanin [e], Lukasz Marciniak [a],[*]

[a] *Institute of Low Temperature and Structure Research, Polish Academy of Sciences, Okólna 2, 50-422, Wroclaw, Poland*
[b] *Nanomaterials for Bioimaging Group (nanoBIG), Departamento de Física Aplicada, Facultad de Ciencias, Universidad Autónoma de Madrid, Madrid, Spain*
[c] *Nanomaterials for Bioimaging Group (nanoBIG), Departamento de Física de Materiales, Facultad de Ciencias, Universidad Autónoma de Madrid, Madrid, Spain*
[d] *Department of Pharmacology and Toxicology, Faculty of Veterinary Medicine, Wrocław University of Environmental and Life Sciences, ul. Norwida 25, 50-375, Wrocław, Poland*
[e] *Center of Excellence for Photoconversion, Vinča Institute of Nuclear Sciences – National Institute of the Republic of Serbia, University of Belgrade, P.O. Box 522, Belgrade, 11001, Serbia*

HIGHLIGHTS

- New type of biocompatible luminescent thermometer was presented.
- Thermometer operates in the ratiometric and lifetime approaches.
- The process of optimization of thermometric performance of thermometer was presented.
- The deposition of a SiO$_2$ shell on a MgTiO$_3$:Cr^{3+},Nd^{3+} slightly elongates the lifetime.
- Low cytotoxicity of the obtained materials was confirmed.

ARTICLE INFO

ABSTRACT

The increasing popularity of luminescent nanothermometry in recent years can be attributed to its application potential in biomedicine. In response to this need, we describe a biocompatible bimodal luminescent thermometer that operates in ratiometric and luminescence lifetime modes based on particles of MgTiO$_3$:Cr^{3+}, Nd^{3+}@SiO$_2$. The introduction of Cr^{3+} and Nd^{3+} dopants enabled the luminescence of Ti^{3+} ions to be observed, and the difference in the thermal quenching rates of Cr^{3+} (^{4}T$_2$→^{4}A$_2$), Ti^{3+} (^{2}T$_2$→^{2}E) and Nd^{3+} (^{4}F$_{3/2}$ → ^{4}I$_{11/2}$) ions enabled the ratiometric thermometers. The highest sensitivity reaching S$_R$ = 1.00%K^{-1} was obtained for MgTiO$_3$:0.1 % Cr^{3+}, 0.1 % Nd^{3+} at 203 K. The shortening of the lifetime of the ^{4}T$_2$ level of Cr^{3+} ions associated with its thermal depopulation allows to develop a lifetime-based thermometer with a relative sensitivity reaching 0.85–1.18%K^{-1} in the physiological temperature range. The deposition of a SiO$_2$ shell on a MgTiO$_3$:Cr^{3+},Nd^{3+} did not introduce significant changes in the shape of the emission spectrum and slightly elongates the lifetime by reducing the probability of surface-related nonradiative processes. More importantly, the thermometric performance of this luminescence thermometer was preserved. The low cytotoxicity of the obtained materials underlines their potential in bioapplications of the described luminescent thermometers.

1. Introduction

Thermal sensing and thermal imaging in biological environments have been found in recent years to be encouraging application fields for the use of luminescence thermometry techniques [1–5]. The temperature readout plays a key role as a diagnostic tool in the detection of inflammation and can also be used for real-time monitoring of hyperthermia treatments [6–8]. Among luminescent thermometers, inorganic

---

* Corresponding author.
** Corresponding author.
E-mail addresses: w.piotrowski@intibs.pl (W.M. Piotrowski), l.marciniak@intibs.pl (L. Marciniak).

materials doped with lanthanide (Ln^{3+}) and transition metal (TM) ions have received particular attention in recent years due to their good chemical- and photo-stability [9,10]. However, the design of a material suitable for thermal imaging in a biomedical context requires several optimization steps.

First, suitable host materials and dopants must be selected. The high susceptibility of the luminescence intensity of the transition metal (TM) ions to temperature changes and the ease of modulation of their spectral range of optical response as well as the thermal quenching rate by the modification of the host material is well known. This makes TM-based phosphors especially attractive for application in luminescent thermometry. The best known representative of TM and most extensively studied for this application is Cr^{3+}, whose intense emission can be associated with the $^2E \rightarrow ^4A_2$ or $^4T_2 \rightarrow ^4A_2$ electronic transitions. In the former case, the emission is usually observed with a maximum in the range of ~680–780 nm, which can make it difficult to select an excitation wavelength convenient for biological application. However, the $^4T_2 \rightarrow ^4A_2$ transition can result in an emission band located in the near infrared (NIR) range, within the range of optical biological windows (NIR-I: ~700–950 nm, NIR-II: 1000–1350 nm, NIR-III: 1500–1800 nm). To observe this broad emission band in the spectrum of Cr^{3+} a host material with weak crystal field strength needs to be selected [11–13]. An example of such a material is $MgTiO_3$, where Cr^{3+} ions occupy the relatively large crystallographic sites of Mg^{2+} ions.

The luminescence thermal quenching effect reduces both the intensity of Cr^{3+} emission and the lifetime of the excited state. This allows for the creation of a temporal luminescence thermometer. In contrast, an intensity-based strategy necessitates the use of a reference signal to calculate the ratio of two intensities. The emission bands of lanthanide ions (Ln^{3+}) can be used for this purpose because their emission intensity is less dependent on temperature than that of the Cr^{3+} band. Nd^{3+} stands out among Ln^{3+} ions in terms of biomedical applications due to its efficient emission in NIR-I and NIR-II. In both strategies, dopant concentrations will have a significant impact on thermometric performance, which must be verified thoroughly. Furthermore, the advantage of the chosen host material i.e. $MgTiO_3$ is the possibility of stabilization of Ti^{3+} ions, which further improves the thermal performance of Cr^{3+} luminescence. Stabilization of 6-fold coordinated Ti^{3+} centers has already been confirmed in the case of substitution of A^{2+} sites in $ATiO_3$ titanate host materials (A = Sr, Ca) by Ln^{3+} ions and is associated with the creation of []-Ti^{3+}-O oxygen vacancies (where [] is an oxygen vacancy) [14–16]. In the case of $MgTiO_3$, the location of both Ln^{3+} and Cr^{3+} ions in Mg^{2+} sites allows the stabilization of optically active Ti^{3+} ions, whose excited state can play the role of additional channel of depopulation of Cr^{3+} ions.

When targeting bioapplications, the cytotoxicity of the phosphor is a very important aspect that should be considered. So far, the low toxicity of $MgTiO_3$ nanostructures has been confirmed in the literature [17–19]. However, concerns about long-term cytotoxicity can stem from ion release. To overcome this issue, the phosphor can be encapsulated in an inorganic shell, minimizing ion release. Silica (SiO_2) is often used as a selling material in this scenario due to its ease in the deposition process, high chemical and mechanical stability, low cytotoxicity and the possibility to easily further functionalize its surface. This is expected to ensure safety when introducing nanoparticles under biological conditions without adversely affecting the tissue or cells. However, an important issue is the investigation of the effect of the envelope on the luminescence and thermometric properties of the enveloped materials, which is often an overlooked step in research.

In this work, we report and compare ratiometric and lifetime-based thermometry in $MgTiO_3$ particles co-doped with Cr^{3+} and Nd^{3+} ions. A detailed structural and luminescence characterization is presented to verify the presence of Ti^{3+} ions stabilized by Cr^{3+} ions and thus correctly assign the observed emission bands. Furthermore, the effect of Cr^{3+} and Nd^{3+} ions concentrations on the spectroscopic and thermometric performance was investigated by two thermometric approaches. Finally,

the effect of SiO_2 shell on the spectroscopic properties of the coated nanoparticles as well as their cytotoxicity in in vitro measurements using three cell lines was verified.

2. Experimental

2.1. Synthesis of $MgTiO_3$ nanoparticles doped with Cr^{3+} and co-doped with Cr^{3+} and Nd^{3+} ions

The $MgTiO_3$:x% Cr^{3+} (x = 0.1; 0.2; 0.5; 1; 2; 5) and $MgTiO_3$:0.1 % Cr^{3+}, y% Nd^{3+} (y = 0.1; 0.5; 1; 2; 5) nanocrystals were synthesized with a modified Pechini method [20]. The following starting materials were used as reagents without further purification: $Mg(NO_3)_2 \cdot 6H_2O$ (99.999 % purity, Alfa Aesar), $Ti(OC_4H_9)_4$ (99+% purity, Alfa Aesar), 2,4-pentanedione ($C_5H_8O_2$, 99 % purity, Alfa Aesar), $Cr(NO_3)_3 \cdot 9H_2O$ (99.999 % purity, Alfa Aesar), Nd_2O_3 (99.99 % purity, Stanford Materials Corporation), citric acid ($C_6H_8O_7$ >99.5 % purity, Alfa Aesar) and HNO_3 (65 % solution, Avantor). The total amount of Mg^{2+}, Cr^{3+} and Nd^{3+} ions was fixed at 2 mmol since x% Cr^{3+} and y% Nd^{3+} were calculated in respect to the number of Mg^{2+} ions. Firstly, appropriate amount of $Mg(NO_3)_2 \cdot 6H_2O$ and $Cr(NO_3)_3 \cdot 9H_2O$ were dissolved in deionized water and mixed together. In the case of Nd^{3+} co-doped nanocrystals, Nd_2O_3 was dissolved in deionized water with the addition of 2 mL of HNO_3, then recrystallized three times to remove the excess nitrogen and added to the water solution of other nitrates. In a separate beaker 2 mmol of $Ti(OC_4H_9)_4$ was mixed with 2,4-pentanedione in a 1:1 M ratio in order to stabilize the $Ti(OC_4H_9)_4$ solution. The contents of the beaker were gently stirred until a transparent, yellowish solution was obtained, which was then combined with the stabilized nitrate solution. Immediately after that, 24 mmol of an anhydrous citric acid was added to a mixture with the molar ratio of citric acid to all metals set to 6:1. Finally, 24 mmol of PEG-200 was added to the mixture in a 1:1 M ratio with respect to citric acid. The resulting solutions were then dried for 3 days at 363 K until resins were formed. Next, the samples were calcined in porcelain crucibles at 1023 K in air for 8 h. Finally, the obtained powders were ground in an agate mortar.

2.2. Coating of $MgTiO_3$:Cr^{3+}, Nd^{3+} nanoparticles with silica

To obtain silica coated $MgTiO_3$:Cr^{3+}, Nd^{3+} nanoparticles, a modified ultrasound-assisted Stöber method was used [21,22]. The following starting materials were used as reagents: $NH_3 \cdot H_2O$ (28 % solution, CHEMPUR), tetraethyl orthosilicate (TEOS; ≥99.0 %, Sigma-Aldrich), ethanol (EtOH; 96 % solution; POL-AURA). Specifically, an ethanolic suspension of $MgTiO_3$:Cr^{3+}, Nd^{3+} nanoparticles (30 mg of powder in 23 cm^3 of EtOH) was placed in an ultrasound bath for 2 h, to obtain well-dispersed nanoparticles, without aggregates. After this time, an ammonia solution (0.55 cm^3/7 cm^3 of distilled H_2O) was added to the dispersed nanoparticles and left for 15 min under continuous stirring. Meanwhile, a solution of TEOS in ethanol (0.75 cm^3/7.5 cm^3 EtOH) was prepared and added dropwise. The mixture prepared in this way was again placed in an ultrasound bath for 90 min. After this time, the obtained $MgTiO_3$:Cr^{3+}, Nd^{3+} @SiO_2 were collected by centrifugation (12000 rpm, 5 min) and washed with ethanol 3 times. The purified NPs were redispersed in ethanol or dried, for further analysis.

2.3. Characterization

All of the synthesized materials were examined by X-ray powder diffraction (XRPD) measurements carried out on PANalitycal X`Pert diffractometer, equipped with an Anton Paar TCU 1000 N temperature control unit, using Ni-filtered Cu-$K_\alpha$ radiation (V = 40 kV, I = 30 mA). Rietveld refinement procedure was carried out with PANalytical X`Pert HighScore Plus software. Transmission electron microscope (TEM) images were taken using a FEI TECNAI G2 X-TWIN microscope. Powders were dispersed in methanol with the aid of ultrasounds and deposited on

2

lacey-type copper grids. The studies were performed with 300 keV parallel beam electron energy. Images were digitally recorded using a Gatan Ultrascan 1000XP camera. The hydrodynamic size of the nanoparticles was determined by dynamic light scattering (DLS), conducted in a Malvern ZetaSizer at room temperature in a polystyrene cuvette, using distilled water as a dispersant.

The emission spectra were measured using the 445 nm excitation lines from a laser diode and a Silver-Nova Super Range TEC spectrometer from Stellarnet (1 nm spectral resolution) as a detector. The low-temperature (83 K) emission and excitation spectra and luminescence decay profiles were recorded using the FLS1000 Fluorescence spectrometer from Edinburgh Instruments with a R5509-72 photomultiplier tube from Hamamatsu in a nitrogen-flow cooled housing as a detector with a 450 W Xenon lamp and 445 nm pulsed work laser diode as an excitation sources. The temperature of the sample was controlled using a THMS 600 heating-cooling stage from Linkam (0.1 K temperature stability and 0.1 K set point resolution).

Thermal dependencies of the luminescence intensity ratio (LIR) were fitted using the Mott–Seitz model (Eq. S1). The average lifetimes of the excited states were calculated with the use of double exponential function according to the procedure described in the Supporting Information (Eq. S2-3).

2.4. Cytotoxicity assessment

The cell lines used in the study included murine fibroblasts 3T3 Swiss Albino, murine macrophages RAW 264.7 (ATCC, Rockville, MD, USA) and canine kidney epithelium line MDCK (Sigma-Aldrich, Steinheim, Germany). All cell lines were cultured in RPMI-1640 medium (Institute of Immunology and Experimental Therapy, Wrocław, Poland) supplemented with 10 % foetal bovine serum (FBS, Sigma, USA), L-glutamine (Sigma, UK) and antibiotics (streptomycin and penicillin, Sigma, Germany). For the cytotoxicity assessment, cells were seeded in 96-well-plates (TTP, Switzerland) at a density of 3×10^3 (3T3, Swiss Albino), 10×10^3 (RAW 264.7) or 2×10^3 (MDCK) cells per well and pre-incubated at 310 K (37 °C) overnight in a humidified atmosphere of 5 % CO_2. After that, dispersions of silica-coated and uncoated $MgTiO_3$: Cr^{3+}, Nd^{3+} were added. The nanoparticles were suspended in 80 % ethanol and bath-sonicated at room temperature for up to 5 min. Next, the stock dispersions were further diluted in sterile 80 % ethanol and dispersions in complete culture medium were prepared so that the concentration of ethanol was 1 % for all nanoparticle dilutions (this concentration was found to be well-tolerated by cells in preliminary experiments). In parallel, the highest nanoparticle concentrations were centrifuged at 30 000 *g* for 1 h and the particle-free supernatants were used as a diluent control (to exclude any possible particle-unrelated effects due to the presence of soluble compounds). Cells were exposed to increasing concentrations (1, 5, 10, 20, 40 μg/ml) of the dispersions for 48 h (5 % CO_2, 310 K). After that, the MTT assay was carried out. This test is based on the enzymatic reduction of the tetrazolium salt MTT [3-(4,5-dimethylthiazol-2-yl)-2,5-diphenyl-tetrazoliumbromide] in living, metabolically active cells. The metabolite, purple-coloured formazan is measured colourimetrically. Preliminary experiments showed no interference of the nanoparticles with MTT in a cell-free system at the concentrations used in this study. After 3.5 h of incubation, cells were lysed with a dedicated buffer (225 mL dimethylformamide, 67.5 g sodium dodecyl sulphate, 275 mL distilled water) and the optical density (OD) was measured after further 24 h using a spectrophotometric microplate reader (Tecan Spark 10 M, Switzerland) at the wavelength of 570 nm (reference 630 nm). The OD of control cells was taken as 100 %. The results were obtained from at least 3 independent experiments and viability values were compared between the control and nanoparticle-exposed cells as well as between both types of nanoparticles using Student's *t*-test (P ≤ 0.05 was considered statistically significant). Additionally, shortly before MTT addition, pictures were taken using an inverted light microscope coupled with a dedicated camera (Axiovert,

Zeiss, Germany).

3. Results and discussion

3.1. Structural and morphological characterization

$MgTiO_3$ crystallizes in a rhombohedral crystal system of the *R*-3 (148) space group. Its structure consists of $(MgO_6)^{10-}$ and $(TiO_6)^{8-}$ octahedra, which form layers in the *ab* plane (Fig. 1a). Due to the presence of two crystallographic sites with the same coordination number (Mg^{2+} and Ti^{4+}), it is of particular interest to consider their substitution mechanism. This is particularly difficult in the case of chromium ions, whose most stable form is Cr^{3+} and occupy only sites with octahedral coordination. For this purpose, a comparison of the effective ionic radii (EIR) of host material ions and dopant ions is most commonly used. In this case, Shannon reports EIR = 72 p.m., 60.5 p.m. and 61.5 p.m. for 6-fold coordinated Mg^{2+}, Ti^{4+} and Cr^{3+} ions, respectively. The smaller difference between the EIR of Ti^{4+} and Cr^{3+} ions clearly suggests that the Ti^{4+} site should be the preferred location of Cr^{3+} ions. However, several works published up to date have discussed the most likely distribution of ions in the $MgTiO_3$ structure after doping it with Cr^{3+} ions [23–25]. Wen-Chen, on the basis of electron paramagnetic resonance (EPR) spectra, reported that Cr^{3+} ions can be located in two sites with distinct surroundings, namely: (A) $Cr_{(Mg)}^{3+}$–$Ti_{(Ti)}^{4+}$ or (B) $Cr_{(Mg)}^{3+}$–$Mg_{(Ti)}^{2+}$ (both cases highlighted in Fig. 1a with a blue glow) [25]. It follows that in case (A), Cr^{3+} ions substitute the crystallographic positions of Mg^{2+} ions, which remain surrounded by Ti^{4+} ions and this situation should be dominant. Case (B), on the other hand, is possible due to the occurrence of the disorder between the Mg^{2+} and Ti^{4+} sublattices in $MgTiO_3$ and implies that Cr^{3+} ions again substitute Mg^{2+} positions, but this also involves the reversed locating of Mg^{2+} ions in Ti^{4+} ion positions. Considering both (A) and (B), the key point is that the Cr^{3+} ions occupy the positions of the larger Mg^{2+} ions rather than the smaller Ti^{4+} ions, which will be also confirmed later in the paper. In the case of Nd^{3+} ions with EIR = 98.3 p.m., they are also expected to substitute Mg^{2+} positions due to the smaller difference between EIR with respect to Ti^{4+} ions. However, by doping $MgTiO_3$ with both Cr^{3+} and Nd^{3+} ions, a charge mismatch is generated. To date, the stabilization of Ti^{3+} ions by Ln^{3+} dopant ions in $SrTiO_3$ and $CaTiO_3$ host materials was confirmed with the use of X-ray photoelectron spectroscopy (XPS) and spectroscopical verification [15,16]. Therefore, the possibility of a similar effect for Nd^{3+} ions in $MgTiO_3$:Cr^{3+}, Nd^{3+} should also be considered here. However, it is possible that a similar situation will occur when the Mg^{2+}-Ti^{4+} pair is replaced by Cr^{3+}-Ti^{3+}. This issue will be discussed later in the paper.

The XRPD patterns of $MgTiO_3$:x% Cr^{3+} nanoparticles have been compared with the reference pattern (ICSD 55285) to verify their phase purity (Fig. 1b). It was found that obtained patterns for $MgTiO_3$:x% Cr^{3+} (where x = 0.1. 0.2 and 0.5) correspond well with reference data. However, additional diffraction reflections were noted for x = 1, 2 and 5. These could be assigned to the impurities of Cr_2MgO_4 (ICSD 250576) and Cr_2O_3 (ICSD 130952). Thus, samples with concentrations higher than 0.5 % of Cr^{3+} ions were not further considered in this work. XRPD patterns of $MgTiO_3$:0.1 % Cr^{3+}, y% Nd^{3+} nanoparticles were also analyzed (Fig. S1). In this case, samples with Nd^{3+} concentration in the range 0.1%–2% do not indicate the presence of a second phase. However, for $MgTiO_3$:0.1 % Cr^{3+}, 5 % Nd^{3+} additional reflections were observed in the diffractograms at 18.18° and 25.53°, which probably correspond to $NdTiO_3$ (ICSD 82008). Therefore, phosphors co-doped maximally with 2 % of Nd^{3+} ions will be included in the following discussion. To investigate the effect of dopants on the unit cell parameters, a Rietveld refinement of the diffractograms was performed (Table S1, Fig. S2). For $MgTiO_3$ singly doped with Cr^{3+}, both *a* and *c* unit cell parameters gradually decrease with an increase of Cr^{3+} concentration (Fig. S3). This observation may suggest that the preferred crystallographic site for Cr^{3+} ions is Mg^{2+} one, since the unit cell shrinkage
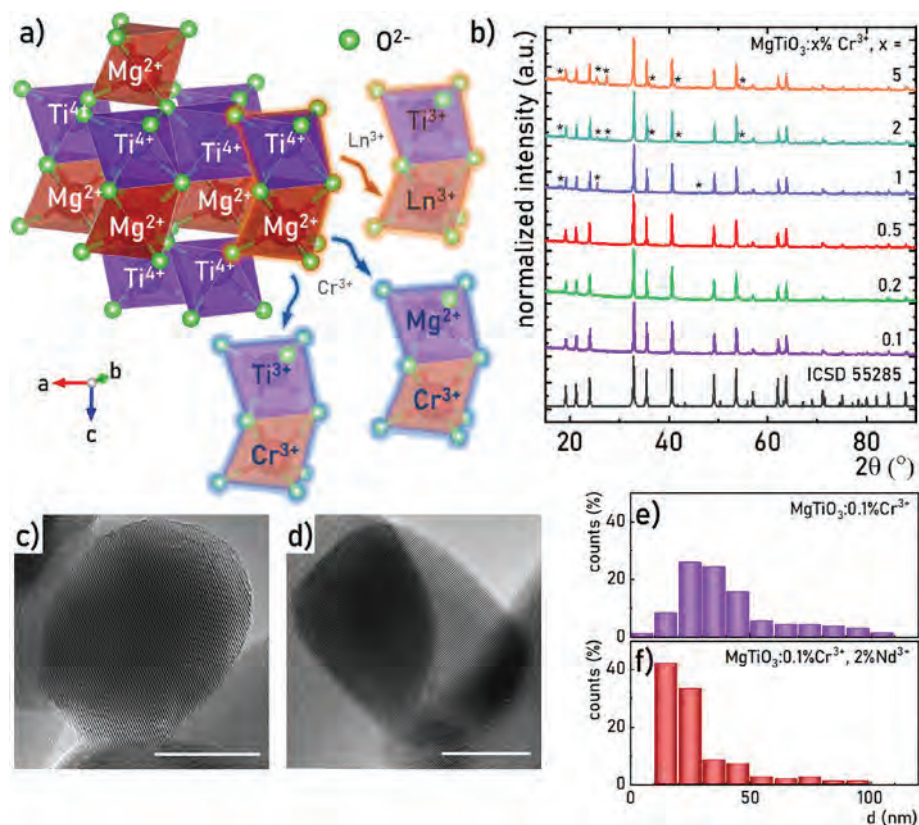
Fig. 1. Crystal structure of half $MgTiO_3$ unit cell – a); X-ray diffraction patterns of $MgTiO_3$ doped with different Cr^{3+} concentration (reflections of the additional phase marked by asterisk) – b); the representative TEM images of $MgTiO_3$:0.1 % Cr^{3+} (scale bar: 20 nm) – c) and $MgTiO_3$:0.1 % Cr^{3+}, 2 % Nd^{3+} (scale bar: 20 nm) – d); particle size distributions for $MgTiO_3$:0.1 % Cr^{3+} – e) and $MgTiO_3$:0.1 % Cr^{3+}, 2 % Nd^{3+} – f).

should be the result of a replacement of larger ions (in this case Mg^{2+} with EIR = 72 p.m.) by a smaller one (Cr^{3+} with EIR = 61.5 p.m.), which would not be the case if Cr^{3+} was replacing Ti^{4+} ions (EIR = 60.5 p.m.). This is consistent with the substitution mechanism mentioned by Wen-Chen [25]. Therefore, on the basis of the presented results, the localization of Cr^{3+} ions in Mg^{2+} positions should be considered as dominant, but there is no direct confirmation that this is the only mechanism for the localization of Cr^{3+} as dopant in $MgTiO_3$. On the other hand, doping with Nd^{3+} ions leads to an expansion of the unit cell, which is in agreement with the substitution of sites of smaller Mg^{2+} ions by larger Nd^{3+} ions. TEM images have been performed for $MgTiO_3$ doped with 0.1 % Cr^{3+} (Fig. 1c and Fig. S4) and 0.1 % Cr^{3+}, 2 % Nd^{3+} (Fig. 1d and Fig. S5). They suggest that the materials are well crystallized and susceptible to agglomeration. In addition, the particle size distribution was determined (Fig. 1e and f, respectively). In both cases, over 90 % of the volume of the material consists of particles smaller than 100 nm. It was observed that co-doping with Nd^{3+} ions yields smaller particles. Specifically, the average particle sizes were determined to be 40 ± 21 nm and 26 ± 16 nm for $MgTiO_3$:0.1%Cr^{3+} and $MgTiO_3$:0.1%Cr^{3+}, 2%Nd^{3+}, respectively. This may suggest that doping with Nd^{3+} ions with charge mismatch in respect to both ions of host material leads to enhanced defect formation, which inhibits the growth of crystallites.

3.2. Luminescent properties characterization

To understand the spectroscopic properties of $MgTiO_3$:Cr^{3+} materials, a configuration coordinate diagram of Cr^{3+} ions should be analyzed (Fig. 2a). Excitation at 445 nm allows the electron to be transferred from the $^4A_2$ ground state to the higher vibronic components of the $^4T_2$ excited state. This is followed by non-radiative depopulation to the bottom of the $^4T_2$ or ^2E parabolas and then radiative relaxation to

the $^4A_2$ ground state, which are manifested by bright emission in the red and near infrared spectral range, respectively. Both transitions are observed in the $MgTiO_3$:0.1 % Cr^{3+} emission spectra, where a sharp emission band at 733.5 nm and a broad emission band with a maximum at 835 nm are present (Fig. 2b). They correspond to spin-forbidden $^2E \rightarrow {}^4A_2$ and spin-allowed $^4T_2 \rightarrow {}^4A_2$ electronic transitions of Cr^{3+}, respectively. However, in the case of $MgTiO_3$:0.1 % Cr^{3+}, an additional sharp emission band at 697 nm with a side band at 713 nm was observed. As presented in previous papers [15,16], in titanates with structure $X^{2+}Ti^{4+}O_3$ it is possible to stabilize the optical centers of Ti^{3+} ions by co-doping with Ln^{3+} ions, locally forming Ln^{3+}-Ti^{3+} pairs. Therefore, it has been verified that in $MgTiO_3$ doped with 1 % of La^{3+} ions (that is optically inactive), the luminescence of Ti^{3+} was observed as a sharp band with side band located in the same spectral range as the previously unassigned emission bands detected for $MgTiO_3$:0.1 % Cr^{3+}. Therefore, it should be inferred that doping with Cr^{3+} ions also allows for the stabilization of Ti^{3+} ions, similarly to La^{3+} ions. According to the energy diagram in Fig. 2a, the use of $\lambda_{exc} = 445$ nm allows also for the excitation of electrons from O^{2-} ligands to Ti^{4+} ions via charge transfer (CT), followed by nonradiative relaxation to the bottom of ^2E parabola of Ti^{3+} ions and eventual radiative depopulation to $^2T_2$ ground state, resulting in an emission band at 697 nm. Comparing the emission spectra of $MgTiO_3$ doped with different concentrations of Cr^{3+} ions, one can see that the contribution of Ti^{3+} emission associated with the $^2E \rightarrow {}^2T_2$ electronic transition decreases sharply with the change of Cr^{3+} content from 0.1 % to 0.2 % (Fig. 2c). To further confirm the presence of emission originating from two different optical centers, excitation spectra of the $MgTiO_3$:Cr^{3+} for $\lambda_{em} = 697$ nm and $\lambda_{em} = 835$ nm are shown in Fig. 2d. It can be clearly seen that the broad band around 340 nm ($\sim$29 410 cm^{-1}) consists of an overlapping bands, corresponding to $^4A_2 \rightarrow {}^4T_1$ transition of Cr^{3+} ions and CT($O^{2-} \rightarrow Ti^{4+}$), respectively.

4

116
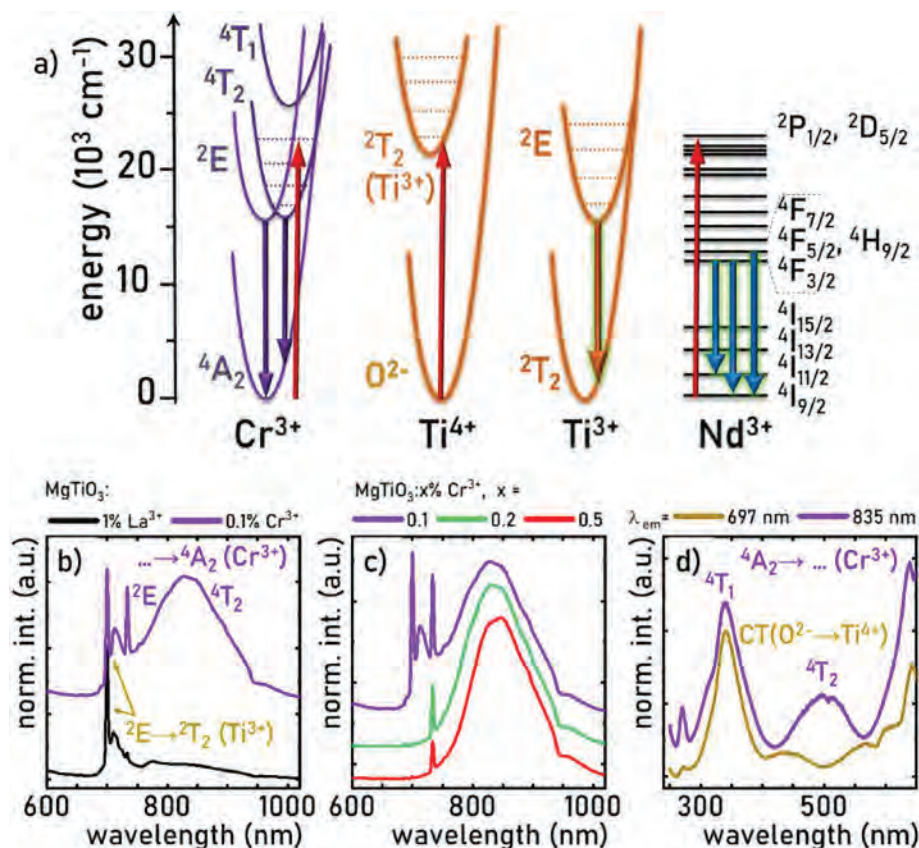
Fig. 2. The simplified configurational coordinate diagram for Cr^{3+}, Ti^{3+} and Nd^{3+} ions – a); comparison of emission spectra ($\lambda_{exc} = 400$ nm) for $MgTiO_3$ doped with 1 % La^{3+} and doped with 0.1 % Cr^{3+} ions performed at low temperature (83 K) – b); the influence of Cr^{3+} concentration on emission spectra of $MgTiO_3$:x% Cr^{3+} materials (83K, $\lambda_{exc} = 445$ nm) – c); comparison of excitation spectra for $\lambda_{em} = 697$ nm and $\lambda_{em} = 835$ nm (83 K) in $MgTiO_3$:0.1 % Cr^{3+} phosphor – d).

Additionally, for $\lambda_{em} = 835$ nm another broad band with a maximum at 504 nm ($\sim$19840 cm^{-1}) was found, which is not present in the excitation spectrum for $\lambda_{em} = 697$ nm and corresponds to $^4A_2 \rightarrow ^4T_2$ electronic transition of Cr^{3+} ions. A similar shape of excitation spectra was obtained for $MgTiO_3$:0.5 % Cr^{3+} (Fig. S6). However, due to the slight shift of the excitation band maxima, a crystal field parameter for Cr^{3+} ions was calculated from Eq. S4–S6. The results summarized in Table S2 indicate that the Dq/B parameter grows from 1.86 to 2.04 as the concentration of Cr^{3+} ions changes from 0.1 % to 0.5 %. This is consistent with the previously presented effect of Cr^{3+} ions concentration on shrinking unit cell parameters, since a smaller unit cell size should lead to higher crystal field strength. On the other hand, one can find in Fig. 2c) that this is inconsistent with a shift of the $^4T_2 \rightarrow ^4A_2$ band maximum of Cr^{3+} ions from 830 nm to 845 nm for 0.1 % and 0.5 % Cr^{3+}, respectively. However, a comparison of the shape of the mentioned emission spectra with that of $MgTiO_3$:1 % La^{3+} may suggest that the broad bands associated with the subsequent Ti^{3+} vibronic states with local maxima at 775 nm and 830 nm, overlap spectrally with the $^4T_2 \rightarrow ^4A_2$ emission band for $MgTiO_3$:0.1 % Cr^{3+}, which is no longer observable for $MgTiO_3$:0.5 % Cr^{3+}, generating an error in the attributing of the actual Cr^{3+} broad band maximum.

As further confirmation of the presence and stabilization of Ti^{3+} ions in doped $MgTiO_3$, emission and excitation spectra for $Ba_xMg_{1-x}TiO_3$ structures were analyzed (Figs. S7–9). This topic is further discussed in the Supporting Information.

3.3. Thermometric properties of Cr^{3+} doped and Cr^{3+} and Nd^{3+} co-doped systems

The correct assignment of emission bands to optical centers in the

$MgTiO_3$:Cr^{3+} emission spectra can also be facilitated by comparing their thermal evolution (Fig. S10). The different quenching rates of the bands located at 697 nm and 713 nm, corresponding to Ti^{3+} emission, and 734 nm and 835 nm, corresponding to Cr^{3+} emission can be clearly seen. Moreover, different quenching rates of Cr^{3+} emission originating from the ^2E and $^4T_2$ levels can also be observed. To allow a quantitative comparison of their characteristics as a function of temperature, the thermal evolution of $^4T_2 \rightarrow ^4A_2$ and $^2E \rightarrow ^4A_2$ emission bands is shown in Figs. S11a–b. In the case of the $^4T_2 \rightarrow ^4A_2$ broad band, the thermal evolution of signal intensity proved to be barely dependent of Cr^{3+} concentration. It decreases slowly from 83 to 143 K reaching $\sim$94 % of the initial intensity. Above this value, the intensity is markedly quenched, at a rate that is faster with increasing Cr^{3+} concentration. Therefore, it is possible to compare the $T_{1/2}$ parameter, defined as the temperature at which the intensity reaches a 50 % of the initial value. $T_{1/2}$ equals 331 K, 295 K and 213 K for 0.1 %, 0.2 % and 0.5 % Cr^{3+}, respectively. Nevertheless, a complete quenching of the emission occurs at $\sim$483 K for all considered concentrations. On the other hand, the ^2E emission intensity decreases rapidly already from 83 K. At 143 K, it reaches 74–81 % of the initial value. It can be seen that in the 83–323 K range the quenching rates of 0.2 % and 0.5 % Cr^{3+} co-doped samples are slightly higher than that of the 0.1 % Cr^{3+} counterpart. Besides, the shape of the thermal evolution of ^2E emission is barely dependent on Cr^{3+} concentration. $T_{1/2}$ equals 243–263 K, while at around 403 K the signal is $\sim$12 % of the initial value. The different thermal quenching rates encourage the determination of the luminescence intensity ratio (LIR) as follows:

$$LIR_1 = \frac{\int\limits_{790\,nm}^{899\,nm} I\left(^4T_2 \rightarrow {}^4A_2\right)\left[Cr^{3+}\right]d\lambda}{\int\limits_{731\,nm}^{736\,nm} I\left(^2E \rightarrow {}^4A_2\right)\left[Cr^{3+}\right]d\lambda} \qquad \text{(Eq. 1)}$$

The resulting thermal evolution of LIR_1 is shown in Fig. S12a. For all Cr^{3+} concentrations the LIR value initially increases, but its maximum value and the temperature at which it is reached decrease as the concentration of Cr^{3+} ions increases. Thus, $LIR_1 = 1.57$ at 303 K, $LIR_1 = 1.37$ at 183 K and $LIR_1 = 1.25$ at 143 K were obtained for 0.1 %, 0.2 % and 0.5 % Cr^{3+}, respectively. Above these values, the monotonicity of the LIR_1 changes and decreases up to ~460 K. To verify the influence of Cr^{3+} concentration on thermal changes of LIR_1 values, the relative sensitivity S_R was calculated according to the following formula (Eq. 2):

$$S_R = \frac{1}{LIR} \frac{\Delta LIR}{\Delta T} \times 100\% \qquad \text{(Eq. 2)}$$

where and ΔLIR represents the change of LIR for the ΔT change of temperature. The obtained S_R results were plotted in Fig. S12b. Firstly, in the temperature range from 83 K to even 291 K negative S_R values were obtained, which are due to the inverse monotonicity of the LIR in respect to the rest of the temperature range. Nevertheless, in the range of 105–114 K the largest S_R values were found to be enhanced with increasing Cr^{3+} concentration and reached $-0.30\%K^{-1}$, $-0.43\%K^{-1}$ and $-0.63\%K^{-1}$ for 0.1 %, 0.2 % and 0.5 % Cr^{3+}, respectively. Besides, the highest S_R values were obtained as follows: $S_R = 0.97\%K^{-1}$ at 450 K, $S_R = 0.65\%K^{-1}$ at 490 K and $S_R = 0.77\%K^{-1}$ at 218 K for 0.1 %, 0.2 % and 0.5 % Cr^{3+}, respectively. Therefore, the MgTiO$_3$:0.1 % Cr^{3+} seems the most encouraging for a potential application. However, to improve the thermometric properties of this luminescent thermometer it was decided to co-dope this material with Nd^{3+} ions. As shown in the energy diagram

in Fig. 2a), the use of $\lambda_{exc} = 445$ nm also allows the excitation of Nd^{3+} ions directly through $^2P_{1/2}$, $^2D_{5/2}$ mixed excited levels. This is followed by the nonradiative depopulation to $^4F_{5/2}$, $^4H_{9/2}$ or $^4F_{3/2}$ excited states, from which the emission can be observed. Indeed, the presence of Nd^{3+} bands was confirmed by the comparison of emission spectra of MgTiO$_3$:0.1 % Cr^{3+}, y% Nd^{3+} for y>0.5 % at 83 K (Fig. 4a). These bands are even more evident when comparing the emission spectra at higher temperature (463 K), when the signal from Cr^{3+} emission decreases, revealing the spectral overlap with the Nd^{3+} bands (Fig. S13). It is noteworthy that the Nd^{3+} ions emission bands are much broader than in previously studied materials and which makes impossible to separate the Stark components of the band. In the case of MgTiO$_3$, this shape of the emission bands is the result of the low local symmetry of the crystallographic site occupied by the Nd^{3+} ions. Due to the low local symmetry of Nd^{3+} sites, the presence of Nd^{3+} ions, regardless of their concentration, slightly affects the shape of the broad excitation bands of Cr^{3+} ions (Fig. S14). Another strand worth mentioning in the shape of the emission spectra of MgTiO$_3$ co-doped with Cr^{3+} and Nd^{3+} ions is the presence of bands associated with the $^2E \rightarrow {}^2T_2$ transition of Ti^{3+} ions (Fig. S15). Comparing the emission spectra for MgTiO$_3$:0.1 % Cr^{3+} and MgTiO$_3$:0.1 % Cr^{3+}, 0.1 % Nd^{3+}, which were normalized to the $^4T_2 \rightarrow {}^4A_2$ emission band, it can be seen that the $^2E \rightarrow {}^2T_2$ vibronic band is about 310 % more intense after co-doping with Nd^{3+} ions. This may suggest that the stabilization of Ti^{3+} ions with Nd^{3+} ions is more efficient than with Cr^{3+}, but in this role the influence of Nd^{3+} and Cr^{3+} ions on Ti^{3+} stabilization add up. Next, Fig. 4b) and Fig. S16 show the thermal evolution of the emission spectra of MgTiO$_3$:0.1 % Cr^{3+}, y% Nd^{3+} materials. Similarly to the emission spectra for MgTiO$_3$:Cr^{3+}, the emission signal coming from several optical centers provides different rates of intensity quenching, depending on the wavelength. From several possibilities, two spectral ranges were found to be the most promising: 1) the one corresponding to the Ti^{3+} emission band associated with the $^2E \rightarrow {}^2T_2$ transition (Fig. 3c) and 2) the other with the spectrally
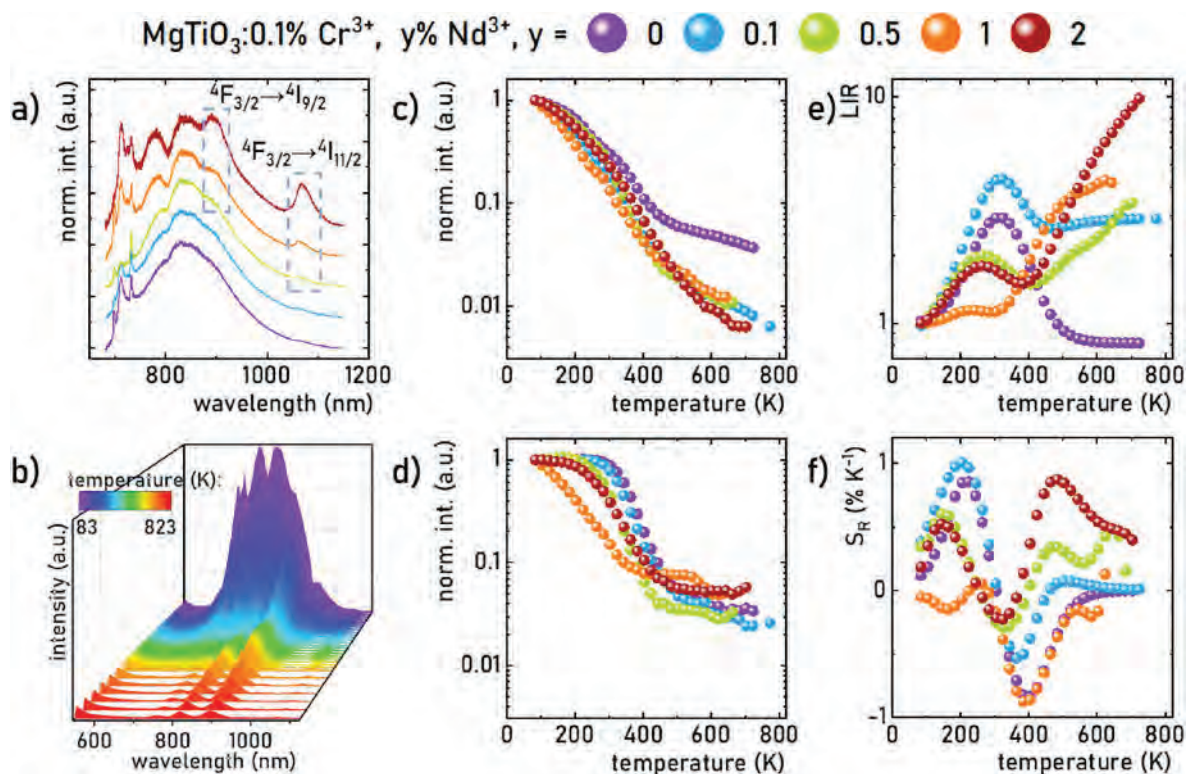
Fig. 3. Influence of Nd^{3+} concentration on the emission spectra of MgTiO$_3$:0.1 % Cr^{3+}, y% Nd^{3+} materials (83K, $\lambda_{exc} = 445$ nm) – a); thermal evolution of emission spectra of MgTiO$_3$:0.1 % Cr^{3+}, 1 % Nd^{3+} phosphor – b); influence of Nd^{3+} concentration on thermal evolution of $^2E \rightarrow {}^2T_2$ (Ti^{3+}) emission band – c); $^4T_2 \rightarrow {}^4A_2$ (Cr^{3+}) + $^4F_{3/2} \rightarrow {}^4I_{9/2}$ (Nd^{3+}) emission band – d); their LIR – e) and relative sensitivity S_R – f).
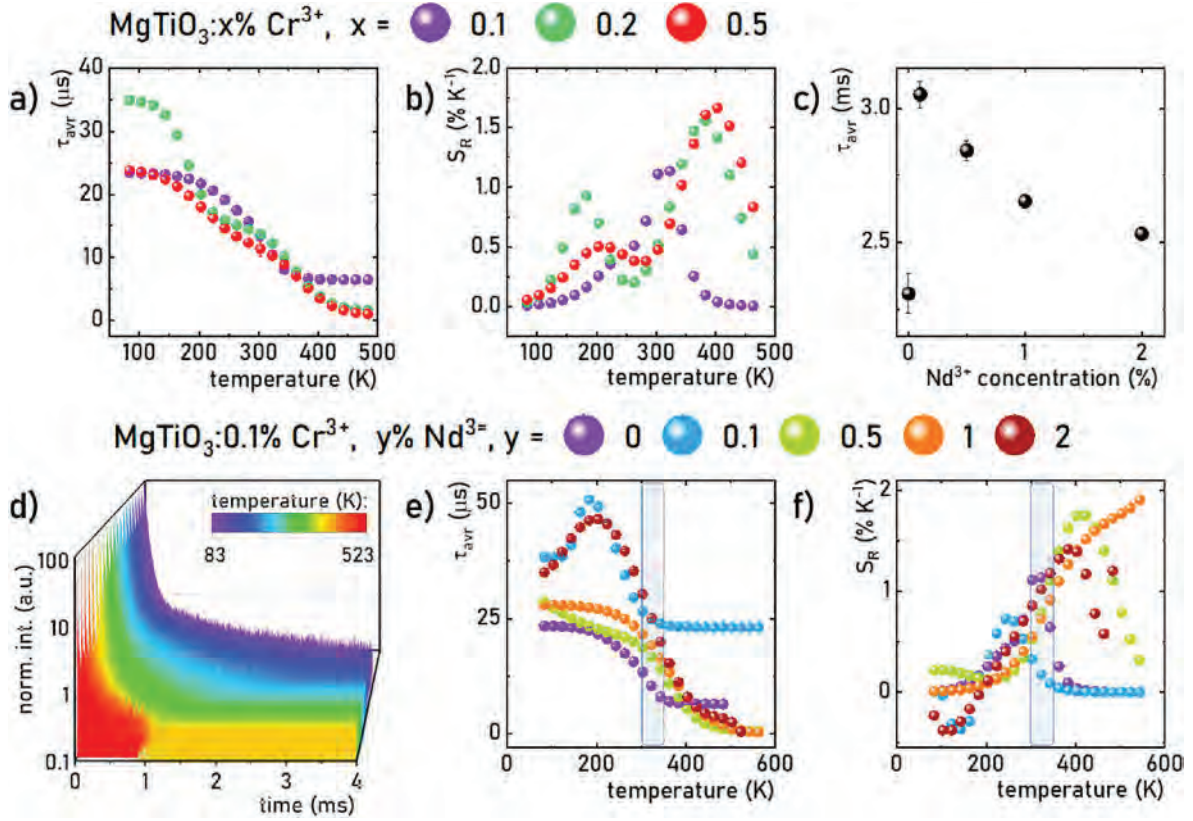
Fig. 4. Thermal evolution of $^4T_2$ excited state lifetime of Cr^{3+} ions – a) and its relative sensitivity for different Cr^{3+} ions concentration in MgTiO$_3$:x% Cr^{3+} materials – b); influence of Nd^{3+} ions concentration on ^2E excited state lifetime of Ti^{3+} ions at 83 K in MgTiO$_3$:0.1 % Cr^{3+}, y% Nd^{3+} – c); thermal evolution of luminescent decay profiles of emission from $^4T_2$ excited state of Cr^{3+} ions in MgTiO$_3$:0.1 % Cr^{3+}, 2 % Nd^{3+} – d); average lifetime – e) and relative sensitivity S$_R$ for MgTiO$_3$:0.1 % Cr^{3+}, y % Nd^{3+} materials – f).

overlapped emission of Cr^{3+} ($^4T_2 \rightarrow ^4A_2$) and Nd^{3+} ions ($^4F_{3/2} \rightarrow ^4I_{9/2}$) (Fig. 3d). In the former case, Ti^{3+} emission intensity quasi-linearly decreases from 83 K to 280 K, regardless of Nd^{3+} content. Above this temperature, the signal of all samples co-doped with Nd^{3+} ions quenches faster than the solely doped with Cr^{3+} ions counterpart. It can be seen that in the case of 1 % Nd^{3+}, the intensity of the signal decreases slightly faster with a value of T$_{1/2}$ = 171 K in comparison with T$_{1/2}$ values in the range 198–222 K achieved for other concentrations. Then, above ~500 K the emission signal remains below 2 % of the initial value. As a result, it can be concluded that the quenching rate of Ti^{3+} ions is not dependent on the presence and content of Nd^{3+} ions, despite the different contributions to the shape of the emission spectra. On the other hand, Fig. 4d shows a noticeable influence of Nd^{3+} content on the thermal evolution of the intensity signal in the spectral range of the overlapped emission bands of Cr^{3+} ($^4T_2 \rightarrow ^4A_2$) and Nd^{3+} ($^4F_{3/2} \rightarrow ^4I_{9/2}$). Firstly, it can be seen that the temperature range, in which the signal remains almost constant shortens. For 0.1 % and 0.5 % Nd^{3+} intensity at 243 K and 203 K is 99 % of the initial value, respectively, in comparison with 263 K for 0 % Nd^{3+}. Above this temperature, gradual thermal quenching occurs. Similar to LIR$_1$, the different thermal quenching rate of the two spectral ranges selected from the emission spectra of MgTiO$_3$:0.1 % Cr^{3+}, y% Nd^{3+} ions is encouraging for the calculation of the LIR$_2$ parameter, as follows:

$$LIR_2 = \frac{\int\limits_{950\ nm}^{967\ nm} I\left(\left(^4T_2 \rightarrow ^4A_2\right)\left[Cr^{3+}\right] + \left(^2F_{9/2} \rightarrow ^4I_{9/2}\right)\left[Nd^{3+}\right]\right)d\lambda}{\int\limits_{710\ nm}^{717\ nm} I\left(^2E \rightarrow ^2T_2\right)\left[Ti^{3+}\right]d\lambda} \qquad \text{(Eq. 3)}$$

The effect of Nd^{3+} concentration on the thermal dependence of LIR$_2$

is shown in Fig. 4e. In the case of MgTiO$_3$ solely doped with Cr^{3+} ions, it is noted that LIR$_2$ increases gradually up to 303 K reaching 292 % of the initial value, and then decreases gradually reaching the same LIR$_2$ value at 483 K as at 83 K. When co-doped with Nd^{3+}, a similar shape of thermal evolution of LIR$_2$ can be found, however, the contribution of the Nd^{3+} band in the denominator of LIR$_2$ is evident in two ways: (I) for 0.1 % Nd^{3+} a rise in LIR$_2$ to a higher value was obtained, i.e. LIR$_2$ = 4.33 at 323 K, followed by a decrease in LIR$_2$ for 2.58 at 443 K, which remained more or less constant until 723 K; (II) for higher concentrations (0.5; 1 and 2 %) a continuous increase in LIR$_2$ was observed from ~400 K onwards. The most dramatic increase in LIR$_2$ was obtained for the sample with 2 % Nd^{3+}, i.e. from 1.54 to 9.85 in the range 403–723 K. Due to the noticeable effect of Nd^{3+} ions concentration on the temperature range in which the largest changes in LIR$_2$ value were observed, relative sensitivities were calculated (Fig. 4f). It is evident that the thermal evolution of S$_R$ for all materials follows a similar shape. However, the S$_R$ values that are obtained for the different Nd^{3+} contents vary significantly. It can be seen that the above-mentioned two processes, which are revealed after co-doping with Nd^{3+} ions, are responsible for the improved sensitivity in respect to the Nd^{3+} non co-doped phosphor. Thus, in the first regime the highest S$_R$ = 1.00%K^{-1} at 203 K was achieved for 0.1 % Nd^{3+} in respect to S$_R$ = 0.85%K^{-1} at this temperature for Cr^{3+} solely doped counterpart. Then, at around 383 K, S$_R$ = −0.87%K^{-1} was achieved for 1 % Nd^{3+} in comparison to a similar value of S$_R$ = −0.85%K^{-1} for the 0 % Nd^{3+} counterpart. As previously mentioned, negative S$_R$ values are indicative of a change in the monotonicity of LIR$_2$, and their potential use in luminescence thermometry would require a determination of the useful temperature range. Finally, for 2 % Nd^{3+} an S$_R$ = 0.87%K^{-1} was obtained at 483 K, while above this temperature the S$_R$ value for the solely Cr^{3+} doped sample tends towards zero. Moreover, LIR$_2$ calculation performed for the heating-cooling cycles also reveals

the thermometric performance of the 2 % Nd^{3+} co-doped materials (Fig. S17). Therefore, luminescence thermometers based on the LIR for $MgTiO_3$ co-doped with Cr^{3+} and Nd^{3+} ions could find a wide range of applications through an appropriate selection of dopant concentrations. However, it should be pointed out that a precisely defined spectral range has to be chosen, which can be a serious practical limitation due to the need to select appropriate optical filters.

Thermal evolution of the luminescence kinetics of Cr^{3+} in Cr^{3+}-doped and Cr^{3+}, Nd^{3+}-co-doped phosphors.

As presented in the case of the emission spectra, the investigated $MgTiO_3:Cr^{3+}$ phosphors contain more than one luminescent center, i.e. co-existing Cr^{3+} and Ti^{3+} ions, and also the emission of Cr^{3+} ions can originate from both the ^2E and $^4T_2$ energy levels. Therefore, the effect of the concentration of Cr^{3+} ions followed by Nd^{3+} ions on the lifetimes of excited states needs to be carefully analyzed. Firstly, the thermal evolution of luminescent decay profiles of the $^4T_2$ excited state of Cr^{3+} ions was performed for $MgTiO_3:Cr^{3+}$ materials (Fig. S18). The $^4T_2$ excited state was chosen because of its broad and intense emission, for which it will be possible to select measurement parameters that do not to overlap spectrally with other emission bands. Comparing decay profiles for different Cr^{3+} concentrations, it can be noted that in the case of $MgTiO_3:0.2$ % Cr^{3+} (below 200 K) longer decay profiles can be observed comparing to samples doped with 0.1 % and 0.5 % Cr^{3+}. To verify this quantitatively, τ_{avr} was calculated (Fig. 4a). Analyzing the τ_{avr} values, it can be seen that for 0.1 % Cr^{3+} the $\tau_{avr} = 23.8$ µs at 83 K remains almost constant until a temperature of 183 K, above which it gradually shortens to 383 K, where it reaches $\tau_{avr} = 6.67$ µs This value remains constant up to 483 K. It is worth noting the elongation of the lifetime to $\tau_{avr} = 34.9$ µs at 83 K for $MgTiO_3:0.2$ % Cr^{3+}. The lifetimes for 0.1 % Cr^{3+} remain longer than the others up to 203 K, when their τ_{avr} starts to be shorter than 20.0 µs However, in this case the change in quenching rate in the range 243–283K is essential, since it suggests the occurrence of an additional depopulation channel. On this basis, it can be inferred that in the range below 200 K the elongation of lifetimes is related to energy transfer to the ^2E state of Ti^{3+} ions. A similar shape of thermal evolution of τ_{avr} was observed for 0.5 % Cr^{3+} ions, but in this case τ_{avr} at 83 K equals 23.8 µs, which is the same as for the 0.1 % Cr^{3+} counterpart. The shortening of the lifetimes in respect to 0.2 % Cr^{3+} may be due to the shortening of the ^2E state of Ti^{3+} ions as the concentration of both Cr^{3+} and Ti^{3+} ions increases. In order to compare the rate of shortening of decay times depending on Cr^{3+} content, their relative sensitivities were calculated (Fig. 4b). Consistent with the previous observation of one process causing a decrease in τ_{avr} for 0.1 % Cr^{3+} and two processes for 0.2 % and 0.5 % Cr^{3+}, the S_R values are characterized by one or two local maxima, respectively. Thus, the S_{Rmax} for $MgTiO_3:0.1$ % Cr^{3+} is 1.13 % K^{-1} at 323 K. On the other hand, lower local maxima of $S_R = 0.93\%K^{-1}$ at 183 K and $S_R = 0.50\%K^{-1}$ at 203 K were reached for 0.2 % Cr^{3+} and 0.5 % Cr^{3+}, respectively. Above these temperatures, there was a decrease in S_R values in both cases, so that 0.2 % Cr^{3+} reached $S_{Rmax} = 1.55\%K^{-1}$ at 383 K and 0.5 % Cr^{3+} reached $S_{Rmax} = 1.67\%K^{-1}$ at 403 K. Despite the higher S_{Rmax} values obtained for 0.2 % and 0.5 % Cr^{3+} doped samples, for the 0.1 % Cr^{3+} S_R reached higher values in the physiological temperature range. Therefore this sample was selected for further study. When co-doping $MgTiO_3:Cr^{3+}$ with Nd^{3+} ions, a marked change in the luminescent decay profiles of ^2E state of Ti^{3+} ions at 83 K was noted, as confirmed by the calculated τ_{avr} values (Fig. S19, Fig. 4c). Importantly, an increase in the lifetimes of Ti^{3+} ions from $\tau_{avr} = 2.31$ ms–3.05 ms was observed for co-doped $MgTiO_3:0.1$ % Cr^{3+} with 0.1 % Nd^{3+} ions. This may suggest that doping with Nd^{3+} ions with charge mismatch and larger EIR in respect to Mg^{2+} ions, leads to the generation of greater lattice distortion in respect to Cr^{3+} ions. As is well known, the local symmetry of a luminescent ion affects the probability of radiative depopulation of the excited state od luminescent ions thus having an impact on their lifetimes. An increase of the local symmetry of the ion and the crystallization degree through the co-doping which leads to the elongation of the luminescence kinetics has been already demonstrated

for lanthanide doped [26,27] changes in local symmetry the co-doping of $MgTiO_3:Cr^{3+}$ with Nd^{3+} can lead to the observed elongation of the Ti^{3+} lifetime. Similar effect was already observed in $SrTiO_3:Ln^{3+}$ [28].

Then, for higher concentrations of Nd^{3+} ions, an expected gradual reduction in the lifetimes of Ti^{3+} ions is observed, up to $\tau_{avr} = 2.53$ ms for 2 % Nd^{3+} ions. The effect of Nd^{3+} concentration was also evaluated for the thermal evolution of Cr^{3+} lifetimes (Fig. 4d and Fig. S20). The calculated τ_{avr} in Fig. 4e confirms the beneficial effect of Nd^{3+} ions on the elongation of Cr^{3+} lifetimes, irrespective of Nd^{3+} concentration. The longest τ_{avr} at 83 K was obtained for 0.1 % Nd^{3+} ions equal to 38.3 µs (~64 % longer than for the solely Cr^{3+} doped counterpart). In this case, up to 183 K there is an increase in lifetimes, reaching 50.9 µs Above this temperature, τ_{avr} decreases until $\tau_{avr} = 23.4$ µs at 363 K. When co-doped with 0.5 % and 1 % of Nd^{3+} ions, $\tau_{avr} = \sim28.0$ µs at 83 K, which is only 20 % higher than the Cr^{3+} solely doped sample. Above 83 K for these two concentrations, no increase in lifetimes was observed either. For concentrations higher than 0.1 % Nd^{3+} above ~220 K, a gradual decrease in τ_{avr} value with increasing temperature can be observed, leading to a value of less than 5 µs after exceeding 443 K. Surprisingly, similar to 0.1 % Nd^{3+}, significant elongation of Cr^{3+} ions lifetimes was obtained for 2 % Nd^{3+}. This may suggest that the concentration of 2 % of Nd^{3+} is sufficient to lead to the greatest lattice distortion affecting the lifetimes of Cr^{3+} ions in respect to other Nd^{3+} concentrations. From 83 to 203 K elongation to 46.6 µs at 203 K and gradual shortening was obtained, similarly to 0.5 % and 1 % Nd^{3+} counterparts. Fig. 4f compares the relative sensitivities calculated for τ_{avr} of $MgTiO_3:Cr^{3+}$, Nd^{3+} materials. The highest values were obtained for 0.5 % Nd^{3+} ions equal to $S_{Rmax} = 1.75\%K^{-1}$ at 413 K, and for 1 % Nd^{3+} the S_R reaches even 1.90%K^{-1} at 543 K. For this reason, co-doping with Nd^{3+} ions should be considered to have a beneficial effect on S_R values. When considering the potential use of phosphors in thermometry operating in the physiological temperature range, it is also worth noting the increase in lifetimes in respect to $MgTiO_3$ solely doped with Cr^{3+} ions, which performed most favorably for samples with 0.5 % and 2 % Nd^{3+} ions. However, of the two materials, the one with 2 % Nd^{3+} achieved S_R values in the range of 0.85–1.18%K^{-1} over 303–343 K in respect to S_R values of less than 0.33%K^{-1} for 0.5 % Nd^{3+} ions. Moreover, heating–cooling cycles performed for $MgTiO_3:0.1$ % Cr^{3+}, 2 % Nd^{3+} confirm a good repeatability in their lifetime-based thermometric performance (Fig. S21). On this basis, the $MgTiO_3:0.1$ % Cr^{3+}, 2 % Nd^{3+} phosphor was selected as the most suitable for further optimization.

3.4. Improving potential of biological application through silica-coating

To improve the application potential of the selected nanoparticles, they were coated with SiO_2 layer using the modified Stöber method, described in detail in the Experimental section. TEM images of SiO_2-coated nanoparticles are shown in Fig. 5a and b and Fig. S22. It can be found that nanoparticles are coated with silica of quasi constant thickness. From the TEM images, the average thickness of the silica shell was determined to be 7 ± 1 nm (Fig. S23). Subsequently, the spectroscopic properties of $MgTiO_3:0.1$ % Cr^{3+}, 2 % Nd^{3+} nanoparticles uncoated and coated with silica were compared. No significant changes in the shape of emission spectra were found (Fig. 5c). Special attention should be paid to the effect of silica coating on the Cr^{3+} excited state lifetimes, conducted in the physiological temperature range 293 K–323 K (Fig. 5d, Fig. S24). At 293 K, a slight increase in τ_{avr} values from 32.2 µs to 32.8 µs for the silica coated sample was observed. A similar trend continues throughout the temperature range, for which an elongation of 0.55 ± 0.16 µs was determined. This phenomenon can be explained by the reduction of the probability of the nonradiative depopulation of the excited state by the surface related quenchers (surface defects, OH molecules attached to the surface etc.) when the SiO_2 is deposited on the $MgTiO_3:Cr^{3+},Nd^{3+}$ surface.

Furthermore, to verify the application potential of nanoparticles coated with silica, cytotoxicity assessments were performed.
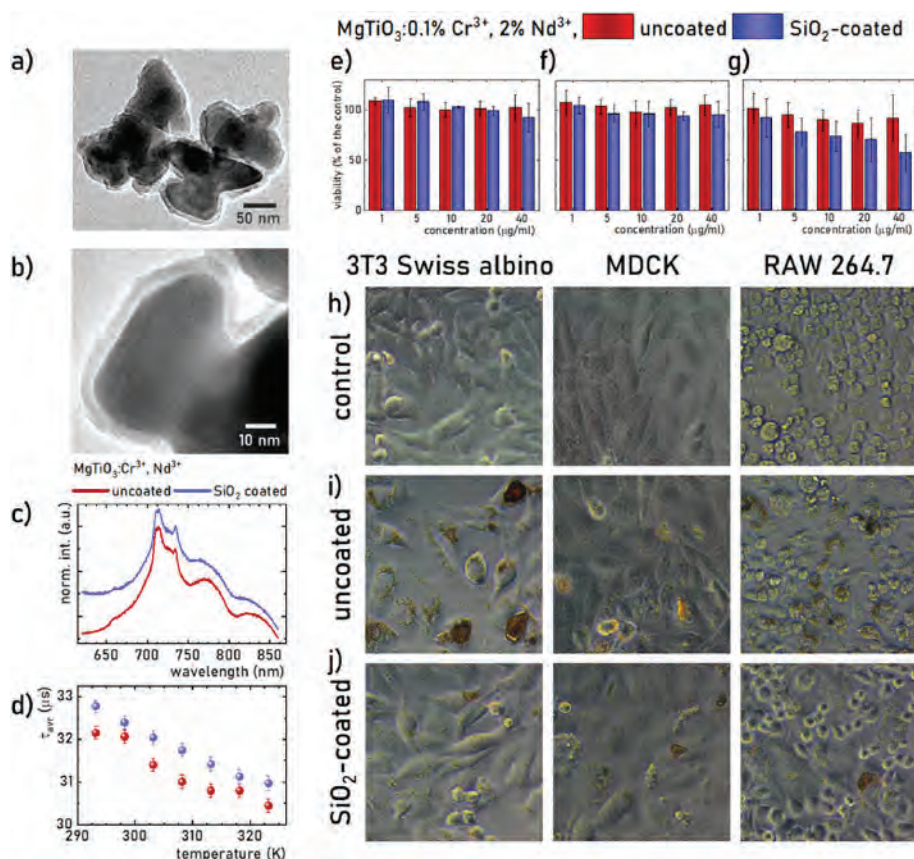
Fig. 5. Representative TEM images of MgTiO$_3$:0.1 % Cr^{3+}, 2 % Nd^{3+} coated with SiO$_2$ layer – a), b); comparison of emission spectra at 83 K – c) and average lifetimes of ^{4}T$_2$ excited state of Cr^{3+} ions in MgTiO$_3$:0.1 % Cr^{3+}, 2 % Nd^{3+} non-coated and coated with SiO$_2$ – d); viability assessment (mean ± SD) using MTT assay in three cell lines exposed to uncoated and silica-coated MgTiO$_3$:0.1 % Cr^{3+}, 2 % Nd^{3+} nanoparticles – d), e), f); control fibroblasts (3T3-Swiss albino), kidney epithelium cells (MDCK) and macrophages (RAW 264.7) (magnification 400 ×) – h); the same cell lines exposed to uncoated MgTiO$_3$:0.1 % Cr^{3+}, 2 % Nd^{3+} nanoparticles at a concentration of 40 μg/ml for 48 h (magnification 400 ×) – i); the same cell lines exposed to silica-coated MgTiO$_3$:0.1 % Cr^{3+}, 2 % Nd^{3+} nanoparticles at a concentration of 40 μg/ml for 48 h (magnification 400 ×) – j).

Cytotoxicity tests were carried out on murine fibroblast (3T3-Swiss albino), murine macrophage (RAW 264.7) and Madin-Darby canine kidney (MDCK) cell lines. Cell lines have been selected as an *in vitro* model based on their wide use in toxicity studies as well as the specific functions these types of cells have in the organism. Fibroblasts are the main cellular component of connective tissues and 3T3 fibroblasts are a standard model to screen for cytotoxicity of implants and biomaterials [29,30]. Under *in vivo* conditions, macrophages form the primary line of defense to foreign bodies e.g. particulate matter, implants or biomaterials [31,32]. Thus they are responsible for the distribution and clearance of nanoparticles and their agglomerates. Lastly, the MDCK kidney cell line was chosen as renal elimination is frequently encountered in metal-based nanoparticles and the risk of nephrotoxicity has been reported [33]. The effects of silica-coated and uncoated MgTiO$_3$: Cr^{3+}, Nd^{3+} nanoparticles on cell viability are summarized in Fig. 5e)-g). For the uncoated nanoparticles, no significant cytotoxicity in any cell line was seen up to the maximum concentration of 40 μg/ml. When exposed to the silica-coated nanoparticles, both 3T3 and MDCK cells showed no decrease in viability. In contrast, the macrophage line RAW 264.7 seemed to show a moderate dose-dependent decrease which never exceeded 50 %. These differences, however, were not found to be significant. Particle-free supernatants of both materials were found to be non-toxic to all three cell lines. Visual inspection of the cells exposed for 48 h to both silica-coated and uncoated MgTiO$_3$:Cr^{3+}, Nd^{3+} suggested some degree of particle internalization in 3T3 and RAW 264.7 cells but not in the MDCK cells (Fig. 5h–j). For the 3T3 fibroblasts the main route of particle internalization are different types of endocytosis [34],

whereas RAW 264.7 cells are known to be efficient in phagocytosis – a route targeting much larger, micron-sized agglomerates [35]. Since the uptake of nanoparticles was clear in both cell lines it seems that nanoparticles could reach the cellular compartment by both phagocytosis (larger agglomerates) and endocytosis (free particles and small agglomerates). Moreover, the uncoated particles seemed to be internalized to a higher degree as the number of cells loaded with optically dense particles was visibly higher as compared to cells exposed to the silica-coated particles. The perinuclear deposition supports the intracellular localization of the material (and not only physical adsorption on the surface). The increased uptake of uncoated particles may be related to two factors: 1) The dispersion of uncoated MgTiO$_3$:Cr^{3+}, Nd^{3+} nanoparticles was visibly less stable as compared to their coated counterparts leading to faster sedimentation and higher dose delivered directly to cells over time [36], and 2) Silica-coated surface created an interface that was not stimulating cellular uptake to a degree observed with the uncoated MgTiO$_3$:Cr^{3+}, Nd^{3+} nanoparticle surface. Quantitative uptake assessment, however, has not been performed in this study.

Surprisingly, the apparently less internalized silica-coated particles seemed to inhibit cell proliferation in the macrophage cell line to a greater extent than the more internalized uncoated particles. This effect is difficult to explain. It seems not to be related to ion release as both supernatants proved to be non-toxic, moreover, internalized material should be more prone to ion release in the acidic environment of the phagosomes [35,37]. Even if internalized, silica shell would be expected to decrease the release of toxic ions from the particle's core. Apart from the presence of silica shell and stability in the dispersion, these two

9

materials differed by their hydrodynamic diameters as measured by DLS in a complete cell culture medium. The coated particles showed a single peak with the mean hydrodynamic diameter of 420 ± 100 nm, whereas the uncoated particles were represented by two peaks of smaller (210 ± 40 nm) and larger particles/agglomerates (740 ± 170 nm). This difference, however, also does not seem to explain the concentration-dependent trend in the viability decrease in RAW 264.7 cells. It seems likely that the protective core itself contributes to this selective sensitivity at higher concentrations. Unmodified silica shell will provide negative surface charge to the nanoparticle system and it is known that negatively charged silica nanoparticles are more toxic to RAW 264.7 cells as compared with positively charged ones [38]. This, however, is typically explained by an increased uptake of negatively charged particles.

The nanoparticles under investigation were found to be biocompatible in the applied *in vitro* model of MDCK and 3T3 cells. On the other hand, the results for RAW 264.7 macrophages suggest a risk of some degree of cytotoxicity to phagocytic cells. More quantitative uptake studies are needed to elucidate the precise mechanisms of cell-specific sensitivity to silica-coated particles.

4. Conclusions

The work presents the step by step investigation of luminescent thermometers based on MgTiO$_3$:Cr^{3+}, Nd^{3+}@SiO$_2$ nanoparticles with potential for bioapplications. At first, it was found that both Cr^{3+} and Nd^{3+} lead to the stabilization of Ti^{3+} ions, whose emission is observed for 0.1 % Cr^{3+} solely doped MgTiO$_3$ and Nd^{3+} co-doped materials. Bands of Ti^{3+} ($^2E \rightarrow ^2T_2$) together with overlapped Cr^{3+} ($^4T_2 \rightarrow ^4A_2$) and Nd^{3+} ($^4F_{3/2} \rightarrow ^4I_{9/2}$) were used to verify the thermometric performance of LIR-based approach. Two main temperature ranges with relatively good sensitivity were obtained for this strategy, i.e. around 203 K with the highest $S_R = 1.00\%K^{-1}$ for 0.1 % Nd^{3+} and at 483 K with the representative $S_R = 0.87\%K^{-1}$ for 2 % Nd^{3+}. Subsequently, the investigation of the luminescent decay profiles of emission from $^4T_2$ excited state of Cr^{3+} ions presented that co-doping with Nd^{3+} ions leads to prolonged Cr^{3+} lifetimes, an important advantage reducing temperature determination uncertainty. For this approach, $S_R = 1.75\%K^{-1}$ at 413 K for 0.5 % Nd^{3+} and even $S_{Rmax} = 1.90\%K^{-1}$ at 543 K for 1 % Nd^{3+} were obtained. Finally, MgTiO$_3$:0.1 % Cr^{3+}, 2 % Nd^{3+} phosphor with S_R ranges between 0.85 and $1.18\%K^{-1}$ over 303–343 K was selected for the silica encapsulation and the cytotoxicity measurements with a view to biorelated applications. It was found that the SiO$_2$ shell does not significantly affect the shape of the emission spectrum, but slightly extends the lifetime, which may be related to a decrease in the probability of surface-related non-radiative processes. The nanoparticles with a silica shell were found to be non-toxic to MDCK and 3T3 cells, although they may adversely affect phagocytic cells.

CRediT authorship contribution statement

Wojciech M. Piotrowski: Methodology, Investigation, Measurements, Visualization, Writing – original draft. **Maja Szymczak:** Methodology, Investigation. **Emma Martín Rodríguez:** Methodology, Investigation. **Riccardo Marin:** Methodology, Investigation, Visualization, Writing – original draft. **Marta Henklewska:** Methodology, Investigation. **Błażej Poźniak:** Methodology, Investigation, Writing – original draft. **Miroslav Dramićanin:** Methodology, Investigation. **Lukasz Marciniak:** Methodology, Investigation, Writing – original draft.

Declaration of competing interest

The authors declare that they have no known competing financial interests or personal relationships that could have appeared to influence the work reported in this paper.

Data availability

Data will be made available on request.

Appendix A. Supplementary data

Supplementary data to this article can be found online at https://doi.org/10.1016/j.matchemphys.2023.128623.

References

[1] X.D. Wang, O.S. Wolfbeis, R.J. Meier, Luminescent probes and sensors for temperature, Chem. Soc. Rev. 42 (2013) 7834–7869, https://doi.org/10.1039/c3cs60102a.

[2] L. Labrador-Páez, M. Pedroni, A. Speghini, J. García-Solé, P. Haro-Gonzalez, D. Jaque, Reliability of rare-earth-doped infrared luminescent nanothermometers, Nanoscale 10 (2018) 22319–22328, https://doi.org/10.1039/c8nr07566b.

[3] D. Jaque, F. Vetrone, Luminescence nanothermometry, Nanoscale 4 (2012) 4301–4326, https://doi.org/10.1039/c2nr30764b.

[4] M. Dramićanin, Luminescence: the basics, methods, and instrumentation, in: M.B. T.-L.T. Dramićanin (Ed.), Lumin. Thermom., Woodhead Publishing, 2018, pp. 33–61, https://doi.org/10.1016/b978-0-08-102029-6.00003-8.

[5] M.D. Dramićanin, Trends in luminescence thermometry, J. Appl. Phys. 128 (2020), 40902, https://doi.org/10.1063/5.0014825.

[6] M. Tan, F. Li, N. Cao, H. Li, X. Wang, C. Zhang, D. Jaque, G. Chen, Accurate in vivo nanothermometry through NIR-II lanthanide luminescence lifetime, Small 16 (2020), 2004118, https://doi.org/10.1002/smll.202004118.

[7] J. Morales-Dalmau, C. Vilches, I. De Miguel, V. Sanz, R. Quidant, Optimum morphology of gold nanorods for light-induced hyperthermia, Nanoscale 10 (2018) 2632–2638, https://doi.org/10.1039/c7nr06825e.

[8] E. Ximendes, R. Marin, Y. Shen, D. Ruiz, D. Gómez-Cerezo, P. Rodríguez-Sevilla, J. Lifante, P.X. Viveros-Méndez, F. Gámez, D. García-Soriano, G. Salas, C. Zalbidea, A. Espinosa, A. Benayas, N. García-Carrillo, L. Cussó, M. Desco, F.J. Teran, B. H. Juárez, D. Jaque, Infrared-Emitting multimodal nanostructures for controlled in vivo magnetic hyperthermia, Adv. Mater. 33 (2021), 2100077, https://doi.org/10.1002/adma.202100077.

[9] E. Martín Rodríguez, G. López-Peña, E. Montes, G. Lifante, J. García Solé, D. Jaque, L.A. Diaz-Torres, P. Salas, Persistent luminescence nanothermometers, Appl. Phys. Lett. 111 (2017), 81901, https://doi.org/10.1063/1.4990873.

[10] S.W. Allison, G.T. Gillies, Remote thermometry with thermographic phosphors: instrumentation and applications, Rev. Sci. Instrum. 68 (1997) 2615–2650, https://doi.org/10.1063/1.1148174.

[11] K. Elzbieciak-Piecka, C. Matuszewska, L. Marciniak, Step by step designing of sensitive luminescent nanothermometers based on Cr3+,Nd3+ co-doped La3:XLuxAl5- yGayO12 nanocrystals, New J. Chem. 43 (2019) 12614–12622, https://doi.org/10.1039/c9nj03167g.

[12] P. Dang, Y. Wei, D. Liu, G. Li, J. Lin, Recent advances in chromium-doped near-infrared luminescent materials: fundamentals, optimization strategies, and applications, Adv. Opt. Mater. 11 (2023), 2201739.

[13] M.G. Brik, C.-G. Ma, Theoretical Spectroscopy of Transition Metal and Rare Earth Ions, 2019, https://doi.org/10.1201/9780429278754.

[14] T. Kubo, H. Nozoye, Surface structure of SrTiO3(1 0 0), Surf. Sci. 542 (2003) 177–191, https://doi.org/10.1016/S0039-6028(03)00998-1.

[15] W. Piotrowski, M. Kuchowicz, M. Dramićanin, L. Marciniak, Lanthanide dopant stabilized Ti3+ state and supersensitive Ti3+ -based multiparametric luminescent thermometer in SrTiO3:Ln3+ (Ln3+ = Lu3+, La3+, Tb3+) nanocrystals, Chem. Eng. J. 428 (2022) 131165.

[16] W.M. Piotrowski, Z. Ristic, M.D. Dramićanin, Marciniak, Modification of the thermometric performance of the lifetime-based luminescent thermometer exploiting Ti3+ emission in SrTiO3 and CaTiO3 by doping with lanthanide ions, J. Alloys Compd. 906 (2022), 164398, https://doi.org/10.1016/j.jallcom.2022.164398.

[17] L. Meng, Z. Ren, W. Zhou, Y. Qu, G. Wang, MgTiO3/MgTi2O5/TiO2 heterogeneous belt-junctions with high photocatalytic hydrogen production activity, Nano Res. 10 (2017) 295–304, https://doi.org/10.1007/s12274-016-1292-6.

[18] X. Wang, J. Cai, Y. Zhang, L. Li, L. Jiang, C. Wang, Heavy metal sorption properties of magnesium titanate mesoporous nanorods, J. Mater. Chem. A 3 (2015) 11796–11800, https://doi.org/10.1039/C5TA02034D.

[19] Y. Suzuki, M. Morimoto, Porous MgTi2O5/MgTiO3 composites with narrow pore-size distribution: in situ processing and pore structure analysis, J. Ceram. Soc. Japan. 118 (2010) 819–822, https://doi.org/10.2109/jcersj2.118.819.

[20] M.P. Pechini, Method of Preparing Lead and Alkaline Earth Titanates and Niobates and Coating Method Using the Same to Form a Capacitor, 1967.

[21] K. Kniec, K.A. Ledwa, L. Marciniak, Role of SiO2 coating on YAG:V3+,Nd3+ nanoparticles in luminescence thermometry, ACS Appl. Nano Mater. 5 (2022) 8271–8278, https://doi.org/10.1021/acsanm.2c01180.

[22] W. Stöber, A. Fink, E. Bohn, Controlled growth of monodisperse silica spheres in the micron size range, J. Colloid Interface Sci. 26 (1968) 62–69, https://doi.org/10.1016/0021-9797(68)90272-5.

[23] A.F.M.Y. Haider, A. Edgar, ESR study of transition metal ions in magnesium titanate, J. Phys. C Solid State Phys. 13 (1980) 6239, https://doi.org/10.1088/0022-3719/13/33/022.

[24] N. Kuganathan, P. Iyngaran, R. Vovk, A. Chroneos, Defects, dopants and Mg diffusion in MgTiO3, Sci. Rep. 9 (2019) 4394, https://doi.org/10.1038/s41598-019-40878-y.

[25] Z. Wen-Chen, EPR study of two Cr3+ sites in MgTiO3 crystal, J. Phys. Chem. Solid. 55 (1994) 647–650.

[26] Y. Li, C. Liu, P. Zhang, J. Huang, H. Ning, P. Xiao, Y. Hou, L. Jing, M. Gao, Doping lanthanide nanocrystals with non-lanthanide ions to simultaneously enhance up- and down-conversion luminescence, Front. Chem. 8 (2020), https://doi.org/10.3389/fchem.2020.00832.

[27] G.B. Kadri, D. Das, S.K. Gupta, K. Sudarshan, Influence of Li+ co-doping on the luminescence of MgO:Eu3+ nanocrystals: probing asymmetry, energy transfer and defects, Solid State Sci. 105 (2020), 106286.

[28] W. Piotrowski, M. Kuchowicz, M. Dramićanin, L. Marciniak, Lanthanide dopant stabilized Ti3+ state and supersensitive Ti3+ -based multiparametric luminescent thermometer in SrTiO3:Ln3+ (Ln3+ = Lu3+, La3+, Tb3+) nanocrystals, Chem. Eng. J. 428 (2021), 131165, https://doi.org/10.1016/j.cej.2021.131165.

[29] W. Geurtsen, F. Lehmann, W. Spahl, G. Leyhausen, Cytotoxicity of 35 dental resin composite monomers/additives in permanent 3T3 and three human primary fibroblast cultures, J. Biomed. Mater. Res. 41 (1998) 474–480, https://doi.org/10.1002/(SICI)1097-4636(19980905)41:3<474::AID-JBM18>3.0.CO;2-I.

[30] S.K. Bhatia, A.B. Yetter, Correlation of visual in vitro cytotoxicity ratings of biomaterials with quantitative in vitro cell viability measurements, Cell Biol. Toxicol. 24 (2008) 315–319, https://doi.org/10.1007/s10565-007-9040-z.

[31] R. Miyata, S.F. van Eeden, The innate and adaptive immune response induced by alveolar macrophages exposed to ambient particulate matter, Toxicol. Appl. Pharmacol. 257 (2011) 209–226, https://doi.org/10.1016/j.taap.2011.09.007.

[32] H.C. Fischer, T.S. Hauck, A. Gómez-Aristizábal, W.C.W. Chan, Exploring primary liver macrophages for studying quantum dot interactions with biological systems, Adv. Mater. 22 (2010) 2520–2524, https://doi.org/10.1002/adma.200904231.

[33] P. Makhdoumi, H. Karimi, M. Khazaei, Review on metal-based nanoparticles: role of reactive oxygen species in renal toxicity, Chem. Res. Toxicol. 33 (2020) 2503–2514, https://doi.org/10.1021/acs.chemrestox.9b00438.

[34] D. Drescher, G. Orts-Gil, G. Laube, K. Natte, R.W. Veh, W. Österle, J. Kneipp, Toxicity of amorphous silica nanoparticles on eukaryotic cell model is determined by particle agglomeration and serum protein adsorption effects, Anal. Bioanal. Chem. 400 (2011) 1367–1373, https://doi.org/10.1007/s00216-011-4893-7.

[35] X. Liu, N. Huang, H. Li, Q. Jin, J. Ji, Surface and size effects on cell interaction of gold nanoparticles with both phagocytic and nonphagocytic cells, Langmuir 29 (2013) 9138–9148, https://doi.org/10.1021/la401556k.

[36] J.G. Teeguarden, P.M. Hinderliter, G. Orr, B.D. Thrall, J.G. Pounds, Particokinetics in vitro: dosimetry considerations for in vitro nanoparticle toxicity assessments, Toxicol. Sci. 95 (2007) 300–312, https://doi.org/10.1093/toxsci/kfl165.

[37] G. Despras, A.I. Zamaleeva, L. Dardevet, C. Tisseyre, J.G. Magalhaes, C. Garner, M. De Waard, S. Amigorena, A. Feltz, J.-M. Mallet, M. Collot, H-Rubies, A new family of red emitting fluorescent pH sensors for living cells, Chem. Sci. 6 (2015) 5928–5937, https://doi.org/10.1039/C5SC01113B.

[38] C. Kembuan, H. Oliveira, C. Graf, Effect of different silica coatings on the toxicity of upconversion nanoparticles on RAW 264.7 macrophage cells, Beilstein J. Nanotechnol. 12 (2021) 35–48, https://doi.org/10.3762/bjnano.12.3.

Supporting Information

Step by step optimization of luminescence thermometry in MgTiO$_3$:Cr^{3+}, Nd^{3+}@SiO$_2$ nanoparticles towards bioapplications

Wojciech M. Piotrowski[1]*, Maja Szymczak[1], Emma Martín Rodríguez[2],

Riccardo Marin[3], Marta Henklewska[4], Błażej Poźniak[4], Miroslav

Dramićanin[5], Lukasz Marciniak[1]*

[1]Institute of Low Temperature and Structure Research, Polish Academy of Sciences, Okólna 2, 50-422 Wroclaw, Poland

[2]Nanomaterials for Bioimaging Group (nanoBIG), Departamento de Física Aplicada, Facultad de Ciencias, Universidad Autónoma de Madrid, Madrid, Spain

[3]Nanomaterials for Bioimaging Group (nanoBIG), Departamento de Física de Materiales, Facultad de Ciencias, Universidad Autónoma de Madrid, Madrid, Spain

[4]Department of Pharmacology and Toxicology, Faculty of Veterinary Medicine, Wrocław University of Environmental and Life Sciences, ul. Norwida 25, 50-375 Wrocław, Poland

[5]Center of Excellence for Photoconversion, Vinča Institute of Nuclear Sciences – National Institute of the Republic of Serbia, University of Belgrade, P.O. Box 522, Belgrade 11001, Serbia

* corresponding author: w.piotrowski@intibs.pl, l.marciniak@intibs.pl

KEYWORDS magnesium titanate, decay, emission, Ti^{3+} ions stabilization, silica-coated nanoparticles, cytotoxicity

The integral intensities of the emission bands to calculate LIR values were fitted with Mott-Seitz equation (Eq. S1):

$$I = \frac{I_0}{C \cdot \exp(-\frac{W}{k \cdot T}) + 1} \qquad \text{(Eq. S1)}$$

where: I – the intensity in temperature T, I_0 – the intensity in the initial temperature,

W - the activation energy, k – Boltzmann constant, C – the dimensionless constant

The average lifetime of the excited states were calculated with the equation Eq. S2:

$$\tau_{avr} = \frac{A_1\tau_1{}^2 + A_2\tau_2{}^2}{A_1\tau_1 + A_2\tau_2}$$
(Eq. S2)

where: τ_1, τ_2 are the decay parameters and A_1, A_2 are amplitudes of the bi-exponential function:

$$I(t) = I_0 + A_1 \cdot \exp\left(-\frac{t}{\tau_1}\right) + A_2 \cdot \exp\left(-\frac{t}{\tau_2}\right)$$
(Eq. S3)

Figure S1. X-ray diffraction patterns of $MgTiO_3$ co-doped with 0.1% Cr^{3+} and different Nd^{3+} concentration (reflection of the additional phase marked by asterisk).

Table S1. Unit cell parameters calculated with Rietveld refinement for $MgTiO_3$:x% Cr^{3+} and $MgTiO_3$:0.1% Cr^{3+}, y% Nd^{3+} materials.

dopant(s)	a (Å)	c (Å)	V (Å³)	R profile (%)	weighted R profile (%)	goodness of fit
0.1% Cr^{3+}	5.0542	13.899	307.47	2.316	2.975	2.099

0.2% Cr^{3+}	5.0538	13.897	307.39	4.813	6.715	2.541
0.5% Cr^{3+}	5.0532	13.896	307.29	3.848	4.840	1.406
0.1% Cr^{3+}, 0.1% Nd^{3+}	5.0545	13.899	307.51	4.282	5.518	1.903
0.1% Cr^{3+}, 0.5% Nd^{3+}	5.0549	13.899	307.57	4.219	5.478	1.891
0.1% Cr^{3+}, 1% Nd^{3+}	5.0548	13.900	307.58	3.882	5.192	1.789
0.1% Cr^{3+}, 2% Nd^{3+}	5.0553	13.900	307.63	3.657	4.598	1.391
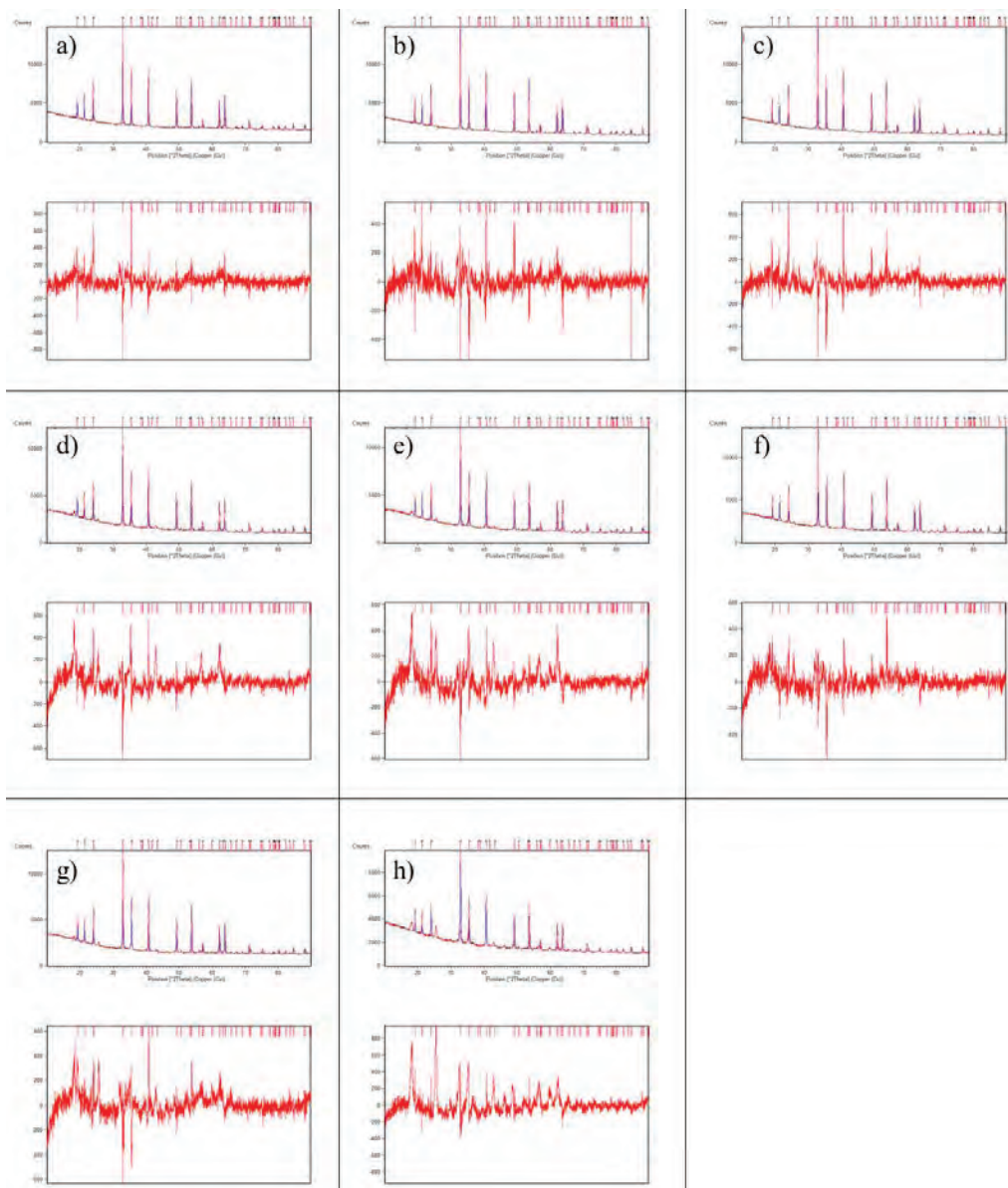
Figure S2. Rietveld refinement of MgTiO$_3$:x% Cr^{3+}, where x = 0.1 – a); 0.2 – b), 0.5 – c) and MgTiO$_3$:0.1% Cr^{3+}, y% Nd^{3+}, where y = 0.1 – d); 0.5 – e); 1 – f); 2 – g); 5 – h).
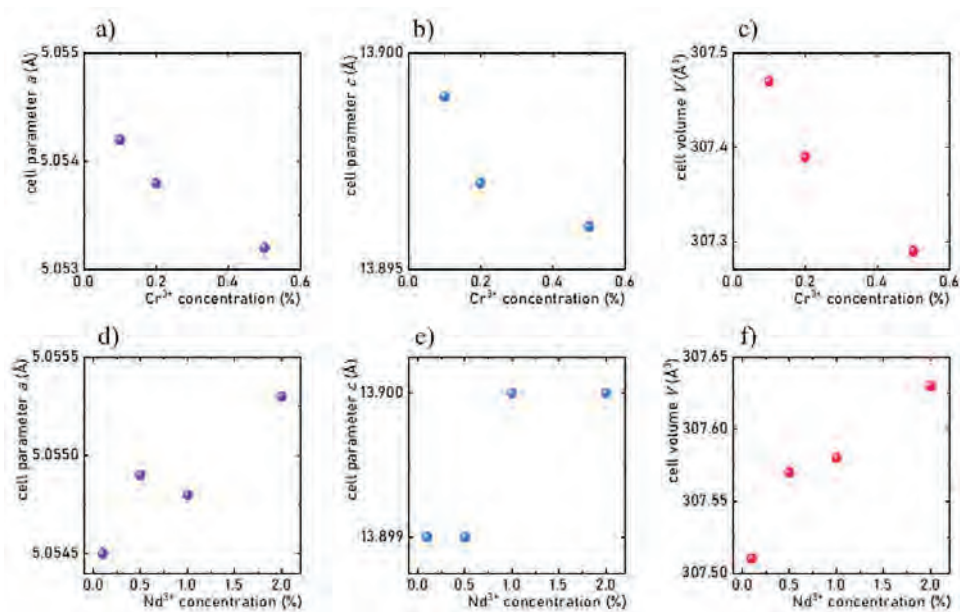
Figure S3. The influence of Cr^{3+} concentration on the calculated cell parameters: a, c and unit cell volume in MgTiO$_3$:x% Cr^{3+}; the influence of Nd^{3+} concentration on the calculated cell parameters: a, c and unit cell volume in MgTiO$_3$:0.1% Cr^{3+}, y% Nd^{3+}.
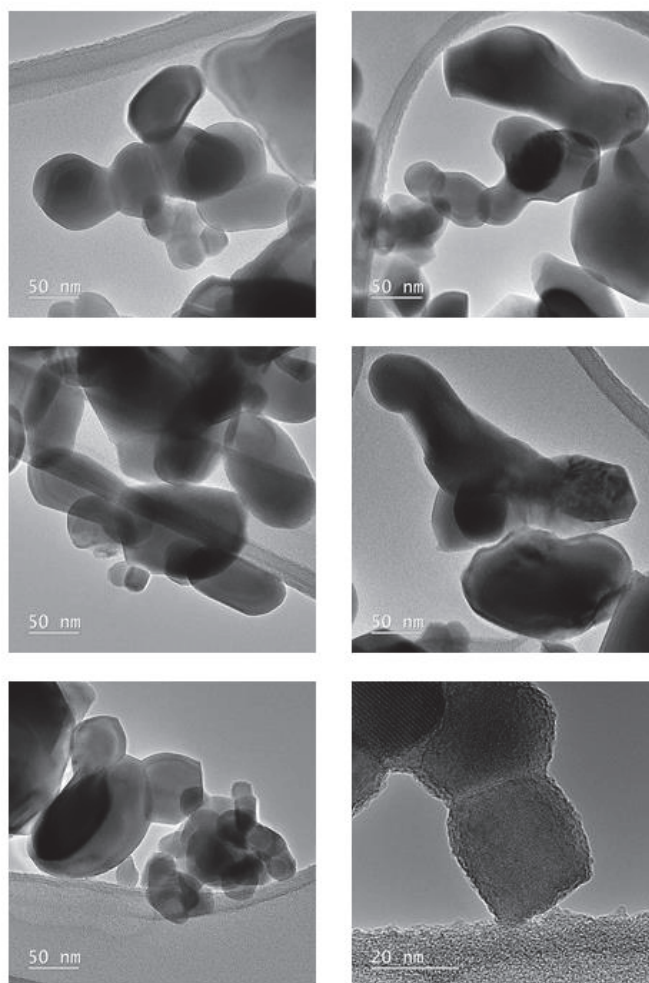
Figure S4. The representative TEM images of MgTiO$_3$:0.1% Cr^{3+}.
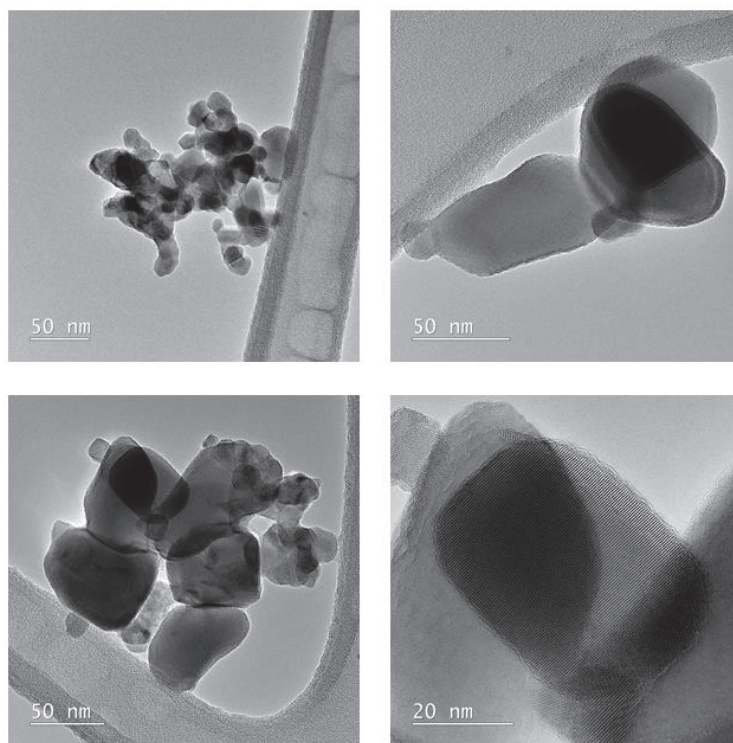
Figure S5. The representative TEM images of MgTiO$_3$:0.1% Cr^{3+}, 2% Nd^{3+}.
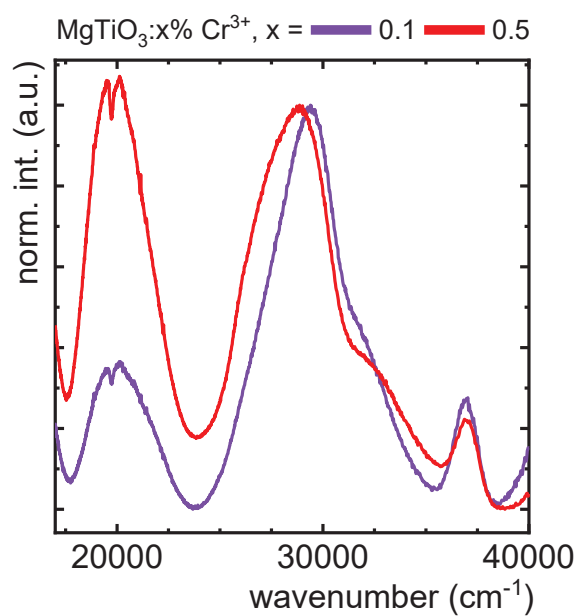
Figure S6. Influence of Cr^{3+} concentration on the excitation spectra for MgTiO$_3$:x% Cr^{3+} detected at 83 K.

The crystal field parameter Dq and Racah parameter B for Cr^{3+} ions were defined based on the energies of $^4A_2 \rightarrow {}^4T_1$ and $^4A_2 \rightarrow {}^4T_2$ bands obtained from excitation spectra. The empirical equations take the following form:

$$E(^4A_2 \rightarrow {}^4T_2) = 10Dq \qquad \text{(Eq. S4)}$$

$$\frac{Dq}{B} = \frac{15\left(\frac{\Delta E}{Dq}-8\right)}{\left(\frac{\Delta E}{Dq}\right)^2 - 10\cdot\frac{\Delta E}{Dq}} \qquad \text{(Eq. S5)}$$

where ΔE was predefined as:

$$\Delta E = E(^4A_2 \rightarrow {}^4T_1) - E(^4A_2 \rightarrow {}^4T_2) \qquad \text{(Eq. S6)}$$

Table S2. The crystal field parameters in $MgTiO_3$:x% Cr^{3+} phosphors.

	Dq [cm^{-1}]	B [cm^{-1}]	Dq/B
$MgTiO_3$:0.1% Cr^{3+}	1983.8	1057.8	1.86
$MgTiO_3$:0.5% Cr^{3+}	1966.6	962.6	2.04

Structural and spectroscopic properties of $Ba_xMg_{1-x}TiO_3$:Cr^{3+} nanopowder materials

$Ba_xMg_{1-x}TiO_3$:Cr^{3+} nanopowder was prepared following the same procedure as $MgTiO_3$:Cr^{3+}. Using the XRPD reference patterns of $BaTiO_3$ (ICSD 67518) and $MgTiO_3$ (ICSD 55285), it can be concluded that $Ba_xMg_{1-x}TiO_3$ does not form solid solutions according to Vegard's law (Figure S5). Nevertheless, XRPD patterns for $BaTiO_3$:0.1% Cr^{3+} and $Ba_{0.9}Mg_{0.1}TiO_3$:0.1% Cr^{3+} correspond well with reference suggesting the formation of a pure phase. Although a different phase was obtained for structures above the 3:1 Ba^{2+}/Mg^{2+} ratio, their emission and excitation spectra taken at 83 K are presented (Figure S6 and S7, respectively). Firstly, it should be noted that for $BaTiO_3$:0.1% Cr^{3+} no emission was observed.

When doping with 10% Mg^{2+} ions, an emission band centered at 757 nm was found. Comparing the emission intensity, it was observed that this band is most intense for 0.25% Mg^{2+} and then its intensity decreases, but is still detectable for 75% Mg^{2+} ions. This may suggest that this is Ti^{3+} emission, which is stabilized by Cr^{3+} ions substituting only Mg^{2+} positions, but in a dominant environment of Ba^{2+} ions. It may be also confirmed by the presence of a single band on the excitation spectra for 25% and 50% Mg^{2+} ions, since it is known that the excitation spectrum of Ti^{3+} ions consists of a single band associated with the $^2T_2 \rightarrow {^2}E$ transition, while the excitation spectrum of Cr^{3+} consists of at least two bands: $^4A_2 \rightarrow {^4}T_2$ and $^4A_2 \rightarrow {^4}T_1$ (Figure S7). Therefore, the unfavorable influence of Ba^{2+} ions on the luminescence of Cr^{3+} ions, the analysis of the luminescence of materials such as $Ba_xMg_{1-x}TiO_3$:Cr^{3+} can have a beneficial effect on the interpretation of the results.
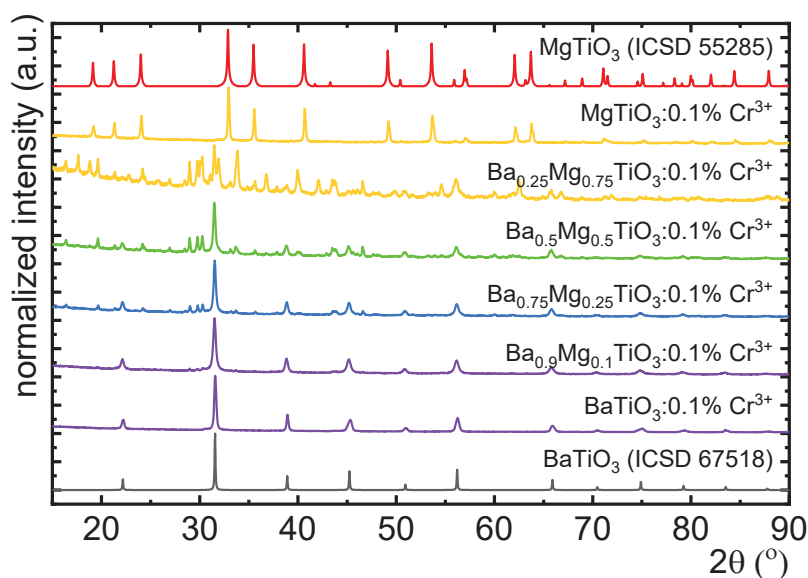
Figure S7. X-ray diffraction patterns of $Ba_{1-x}Mg_xTiO_3$:0.1% Cr^{3+} materials.
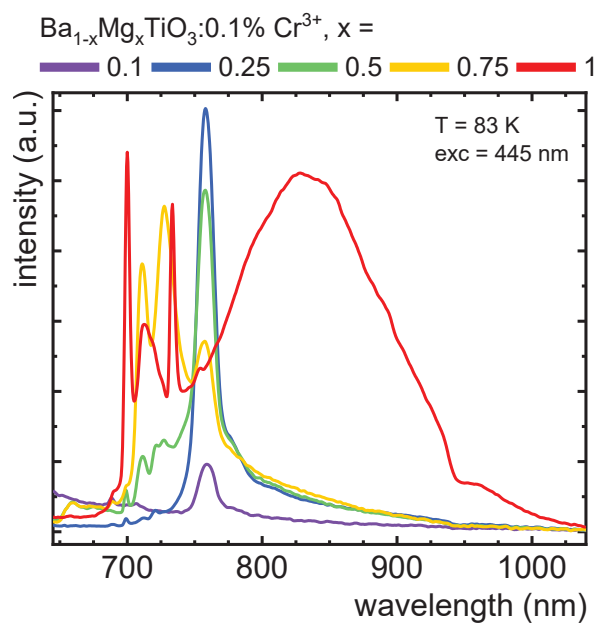
Figure S8. Influence of host composition on the emission spectra for $Ba_{1-x}Mg_xTiO_3$:0.1% Cr^{3+} excited by λ_{exc} = 445 nm and detected at 83 K.
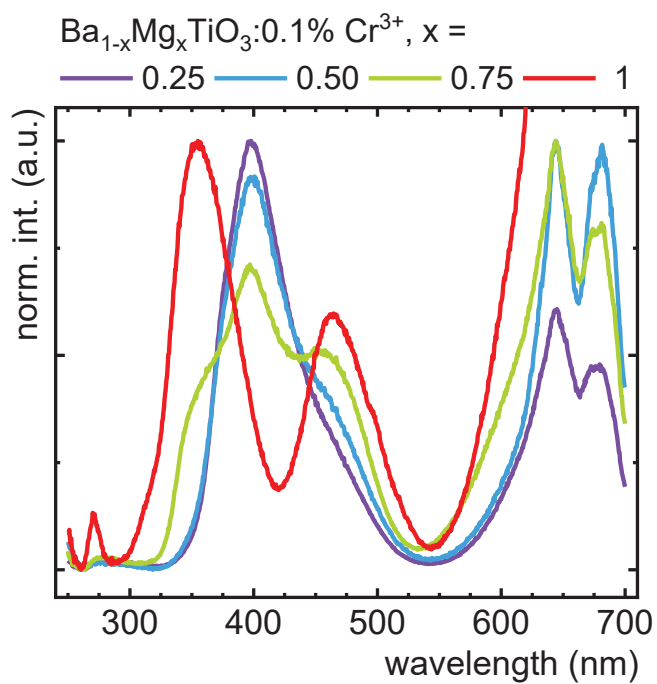
Figure S9. Influence of host composition on the excitation spectra for $Ba_{1-x}Mg_xTiO_3$:0.1% Cr^{3+} detected at 83 K.
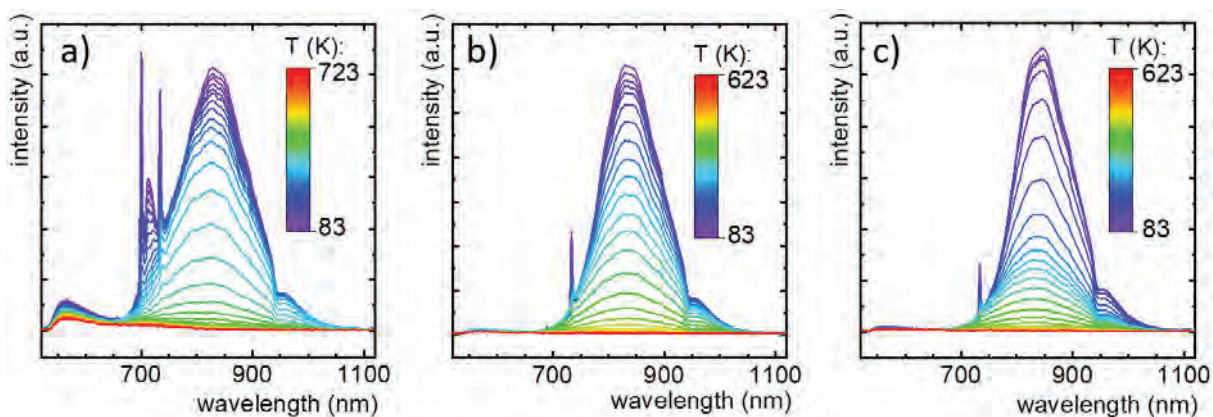
Figure S10. Thermal evolution of emission spectra of $MgTiO_3$ doped with 0.1% – a); 0.2% – b) and 0.5% excited by λ_{exc} = 445 nm – c).
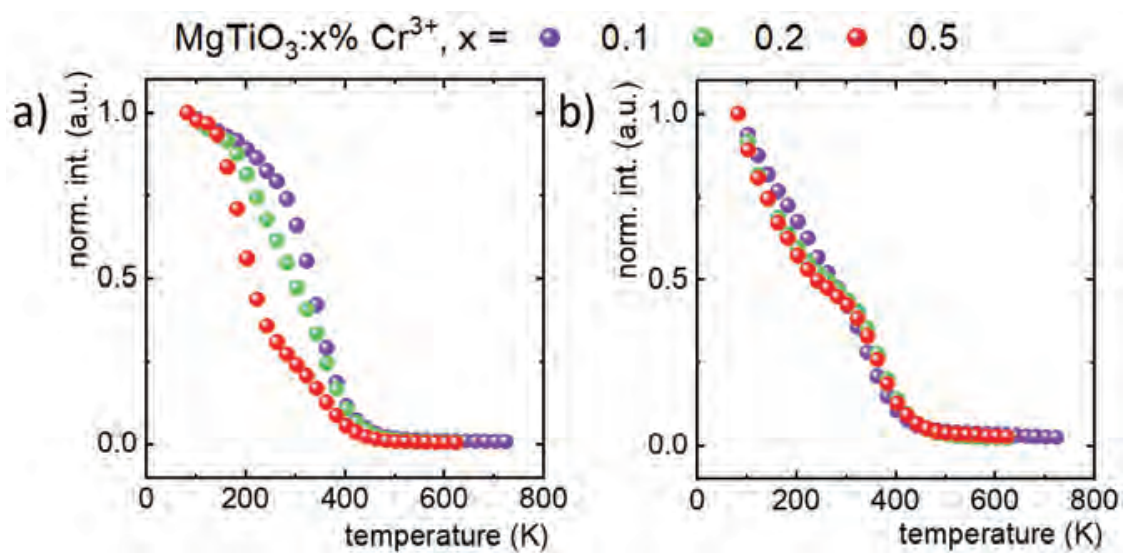
Figure S11. Thermal evolution of $^4T_2 \rightarrow {}^4A_2$ (Cr^{3+}) emission band (790-899 nm) – a) and $^2E \rightarrow {}^4A_2$ (Cr^{3+}) emission band (731-736 nm) in $MgTiO_3$:x% Cr^{3+}.
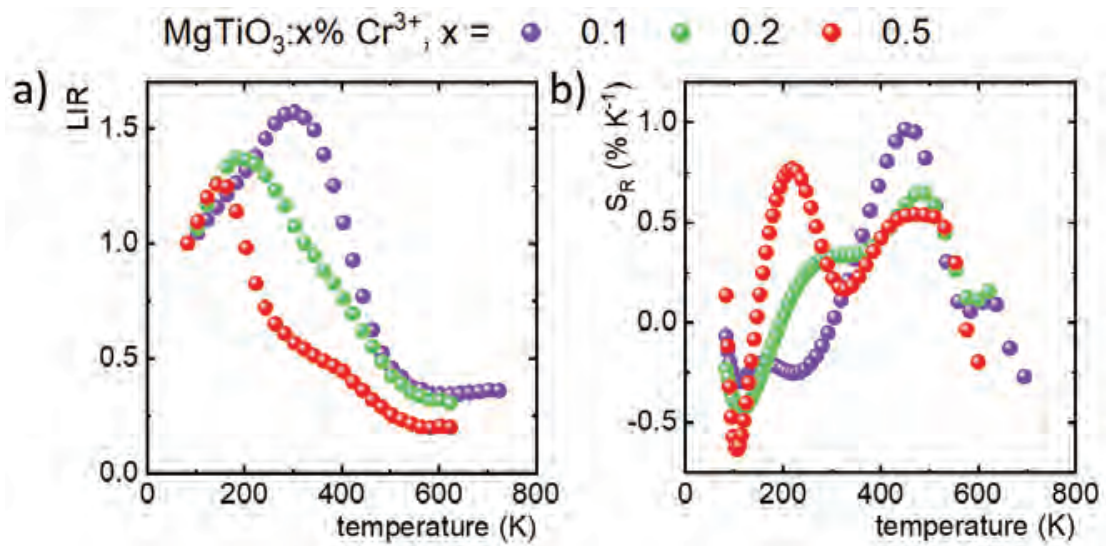
Figure S12. Thermal evolution of LIR = $^4T_2 \rightarrow ^4A_2 / ^2E \rightarrow ^4A_2$ – a) and their relative sensitivity S_R in MgTiO$_3$:x% Cr^{3+}.
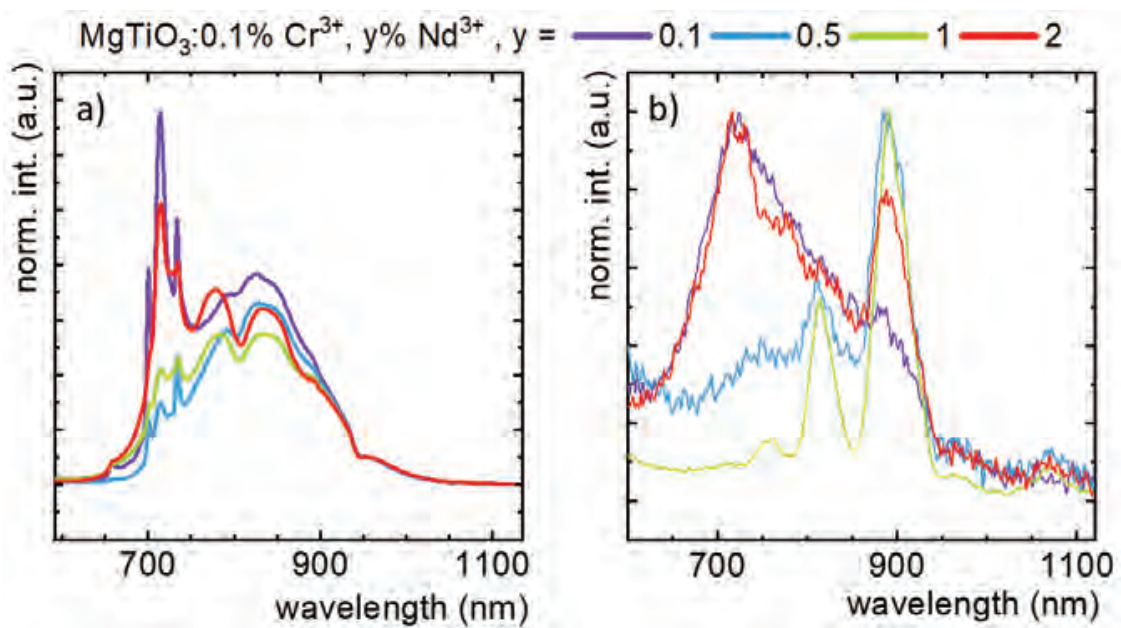
Figure S13. Influence of Nd^{3+} concentration on emission spectra of MgTiO$_3$:0.1% Cr^{3+}, y% Nd^{3+} measured at 83 K – a) and 463 K – b).
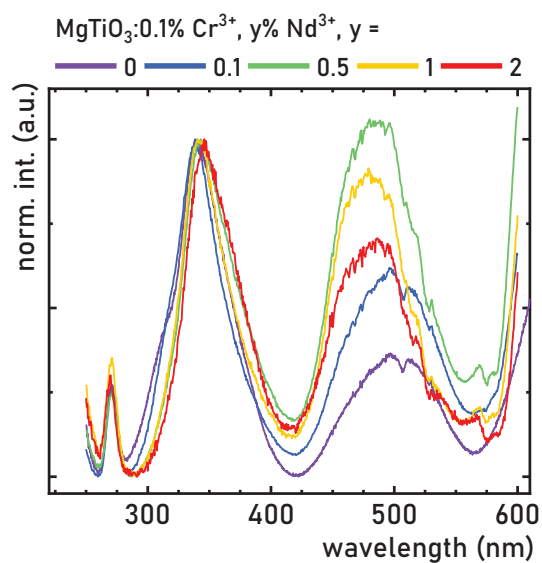
Figure S14. The influence of Nd^{3+} concentration on the excitation spectra (λ_{em} = 835 nm, 83K) in $MgTiO_3$:0.1% Cr^{3+}, y% Nd^{3+}.
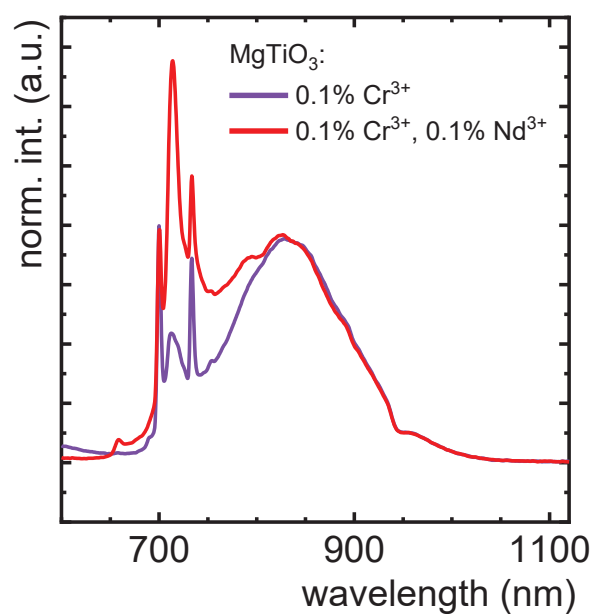
Figure S15. Comparison of low temperature (83 K) emission spectra for $MgTiO_3$ doped with 0.1% Cr^{3+} and co-doped with 0.1% Cr^{3+}, 0.1% Nd^{3+}.
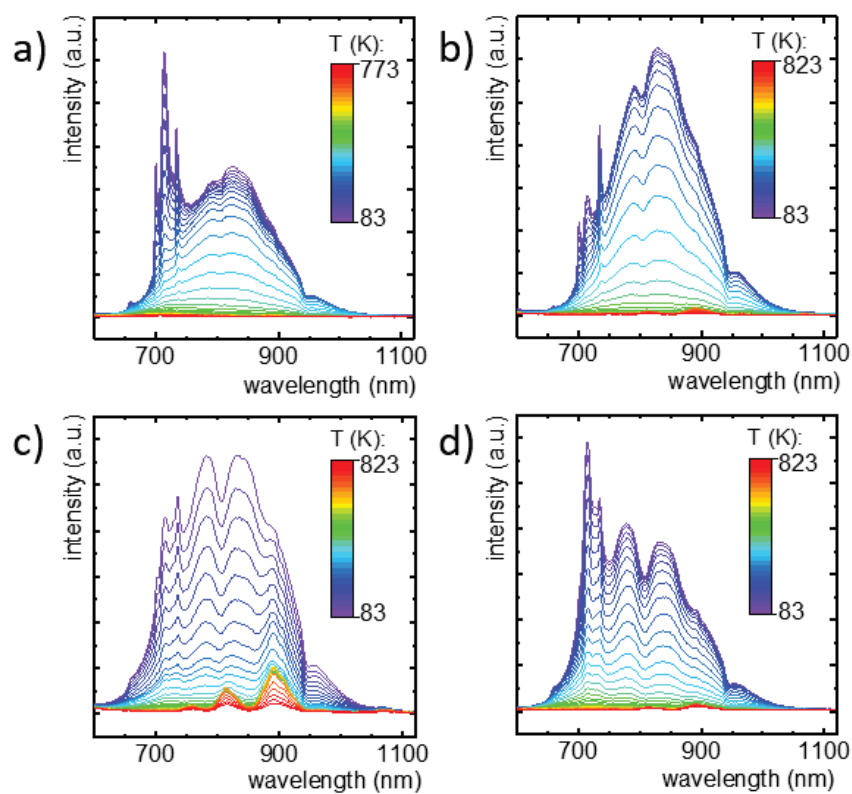
Figure S16. Thermal evolution of emission spectra of MgTiO$_3$:0.1% Cr^{3+}, y% Nd^{3+} where 0.1% – a); 0.5% – b)

1% – c) and 2% excited by λ_{exc} = 445 nm – d).
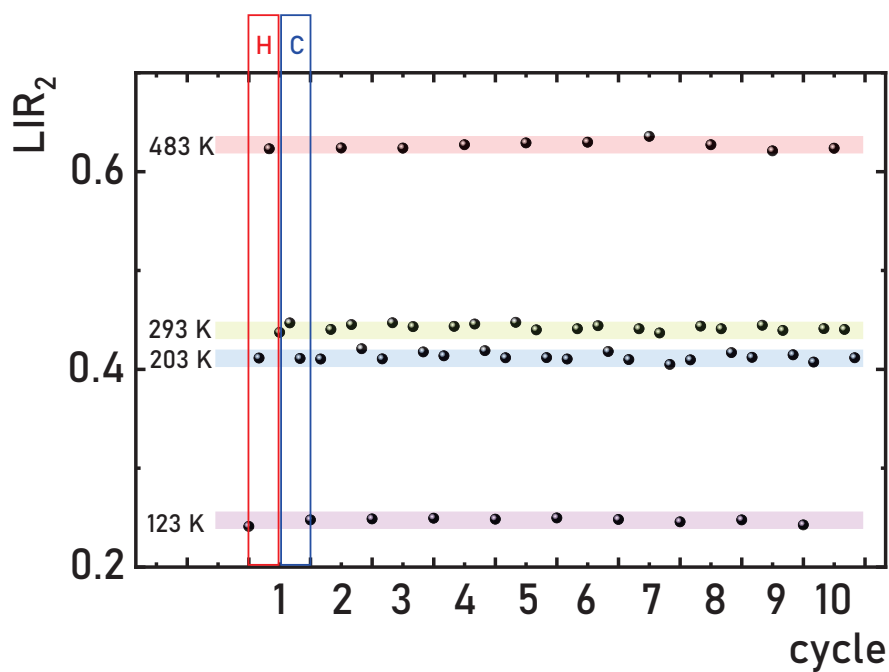
Figure S17. The LIR$_2$ measured within several heating–cooling cycles in MgTiO$_3$:0.1% Cr^{3+}, 2% Nd^{3+}

(H – heating, C – cooling).
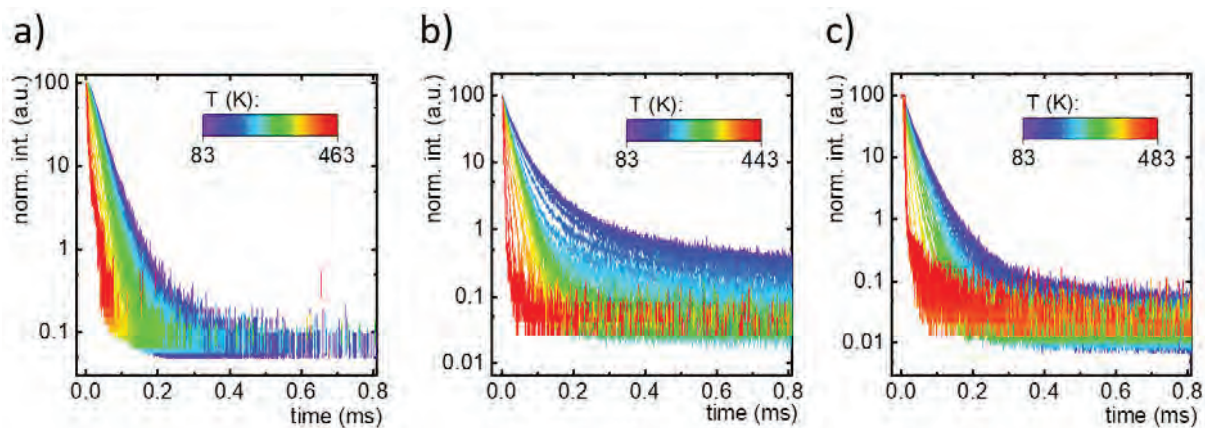
Figure S18. Thermal evolution of luminescence decays of ^2E excited state of Cr^{3+} ions (λ_{em} = 835 nm) for MgTiO$_3$:x% Cr^{3+}, where x = 0.1% – a); 0.2% – b) and 0.5% – c).
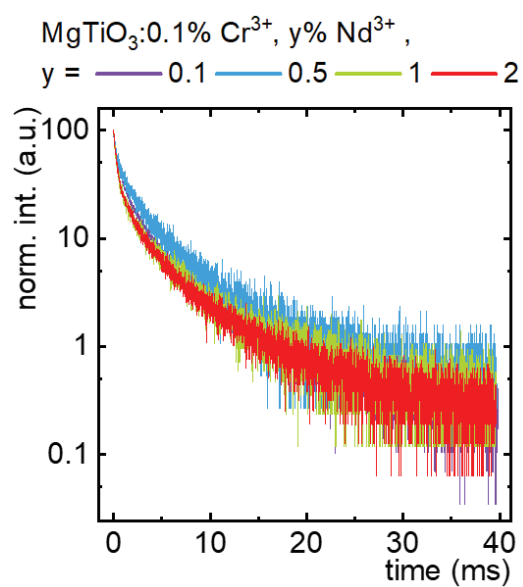
Figure S19. Influence of Nd^{3+} concentration on low temperature (83 K) luminescence decays of ^2E excited state of Ti^{3+} ions (λ_{em} = 713 nm) for MgTiO$_3$:0.1% Cr^{3+}, y% Nd^{3+}.
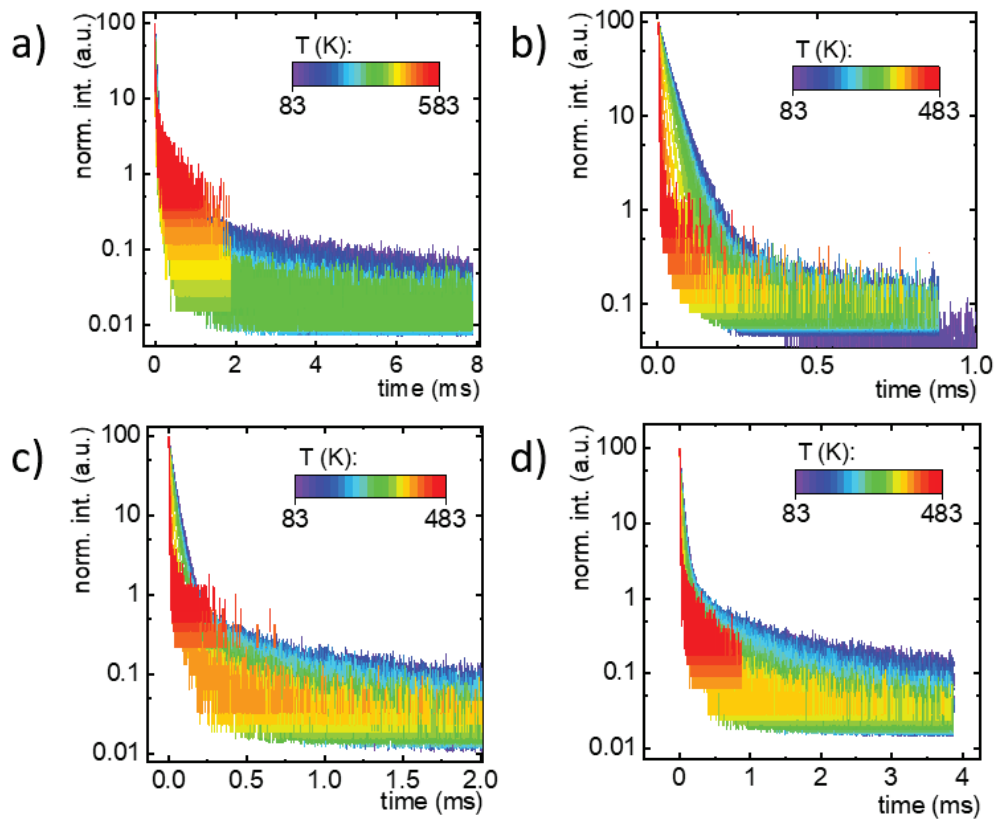
Figure S20. Thermal evolution of luminescence decays of ^2E excited state of Cr^{3+} ions (λ_{em} = 835 nm) for

MgTiO$_3$:0.1% Cr^{3+}, y% Nd^{3+} where y = 0.1% – a); 0.5% – b); 1% – c) and 2% – d).
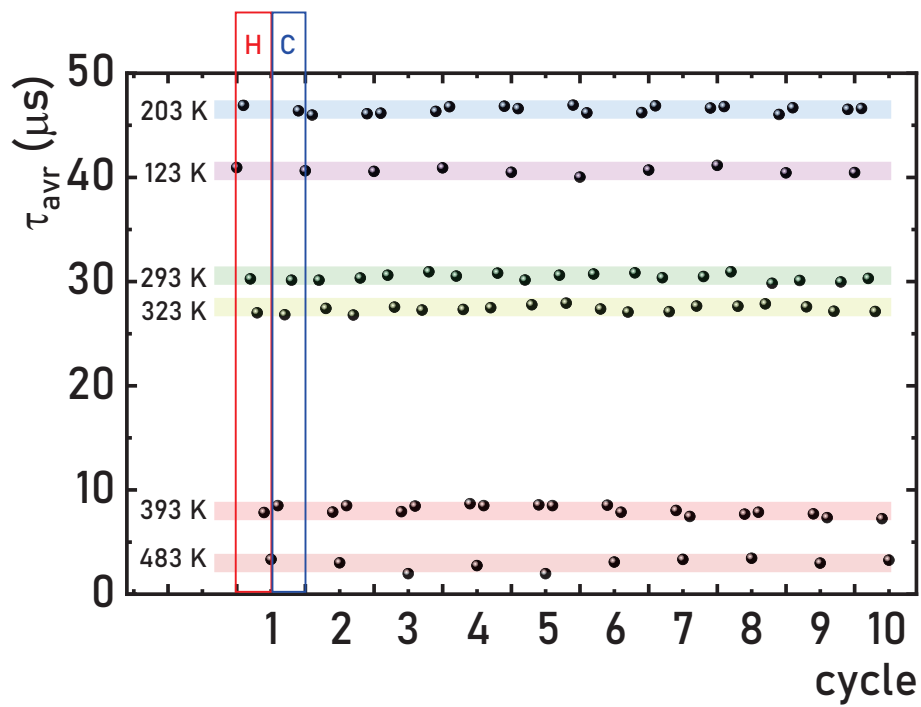
Figure S21. The average lifetime of Cr^{3+} ions measured within several heating–cooling cycles

in MgTiO$_3$:0.1% Cr^{3+}, 2% Nd^{3+} (H – heating, C – cooling).
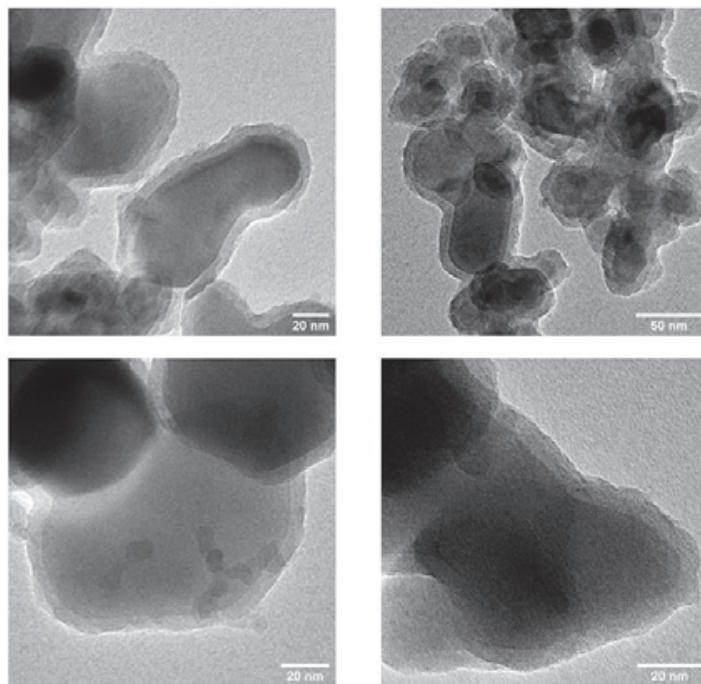
Figure S22. The representative TEM images of MgTiO$_3$:0.1% Cr^{3+}, 2% Nd^{3+} particles coated with silica.
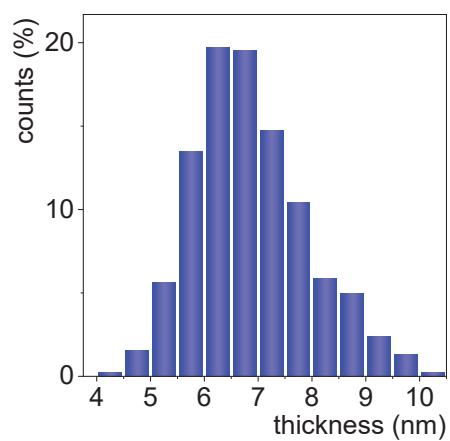
Figure S23. Thickness distribution of silica coating of MgTiO$_3$:0.1% Cr^{3+}, 2% Nd^{3+} particles.
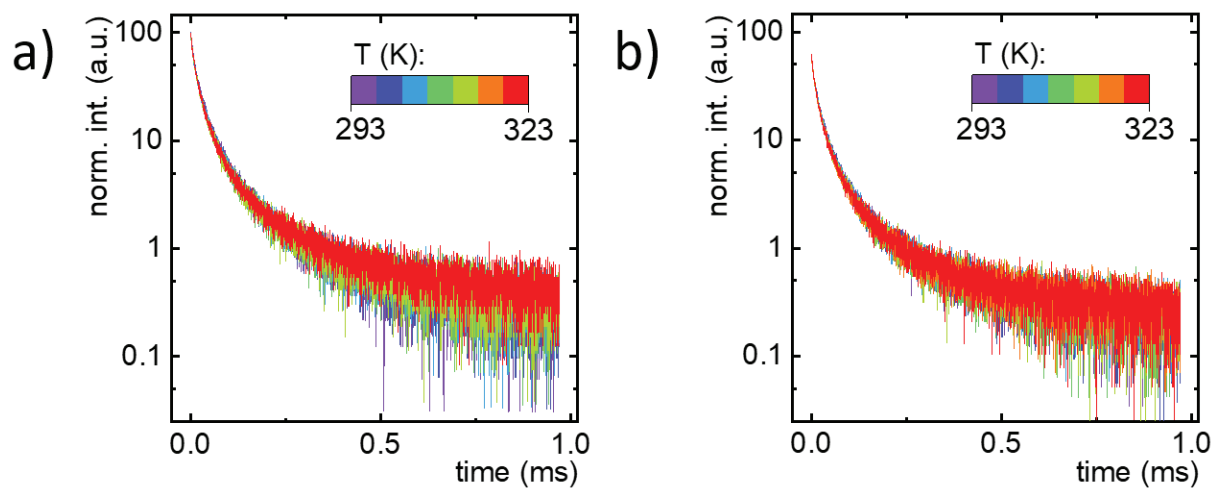
Figure S24. Thermal evolution of luminescence decays of ^2E excited state of Cr^{3+} ions (λ_{em} = 835 nm) for non-coated – a) and silica coated $MgTiO_3$:0.1% Cr^{3+}, 2% Nd^{3+} nanoparticles – b).

Enhancement of the Ln³⁺ ratiometric nanothermometers by sensitization with transition metal ions

W. Piotrowski, K. Kniec, L. Marciniak*

Institute of Low Temperature and Structure Research, Polish Academy of Sciences, Okólna 2, 50-422 Wrocław, Poland

ABSTRACT

One of the most important parameters that affect the thermal resolution in the luminescent thermometry is the relative sensitivity of phosphor to temperature changes. Therefore various approaches to enhance its value are intensively investigated. The strategy of the relative sensitivity enhancement of the ratiometric lanthanide ions based luminescent thermometer by the sensitization with the transition metal ions is proposed in this work. It was found that by taking advantage of the temperature dependent energy transfer from transition metal ion (Mn^{4+}-, Cr^{3+}- and $Ti^{3+/4+}$-) to the Tb^{3+} and Eu^{3+} ions in the YAG powder, the thermal variation of the Tb^{3+} to Eu^{3+} luminescence intensity ratio increases leading to the improvement of its thermometric properties even by 300%. Therefore, the maximal relative sensitivity increases from $S_R = 0.09\%/°C$ for unco-doped powder up to $S_R = 0.15, 0.28, 0.30\%/°C$, for powders co-doped with Cr^{3+}, Mn^{4+} and $Ti^{3+/4+}$, respectively. The beneficial influence of the transition metal to lanthanides energy transfer was investigated in a function of the transition metal ion concentration.

© 2021 Elsevier B.V. All rights reserved.

1. Introduction

The temperature monitoring using the luminescent thermometry (LT) technique is one of the most attractive applications of the photoluminescence materials intensively investigated in recent years [1–4]. The relevant advantage of this technique is the non-contact readout mode which, in contrary to other noncontact techniques like infrared thermography, enables to receive accurate information about the phosphor temperature without knowing the emissivity of the material, even through the disrupting layers like glass, polymeric layers or even skin [1,5,6]. Therefore, the possibilities of temperature readout provided by LT are especially attractive, among others, for biological in vitro or in vivo applications [7–9], where LT was proved to provide information about the brain activity monitoring through real-time thermal sensing or the intratumoral temperature during the in vivo photothermal therapy. On the other hand, the LT presents a highly applicative potential in the analysis of the turbulent gas or liquid flows and the surface coated thermography in the diesel engines [10–12]. Among different classes of temperature sensors distinguished based on the type of the thermally induced changes of the spectroscopic properties of the phosphor, the ratiometric approach is one of the most extensively

investigated because of the easiness of its practical implementation and its high accuracy [13–22]. In this case, the change in the relative emission intensity of two emission signals is analysed. In order to provide a reliable temperature readout, the well spectrally separated bands are desired. Therefore spectrally narrow and well secluded emission bands of lanthanide ions (Ln³⁺) ions are especially beneficial from this perspective. Moreover, a well-defined and complex energy level scheme of Ln³⁺ ions enables the design of the composition of the emission spectrum almost on demand [23–26]. These unique features of Ln³⁺ as dopants together with the high physico-chemical and photochemical stability of the inorganic compounds as a host material generate high research interest in this kind of materials for noncontact thermometry [4,8,27–30]. The accuracy and temperature determination uncertainty provided by LT depend on the sensitivity of LT [31]. Therefore much effort is put into the development of different approaches to enhance the sensitivity of luminescent temperature sensors including optimization of the host material composition, dopant concentration, excitation wavelength and excitation density used etc [32,33]. However, little attention has been paid to the issue of the possibility of increasing the sensitivity of the LT based on the ratio of the intensity of the emission of the Ln³⁺ bands through the phenomenon of sensitization. In this case, when the energy of the excited state of the sensitizer is not in resonance with the energy of the excited states of Ln³⁺ ions, the probability of sensitizer-to-Ln³⁺ energy transfer will occur with the assistance of phonon and thus will be dependent on temperature.

Hence the emission intensity of Ln^{3+} should be governed not only by the thermally induced depopulation processes of their excited states (i.e. multiphonon nonradiative depopulation, thermally induced cross relaxation, energy transfer between ions) but also by the populating processes i.e. the probability of sensitizer-to-Ln^{3+} energy transfer. An additional advantage of this kind of approach is the fact that by the deliberate selection of the sensitizer, the spectral range of the excitation wavelength enabling Ln^{3+} emission generation becomes wider. The significantly higher absorption cross section of the transition metal ions (TM) with respect to the Ln^{3+} ions makes them very promising candidates as Ln^{3+} sensitizers [34–38].

The concept of the sensitization of the luminescence of Ln^{3+} by the use of TM ions is not new and has been extensively investigated in the last decades as an approach to enhance the efficiency of the solar cells [39,40], to increase the pumping efficiency in the laser systems [41–45] or to boost the luminescence intensity of the Ln^{3+} doped phosphors [46–51]. The TM have already been used in order to modify the spectroscopic properties of the Ln^{3+}-based phosphors i.e. the shape of the emission spectra, luminescence decay profiles or emission bandwidth [52–59]. In the case of the luminescent thermometers the TM ions have been mostly used for up-converting Ln^{3+} based thermographic phosphors to enhance their brightness by means of creating the Yb^{3+},TM ionic pair which serves as an electron reservoir and provides the more efficient pumping of the excited states of emitting ions [60]. The Cr^{3+} and Mn^{2+} ions are usually applied for this purpose. Nannuri et al. show that when the $NaYF_4$:Yb^{3+}, Er^{3+} submicron crystals were doped with 5% of Cr^{3+} ions the intensity of the Er^{3+} luminescence was doubled with respect to the uncodoped counterpart, without any negative effect on its thermometric properties [61]. Xu et al. reported even higher, 4-fold, enhancement of the green emission of Er^{3+} ions in the $CaWO_4$: Er^{3+}, Yb^{3+}, Cr^{3+} system when the 3% of Cr^{3+} was used [62]. The introduction of the TM, however, may also modify the thermometric performance of the thermographic phosphor boosting its relative sensitivity to temperature changes. Therefore in this system an increase from the S_R = 1.36%/°C for $CaWO_4$: Er^{3+}, Yb^{3+} to 1.91%/°C for $CaWO_4$: Er^{3+}, Yb^{3+}, 9%Cr^{3+} was obtained. This effect was discussed in terms of efficient energy transfer between Er^{3+}, Yb^{3+} and Cr^{3+} ions. Cui et al. reported that the introduction of the Mn^{2+} co-dopant in the $KMnF_3$:Yb^{3+}, Er^{3+} system enables thermal coupling between $^4F_{9/2}$ and $^4S_{3/2}$ states boosting the sensitivity of green to red emission intensity ratio based LT up to 5.7%/°C at 30 °C [63]. On the other hand, the introduction of Cr^{3+} may have a negative influence on the Yb^{3+}, Er^{3+} based thermometer. Mikalauskaite et al. reported that the introduction of the Cr^{3+} ions in the $NaGd_{0.78−x}F_4$:$Yb_{0.2}$/$Er_{0.02}$/Cr_x lowers the relative sensitivity of $^2H_{11/2}{\rightarrow}^4I_{15/2}$ to $^4S_{3/2}{\rightarrow}^4I_{15/2}$ based thermometer [64]. Chen et al. indicated that the presence of the Cr^{3+} dopant in the YF_3:Er^{3+}, Yb^{3+} + Ga_2O_3:Cr^{3+} glass-ceramics leads to the activation of the additional nonradiative depopulation channel of the $^4S_{3/2}$ state of the Er^{3+} efficiently quenching its emission [65]. The main concept of the approach proposed in this manuscript is schematically presented in Fig. 1. In order to validate the this idea in the most tangible way, the yttrium aluminium garnet ($Y_3Al_5O_{12}$, YAG) co-doped with Tb^{3+} and Eu^{3+} ions was used as a representative thermographic phosphor [66–68]. This was motivated by the fact that inorganic LT co-doped with Eu^{3+} and Tb^{3+} are well known for their low relative sensitivity to temperature changes. Moreover, YAG structure possesses octahedral Al sites that are preferentially occupied by the TM ions like Cr^{3+} or Mn^{4+}. Therefore the doping with TM ions does not provide significant structural changes in the YAG structure (Fig. 1a and b). When the excitation wavelength ($\lambda_{exc(Ln)}$) of the energy corresponding to the difference between ground and excited states of Tb^{3+} ions is used the $^5D_4$ and $^5D_3$ multiplets of Tb^{3+} ions are populated followed by their radiative depopulation (Fig. 1c). The increase of temperature leads to an increase of the $^5D_0$ state of the Eu^{3+} ion population by the $Tb^{3+}{\rightarrow}Eu^{3+}$ phonon assisted energy

transfer. Therefore the emission intensity ratio of the bands associated with the electronic transitions from $^5D_4$ state of Tb^{3+} to the one from $^5D_0$ state of Eu^{3+} can be used as a ratiometric temperature probe. However, when the TM ions are introduced to the nanoparticles and the $\lambda_{exc(TM)}$ is used, the population of the excited state of TM is followed by the phonon assisted energy transfer to the Ln^{3+} ions. The energy mismatch between the excited states of TM and Ln^{3+} leads to the strong thermal dependence of the probability of these energy transfers causing the enhancement of the sensitivity of LT to temperature changes. Taking advantage of this approach, the usable spectral range that enables the generation of the Ln^{3+} luminescence becomes wider (Fig. 1d) and the boost of the thermal response of the luminescence signal can be achieved (Fig. 1e and f). Three the most representative TM, namely Cr^{3+}, Mn^{4+} and Ti^{3+}/ Ti^{4+} were used as sensitizers in this manuscript [26,69–78]. The Cr^{3+} ions which emit in the red/near infrared spectral region are characterized by $3d^3$ electronic configuration with 8 LS terms. As it is well known the shape of the emission spectrum of Cr^{3+} ions depends on the crystal field strength (CFS) [79,80]. In the case of another TM of $3d^3$ configuration – Mn^{4+}, owing to its high positive effective change, the CFS is usually stronger than for Cr^{3+} and it affects the rate of thermal quenching of sharp red emission band [21]. The last proposed TM ion is $Ti^{3+/4+}$ with only one or none electron on the 3d orbital, respectively. The $3d^1$ configuration of Ti^{3+} leads to the limitation of transition possibilities to the ones between ^2E and $^4T_2$ states caused by the deformations of the oxygen octahedrons. On the other hand, the Ti^{4+} excitation is based on charge transfer (CT) transition from the ligand (O^{2-}) state and the population of Ti^{3+} ground state (^2E). Summing up, the $Ti^{3+/4+}$-doped samples may be characterized by two broad emission bands [77,81]. The difference in the energy diagram of those TM provides the flexibility in the modulation of the thermometric performance of TM sensitized Ln^{3+}-based LT, which will be discussed in this manuscript.

2. Experimental

The powders of YAG:Tb^{3+}, Eu^{3+} and YAG:Tb^{3+}, Eu^{3+}, TM (TM = Mn^{4+}, Cr^{3+}, $Ti^{3+/4+}$) nanocrystals were synthesised by the use of the modified Pechini method. The $Al(NO_3)_3 \cdot xH_2O$ (x ≈ 9; 99.999% purity, Alfa Aesar), Y_2O_3 (99.999% purity, Stanford Materials Corporation), Tb_4O_7 (99.999% purity, Stanford Materials Corporation), Eu_2O_3 (99.99% purity, Stanford Materials Corporation), $C_6H_8O_7$ (> 99.5% purity, Alfa Aesar), $H(OCH_2CH_2)_nOH$, (PEG-200, n = 200, Alfa Aesar) and $Mn(NO_3)_2 \cdot 4H_2O$ (99.99% purity, Sigma Aldrich), $Cr(NO_3)_3 \cdot 9H_2O$ (99.99% purity, Alfa Aesar) and $TiCl_3$ (solution about 30%, Sigma Aldrich) were used as starting materials. Stoichiometric amounts of aluminium nitrate and manganese or chromium nitrates or titanium chloride, respectively, were dissolved in deionized water in separate glasses and then mixed together. Yttrium, terbium and europium oxides were dissolved in deionized water with the addition of a small amount of HNO_3 (65% purity, Avantor), then recrystallized three times to remove the excess of nitric acid and added to the water solution of nitrates and chlorides. After that, an anhydrous citric acid and polyglycol were added to the mixture. The molar ratio of citric acid to all metals was set up as 6:1, meanwhile PEG-200 and citric acid were used in a 1:1 molar ratio. Subsequently, the obtained solution was dried for 7 days at 90 °C until a resin was formed. The produced resin of the samples with 1% Tb^{3+} and 1% Eu^{3+} concentration with respect to the moles of Y^{3+} ions and x% molar TM concentration (x = 0.1, 0.5, 1, 5, 10, 20 Mn^{4+} and $Ti^{3+/4+}$ and 0.1, 0.5, 1, 2, 3, 5, 10 for Cr^{3+}) in respect to Al^{3+} ions were annealed in porcelain crucibles for 12 h in air at a temperature of 1100 °C. All of the synthesized materials were examined by X-ray powder diffraction (XRPD) measurements carried out on PANalitycal X′Pert diffractometer, equipped with an Anton Paar TCU 1000 N temperature control unit, using Ni-filtered Cu-K_α radiation (V = 40 kV, I = 30 mA).

2

144
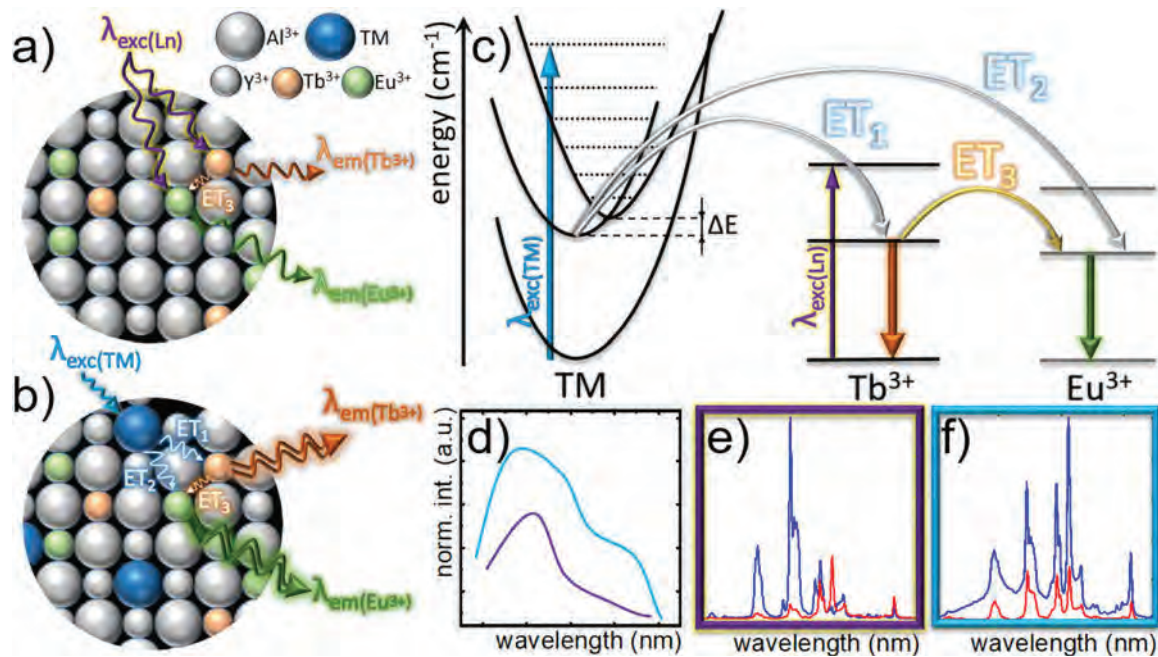
Fig. 1. The visualization of the concept of the proposed approach: schematic representation of the matrix co-doped with Tb^{3+} and Eu^{3+} ions – without (a) and with TM (b) as a sensitizer; simplified energy diagram of TM, Tb^{3+} and Eu^{3+} ions (c); the comparison of the excitation spectra of Eu^{3+} ions with (blue) and without (violet) TM as a sensitizer (d) and the difference between the low at high temperature emission spectra of the Tb^{3+}, Eu^{3+} co-doped sample without (e) and with (f) TM as a sensitizer.

Transmission electron microscope (TEM) images were taken using Philips CM-20 SuperTwin TEM microscope. The samples were dispersed in methanol, and a droplet of such suspension was put on a microscope copper grid. Next, the samples were dried and purified in a plasma cleaner. Studies were performed in a conventional TEM procedure with 160 kV parallel beam electron energy.

The emission spectra were measured using the 266 nm (20 mW) and 445 nm (50 mW) excitation lines from a laser diode and a Silver-Nova Super Range TEC spectrometer from Stellarnet (1 nm spectral resolution) as a detector. The temperature of the sample was controlled using a THMS 600 heating-cooling stage from Linkam (0.1 °C temperature stability and 0.1 °C set point resolution).

The excitation spectra and luminescence decay profiles were recorded using a FLS980 Fluorescence spectrometer from Edinburgh Instruments with a 450 W xenon lamp and μFlash lamp as excitation sources and a R928P side window photomultiplier tube from Hamamatsu as a detector. Owing to obtain the results of relative sensitivity with lower uncertainty, all of the LIR values were fitted according to the Mott-Seitz equation (Eq. (S1)). The average lifetimes of the excited states were calculated with the use of doubleexponential function using (Eq. (S2)).

3. Results and discussion

The YAG structure is well known for its superior thermal, chemical and optical properties serving as an excellent host material for both lanthanides and transition metal ions because it consists of dodecahedral sites of Y^{3+} (suitable for Ln^{3+} substitutions) and octahedral and tetrahedral sites of Al^{3+} (suitable for TM substitutions) (Fig. 2a) [72,82,83]. The analysis of the ionic radii of TM and Al^{3+} ions reveals that because of the similarities in their length even a high concentration of TM ions is possible to introduce in this host material. This is an especially beneficial feature of the YAG structure because an increase of the TM ions concentration facilitates the TM→Ln^{3+} energy transfer thus their high content is especially desired. In order to validate the influence of dopant concentration on the crystallographic structure of the synthesized nanocrystalline powders, the XRPD patterns were analyzed (Figs. 2b, S1–S4). All the

peaks observed in the patterns correspond with the reference data (ICSD 23848) confirming that obtained nanocrystals crystallize in a pure cubic YAG structure of a Ia3d space group. However, in the case of Ti^{3+}/Ti^{4+} co-doped YAG:Eu^{3+}, Tb^{3+} for 10% of Ti^{3+}/Ti^{4+} ions, the additional peaks associated with the TiO_2 (ICSD 1530026) and AlO_2 (ICSD 4124783). The slight shift of the diffraction peaks toward smaller 2θ angles indicates an increase of the cell parameter caused by the difference in the ionic radii between Al^{3+} and TM ions. This is especially clearly indicated for Cr^{3+} co-dopant (Fig. S5). The morphological studies indicate that there is no significant influence of the TM dopant ions on the morphology of obtained YAG powders. The synthesized powders consist of strongly aggregated particles of average size around 90 nm (Figs. 2c–f, S6–S9 and histograms S10).

The spectroscopic properties of Eu^{3+} and Tb^{3+} ions (Fig. S11) are well known and widely described in the literature [30,84–86]. Therefore only a brief description will be given here: the λ_{exc} = 266 nm excitation wavelength is absorbed by the Eu^{3+} ion through $O^{2-}\rightarrow Eu^{3+}$ charge transfer transition followed by the nonradiative population of the $^5D_0$ metastable state of Eu^{3+} ions (Figs. S12 and S13). As a consequence of its radiative depopulation, several emission bands appear in the Eu^{3+} emission spectrum at 584 nm ($^5D_0\rightarrow^7F_0$), 592 nm ($^5D_0\rightarrow^7F_1$), 611 nm ($^5D_0\rightarrow^7F_2$), 629 nm ($^5D_0\rightarrow^7F_3$) and 711 nm ($^5D_0\rightarrow^7F_4$). The emission intensity of $^5D_0\rightarrow^7F_J$ is marginally susceptible to thermal quenching by the multiphonon depopulation process because of the high energy separation between $^5D_0$ and the $^7F_6$ states (around 12200 cm^{-1}). In the case of the Tb^{3+} ions the luminescence is expected to occur via radiative depopulation of $^5D_3$ and $^5D_4$ states. However, because of the high probability

Table 1
Shannon ionic radii of matrix and dopant ions.

Site	Coordination number	Effective ionic radii (pm)			
dodecahedral	VIII (8-fold)	Y^{3+}	Tb^{3+}	Eu^{3+}	–
		101.9	104	106.6	–
octahedral	VI (6-fold)	Al^{3+}	Mn^{4+}	Cr^{3+}	$Ti^{3+/4+}$
		53.5	53	61.5	67/60.5
tetrahedral	IV (4-fold)	Al^{3+}	Mn^{4+}	Cr^{3+}	Ti^{4+}
		39	39	–	42
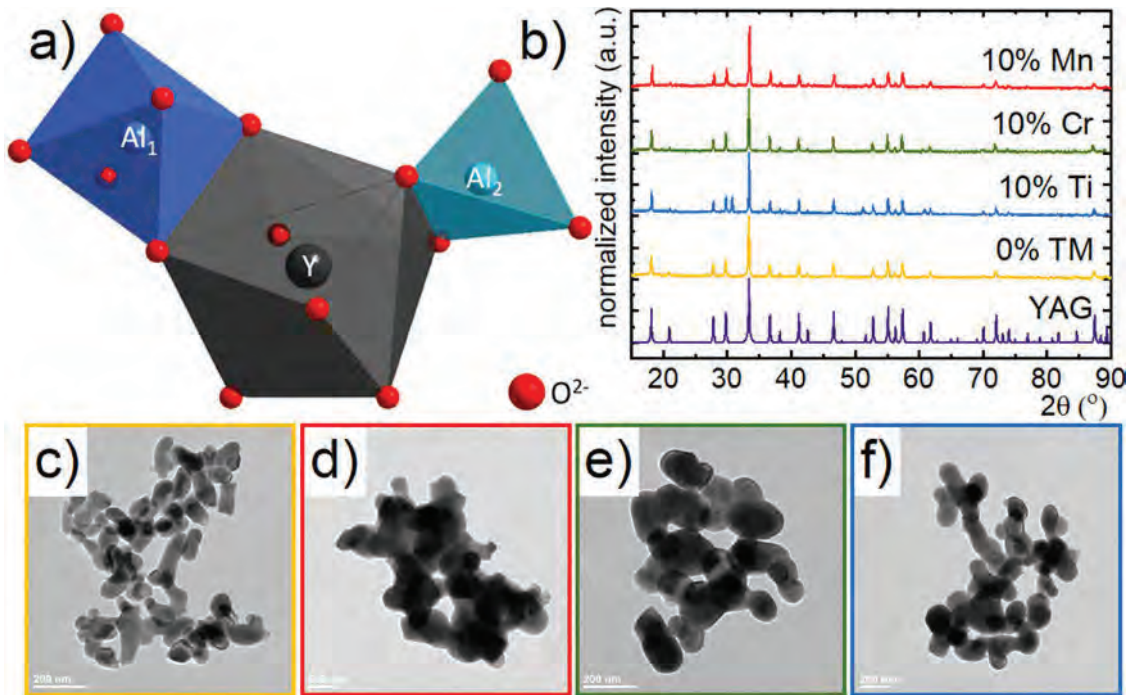
3

Fig. 2. Structural characterization of synthesized materials: the visualization of the polyhedras of Y^{3+} and Al^{3+} in YAG structure (a); the X-ray diffraction patterns of YAG:1% Tb^{3+}, 1% Eu^{3+} powders with different TM dopants – (b); The representative TEM images of YAG:1% Tb^{3+}, 1% Eu^{3+} undoped TM ions – (c) and co-doped with Mn^{4+} – (d), Cr^{3+} – (e), $Ti^{3+/4+}$ – (f).

of $\{^5D_3, {}^7F_6\} \leftrightarrow \{^5D_4, {}^7F_0\}$ cross relaxation process, the $^5D_4 \rightarrow {}^7F_J$ emission bands are usually dominant in the spectra. The radiative de-population of the $^5D_4$ state causes the generation of the emission bands at 492 nm ($^5D_4 \rightarrow {}^7F_6$), 545 nm ($^5D_4 \rightarrow {}^7F_5$), 589 nm ($^5D_4 \rightarrow {}^7F_4$) and 622 nm ($^5D_4 \rightarrow {}^7F_3$). Analogously, in this case also thermally stable emission of Tb^{3+} is expected (energy separation between $^5D_4$ and $^7F_0$ is around 14,700 cm^{-1}). However, when both ions are used as co-dopants the small energy difference between $^5D_4$ state of Tb^{3+}

and $^5D_0$ state of Eu^{3+} facilitates phonon assisted energy transfer between them which is thermally dependent.

3.1. The use of Mn^{4+} ions as a co-dopants

In order to understand the energy transfer processes which take place between TM and Ln^{3+} ions the simplified configurational energy diagram of Mn^{4+} ion is presented in Fig. 3a. Due to the higher
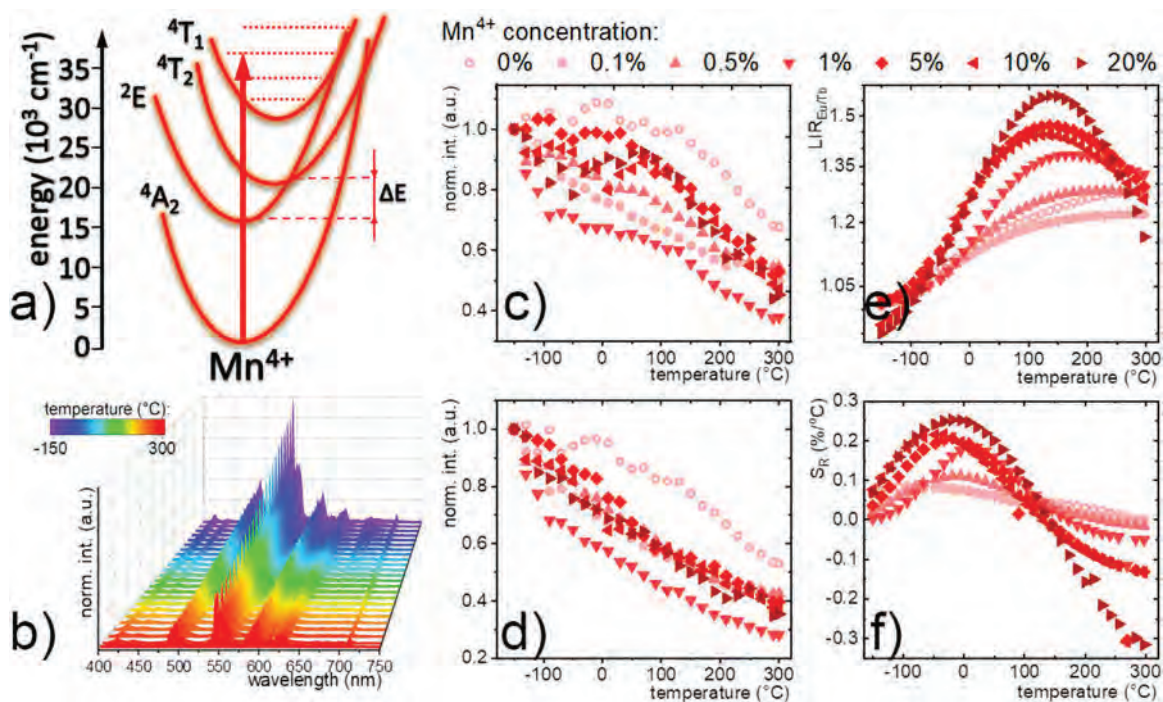
Fig. 3. Configurational coordinate diagram of Mn^{4+} ion (a); thermal evolution of emission spectra for YAG:1% Tb^{3+}, 1% Eu^{3+}, 10% Mn^{4+} (b); thermal evolution of integral band intensities of $^5D_0 \rightarrow {}^7F_1$ transition of Eu^{3+} ion (c) and $^5D_4 \rightarrow {}^7F_5$ electronic transition of Tb^{3+} ion (d); LIR (e) and S_R for different Mn^{4+} concentration (f).

absorption cross section of Mn^{4+} with respect to the Eu^{3+} ions, the $\lambda_{exc} = 266$ nm is mainly absorbed by the $^4A_2 \rightarrow ^4T_1$ transition of Mn^{4+} ions. Subsequently, nonradiative relaxation processes lead to the population of ^2E state from which usually red emission of Mn^{4+} takes place. However, in this case the Mn^{4+} luminescence was found only for Mn^{4+} concentration below 2% confirming the efficient non-radiative $Mn^{4+} \rightarrow Ln^{3+}$ energy transfer. As it can be seen on the representative thermal evolution of the emission spectra, an increase of the temperature causes the reduction of the Tb^{3+} and Eu^{3+} bands intensity (Figs. 3b and S13). However, Tb^{3+} luminescence is quenched faster with respect to the Eu^{3+} counterpart. In order to quantify observed changes the integral emission intensities of Eu^{3+} and Tb^{3+} were analyzed (Fig. 3c and d, respectively). In the case of Mn^{4+} unco-doped nanocrystals, the integral emission intensity of Eu^{3+} decreases by 35% in the considered temperature range while the Tb^{3+} emission intensity decreases by around 42%. However, when the concentration of the Mn^{4+} ions increases the rate of thermal quenching of both ions also gradually rises, however, more spectacular changes are observed in the case of Tb^{3+} ions. Therefore the decline of the intensity of Eu^{3+} even by 70% and by 92% for Tb^{3+} can be found when 20% of Mn^{4+} ions is used. The difference in the thermal quenching rate of the emission intensities of both ions enables to establish a thermally-dependent parameter based on their luminescence intensity ratio (LIR) (Fig. 3e):

$$LIR = \frac{\int I(Eu^{3+})d\lambda}{\int I(Tb^{3+})d\lambda} \tag{1}$$

The slight increase of LIR value (from 0.98 to 1.22) with its saturation above 200 °C is observed for the Mn^{4+}-unco-doped powder in the −150–300 °C temperature range. However, when the Mn^{4+} dopant concentration increases, the gradual enhancement of the LIR can be found with the maximum at around 120–200 °C followed by the decline in LIR values. The most spectacular thermal change of LIR can be found for 20% of Mn^{4+} where LIR increases from 0.9 at −150 °C to 1.6 at 120 °C. The reduction of LIR values observed at higher temperatures is associated with the enhancement of Eu^{3+} thermal quenching rate with respect to the Tb^{3+} ones. To quantify the observed thermally-induced variation of LIR, the relative sensitivity of nanopowders to temperature changes was calculated as follows:

$$S_R = \frac{1}{LIR} \cdot \frac{\Delta LIR}{\Delta T} \times 100\% \tag{2}$$

where ΔLIR represents change of LIR corresponding to ΔT change of temperature (Fig. 3f). The small changes of LIR for Mn^{4+} unco-doped powders are reflected in the value of $S_R = 0.09\%/°C$ at −80 °C. On the other hand, for Mn^{4+} co-doped nanocrystals the increase of the S_R up to $S_R = 0.28\%/°C$ at −25 °C and decrease to $S_R = −0.33\%/°C$ at 300 °C can be found. These results confirm that the introduction of the Mn^{4+} as a sensitizer enables the enhancement of the S_R by over 300% with respect to the unco-doped counterpart. The negative values of the S_R result from the change of the LIR's monotonicity and lead to the distinguishing of the two usable temperature ranges. Observed growth of the S_R causes the reduction of the temperature determination uncertainty calculated in accordance with Eq. (S6) (Fig. S14). In this case, the $\delta T = 4$ °C was calculated for the range of −150–200 °C what is expected in the materials with relatively low S_R.

The excitation spectra of Mn^{4+} monitored at $\lambda_{em} = 652$ nm consist among others of the bands of $^4A_2 \rightarrow ^4T_1$ (with a maximum around 350 nm) and $^4A_2 \rightarrow ^4T_2$ (centered at ~484 nm) electronic transitions and intense band in the ultraviolet part of the spectrum which is the superposition of $Mn^{4+} \rightarrow O^{2+}$ charge transfer transition and the tail of the $^4A_2 \rightarrow ^4T_1$ (Figs. S15–S17). Performed calculations (Eqs. (S3)–(S5)) indicate a decline of the CFS with the increase of Mn^{4+} concentration as follows: 2.72, 2.67, 2.63 for the YAG sample with 0.1; 0.5; 1% Mn^{4+},

respectively. However, the lack of the $^4A_2 \rightarrow ^4T_2$ band in the excitation spectrum for the concentration above 1% of Mn^{4+} ions, associated with the quenching of the Mn^{4+} emission intensity, prevented the further CFS analysis. The presence of the absorption bands of Ln^{3+} in the excitation spectra allows confirming the occurrence of the energy transfer between dopant ions. The narrow bands with the maximum at 393, 395.5 and 404.5 nm (25445, 25284, 24722 cm^{-1}, respectively) correspond to the transition from the $^7F_0$ ground state to the $^5L_7$, $^5L_6$, $^5D_3$ states of Eu^{3+}, respectively. However, the band at 447.5 nm (22346 cm^{-1}) originates from $^7F_0 \rightarrow ^5D_2$ of Eu^{3+} and occurs only above 5% of Mn^{4+} ions in the YAG matrix what is the statement confirming the ET from Mn^{4+} to the Eu^{3+} ions. The excitation spectra measured at the emission of Tb^{3+} ions indicate that there is no influence of the Mn^{4+} ions on the character of the Tb^{3+} excited states population (Fig. S15b). On the other hand, in the case of the excitation spectra of Eu^{3+} ions, an intense absorption band of Mn^{4+} in the UV part occurs (Fig. S15c). Additionally, its intensity increases with temperature confirming that higher temperature facilitates $Mn^{4+} \rightarrow Eu^{3+}$ energy transfer. For low Mn^{4+} concentration (0.1; 0.5; 1%) the $^7F_0 \rightarrow ^5D_4$ (362 nm) and $^7F_0 \rightarrow ^5D_3$ (404 nm) of Eu^{3+} bands and $^7F_0 \rightarrow ^5D_3$ (380 nm) of Tb^{3+} band are noted, while when Mn^{4+} concentration increases (5; 10; 20%) additional $^7F_0 \rightarrow ^5D_2$ (448 nm) of Eu^{3+} and $^7F_0 \rightarrow ^5D_4$ (477 nm) of Tb^{3+} bands occur. Riseberg et al. reported a radiative lifetime of ^2E level in YAG:Mn^{4+} crystals of around 2 ms at −196°C which starts to rapidly decrease above 30 °C [87]. In the case of the YAG:Eu^{3+}, Tb^{3+} Mn^{4+} powders discussed in this manuscript similar behaviour has been observed. However when the concentration of Mn^{4+} increases the lifetime of the ^2E state of Mn^{4+} ions significantly shortens, which can be explained in terms of the combination of the energy transfers between Mn^{4+} ions and the $Mn^{4+} \rightarrow Ln^{3+}$ energy transfer. Above 5% of Mn^{4+} concentration, the $^2E \rightarrow ^4A_2$ emission band was completely quenched (Figs. S18–S20). In order to better understanding the energy transfer between Mn^{4+} and Ln^{3+} ions the kinetics of the excited states of the Tb^{3+} and Eu^{3+} ions were analysed (Fig. S21). The calculated average lifetimes $<\tau>$ indicate the shortening of their value with the increase of Mn^{4+} ions concentration. This suggests that not only the $Mn^{4+} \rightarrow Ln^{3+}$ but also the back energy transfer occurs in the considered system which is beneficial from the thermometric performance perspective (Fig. S22).

3.2. The use of Cr^{3+} ions as a co-dopants

Although the Cr^{3+} ions possess exactly the same $3d^3$ configuration as Mn^{4+} their energy levels schemes differ. Therefore in order to understand the sensitization process through Cr^{3+} ions the simplified configurational coordinate diagram is presented in Fig. 4a. In this case, the excitation wavelength leads to the population of the $^4T_2$ state followed by the nonradiative transitions to the ^2E state. In YAG structure the strong crystal field approximation can be used to explain the luminescent properties of the Cr^{3+}. Therefore narrow emission line associated with the $^2E \rightarrow ^4A_2$ electronic transition is expected to occur. Relatively broad absorption bands at 450 nm ($^4A_2 \rightarrow ^4T_1$) and 600 nm ($^4A_2 \rightarrow ^4T_2$) usually observed in the excitation spectra of YAG:Cr^{3+} are especially favourable for the sensitization process. The $^2E \rightarrow ^4A_2$ luminescence of Cr^{3+} is well known for its high intensity, therefore the Cr^{3+} emission band dominates in the YAG:Tb^{3+},Eu^{3+}, Cr^{3+} co-doped nanocrystals (Figs. 4b and S23). The comparison of the excitation spectra of the considered nanocrystals measured for $\lambda_{em} = 712$ nm (Cr^{3+} ions emission) indicates the presence of the $O^{2-} \rightarrow Eu^{3+}$ charge transfer band confirming the $Eu^{3+} \rightarrow Cr^{3+}$ energy transfer, which becomes less efficient in the case of the higher Cr^{3+} concentrations. The spectral positions of the $^4A_2 \rightarrow ^4T_1$ (440 nm) and $^4A_2 \rightarrow ^4T_2$ (594 nm) shifts slightly toward shorter wavelengths with an increase of Cr^{3+} concentration suggesting that there is a change in the CFS ^{4}induced by high dopant
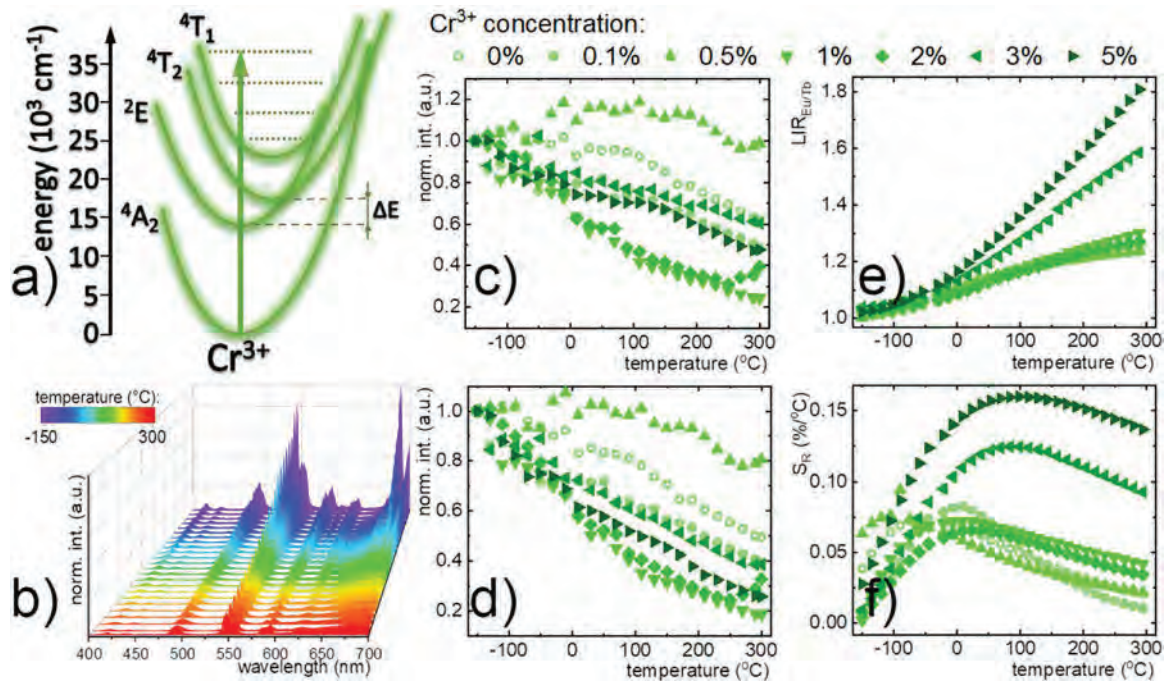
Fig. 4. The simplified configurational coordinate diagram of Cr^{3+} ion (a); thermal evolution of emission spectra for YAG:1% Tb^{3+}, 1% Eu^{3+}, 1% Cr^{3+} (b); the integral emission intensity of $^5D_0\rightarrow^7F_1$ emission band of Eu^{3+} ion (c) and $^5D_4\rightarrow^7F_5$ emission band of Tb^{3+} ion (d) as a function of temperature, LIR (e) and relative sensitivity S_R for different Cr^{3+} concentrations (f).

concentration [88]. The calculations of the CFS (Eqs. (S3)–(S5)) indicate the gradual enhancement from Dq/B = 2.74 for 0.1% of Cr^{3+} to Dq/B = 3.02 for 5% of Cr^{3+} ion related to the difference in Al^{3+} and Cr^{3+} ionic radii (see Table 1). Moreover, the narrow peaks are noted in the excitation spectra as a consequence of Tb^{3+} transitions to $^5H_7$ (320 nm), $^5G_5$ (362 nm) and $^5D_3$ (382 nm) states as well as of the $^7F_0\rightarrow^5L_6$ of Eu^{3+} ions were observed. That confirms the expected $Tb^{3+}\rightarrow Cr^{3+}$ and $Eu^{3+}\rightarrow Cr^{3+}$ ETs (Figs. S24–S26). The excitation spectra measured at the Tb^{3+} emission consist of characteristic f-f absorption bands of Tb^{3+} ions related to $^7F_6\rightarrow^5D_1$ (324 nm), $^7F_6\rightarrow^5D_2$ (354 nm), $^7F_6\rightarrow^5G_5$ (360 nm) and $^7F_6\rightarrow^5D_3$ (372.5 nm) transitions. Additionally, the bands associated with the $^7F_0\rightarrow^5L_8$ (371 nm) and $^7F_0\rightarrow^5G_5$ (378 nm) transitions of Eu^{3+} ions confirm the $Eu^{3+}\rightarrow Tb^{3+}$ energy transfer. On the other hand, the excitation spectra measured for Eu^{3+} emission consist the several transitions of the Eu^{3+}: $^7F_0\rightarrow^5D_1$ (324 nm), $^7F_0\rightarrow^5H_3$ (327 nm), $^7F_0\rightarrow^5D_4$ (362 nm), $^7F_0\rightarrow^5G_5$ (379 nm), $^7F_0\rightarrow^5L_7$ (388.5 nm), $^7F_0\rightarrow^5L_6$ (394 nm) and $^7F_0\rightarrow^5D_3$ (405 nm) as well as the $^4A_2\rightarrow^4T_1$ of Cr^{3+} (440 nm). When the temperature increases, the intensity of the band at 440 nm associated with $^4A_2\rightarrow^4T_1$ transition of Cr^{3+} ions increases. This suggests that the Eu^{3+} ions may be populated by the $Cr^{3+}\rightarrow Eu^{3+}$ energy transfer and the probability of this process increases at elevated temperatures. It is worth noting that the average decay times of $^5D_4$ (Tb^{3+}), $^5D_0$ (Eu^{3+}) and ^2E (Cr^{3+}) decreases with enlargement of the Cr^{3+} concentration (Figs. S27, S28), which is related to the $Cr^{3+}\rightarrow Ln^{3+}$ and $Ln^{3+}\rightarrow Cr^{3+}$ energy transfers. The integral emission intensity of Eu^{3+} ions was found to be very sensitive to Cr^{3+} dopant concentration. In the case of the Cr^{3+}-unco-doped nanocrystals its intensity is constant up to 100 °C and above this threshold starts to gradually decrease up to 60% of its initial value (at − 150 °C). However, when the concentration of the Cr^{3+} sensitizer rises the Eu^{3+} emission intensity starts to decrease already from − 130 °C and reached 40% of its initial value at 300 °C. This is in agreement with the expectations since the strong quenching of the Cr^{3+} states population and $Cr^{3+}\rightarrow Eu^{3+}$ energy transfer lead to the decrease of Eu^{3+} emission intensity. The Tb^{3+} luminescence intensity is much more susceptible to luminescence thermal quenching and for high Cr^{3+} dopant concentration the Tb^{3+}

integral intensity reached almost 20% of its initial intensity. The analysis of the thermal dependence of luminescence lifetime of the ^2E state of the Cr^{3+} ion indicates that in the case of 0.1%Cr^{3+} ions in YAG:Eu^{3+}, Tb^{3+}, Cr^{3+} phosphor the lifetime decreases from 6.6 ms at − 150 °C up to 400 µs at 300 C (Figs. S29, S30). The rate of this quenching is very similar with respect to the one reported by My-khaylyk et al. for the YAG:Cr^{3+} crystals. When the concentration of Cr^{3+} ions increases a significant shortening of the lifetime of ^2E state can be noticed [89]. As a consequence the low temperature lifetime of ^2E state in the case of YAG:Tb^{3+},Eu^{3+} 5%Cr^{3+} reached 0.7 ms. This reduction of the lifetime is associated with two effects (i) concentration quenching of the Cr^{3+} ions and the $Cr^{3+}\rightarrow Ln^{3+}$ which has been already confirmed and discussed. The calculations of the LIR values as a function of temperature for different sensitizer concentrations depict that below 2% Cr^{3+} no significant changes can be found in the thermal trend of LIR. However, above this threshold, the higher the Cr^{3+} concentration the stronger enhancement of the LIR value, even up to 80% enhancement in the − 150–300 °C temperature range observed for 5% of Cr^{3+} ions. Therefore the increase of the Cr^{3+} concentration causes the enhancement of the S_R values up to 0.16%/ °C at 100 °C for 5% Cr^{3+} ions, while the maximal S_R for a powder without Cr^{3+} was only S_R = 0.075%/°C at − 60 °C. It is worth noting that in this case the S_R above 0.15%/°C was maintained over a 20–200 °C temperature range. Obtained results corroborate that the introduction of Cr^{3+} ions to the YAG:Eu^{3+},Tb^{3+} structure enables the growth of S_R by 200%. The general conclusion can be drawn that the higher Cr^{3+} concentration the more spectacular increase of the S_R can be observed in the analyzed concentration range. However, it needs to be noted that an increase of Cr^{3+} concentration leads to the reduction of the Ln^{3+} emission intensity due to the increase of the probability of the back $Ln^{3+}\rightarrow Cr^{3+}$ energy transfer. Since the temperature determination uncertainty depends on the emission intensity of the phosphor, further enhancement of the Cr^{3+} concentration will not be beneficial from the thermometric perspective. The LIR uncertainty values were obtained below $\delta T = 3$ °C in the − 150–300 °C range for the samples with 3% and 5% of Cr^{3+} (Eq. (S6), Fig. S31).

6
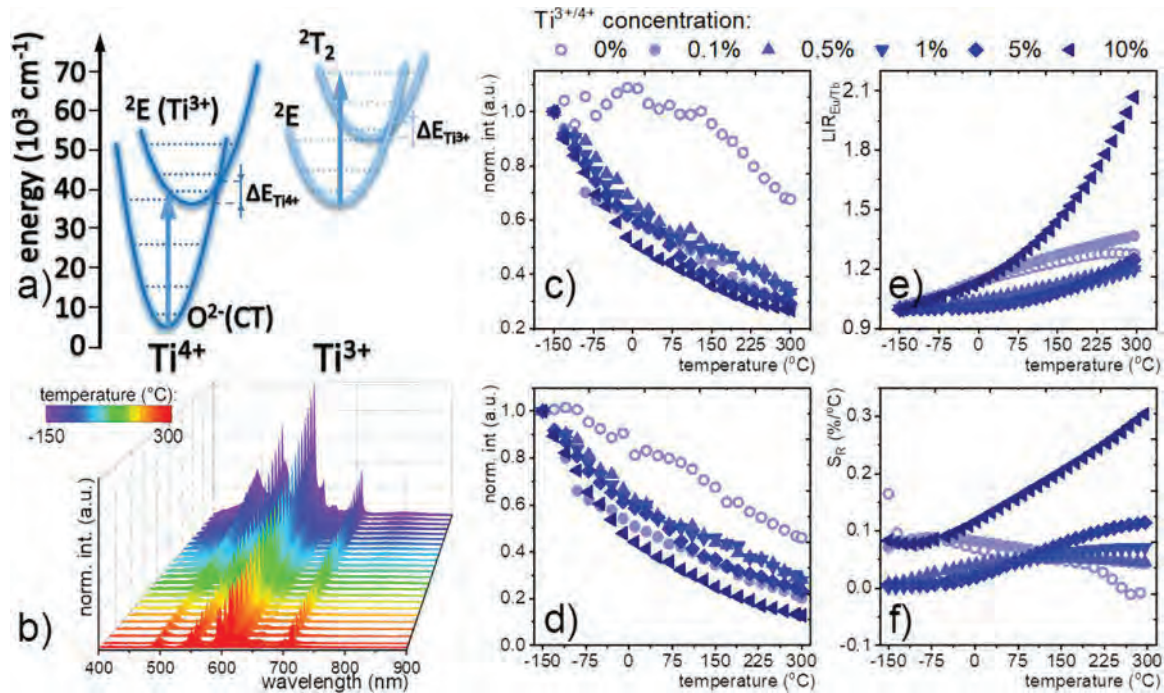
Fig. 5. Configurational coordinate diagrams of $Ti^{3+/4+}$ ions (a); thermal evolution of emission spectra for YAG:1%Tb^{3+}, 1%Eu^{3+}, 10%$Ti^{3+/4+}$ (b); thermal evolution of band integral intensities for $^5D_0{\rightarrow}^7F_1$ emission band of Eu^{3+} ion (c) and $^5D_4{\rightarrow}^7F_5$ emission band of Tb^{3+} ion (d), LIR (e) and relative sensitivity S_R for different $Ti^{3+/4+}$ concentrations (f).

3.3. The use of $Ti^{3+/4+}$ ions as a co-dopants

The last of the proposed sensitizers of Ln^{3+}-based ratiometric thermometer are Ti ions. As it has already been reported due to the highly defected surface part of the nanocrystal the Ti^{4+} oxidation state was found in the surface part while the Ti^{3+} in the inner part of the particle [77,90]. It was also found that the increase of the size of the particle modulates the relative emission intensity ratio between those two oxidation states. The ratio of the Ti^{3+} to the Ti^{4+} ions is constant and proportional to the size of the nanocrystals. Analogously in the considered in this manuscript case, two oxidation states of titanium ions were found. Due to its mixed valence character, the appearance of the Ti^{3+} and Ti^{4+} ions in the YAG matrix leads to occurring two different kinds of radiative processes which are described in the energy diagrams in Fig. 5a. The configurational coordination diagram of $3d^1$ configuration of Ti^{3+} ion consists of only two energy levels, namely ^2E and $^2T_2$. In this case, the excitation wavelength of 266 nm enables the electron transfer from the ground state ^2E to excited $^2T_2$. The return radiative $^2T_2{\rightarrow}^2E$ transition leads to the generation of the broad emission band centered at ~800 nm. On the other hand the Ti^{4+} of $3d^0$ electronic configuration, due to unfiled d orbitals, are able to absorb the light only via the $O^{2-}{\rightarrow}Ti^{4+}$ electronic transition, which leads to the ^2E state population of Ti^{3+}. The charge transfer emission band occurs at around 520 nm. However, in our approach the part of energy may be transferred to the Tb^{3+} and Eu^{3+} ions. The thermal evolution of the emission spectra of YAG:Tb^{3+}, Eu^{3+}, $Ti^{3+/4+}$ powders with different $Ti^{3+/4+}$ concentration upon 266 nm excitation indicates that the besides the Eu^{3+} and Tb^{3+} bands the emission spectra consists of broad band of very low intensity associated with the $^2T_2{\rightarrow}^2E$ electronic transition of Ti^{3+} ions and broad CT band at 520 nm of Ti^{4+} ions (Figs. 5b and S32). The Ti^{3+} emission band can be observed only at low temperatures and for low Ti^{3+} dopant concentrations. Its intensity is rapidly quenched when temperature increases. The significantly faster rate of the thermal quenching of Ti^{3+} luminescence observed in YAG: Eu^{3+}, Tb^{3+}, $Ti^{3+/4+}$ powders with respect to the $Ti^{3+/4+}$ unco-doped powders confirms the thermal activation of $Ti^{3+/4+}{\rightarrow}Ln^{3+}$ energy transfer [77]. It is

worth noting that the CT emission of Ti^{4+} ions spectrally overlaps with the Eu^{3+} and Tb^{3+} emission bands. The integral emission intensities of Eu^{3+} and Tb^{3+} bands as a function of temperature reveal that the doping even with the small amount of $Ti^{3+/4+}$ ions strongly affects the thermal quenching rates of both ions (Fig. 5c and d). The Eu^{3+} emission intensity decreases to 35% of its initial value for 0.1% Ti^{3+} and the further increase of sensitizer concentration causes the quenching of the Eu^{3+} emission intensity up to 28% at 300 °C. On the other hand the quenching rate of the Tb^{3+} intensity increases gradually with the sensitizer concentration and the 18% of initial Tb^{3+} luminescence intensity was found for 10% of Ti^{3+} ions. Spectral overlap of the Ti^{4+} emission band with the Eu^{3+} and Tb^{3+} and its high thermal quenching rate may affect the thermal evolution of the Ln^{3+} bands intensities. Therefore in the case of the Eu^{3+} the integral emission intensity of the $^5D_0{\rightarrow}^7F_4$ band at 710 nm was calculated and the comparison with the one obtained for $^5D_0{\rightarrow}^7F_1$ indicates that indeed the bands intensity at 590 was 10% stronger quenched than 710 nm counterpart. In the case of the Tb^{3+} luminescence such analysis was impossible to perform. The lack of an evident correlation between sensitizer concentration and the thermal change of LIR value may be related with the contribution of the Ti^{4+} luminescence to the calculated intensities of Ln^{3+} ions. However, in the case of the 10% $Ti^{3+/4+}$ concentration when the Ti^{3+} and Ti^{4+} emission bands are totally quenched, the spectacular increase of LIR from 0.94 to 2.1 was observed. Hence the implementation of 10% of Ti^{3+} enables an enhancement of the S_R values in the 0–300 °C temperature range with respect to the $Ti^{3+/4+}$-unco-doped counterpart. The maximum of $S_R = 0.30\%$/°C was obtained at 285 °C, while only $S_R = 0.01\%$/°C for YAG:Tb^{3+}, Eu^{3+} powder. The lowest temperature determination uncertainty calculated in the temperature range of − 150–300 °C was below $\delta T = 3$ °C for the YAG:Tb^{3+}, Eu^{3+}, 10% $Ti^{3+/4+}$ powder (Fig. S33).

The excitation spectra measured for $\lambda_{em} = 612$ nm indicate the presence of an additional, $O^{2-}{\rightarrow}Ti^{4+}$ CT aborting band with the maxima at around 300 nm which spectrally overlaps with the $O^{2-}{\rightarrow}Eu^{3+}$ CT band (Figs. S34, S35). In general in the nanocrystalline materials it is difficult to register excitation bands of Ti^{3+} and Ti^{4+} upon lamp excitation due to their low intensities[77,90]. In order to
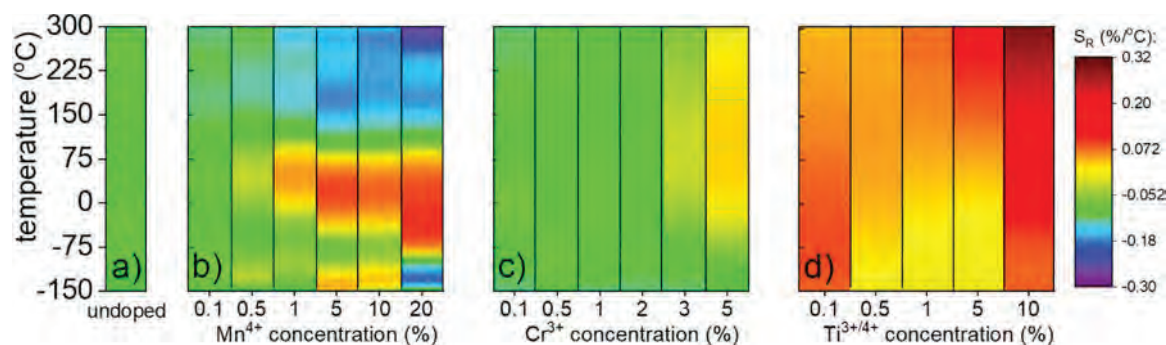
Fig. 6. Influence of TM ions concentration on the thermal evolution of relative sensitivity S_R in YAG:Tb^{3+}, Eu^{3+} (a) and YAG:Tb^{3+}, Eu^{3+}, TM powders where TM = Mn^{4+} (b); Cr^{3+} (c); Ti$^{3+/4+}$ (d).

confirm the presence of ET processes, the measurements of the lifetimes of the excited states measurements of Tb^{3+} and Eu^{3+} were performed for different Ti$^{3+/4+}$ concentrations (Figs. S36 and S37). Additionally, the shortening of the average lifetime of the Ln^{3+} ions with the increase of the Ti$^{3+/4+}$ concentration indicates the Ln^{3+}→Ti$^{3+/4+}$ energy transfer. However, observed shortening was not as spectacular as in the case of Cr^{3+} and Mn^{4+} sensitizers.

An evident influence of the Mn^{4+}, Cr^{3+} and Ti$^{3+/4+}$ ions on the thermal evolution of the Eu^{3+} and Tb^{3+} ions emission intensities may be caused either by the population (TM→Ln^{3+} energy transfer) or depopulation (Ln^{3+}→TM energy transfer) mechanisms of the Ln^{3+} excited states. The shortening of the Ln^{3+} excited state lifetimes indicates that the TM→Ln^{3+} is probable. In order to verify which of those processes plays a dominant role in the change of the LIR the kinetics of the Tb^{3+} and Eu^{3+} excited states were investigated as a function of temperature (Figs. S38–S45). Obtained results clearly demonstrate that $<\tau>$ are in most cases temperature independent. These results indicate that the TM→Ln^{3+} energy transfer is temperature independent and should not affect the change of the thermal dependence of Ln^{3+} emission intensities. Moreover, in the case of Tb^{3+} lifetime in YAG:Eu^{3+}, Tb^{3+}, Mn^{4+} and even more spectacular in YAG:Eu^{3+}, Tb^{3+}, Cr^{3+} increases at elevated temperatures. This effect confirms that the probability of the Ln^{3+}→TM parasitic quenching process decreases. If the quenching process will be responsible for change of the thermal evolution of LIR, the reduction of the Tb^{3+} quenching manifested as an increase of the $<\tau>$ of the $^5D_4$ state would lead to the reduction of the thermally induced changes of Tb^{3+} emission intensity. This is in contrary to the obtained results. Therefore it can be concluded that the sensitization process (TM→Ln^{3+} energy transfer) is responsible for LIR and hence S_R enhancement. The obtained S_R values for different TM are compared in Fig. 6. When the Mn^{4+} ions are used as a sensitizer the gradual enhancement of the S_R can be observed, what is especially clearly seen in the 0–100 °C temperature range. In the case of the 20% of Mn^{4+} ions the 300% enhancement of S_R was found. However, the observed negative values of S_R indicates that the usable temperature range (UTR) becomes narrower with the enlargement of the Mn^{4+} concentration. Hence for the YAG:Eu^{3+}, Tb^{3+}, 20% Mn^{4+} the two UTR can be distinguished depending on the type of the application: 1st in the range of − 100–100 °C and 2nd: 150–300 °C. The introduction of the Cr^{3+} ions leads to the less spectacular changes of S_R. However, for YAG:Eu^{3+}, Tb^{3+}, 5% Cr^{3+} the 200% enhancement of S_R was observed and this high value of the S_R maintained over 20–300 °C temperature range. The advantage of the use of this sensitizer is that the UTR does not become narrower. For Ti$^{3+/4+}$ ions used as a sensitizer the less regular changes of the S_R as a function of sensitizer concentration were observed which results from the spectral overlap of the sensitizer and Ln^{3+} emission. However, for YAG:Eu^{3+}, Tb^{3+}, 10% Ti^{3+} the

significantly higher values of S_R (with respect to the unco-doped counterpart) were obtained in a very wide temperature range (− 150–300 °C). The presented comparison confirms the positive role of the use of TM as a sensitizers of the Ln^{3+} ions from the luminescent thermometry perspective. The significant improvement of thermographic properties of YAG:Eu^{3+}, Tb^{3+} luminescent thermometer indicates that further work on this approach may lead to the design of the TM-sensitized highly sensitive luminescent thermometer.

4. Conclusions

An approach of enhancing the relative sensitivity of Tb^{3+}, Eu^{3+}-based ratiometric luminescent thermometer by their sensitization with three different transition metal ions (TM = Mn^{4+}, Cr^{3+}, Ti$^{3+/4+}$) in YAG structure was investigated as a function of sensitizer ions concentration. The structural studies of YAG:Tb^{3+}, Eu^{3+}, TM indicate that doping with high sensitizer concentration up to 20% of Mn^{4+}, 5% of Cr^{3+} and 10% of Ti$^{3+/4+}$ ions does not lead to the generation of any significant structural changes of YAG host material. It was found that the thermally induced changes of Eu^{3+} to Tb^{3+} luminescence intensity ratio significantly increases when the concentration of TM increases. This effect was discussed in terms of the temperature dependent TM→Ln^{3+} energy transfer process, that was confirmed by the excitation spectra measurements. The detailed analysis of the kinetics of the excited state of Ln^{3+} ions reveals that also Ln^{3+} → TM back energy transfer occurs in the considered system. However the thermal dependence of the Ln^{3+} lifetimes confirmed that the sensitization via TM→Ln^{3+} energy transfer is a dominant process responsible for thermal variation of LIR value. The proposed approach enables to enhance the relative sensitivity even by 300% from S_R = 0.09%/°C for YAG:Eu^{3+},Tb^{3+} to S_R = 0.28%/°C for Mn^{4+}, 0.15%/°C for Cr^{3+} and 0.30%/°C for Ti$^{3+/4+}$ co-dopant. Hence, the sensitization effect is significant, in the order of 200–300% higher in comparison with TM-unco-doped YAG:Tb^{3+}, Eu^{3+} powder ($S_{R(max)}$ = 0.09%/°C). These first optimistic results confirm the beneficial influence of the sensitization with transition metal ions process for enhancing the relative sensitivity of Ln^{3+} based luminescent thermometer. Therefore further development of this approach may lead to the creation of highly sensitive luminescent thermometers.

CRediT authorship contribution statement

Wojciech Piotrowski: Methodology, Investigation, Writing - original draft, Writing - review & editing. **Karolina Kniec:** Methodology, **Lukasz Marciniak:** Conceptualization, Writing - original draft, Writing - review & editing.

Declaration of Competing Interest

The authors declare that they have no known competing financial interests or personal relationships that could have appeared to influence the work reported in this paper.

Acknowledgements

Appendix A. Supporting information

Supplementary data associated with this article can be found in the online version at doi:10.1016/j.jallcom.2021.159386.

References

[1] L.D. Carlos, F. Palacio, Thermometry at the Nanoscale, The Royal Society of Chemistry, 2016, https://doi.org/10.1039/9781782622031

[2] M. Dramićanin, Chapter 11 - temperature measurements at the nanoscale, in: M.B.T.-L.T. Dramićanin (Ed.), Woodhead Publishing Series in Electronic and Optical Materials, Woodhead Publishing, 2018, pp. 251–263, https://doi.org/10.1016/B978-0-08-102029-6.00011-7

[3] D. Jaque, F. Vetrone, Luminescence nanothermometry, Nanoscale 4 (2012) 4301–4326, https://doi.org/10.1039/c2nr30764b

[4] M. Runowski, N. Stopikowska, D. Szeremeta, S. Goderski, M. Skwierczyńska, S. Lis, Upconverting lanthanide fluoride core@shell nanorods for luminescent thermometry in the first and second biological windows: β-NaYF$_4$:Yb^{3+}-Er^{3+}@SiO$_2$ temperature sensor, ACS Appl. Mater. Interfaces 11 (2019) 13389–13396, https://doi.org/10.1021/acsami.9b00445

[5] H.D.A. Santos, D. Ruiz, G. Lifante, C. Jacinto, B.H. Juarez, D. Jaque, Time resolved spectroscopy of infrared emitting Ag$_2$S nanocrystals for subcutaneous thermometry, Nanoscale 9 (2017) 2505–2513, https://doi.org/10.1039/c6nr08534b

[6] E.C. Ximendes, W.Q. Santos, U. Rocha, U.K. Kagola, F. Sanz-Rodríguez, N. Fernández, A.D.S. Gouveia-Neto, D. Bravo, A.M. Domingo, B. Del Rosal, C.D.S. Brites, L.D. Carlos, D. Jaque, C. Jacinto, Unveiling in vivo subcutaneous thermal dynamics by infrared luminescent nanothermometers, Nano Lett. 16 (2016) 1695–1703, https://doi.org/10.1021/acs.nanolett.5b04611

[7] X. Qiu, Q. Zhou, X. Zhu, Z. Wu, W. Feng, F. Li, Ratiometric upconversion nanothermometry with dual emission at the same wavelength decoded via a time-resolved technique, Nat. Commun. 11 (2020) 4, https://doi.org/10.1038/s41467-019-13796-w

[8] A.M. Kaczmarek, M. Suta, H. Rijckaert, A. Abalymov, I. Van Driessche, A.G. Skirtach, A. Meijerink, P. Van Der Voort, Visible and NIR upconverting Er^{3+}–Yb^{3+} luminescent nanorattles and other hybrid PMO-inorganic structures for in vivo nanothermometry, Adv. Funct. Mater. 30 (2020) 2003101, https://doi.org/10.1002/adfm.202003101

[9] Y. Shen, J. Lifante, N. Fernández, D. Jaque, E. Ximendes, In vivo spectral distortions of infrared luminescent nanothermometers compromise their reliability, ACS Nano 14 (2020) 4122–4133, https://doi.org/10.1021/acsnano.9b08824

[10] C. Abram, B. Fond, F. Beyrau, Temperature measurement techniques for gas and liquid flows using thermographic phosphor tracer particles, Prog. Energy Combust. Sci. 64 (2018) 93–156, https://doi.org/10.1016/j.pecs.2017.09.001

[11] A. Mendieta, B. Fond, P. Dragomirov, F. Beyrau, A delayed gating approach for interference-free ratio-based phosphor thermometry, Meas. Sci. Technol. 30 (2019) 074002, https://doi.org/10.1088/1361-6501/ab1b0c

[12] C. Binder, F. Abou Nada, M. Richter, A. Cronhjort, D. Norling, Heat loss analysis of a steel piston and a YSZ coated piston in a heavy-duty diesel engine using phosphor thermometry measurements, SAE Int. J. Engines 10 (2017) 1954–1968, https://doi.org/10.4271/2017-01-1046

[13] M. Runowski, P. Woźny, N. Stopikowska, I.R. Martín, V. Lavín, S. Lis, Luminescent nanothermometer operating at very high temperature-sensing up to 1000 K with upconverting nanoparticles (Yb^{3+}/Tm^{3+}), ACS Appl. Mater. Interfaces 12 (2020) 43933–43941, https://doi.org/10.1021/acsami.0c13011

[14] M.W. Khalid, C. Whitehouse, R. Ahmed, M.U. Hassan, H. Butt, Remote thermal sensing by integration of corner-cube optics and thermochromic materials, Adv. Opt. Mater. 7 (2019) 1801013, https://doi.org/10.1002/adom.201801013

[15] A. Skripka, V. Karabanovas, G. Jarockyte, R. Marin, V. Tam, M. Cerruti, R. Rotomskis, F. Vetrone, Decoupling theranostics with rare earth doped nanoparticles, Adv. Funct. Mater. 29 (2019) 1807105, https://doi.org/10.1002/adfm.201807105

[16] F. Yang, A. Skripka, A. Benayas, X. Dong, S.H. Hong, F. Ren, J.K. Oh, X. Liu, F. Vetrone, D. Ma, An integrated multifunctional nanoplatform for deep-tissue dual-mode imaging, Adv. Funct. Mater. 28 (2018) 1706235, https://doi.org/10.1002/adfm.201706235

[17] A.M. Kaczmarek, M.K. Kaczmarek, R. Van Deun, Er^{3+} -to-Yb^{3+} and Pr^{3+} -to-Yb^{3+} energy transfer for highly efficient near-infrared cryogenic optical temperature sensing, Nanoscale 11 (2019) 833–837, https://doi.org/10.1039/c8nr08348g

[18] M. Suta, Ž. Antić, V. Đorđević, S. Kuzman, M.D. Dramićanin, A. Meijerink, Making Nd^{3+} a sensitive luminescent thermometer for physiological temperatures—an account of pitfalls in Boltzmann thermometry, Nanomaterials 10 (2020) 543, https://doi.org/10.3390/nano10030543

[19] I.K. van Ravenhorst, R.G. Geitenbeek, M.J. van der Eerden, J. Tijn van Omme, H.H. Peréz Garza, F. Meirer, A. Meijerink, B.M. Weckhuysen, In situ local temperature mapping in microscopy nano-reactors with luminescence thermometry, ChemCatChem 11 (2019) 5505–5512, https://doi.org/10.1002/cctc.201900985

[20] A.S. Souza, L.A.O. Nunes, I.G.N. Silva, F.A.M. Oliveira, L.L. Da Luz, H.F. Brito, M.C.F.C. Felinto, R.A.S. Ferreira, S.A. Júnior, L.D. Carlos, O.L. Malta, Highly-sensitive Eu^{3+} ratiometric thermometers based on excited state absorption with predictable calibration, Nanoscale 8 (2016) 5327–5333, https://doi.org/10.1039/c6nr00158k

[21] W. Piotrowski, K. Trejgis, K. Maciejewska, K. Ledwa, B. Fond, L. Marciniak, Thermochromic luminescent nanomaterials based on Mn^{4+}/Tb^{3+} codoping for temperature imaging with digital cameras, ACS Appl. Mater. Interfaces 12 (2020) 44039–44048, https://doi.org/10.1021/acsami.0c11730

[22] L. Marciniak, A. Bednarkiewicz, D. Kowalska, W. Strek, A new generation of highly sensitive luminescent thermometers operating in the optical window of biological tissues, J. Mater. Chem. C 4 (2016) 5559–5563, https://doi.org/10.1039/c6tc01484d

[23] J.C.G. Bünzli, C. Piguet, Taking advantage of luminescent lanthanide ions, Chem. Soc. Rev. 34 (2005) 1048, https://doi.org/10.1039/b406082m

[24] S.V. Eliseeva, J.C.G. Bünzli, Lanthanide luminescence for functional materials and bio-sciences, Chem. Soc. Rev. 39 (2010) 189–227, https://doi.org/10.1039/b905604c

[25] J.C.G. Bünzli, Lanthanide luminescence for biomedical analyses and imaging, Chem. Rev. 110 (2010) 2729–2755, https://doi.org/10.1021/cr900362e

[26] V. Lupei, A. Lupei, G. Boulon, Characteristics of sensitized emission in laser crystals, Phys. Rev. B 53 (1996) 14818–14827, https://doi.org/10.1103/PhysRevB.53.14818

[27] L.B. Guimarães, A.M.P. Botas, M.C.F.C. Felinto, R.A.S. Ferreira, L.D. Carlos, O.L. Malta, H.F. Brito, Highly sensitive and precise optical temperature sensors based on new luminescent Tb^{3+}/Eu^{3+} tetrakis complexes with imidazolic counterions, Mater. Adv. 1 (2020) 1988–1995, https://doi.org/10.1039/d0ma00201a

[28] L. Li, X. Qi, F. Qin, L. Li, H. Gao, Y. Zheng, Z. Zhang, Highly sensitive optical ratiometric thermometry by exciting Eu^{3+}/Tb^{3+}'s unusual absorption lines, Phys. Chem. Chem. Phys. 21 (2019) 24308–24315, https://doi.org/10.1039/c9cp04094c

[29] N. Rakov, Y. Xing, G.S. Maciel, Optical thermometry operation within all three biological windows using Nd^{3+}:Er^{3+}:Y$_2$O$_3$ nanocomposite phosphors, ACS Appl. Nano Mater. 3 (2020) 10479–10486, https://doi.org/10.1021/acsanm.0c02397

[30] A.N. Carneiro Neto, R.T. Moura, A. Shyichuk, V. Paterlini, F. Piccinelli, M. Bettinelli, O.L. Malta, Theoretical and experimental Investigation of the Tb^{3+}→Eu^{3+} energy transfer mechanisms in cubic A$_3$Tb$_{0.90}$Eu$_{0.10}$(PO$_4$)$_3$ (A = Sr, Ba) materials, J. Phys. Chem. C 124 (2020) 10105–10116, https://doi.org/10.1021/acs.jpcc.0c00759

[31] C.D.S. Brites, A. Millán, L.D. Carlos, Lanthanides in luminescent thermometry, Handbook on the Physics and Chemistry of Rare Earths, 49 (2016) 339–427. doi:10.1016/bs.hpcre.2016.03.005.

[32] L. Marciniak, K. Waszniewska, A. Bednarkiewicz, D. Hreniak, W. Strek, Sensitivity of a nanocrystalline luminescent thermometer in high and low excitation density regimes, J. Phys. Chem. C 120 (2016) 8877–8882, https://doi.org/10.1021/acs.jpcc.6b01636

[33] J. Zhang, J. Chen, C. Jin, The effect of dopant concentration and pump power on sensitivities of optical thermometry in LiLa$_9$Si$_6$O$_{26}$:Yb^{3+}-Er^{3+}/Ho^{3+} phosphors based on upconversion luminescence, J. Alloy. Compd. 846 (2020) 156397, https://doi.org/10.1016/j.jallcom.2020.156397

[34] M.D. Ward, Transition-metal sensitised near-infrared luminescence from lanthanides in d-f heteronuclear arrays, Coord. Chem. Rev. 251 (2007) 1663–1677, https://doi.org/10.1016/j.ccr.2006.10.005

[35] B. Yan, Lanthanide-functionalized metal-organic framework hybrid systems to create multiple luminescent centers for chemical sensing, Acc. Chem. Res. 50 (2017) 2789–2798, https://doi.org/10.1021/acs.accounts.7b00387

[36] B. Alpha, R. Ballardini, V. Balzani, J. -M Lehn, S. Perathoner, N. Sabbatini, Antenna effect in luminescent lanthanide cryptates: a photophysical study, Photochem. Photobiol. 52 (1990) 299–306, https://doi.org/10.1111/j.1751-1097.1990.tb04185.x

[37] J. Massue, S.J. Quinn, T. Gunnlaugsson, Lanthanide luminescent displacement assays: the sensing of phosphate anions using Eu(III)-cyclen-conjugated gold nanoparticles in aqueous solution, J. Am. Chem. Soc. 130 (2008) 6900–6901, https://doi.org/10.1021/ja800361e

[38] N.M. Shavaleev, L.P. Moorcraft, S.J.A. Pope, Z.R. Bell, S. Faulkner, M.D. Ward, Sensitized near-infrared emission from complexes of YbIII, NdIII and ErIII by energy-transfer from covalently attached PtII-based antenna units, Chem. A Eur. J. 9 (2003) 5283–5291, https://doi.org/10.1002/chem.200305132

[39] P.K. Tawalare, V.B. Bhatkar, S.K. Omanwar, S.V. Moharil, Cr^{3+} sensitized near infrared emission in Al$_2$O$_3$:Cr,Nd/Yb phosphors, J. Alloy. Compd. 790 (2019) 1192–1200, https://doi.org/10.1016/j.jallcom.2019.03.201

[40] L. Dong, L. Zhang, Y. Jia, Y. Xu, S. Yin, H. You, Realizing broadband spectral conversion in novel Ce^{3+}, Cr^{3+}, Ln^{3+} (Ln = Yb, Nd, Er) tridoped near-infrared phosphors via multiple energy transfers, Ceram. Int. 47 (2021) 3127–3135, https://doi.org/10.1016/j.ceramint.2020.09.149

[41] T. Härig, G. Huber, I.A. Shcherbakov, Cr^{3+} sensitized Nd^{3+}: Li-La-phosphate glass laser, J. Appl. Phys. 52 (1981) 4450–4452, https://doi.org/10.1063/1.329369

9

[42] M. Yamaga, Y. Oda, H. Uno, K. Hasegawa, H. Ito, S. Mizuno, Formation probability of Cr-Nd pair and energy transfer from Cr to Nd in $Y_3Al_5O_{12}$ ceramics codoped with Nd and Cr, J. Appl. Phys. 112 (2012) 063508, https://doi.org/10.1063/1.4752403

[43] Y. Wang, Z. You, J. Li, Z. Zhu, E. Ma, C. Tu, Crystal growth and optical properties of Cr^{3+}, Er^{3+}, RE^{3+}: $Gd_3Ga_5O_{12}$ (RE = Tm, Ho, Eu) for mid-IR laser applications, J. Lumin. 132 (2012) 693–696, https://doi.org/10.1016/j.jlumin.2011.10.020

[44] Z.J. Kiss, R.C. Duncan, Cross-pumped Cr^{3+}–Nd^{3+}:YAG laser system, Appl. Phys. Lett. 5 (1964) 200–202, https://doi.org/10.1063/1.1723587

[45] Y. Ding, N. Guo, X. Lü, H. Zhou, L. Wang, R. Ouyang, Y. Miao, B. Shao, None-rare-earth activated $Ca_{14}Al_{10}Zn_6O_{35}$:Bi^{3+},Mn^{4+} phosphor involving dual luminescent centers for temperature sensing, J. Am. Ceram. Soc. 102 (2019) 7436–7447, https://doi.org/10.1111/jace.16660

[46] X. Gao, W. Li, X. Yang, X. Jin, S. Xiao, Near-infrared emission of Er^{3+} sensitized by Mn^{4+} in $Ca_{14}Zn_6Al_{10}O_{35}$ matrix, J. Phys. Chem. C. 119 (2015) 28090–28098, https://doi.org/10.1021/acs.jpcc.5b05825

[47] W. Li, T. Chen, W. Xia, X. Yang, S. Xiao, Near-infrared emission of Yb^{3+} sensitized by Mn^{4+} in La_2MgTiO_6, J. Lumin. 194 (2018) 547–550, https://doi.org/10.1016/j.jlumin.2017.04.063

[48] J. Liao, L. Kong, Q. Wang, J. Li, G. Peng, Y. Sun, H. Wen, Sol-gel preparation and near-infrared emission properties of Yb^{3+} sensitized by Mn^{4+} in double-perovskite La_2ZnTiO_6, Opt. Mater. 84 (2018) 82–88, https://doi.org/10.1016/j.optmat.2018.06.055

[49] W. Li, X. Gao, X. Yang, X. Jin, S. Xiao, Intense 1.85 μm emission of Tm^{3+} sensitized by Mn^{4+}/Tm^{3+} co-doped $Ca_{14}Zn_6Al_{10}O_{35}$ phosphor, J. Alloy. Compd. 664 (2016) 181–187, https://doi.org/10.1016/j.jallcom.2015.12.217

[50] Y. Duan, Y. Liu, G. Zhang, L. Yao, Q. Shao, Broadband Cr^{3+}-sensitized upconversion luminescence of $LiScSi_2O_6$:Cr^{3+}/Er^{3+}, J. Rare Earths (2020), https://doi.org/10.1016/j.jre.2020.08.007

[51] K. Prorok, A. Bednarkiewicz, Energy migration up-conversion of Tb^{3+} in Yb^{3+} and Nd^{3+} codoped active-core/active-shell colloidal nanoparticles, ACS Chem. Mater. 28 (2016) 2295–2300, https://doi.org/10.1021/acs.chemmater.6b00353

[52] R. Martín-Rodríguez, R. Valiente, M. Bettinelli, Room-temperature green up-conversion luminescence in $LaMgAl_{11}O_{19}$:Mn^{2+}, Yb^{3+} upon infrared excitation, Appl. Phys. Lett. 95 (2009) 091913, https://doi.org/10.1063/1.3220059

[53] D. Imbert, M. Cantuel, J.-C.G. Bünzli, G. Bernardinelli, C. Piguet, Extending lifetimes of lanthanide-based near-infrared emitters (Nd, Yb) in the millisecond range through Cr(III) sensitization in discrete bimetallic edifices, J. Am. Chem. Soc. 125 (2003) 15698–15699, https://doi.org/10.1021/ja0386501

[54] S. Torelli, D. Imbert, M. Cantuel, G. Bernardinelli, S. Delahaye, A. Hauser, J.-C.G. Bünzli, C. Piguet, Tuning the decay time of lanthanide-based near infrared luminescence from micro- to milliseconds through d→f energy transfer in discrete heterobimetallic complexes, Chem. A Eur. J. 11 (2005) 3228–3242, https://doi.org/10.1002/chem.200401158

[55] D. Chen, Y. Chen, H. Lu, Z. Ji, A bifunctional Cr/Yb/Tm:$Ca_3Ga_2Ge_3O_{12}$ phosphor with near-infrared long-lasting phosphorescence and upconversion luminescence, Inorg. Chem. 53 (2014) 8638–8645, https://doi.org/10.1021/ic501238u

[56] P.A. Tanner, Z. Pan, Luminescence properties of lanthanide and transition metal ion-doped Ba_2LaNbO_6: detection of MnO_6^{8-} and CrO_6^{9-} clusters, Inorg. Chem. 48 (2009) 11142–11146, https://doi.org/10.1021/ic9015178

[57] S. Heer, K. Petermann, H.U. Güdel, Upconversion excitation of Cr^{3+} emission in $YAlO_3$ codoped with Cr^{3+} and Yb_3, J. Lumin. 102– 103 (2003) 144–150, https://doi.org/10.1016/S0022-2313(02)00490-8

[58] C. Wang, X. Cheng, Influence of Cr^{3+} ions doping on growth and upconversion luminescence properties of β-$NaYF_4$:Yb^{3+}/Er^{3+} microcrystals, J. Alloy. Compd. 649 (2015) 196–203, https://doi.org/10.1016/j.jallcom.2015.07.024

[59] H. Luo, P. Dorenbos, The dual role of Cr^{3+} in trapping holes and electrons in lanthanide co-doped $GdAlO_3$ and $LaAlO_3$, J. Mater. Chem. C 6 (2018) 4977–4984, https://doi.org/10.1039/C8TC01100A

[60] Y. Guo, L. Zhao, Y. Fu, H. Yu, Tailoring up-conversion luminescence for single band located in first biological windows and optical thermometry of Yb^{3+}/Ln^{3+} (Ln = Er, Tm) doped oxyfluoride ceramics via Cr^{3+} doping, J. Lumin. 215 (2019) 116629, https://doi.org/10.1016/j.jlumin.2019.116629

[61] S.H. Nannuri, A.R. Samal, C.K. Subash, C. Santhosh, S.D. George, Tuning of structural, laser power-dependent and temperature dependent luminescence properties of $NaYF_4$:Yb, Er (Y: 88%, Yb: 10 and Er: 2%) submicron crystals using Cr^{3+} ion doping, J. Alloy. Compd. 777 (2019) 894–901, https://doi.org/10.1016/j.jallcom.2018.11.035

[62] W. Xu, Y. Hu, L. Zheng, Z. Zhang, W. Cao, Improved green upconversion emissions from $CaWO_4$: Er^{3+}-Yb^{3+} by Cr^{3+} codoping for optical thermometry, J. Lumin. 215 (2019) 116617, https://doi.org/10.1016/j.jlumin.2019.116617

[63] X. Cui, Y. Cheng, H. Lin, F. Huang, Q. Wu, J. Xu, Y. Wang, Towards ultra-high sensitive colorimetric nanothermometry: constructing thermal coupling channel for electronically independent levels, Sens. Actuators B Chem. 256 (2018) 498–503, https://doi.org/10.1016/j.snb.2017.10.131

[64] I. Mikalauskaite, G. Pleckaityte, M. Skapas, A. Zarkov, A. Katelnikovas, A. Beganskiene, Emission spectra tuning of upconverting $NaGdF_4$:20% Yb, 2% Er nanoparticles by Cr^{3+} co-doping for optical temperature sensing, J. Lumin. 213 (2019) 210–217, https://doi.org/10.1016/j.jlumin.2019.05.032

[65] D. Chen, Z. Wan, Y. Zhou, X. Zhou, Y. Yu, J. Zhong, M. Ding, Z. Ji, Dual-phase glass ceramic: structure, dual-modal luminescence, and temperature sensing behaviors, ACS Appl. Mater. Interfaces 7 (2015) 19484–19493, https://doi.org/10.1021/acsami.5b06036

[66] W.S. Silveira, P.A.M. Nascimento, A.J.S. Silva, M.V. do. S. Rezende, Luminescent properties and energy transfer mechanism from Tb^{3+} to Eu^{3+} doped in $Y_3Al_5O_{12}$ phosphors, J. Alloy. Compd. 822 (2020) 153651, https://doi.org/10.1016/j.jallcom.2020.153651

[67] D. Balaji, A. Durairajan, K. Kavirasu, S.M. Babu, Investigation on the luminescence properties of Eu^{3+}/Tb^{3+}:$Y_3Al_5O_{12}$ phosphors, in: AIP Conference Proceedings, (2015). doi:10.1063/1.4918214.

[68] A.M. Chinie, A. Stefan, S. Georgescu, O. Toma, E. Borca, M. Bercu, Structural and spectroscopical characterization of RE^{3+}(RE = Er, Eu, Tb) doped nanocrystalline YAG produced by a sol-gel method, J. Optoelectron. Adv. Mater. (2006) 95–98.

[69] D. Chen, Y. Zhou, W. Xu, J. Zhong, Z. Ji, W. Xiang, Enhanced luminescence of Mn^{4+}:$Y_3Al_5O_{12}$ red phosphor via impurity doping, J. Mater. Chem. C 4 (2016) 1704–1712, https://doi.org/10.1039/c5tc04133c

[70] K. Trejgis, L. Marciniak, The influence of manganese concentration on the sensitivity of bandshape and lifetime luminescent thermometers based on $Y_3Al_5O_{12}$:Mn^{3+},Mn^{4+},Nd^{3+} nanocrystals, Phys. Chem. Chem. Phys. 20 (2018) 9574–9581, https://doi.org/10.1039/c8cp00558c

[71] M. Chaika, R. Tomala, O. Vovk, S. Nizhankovskyi, G. Mancardi, W. Strek, Upconversion luminescence in Cr^{3+}:YAG single crystal under infrared excitation, J. Lumin. 226 (2020) 117467, https://doi.org/10.1016/j.jlumin.2020.117467

[72] H. Yagi, T. Yanagitani, H. Yoshida, M. Nakatsuka, K.I. Ueda, Highly efficient flashlamp-pumped Cr^{3+} and Nd^{3+} codoped $Y_3Al_5O_{12}$ ceramic laser, Jpn. J. Appl. Phys. Part 1 Regul. Pap. Short Notes Rev. Pap. 45 (2006) 133–135, https://doi.org/10.1143/JJAP.45.133

[73] J.P. Hehir, M.O. Henry, J.P. Larkin, G.F. Imbusch, Nature of the luminescence from YAG:Cr^{3+}, J. Phys. C Solid State Phys. 7 (1974) 2241–2248, https://doi.org/10.1088/0022-3719/7/12/017

[74] W.A. Wall, J.T. Karpick, B. Di Bartolo, Temperature dependence of the vibronic spectrum and fluorescence lifetime of YAG:Cr^{3+}, J. Phys. C Solid State Phys. 4 (1971) 3258–3264, https://doi.org/10.1088/0022-3719/4/18/031

[75] V. Lupei, L. Lout, G. Boulon, A. Lupei, On the origin of the satellite structure of luminescent spectra of Cr^{3+} in YAG, J. Phys. Condens. Matter 5 (1993) L35–L38, https://doi.org/10.1088/0953-8984/5/3/003

[76] J.A. Mares, W. Nie, G. Boulon, Energy transfer processes between various Cr^{3+} and Nd^{3+} multisites in YAG:Nd, Cr, J. Lumin. 48–49 (1991) 227–231, https://doi.org/10.1016/0022-2313(91)90110-H

[77] J. Drabik, Ł. Marciniak, B.B. Cichy, L. Marciniak, New type of nanocrystalline luminescent thermometers based on Ti^{3+}/Ti^{4+} and Ti^{4+}/Ln^{3+} (Ln^{3+} = Nd^{3+}, Eu^{3+}, Dy^{3+}) luminescence intensity ratio, J. Phys. Chem. C 122 (2018) 14928–14936, https://doi.org/10.1021/acs.jpcc.8b02328

[78] L. Marciniak, A. Bednarkiewicz, J. Drabik, K. Trejgis, W. Strek, Optimization of highly sensitive YAG:Cr^{3+},Nd^{3+} nanocrystal-based luminescent thermometer operating in an optical window of biological tissues, Phys. Chem. Chem. Phys. 19 (2017) 7343–7351, https://doi.org/10.1039/c6cp07213e

[79] N.M. Avram, M.G. Brik, Optical properties of 3d-ions in crystals: spectroscopy and crystal field analysis, 2013. doi:10.1007/978-3-642-30838-3.

[80] K. Elzbieciak, A. Bednarkiewicz, L. Marciniak, Temperature sensitivity modulation through crystal field engineering in Ga^{3+} co-doped $Gd_3Al_{5-x}Ga_xO_{12}$:Cr^{3+}, Nd^{3+} nanothermometers, Sens. Actuators B Chem. 269 (2018) 96–102, https://doi.org/10.1016/j.snb.2018.04.157

[81] G.H. Pan, L.L. Zhang, H.H. Wu, X. Qu, H.H. Wu, Z. Hao, L.L. Zhang, X. Zhang, J. Zhang, On the luminescence of Ti^{4+} and Eu^{3+} in monoclinic ZrO_2: high performance optical thermometry derived from energy transfer, J. Mater. Chem. C 8 (2020) 4518–4533, https://doi.org/10.1039/c9tc06992e

[82] A.P. Vink, A. Meijerink, Electron-phonon coupling of Cr^{3+} in YAG and YGG, J. Lumin. 87–89 (2000) 601–604, https://doi.org/10.1016/S0022-2313(99)00308-7

[83] S.M. Kaczmarek, W. Chen, G. Boulon, Recharging processes of Cr ions in Mg_2SiO_4 and $Y_3Al_5O_{12}$ crystals under influence of annealing and γ - irradiation, Cryst. Res. Technol. 41 (2006) 41–47, https://doi.org/10.1002/crat.200410527

[84] M. Bettinelli, C.D. Flint, Non-resonant energy transfer between Tb^{3+} and Eu^{3+} in the cubic hexachloroelpasolite crystals $Cs_2NaTb_{1-x}Eu_xCl_6$ (x = 0.01–0.15), J. Phys. Condens. Matter 2 (1990) 8417–8426, https://doi.org/10.1088/0953-8984/2/42/018

[85] U. Caldiño, E. Álvarez, A. Speghini, M. Bettinelli, New greenish-yellow and yellowish-green emitting glass phosphors: Tb^{3+}/Eu^{3+} and Ce^{3+}/Tb^{3+}/Eu^{3+} in zinc phosphate glasses, J. Lumin. 135 (2013) 216–220, https://doi.org/10.1016/j.jlumin.2012.10.013

[86] F. Piccinelli, C. De Rosa, A. Lazarowska, S. Mahlik, M. Grinberg, T. Nakanishi, S. Omagari, M. Bettinelli, Optical properties of Eu(III) and Tb(III) complexes with pyridine- and quinoline- based ligands under high hydrostatic pressure, Inorg. Chim. Acta 499 (2020) 119179, https://doi.org/10.1016/j.ica.2019.119179

[87] L.A. Riseberg, M.J. Weber, Spectrum and anomalous temperature dependence of the ^2E→$^4A_2$ emission of $Y_3Al_5O_{12}$: Mn^{4+}, Solid State Commun. 9 (1971) 791–794, https://doi.org/10.1016/0038-1098(71)90565-5

[88] K. Elzbieciak, L. Marciniak, The impact of Cr^{3+} doping on temperature sensitivity modulation in Cr^{3+} doped and Cr^{3+}, Nd^{3+} Co-doped $Y_3Al_5O_{12}$, $Y_3Al_2Ga_3O_{12}$, and $Y_3Ga_5O_{12}$ nanothermometers, Front. Chem. 6 (2018) 1–8, https://doi.org/10.3389/fchem.2018.00424

[89] V. Mykhaylyk, H. Kraus, V. Zhydachevskyy, V. Tsiumra, A. Luchechko, A. Wagner, A. Suchocki, Multimodal non-contact luminescence thermometry with Cr-doped oxides, Sensors 20 (2020) 5259, https://doi.org/10.3390/s20185259

[90] J. Drabik, L. Marciniak, The influence of Eu^{3+} concentration on the spectroscopic properties of YAG:Ti, Eu^{3+} nanocrystalline luminescent thermometer, J. Lumin. 208 (2019) 213–217, https://doi.org/10.1016/j.jlumin.2018.12.054

Enhancement of the Ln^{3+} ratiometric nanothermometers by sensitization with transition metal ions

W. Piotrowski[1], K. Kniec[1], L. Marciniak[1]*

[1]Institute of Low Temperature and Structure Research, Polish Academy of Sciences, Okólna 2, 50-422 Wroclaw, Poland

* corresponding author: *l.marciniak@intibs.pl*

The integral intensities of the Tb^{3+} and Eu^{3+} bands to calculate LIR values were fitted with Mott-Seitz equation (Eq. S1):

$$I = \frac{I_0}{C \cdot \exp(-\frac{W}{k \cdot T}) + 1}$$
(Eq. S1)

where: I – the intensity in temperature T, I_0 – the intensity in the initial temperature, W - the activation energy, k – Boltzmann constant, C – the dimensionless constant

The average lifetime of the excited states were calculated with the equation Eq. S2:

$$\langle \tau \rangle = \frac{A_1 \tau_1^2 + A_2 \tau_2^2}{A_1 \tau_1 + A_2 \tau_2}$$
(Eq. S2a)

where: τ_1, τ_2 – the average time, which is in accordance with the relation $\tau = t \cdot \ln(2)$ and A_1, A_2 – amplitude, which are the parameters of the doubleexponential function:

$$y = y_0 + A_1 \cdot \exp(-\frac{x}{t_1}) + A_2 \cdot \exp(-\frac{x}{t_2})$$
(Eq. S2b)

The crystal field strength (CFS) for the Mn^{4+} and Cr^{3+} ions with $3d^3$ configuration was calculated in accordance with the Eq. S3-5:

$$CFS \equiv \frac{Dq}{B} = \frac{15(x-8)}{x^2 - 10x}$$
(Eq. S3)

where: CFS – the crystal field strength which is defined by the relation of the Racah parameter B and the local field Dq:

$$Dq = \frac{E_a(^4A_2 \rightarrow {}^4T_2)}{10} \qquad \text{(Eq. S4)}$$

The experimental equation of the CFS calculation is based on the parameter x defined with the following equation:

$$x = \frac{E_a(^4A_2 \rightarrow {}^4T_1) - E_a(^4A_2 \rightarrow {}^4T_2)}{Dq} \qquad \text{(Eq. S5)}$$

where: E_a are the average band energies.

Temperature determination uncertainty was calculated using Eq. S6:

$$\delta T = \frac{1}{S_R} \cdot \frac{\delta LIR}{LIR} \qquad \text{(Eq. S6)}$$

S_R is the relative sensitivity and $\delta LIR/LIR$ determines the uncertainty of the LIR determination, where $\delta LIR/LIR$ was determined as follows:

$$\frac{\delta LIR}{LIR} = \sqrt{\left(\frac{\delta I_{Tb}}{I_{Tb}}\right)^2 + \left(\frac{\delta I_{Eu}}{I_{Eu}}\right)^2} \qquad \text{(Eq. S7)}$$
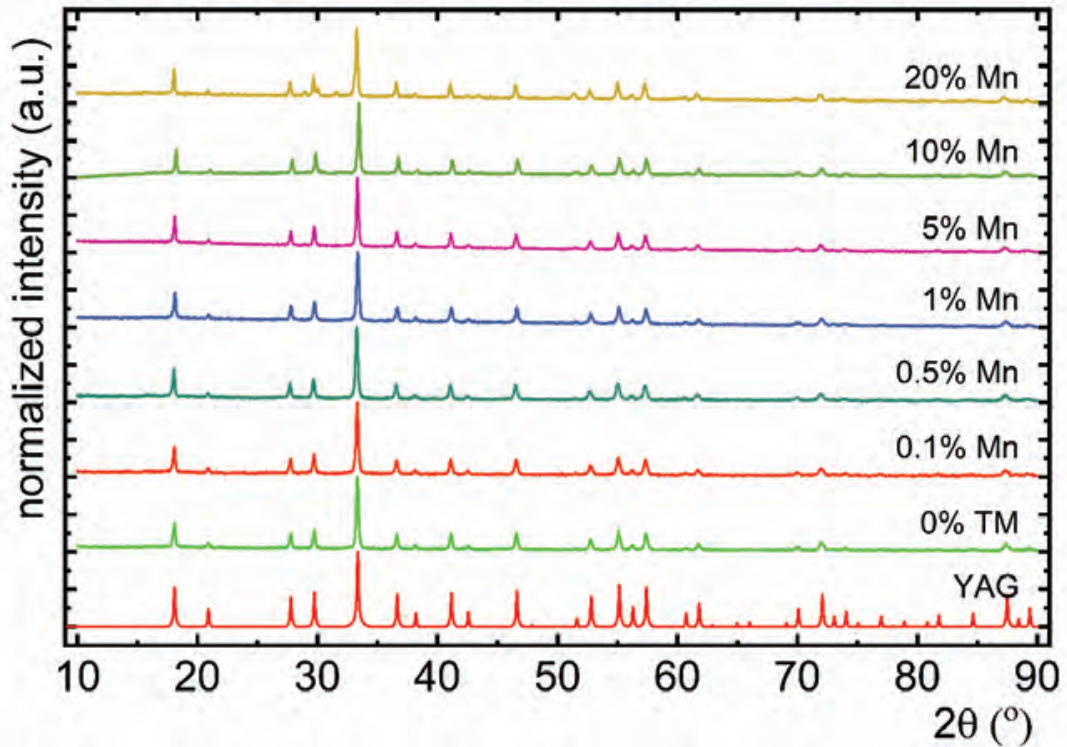
Figure S1. The X-ray diffraction patterns of YAG:1% Tb^{3+}, 1% Eu^{3+}, x% Mn^{4+} powders with different Mn^{4+} concentration.

154
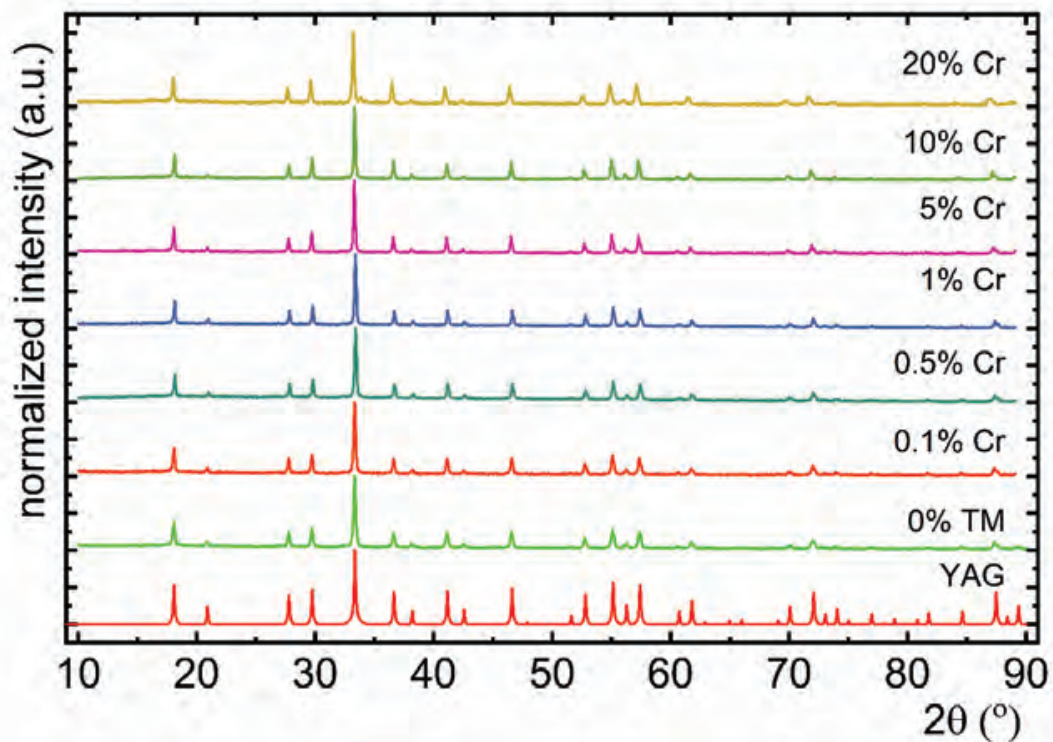
Figure S2. The X-ray diffraction patterns of YAG:1% Tb^{3+}, 1% Eu^{3+}, x% Cr^{3+} powders with different Cr^{3+} concentration.
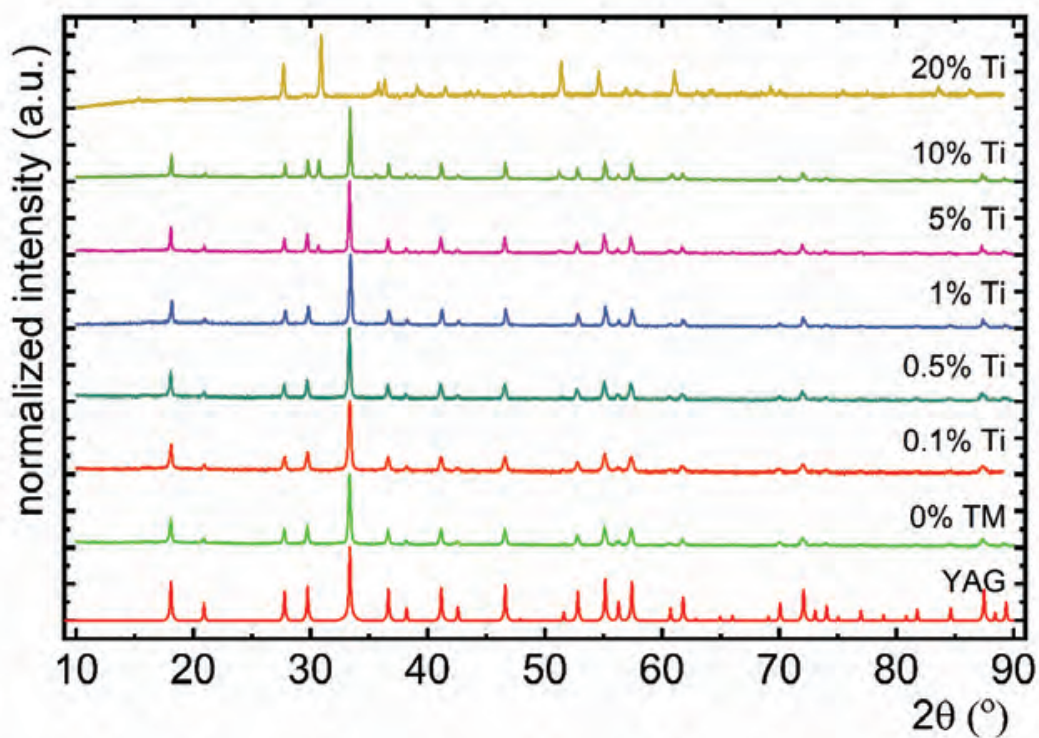
Figure S3. The X-ray diffraction patterns of YAG:1% Tb^{3+}, 1% Eu^{3+}, x% $Ti^{3+/4+}$ powders with different $Ti^{3+/4+}$ concentration.
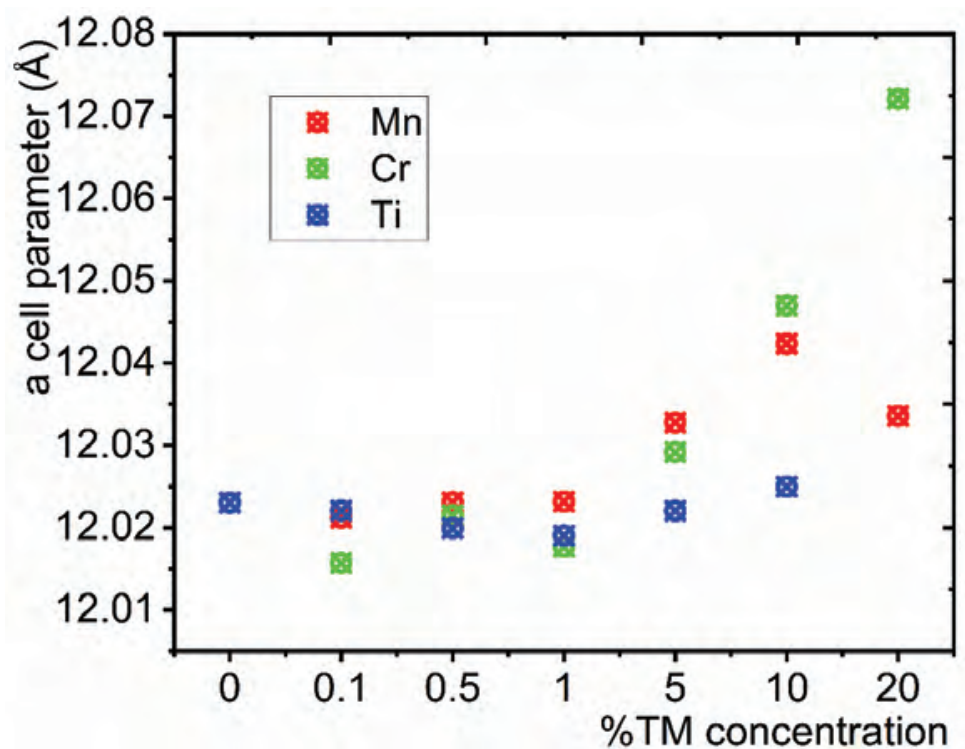
Figure S4. The *a* cell parameter in the function of TM concentration in the YAG:1% Tb^{3+}, 1% Eu^{3+}, x% TM powders, where TM = Mn^{4+}, Cr^{3+} and $Ti^{3+/4+}$.
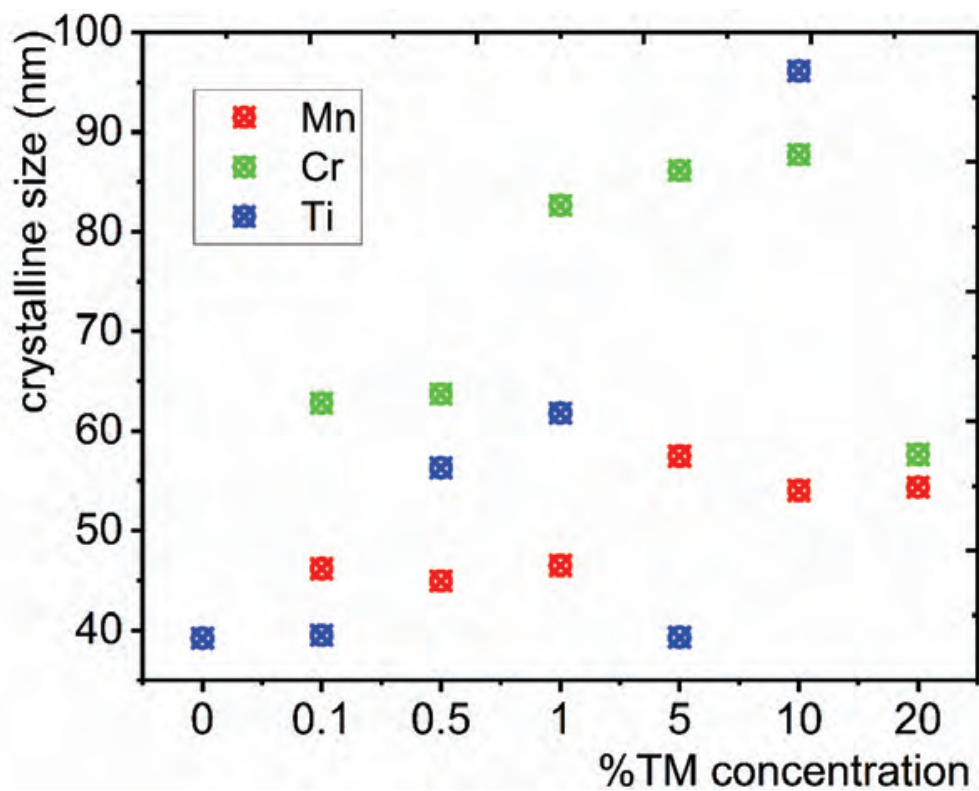
Figure S5. The crystalline size of the YAG:1% Tb^{3+}, 1% Eu^{3+}, x% TM powders for different TM concentration, where TM = Mn^{4+}, Cr^{3+} and $Ti^{3+/4+}$.
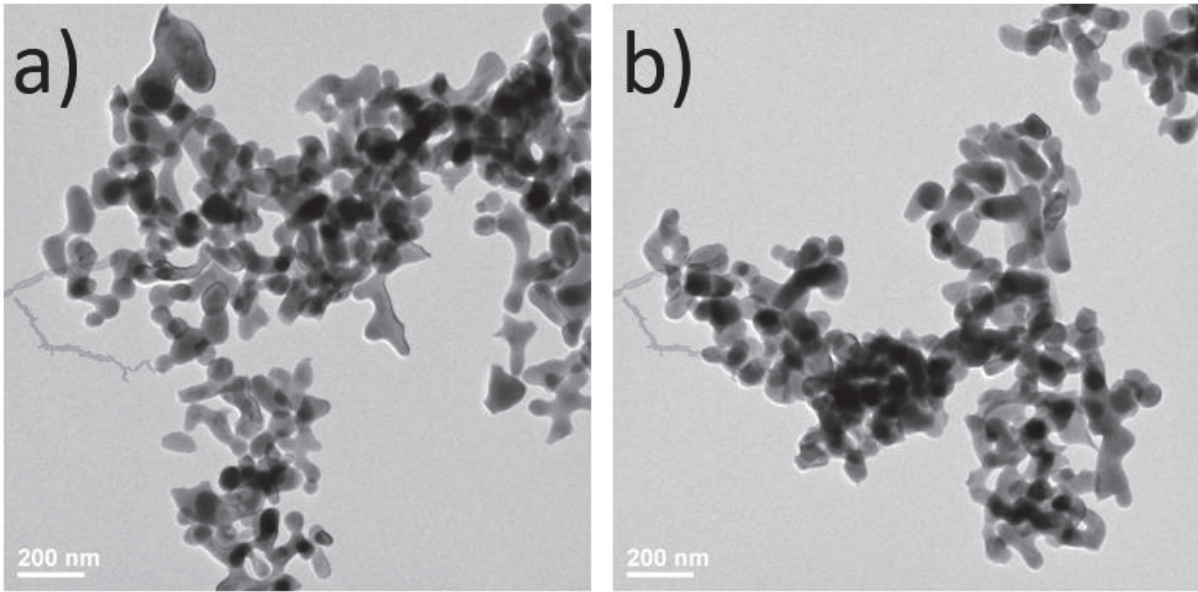
Figure S6.Representative TEM images of YAG:Tb^{3+}, Eu^{3+}
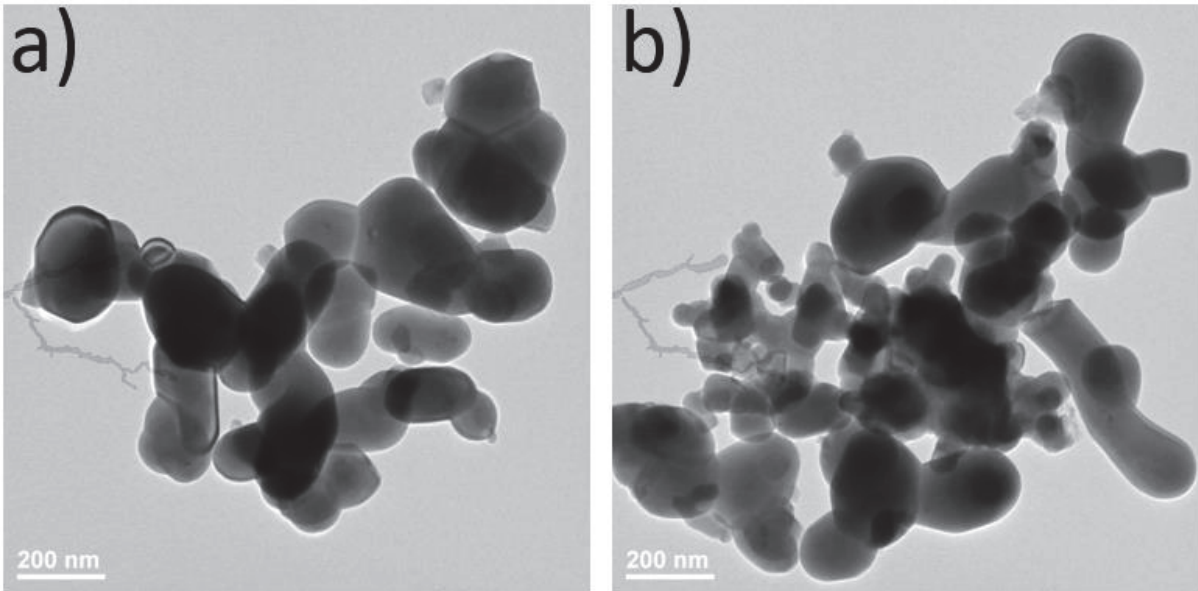
Figure S7.Representative TEM images of YAG:Tb^{3+}, Eu^{3+} Mn^{4+}
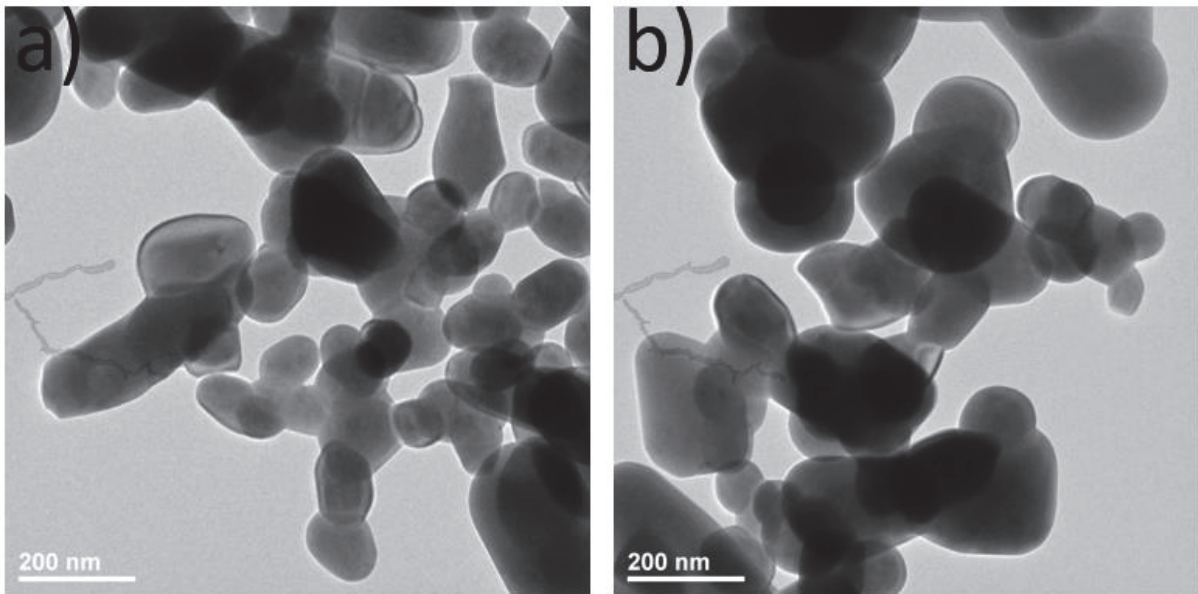
Figure S8. Representative TEM images of YAG:Tb^{3+}, Eu^{3+} Cr^{3+}
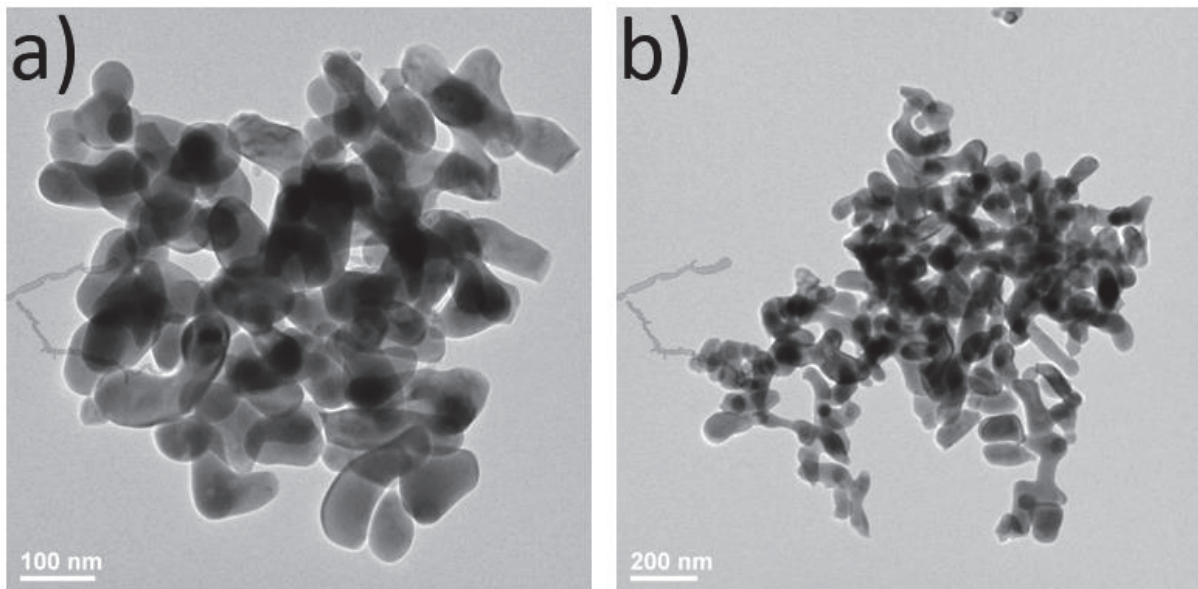
Figure S9. Representative TEM images of YAG:Tb^{3+}, Eu^{3+} $Ti^{3+/4+}$
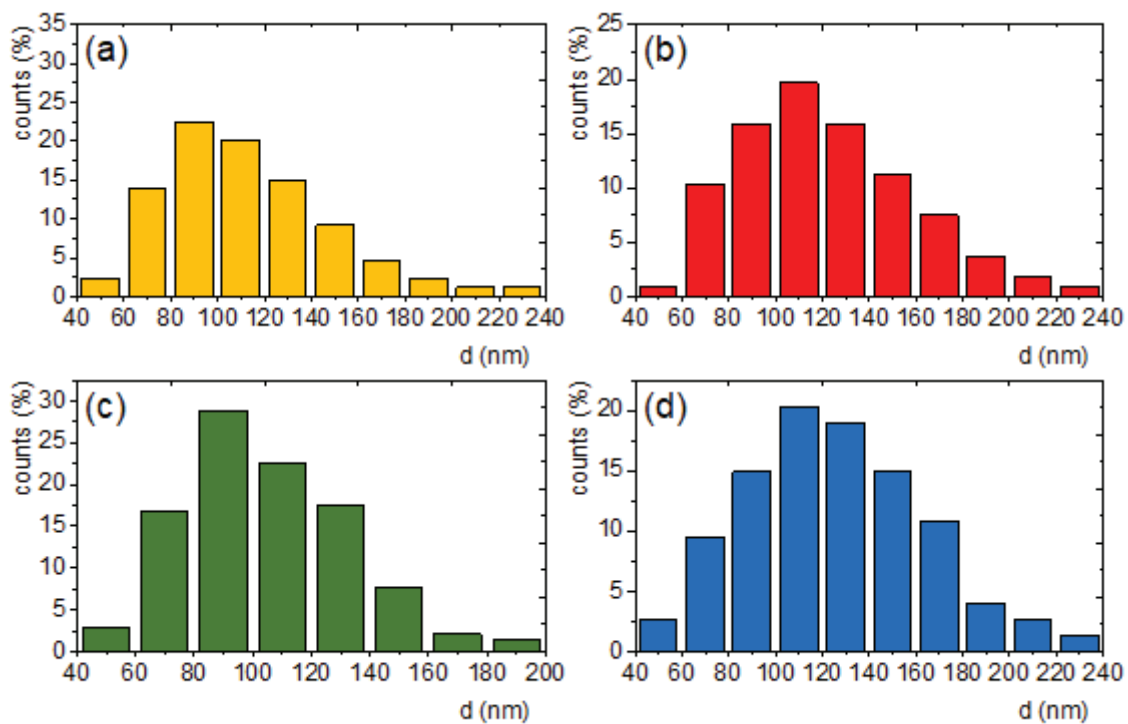
Figure S10. The particle size distributions for YAG:1% Tb^{3+}, 1% Eu^{3+} (a) and the representative YAG:1% Tb^{3+}, 1% Eu^{3+}, 10% TM powders, where TM = Mn^{4+} (b), Cr^{3+} (c) and $Ti^{3+/4+}$ (d).
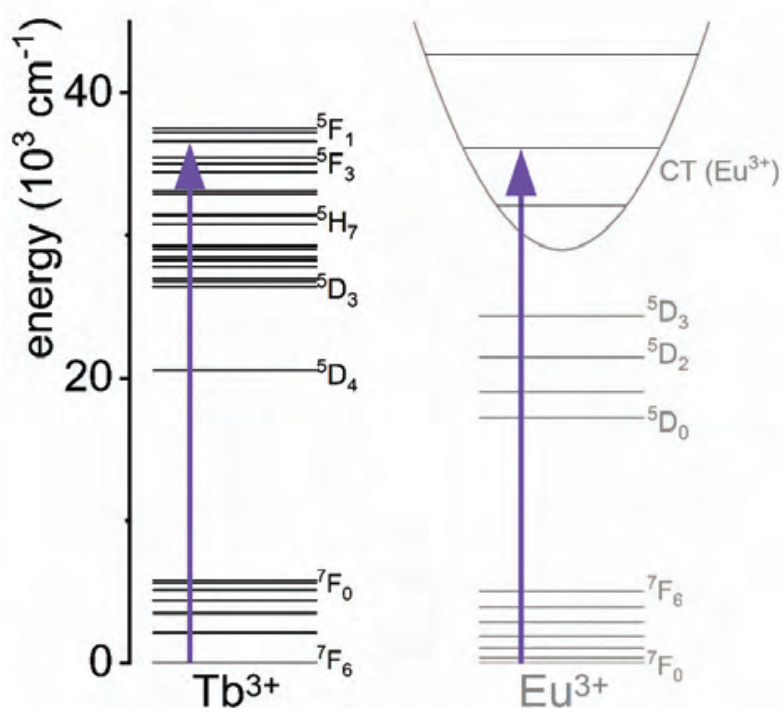
Figure S11. The configurational coordinate diagram for Tb^{3+} and Eu^{3+} ions.
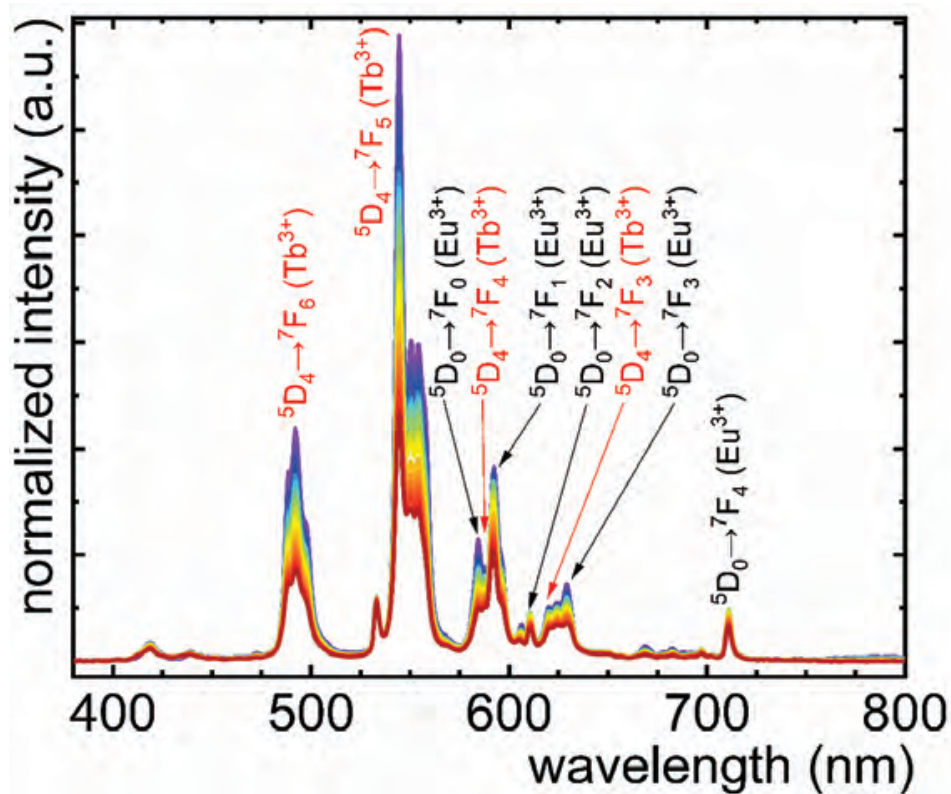
Figure S12. The thermal evolution of the emission spectra of YAG:1% Tb^{3+}, 1% Eu^{3+} powder.
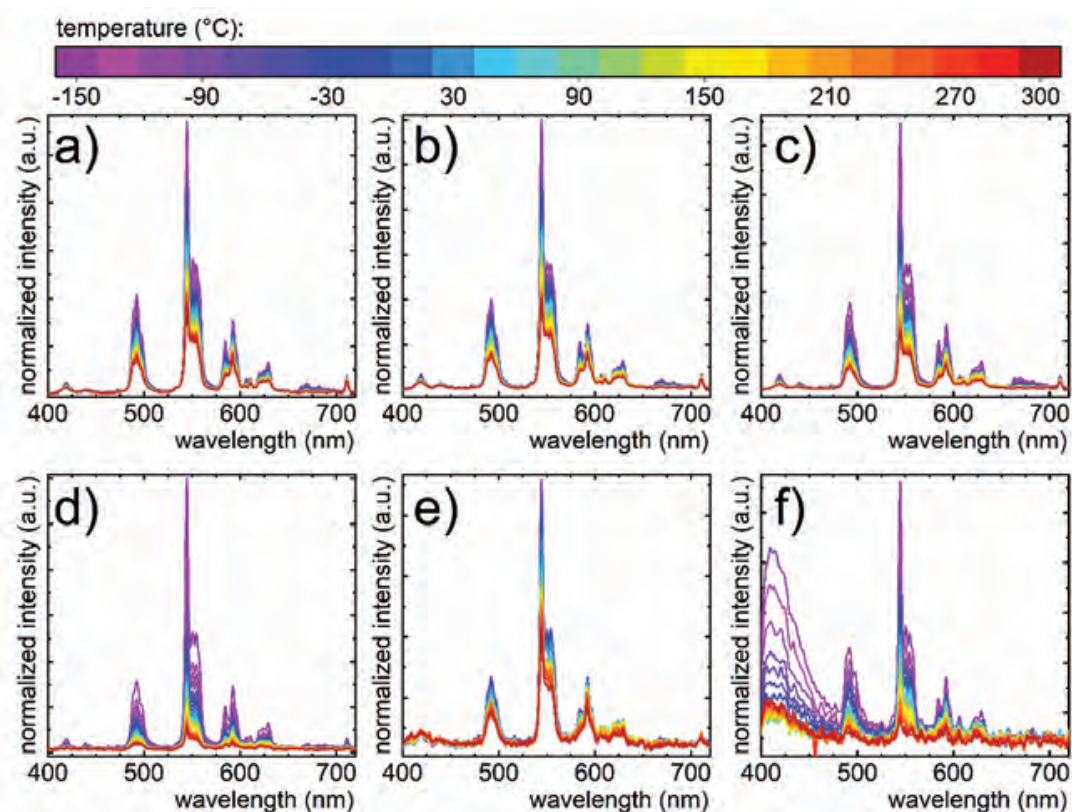
Figure S13. The thermal evolution of the emission spectra of YAG:1% Tb^{3+}, 1% Eu^{3+}, x% Mn^{4+} powders, where x = 0.1 (a), 0.5 (b), 1 (c), 5 (d), 10 (e), 20 (f).
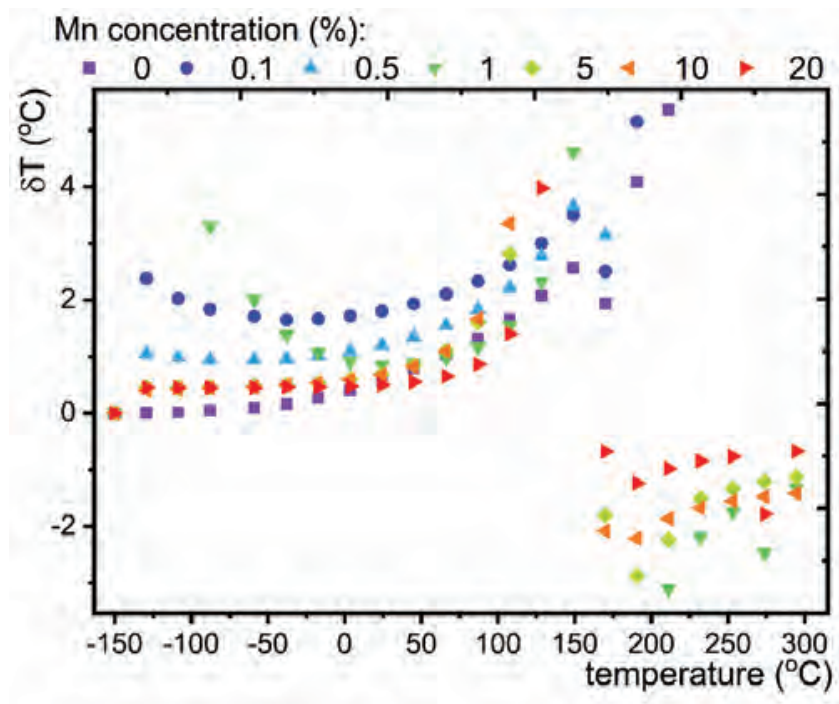
Figure S14. The thermal dependence of temperature estimation uncertainty for different Mn^{4+} concentration in the YAG:1% Tb^{3+}, 1% Eu^{3+}, x% Mn^{4+}.
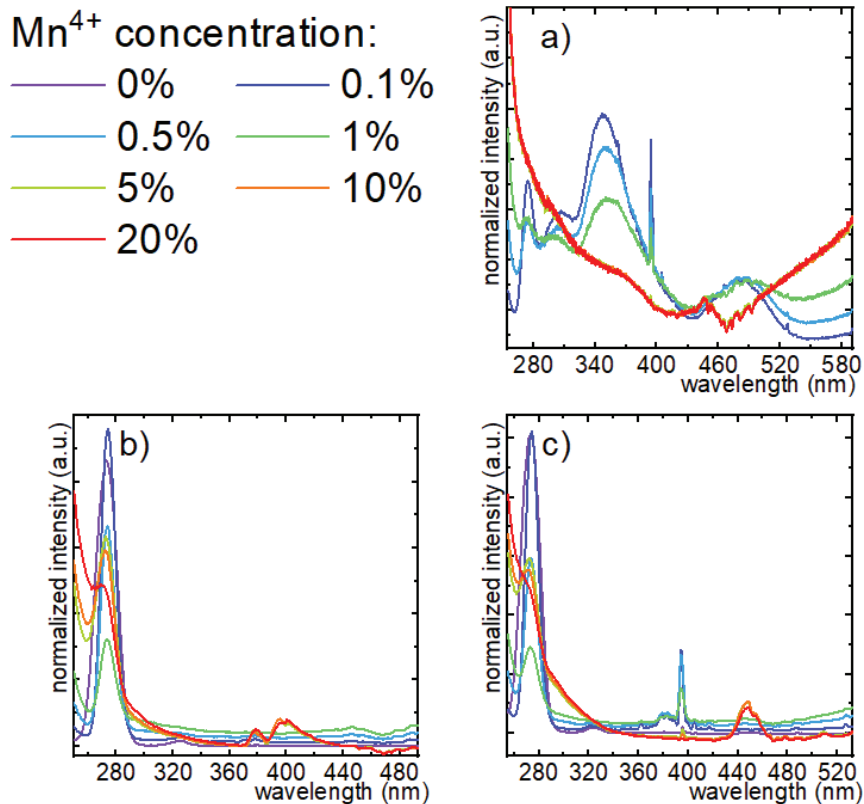
Figure S15. The influence of Mn^{4+} ions concentration on excitation spectra in YAG:1% Tb^{3+}, 1% Eu^{3+}, x% Mn^{4+} for 652 nm (a), 545 nm (b) and 592 nm (c).
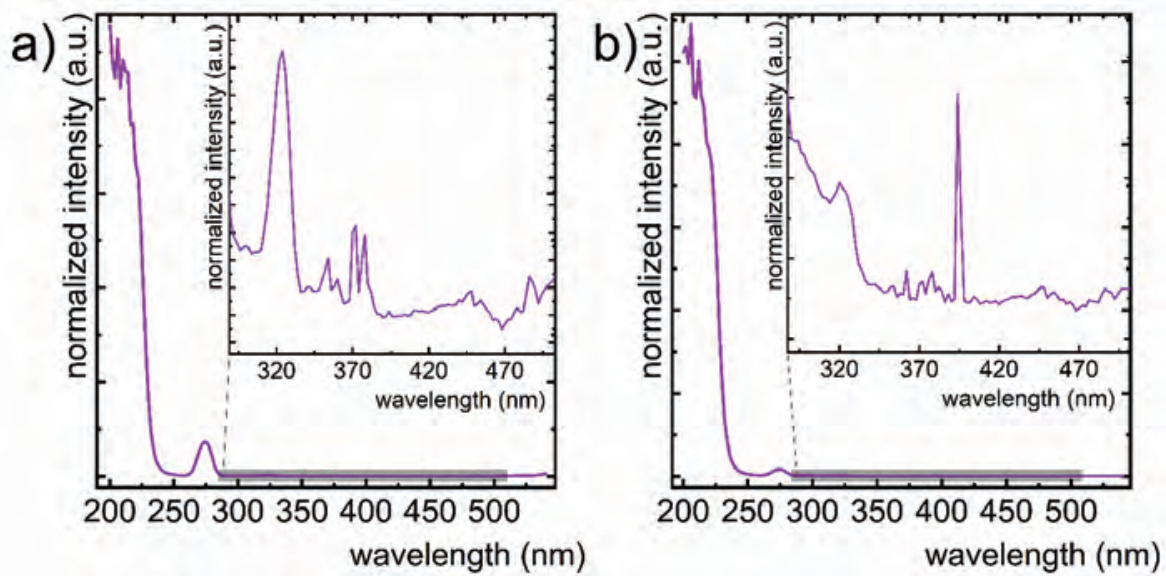
Figure S16. The excitation spectra in YAG:1% Tb^{3+}, 1% Eu^{3+} for 550 nm (a) and 620 nm (b).
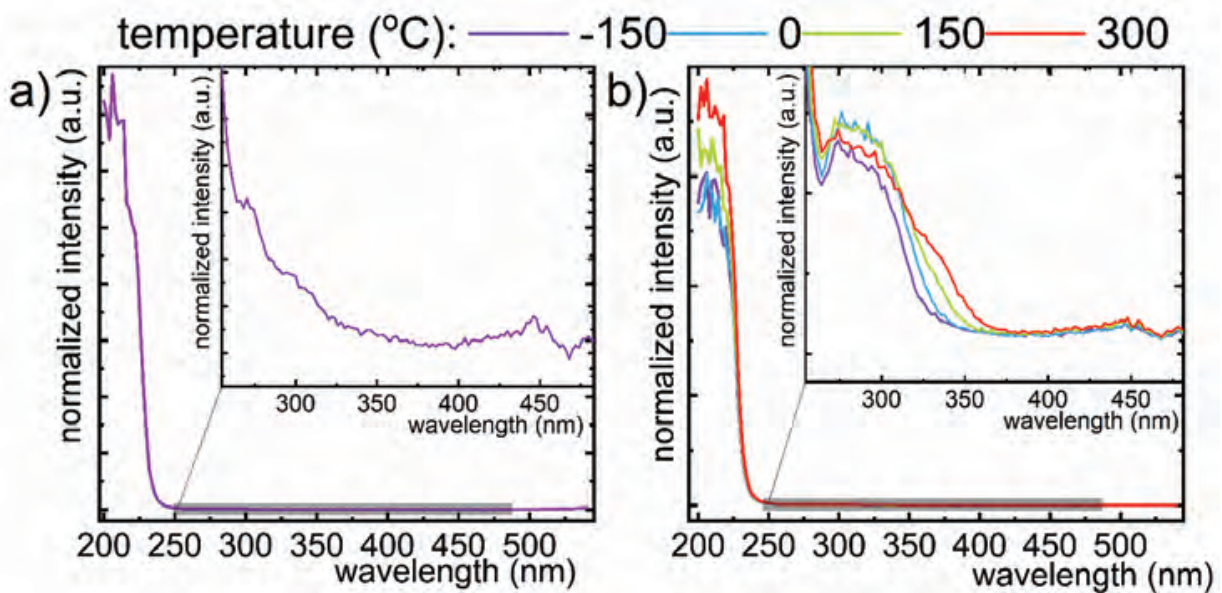
Figure S17. The representative excitation spectra in YAG:1% Tb^{3+}, 1% Eu^{3+}, 10% Mn^{4+} for 550 nm (a) and 620 nm (b).
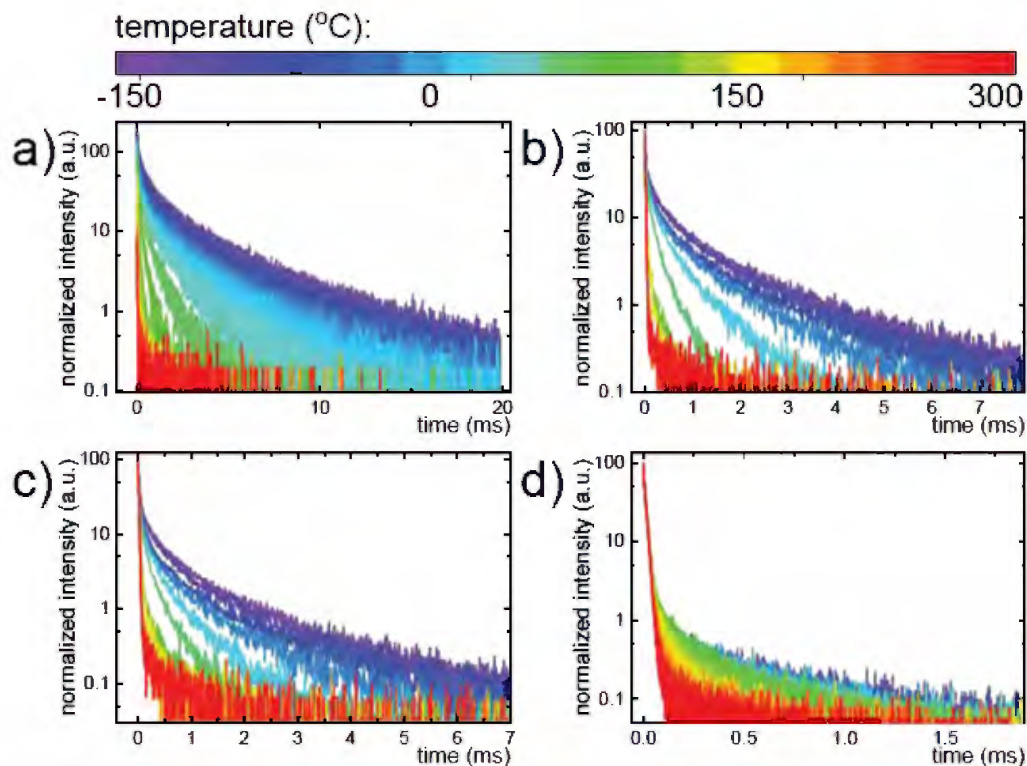
Figure S18. The thermal evolution of luminescent decays in YAG:1% Tb^{3+}, 1% Eu^{3+}, x% Mn^{4+} for 652 nm, where x = 0.1 (a), 0.5 (b), 1 (c) and 5 (d).
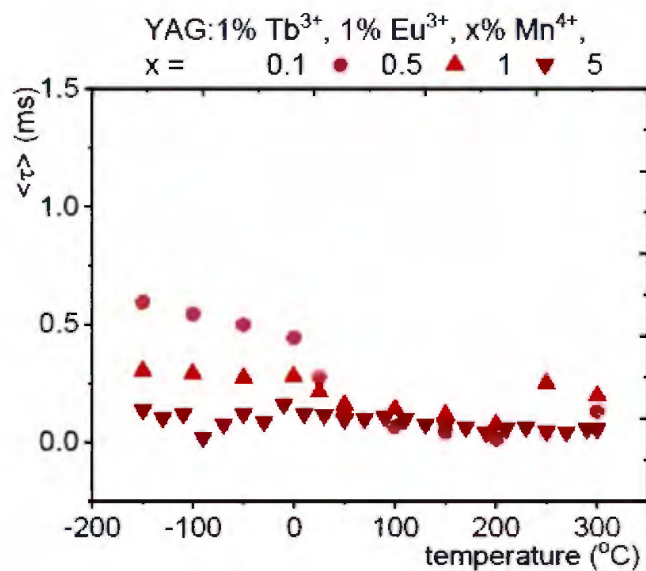
Figure S19. The thermal evolution of the average lifetime of Mn^{4+} in YAG:1% Tb^{3+}, 1% Eu^{3+}, x% Mn^{4+}.
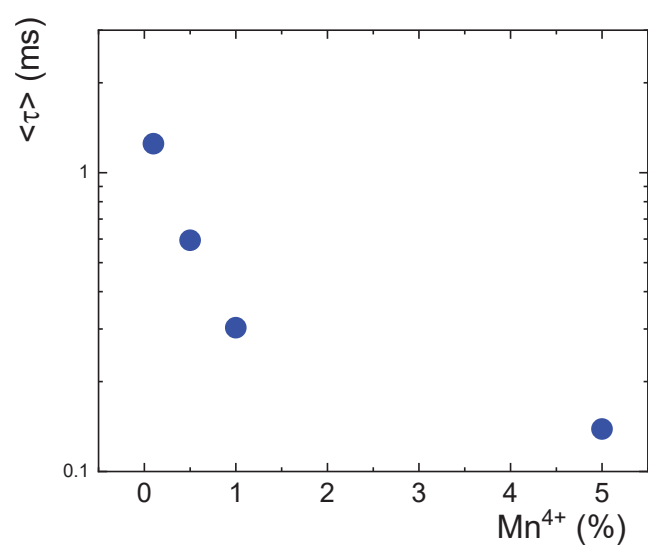
Figure S20. The average lifetime of ^2E state of Mn^{4+} ions in YAG:1% Tb^{3+}, 1% Eu^{3+}, x% Mn^{4+} at -150°C as a function of Mn^{4+} concentration
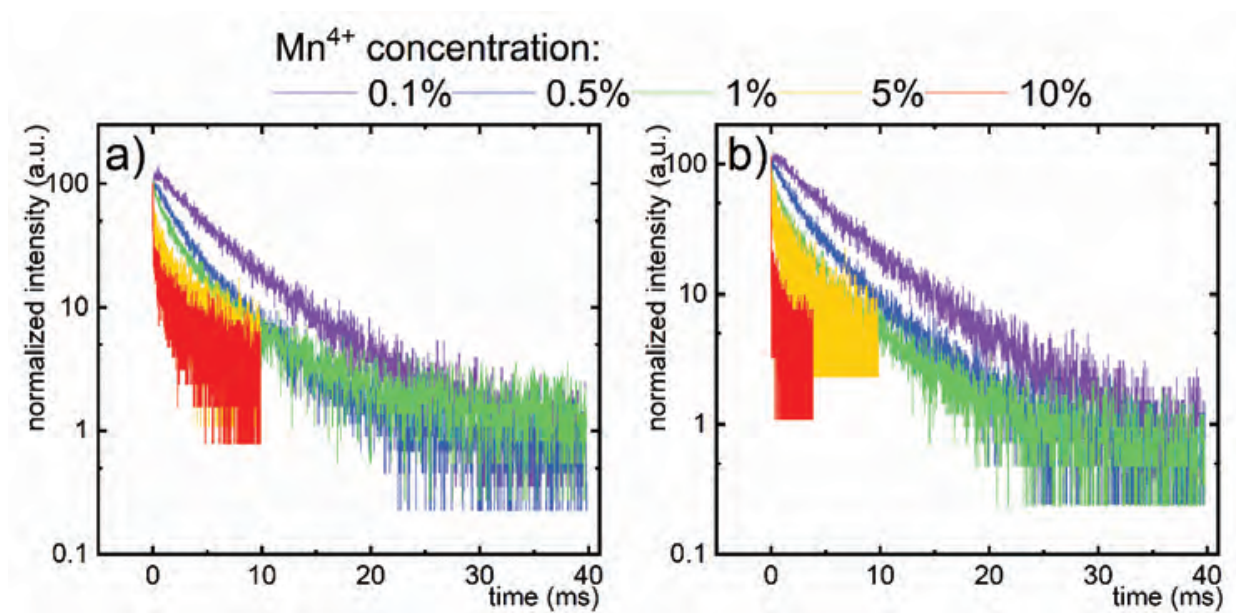
Figure S21. The influence of Mn^{4+} ions concentration on luminescent decays in YAG:1% Tb^{3+}, 1% Eu^{3+}, x% Mn^{4+} for 545 nm (a) and 592 nm (b).
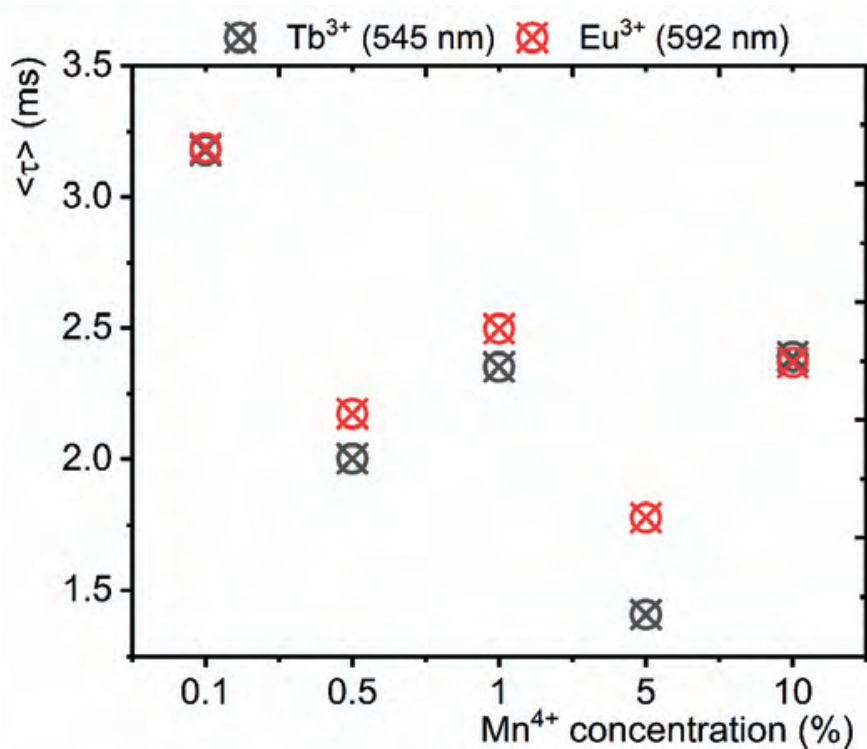
Figure S22. The average lifetime of Tb^{3+} and Eu^{3+} excited states as a function of Mn^{4+} concentration for YAG:1% Tb^{3+}, 1% Eu^{3+}, x% Mn^{4+} powders.
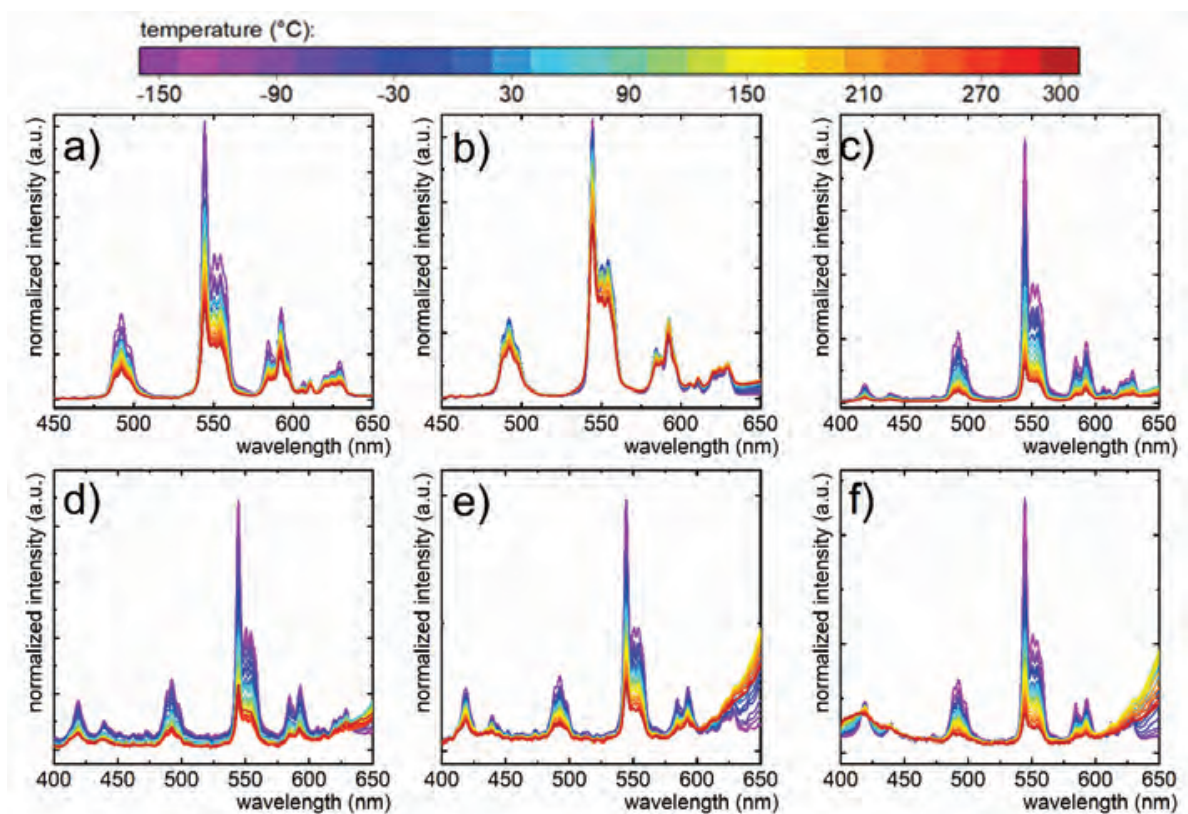
Figure S23. The thermal evolution of the emission spectra of YAG:1% Tb^{3+}, 1% Eu^{3+}, x% Cr^{3+} powders, where x = 0.1 (a), 0.5 (b), 1 (c), 2 (d), 3 (e), 5 (f).
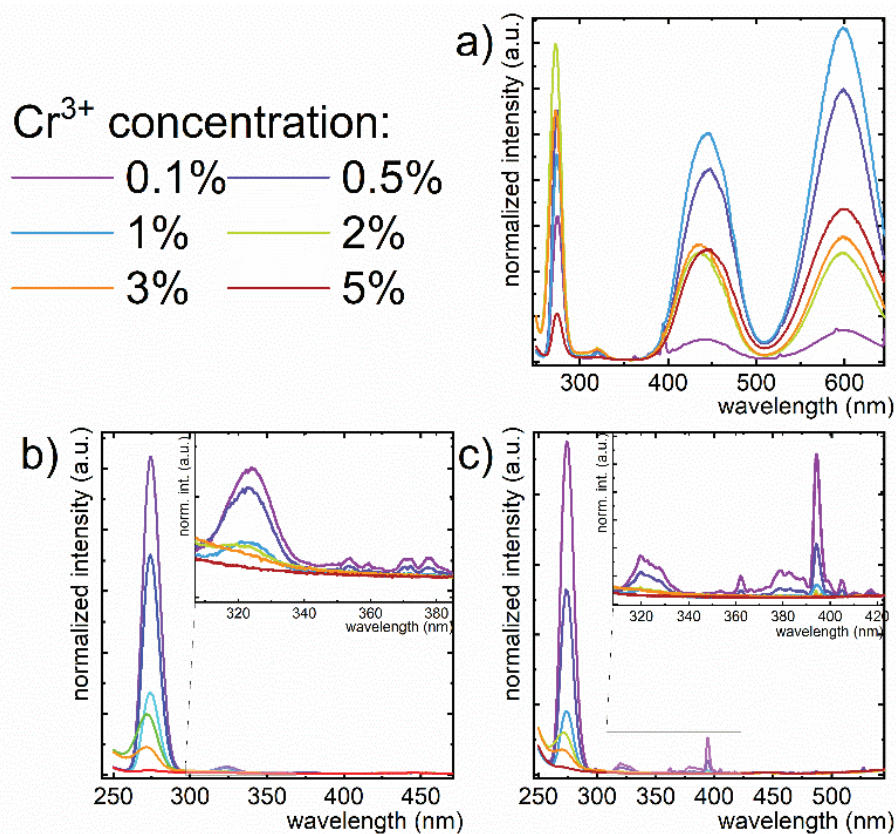
Figure S24. The influence of Cr^{3+} ions concentration on excitation spectra in YAG:1% Tb^{3+}, 1% Eu^{3+}, x% Cr^{3+} for 712 nm (a), 545 nm (b) and 592 nm (c).
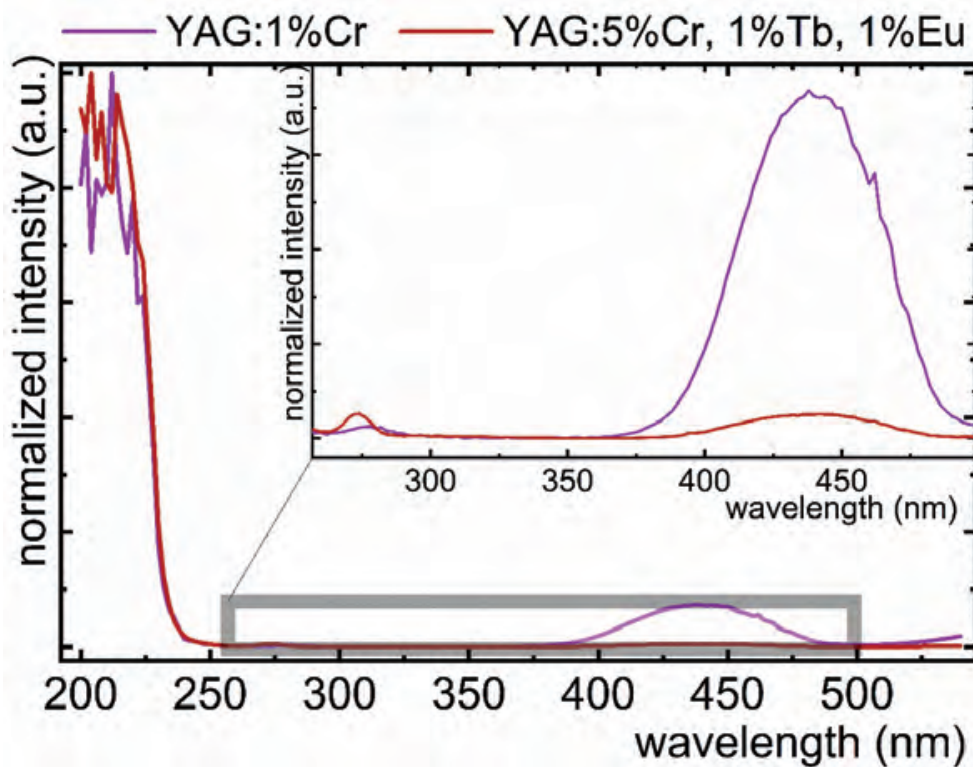
Figure S25. The excitation spectra in YAG:1% Cr^{3+} and YAG:1% Tb^{3+}, 1% Eu^{3+}, 5% Cr^{3+} for 712 nm.
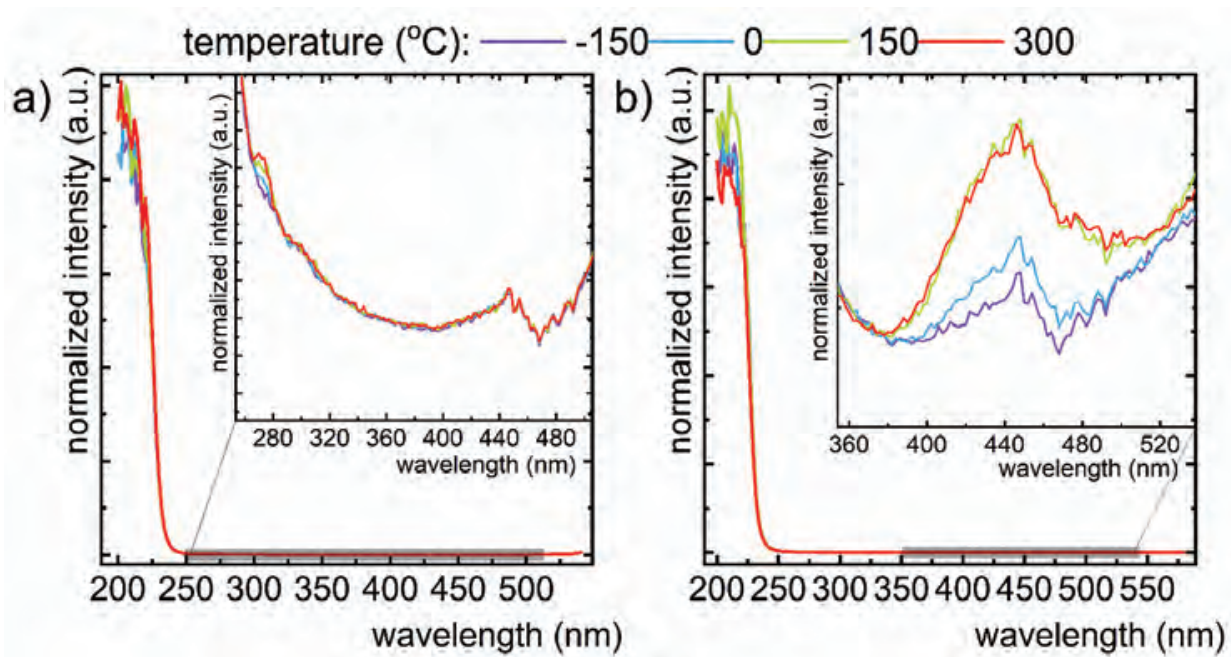
Figure S26. The temperature evolution of the excitation spectra in YAG:1% Tb^{3+}, 1% Eu^{3+}, 5% Cr^{3+} for 550 nm (a) and 620 nm (b).
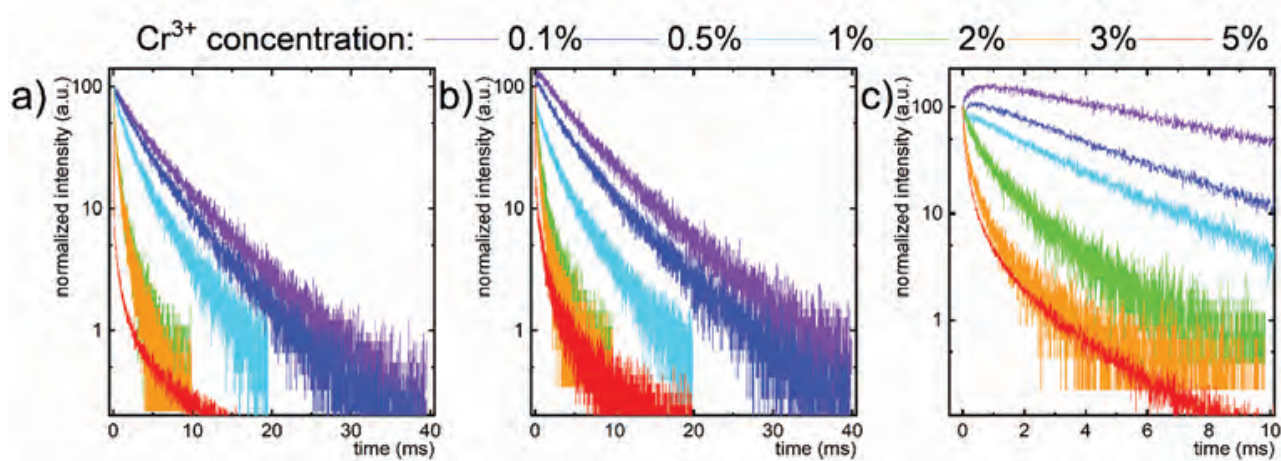
Figure S27. The influence of Cr^{3+} ions concentration on luminescent decays in YAG:1% Tb^{3+}, 1% Eu^{3+}, x% Cr^{3+} for 545 nm (a), 592 nm (b) and 712 nm (c).
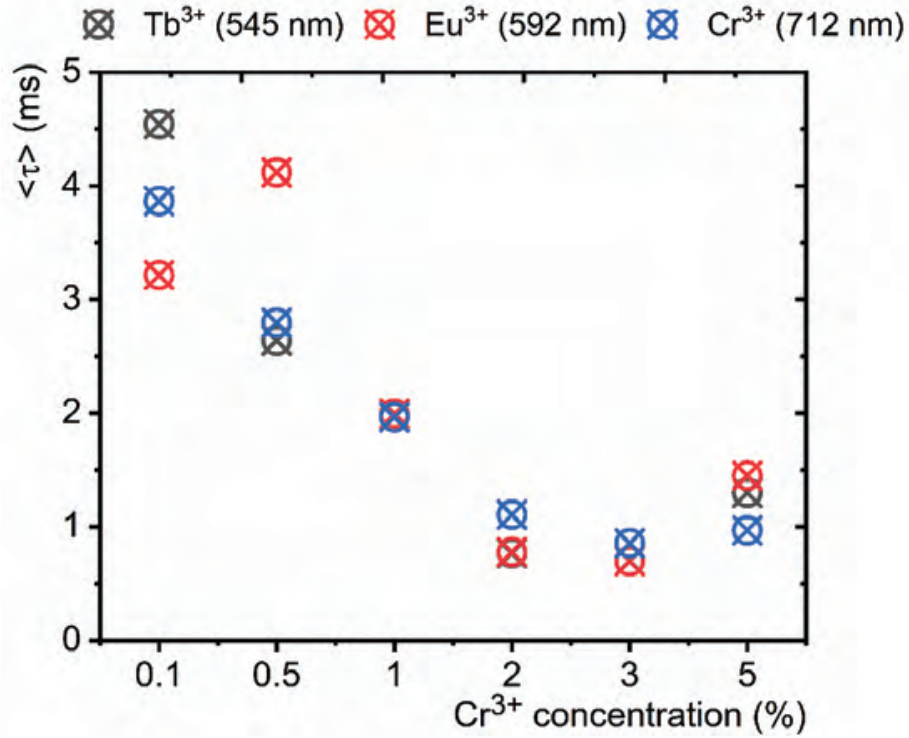
Figure S28. The average lifetime of Tb^{3+}, Eu^{3+} and Cr^{3+} excited states as a function of Cr^{3+} concentration for YAG:1% Tb^{3+}, 1% Eu^{3+}, x% Cr^{3+} powders.
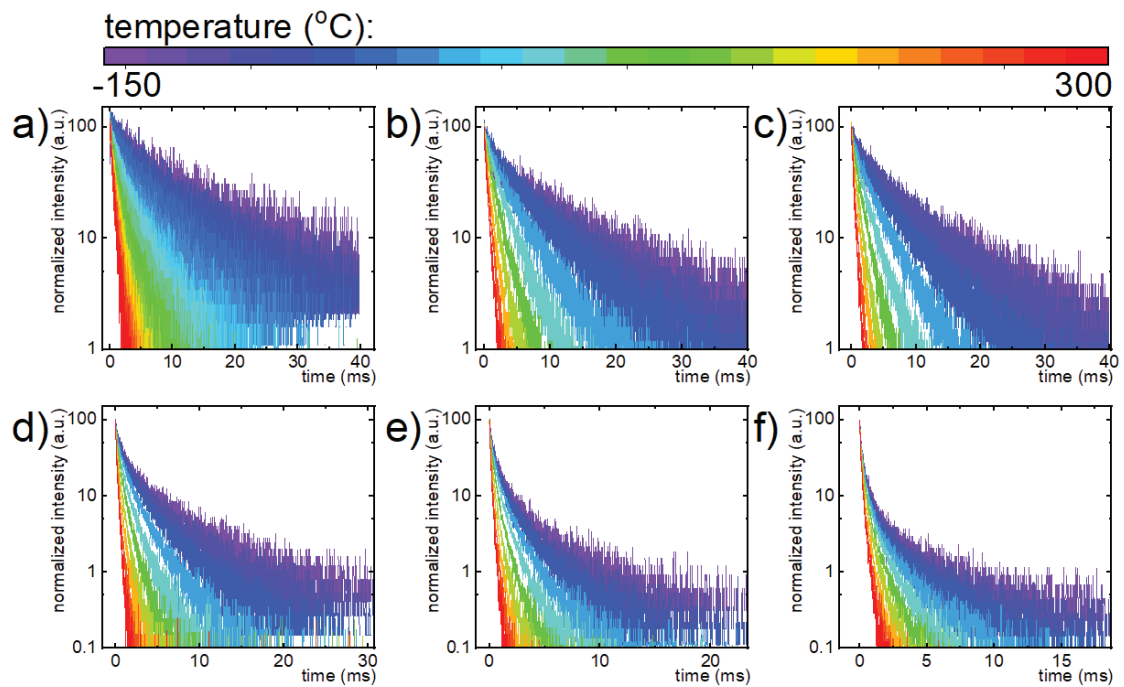
Figure S29. The thermal evolution of luminescent decays in YAG:1% Tb^{3+}, 1% Eu^{3+}, x% Cr^{3+} for 689 nm, where x = 0.1 (a), 0.5 (b), 1 (c), 2 (d), 3 (e) and 5 (f).
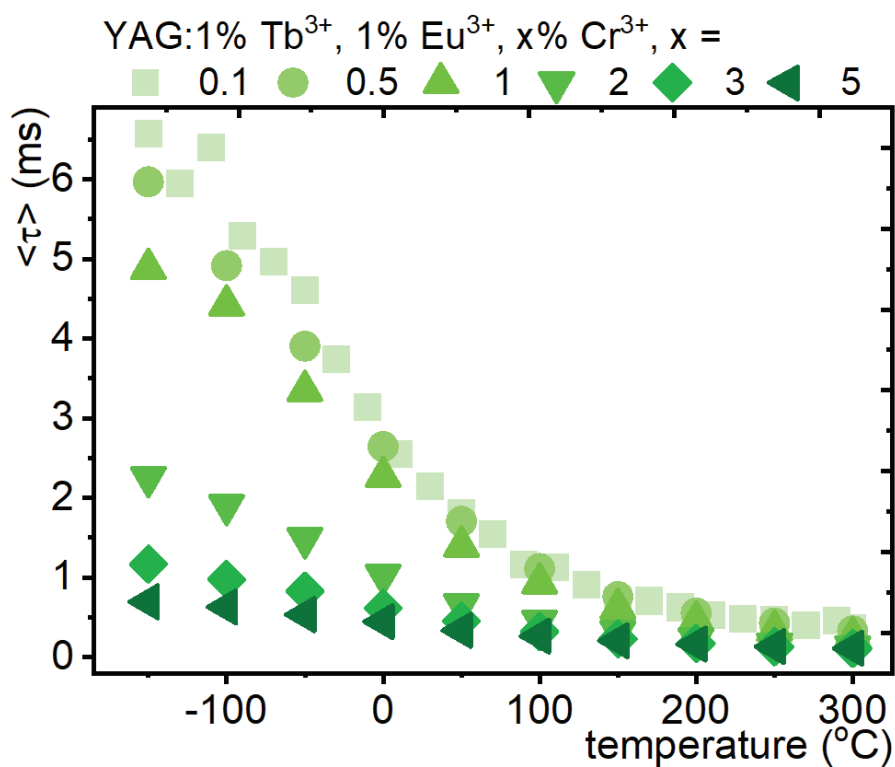
Figure S30. The thermal evolution of average lifetime of Cr^{3+} excited states with different Cr^{3+} concentration for YAG:1% Tb^{3+}, 1% Eu^{3+}, x% Cr^{3+} powders.
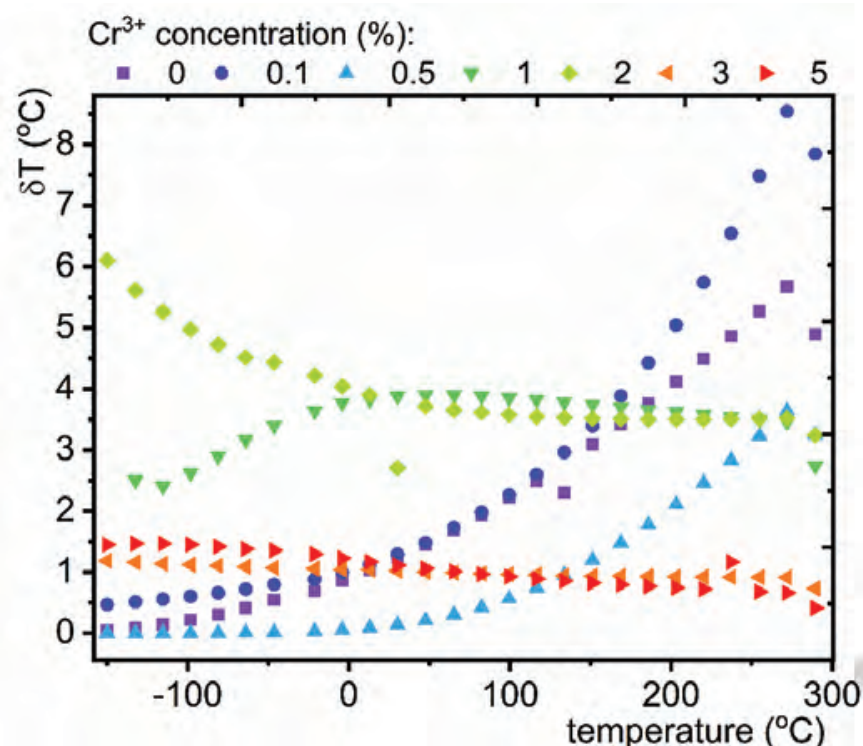
Figure S31. The thermal dependence of temperature estimation uncertainty for different Cr^{3+} concentration in the YAG:1% Tb^{3+}, 1% Eu^{3+}, x% Cr^{3+}.
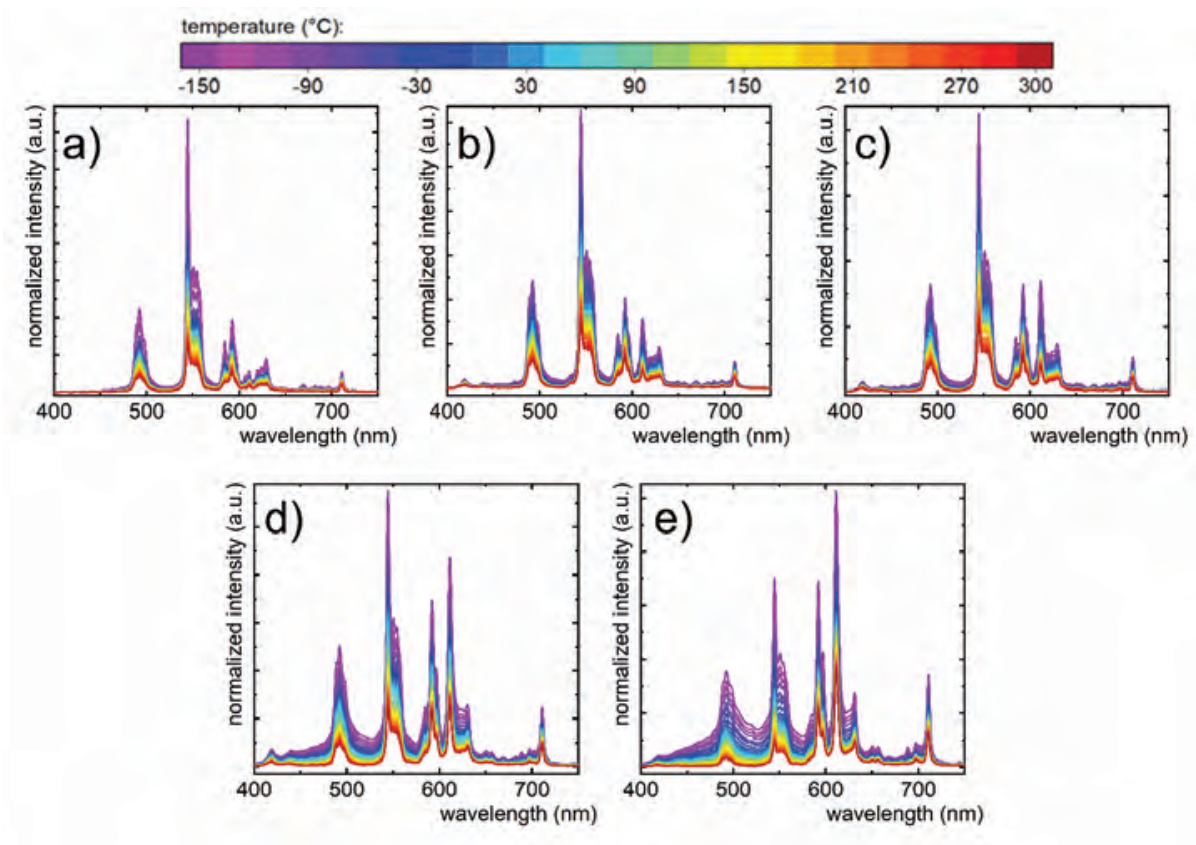
Figure S32. The thermal evolution of the emission spectra of YAG:1% Tb^{3+}, 1% Eu^{3+}, x% $Ti^{3+/4+}$ powders, where x = 0.1 (a), 0.5 (b), 1 (c), 5 (d), 10 (e).
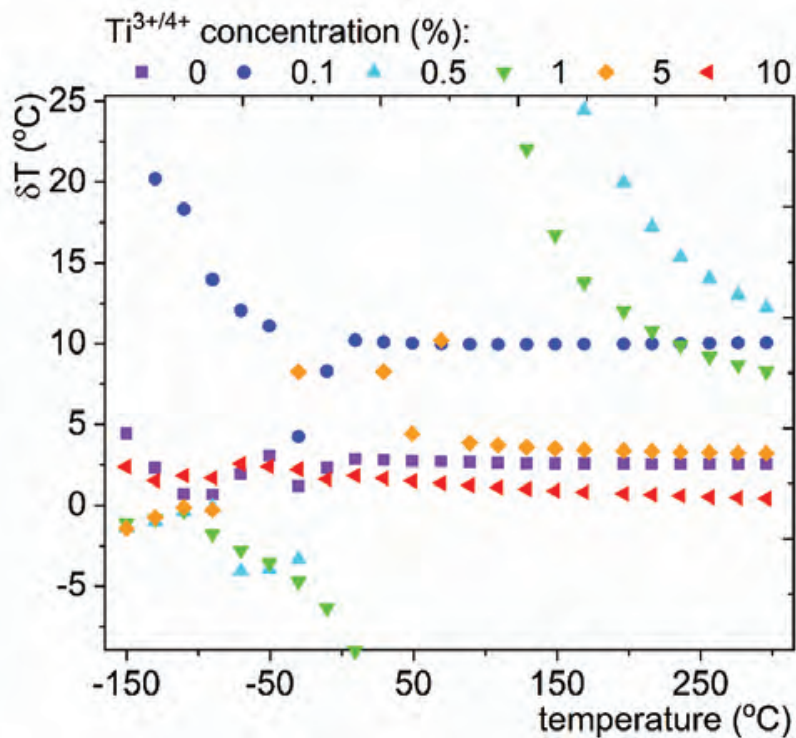
Figure S33. The thermal dependence of temperature estimation uncertainty for different $Ti^{3+/4+}$ concentration in the YAG:1% Tb^{3+}, 1% Eu^{3+}, x% $Ti^{3+/4+}$.
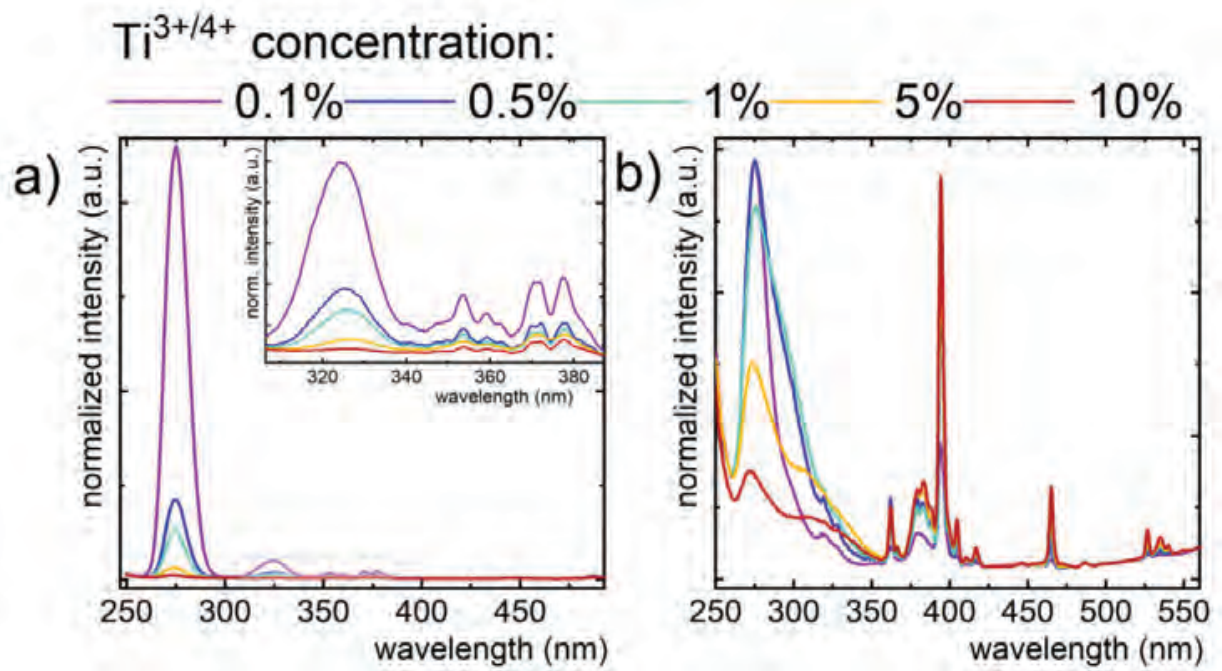
Figure S34. The influence of $Ti^{3+/4+}$ ions concentration on excitation spectra in YAG:1% Tb^{3+}, 1% Eu^{3+}, x% $Ti^{3+/4+}$ for 545 nm (a) and 612 nm (b).
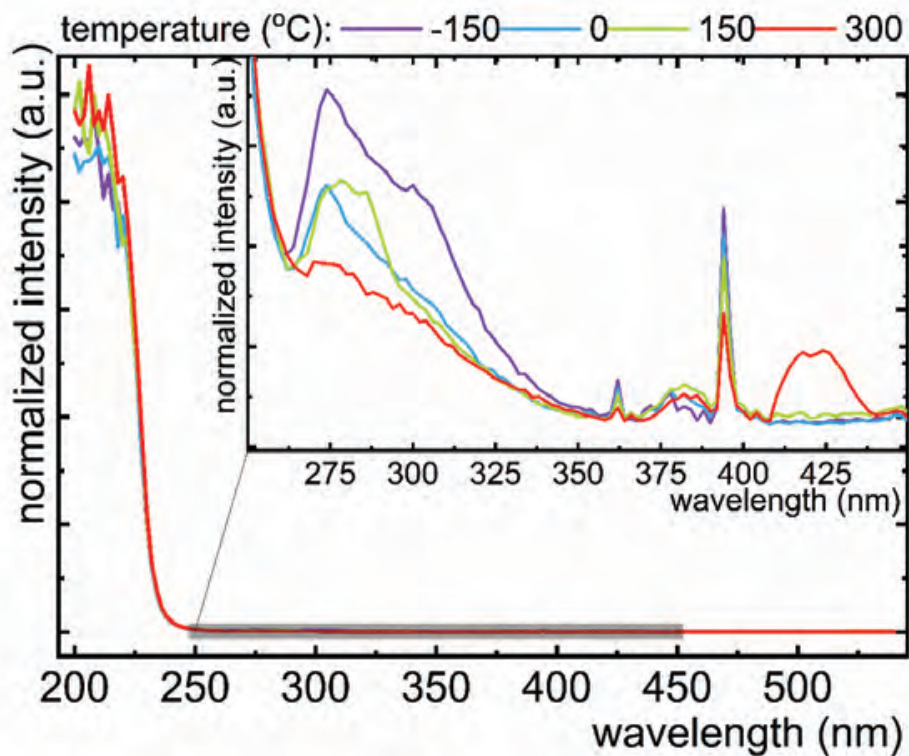
Figure S35. The thermal evolution of the excitation spectra in YAG:1% Tb^{3+}, 1% Eu^{3+}, 10% $Ti^{3+/4+}$ for 620 nm.
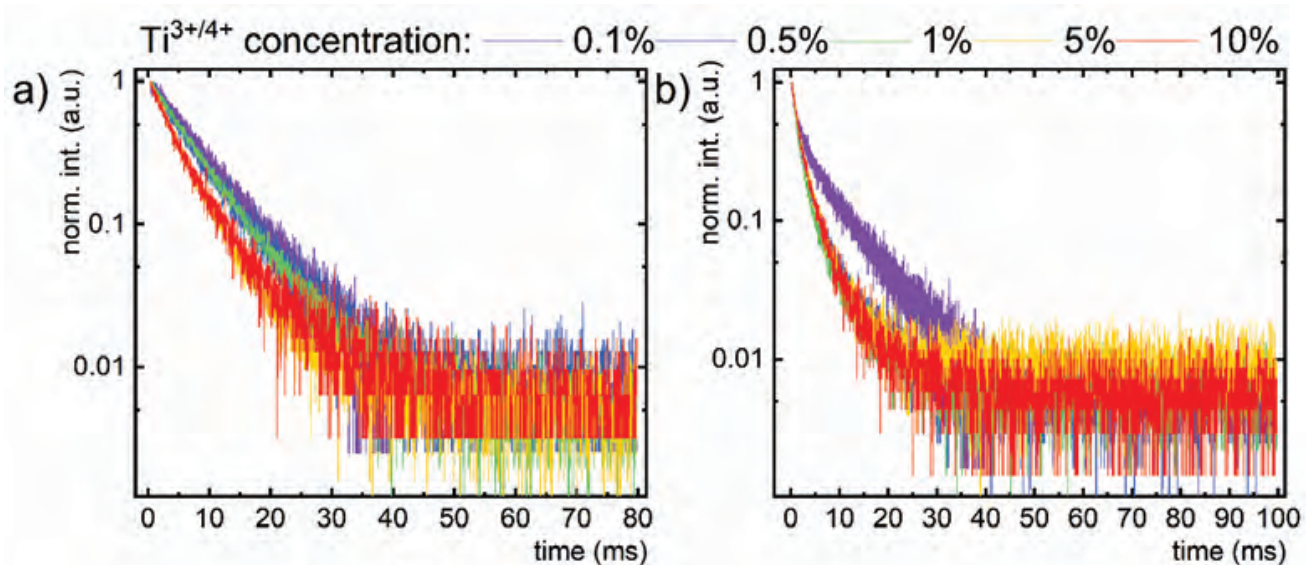
Figure S36. The influence of $Ti^{3+/4+}$ ions concentration on excitation spectra in YAG:1% Tb^{3+}, 1% Eu^{3+}, x% $Ti^{3+/4+}$ for 545 nm (a) and 592 nm (b).
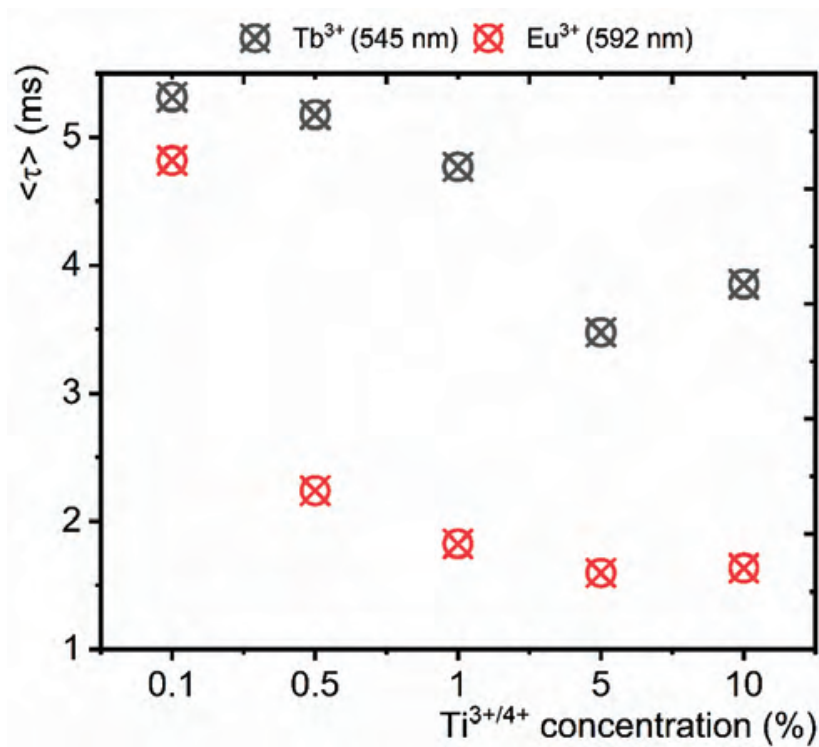
Figure S37. The average lifetime of Tb^{3+} and Eu^{3+} excited states as a function of $Ti^{3+/4+}$ concentration for YAG:1% Tb^{3+}, 1% Eu^{3+}, x% $Ti^{3+/4+}$ powders.
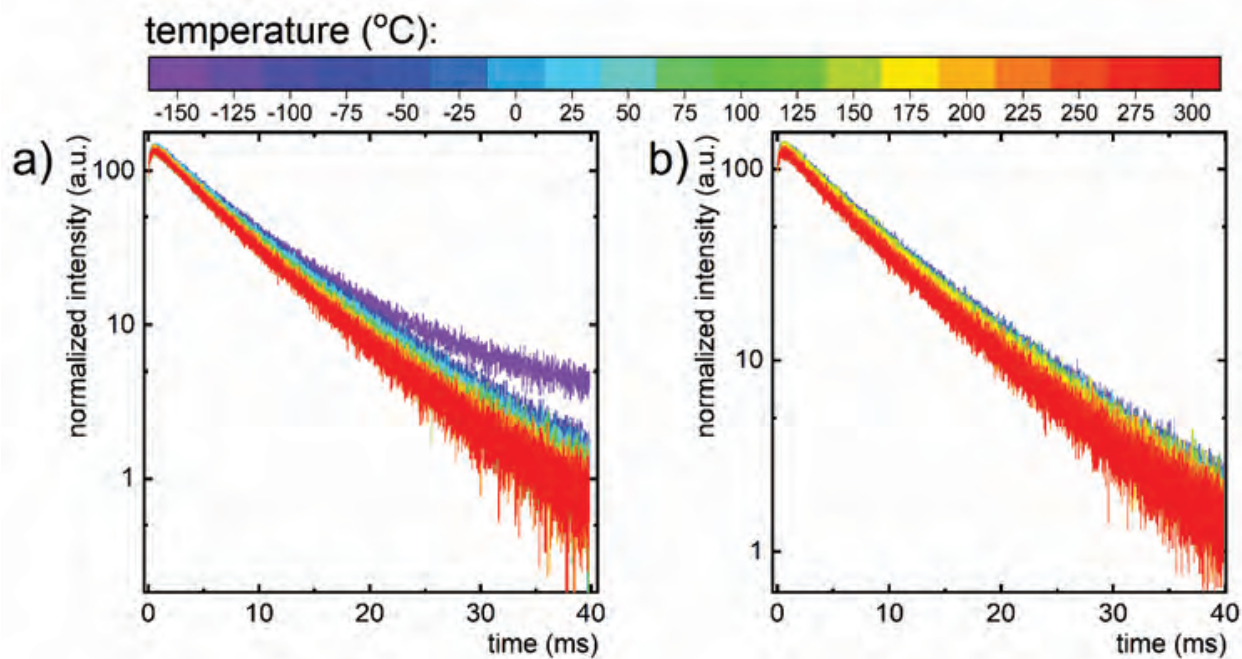
Figure S38. The thermal evolution of luminescent decays in YAG:1% Tb^{3+}, 1% Eu^{3+} for 545 nm (a) and 592 nm (b).
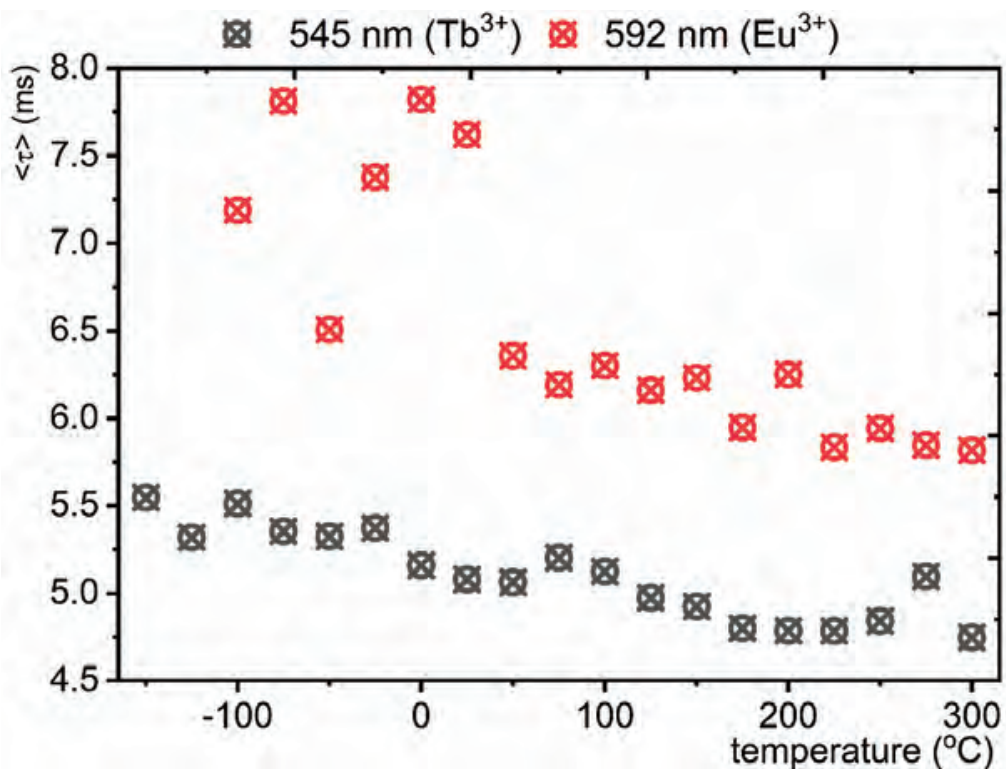
Figure S39. The thermal evolution of average lifetime of Tb^{3+} and Eu^{3+} excited states for YAG:1% Tb^{3+}, 1% Eu^{3+} powders.
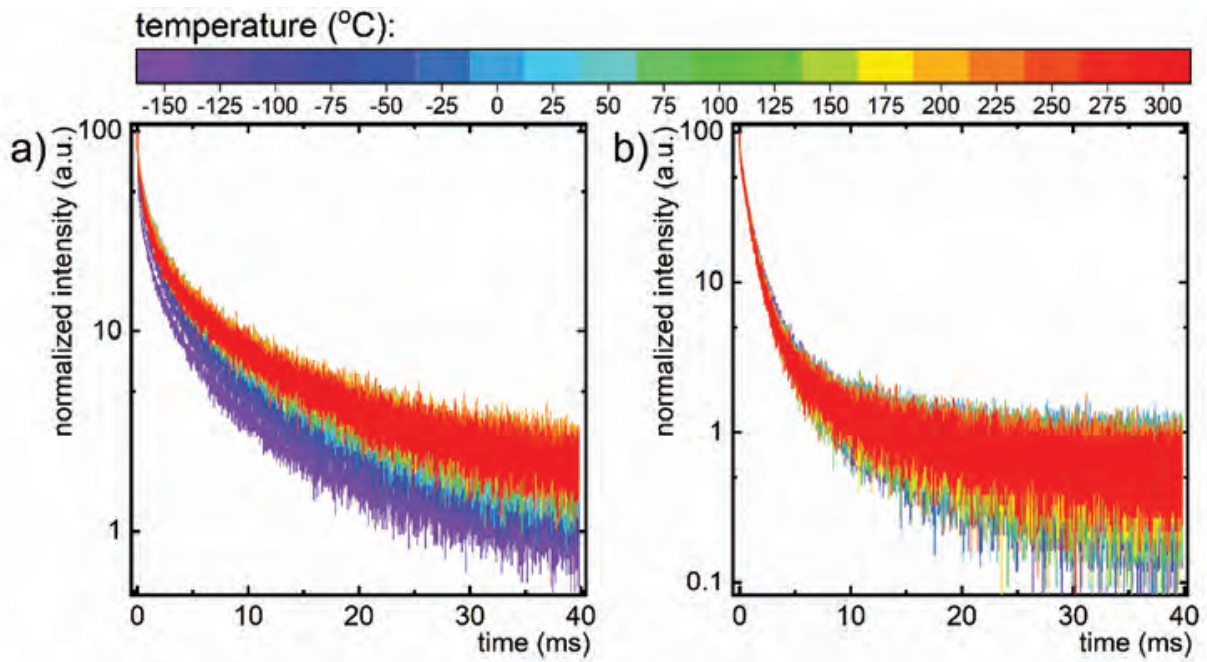
Figure S40. The thermal evolution of luminescent decays in YAG:1% Tb^{3+}, 1% Eu^{3+}, 10% Mn^{4+} for 545 nm (a) and 592 nm (b).
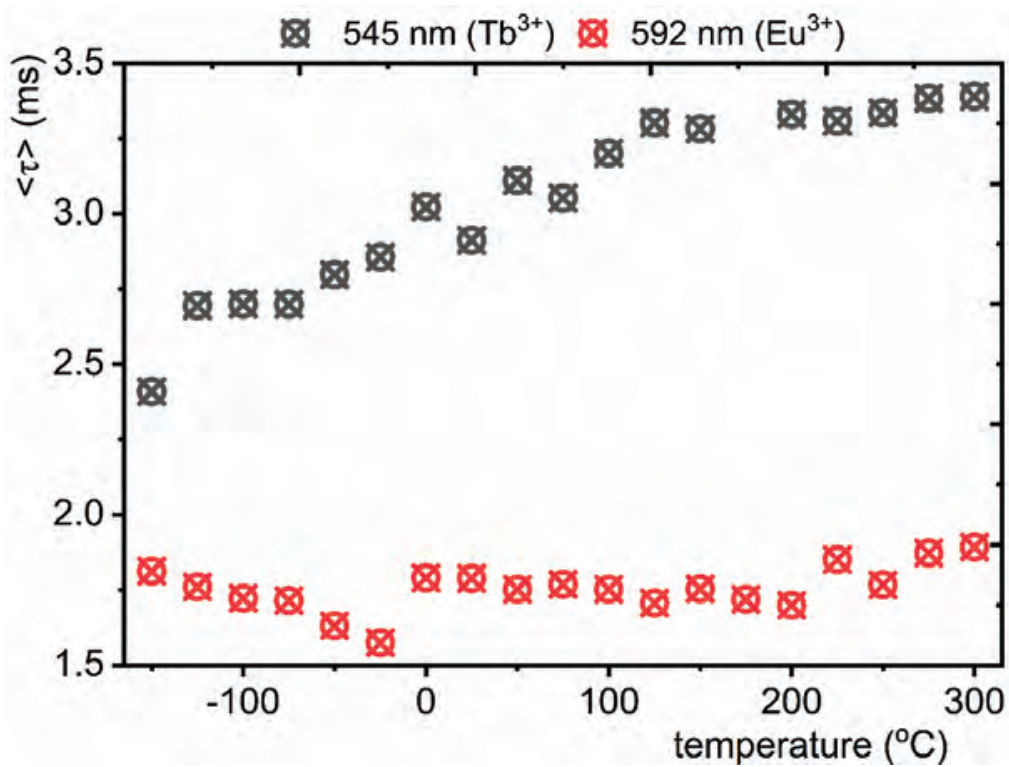
Figure S41. The thermal evolution of average lifetime of Tb^{3+} and Eu^{3+} excited states for YAG:1% Tb^{3+}, 1% Eu^{3+}, 10% Mn^{4+} powders.
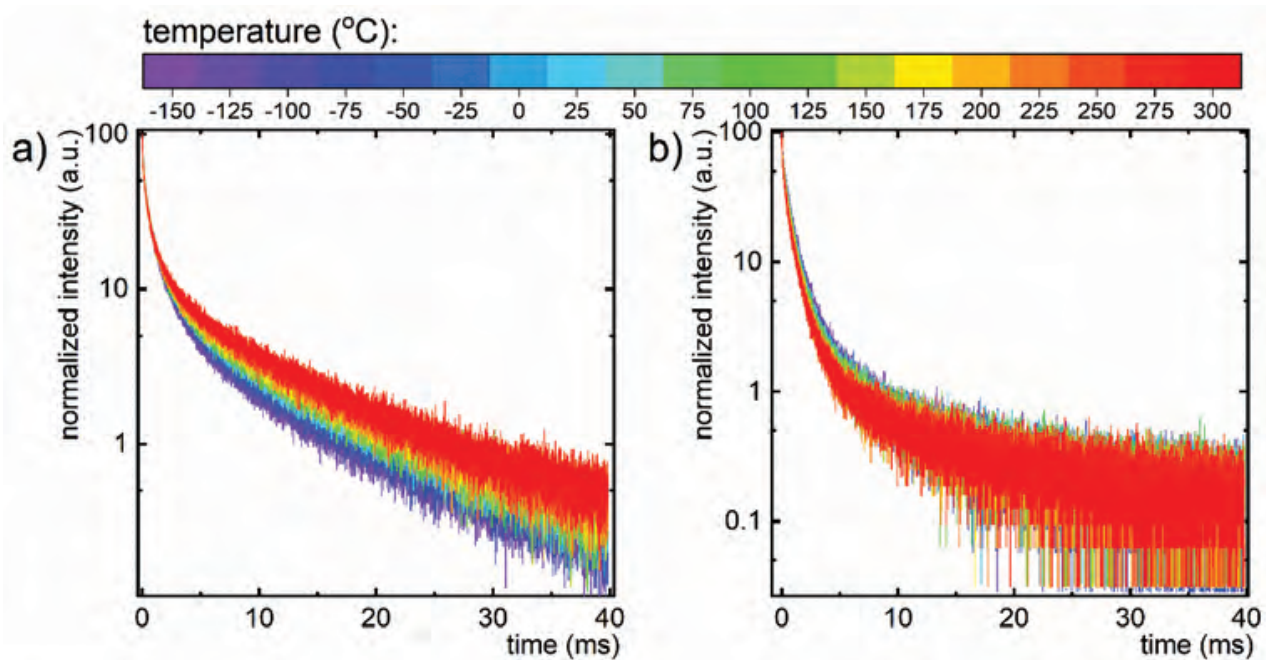
Figure S42. The thermal evolution of luminescent decays in YAG:1% Tb^{3+}, 1% Eu^{3+}, 5% Cr^{3+} for 545 nm (a) and 592 nm (b).
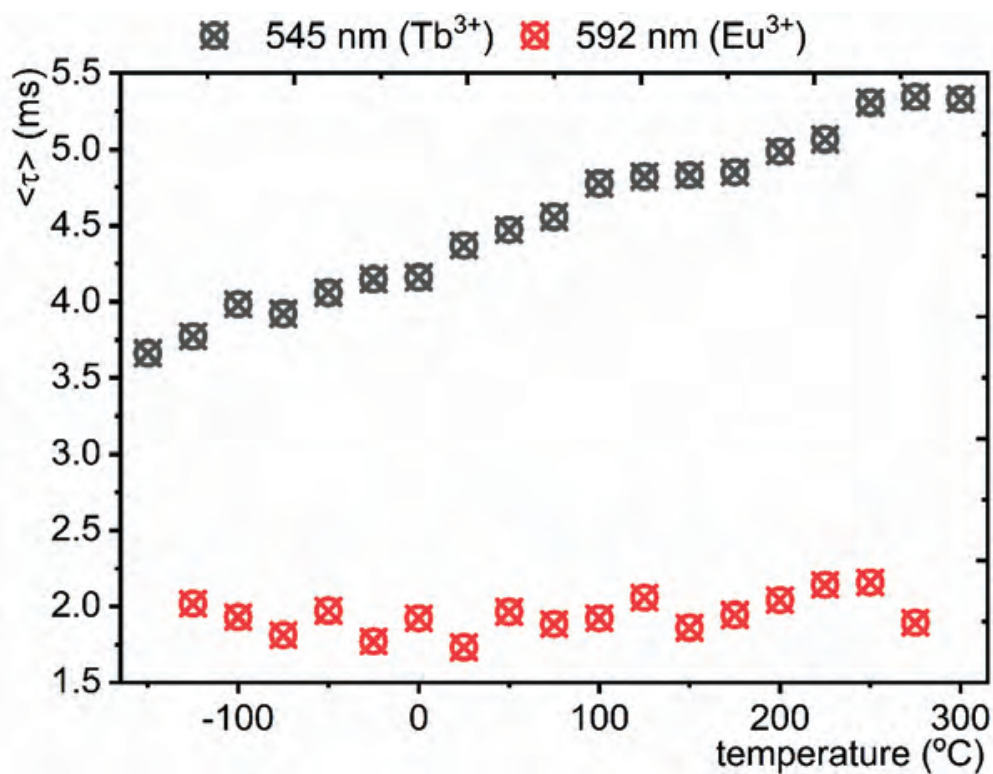
Figure S43. The thermal evolution of average lifetime of Tb^{3+} and Eu^{3+} excited states for YAG:1% Tb^{3+}, 1% Eu^{3+}, 5% Cr^{3+} powders.
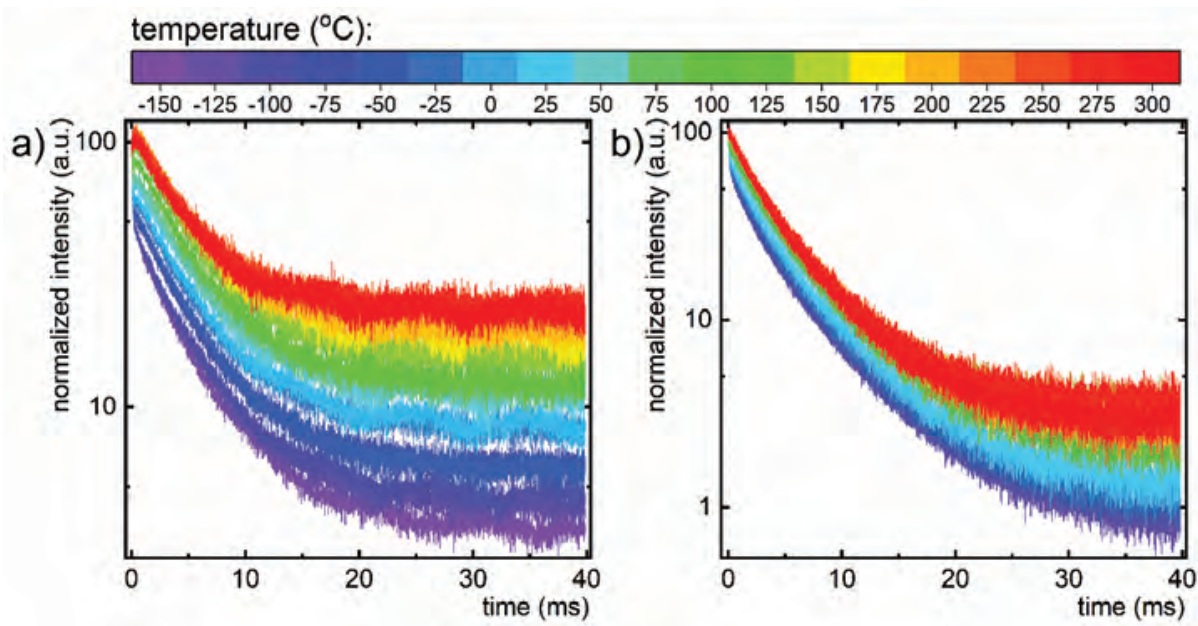
Figure S44. The thermal evolution of luminescent decays in YAG:1% Tb^{3+}, 1% Eu^{3+}, 5% $Ti^{3+/4+}$ for 545 nm (a) and 592 nm (b).
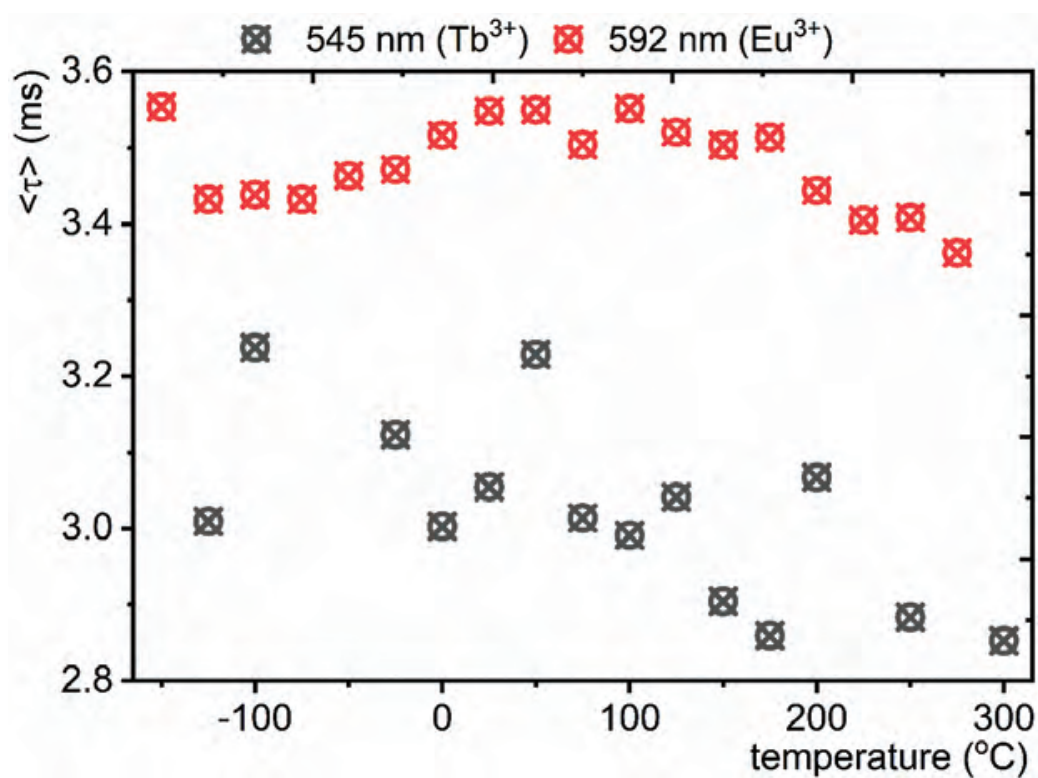
Figure S45. The thermal evolution of average lifetime of Tb^{3+} and Eu^{3+} excited states for YAG:1% Tb^{3+}, 1% Eu^{3+}, 5% $Ti^{3+/4+}$ powders.

ROYAL SOCIETY OF CHEMISTRY

PAPER

Check for updates

The role of Cr^{3+} and Cr^{4+} in emission brightness enhancement and sensitivity improvement of NIR-emitting Nd^{3+}/Er^{3+} ratiometric luminescent thermometers†

W. Piotrowski, [ID] [a] L. Dalipi,[b] R. Szukiewicz, [ID] [c] B. Fond, [ID] [b] M. Dramicanin [ID] [d] and L. Marciniak [ID] *[a]

Despite the numerous advantages of lanthanide based luminescent thermometers, a major limitation is the limited brightness associated with the low absorption cross section of the 4f–4f transitions. In this paper, co-doping with Cr$^{3+/4+}$ is proposed as a strategy to enhance the near-infrared luminescence emission of Nd^{3+}/Er^{3+}-based luminescent thermometers, as well as to modulate the temperature sensitivity of the ratio of Nd^{3+} to Er^{3+} in YAG microcrystals. It was found that an increase in the Cr^{3+} concentration leads to the enhancement of the YAG:Nd^{3+},Er^{3+} emission intensity *via* the Cr^{3+} → Ln^{3+} sensitization process. The quantitative analysis of the absolute brightness indicates the 30-fold enhancement of their near infrared emission upon broad white light excitation for 20% Cr^{3+} with respect to the non co-doped with the Cr^{3+} counterpart. In addition, the phonon-assisted nature of the simultaneously occurring Cr^{3+} → Ln^{3+} and Nd^{3+} → Cr^{4+} → Er^{3+} energy transfers leads to a 7-fold increase of the relative temperature sensitivity of the ratio of Nd^{3+} to Er^{3+} emission. In conclusion, co-doping with transition metals can enhance simultaneously the luminescence brightness and the temperature sensitivity of NIR luminescent thermometers, holding promise for sensitive and robust remote temperature sensing at physiological temperatures.

1. Introduction

Inorganic particles doped with lanthanide ions are commonly used as probes for luminescence thermometry due to their numerous advantages such as high thermal and chemical stability, narrow emission lines which facilitate spectral separation of the emission bands for ratiometric readout, relatively long lifetimes, and finally the unique energy level configuration which enables the activation of different temperature-dependent energy transfer processes and affects the spectroscopic properties of thermographic phosphors *etc.*[1–7] However, one of the most severe limitations of Ln^{3+} ions is their low absorption cross section, which constricts their luminescence brightness. Additionally, in the case of Ln^{3+} co-doped luminescent thermometers, the observed increase of the relative sensitivity of phosphors usually corresponds to the temperature

range in which the quenching of the luminescence is observed which further hampers the emission signal collection.[8–12]

The low emission intensity limitation of Ln^{3+} thermometers may be overcome by the additional sensitization process that exploits co-dopant ions or organic molecules *via* the so-called antenna effect.[13–19] Since the thermal and chemical stability of organic molecules is low especially at higher temperatures, sensitization by co-doping appears to be a more universal strategy. The high absorption cross-section of transition metal (TM) ions makes them excellent candidates for this purpose.[17–21] The high efficiency of this strategy to enhance the emission brightness of Ln^{3+} has already been proved. However, the additional advantage of this approach, especially important from the thermometric perspective, is that due to the small mismatch in the energy of the excited states of TM and Ln^{3+} the probability of TM → Ln^{3+} is strongly susceptible to temperature changes which enhances the relative sensitivity of Ln^{3+} based luminescent thermometers.[22] Additionally, one can benefit from the easiness in the modification of the spectroscopic properties of the TM by the engineering of the crystal field strength and, thus, the alteration of the energy level configuration customizing the thermal dependence of energy transfer probabilities.[23–25] Therefore, by TM co-doping, not only the emission intensity but also the thermometric

[a] Institute of Low Temperature and Structure Research, Polish Academy of Sciences, Okólna 2, 50-422 Wroclaw, Poland. E-mail: l.marciniak@intibs.pl

[b] Institute of Fluid Dynamics and Thermodynamics, Otto-von-Guericke University Magdeburg, 39106 Magdeburg, Germany

[c] Institute of Experimental Physics, Faculty of Physics and Astronomy, University of Wroclaw, Wroclaw 50-204, Poland

[d] Vinča Institute of Nuclear Sciences – National Institute of the Republic of Serbia, University of Belgrade, P.O. Box 522, Belgrade 11001, Serbia

† Electronic supplementary information (ESI) available. See DOI: 10.1039/d1tc03046a

performance of the thermographic phosphor can be enhanced. It was shown that by the introduction of the Cr^{3+} ions into the Eu^{3+},Tb^{3+} co-doped system the S_R increases by two orders of magnitude with respect to the non co-doped with Cr^{3+} counterparts.[20] However, in previous studies, the limitation of the proposed approach was caused by the spectral overlap between the absorption bands of the TM with the emission bands of Ln^{3+} which by the self-filtering effect reduced the Ln^{3+} emission intensity. The enhancement of the thermometric properties of the near infrared emitting Ln^{3+} based luminescent thermometer by the TM co-doping has not been explored so far.

In this paper, the influence of the Cr^{3+} and Cr^{4+} ions on the thermometric properties of the Nd^{3+}/Er^{3+} luminescent thermometer has been investigated in a wide range of Cr doping concentrations. The increase in the absorption cross section for broadband illumination provided by Cr^{3+} doping was quantified using particle dispersions. Additionally, the concept of the use of Cr^{4+} as an energy bridge that facilitates energy transfer between Nd^{3+} and Er^{3+} ions is being reported here and studied, to the best of our knowledge, for the first time. The unique configuration of the energy level diagram of the Cr^{4+} enhances the thermometric properties of both ratiometric and lifetime-based luminescent thermometers.

2. Experimental section

The powders of the yttrium aluminium garnet YAG:Nd^{3+},Er^{3+} and YAG:Nd^{3+},Er^{3+},$Cr^{3+/4+}$ nanocrystals were synthesised by the use of the solid-state method. $Al(NO_3)_3 \cdot xH_2O$ ($x \approx 9$; 99.999% purity, Alfa Aesar), Y_2O_3 (99.999% purity, Stanford Materials Corporation), Nd_2O_3 (99.999% purity, Stanford Materials Corporation), Er_2O_3 (99.99% purity, Stanford Materials Corporation) and $Cr(NO_3)_3 \cdot 9H_2O$ (99.99% purity, Alfa Aesar) were used as starting materials. The stoichiometric amounts of compounds were mixed in n-hexane and ground well in an agate mortar three times until the n-hexane evaporated. Next, the powder was first calcined in porcelain crucibles at 1000 °C in air for 24 h. The pre-annealed powders with 1% Nd^{3+} and 1% Er^{3+} concentrations with respect to the number of moles of Y^{3+} ions and x% molar $Cr^{3+/4+}$ concentration (x = 0, 1, 2, 5, 10, 20) with respect to Al^{3+} ions were subsequently ground again with the same procedure and sintered in corundum crucibles in air at 1600 °C for 24 h. All of the synthesized materials were examined by X-ray powder diffraction (XRPD) measurements carried out on a PANalytical X'Pert diffractometer, equipped with an Anton Paar TCU 1000 N temperature control unit, using Ni-filtered Cu-K$_\alpha$ radiation (V = 40 kV, I = 30 mA).

Scanning Electron Microscopy (SEM) images were taken with a Field Emission Scanning Electron Microscope (FEI Nova NanoSEM 230) equipped with an energy-dispersive spectrometer (EDAX Genesis XM4). The sample was ground in a mortar and dispersed in methanol and then a drop of the suspension was placed on the carbon stub and dried. X-ray Photoelectron Spectroscopy (XPS) has been used for surface chemical composition analysis. The non-monochromatized X-ray Mg Kα excitation source was used. All measurements have been performed using an AES/XPS system EA10 (Leybold-Heraeus GmbH, Cologne, Germany). The overall resolution of the spectrometer during the measurements was 0.96 eV as a full width of half maximum (FWHM) of the Ag $3d_{5/2}$ line. During measurements the pressure was kept in the 10^{-9} mbar range. All acquired spectra were calibrated to adventitious carbon C1s at 285 eV. After subtraction of the Shirley-type background, the core-level spectra were decomposed into main components with mixed Gaussian–Lorentzian lines (70% G + 30% L for majority of photo-peaks) by a non-linear least squares curve-fitting procedure, using CasaXPS software. The atomic concentration was determined based on XPS spectra analysis, taking into account the presence of individual elements O, C, Y, Al, N and Cr.

The emission spectra were measured using the 445 nm (50 mW) excitation lines from a laser diode and a NIRQUEST spectrometer from Ocean Optics (1.5 nm spectral resolution) as a detector. The temperature of the sample was controlled using a THMS 600 heating–cooling stage from Linkam (0.1 °C temperature stability and 0.1 °C set point resolution).

The excitation spectra and luminescence decay profiles were recorded using a FLS1000 Fluorescence spectrometer from Edinburgh Instruments with a 450 W xenon lamp and a μFlash lamp as excitation sources and a R928P side window photomultiplier tube from Hamamatsu as a detector. Thermal dependencies of the luminescence intensity ratio (LIR) were fitted using the Mott–Seitz model (eqn (S1), ESI†). The average lifetimes of the excited states were calculated with the use of double exponential function according to the procedure described in the ESI† (eqn (S2)).

To quantify the enhancement in Nd^{3+} emission offered by Cr^{3+} sensitization, the luminescence emission was quantified from suspensions of particles in water. For each sample, 10 mg of the phosphor powder was dispersed in 20 mL deionized water, yielding a standard dispersion with a concentration of 500 mg L^{-1}. An ultrasonic homogenizer (Bandelin Sonopuls HD 2200) was used to disperse and break agglomerated particles. The stirred suspensions were illuminated by a white LED (Thorlabs MCWHL5), focused using a 85 mm objective lens (Zeiss 85 mm f/1.4) and a f = +75 mm plano-convex lens to yield an intensity of 930 mW cm^{-2} in the measurement region. A visible 315–710 nm band-pass filter (Schott KG3) was positioned between the LED and the beaker to block any IR light. For visualization, images of 1064 nm emission were captured using a CMOS camera (Basler acA1300–200 μm), equipped with a 50 mm objective lens (Nikon 50 mm f/1.4) and an IR long-pass filter (Schott RG 1000) to block the scattered light from the LED beam. For quantitative spectroscopic measurements, the luminescence was collected from the dispersions using a 50 mm objective lens (Nikon 50 mm f/4) and focused onto the entrance slit of a monochromator (Spectrapro: HRS-300, Princeton Instruments), and detected using a non-amplified silicon photodiode (Thorlabs DET1002A). The grating (100 grooves per mm blazed at 450 nm) was centered at 1065 nm with the

entrance and exit slit set to provide a bandwidth (FWHM) of 60 nm. For low-noise interference-free detection, the LED was modulated at 8 Hz and the current from the photodiode amplified using a lock-in amplifier (Stanford Research Systems SR510) and temporally filtered. To account for potential differences in dispersion stability, prior to luminescence measurements, the particle suspensions were illuminated by a 375 nm diode laser (PhoxX-Omicron Lasers), and the scattered light from the particles recorded using the monochromator at 375 nm and the photodiode. The amplitude of the scattered light was read from the lock-in amplifier. Variations in particle scattering between the dispersions of various samples were within a factor of 2.6, and to compare luminescence signals for the same amount of particles in the probe volume, the measured luminescence emission was corrected by dividing by its normalized scattering intensity. To convert measured amplifier voltage to photons per s per mg, the various components of the systems were taken into consideration following the procedure described previously.[26]

3. Results and discussion

The yttrium aluminum garnet $Y_3Al_2(AlO_4)_3$ (YAG) is one of the most representative and well-described compounds of the family of the synthetic garnets with the general chemical formula $C_3A_2D_3O_{12}$ with cubic space group $Ia\bar{3}d$ (no. 230).[27–29] The YAG crystal consists of Y^{3+} ions occupying dodecahedral "C" sites with D_2 local symmetry and Al^{3+} ions in both the octahedral "A" and tetrahedral "D" sites with C_{3i} and S_4 local symmetries, respectively (Fig. 1a). In the case of YAG doped

with neodymium, erbium and chromium ions, a slight difference between the effective ionic radii of Y^{3+} (101.9 pm) and Ln^{3+} ions reveals that Nd^{3+} and Er^{3+} ions substitute the eight-fold coordinated "C" site (110.9 and 100.4 pm for Nd^{3+} and Er^{3+} ions, respectively). From numerous studies, it is well known that the favored oxidation state of chromium ions incorporated into YAG is Cr^{3+} due to the electrical charge match with Al^{3+}. However, some literature reports suggest that also higher oxidation states of chromium ions like Cr^{4+} and even Cr^{6+} can be noticed in the YAG structure.[30–37] In particular the surface states of the nano and microcrystalline powders due to the strongly defected structure are the phosphor areas expected to be occupied by the higher oxidation states of the transition metal ions. The Cr^{3+} ions preferentially occupy the six-fold coordinated Al^{3+} site "A" positions (compare Al_2 in Fig. 1a). The strong octahedral ligand field induces the additional thermodynamic stabilization of Cr in its trivalent oxidation state since only t_{2g}-transforming orbitals are occupied in such an environment. Considering its smaller effective ionic radii, the Cr^{4+} ions may substitute Al^{3+} at both the octahedral and tetrahedral sites (55 pm and 41 pm for 6-fold and 4-fold coordinated Cr^{4+} ions, respectively). In accordance with Eilers *et al.*,[38] the spectroscopic properties of YAG:Cr^{4+} are dominated by Cr^{4+} in the tetrahedral position (Al_1 in Fig. 1a) where Cr^{4+} ions modify the local symmetry to D_{2d} with the oxygen tetrahedron elongated along the z-axis.[39]

To verify the phase purity of the synthesized powders and to investigate the influence of dopant concentration on the crystallographic structure of the synthesized YAG powders, the XRPD patterns were analysed (Fig. 1b, see also Table S1 (ESI†) for Rietveld refinement parameters). All of the obtained
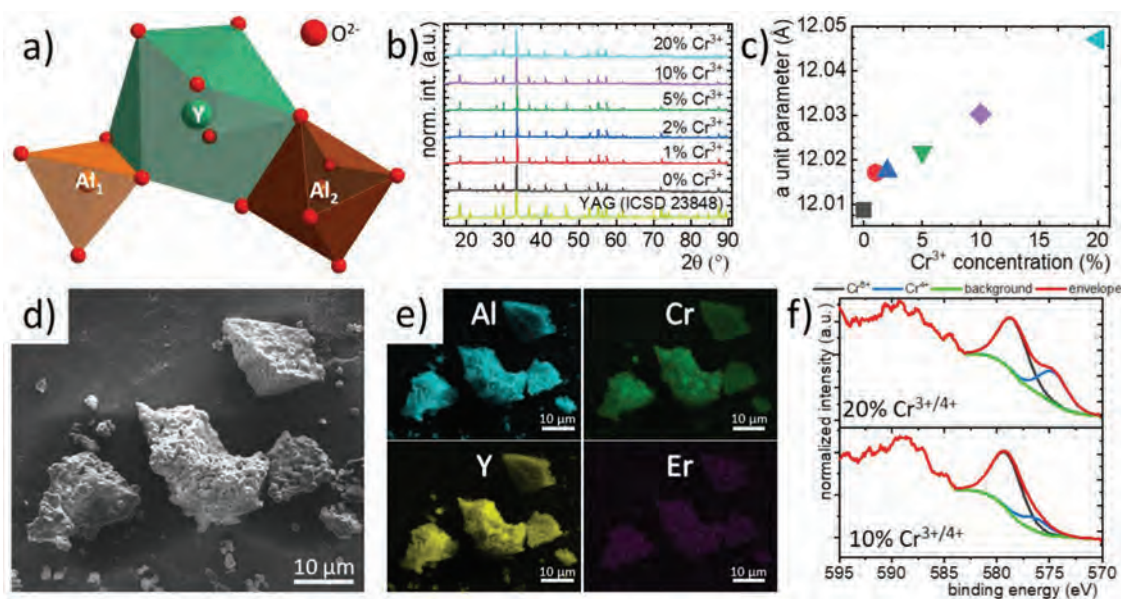
Fig. 1 Structural characterization of synthesized materials: the visualization of the polyhedra of Y^{3+} and Al^{3+} in the YAG structure (a); the X-ray diffraction patterns of YAG:1%Nd^{3+},1%Er^{3+},x%Cr^{3+} powders with different $Cr^{3+/4+}$ concentrations (b); the a unit cell parameter as a function of $Cr^{3+/4+}$ concentration (c); the representative SEM images of YAG:1%Nd^{3+},1%Er^{3+} undoped with $Cr^{3+/4+}$ ions (d) the ionic distribution maps (e), and the XPS binding energy spectrum (f).

diffraction reflection corresponds with the reference pattern (ICSD 23848) confirming the phase purity of the synthesized phosphors. The increase of the Cr^{3+} concentration up to 20 molar% with respect to Al^{3+} ions does not lead to the occurrence of additional reflection in the pattern. However, a slight shift of the reflection toward smaller 2 theta angles was observed at an elevated Cr^{3+} amount, which is related to the expansion of the crystallographic unit cell associated with the difference in the ionic radii between the dopant and substituted ions. The detailed Rietveld refinement reveals that the *a* unit cell parameter increases from 12.01 for 0.1%Cr^{3+} to 12.047 Å for 20% of Cr^{3+} ions (Fig. 1c). A slight increase of the lattice constant value was observed for YAG:1%Nd^{3+},1%Er^{3+} with respect to the model pattern *a* = 12.004 Å. Furthermore, the introduction of $Cr^{3+/4+}$ ions enables almost linear growth of the unit cell up to 12.047 Å for 20% $Cr^{3+/4+}$. The morphology of the obtained powders is presented in Fig. 1d (see also Fig. S1, ESI†). The analysis of the EDS data indicates homogenous ion distributions (Fig. 1e, see also Table S2 and Fig. S2, ESI†). The XPS measurements indicate that on the surface of phosphor particles mostly two oxidation states of chromium ions can be found, namely Cr^{6+} and Cr^{4+}, while the signal is dominated by the band associated with the Cr^{6+} oxidation state (Fig. S1f and Table S3, ESI†). Additionally, it was found that the increase in the chromium concentration results in the increase of the relative signal intensity associated with the Cr^{4+} with respect to the Cr^{6+}. The mechanism of change of the oxidation state of the chromium ion from Cr^{3+} to Cr^{4+} in the YAG matrix was described in detail by many authors.[30–38,40–43] However previous reports have considered the YAG:Cr^{4+} or mixed YAG:Cr^{3+}/Cr^{4+} structure in the single crystal[44] or ceramics[37] in contrast to the microcrystalline powder demonstrated in this manuscript. In this case, when any of the charge compensation ions were introduced into the structure oxidation of the Cr^{3+} ions is caused by the high annealing temperature.[37] As shown in the later part of the study, the annealing-induced change of the oxidation state is stable and independent of the temperature change up to 600 K. In the course of our previous studies, higher oxidation states of other transition metal ions on the surface part of the particles with respect to the ones observed in the core part were confirmed in the case of the vanadium ions (where the presence of V^{5+} on the surface was confirmed)[45,46] and titanium (Ti^{4+}, was found).[47] In the case of YAG:Cr^{3+} the random distribution of dopant ions within the particle leads to the conclusion that the increase of the dopant concentration leads to the increase of the number of chromium ions localized in the surface part of the crystal and thus a higher amount of Cr^{4+} and Cr^{6+} is expected to occur in heavily doped particles. The fact that no signal in the XPS analysis from the Cr^{3+} was found results from the fact that the strongly defected structure observed on the surface of the particle prevents the formation of eight-fold coordinated sites which could be occupied by the Cr^{3+} ions.

To understand the spectroscopic properties of the Cr^{3+}, Nd^{3+}, Er^{3+} and Cr^{3+}, Nd^{3+}, Cr^{4+}, Er^{3+} co-doped systems, simplified configurational coordinate energy diagrams for Cr^{3+} and
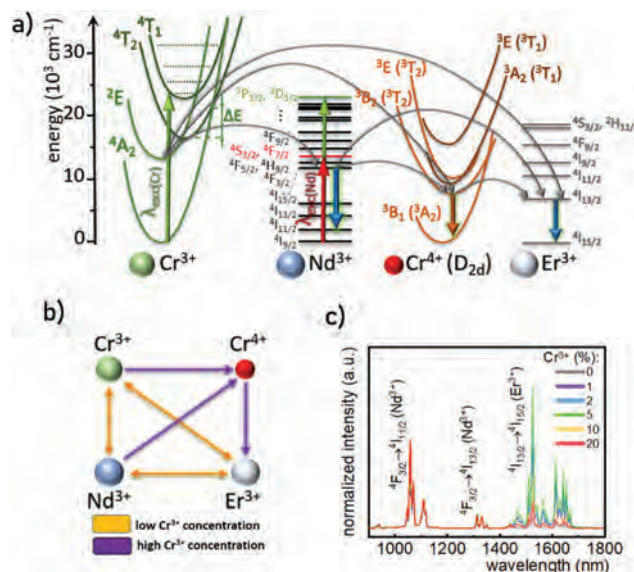
Fig. 2 Configurational coordinate diagram for Cr^{3+}, Nd^{3+}, Cr^{4+} and Er^{3+} ions (a); the schematic diagram explaining the directions of the energy transfer between dopant ions at low and high Cr^{3+} concentrations obtained at λ_{exc} = 445 nm (b); and the comparison of the low temperature (123 K) emission spectra of YAG:1%Nd^{3+},1%Er^{3+},x%$Cr^{3+/4+}$ powders with different Cr^{3+} concentrations (c).

Cr^{4+} with the energy level diagrams of Nd^{3+} and Er^{3+} ions are presented in Fig. 2a. The YAG:Nd^{3+},Er^{3+},$Cr^{3+/4+}$ powders were excited at λ_{exc} = 445 nm ($\sim$22 500 cm^{-1}), represented by the green arrow, to match the $^4A_2 \rightarrow {}^4T_1$ electronic transition of Cr^{3+} ions. For powders without Cr^{3+}, at this wavelength, weak absorption takes place *via* the $^4I_{9/2} \rightarrow ({}^2P_{1/2}, {}^2D_{5/2})$ electronic transition of Nd^{3+} ions which populates the high energy Nd^{3+} levels followed by the fast non-radiative transitions to the $^4F_{3/2}$ metastable state. The radiative depopulation of this multiplet generates three characteristic emission bands at 880 nm, 1064 nm and 1350 nm corresponding to the $^4F_{3/2} \rightarrow {}^4I_{9/2}$, $^4F_{3/2} \rightarrow {}^4I_{11/2}$ and $^4F_{3/2} \rightarrow {}^4I_{13/2}$ electronic transitions respectively. However, when the distance between Nd^{3+} and Er^{3+} ions is sufficiently short, the $Nd^{3+} \rightarrow Er^{3+}$ energy transfer may occur *via* the $^4I_{11/2}$ state of Er^{3+}, which followed by non-radiative processes leads to the population of the $^4I_{13/2}$ state of Er^{3+} ions. The radiative depopulation of this state *via* the $^4I_{13/2} \rightarrow {}^4I_{15/2}$ electronic transition generates the emission band at 1550 nm. The energy mismatch between the $^4F_{3/2}$ state of Nd^{3+} ions and the $^4I_{13/2}$ state of Er^{3+} ions makes the inter-ionic energy transfer feasible to occur only with the assistance of the phonon. The probability of such a process is strongly dependent on the temperature which makes such a system especially interesting from the thermometric perspective.

However, when the Cr^{3+} co-dopant ions are introduced into the host material, their significantly higher absorption cross section at this excitation wavelength makes sensitization of lanthanide ions more probable with respect to their direct excitation. In this case, the absorption at the 445 nm excitation wavelength populates the $^4T_1$ state which is followed by non-radiative transitions resulting in the population of the ^2E state of Cr^{3+} ions. The emission band at 712 nm originates mainly

from the $^2E \rightarrow {^4A_2}$ electronic transition in Cr^{3+} ions with small contribution from the $^4T_2 \rightarrow {^4A_2}$ spin-allowed transition. From the ^2E state of Cr^{3+} ions, the $Cr^{3+} \rightarrow Nd^{3+}$ and $Cr^{3+} \rightarrow Er^{3+}$ energy transfers can occur and they are phonon-assisted due to the energy mismatch. The specific energy level configuration of Cr^{4+} ions enables them to act as mediators in the energy transfer between Nd^{3+} and Er^{3+} ions. For that matter, the $^3B_2$ ($^3T_2$) excited state of the Cr^{4+} ions may be populated either by the $Cr^{3+} \rightarrow Cr^{4+}$ or $Nd^{3+} \rightarrow Cr^{4+}$ energy transfer. The electrons populating the $^3B_2(^3T_2)$ state can be either transferred non-radiatively to the $^4I_{13/2}$ state of Er^{3+} ions or radiatively transferred to the ground state of Cr^{4+} ions *via* the $^3B_2(^3T_2) \rightarrow {^3B_1(^3A_2)}$ electronic transition. The presence of Cr^{4+} ions in the samples was confirmed on account of the low-intensity emission band from the $^3B_2(^3T_2) \rightarrow {^3B_1(^3A_2)}$ transition observed around 1400 nm at low temperatures (see Fig. S3, ESI†). However, this emission rapidly disappeared due to a strong thermal quenching. As already stated, the number of Cr^{4+} ions is proportional to the number of introduced Cr^{3+} ions, and their number observed for the low Cr^{3+} concentration may be neglected. The direction of the inter-ionic energy transfer observed in this system has been schematically depicted in Fig. 2b. At low Cr^{3+} dopant concentration, the sensitization of Nd^{3+} and Er^{3+} ions *via* Cr^{3+} is a dominant process while at a higher Cr^{3+} amount the mediation of the energy transfer *via* Cr^{4+} ions starts to be activated. The comparison of the emission spectrum of YAG:Nd^{3+},Er^{3+},$Cr^{3+/4+}$ powders normalized to the emission intensity of the $^4F_{3/2} \rightarrow {^4I_{11/2}}$ emission band of Nd^{3+} ions, shown in Fig. 2c, revealed that the increase of the Cr^{3+} ions up to 5% results in a gradual increase of the intensity of the band associated with the $^4I_{13/2} \rightarrow {^4I_{15/2}}$ electronic transition of Er^{3+} ions with respect to the Nd^{3+} emission intensity. A further Cr^{3+} increase causes the lowering of its intensity.

Co-doping with Cr^{3+} has a significant effect on the excitation properties. Excitation spectra recorded for Nd^{3+} emission ($^4F_{3/2} \rightarrow {^4I_{11/2}}$ transition) for non co-doping with Cr^{3+} and co-doping with 20% of Cr^{3+} ions are shown in Fig. 3a. Both spectra are normalized to the intensity of the strongest Nd^{3+} excitation band, which is related to the $^4I_{9/2} \rightarrow {^4F_{5/2}},^2H_{9/2}$ electronic transition of Nd^{3+} ions. In the excitation spectra of YAG:Nd^{3+},Er^{3+} powders monitored at Nd^{3+} emission $\lambda_{em} = 1064$ nm the numerous narrow bands which can be assigned to the transitions from the $^4I_{9/2}$ level to the $^4D_{3/2}$ (353.5 nm), $^2P_{1/2}$ (431 nm), $^2K_{15/2}$ and $^4G_{11/2}$ (458.5 nm), $^2K_{13/2}$ and $^4G_{9/2}$ (510 nm), $^4G_{7/2}$ (523.5 nm), $^4G_{5/2}$ (578 nm), $^4F_{9/2}$ (675 nm), $^4F_{7/2}$ (736 nm), $^2H_{9/2}$ and $^4F_{5/2}$ (795 nm) (Fig. 3a and Fig. S4a, ESI†) excited levels can be observed. However, the fact that some additional bands originated from the electronic transitions of Er^{3+} ions like $^4I_{15/2} \rightarrow {^4F_{7/2}}$ (480.5 nm), $^4I_{15/2} \rightarrow {^2H_{11/2}}$ (518 nm), $^4I_{15/2} \rightarrow {^4S_{3/2}}$ (530.5 nm), and $^4I_{15/2} \rightarrow {^4I_{9/2}}$ (804 nm) can be found confirms the $Er^{3+} \rightarrow Nd^{3+}$ energy transfer. In the samples co-doped with 20% $Cr^{3+/4+}$, the two wide band characteristics of the $^4A_2 \rightarrow {^4T_1}$ electronic transitions of Cr^{3+} appear. The peak intensity of these two bands for 20% $Cr^{3+/4+}$
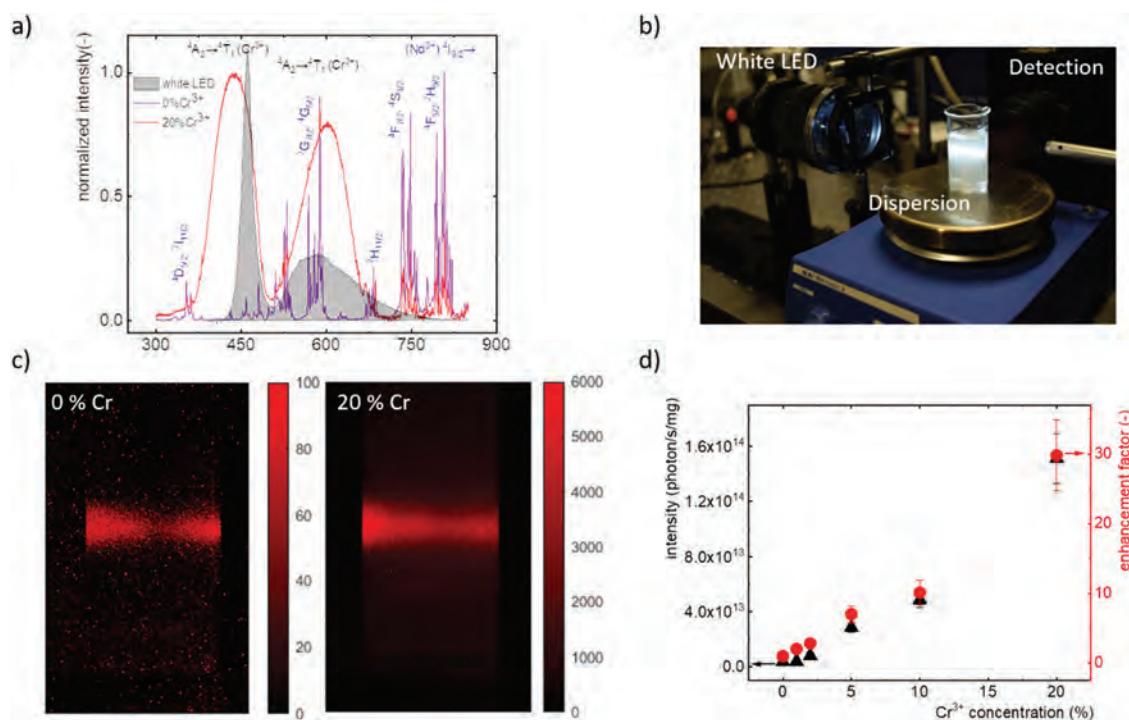
Fig. 3 Excitation spectra measured for Nd^{3+} emission ($\lambda_{em} = 1064$ nm) in YAG:1%Nd^{3+},1%Er^{3+} and YAG:1%Nd^{3+},1%Er^{3+},20%$Cr^{3+}/^{4+}$ powders, and the emission spectrum of the white LED used (a). Setup for quantitative luminescence emission measurements from dispersed particles (b). Filtered luminescence image from dispersion for YAG:1%Nd^{3+},1%Er^{3+} and YAG:1%Nd^{3+},1%Er^{3+},20%$Cr^{3+/4+}$ (c). Absolute emission intensity at 1064 nm for white light illumination (930 mW cm^{-2}) and derived enhancement factor. Error bars are derived from repeated measurements (d).

is more than 2 times higher than that of the narrow $^4I_{9/2} \rightarrow {}^4F_{5/2}$, $^2H_{9/2}$ transitions of Nd^{3+}. To quantify both the effect of the increase in width and the peak of the excitation bands, the contribution parameter δ is proposed as a function of $Cr^{3+/4+}$ concentration with the following equation (Fig. S4b, ESI†):

$$\delta = \frac{\int I\left(^4A_2 \rightarrow {}^4T_1\right)\left(Cr^{3+}\right)d\lambda}{\int I\left(^4I_{9/2} \rightarrow {}^4F_{7/2}\right)\left(Nd^{3+}\right)d\lambda}. \tag{1}$$

The obtained results indicate that the intensity of the $^4A_2 \rightarrow {}^4T_1$ band at 445 nm is almost 50-fold more intense with respect to the $^4I_{9/2} \rightarrow \left(^2P_{1/2}, {}^2D_{5/2}\right)$ band of Nd^{3+} ions (see Fig. S4, ESI†).

In addition, in the Cr^{3+}, Er^{3+}, Nd^{3+} co-doped case the $Cr^{3+} \rightarrow Er^{3+}$ energy transfer can be observed corroborating the sensitization of Er^{3+} luminescence by Cr^{3+} ions. Interestingly, one can notice that the increase of the Cr^{3+} concentration results also in the spectral shift of the absorption bands toward longer wavelengths which indicates the lowering of the crystal field strength. A similar effect has been already reported for the Cr^{3+} doped garnets.[48] The excitation spectra were measured also for Cr^{3+} ions, by monitoring the luminescence at 708 nm (Fig. S4d, ESI†). The obtained results revealed the presence of the reabsorption peaks on the absorption bands of Cr^{3+} ions corresponding to the 4f–4f electronic transition of Nd^{3+} ions, and thus the nonradiative nature of the energy transfer between these ions was revealed.

To quantify unambiguously the increased brightness that Cr^{3+} sensitisation offers to luminescent thermometers, the absolute emission intensity of the 1064 nm band was quantified by probing dilute particle dispersions using the setup shown in Fig. 3b. This state avoids complex scattering and re-absorption phenomena which make it difficult to quantify increased absorption when probing phosphors in bulk powders. It also allows absolute quantification of the light emitted by each particle.[26] Excitation with a white LED was chosen to efficiently excite both Nd^{3+}/Er^{3+} and Cr^{3+} bands as shown in Fig. 3a, so as to offer a fairer comparison. A comparison based on narrow laser illumination would strongly depend on the match of the laser wavelength with narrow Nd^{3+}/Er^{3+} excitation features. To visualize the luminescence beam and reject the beam of scattered white light shown in Fig. 3(b), images were recorded with a 1000 nm long-pass IR filter and are shown in Fig. 3(c) for both 0% and 20% Cr^{3+} dopant concentrations. As shown, the luminescence emission is more than one order of magnitude larger for the sample co-doped with Cr^{3+} than for the sample without Cr^{3+} co-doping. Quantitative spectroscopic measurements show that for an excitation power of 930 mW cm^{-2}, the absolute emission intensity at 1064 nm increases from 5×10^{12} photons per s per mg for a sample without Cr^{3+} to 1.6×10^{14} photons per s per mg for 20% $Cr^{3+/4+}$, corresponding to an enhancement by a factor of 30 (Fig. 3d). The emission intensity increases quasi linearly with Cr^{3+} concentration. These results confirm the positive impact of co-doping of YAG:1%Nd^{3+},1%Er^{3+} with Cr^{3+}, benefiting from the larger absorption cross section of Cr^{3+} than those of Nd^{3+}/Er^{3+} ions, and the efficient $Cr^{3+} \rightarrow Nd^{3+}/Er^{3+}$ energy transfer.

As already stated, the probability of the $Nd^{3+} \rightarrow Er^{3+}$ phonon assisted energy transfer is strongly temperature dependent. An increase in temperature results in the gradual lowering of the emission intensity of the Nd^{3+} band associated with the $^4F_{3/2} \rightarrow {}^4I_{11/2}$ electronic transition and in a simultaneous increase in the intensity of the $^4I_{13/2} \rightarrow {}^4I_{15/2}$ band of Er^{3+} ions as shown in Fig. 4a (see Fig. S5, ESI†). To evaluate the influence of Cr^{3+} dopant concentration on the thermal changes of the emission
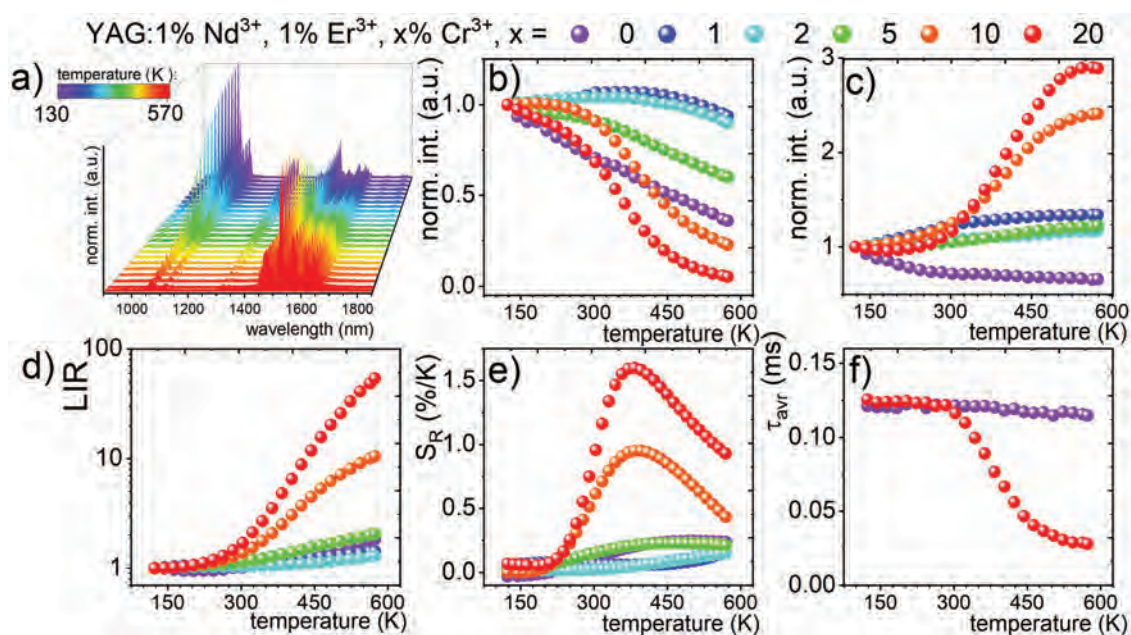
Fig. 4 Thermal evolution of emission spectra of YAG:1%Nd^{3+},1%Er^{3+},20%$Cr^{3+/4+}$ (a); thermal evolution of integral emission intensities of the $^4F_{3/2} \rightarrow {}^4I_{11/2}$ emission band of the Nd^{3+} ion (b) and $^4I_{13/2} \rightarrow {}^4I_{15/2}$ emission band of the Er^{3+} ion (c); LIR (d) and S_R for different $Cr^{3+/4+}$ concentrations (e); and the comparison of the thermal dependence of τ_{avr} for the Nd^{3+} $^4F_{3/2}$ emission in YAG:1%Nd^{3+},1%Er^{3+} and YAG:1%Nd^{3+},1%Er^{3+},20%Cr^{3+} (f).

intensities of Nd^{3+} and Er^{3+} ions their integral emission intensities measured as a function of temperature were calculated (Fig. 4b and c for emission intensities of Nd^{3+} and Er^{3+} ions, respectively). It was found that in the case of non co-doped with Cr^{3+} powders the Nd^{3+} emission intensity obtained at λ_{exc} = 445 nm decreases gradually reaching at 573 K 40% of its intensity at 123 K. However, the introduction of Cr^{3+} strongly affects the thermal dependence of Nd^{3+} ions. Initially for 1% Cr^{3+} and 2% Cr^{3+} the increase of temperature results in a slight enhancement followed by the quenching of Nd^{3+} intensity. A further increase of the dopant concentration enhances the thermal quenching of Nd^{3+} ions leading to the situation where for 20% of Cr^{3+} above 300 K rapid thermal quenching occurs. In the case of the Er^{3+} emission intensity, the influence of Cr^{3+} on the thermal behavior is totally different. A slow quenching is found in the case of Nd^{3+}, Er^{3+} powders not co-doped with Cr^{3+}. Upon addition of Cr^{3+} concentration, the Er^{3+} emission intensity is thermally enhanced. For the powders doped with 20% of Cr^{3+}, a 3-fold enhancement of the $^4I_{13/2} \rightarrow {}^4I_{15/2}$ emission band was noticed in the 123–573 K temperature range. To provide a deeper insight into the mechanism responsible for such changes in the thermal dependences of the emission intensity of those lanthanide ions, an additional measurement was performed in which direct Nd^{3+} excitation was used (λ_{exc} = 793 nm, see Fig. S6 and S7, ESI†). It was found that for the Cr^{3+} concentration below 5%, the quenching of the Nd^{3+} emission is independent of the co-dopant amount. This suggests that the changes of the Nd^{3+} emission intensity observed upon λ_{exc} = 445 nm excitation results from the $Cr^{3+} \rightarrow Nd^{3+}$ sensitization process. The analogous emission intensity of Er^{3+} ions was barely dependent on the Cr^{3+} amount for low co-dopant concentration. However, when the Cr^{3+} amount exceeds 10% the quenching rate of Nd^{3+} becomes faster, while the enhancement of the Er^{3+} emission intensity was observed above 373 K. This effect can be explained in the statistical increase amount of Cr^{4+} ions which mediates in the exchange of energy between Nd^{3+} and Er^{3+} ions. The opposite thermal dependency of Nd^{3+} and Er^{3+} emission intensities can be utilized in the ratiometric approach of luminescence thermometry where their ratio (LIR) is used as a thermometric parameter:

$$\text{LIR} = \frac{\int I\left(Nd^{3+}\right)d\lambda}{\int I\left(Er^{3+}\right)d\lambda} = \frac{\int \left({}^4F_{3/2} \rightarrow {}^4I_{11/2}\right)d\lambda}{\int \left({}^4I_{13/2} \rightarrow {}^4I_{15/2}\right)d\lambda} \qquad (2)$$

The calculated values of the LIR for increased concentration of Cr^{3+} ions presented in Fig. 4d reveal that while only a 2-fold increase of the LIR over the 123–573 K temperature range was found for the non co-doped with Cr^{3+} powders, an 80-fold increase was observed for 20% Cr^{3+} (see Fig. S8, ESI†). To quantify the observed changes, the relative sensitivity was calculated according to the following formula:

$$S_R = \frac{1}{\Omega} \cdot \frac{\Delta\Omega}{\Delta T} \times 100\%, \qquad (3)$$

where Ω is the thermometric parameter (in this case the LIR) and $\Delta\Omega$ represents its change for the ΔT change of temperature (Fig. 4e). The maximal value of the S_R for powders doped only

with Nd^{3+} and Er^{3+} ions was found to be 0.25% K^{-1} at 468 K, while its value increases up to 1.67% K^{-1} at 300 K when 20% of Cr^{3+} was introduced in the host. The drastic difference in the thermal behavior of the Er^{3+} and Nd^{3+} intensities between 5%Cr^{3+} and 10%Cr^{3+} doping, which is reflected by the strong increase in S_R, coincides with the level of doping where the presence of Cr^{4+} was noticed. This shows that both Cr^{3+} and Cr^{4+} ions beneficially influenced the thermometric properties of the Nd^{3+}, Er^{3+} based luminescent thermometer. The Cr^{4+} ions may modify the thermal dependence of Nd^{3+} emission intensity in two possible ways: (i) by depopulation of the $^4F_{3/2}$ state of Nd^{3+} or (ii) by the additional sensitization process as a $Cr^{4+} \rightarrow Ln^{3+}$ energy transfer. To verify which of these processes is dominant the luminescence decay profiles of the $^4F_{3/2}$ state were measured for the samples without and with 20% Cr^{3+} ions (Fig. 4f, see also Fig. S9 and S10, ESI†). The thermal dependence of the average lifetimes indicates that the $^4F_{3/2}$ state is barely shortened in the analyzed temperature range, while for the samples with the high Cr^{3+} doping, its lifetime undergoes drastic shortening above 300 K reaching τ_{avr} = 28 μs at 573 K (τ_{avr} = 120 μs was noticed at 123 K). The fact that the τ_{avr} of the $^4F_{3/2}$ state of the Nd^{3+} ions in the YAG:Nd^{3+},Er^{3+} phosphor is barely dependent on temperature is the result of the low efficiency of its thermal depopulation by nonradiative processes in the considered temperature range. This is in agreement with the previously reported results according to which the thermal shortening of the $^4F_{3/2}$ lifetime is not evident at temperatures below 650 K.[49,50] The fact that at the same time the lifetime of the $^4I_{13/2}$ state is thermally stable independently of Cr^{3+} concentration (except the powder with 20% Cr^{3+}) (Fig. S11 and S12, ESI†) confirms that the Cr^{4+} mediates in the transfer of the energy between ions beneficially influencing the thermometric properties of the luminescent thermometer based on the LIR. The shortening of the lifetime of the $^4F_{3/2}$ state of the Nd^{3+} ions observed at elevated temperatures for the samples co-doped with 20% of the Cr^{3+} ions can also be explained by a $Nd^{3+} \rightarrow Cr^{3+}$ back energy transfer. Unfortunately, due to the shorter lifetime of the Nd^{3+} emitting state than that of the ^2E state of Cr^{3+}, the thermal behaviour of the lifetime cannot support or refutes this hypothesis. However, back energy transfer cannot explain the significant thermal enhancement of the Er^{3+} emission intensity shown in Fig. 4c. On the other hand, the more probable hypothesis is that the presence of Cr^{4+} induces the $Nd^{3+} \rightarrow Cr^{3+} \rightarrow Er^{3+}$ energy transfer, which results in both the shortening of the $^4F_{3/2}$ state lifetime and an enhancement of the Er^{3+} emission intensity at elevated temperatures. Additionally, the temperature determination uncertainty was found to be lower than δT = 0.2 K in the range of 303–573 K for YAG:Nd^{3+},Er^{3+},$Cr^{3+/4+}$ powders (eqn (3) and Fig. S13, ESI†).

The strong susceptibility of the τ_{avr} of the $^4F_{3/2}$ state of Nd^{3+} to temperature changes indicates that the high concentration of Cr^{3+} and Cr^{4+} ions may also be beneficial for the thermometric parameters of the lifetime-based luminescence thermometry. The most spectacular changes in the luminescence decay profiles at elevated temperatures were observed when
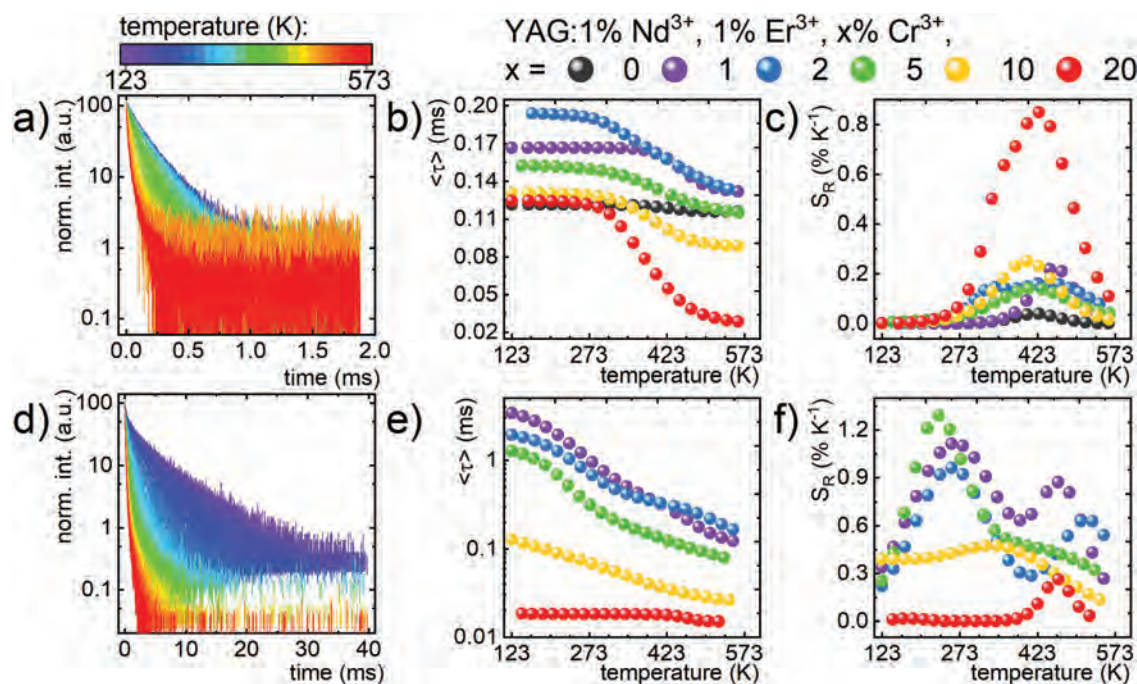
Fig. 5 The luminescence decay profiles of the Nd^{3+} ions ($^4F_{3/2}$ state λ_{em} = 1064 nm) for YAG:1%Nd^{3+},1%Er^{3+},20%$Cr^{3+/4+}$ (a); thermal dependence of τ_{avr} of this state (b) and corresponding S_R (c); the luminescence decay profiles of the Cr^{3+} ions (^2E state, λ_{em} = 712 nm) for the YAG:1%Nd^{3+},1%Er^{3+},1%Cr^{3+} (d); thermal dependence of τ_{avr} of this state (e) and corresponding S_R (f).

20% Cr^{3+} ions were used for doping (Fig. 5a). However, even low amounts of Cr^{3+}/Cr^{4+} ions activate the shortening of the τ_{avr}, as can be seen in Fig. 5b. An enlargement of the Cr^{3+} amount gradually shortens the τ_{avr} at elevated temperatures. This effect is reflected in the S_R determined based on the kinetics of the excited state, which increases from the S_R = 0.042% K^{-1} at 423 K for YAG:Nd^{3+},Er^{3+} to 0.86% K^{-1} at the same temperature for YAG:Nd^{3+},Er^{3+},$Cr^{3+/4+}$ powders. This spectacular 20-fold enhancement of the relative sensitivity undoubtedly confirms that the presence of Cr^{4+} ions has an extremely favorable effect on the thermometric parameters of luminescent thermometers operating in ratiometric and lifetime-based approaches. It is worth emphasizing that contrary to often observed cases, the presence of the quenching ions (in this case Cr^{4+} ions) does not lead to the quenching of the low temperature τ_{avr} values. This is a very important finding since the duration of the decay time predefines the maximal available acquisition time in the thermal imaging and, hence, the intensity of the signal collected. The fact that Cr^{3+} ions so efficiently sensitize the Nd^{3+} and Er^{3+} luminescence should lead to the shortening of the lifetime of its ^2E excited state (Fig. S14 and S15, ESI†). According to the expectation, a decrease in the lifetime of the ^2E upon doping with Nd^{3+} and Er^{3+} was observed, as shown in Fig. 5d. The lifetime τ_{avr} measured at 123 K decreases slowly from 1 to 5% Cr^{3+} and then by an order of magnitude from 5 to 10% and another from 10% to 20%, as a result of the $Cr^{3+} \rightarrow Ln^{3+}$ energy transfer. The lifetime is also temperature dependent, which is also observed for YAG:Cr^{3+} particles. The Cr^{3+} concentration has a small influence on this temperature dependence for 1 to 5%, and this response has the highest S_R, S_R = 1.28% K^{-1} at

253 K for a dopant concentration of 5% of Cr^{3+}. Above 10%, the temperature dependence of the lifetime ^2E is much less pronounced than for lower concentration.

To summarize, the presented results confirm the advantageous influence of the Cr^{3+},Cr^{4+} co-doping on the emission intensity and the thermometric properties of the ratiometric Nd^{3+}, Er^{3+} and the lifetime-based ($^4F_{3/2}$ state of Nd^{3+} ions) luminescent thermometers in YAG:Nd^{3+},Er^{3+},$Cr^{3+/4+}$ powders.

4. Conclusions

The influence of $Cr^{3+/4+}$ ions as a sensitizer of luminescence (Cr^{3+}) and as a mediator in the energy exchange (Cr^{4+}) were investigated for the improvement of luminescence and thermometric parameters in YAG:Nd^{3+},Er^{3+} powders. It was found that due to the significantly higher absorption cross section of Cr^{3+} ions with respect to the Nd^{3+} ones, the introduction of the Cr^{3+} ions into the YAG:Nd^{3+},Er^{3+} powders enhances *via* the $Cr^{3+} \rightarrow Nd^{3+}/Er^{3+}$ sensitization process the emission intensity of Nd^{3+} and Er^{3+} upon white light excitation by a factor of 30 with respect to samples without Cr^{3+} doping. Moreover, it was noticed that for higher Cr^{3+} concentration the oxidation of chromium ions to Cr^{4+} and even Cr^{6+} was observed. Hence the presence of chromium ions leads to the improvement of the thermometric properties of the Nd^{3+},Er^{3+} ratiometric luminescent thermometer by the superposition of two effects: the temperature dependence of the phonon-assisted $Cr^{3+} \rightarrow Nd^{3+}$ and $Cr^{3+} \rightarrow Er^{3+}$ energy transfer processes and the mediation of the Cr^{4+} ion in the energy exchange between lanthanide ions *via*

the $Nd^{3+} \rightarrow Cr^{4+} \rightarrow Er^{3+}$ energy transfer process, which is observed at higher Cr^{3+} concentration. As a result the relative sensitivity of the ratiometric luminescent thermometer based on the Er^{3+} and Nd^{3+} emission increased by 700% from 0.25% K^{-1} at 468 K for YAG:Nd^{3+},Er^{3+} to 1.67% K^{-1} at 300 K for YAG:Nd^{3+},Er^{3+},20%$Cr^{3+/4+}$. Moreover, the presence of the Cr^{4+} ions induces the additional thermally activated depopulation channel of the $^4F_{3/2}$ state of Nd^{3+} which enables the development of a highly sensitive luminescent thermometer based on the lifetime of the $^4F_{3/2}$ excited state of Nd^{3+} ions on the highest sensitivity, enhanced by 2000% with respect to the non co-doped with $Cr^{3+/4+}$ powders, reached at 423 S_R = 0.86% K^{-1}. Notably, the presence of the Cr^{4+} ions does not affect the value of the low temperature lifetime of the $^4F_{3/2}$ state. Additionally the efficient $Cr^{3+} \rightarrow Nd^{3+}/Er^{3+}$ energy transfer process leads to the shortening of the ^2E lifetime of the Cr^{3+} ions which can be exploited for the development of the lifetime based luminescent thermometer with the highest S_R = 1.28% K^{-1} at 253 K notified for the YAG:Nd^{3+},Er^{3+},5%$Cr^{3+/4+}$ ions. This research clearly confirms the highly beneficial influence of the co-doping process with Cr^{3+}/Cr^{4+} ions on the emission intensity as well as the thermometric properties of the luminescent thermometers operating in the ratiometric and temporal approaches. This material holds significant promise as a sensitive and robust NIR thermometer operating in the physiological temperature range. However, before its biomedical application, several factors of the phosphor itself, like the size of the particles, need to be optimized. Therefore, in further works, the optimization of these parameters will be considered to demonstrate the thermometric performance of this kind of luminescent thermometer.

Conflicts of interest

There are no conflicts to declare.

Acknowledgements

References

1 M. Runowski, P. Wozny, N. Stopikowska, I. R. Martín, V. Lavín and S. Lis, *ACS Appl. Mater. Interfaces*, 2020, **12**, 43933–43941.

2 M. Runowski, J. Marciniak, T. Grzyb, D. Przybylska, A. Shyichuk, B. Barszcz, A. Katrusiak and S. Lis, *Nanoscale*, 2017, **9**, 16030–16037.

3 M. Runowski, A. Shyichuk, A. Tymiński, T. Grzyb, V. Lavín and S. Lis, *ACS Appl. Mater. Interfaces*, 2018, **10**, 17269–17279.

4 A. M. Kaczmarek, M. Suta, H. Rijckaert, A. Abalymov, I. Van Driessche, A. G. Skirtach, A. Meijerink and P. Van Der Voort, *Adv. Funct. Mater.*, 2020, **30**, 2003101.

5 M. Suta, Ž. Antić, V. Dordević, S. Kuzman, M. D. Dramićanin and A. Meijerink, *Nanomaterials*, 2020, **10**, 543.

6 A. Benayas, B. Del Rosal, A. Pérez-Delgado, K. Santacruz-Gómez, D. Jaque, G. A. Hirata and F. Vetrone, *Adv. Opt. Mater.*, 2015, **3**, 687–694.

7 A. Nexha, J. J. Carvajal, M. C. Pujol, F. Díaz and M. Aguiló, *Nanoscale*, 2021, **13**, 7913–7987.

8 M. Suta and A. Meijerink, *Adv. Theor. Simul.*, 2020, **3**, 2000176.

9 D. Jaque and F. Vetrone, *Nanoscale*, 2012, **4**, 4301–4326.

10 C. D. S. Brites, S. Balabhadra and L. D. Carlos, *Adv. Opt. Mater.*, 2019, **7**, 1801239.

11 M. D. Dramićanin, *J. Appl. Phys.*, 2020, **128**, 40902.

12 A. Bednarkiewicz, L. Marciniak, L. D. Carlos and D. Jaque, *Nanoscale*, 2020, **12**, 14405–14421.

13 B. Yan, *Acc. Chem. Res.*, 2017, **50**, 2789–2798.

14 B. Alpha, R. Ballardini, V. Balzani, J.-M. Lehn, S. Perathoner and N. Sabbatini, *Photochem. Photobiol.*, 1990, **52**, 299–306.

15 J. Massue, S. J. Quinn and T. Gunnlaugsson, *J. Am. Chem. Soc.*, 2008, **130**, 6900–6901.

16 N. M. Shavaleev, L. P. Moorcraft, S. J. A. Pope, Z. R. Bell, S. Faulkner and M. D. Ward, *Chem. – Eur. J.*, 2003, **9**, 5283–5291.

17 P. K. Tawalare, V. B. Bhatkar, S. K. Omanwar and S. V. Moharil, *J. Alloys Compd.*, 2019, **790**, 1192–1200.

18 T. Härig, G. Huber and I. A. Shcherbakov, *J. Appl. Phys.*, 1981, **52**, 4450–4452.

19 M. Yamaga, Y. Oda, H. Uno, K. Hasegawa, H. Ito and S. Mizuno, *J. Appl. Phys.*, 2012, **112**, 63508.

20 W. Piotrowski, K. Kniec and L. Marciniak, *J. Alloys Compd.*, 2021, **870**, 159386.

21 Z. J. Kiss and R. C. Duncan, *Appl. Phys. Lett.*, 1964, **5**, 200–202.

22 T. Miyakawa and D. L. Dexter, *Phys. Rev. B: Solid State*, 1970, **1**, 2961–2969.

23 M. Back, J. Ueda, M. G. Brik and S. Tanabe, *ACS Appl. Mater. Interfaces*, 2020, **12**, 38325–38332.

24 K. Kniec, W. Piotrowski, K. Ledwa, M. Suta, L. D. Carlos and L. Marciniak, *J. Mater. Chem. C*, 2021, **9**, 6268–6276.

25 K. Elzbieciak, A. Bednarkiewicz and L. Marciniak, *Sens. Actuators, B*, 2018, **269**, 96–102.

26 B. Fond, C. Abram, M. Pougin and F. Beyrau, *Opt. Mater.*, 2019, **89**, 615–622.

27 A. Yoshikawa, G. Boulon, L. Laversenne, H. Canibano, K. Lebbou, A. Collombet, Y. Guyot and T. Fukuda, *J. Appl. Phys.*, 2003, **94**, 5479–5488.

28 T. Epicier, G. Boulon, W. Zhao, M. Guzik, B. Jiang, A. Ikesue and L. Esposito, *J. Mater. Chem.*, 2012, **22**, 18221–18229.

29 G. Blasse and A. Bril, *Appl. Phys. Lett.*, 1967, **11**, 53–55.

30 W. Jia, H. Eilers, W. M. Dennis, W. M. Yen and A. V. Shestakov, in *Advanced Solid State Lasers*, ed. P. Chase, Optical Society of America, Santa Fe, NM, 1992, vol. 13, p. CL8.

31 Z. Burshtein, P. Blau, Y. Kalisky, Y. Shimony and M. R. Kikta, *IEEE J. Quantum Electron.*, 1998, **34**, 292–299.

32 Y. Shimony, Z. Burshtein and Y. Kalisky, *IEEE J. Quantum Electron.*, 1995, **31**, 1738–1741.

33 J. Dong and P. Deng, *J. Lumin.*, 2003, **104**, 151–158.

34 M. Chaika and W. Strek, *J. Lumin.*, 2021, **233**, 117935.

35 M. A. Chaika, A. G. Doroshenko, S. V. Parkhomenko, E. G. Chernomorets, P. V. Mateichenko and R. P. Yavetskiy, *Sci. Res. Refract. Techn. Ceram.*, 2017, **117**, 196–211.

36 M. A. Chaika, P. Dluzewski, K. Morawiec, A. Szczepanska, K. Jablonska, G. Mancardi, R. Tomala, D. Hreniak, W. Strek, N. A. Safronova, A. G. Doroshenko, S. V. Parkhomenko and O. M. Vovk, *J. Eur. Ceram. Soc.*, 2019, **39**, 3344–3352.

37 M. A. Chaika, R. Tomala, W. Strek, D. Hreniak, P. Dluzewski, K. Morawiec, P. V. Mateychenko, A. G. Fedorov, A. G. Doroshenko, S. V. Parkhomenko, K. Lesniewska-Matys, D. Podniesinski, A. Kozłowska, G. Mancardi and O. M. Vovk, *J. Chem. Phys.*, 2019, **151**, 134708.

38 H. Eilers, U. Hömmerich, S. M. Jacobsen, W. M. Yen, K. R. Hoffman and W. Jia, *Phys. Rev. B: Condens. Matter Mater. Phys.*, 1994, **49**, 15505–15513.

39 M. G. Brik, N. M. Avram, C. N. Avram and I. Tanaka, *EPJ Appl. Phys.*, 2005, **29**, 239–245.

40 A. G. Okhrimchuk and A. V. Shestakov, *Opt. Mater.*, 1994, **3**, 1–13.

41 D. Li, S. Zhao, G. Li and K. Yang, *Opt. Laser Technol.*, 2009, **41**, 272–279.

42 Y. Shimony, Z. Burshtein, A. B. Baranga, Y. Kalisky and M. Strauss, *IEEE J. Quantum Electron.*, 1996, **32**, 305–310.

43 Y. Bai, N. Wu, J. Zhang, J. Li, S. Li, J. Xu and P. Deng, *Appl. Opt.*, 1997, **36**, 2468–2472.

44 A. Sugimoto, Y. Nobe and K. Yamagishi, *J. Cryst. Growth*, 1994, **140**, 349–354.

45 K. Kniec and L. Marciniak, *Sens. Actuators, B*, 2018, **264**, 382–390.

46 K. Kniec and L. Marciniak, *Phys. Chem. Chem. Phys.*, 2018, **20**, 21598–21606.

47 J. Drabik, B. Cichy and L. Marciniak, *J. Phys. Chem. C*, 2018, **122**, 14928–14936.

48 K. Elzbieciak and L. Marciniak, *Front. Chem.*, 2018, **6**, 1–8.

49 Y. Honda, S. Motokoshi, T. Jitsuno, N. Miyanaga, K. Fujioka, M. Nakatsuka and M. Yoshida, *J. Lumin.*, 2014, **148**, 342–346.

50 P. Hong, X. X. Zhang, C. W. Struck and B. Di Bartolo, *J. Appl. Phys.*, 1995, **78**, 4659–4667.

Supporting Information

The role of Cr^{3+} and Cr^{4+} in emission brightness enhancement and sensitivity improvements of NIR-emitting Nd[3+]/Er[3+] ratiometric luminescence thermometers

W. Piotrowski[1], L. Dalipi[2], R. Szukiewicz[3], B. Fond[2], M. Dramicanin[4], L. Marciniak[1]*

[1]Institute of Low Temperature and Structure Research, Polish Academy of Sciences, Okólna 2, 50-422 Wroclaw, Poland

[2] Institute of Fluid Dynamics and Thermodynamics, Otto-von-Guericke University Magdeburg, 39106 Magdeburg, Germany

[3] Institute of Experimental Physics, Faculty of Physics and Astronomy, University of Wroclaw, Wroclaw 50-204, Poland

[4]Vinča Institute of Nuclear Sciences - National Institute of the Republic of Serbia, University of Belgrade, P.O. Box 522, Belgrade 11001, Serbia.

* corresponding author: *l.marciniak@intibs.pl*

KEYWORDS luminescent thermometry, triple-doped nanocrystals, sensitization by transition metals, host-sensitizer-emitter systems, lanthanide ions

The integral intensities of the Nd[3+] and Er[3+] bands to calculate LIR values were fitted with Mott-Seitz equation (Eq. S1):

$$I = \frac{I_0}{C \cdot \exp(-\frac{W}{k \cdot T}) + 1}$$ (Eq. S1)

where: I – the intensity in temperature T, I_0 – the intensity in the initial temperature, W - the activation energy, k – Boltzmann constant, C – the dimensionless constant

The average lifetime of the excited states were calculated with the equation Eq. S2:

$$\langle \tau \rangle = \frac{A_1 \tau_1^2 + A_2 \tau_2^2}{A_1 \tau_1 + A_2 \tau_2}$$ (Eq. S2a)

where: τ_1, τ_2 – the average time, which is in accordance with the relation $\tau = t \cdot \ln(2)$ and A_1, A_2 – amplitude, which are the parameters of the doubleexponential function:

$$y = y_0 + A_1 \cdot \exp(-\frac{x}{t_1}) + A_2 \cdot \exp(-\frac{x}{t_2}) \qquad \text{(Eq. S2b)}$$

Temperature determination uncertainty was calculated using Eq. S6:

$$\delta T = \frac{1}{S_R} \cdot \frac{\delta LIR}{LIR} \qquad \text{(Eq. S3a)}$$

S_R is the relative sensitivity and $\delta LIR/LIR$ determines the uncertainty of the LIR determination, where $\delta LIR/LIR$ was determined as follows:

$$\frac{\delta LIR}{LIR} = \sqrt{\left(\frac{\delta I_{Tb}}{I_{Tb}}\right)^2 + \left(\frac{\delta I_{Eu}}{I_{Eu}}\right)^2} \qquad \text{(Eq. S3b)}$$

Table S1. The Rietveld refinement parameters of XRD patterns for YAG:Nd^{3+}, Er^{3+}, $Cr^{3+/4+}$ powders

Sample	Rexp	Rprofile	weigth R profile	D statisctics	weight S-Statistics
YAG:1%Nd^{3+}, 1%Er^{3+}	1.52919	1.96616	3.1929	1.33710	1.07269
YAG:1%Nd^{3+}, 1%Er^{3+}, 1%Cr^{3+}	1.55303	3.36102	4.73781	0.40631	0.25277
YAG:1%Nd^{3+}, 1%Er^{3+}, 2%Cr^{3+}	1.53677	2.51937	3.52202	0.70730	0.49693
YAG:1%Nd^{3+}, 1%Er^{3+}, 5%Cr^{3+}	1.52759	2.66131	3.75056	0.57502	0.39426
YAG:1%Nd^{3+}, 1%Er^{3+}, 10%Cr^{3+}	1.55828	1.66312	2.39261	0.81267	0.73250
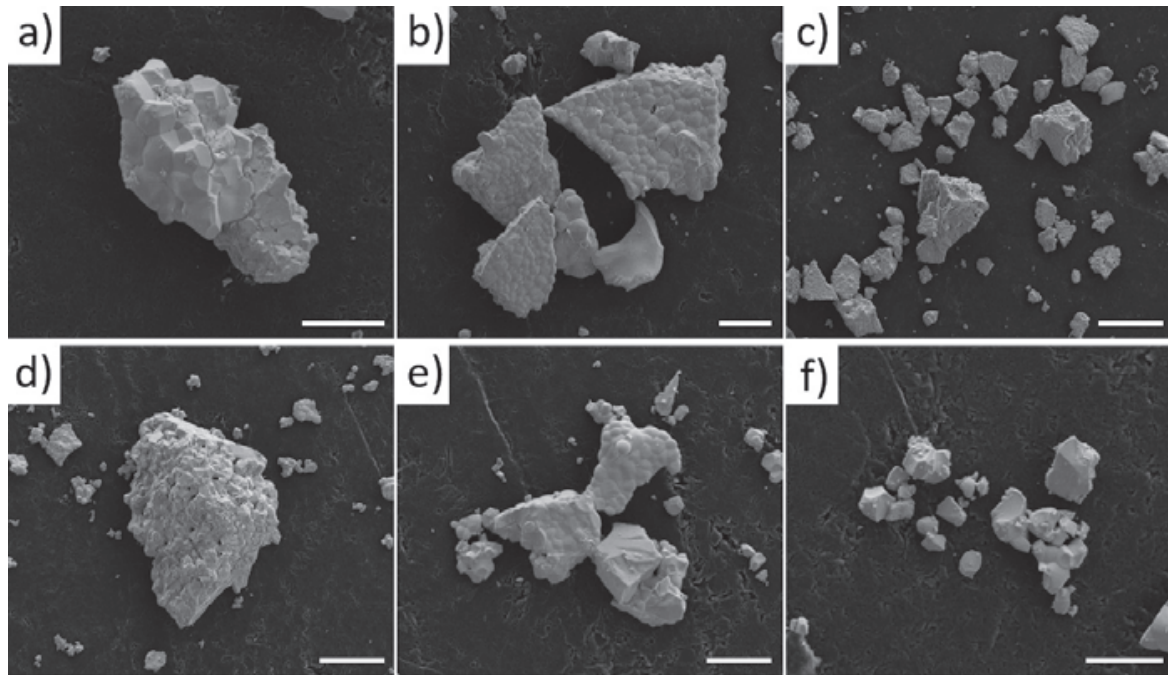
Figure S1. The representative SEM images of YAG:Nd^{3+}, Er^{3+} – scale bar: 4 µm (a), 5 µm (b), 20 µm (c) and YAG:Nd^{3+}, Er^{3+}, 10% $Cr^{3+/4+}$ – scale bar: 10 µm (d), 5 µm (e), 3 µm (f).

YAG:1%Nd^{3+}, 1%Er^{3+}, 20%Cr^{3+}	1.56894	1.82007	2.74488	0.78064	0.69035

Table S2. Atomic concentration of the surface of the analysed samples by EDS method.

| | YAG:1% Nd^{3+}, 1%Er^{3+}, | | | | | |
| | Cr$^{3+/4+}$-unco-doped | | | doped with 10% Cr$^{3+/4+}$ | | |
Element	at% (%)	+/-	r_{conc} (%)	at% (%)	+/-	r_{conc} (%)
Y	13.630	0.166		14.097	0.284	
Nd	0.180	0.022	1.321	0.187	0.045	1.324
Er	0.163	0.012	1.198	0.180	0.008	1.277
Al	25.877	0.337		24.773	0.198	
Cr	-	-		1.947	0.123	7.858
O	60.147	0.373		58.817	0.358	

at% - atomic percentage
r_{conc} – the ratio of the dopant concentration in respect to the content of the element which it substitutes (Nd, Er substitutes Y sites, Cr substitutes Al sites)
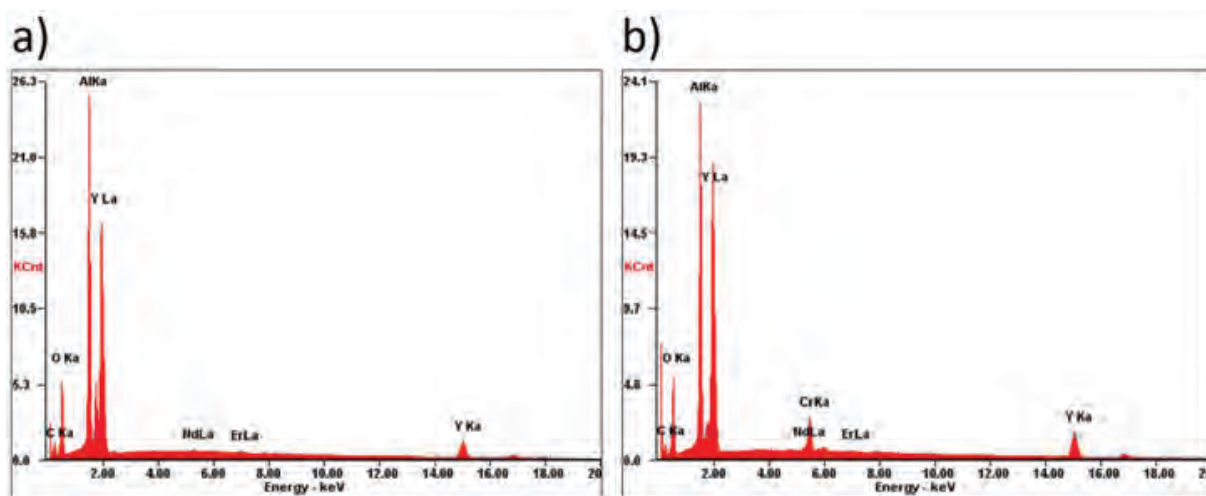
Figure S2. The representative EDS spectra for YAG:Nd^{3+}, Er^{3+} (a) and YAG:Nd^{3+}, Er^{3+}, 10% Cr$^{3+/4+}$ (b).

190

Table S3. Atomic concentration from the analyzed samples by XPS method.

	The concentration of elements for the YAG:1% Nd^{3+}, 1% Er^{3+}, x% $Cr^{3+/4+}$ samples (%):			
Element	x = 1%	x = 5%	x = 10%	x = 20%
Al	11.74	12.97	10.4	7.25
Y	6.73	8.21	6.9	4.6
C	40.25	32.23	43.28	50
O	36.58	42.24	35.07	34.1
N	4.54	4.17	3.96	3.48
Cr	0	0.17	0.39	0.56
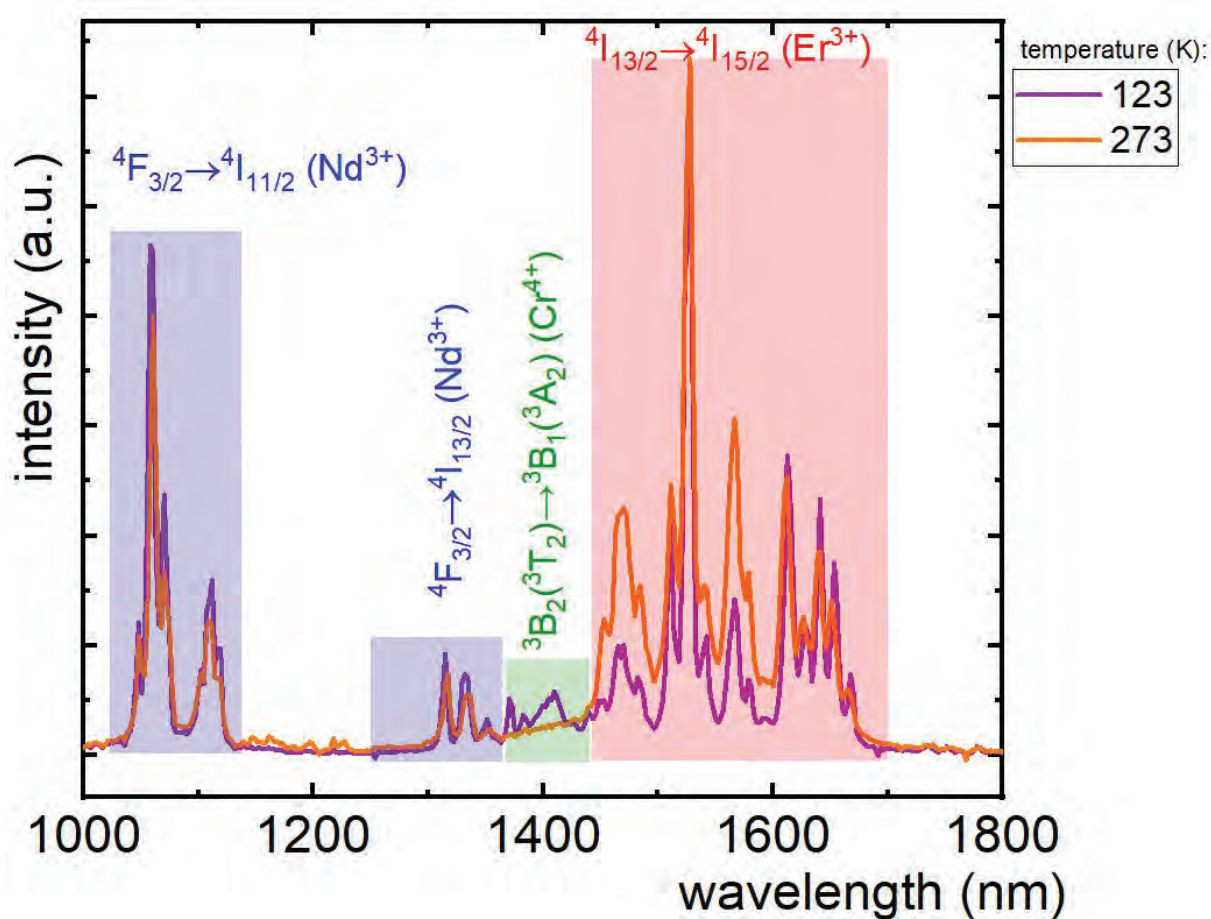
Figure S3. The emission spectra of YAG:1% Nd^{3+}, 1% Er^{3+}, 5% $Cr^{3+/4+}$ at 123 K and at 273K .
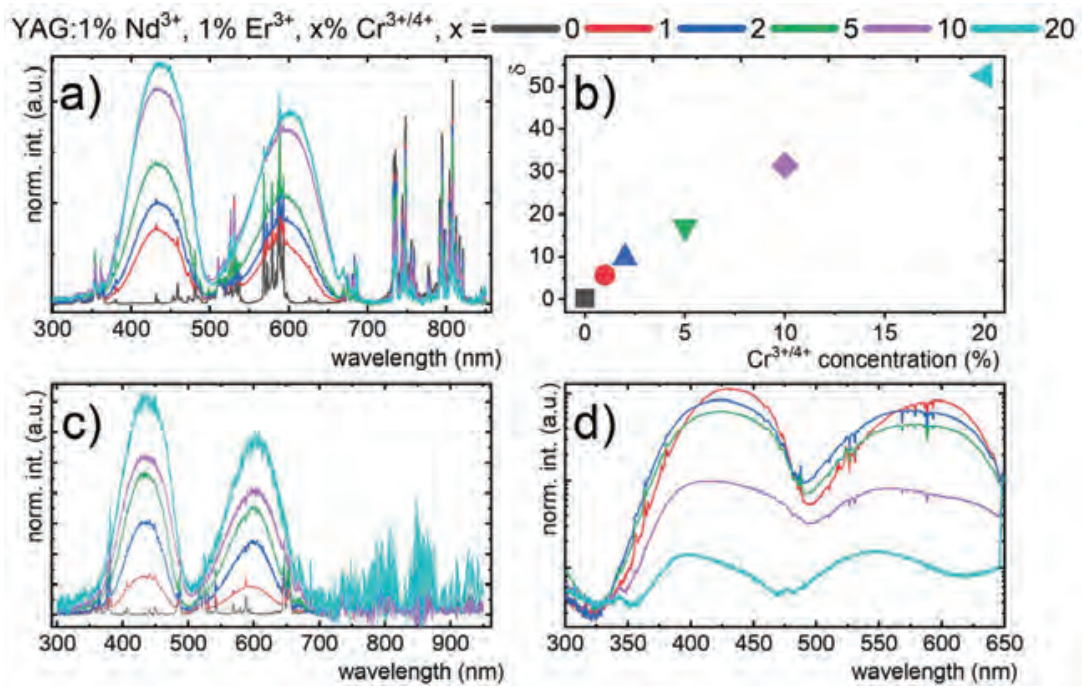
Figure S4. The influence of $Cr^{3+/4+}$ ions concentration on excitation spectra in YAG:1% Nd^{3+}, 1% Er^{3+}, x% $Cr^{3+/4+}$ for 1064 nm (a) and on the contribution parameter δ (b), for 1530 nm (c) and for 445 nm (d).
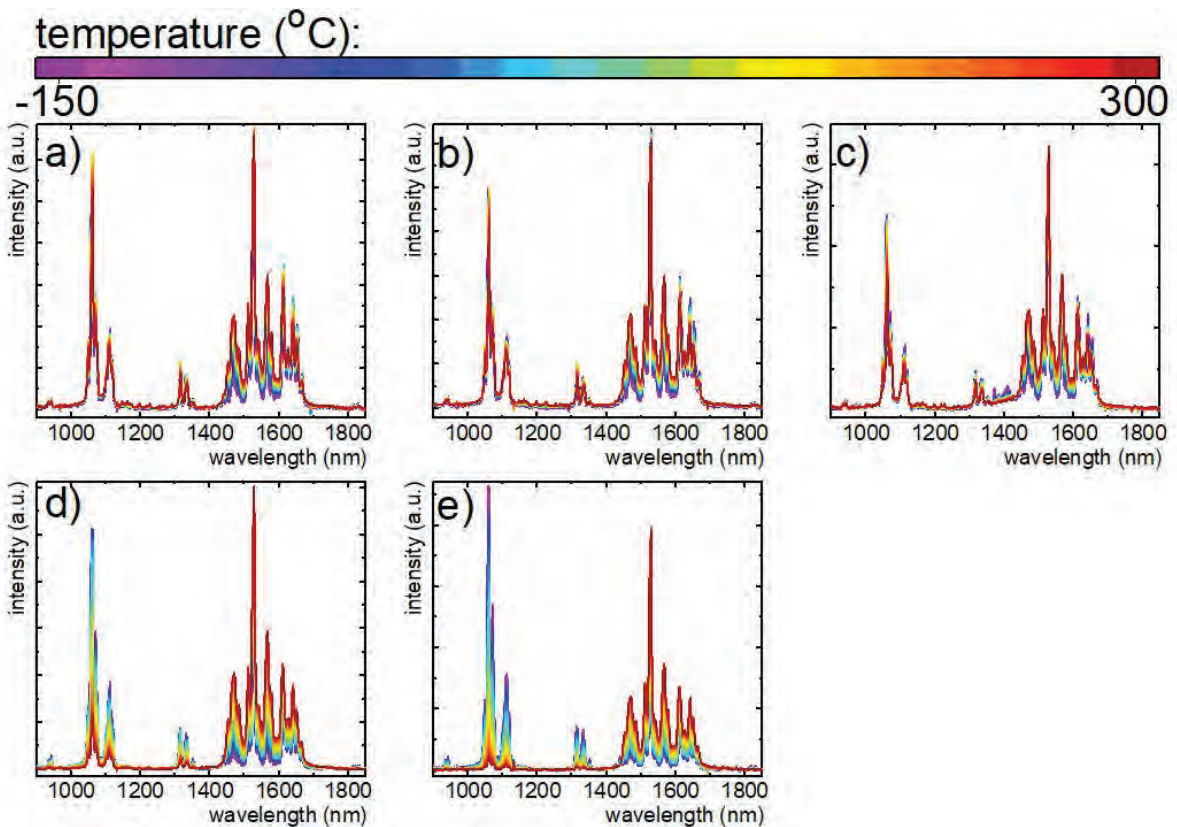
Figure S5. The thermal evolution of the NIR range of emission spectra of YAG:1% Nd^{3+}, 1% Er^{3+}, x% $Cr^{3+/4+}$ powders with λ_{exc} = 445 nm, where x = 1 (a), 2 (b), 5 (c), 10 (d), 20 (e).
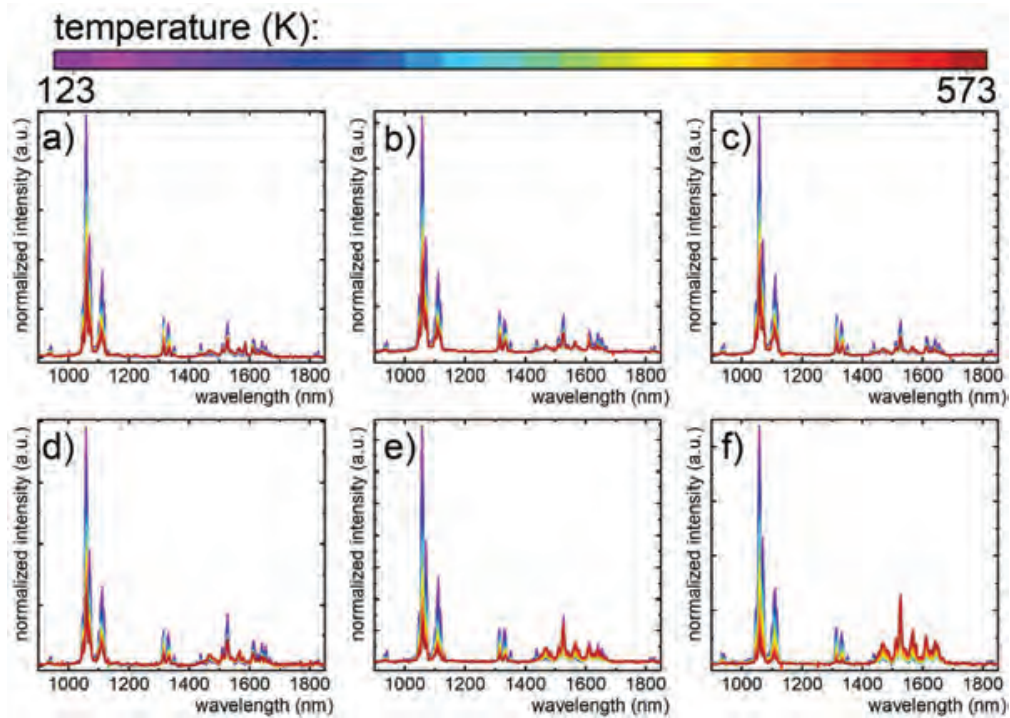
Figure S6. The thermal evolution of emission spectra of YAG:1% Nd^{3+}, 1% Er^{3+}, x% $Cr^{3+/4+}$ powders with λ_{exc} = 793 nm, where x = 0 (a), 1 (b), 2 (c), 5 (d), 10 (e), 20 (f).
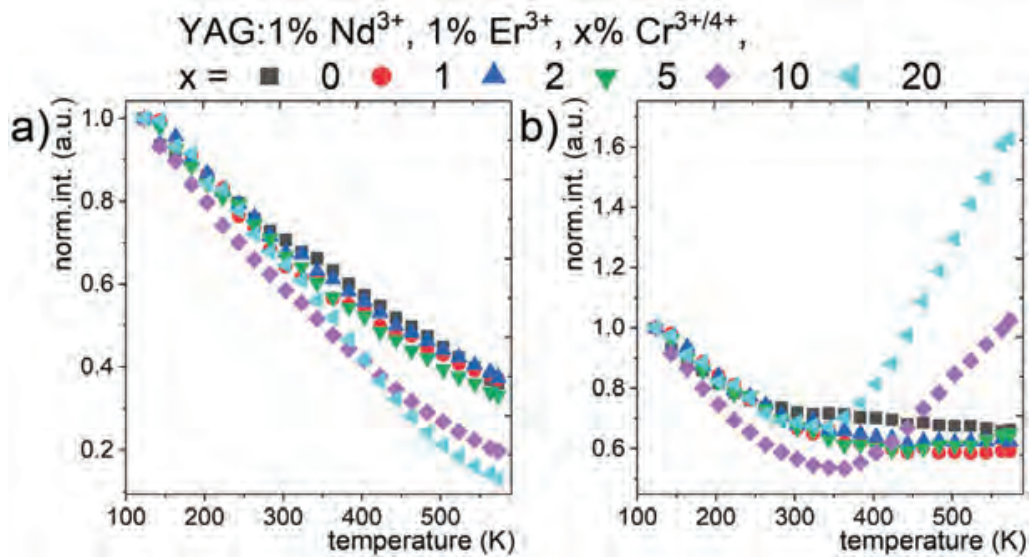
Figure S7. The thermal evolution of integral band intensities of $^4F_{3/2} \rightarrow ^4I_{11/2}$ transition of Nd^{3+} ion (a) and $^4I_{13/2} \rightarrow ^4I_{15/2}$ electronic transition of Er^{3+} ion (b) excited by λ_{exc} = 793 nm.
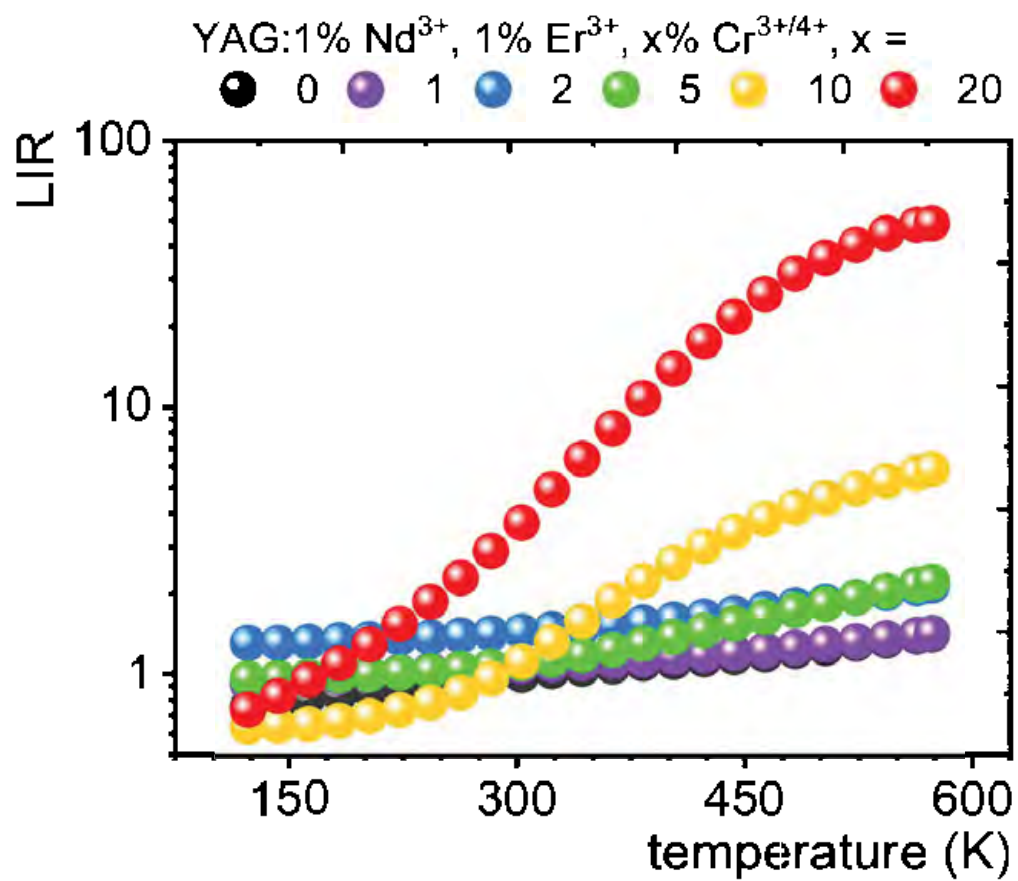
Figure S8. Thermal dependence of LIR calculated on the unnormalized data for different Cr3+/Cr4+ dopant concentration
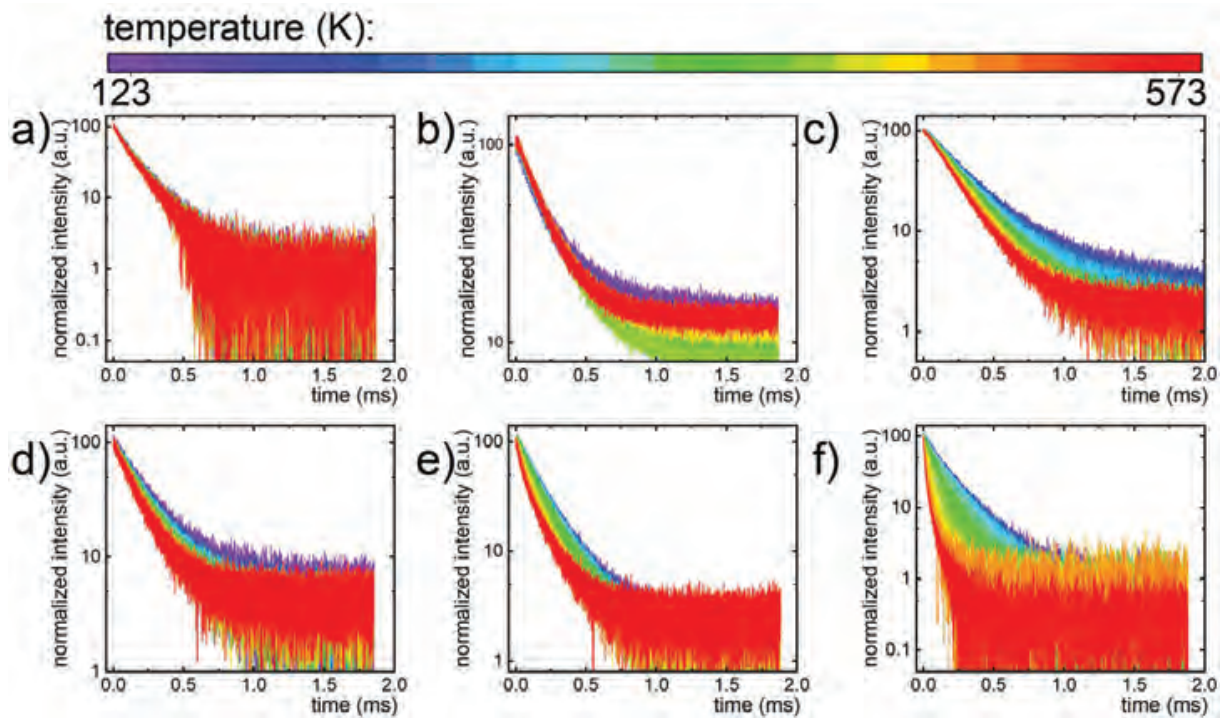
Figure S9. The thermal evolution of luminescent decays in YAG:1% Nd^{3+}, 1% Er^{3+}, x% $Cr^{3+/4+}$ for 1064 nm (Nd^{3+} excited state), where x = 0 (a), 1 (b), 2 (c), 5 (d), 10 (e), 20 (f).
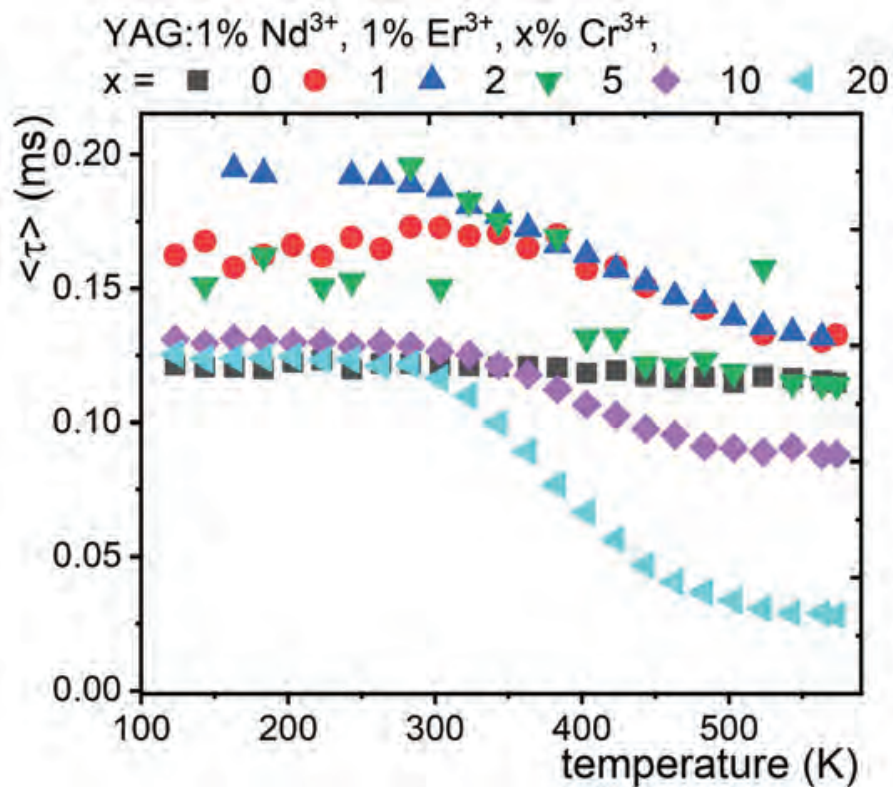
Figure S10. The thermal evolution of average lifetime of Nd^{3+} excited state for YAG:1% Nd^{3+}, 1% Er^{3+}, x% $Cr^{3+/4+}$ powders.
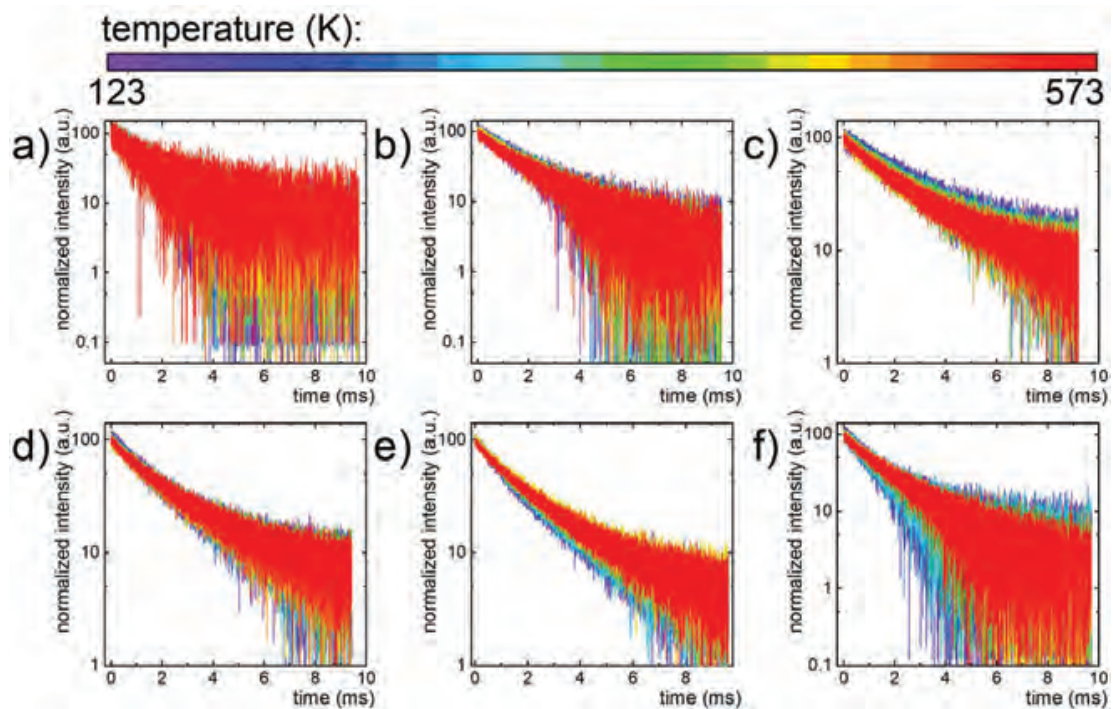
Figure S11. The thermal evolution of luminescent decays in YAG:1% Nd^{3+}, 1% Er^{3+}, x% $Cr^{3+/4+}$ for 1530 nm (Er^{3+} excited state), where x = 0 (a), 1 (b), 2 (c), 5 (d), 10 (e), 20 (f).
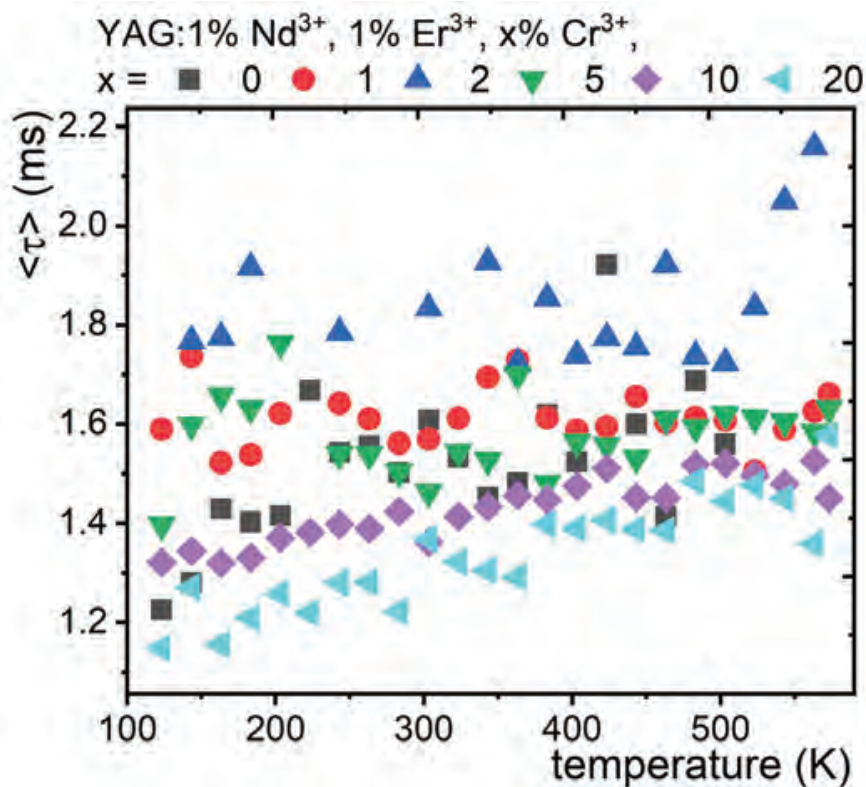
Figure S12. The thermal evolution of average lifetime of Er^{3+} excited state for YAG:1% Nd^{3+}, 1% Er^{3+}, x% $Cr^{3+/4+}$ powders.
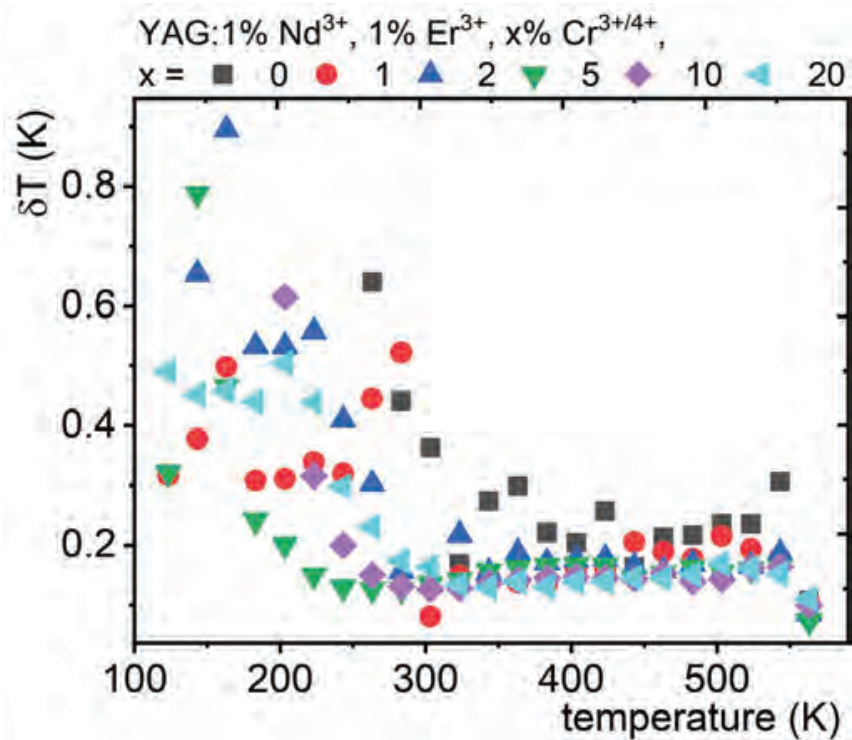
Figure S13. The thermal dependence of temperature estimation uncertainty for different $Cr^{3+/4+}$ concentration in the YAG:1% Nd^{3+}, 1% Er^{3+}, x% $Cr^{3+/4+}$.
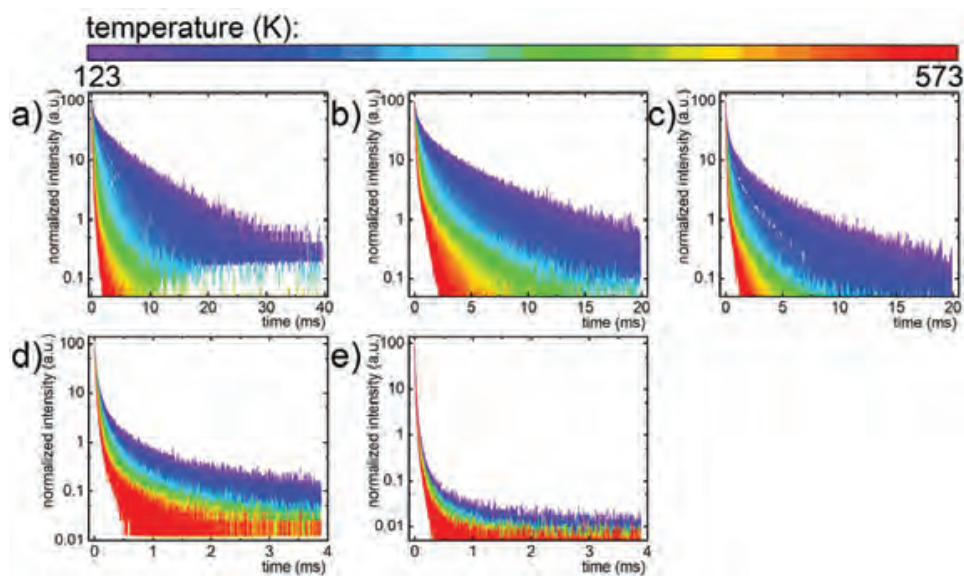
Figure S14. The thermal evolution of luminescent decays in YAG:1% Nd^{3+}, 1% Er^{3+}, x% $Cr^{3+/4+}$ for 445 nm (Cr^{3+} excited state), where x = 1 (a), 2 (b), 5 (c), 10 (d), 20 (e).
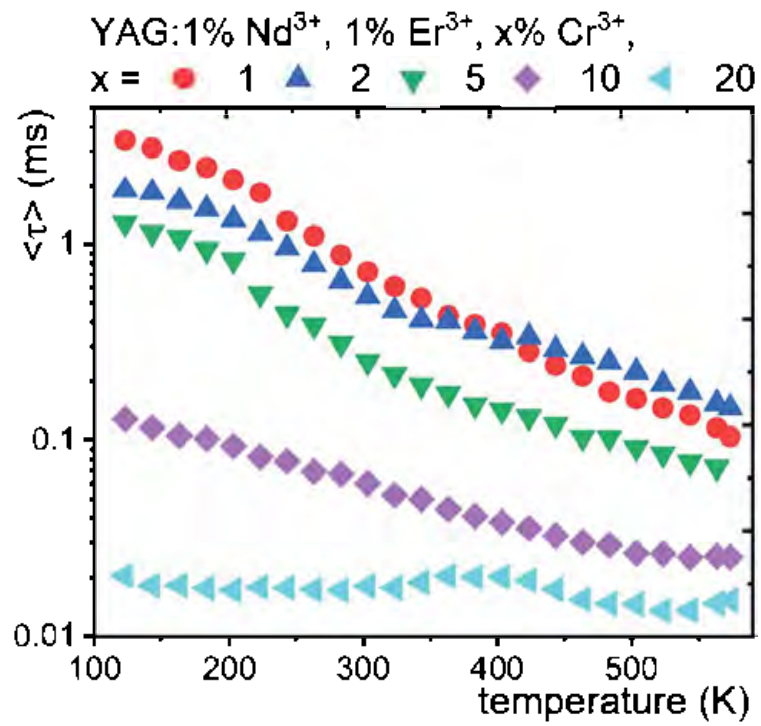
Figure S15. The thermal evolution of average lifetime of Cr^{3+} excited state for YAG:1% Nd^{3+}, 1% Er^{3+}, x% $Cr^{3+/4+}$ powders.
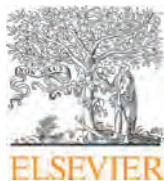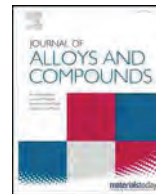
Cr³⁺ ions as an efficient antenna for the sensitization and brightness enhancement of Nd³⁺, Er³⁺-based ratiometric thermometer in GdScO₃ perovskite lattice

W.M. Piotrowski[a], K. Maciejewska[a], L. Dalipi[b], B. Fond[b], L. Marciniak[a,*]

[a] Institute of Low Temperature and Structure Research, Polish Academy of Sciences, Okólna 2, 50-422 Wroclaw, Poland
[b] Institute of Fluid Dynamics and Thermodynamics, Otto-von-Guericke University Magdeburg, 39106 Magdeburg, Germany

ARTICLE INFO

ABSTRACT

Although the technique of luminescence thermometry using luminescence of lanthanide ions (Ln³⁺) is at a high level of sophistication, its main limitations are the relatively low luminescence brightness and the need for precisely selected optical excitation sources. This is due to their relatively low absorption cross-section and the spectrally narrow nature of the $4–4f$ absorption bands. In this work, we propose a strategy that, through exploiting chromium (Cr³⁺) to Ln³⁺ energy transfer, circumvent these limitations. It is shown that as the concentration of Cr³⁺ ions increases up to 15 %, the brightness of a luminescent thermometer based on GdScO₃:Nd³⁺,Er³⁺ increases 25-fold in respect to the non co-doped counterpart. Additionally, due to the temperature dependence of the Cr³⁺→Nd³⁺, Cr³⁺→Er³⁺ energy transfer rate, the sensitivity of this thermometer increases threefold. The described studies confirm the beneficial effect of sensitization of Ln³⁺ ions by Cr³⁺ ions on the thermometric parameters of this type of luminescent thermometers.

1. Introduction

Lanthanide (Ln³⁺) ions are well known and widely investigated as active ions for luminescence thermometry due to their narrow emission lines which facilitate spectral separation of the bands considered in the ratiometric readout approach [1–4]. Especially the inorganic phosphors doped with Ln³⁺ ions are desirable for thermometric applications due to their high thermal and mechanical stability [5–7]. However, the main limitation of luminescent materials doped with Ln³⁺ ions is their low absorption cross-section, resulting in their limited emission brightness. Moreover, the narrow absorption bands associated with the $4–4f$ electronic transitions of Ln³⁺ impose the necessity of using excitation light sources which matches the narrow absorption bands [1,8]. Therefore, new strategies that offer improvements of their brightness and enable excitation in wide spectral range are necessary. One of the most promising strategy, verified experimentally recently, was the sensitization of the Ln³⁺ ions luminescence via the energy transfer from transition metal ions (TM) to Ln³⁺[9,10]. The concept of this approach is schematically presented in Fig. 1. When the ratiometric readout is realized on the Ln³⁺ doped system (in this case Nd³⁺ and Er³⁺ ions),

the excitation wavelength of the energy that enables the population of the excited state of Nd³⁺ is used. The energy transfer between Nd³⁺ and Er³⁺ ions enables the population of the excited states of Er³⁺ ions and thus to achieve their emission [11–13]. Since the assistance of the phonon is required to provide such transfer, thermal dependence is expected of the Nd³⁺ to Er³⁺ luminescence intensities ratio (LIR). However, the sensitivity of such thermometer is found to be not very high ($S_R < 0.5$ %/K). Moreover, the narrow and not intense absorption bands of such system hinder to receive high luminescence brightness of such phosphor. Therefore, the use of the Cr³⁺ co-dopant, which is well known for its broad and intense absorption bands enables the enhancement of the Ln³⁺ emission brightness due to much higher absorption cross section of Cr³⁺ and high Cr³⁺→Ln³⁺ energy transfer. Additionally, due to the significant energy difference between the metastable levels of Cr³⁺ and Nd³⁺ and Er³⁺ ions, the probability of Cr³⁺→Ln³⁺ is expected to be strongly thermally dependent. Therefore, as a consequence of co-doping with Cr³⁺ ions, the bright luminescent thermometer of high sensitivity can be developed. This approach has been already successfully implemented in the YAG:Cr³⁺,Nd³⁺,Er³⁺ phosphor [10]. However, in that case a significant contribution of the Cr⁴⁺ oxidation state in the Nd³⁺→Er³⁺ energy transfer was found. This was due to the fact that the YAG structure contains both octahedrally and tetrahedrally coordinated sites of Al³⁺ ions, that can be occupied by the chromium ions. The tetrahedral site of the Al³⁺ is especially preferred by the Cr⁴⁺, hence

199
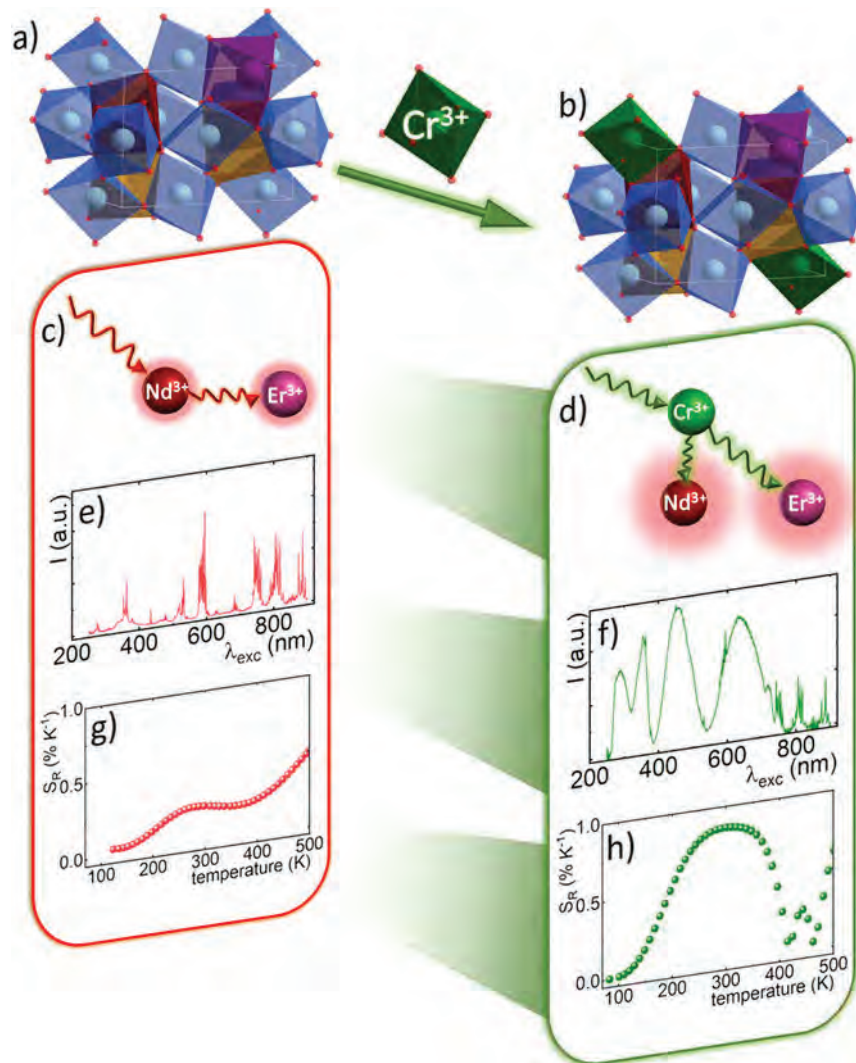
Fig. 1. The visualization of the concept of the proposed approach: the schematic presentation of GdScO$_3$ matrix doped with Nd^{3+}, Er^{3+} - a) and co-doped with Cr^{3+} - b); the simplified visualization of the excitation processes for Nd^{3+}-Er^{3+} ions pair without – c) and with Cr^{3+} as a sensitizer – d); excitation spectra of Nd^{3+} ions (λ_{em}=1082 nm) in GdScO$_3$:Nd^{3+}, Er^{3+} – e) and in GdScO$_3$:Nd^{3+}, Er^{3+}, 20 % Cr^{3+} – f); thermal evolution of the relative sensitivity S$_R$(LIR) for GdScO$_3$:Nd^{3+}, Er^{3+} unco-doped with Cr^{3+} – g) and co-doped with 20 % Cr^{3+} – h).

for a high concentration of chromium ions their small fraction undergoes of oxidation to Cr^{4+}. Therefore, in order to prove that the enhancement of the sensitivity of Er^{3+}, Nd^{3+} based ratiometric luminescent thermometer can be provided by implementing even when solely Cr^{3+} ions are doped as a sensitizer, the host material that prevents the Cr^{4+} stabilization should be examined.

Therefore, in this work the GdScO$_3$ host material was used that contains only the octahedrally coordinated Sc^{3+} site that can be occupied by the Cr^{3+} ions[14–17]. The spectroscopic properties of the GdScO$_3$:Er^{3+}, Nd^{3+} and GdScO$_3$:Er^{3+}, Nd^{3+}, Cr^{3+} were investigated in a wide range of temperature in order to evaluate thermometric properties of Er^{3+}, Nd^{3+} based ratiometric luminescent thermometer. The investigations were conducted for various Cr^{3+} concentration in order to verify the beneficial influence of the sensitization effect via Cr^{3+} ions on the enhancement of the emission brightness and increase of the relative sensitivity of the luminescent thermometer.

2. Experimental

The powders of GdScO$_3$:1 % Nd^{3+}, 1 % Er^3, x % Cr^{3+} (where x = 0; 0.5; 1; 2; 5; 10; 15; 20) microcrystals were synthesised with a solid-state synthesis method. The following starting materials were used

as reagents without further purification: Gd$_2$O$_3$ (99.995 % purity from Stanford Materials Corporation), Sc$_2$O$_3$ (99.99 % purity, Alfa Aesar), Nd$_2$O$_3$ (99.998 % purity, Stanford Materials Corporation), Er$_2$O$_3$ (99.99 % purity, Stanford Materials Corporation) and Cr (NO$_3$)$_3$·9H$_2$O (99.99 % purity, Alfa Aesar). The stoichiometric amounts of compounds were mixed in n-hexane and ground in an agate mortar three times until the n-hexane evaporated. Next, the powder was first calcined in porcelain crucibles at 1000 °C in air for 24 h. The pre-annealed powders with 1 % Nd^{3+} and 1 % Er^{3+} molar concentrations with respect to the Gd^{3+} ions and x % molar Cr^{3+} concentration with respect to Sc^{3+} ions were subsequently ground again with the same procedure and sintered in corundum crucibles in air at 1600 °C for 24 h. Finally, the obtained perovskite powders were ground in an agate mortar.

All of the synthesized materials were examined by X-ray powder diffraction (XRPD) measurements carried out on PANalitycal X′Pert diffractometer, equipped with an Anton Paar TCU 1000 N temperature control unit, using Ni-filtered Cu-K$_\alpha$ radiation (V = 40 kV, I = 30 mA) with a step 2Θ= 0.026°. Scanning Electron Microscopy (SEM) images were taken with a Field Emission Scanning Electron Microscope (FEI Nova NanoSEM 230) equipped with an energy-dispersive spectrometer (EDAX Genesis XM4). The sample was ground

2
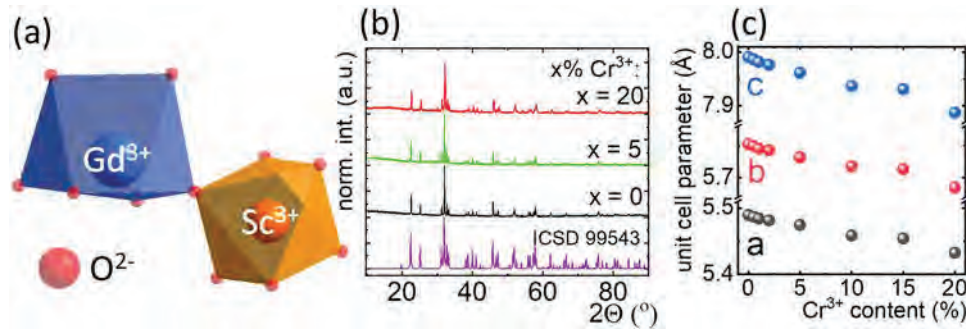
Fig. 2. Structural characterization of synthesized materials: the visualization of the polyhedra of Gd^{3+} and Sc^{3+} in the $GdScO_3$ structure – a); the X-ray diffraction patterns of $GdScO_3$:Nd^{3+}, Er^{3+} x % Cr^{3+} powders with different Cr^{3+} concentrations – b); the influence of the Cr^{3+} concentration on the unit cell parameters in $GdScO_3$:Nd^{3+}, Er^{3+} x % Cr^{3+} – c).

in a mortar and dispersed in methanol and then a drop of the suspension was placed on the carbon stub and dried.

The emission spectra were measured using the 445 nm (50 mW) excitation lines from a laser diode and a NIRQUEST spectrometer from Ocean Optics (1.5 nm spectral resolution) as a detector. The excitation spectra and luminescence decay profiles were recorded using the FLS1000 Fluorescence spectrometer from Edinburgh Instruments with a R928P side window photomultiplier tube from Hamamatsu as a detector with a 450 W halogen lamp and 445 nm pulsed work laser diode as an excitation sources. The temperature of the sample was controlled using a THMS 600 heating-cooling stage from Linkam (0.1 K temperature stability and 0.1 K set point resolution). To estimate relative sensitivities with lower uncertainty, all of the intensity vs temperature plots were fitted according to the Mott-Seitz equation (Eq. S2). In the case of the average lifetime of the excited states, they were calculated with the use of bi-exponential function according to the procedure described in the Supporting Information (SI) (Eq. S4).

To verify the increase of the emission brightness of $GdScO_3$:Nd^{3+}, Er^{3+} when co-doping with Cr^{3+}, a spectroscopic study of liquid dispersions of the particles was performed. The experimental approach is similar to that outlined in Ref. [18].

The particles were dispersed in deionized water at a concentration of 500 mg/L and placed in a borosilicate beaker. These dispersions were probed with two different light sources, namely a white LED (Thorlabs MCWHL5), with an emission spectrum which consisted of two bands: a narrow band with a center wavelength around 460 nm and a 20 nm full width at half maximum (FWHM) and a broad band with a center wavelength of 580 nm with a FWHM of 130 nm; and a blue LED (Thorlabs M455L3) centered at 455 nm with a 20 nm FWHM. The LED emission was focused by an 85 mm objective lens (Zeiss 85 mm f/1.4) and a f = +75 mm plano-convex lens onto the center of the beaker, with a power density of 860 and 960 W/cm^2, for the blue and white LED respectively. The difference between the two LEDs do not allow IR radiation from the white LED was blocked by a visible band pass filter (Schott KG3). The luminescence from the stirred dispersions was collected by a 50 mm objective lens (Nikon 50 mm f/4) and imaged onto the entrance slit of a monochromator (Spectrapro: HRS-300, Princeton Instruments) with a grating (100 grooves per mm blazed at 450 nm). To reject the LED illumination, a an IR long-pass filter (Schott RG 1000) was used. A non-amplified silicon photodiode (Thorlabs DET1002A) was placed at the exit slit of the monochromator to collect the 1064 nm emission with a 60 nm bandwidth (FWHM). The photodiode current was further amplified using a lock-in amplifier (Stanford Research Systems SR510) referenced at 8 Hz, at the same modulation frequency of the excitation source. To account for difference in dispersion stability, Mie scattering measurements were also performed before and after the luminescence measurements. For this, the particles were illuminated with a 375 nm diode laser (PhoxX-

Omicron Lasers), and the scattered intensity was recorded with the same system for a monochromator center wavelength of 375 nm. For these measurements, both filters were removed and the LED were turned off. The comparison of brightness of the luminescent thermometers was performed based on the ratio of collected luminescence signal and Mie scattering signal for each dispersion.

To evaluate possible signal leakage between the excitation source and the detection and luminescence from the beaker to the non-luminescent Al_2O_3 particles (Phosphor Technology) with 3 μm average particle size were dispersed in water and illuminated with the white and blue LED, while the emission at 1064 nm was recorded. The signal detected at 1064 nm for aluminum oxide particles was used as a background for luminescence intensities and subtracted. To account for the contribution of the beaker wall to the scattering signal when illuminated at 375 nm, a background signal was also recorded with the beaker filled with deionized water in the absence of phosphor particles.

3. Results and discussion

3.1. Structural and morphological characterization

$GdScO_3$ crystallizes in an orthorhombic system of *Pnma* (62) space group and is a representative of the perovskite family of the general formula ABX_3 (where A and B represents the metallic sites, while X = O^{2-} anion)[14–17]. In this case, the Gd^{3+} and Sc^{3+} cations are located in the 'A' and 'B' sites, respectively. The Sc^{3+} ions together with surrounding O^{2-} ions form corner-sharing distorted octahedra, while triangular prisms of Gd^{3+} ions are found in vacancies between these octahedra (Fig. 2a). It is noteworthy, both Gd^{3+} and Sc^{3+} have the same electric charge and are surrounded by the same number of oxide ions O^{2-} in the first coordination sphere, which could make it difficult to determine where substitution of dopant ions is to be expected. However, the differences between the effective ionic radii (EIR) allow unambiguous assignment of the sites that will be favoured for the dopant ions. Therefore, since the Shannon ionic radius of Sc^{3+} equals 74.5 pm and for Gd^{3+} it is 93.8 pm, it is expected that Ln^{3+} ions such as Nd^{3+} and Er^{3+} will occupy the Gd^{3+} site (EIR_{Er3+}/EIR_{Gd3+} = 89 pm/93.8 pm ≈ 94.9 % and EIR_{Nd3+}/EIR_{Gd3+} = 98.3 pm/93.8 pm ≈ 105.0 %)[19]. On the other hand, the smaller site of Sc^{3+} should be more suitable for the transition metal ions like Cr^{3+} with an effective ionic radius equal to 61.5 pm (EIR_{Cr3+}/EIR_{Sc3+} = 61.5 pm/74.5 pm ≈ 82.5 %). The analysis of the calculated Goldschmidt tolerance factor *t* (Eq. S1), reveals that for the un-doped $GdScO_3$ structure, *t* = 0.771, which is consistent with the classification of this structure as orthorhombic[17,20]. However the co-doping the structure with 1 % of Nd^{3+} and Er^{3+} ions causes the increase of *t* to 0.776, and with increasing concentration of Cr^{3+} ions *t* increases even more, reaching *t* = 0.786 for the microcrystals co-doped with 20 % Cr^{3+} ions (Fig. S1).

To verify the crystallographic purity of prepared micromaterials, the patterns obtained from X-ray powder diffraction (XRPD) measurements were compared with reference data (ICSD 99543) (Fig. 2b, see also Fig. S2 – S4). Performed analysis indicates the lack of additional intense Bragg reflections in the XRPD patterns confirming the phase purity of the GdScO$_3$:Nd^{3+}, Er^{3+}, Cr^{3+} even for 20 % Cr^{3+} ions. It should be noted that the most intense reflection at 2theta= 32° undergoes broadening for 20 %Cr^{3+} which may suggest a lowering of the crystallization level for such high concentrations of dopant ions. Moreover, careful analysis reveals that at ca. 2theta= 30° for 5 %Cr^{3+} and 10 %Cr^{3+} samples additional reflections of low intensity (< 3 % intensity of the most intense reflection of GdScO$_3$) are observed. As further spectroscopic investigations will show, the presence of this impurity does not influence significantly the luminescence properties of the phosphors analyzed. The observed gradual shift of the diffraction peaks towards higher 2Θ degrees with increasing Cr^{3+} concentration (by 0.21° for 20 % Cr^{3+} with respect to the Cr^{3+} undoped sample) indicates a contraction of the unit cell from V = 250.75 Å for Nd^{3+}, Er^{3+}-doped GdScO$_3$ material to V = 242.07 Å for the sample doped with 20 % Cr^{3+} ions, which is expected due to substitution of Sc^{3+} ions by smaller Cr^{3+} ions (Fig. S5). Accordingly, a nearly linear increase in the Goldschmidt tolerance factor with the decreasing unit cell volume was found, indicating that with the gradual substitution of Sc^{3+} ions by Cr^{3+} ions the angle between Sc^{3+}/Cr^{3+} octahedra tends towards the 90° found in an ideal cubic structure such as SrTiO$_3$ (Fig. S6). The SEM analysis of the obtained phosphors reveals that independently on the Cr^{3+} concentration synthesized powders consists of aggregated particles of around 2 µm in diameter (Fig. S7).

3.2. Luminescent properties characterization

In order to understand the sensitization process of Ln^{3+} luminescence occurring in GdScO$_3$ nanocrystals doped with Nd^{3+}, Er^{3+} and co-doped with Cr^{3+} ions, the configurational-coordinate diagram for Cr^{3+} ions and the energy level diagrams of Nd^{3+} and Er^{3+} ions are presented in Fig. 3a. In the case of the luminescent system doped solely with Ln^{3+} ions, it is possible to populate their excited states by using an excitation wavelength matched to the one of the narrow absorption bands of Nd^{3+} or Er^{3+} ions, e.g. Nd^{3+} through λ_{exc} = 808 nm ($^4I_{9/2} \rightarrow ^4F_{5/2}, ^4S_{3/2}$ electronic transition). As a consequence of nonradiative transitions, the metastable $^4F_{3/2}$ state is populated. Its radiative depopulation results in the occurrence of three characteristic emission bands at 880 nm, 1080 nm and 1348 nm corresponding to the $^4F_{3/2} \rightarrow ^4I_{9/2}$, $^4F_{3/2} \rightarrow ^4I_{11/2}$ and $^4F_{3/2} \rightarrow ^4I_{13/2}$ electronic transitions, respectively. Since only a small energy difference is found between the $^4F_{3/2}$ state of Nd^{3+} ions and the $^4I_{11/2}$ state of Er^{3+} ions, the interionic Nd$^{3+} \rightarrow$ Er^{3+} energy transfer can occur, which then is followed by non-radiative processes to the $^4I_{13/2}$ state of Er^{3+} ions. From this level, the $^4I_{13/2} \rightarrow ^4I_{15/2}$ electronic transition generates the emission band at 1540 nm.

However, when the system is co-doped with Cr^{3+} ions, it is possible to populate excited states of Ln^{3+} through the Cr$^{3+} \rightarrow$Ln^{3+} energy transfer. This is due to the fact that Cr^{3+} is characterized by the very broad and intense absorption bands in the visible part of the spectrum, that are associated with the spin-allowed $^4A_2 \rightarrow ^4T_1$ and $^4A_2 \rightarrow ^4T_2$ electronic transitions. When the λ_{exc} = 445 nm excitation line is used ($^4A_2 \rightarrow ^4T_1$ electronic transition) the population of the $^4T_1$ state followed by the nonradiative transitions to the bottom of the $^4T_2$ state parabola. As presented by Wang et al.[14], the radiative depopulation of this state at room temperature results in the observation of broad emission bands with a maximum at 767 nm. However, in a system co-doped with Ln^{3+} ions it is also possible that energy transfer processes Cr$^{3+} \rightarrow$Nd^{3+} and Cr$^{3+} \rightarrow$Er^{3+} occur. It should be emphasized that considering the energy mismatch between Cr^{3+} excited states and $^4F_{7/2}$ of Nd^{3+} and $^4I_{11/2}$ of Er^{3+}, both energy

transfers require the assistance of phonons, making them highly temperature-dependent processes, which is advantageous from a thermometric point of view. The emission spectra measured at T = 83 K (Fig. 3b) confirm these phenomenological predictions. Upon λ_{exc} = 445 nm optical excitation for the GdScO$_3$ microcrystals doped with Cr^{3+} ions, two bands originating from $^4F_{3/2} \rightarrow ^4I_{11/2}$ and $^4F_{3/2} \rightarrow ^4I_{13/2}$ electronic transitions of Nd^{3+} ions with maxima at 1180 nm and 1348 nm can be found and one emission band associated with the $^4I_{13/2} \rightarrow ^4I_{15/2}$ electronic transition of Er^{3+} ions at 1540 nm. This confirms the Cr$^{3+} \rightarrow$Ln^{3+} energy transfer. However, the comparison of the emission spectra obtained upon λ_{exc}= 445 nm (Cr^{3+} sensitization) and λ_{exc} = 808 nm (direct Nd^{3+} excitation) reveals that both Cr$^{3+} \rightarrow$Nd^{3+} and Cr$^{3+} \rightarrow$Er^{3+} energy transfer take place in the Cr^{3+} co-doped systems. Upon direct Nd^{3+} excitation the emission band of Er^{3+} ions reached about 7 % of the emission intensity of $^4F_{3/2} \rightarrow ^4I_{11/2}$ emission band of Nd^{3+} ions. However, when the λ_{exc}= 445 nm is used for the 0.5 % Cr^{3+}, the Er^{3+} intensity increases up to 45 % of the Nd^{3+} intensity (Fig. S8). Higher concentrations of Cr^{3+} lead to some reduction of the contribution of Er^{3+} emission intensity in the luminescence spectrum of the analysed samples (up to 13.5 % of Nd^{3+} band intensity for 20 %Cr^{3+}). This is probably related to the high concentration of Cr^{3+} ions, which transfer energy less efficiently to Ln^{3+} co-dopants due to the higher probability of occurrence of so-called concentration quenching between Cr^{3+} ions. To verify this, the comparison of the average distance between Cr^{3+} ions (R) and a critical distance (R_c) should be analysed. The R can be calculated by the formalism introduced and explained by Blasse and Grabmaier with the following equation (Eq. 1)[21,22]:

$$R = 2\left(\frac{3V}{4\pi x N}\right)^{1/3} \tag{1}$$

where N is the number of positions in which the dopant can be located in the unit cell with the volume V and x is the concentration of the optically active dopant (Cr^{3+} in this case). Since there are 12 Sc^{3+} ions in the unit cell, N = 12 and it is possible to determine R for different Cr^{3+} concentration: R = 43.04 Å; 15.85 Å; 12.57 Å; 9.25 Å; 7.32 Å; 6.38 Å and 5.78 Å for 0.5; 1; 2; 5; 10; 15 % and 20 % Cr^{3+} concentration, respectively. The critical distance for energy transfer R_c is defined as the distance for which the rate of transfer between two optical centres equals the radiative rate in one of these centres. Therefore, when R_c < R the energy transfer between Cr^{3+} ions dominates and when R_c > R the radiative transition or the Cr$^{3+} \rightarrow$Ln^{3+} is more probable. Since the optical transitions between ^2E states of two Cr^{3+} ions are forbidden electric-dipole transitions, the R_c value should be around 5–8 Å to occur the transfer over the multipolar interaction[22].

The beneficial effect of the Cr^{3+} co-doping on the excitation efficiency is presented in the excitation spectra of the GdScO$_3$:Cr^{3+}, Nd^{3+}, Er^{3+} powders measured on the emission of Nd^{3+} ions (λ_{em} = 1082 nm) (Fig. 3c). For the GdScO$_3$:Nd^{3+}, Er^{3+} powders, the Nd^{3+} excitation spectrum consists of several narrow excitation bands, which can be attributed to electronic transitions occurring from the $^4I_{9/2}$ ground state of Nd^{3+} ions to: $^2F_{5/2}$ (275 nm), $^4D_{3/2},^4D_{1/2}$ (362 nm), $^4D_{5/2}$ (378 nm), $^2P_{1/2},^2D_{5/2}$ (434 nm), $^4G_{9/2},^2D_{3/2}$ (447 nm), $^4G_{9/2},^2K_{13/2}$ (519 nm), $^4G_{5/2},^2G_{7/2}$ (595 nm) $^2H_{11/2}$ (627 nm), $^4F_{9/2}$ (683 nm), $^4F_{7/2},^4S_{3/2}$ (745 nm), $^4F_{5/2},^2H_{9/2}$ (805 nm) and $^4F_{3/2}$ (875 nm), but also several Er^{3+} bands, related to the $^4I_{15/2} \rightarrow ^4G_{7/2}, ^2K_{13/2}$ (312 nm), $^4I_{15/2} \rightarrow ^2H_{11/2}$ (520 nm), $^4I_{15/2} \rightarrow ^4S_{3/2}$ (542 nm) and $^4I_{15/2} \rightarrow ^4I_{9/2}$ (800 nm) transitions (Fig. S8). The occurrence of weak Er^{3+} bands in the excitation spectrum of Nd^{3+} indicates a Er$^{3+} \rightarrow$Nd^{3+} energy transfer. Also for the excitation spectra of Er^{3+} ions taken for the emission wavelength of 1525 nm, many narrow bands of both Nd^{3+} and Er^{3+} ions were found (Fig. S9). These include the excitation bands corresponding to the population of the following Er^{3+} states: $^4G_{9/2}$ (281 nm), $^4G_{7/2}$ +$^2K_{13/2}$ (301 nm), $^4G_{11/2}$ (378 nm), $^4F_{7/2}$ (486 nm), $^2H_{11/2}$ (521 nm), $^4S_{3/2}$ (542 nm), $^4F_{9/2}$ (655 nm) and $^4I_{9/2}$
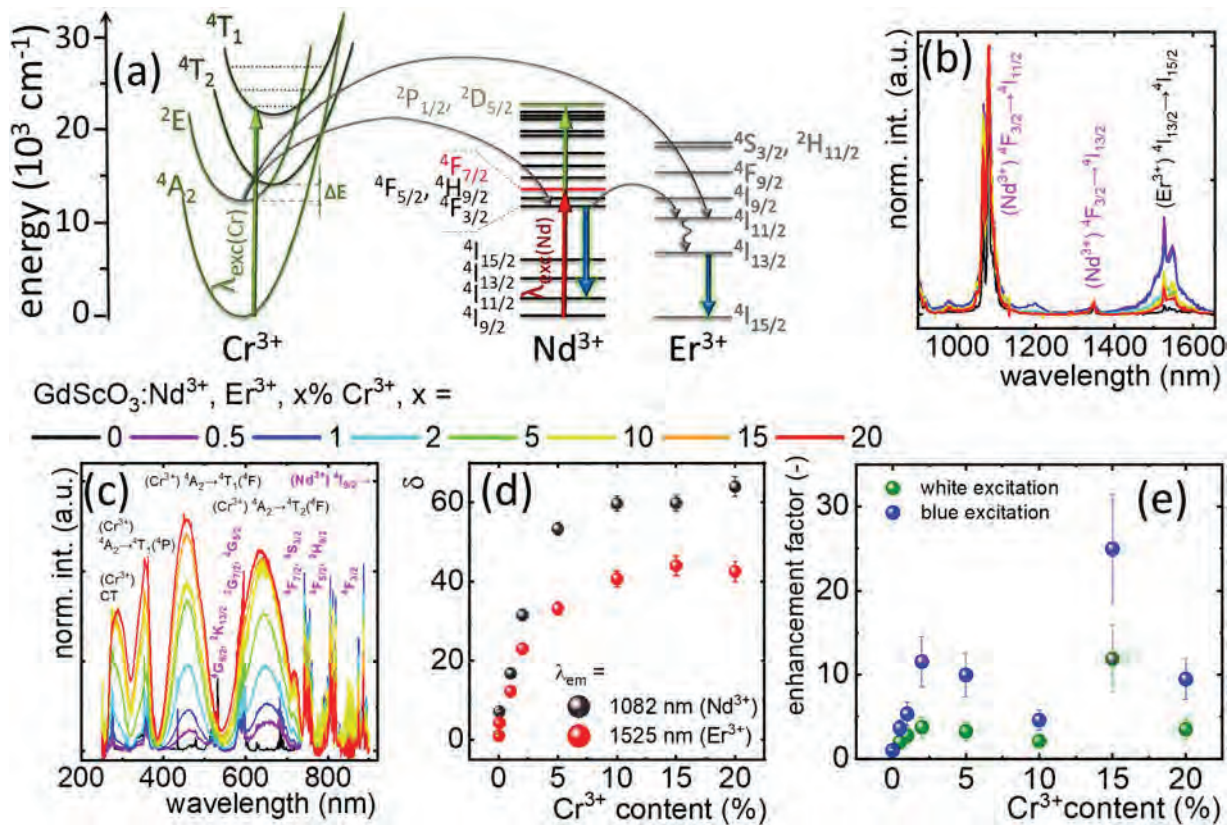
Fig. 3. The configurational-coordinate diagram of Cr^{3+} and energy levels diagram of Nd^{3+} and Er^{3+} ions – a); the comparison of the low temperature (83 K) emission (λ_{exc} = 445 nm) – b) and excitation spectra of Nd^{3+} ions (λ_{em} = 1082 nm) of $GdScO_3$:Nd^{3+}, Er^{3+} x % Cr^{3+} microcrystals with different Cr^{3+} concentration – c); the influence of the Cr^{3+} concentration on the contribution parameter δ – d); the luminescence intensity enhancement factors for $GdScO_3$:1 %Nd^{3+}, 1 %Er^{3+}, x %Cr^{3+} phosphors. The errors bars were computed from the mean standard deviations of the ratios from repeated measurements with newly prepared dispersions – e).

(805 nm) and also Nd^{3+} excited states: $^4D_{3/2}$ +$^4D_{1/2}$ (360 nm), $^4G_{9/2}$ +$^2D_{3/2}$ (480 nm), $^4G_{9/2}$ +$^2K_{13/2}$ (518 nm), $^4G_{5/2}$ +$^2G_{7/2}$ (594 nm) and $^2H_{9/2}$ +$^4F_{5/2}$ (805 nm). The Nd^{3+} excitation bands in the spectrum taken for Er^{3+} emission confirm the expected $Nd^{3+}{\rightarrow}Er^{3+}$ energy transfer. In both cases of the Nd^{3+} and Er^{3+} excitation spectra, with increasing Cr^{3+} ion concentration the occurrence of several broad bands is observed, which can be assigned to the electronic transitions of $^4A_2{\rightarrow}^4T_1(^4P)$ (~353 nm), $^4A_2{\rightarrow}^4T_1(^4F)$ (~456 nm), $^4A_2{\rightarrow}^4T_2(^4F)$ (~632 nm) and $^4A_2{\rightarrow}^2E$ (~718 nm). Such an unusually rich excitation spectrum is associated with a large optical bandgap (> 5.5 eV) that is characteristic of the rare earth scandate crystals ($REScO_3$, where RE - the rare earth ion)[23–25]. Additionally, it is worth noting that the $^4A_2{\rightarrow}^2E$ excitation band is rarely observed, but has been previously reported in a Sc^{3+} site characterised by a weak crystal field in $Ca_3Sc_2Si_3O_{12}$ garnet[26]. From the energetical location of the $^4A_2{\rightarrow}^4T_1$ and $^4A_2{\rightarrow}^4T_2$ bands, the crystal field strength Dq, the Racah parameter B and their ratio Dq/B can be determined according to empirical formulae determined from Tanabe-Sugano diagrams (Eqs. 2–4):

$$Dq = \frac{E_a(^4A_2 \rightarrow {}^4T_2)}{10} \quad (2)$$

$$x = \frac{E_a(^4A_2 \rightarrow {}^4T_1) - E_a(^4A_2 \rightarrow {}^4T_2)}{Dq} \quad (3)$$

$$\frac{Dq}{B} = \frac{15(x-8)}{x^2 - 10x} \quad (4)$$

The obtained results show that the weak crystal field strength affects the Cr^{3+} ions in $GdScO_3$:Nd^{3+}, Er^{3+}, Cr^{3+} materials (for Cr^{3+} concentration below 2 % - Dq/B ≈ 2.05) (Table 1). With increasing

Cr^{3+} content above 5 % the parameter Dq/B increases from 2.27 to 2.48 for $GdScO_3$:Nd^{3+}, Er^{3+}, 20 % Cr^{3+} crystals. The increase of Dq/B ratio with Cr^{3+} content is expected due to the smaller radius of Cr^{3+} ions with respect to Sc^{3+} host ions and the well-known inverse relationship between crystal field strength 10Dq and a metal-ligand distance $R(Sc^{3+}/Cr^{3+}\text{-}O^{2-})$ presented by Tanabe and Sugano for $3d^3$ electronic configuration [27,28]. The crystal field strength affecting the Cr^{3+} ion located in the octahedral symmetry is inversely proportional to R^{-5} (where R is the Cr^{3+} -O^{2-} distance). Due to the large difference in ionic radii between Sc^{3+} and Cr^{3+} as the dopant ion concentration increases, a change in the average Cr^{3+}-O^{2-} distance resulting in a change in crystal field strength is expected. Such effect has been previously reported for $Y_3Ga_5O_{12}$:Cr^{3+}, among others [29]. The obtained results differ from the values previously reported in the literature (Dq = 1553 cm^{-1}, B = 574 cm^{-1}, Dq/B = 2.71) [14]. It should be noticed here, that when the Dq/B is below 2.3 the low crystal field affects the Cr^{3+} ions, where the energy of the $^4T_2$ state is lower compared to the ^2E state. Hence, the obtained Dq/B < 2.1 for low Cr^{3+} concentrations are consistent with the emission spectra reported in that work consisting of a broad band characteristic of the

Table 1
Comparison of crystal field parameters for $GdScO_3$:Nd^{3+}, Er^{3+}, x % Cr^{3+} microcrystals.

Cr^{3+} concentration	Dq (cm^{-1})	B (cm^{-1})	Dq/B
0.5 %	1535	752	2.04
1 %	1539	755	2.03
2 %	1544	758	2.05
5 %	1585	699	2.27
10 %	1606	678	2.37
15 %	1631	661	2.47
20 %	1646	664	2.48

5

spin-allowed $^4T_2 \rightarrow {}^4A_2$ transition. This disagreement may be due to differences in the temperature at which the excitation spectra were measured (room temperature in[14] comparing to the T = 83 K in this work).

To quantify the growing contribution of the Cr^{3+} absorption bands in the excitation spectrum of $GdScO_3$:Cr^{3+},Nd^{3+},Er^{3+} powders recorded on the Nd^{3+} emission and Er^{3+} emission the δ_{Nd3+} and δ_{Er3+} parameters were calculated, respectively, as follows:

$$\delta_{Nd3+} = \frac{\int I(^4A_2 \rightarrow {}^4T_1)(Cr^{3+})d\lambda}{\int I(^4I_{9/2} \rightarrow {}^4G_{7/2})(Nd^{3+})d\lambda} \tag{5}$$

$$\delta_{Er3+} = \frac{\int I(^4A_2 \rightarrow {}^4T_1)(Cr^{3+})d\lambda}{\int I(^4I_{15/2} \rightarrow {}^2H_{11/2})(Er^{3+})d\lambda} \tag{6}$$

The analysis of the influence of the Cr^{3+} concentration on values of these parameters indicates that even for the powders co-doped with 2 % Cr^{3+}, the excitation band $^4A_2 \rightarrow {}^4T_1$ of Cr^{3+} ions is above 23 times more intense than the band corresponding to $^4I_{15/2} \rightarrow {}^2H_{11/2}$ transition for Er^{3+} emission and 31 times more intense than the band $^4I_{9/2} \rightarrow {}^4G_{7/2}$ of Nd^{3+} ions. Subsequently, the increase in the intensity of bands originating from Cr^{3+} ions increases less rapidly, reaching a maximum of $\delta_{Er3+} \approx 41$ and $\delta_{Nd3+} \approx 64$ for 20 % Cr^{3+} doped microcrystals.

To exploit the impact of Cr^{3+} co-doping in $GdScO_3$:1 %Nd^{3+}, 1 % Er^{3+}, x %Cr^{3+} (x = 0, 0.5, 1, 2, 5, 10, 15, 20 %) luminescent thermometers' brightness, spectroscopic measurements were conducted in water dispersions. Probing particle dispersions, which is an optically thin state, serves two aims: 1) the enhancement observed will be valid in applications benefiting from sensitization, where generally the concentration of luminescence thermometers is limited (fluid metrology, biomedical applications). 2) the enhancement is a linear function of the enhancements of both absorption cross section and quantum efficiency. In bulk powders, the attenuation length due to absorption and multiple scattering is smaller than the thickness of the powder sample itself. As a result, in this optically thick state, there is a sub-linear and unknown dependence on the absorption cross section. The enhancement factors obtained in dispersion are therefore less ambiguous and more transferrable than those which could be observed in the powder state.

In terms of excitation source, the blue LED with an emission peak centered at 455 nm has an excellent overlap with the $^4A_2 \rightarrow {}^4T_1$ band of Cr^{3+}. On the other hand, it does not cover an Er^{3+} excitation line and can only excite Nd^{3+} into a weak $^4G_{9/2}$,$^2D_{3/2}$ band at 447 nm. As a result, it can be used to probe the enhancement of the luminescence signal due to the apparition of an excitation band with Cr^{3+} co-doping. In comparison, the broad white LED allows the excitation into several excitation bands of each of the three ions. As a result, luminescent signal variations would be the result of differences in the involved absorption strengths of the different transitions, irrespective of the quality of the overlap between the LED emission spectrum and the specific excitation peaks. This means the difference in absorption cross sections of excitation transitions of Cr^{3+} and those of Nd^{3+} and Er^{3+} can be investigated.

The brightness enhancement factors for each excitation source were derived as the ratio of Nd^{3+} 1064 nm emission intensity of a luminescence thermometer with respect to that of the non Cr^{3+} co-doped phosphor. Enhancement factors are derived for each of the two illumination, which by their ratiometric nature, can be compared despite the slight mismatch in power densities between the two illumination sources used. In contrast to the previously reported similar study on YAG:1 %Nd^{3+}, 1 %Er^{3+}, x %Cr^{3+} microcrystals where the phosphor brightness increased continuously with Cr^{3+} concentration[18], $GdScO_3$ host show a non monotonic behaviour with sensitizer concentration for both blue and white light illumination (Fig. 3e). From 0 % to 2 % Cr^{3+}, the emission intensity significantly

increases with Cr^{3+} content, while between 2 % and 5 %, the intensity is similar. At 10 %, the intensity has decreased to a similar level as at 1 %. However, the highest intensity has been found for 15 % Cr^{3+} ions with a two-fold increase with respect to the first maximum while at 20 % Cr^{3+}, the emission intensity has dropped to the level of that plateau. The reason for the double maximum in the curve is not clear, but it has to do with a competition between increase an absorption cross section with the concentration of chromium and a competition between the rate of $Cr^{3+} \rightarrow Cr^{3+}$ energy transfer (ET), $Cr^{3+} \rightarrow Nd^{3+}$ ET, $Nd^{3+} \rightarrow Cr^{3+}$ back energy transfer and Cr^{3+} to defects ET, which influence the quantum efficiency for the Nd^{3+} emission. Eventually concentration quenching dominates and the intensity decreases.

The same behaviour is observed for both LEDs, with the enhancement being systematically 2–3 times larger with the blue excitation than with the white excitation. The maximal enhancement, obtained at 15 % is 12 and 25, for white and blue LED respectively. This is expected as the match of the blue LED excitation bands is far better in the case of Cr^{3+} excitation features than for Ln^{3+} excitation bands, therefore the appearance of the Cr^{3+} has a significant effect on the brightness. Since the white LED excitation covers both Nd^{3+} and Cr^{3+} excitation bands, the enhancement due to the addition of the Cr^{3+} excitation is less pronounced than for the blue LED.

The observed brightness increase for highly co-doped phosphors would indicate that the enhancement of the total absorption cross-section of the particle co-doped with Cr^{3+} is stronger than the effect of concentration quenching, which has been mentioned earlier in the manuscript. At this point, it is worth emphasizing, that, the emission intensity for particle dispersion is a result of the product of quantum efficiency and absorption coefficient[30]. Moreover, concentration quenching analysis is often performed in powders, and in this state, the contribution of the total absorption cross section to the overall signal is reduced due to the thickness of the medium. Therefore, it could be concluded that the powder measurements tend to reflect more the effect of quantum efficiency loss with increase in concentration and minimize the effect of the increase of the total absorption cross section with concentration.

3.3. Thermometric properties characterization

Apart from the brightness enhancement, another aspect of luminescent thermometers equally important especially from the application point of view and which can be enhanced by the through Cr^{3+} sensitization, are the thermometric properties of the investigated thermometer. In order to verify the influence of the Cr^{3+} ions concentration on the thermal dependence of emission bands intensities of Nd^{3+} and Er^{3+} ions, thermal dependence of emission spectra of $GdScO_3$:Nd^{3+}, Er^{3+}, Cr^{3+} powders were measured (Fig. 4a, Fig. S10). It was found that for the $GdScO_3$:Nd^{3+}, Er^{3+} sample the luminescence of both bands decreases slowly at elevated temperature and their emission intensities are not completely quenched until 743 K. However, with increasing Cr^{3+} ion concentration, a more rapid decrease of their intensity was found.

The analysis of the thermal dependence of the integral emission intensities of Ln^{3+} indicates that in the case of the Nd^{3+} band for the Cr^{3+} un-doped powders in the temperature range of 83–143 K a slight increase of the intensity up to 115 % of the initial value is observed. Above this temperature the emission intensity remains almost constant up to 200 K and above this temperature there is a gradual decrease of the intensity which at 743 K reaches 37 % of the initial value (Figs. 4b, 4c). The slight increase in emission intensity for the sample undoped with Cr^{3+} ions observed in the 100–130 K temperature range is due to the thermally induced increase in the absorption cross section for this wavelength. The optical excitation of λ_{exc}= 445 nm reached a sideband of the $^4I_{9/2} \rightarrow {}^2G_{9/2}$,$^2D_{3/2}$,$^4G_{11/2}$,$^2K_{13/2}$ absorption band of Nd^{3+}. Its spectral broadening observed at
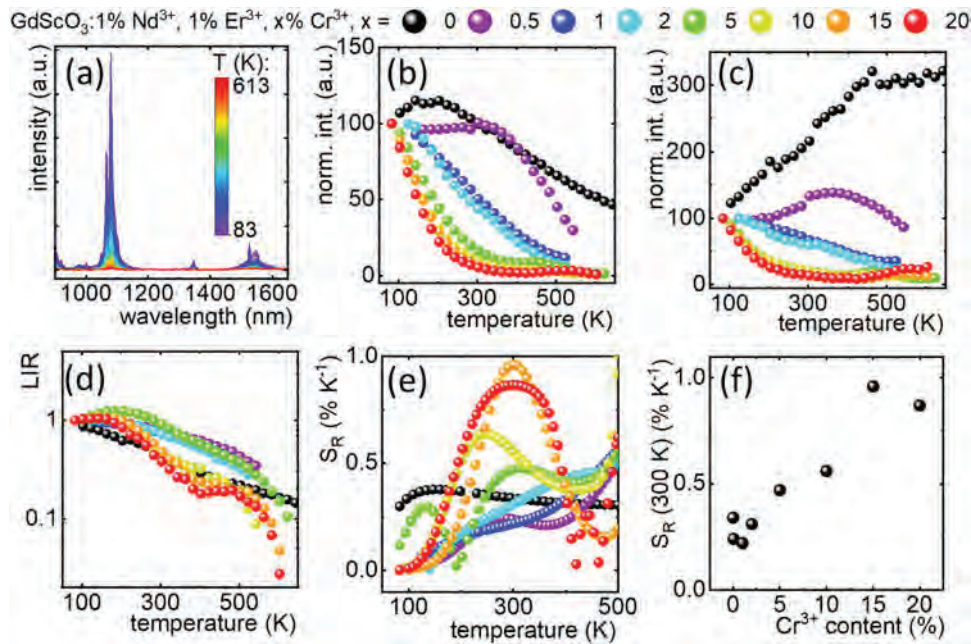
6

Fig. 4. Thermal evolution of the emission spectra of GdScO$_3$:Nd^{3+}, Er^{3+}, 5 % Cr^{3+} (λ_{exc} = 445 nm) – a); thermal evolution of the normalized intensity of the Nd^{3+} emission band – b), and of the Er^{3+} emission band – c), LIR of their values – d) and its relative sensitivity of GdScO$_3$: Nd^{3+}, Er^{3+}, x % Cr^{3+} with different Cr^{3+} concentration – e); the influence of Cr^{3+} concentration on the relative sensitivity and temperature uncertainty at 300 K – f).

elevated temperatures results in more efficient optical pumping and thus a slight increase in luminescence intensity. However, when the Cr^{3+} ions are introduced to the structure, significant changes in the thermal dependence of the LIR were observed. For the low dopant concentration regime (below 0.5 % Cr^{3+}) the intensity of the Nd^{3+} band remains almost constant in the 83–300 K temperature range, and then drastically decreases reaching 50 % of its original value at T$_{1/2}$ = 490 K. For the intermediate Cr^{3+} concentrations (0.5–2 % Cr^{3+}) the intensity of the ^{4}F$_{3/2}$→^{4}I$_{11/2}$ band decreases monotonically over the entire investigated range, reaching 50 % at T$_{1/2}$ = 300 K and 290 K, respectively. However, for the high dopant concentration (above 5 % Cr^{3+}) the rapid decrease in the intensity of the Nd^{3+} band emission occurs already at 83 K. The value of quenching temperature T$_{1/2}$ decreases from 190 K for 5 % Cr^{3+} to 145 K for 20 % Cr^{3+}. On the other hand for Er^{3+} luminescence without Cr^{3+} co-doping, the intensity continuously increases with temperature reaching a 3-fold enhancement at 440 K and remained at a similar level up to 580 K. Its thermal behaviour is completely changed when Cr^{3+} sensitization is activated. In the sample with 0.5 % Cr^{3+} a slight 40 % increase in the emission intensity of Er^{3+} ions was recorded from 200 to 360 K, followed by a slow decrease in the intensity, reaching at 543 K 87 % of the value at 83 K. In this case, the increase in intensity in the range between 200 and 360 K may result from the thermally dependent activation of the energy transfer process from Cr^{3+} to Er^{3+} ions. For 1 % and 2 % Cr^{3+}-co-doped compounds, similarly as in the case of Nd^{3+} emission, the Er^{3+} emission decreases continuously over the entire measurement range, but with slower quenching rate with respect to the Nd^{3+} band counterpart. Therefore, T$_{1/2}$ was determined at 390 K and 360 K for 1 % and 2 % Cr^{3+}, respectively. Finally, in the last group of x = 5–20 % Cr^{3+} in GdScO$_3$:Nd^{3+}, Er^{3+}, x % Cr^{3+} the thermal quenching of the ^{4}I$_{13/2}$→^{4}I$_{15/2}$ band was even more drastic than for the Nd^{3+} band. This is confirmed by T$_{1/2}$ = 160–140 K for samples with 5–20 % Cr^{3+}. On the other hand, the intensity reduction is smaller at higher temperatures, when for 400 K and 380 K in samples doped with 5 % and 10 % Cr^{3+}, the intensity of the Er^{3+} band is 13 % of the initial intensity, and then the intensity for 5 % Cr^{3+} slightly increases to 20 % at T = 460 K, while for 10 % Cr^{3+} it remains constant at 13 % until 540 K. The comparison with the intensity at

the stage of 10 % of initial signal with Nd^{3+} emission is possible for 15 % and 20 % Cr^{3+}-co-doped samples, for which 10 % intensity from 80 K was observed at about 360 K. The relative thermal changes of the Nd^{3+} and Er^{3+} emission bands intensities were quantified by means of the calculation of their luminescence intensity ratio (LIR) as follows (Eq. 6, Fig. 4d):

$$LIR = \frac{\int I(^4F_{3/2} \rightarrow {}^4I_{11/2})(Nd^{3+})d\lambda}{\int I(^4I_{11/2} \rightarrow {}^4I_{15/2})(Er^{3+})d\lambda} \quad (6)$$

For Cr^{3+}-un-doped GdScO$_3$:Nd^{3+}, Er^{3+} the LIR value monotonically decreases reaching 48 % and 18 % at T = 300 K and 560 K, respectively. For the 0.5 %, 1 % and 2 % doped samples, the LIR curve at temperature follows a similar pattern and changes slowly from 80 K to 520 K eventually reaching values of 0.38, 0.33 and 0.28 respectively. Above 5 % Cr^{3+}, in the range from 80 to 200 K there is a slight increase in the LIR to the value of 1.24, followed by gradual decrease to 0.37 at 500 K and a drastic fall to 0.10 at 620 K. For GdScO$_3$:Nd^{3+}, Er^{3+}, 10 % Cr^{3+} a slight increase to LIR = 1.04 at 140 K was detected, followed by a decrease in value to 0.18 at 500 K. Similar LIR changes with increasing temperature were determined for 15 % and 20 % Cr^{3+}. On the other hand, for 20 % Cr^{3+} the decrease from LIR = 1.02 at 160 K was obtained at a lower temperature to 0.18 at 400 K, while above this temperature a slight increase to 0.20 at 480 K and then reduction of LIR to 3 % at 600 K was observed. Moreover, to verify the influence of Cr^{3+} concentration on thermal changes of LIR values in quantitative way, the relative sensitivity S$_R$ was calculated according to the following formula (Eq. 7):

$$S_R = \frac{1}{\Omega} \frac{\Delta\Omega}{\Delta T} \times 100\% \quad (7)$$

where Ω is the thermometric parameter (in this case LIR) and $\Delta\Omega$ represents its change for the ΔT change of temperature. The obtained S$_R$ results were plotted at Fig. 4e. For the 0 % Cr^{3+} sample, S$_R$ remains slightly above 0.3 % K^{-1} over a wide range of 80–480 K with a maximum value of 0.38 % K^{-1} at 150 K. Co-doping with Cr^{3+} ions at a concentration of 0.5 % did not act favourably to improve the relative sensitivity in this range, with a S$_{Rmax}$ = 0.24 % K^{-1} at 270 K. A lower S$_R$ value is also obtained for 1 % and 2 % Cr^{3+}. However, above

5 % Cr^{3+} an improvement in the maximum relative sensitivity can be noticed with respect to non Cr-co-doped samples. For $GdScO_3$:Nd^{3+}, Er^{3+}, 5 % Cr^{3+}, S_{Rmax} = 0.48 % K^{-1} at 310 K was obtained, while for 10 % it is 0.64 % K^{-1} at 245 K. Finally, for 15 % and 20 % Cr^{3+} samples a significant improvement in the relative sensitivity was noted. For 15 % Cr^{3+} the S_R is maintained above 0.5 % K^{-1} in the temperature range between 225 and 380 K with a maximum of S_{Rmax} = 0.96 % K^{-1} at 300 K. When co-doping gadolinium scandate with 20 % Cr^{3+}, the range in which a relative sensitivity exceeded 0.5 % K^{-1} was wider (195–390 K), at the expense of a slight decrease in maximum sensitivity with S_{Rmax} = 0.87 % K^{-1} at 295 K. The comparison of the S_R at room temperature (300 K) presented in Fig. 4f confirms the beneficial effect of the Cr^{3+} dopant concentration to thermometric properties of Nd^{3+}/Er^{3+} based ratiometric thermometer. The highest S_R(300 K) value equal to 0.96 % K^{-1} was obtained for 15 % Cr^{3+}, which represents a 2.8-fold enhancement with respect to the Cr^{3+}-undoped counterpart. For 20 % Cr^{3+} the sensitisation effect was slightly lower and with S_R(300 K) = 0.87 % K^{-1} was 255 % of the value for 0 % Cr^{3+}.

In order to understand the energy transfer process between Cr^{3+} and Ln^{3+} ions the influence of the Cr^{3+} ion on the kinetics of the Ln^{3+} luminescence was analysed (Fig. 5, see also Fig. S12). For the sample doped with Nd^{3+} and Er^{3+} ions, the lifetime of the Nd^{3+} $^4F_{3/2}$ excited state (τ_{avr}) 60 μs, which is in agreement with the previously reported lifetimes for $GdScO_3$:3 % Nd^{3+} single crystal by Amanyan et al.[31]. When a small concentration of Cr^{3+} ions was introduced the elongation of the τ_{avr} was observed. This elongation was already reported by Saiki et al.[32]. for Cr^{3+}, Nd^{3+} co-doped systems and was discussed in terms of the pumping of the $^4F_{3/2}$ state by the $Cr^{3+}\rightarrow Nd^{3+}$ energy transfer. Since the lifetime of the excited state of Cr^{3+} is usually longer with respect to the $^4F_{3/2}$ counterpart the continuous energy transfer process results in the elongation of the latter one [32]. The further increase in Cr^{3+} concentration results in gradual shortening of the τ_{avr} up to τ_{avr} = 0.053 ms at 83 K for 20 % Cr^{3+}. For higher concentration of Cr^{3+} the quenching of the population of the

Cr^{3+} excited state results in the reduction of the contribution of Cr^{3+} ions in the elongation process and the shortening of the τ_{avr} due to the back $Nd^{3+}\rightarrow Cr^{3+}$ energy transfer. It is worth noting that the τ_{avr} of the $^4F_{3/2}$ state upon direct excitation into $^4F_{5/2}$ state of the Nd^{3+} ions (λ_{exc}=808 nm) remains almost independent on the Cr^{3+} concentration (Fig. S14). This confirms that $Cr^{3+}\rightarrow Nd^{3+}$ energy transfer is responsible for results presented in Fig. 5a), whereas the $Nd^{3+}\rightarrow Er^{3+}$ energy transfer probability is independent on Cr^{3+} ions amount. The thermal evolution of τ_{avr} of $^4F_{3/2}$ state for $GdScO_3$:Nd^{3+}, Er^{3+}, x % Cr^{3+} with different Cr^{3+} concentration was performed (Fig. 5b, Fig. S13). For the sample undoped with Cr^{3+} ions, a slight increase in lifetime from 60 μs at 83 K to 71 μs at 273 K was noted and was similarly observed from 160 μs at 77 K to 170 μs at 300 K for $GdScO_3$:1 % Nd^{3+} in the literature[31,32]. In the case of $GdScO_3$:Nd^{3+}, Er^{3+}, x % Cr^{3+} where x = 1, 2, 5 up to 200 K the τ_{avr} remains constant and above this temperature it starts to shorten. Since the τ_{avr} lifetime in this case is longer than the counterpart measured for Cr^{3+} undoped system, this shortening can be explained in terms of the thermal activation of the $Cr^{3+}\rightarrow Nd^{3+}$ energy transfer that results in shortening of the lifetime of the donor state of Cr^{3+}. The thermal shortening of the lifetime of the Nd^{3+} state can be used as a thermometric parameter of the lifetime based luminescence thermometer. Therefore the S_R was calculated according to Eq. 7 (Fig. S15). In this case, the highest sensitivity values S_{Rmax} were obtained for 10 % Cr^{3+} with the value of S_{Rmax} = 0.66 % K^{-1} at 266 K, which is a 5-fold improvement over 0.13 % K^{-1} at 120 K for Cr^{3+}-un-doped phosphor. Similar behaviour to the lifetimes of the Nd^{3+} excited state at 83 K under doping with Cr^{3+} ions was also observed for the $^4I_{13/2}$ state of Er^{3+} ions (Fig. 5c, Fig. S16). For the $GdScO_3$:Nd^{3+}, Er^{3+} sample the average lifetime was 0.83 ms, while for 1 % Cr^{3+} it was already τ_{avr} = 2.17 ms. When considering the τ_{avr} of the $^4I_{13/2}$ state of Er^{3+} ions very similar effect of concentration of Cr^{3+} ions can be found. In the case of the Cr^{3+} un-doped sample the τ_{avr} is almost temperature independent. However an increase in the Cr^{3+} amount results in the initiation of the thermal shortening of the τ_{avr}. For as high as 20 % of Cr^{3+}, a shortening of the lifetime was observed already from 83 K, when it was 1.32 ms, whereas τ_{avr} = 0.55 ms at 283 K (Fig. 5d, Fig. S17a). Based on the thermal evolution of average lifetime of the Er^{3+} excited state, a S_{Rmax} value of 0.46 % K^{-1} at 217 K was calculated (Fig. S17b).

4. Conclusions

In this work, the effect of Cr^{3+} ion concentration on the thermometric properties of $GdScO_3$:Er^{3+},Nd^{3+} luminescent thermometer exploiting the luminescence intensity ratio of Nd^{3+} to Er^{3+} ions as a thermometric parameter was investigated. As shown, doping with Cr^{3+} ions allowed for an up to 25-fold enhancement of the emission intensity of Ln^{3+} ions through a high absorption cross section of Cr^{3+} ions in respect to Ln^{3+} ions and an efficient $Cr^{3+}\rightarrow Ln^{3+}$ energy transfer. In addition, due to the large spectral width of the absorption bands of Cr^{3+} ions, the spectral range of optical excitation at which the emission of Nd^{3+} and Er^{3+} ions can be generated has been significantly extended. The fact of the energy mismatch between the ^2E level of Cr^{3+} ions and the excited levels of Nd^{3+} and Er^{3+} ions, the probability of inter-ion energy transfer shows a strong susceptibility to temperature changes. Therefore, increasing the concentration of Cr^{3+} ions to 15 mol % made it possible to increase the maximum relative sensitivity value threefold from 0.3 % K^{-1} at 300 for $GdScO_3$:Nd^{3+},Er^{3+} to 0.96 % K^{-1} for $GdScO_3$:15 %Cr^{3+}, Nd^{3+}, Er^{3+}.

In conclusion, the proposed strategy of using Cr^{3+} ions as luminescence sensitizers of Ln^{3+} ions has a favourable effect on the thermometric performance of this type of ratiometric luminescence thermometers and may make it possible to expand the scope of their applicability in the future.
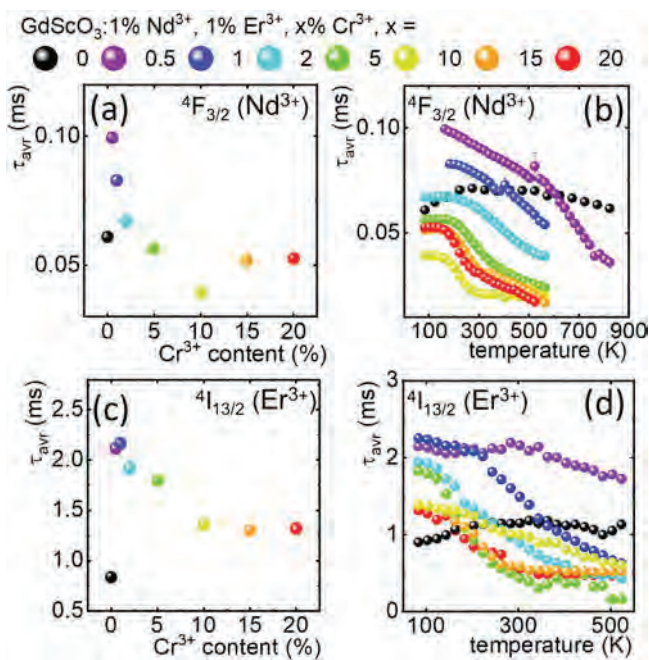
Fig. 5. The influence of Cr^{3+} concentration on the average lifetime of Nd^{3+} excited state $^4F_{3/2}$ (λ_{exc} = 1082 nm) at 83 K in $GdScO_3$: Nd^{3+}, Er^{3+}, x % Cr^{3+} – a); thermal evolution of Nd^{3+} excited state $^4F_{3/2}$ for $GdScO_3$: Nd^{3+}, Er^{3+}, x % Cr^{3+} with different Cr^{3+} concentration – b); the influence of Cr^{3+} concentration on the average lifetime of Er^{3+} excited state $^4I_{13/2}$ (λ_{exc} = 1525 nm) at 83 K in $GdScO_3$: Nd^{3+}, Er^{3+}, x % Cr^{3+} – c); thermal evolution of Er^{3+} excited state $^4I_{13/2}$ for $GdScO_3$: Nd^{3+}, Er^{3+}, 20 % Cr^{3+} – d).

CRediT authorship contribution statement

Wojciech M. Piotrowski: Methodology, Investigation, Writing – original draft. **Kamila Maciejewska:** Methodology, Investigation. **Linda Dalipi:** Methodology, Investigation. **Benoit Fond:** Conceptualization, Writing – original draft, Writing – review & editing. **Lukasz Marciniak:** Conceptualization, Writing – original draft, Writing – review & editing.

Data Availability

Data will be made available on request.

Declaration of Competing Interest

The authors declare the following financial interests/personal relationships which may be considered as potential competing interests: Lukasz Marciniak reports financial support was provided by National Science Centre Poland.

Appendix A. Supporting information

Supplementary data associated with this article can be found in the online version at doi:10.1016/j.jallcom.2022.166343.

References

[1] L. Labrador-Páez, M. Pedroni, A. Speghini, J. García-Solé, P. Haro-González, D. Jaque, Reliability of rare-earth-doped infrared luminescent nanothermometers, Nanoscale 10 (2018) 22319–22328.

[2] M. Dramićanin, Luminescence: the basics, methods, and instrumentation, in: M.B.T.-L.T. Dramićanin (Ed.), Lumin. Thermom. Woodhead Publishing, 2018, pp. 33–61.

[3] M.D. Dramićanin, Trends in luminescence thermometry, J. Appl. Phys. 128 (2020) 40902.

[4] M. Suta, A. Meijerink, A. Theoretical, Framework for ratiometric single ion luminescent thermometers—thermodynamic and kinetic guidelines for optimized performance, Adv. Theory Simul. 3 (2020) 2000176.

[5] D. Jaque, F. Vetrone, Luminescence nanothermometry, Nanoscale 4 (2012) 4301–4326.

[6] C.D.S. Brites, A. Millán, L.D. Carlos, Lanthanides in Luminescent Thermometry, in: B. Jean-Claude, P.B.T.-H. on the P. and C. of R.E. Vitalij K. (Eds.), Handb. Phys. Chem. Rare Earths, Elsevier, 2016: pp. 339–427.

[7] J. Zhou, B. del Rosal, D. Jaque, S. Uchiyama, D. Jin, Advances and challenges for fluorescence nanothermometry, Nat. Methods 17 (2020) 967–980.

[8] A. Bednarkiewicz, L. Marciniak, L.D. Carlos, D. Jaque, Standardizing luminescence nanothermometry for biomedical applications, Nanoscale 12 (2020) 14405–14421.

[9] W. Piotrowski, K. Kniec, L. Marciniak, Enhancement of the Ln³⁺ ratiometric nanothermometers by sensitization with transition metal ions, J. Alloy. Compd. 870 (2021) 159386.

[10] W. Piotrowski, L. Dalipi, R. Szukiewicz, B. Fond, M. Dramicanin, L. Marciniak, The role of Cr³⁺ and Cr⁴⁺ in emission brightness enhancement and sensitivity improvement of NIR-emitting Nd³⁺/Er³⁺ ratiometric luminescent thermometers, J. Mater. Chem. C. 9 (2021) 12671–12680, https://doi.org/10.1039/d1tc03046a

[11] Y. Bao, Z. Zhang, B. Cao, Y. Liu, J. Shang, Y. Yang, B. Dong, Energy transfer from Er to Nd ions by the thermal effect and promotion of the photocatalysis of the NaYF₄:Yb,Er,Nd/W₁₈O₄₉ heterostructure, Nanoscale 11 (2019) 7433–7439.

[12] T. Miyakawa, D.L. Dexter, Phonon sidebands, multiphonon relaxation of excited states, and phonon-assisted energy transfer between ions in solids, Phys. Rev. B. 1 (1970) 2961–2969.

[13] X. Shen, Q. Nie, T. Xu, S. Dai, X. Wang, Investigation on energy transfer from Er3+ to Nd³⁺ in tellurite glass, J. Rare Earths 26 (2008) 899–903.

[14] D. Wang, W. Hou, N. Li, Y. Xue, Q. Wang, X. Xu, D. Li, H. Zhao, J. Xu, Growth, spectroscopic properties and crystal field analysis of Cr³⁺ doped GdScO₃ crystal, Opt. Mater. Express 9 (2019) 4218–4227.

[15] J. Shi, B. Liu, Q. Wang, H. Tang, F. Wu, D. Li, H. Zhao, Z. Wang, W. Deng, X. Xu, J. Xu, Crystal growth, spectroscopic characteristics, and Judd-Ofelt analysis of Dy:Lu₂O₃ for yellow laser, Chin. Phys B 27 (2018) 77802.

[16] R. Uecker, B. Velickov, D. Klimm, R. Bertram, M. Bernhagen, M. Rabe, M. Albrecht, R. Fornari, D.G. Schlom, Properties of rare-earth scandate single crystals (Re= Nd−Dy), J. Cryst. Growth 310 (2008) 2649–2658.

[17] B. Veličkov, V. Kahlenberg, R. Bertram, M. Bernhagen, Crystal chemistry of GdScO₃, DyScO₃, SmScO₃ and NdScO₃, Z. Für Krist. 222 (2007) 466–473.

[18] B. Fond, C. Abram, M. Pougin, F. Beyrau, Characterisation of dispersed phosphor particles for quantitative photoluminescence measurements, Opt. Mater. 89 (2019) 615–622.

[19] R.D. Shannon, Revised effective ionic radii and systematic studies of interatomic distances in halides and chalcogenides, Acta Crystallogr. Sect. A 32 (1976) 751–767.

[20] M. Johnsson, P. Lemmens, Crystallography and chemistry of perovskites, Handb. Magn. Adv. Magn. Mater. (2007).

[21] G. Blasse, Energy transfer in oxidic phosphors, Phys. Lett. A 28 (1968) 444–445.

[22] G. Blasse, B.C. Grabmaier, Energy Transfer BT - Luminescent Materials, in: G. Blasse, B.C. Grabmaier (Eds.), Springer Berlin Heidelberg, Berlin, Heidelberg, 1994: pp. 91–107.

[23] G. Lucovsky, Y. Zhang, J.L. Whitten, D.G. Schlom, J.L. Freeouf, Separate and independent control of interfacial band alignments and dielectric constants in transition metal rare earth complex oxides, Microelectron. Eng. 72 (2004) 288–293.

[24] H.M. Christen, G.E. Jellison, I. Ohkubo, S. Huang, M.E. Reeves, E. Cicerrella, J.L. Freeouf, Y. Jia, D.G. Schlom, Dielectric and optical properties of epitaxial rare-earth scandate films and their crystallization behavior, Appl. Phys. Lett. 88 (2006) 262906.

[25] S.-G. Lim, S. Kriventsov, T.N. Jackson, J.H. Haeni, D.G. Schlom, A.M. Balbashov, R. Uecker, P. Reiche, J.L. Freeouf, G. Lucovsky, Dielectric functions and optical bandgaps of high-K dielectrics for metal-oxide-semiconductor field-effect transistors by far ultraviolet spectroscopic ellipsometry, J. Appl. Phys. 91 (2002) 4500–4505.

[26] Z. Jia, C. Yuan, Y. Liu, X.-J. Wang, P. Sun, L. Wang, H. Jiang, J. Jiang, Strategies to approach high performance in Cr³⁺-doped phosphors for high-power NIR-LED light sources, Light Sci. Appl. 9 (2020) 86.

[27] Y. Tanabe, S. Sugano, On the absorption spectra of complex ions, J. Phys. Soc. Jpn. 9 (1954) 753–766.

[28] Y. Tanabe, H. Kamimura, On the absorption spectra of complex ions Iv. the effect of the spin-orbit interaction and the field of lower symmetry on d electrons in cubic field, J. Phys. Soc. Jpn. 13 (1958) 394–411.

[29] K. Elzbieciak, L. Marciniak, The Impact of Cr³⁺ doping on temperature sensitivity modulation in Cr³⁺ Doped and Cr³⁺, Nd³⁺ Co-doped Y₃Al₅O₁₂, Y₃Al₂Ga₃O₁₂, and Y₃Ga₅O₁₂ nanothermometers, Front. Chem. 6 (2018) 424.

[30] A.H. Khalid, K. Kontis, Progress towards absolute intensity measurements of emissions from high temperature thermographic phosphors, J. Lumin. 131 (2011) 1312–1321.

[31] S.N. Amanyan, P.A. Arsen'ev, K.S. Bagdasarov, A.M. Kevorkov, D.I. Korolev, A.V. Potemkin, V.V. Femin, Synthesis and examination of GdScO₃ single crystals activated by Nd³⁺, J. Appl. Spectrosc. 38 (1983) 343–348.

[32] T. Saiki, M. Nakatsuka, K. Fujioka, S. Motokoshi, K. Imasaki, Y. Iida, Increase in effective fluorescence lifetime by cross-relaxation effect depending on temperature of Nd/Cr: YAG ceramic using white-light pump source, Opt. Photonics Lett. 6 (2013) 1350003.

Cr³⁺ ions as an efficient antenna for the sensitization and brightness enhancement of Nd³⁺, Er³⁺-based ratiometric thermometer in GdScO₃ perovskite lattice

W. M. Piotrowski[1], K. Maciejewska[1], L. Dalipi[2], B. Fond[2], L. Marciniak[1]*

[1]Institute of Low Temperature and Structure Research, Polish Academy of Sciences, Okólna 2, 50-422 Wroclaw, Poland

[2]Institute of Fluid Dynamics and Thermodynamics, Otto-von-Guericke University Magdeburg, 39106 Magdeburg, Germany

* corresponding author: *l.marciniak@intibs.pl*

The Goldschmidt tolerance factor were calculated involving dopant concentrations with the following equation (Eq. S1):

$$t = \frac{1}{\sqrt{2}} \frac{0.998 \cdot r_{Gd^{3+}} + 0.01 \cdot r_{Nd^{3+}} + 0.01 \cdot r_{Er^{3+}} + r_{O^{2-}}}{(1-x) \cdot r_{Sc^{3+}} + x \cdot r_{Cr^{3+}} + r_{O^{2-}}} \qquad \text{(Eq. S1)}$$

where: r_{Gd3+}, r_{Nd3+}, r_{Er3+}, r_{Sc3+}, r_{Cr3+}, r_{O2-} – effective ionic radii of Gd^{3+}, Nd^{3+}, Er^{3+}, Sc^{3+}, Cr^{3+} and O^{2-}, respectively, x – the concentration of Cr^{3+} ions.
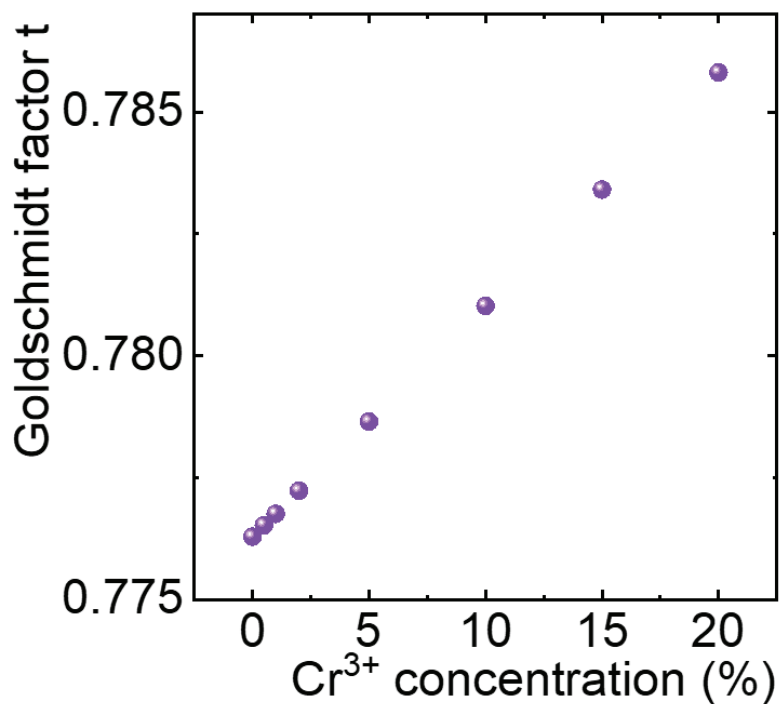
Figure S1. The effect of the Cr^{3+} concentration on the value of the Goldschmidt tolerance factor t in $GdScO_3$:1% Nd^{3+}, 1% Er^{3+}, x% Cr^{3+}.
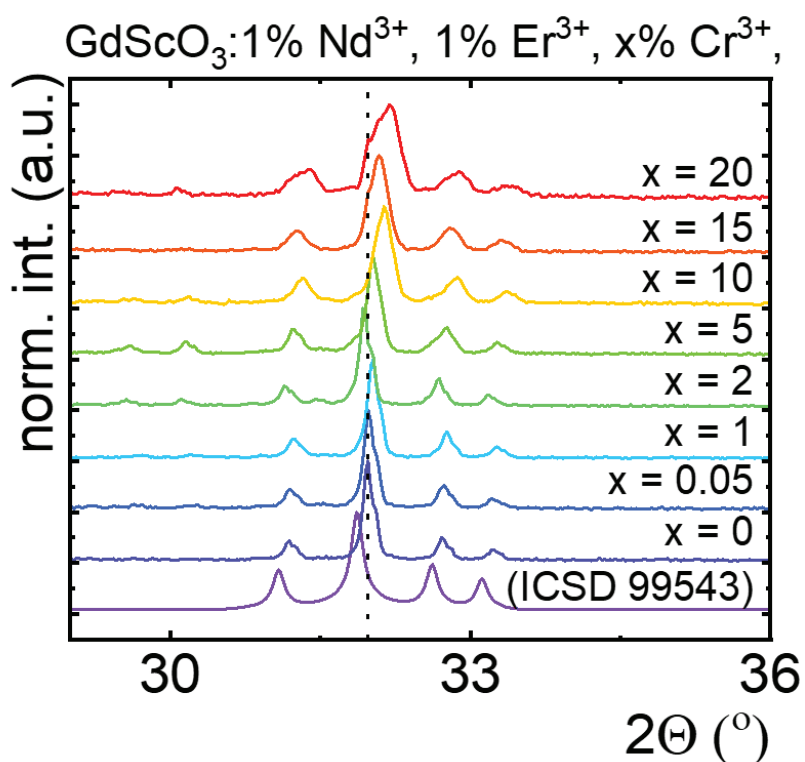
Figure S2. The zoom of the X-ray diffraction patterns of $GdScO_3$:Nd^{3+}, Er^{3+}, x% Cr^{3+} powders with different Cr^{3+} concentration.
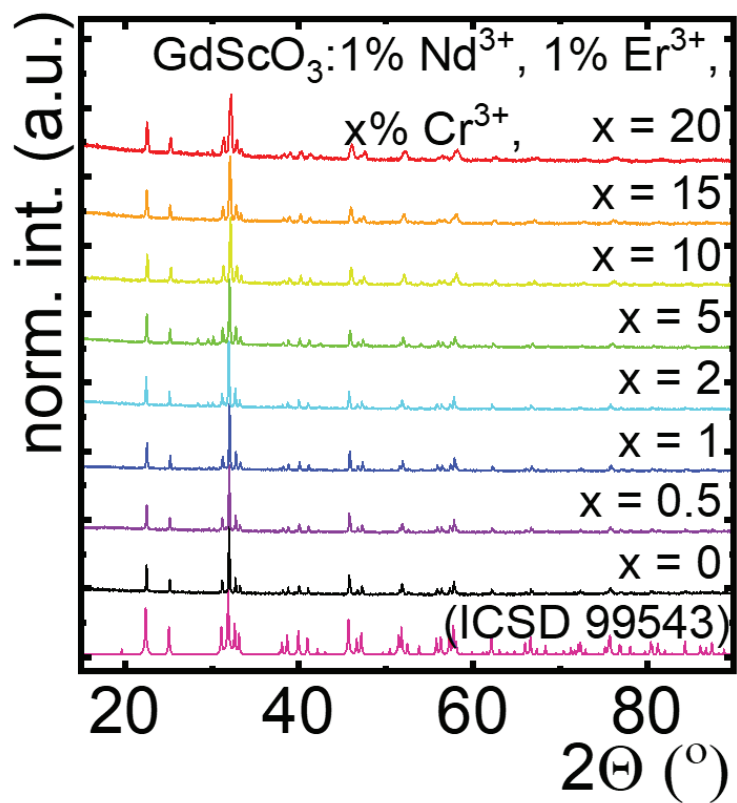
Figure S3. The XRD patterns of $GdScO_3$:Nd^{3+},Er^{3+},Cr^{3+} with different concentration of Cr^{3+} ions.
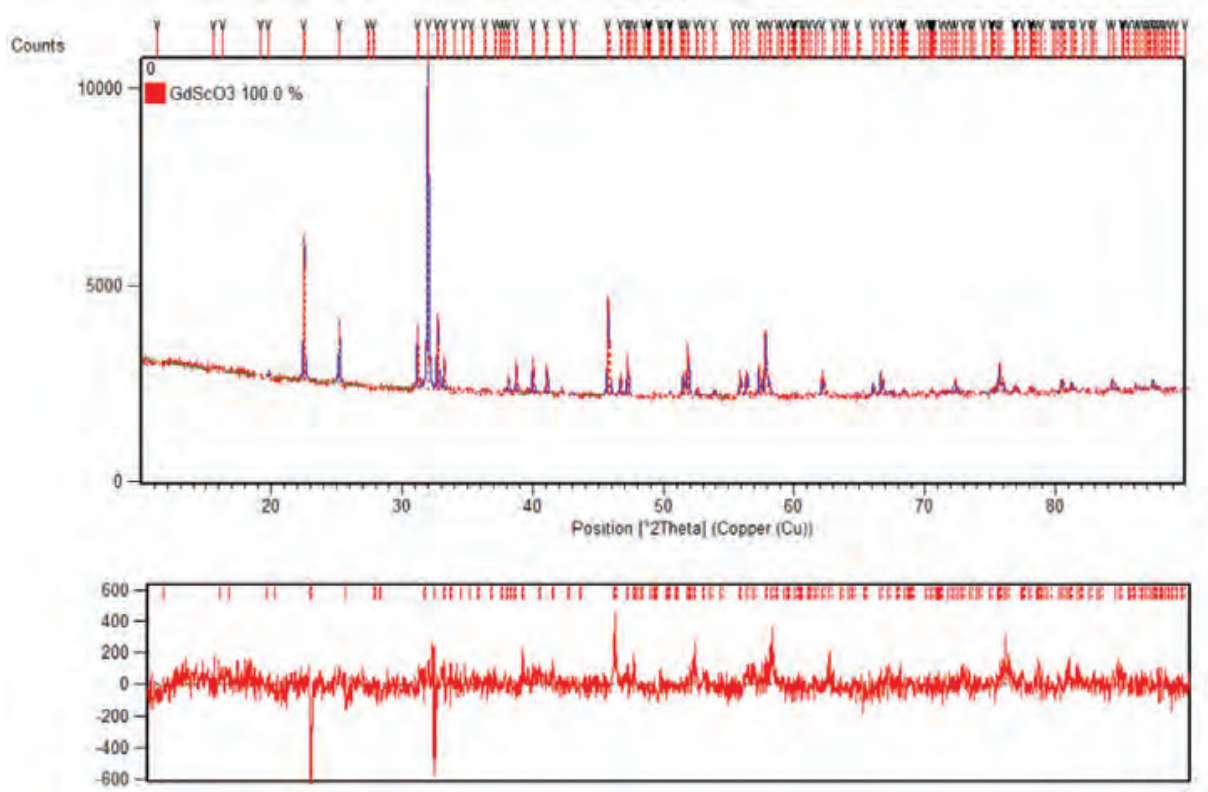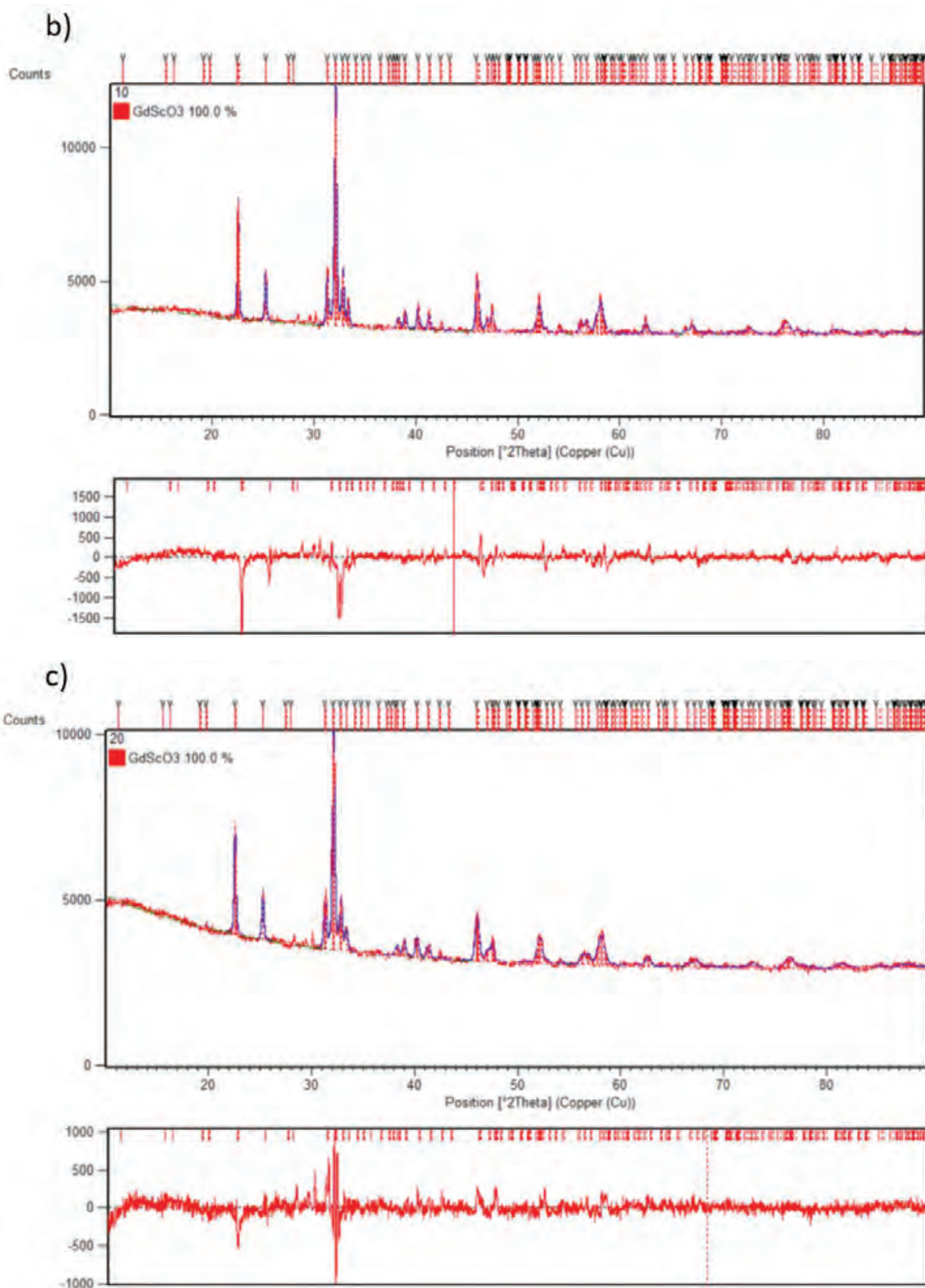
Figure S4. Representative of the Rietveld refinement results for GdScO$_3$:Nd^{3+},Er^{3+} co-doped with 0%Cr^{3+}-a), 10%Cr^{3+}-b) and 20%Cr^{3+}-c).
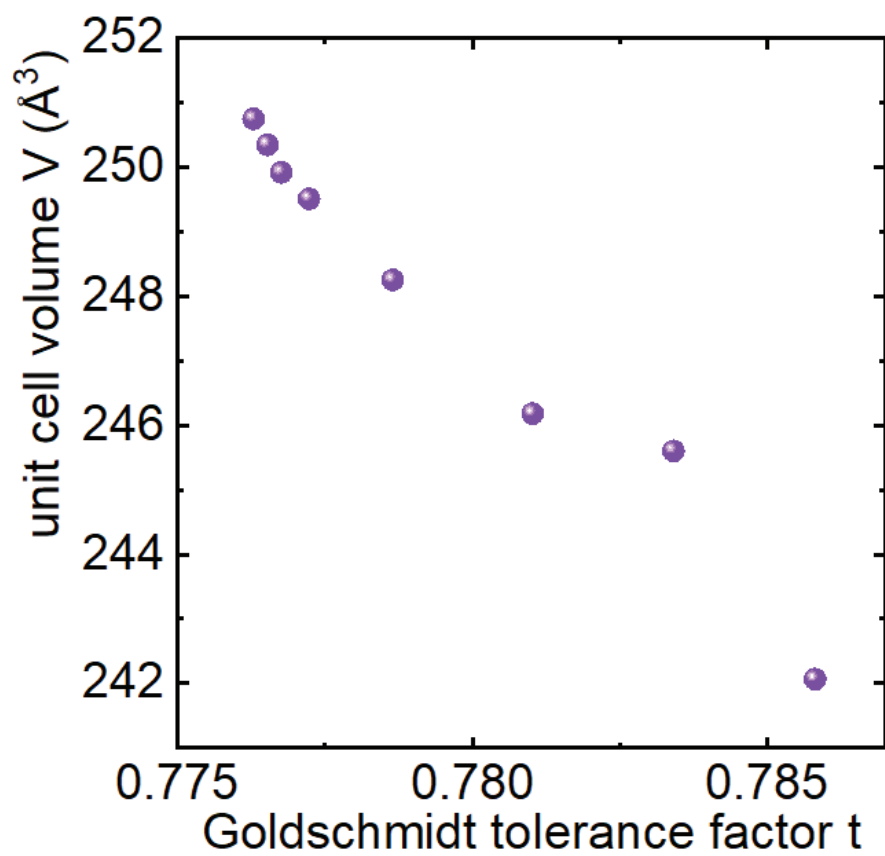
Figure S5. The Goldschmidt tolerance factor t in the function of the experimental unit cell volume of $GdScO_3$:Nd^{3+}, Er^{3+}, x% Cr^{3+} with different Cr^{3+} concentration.
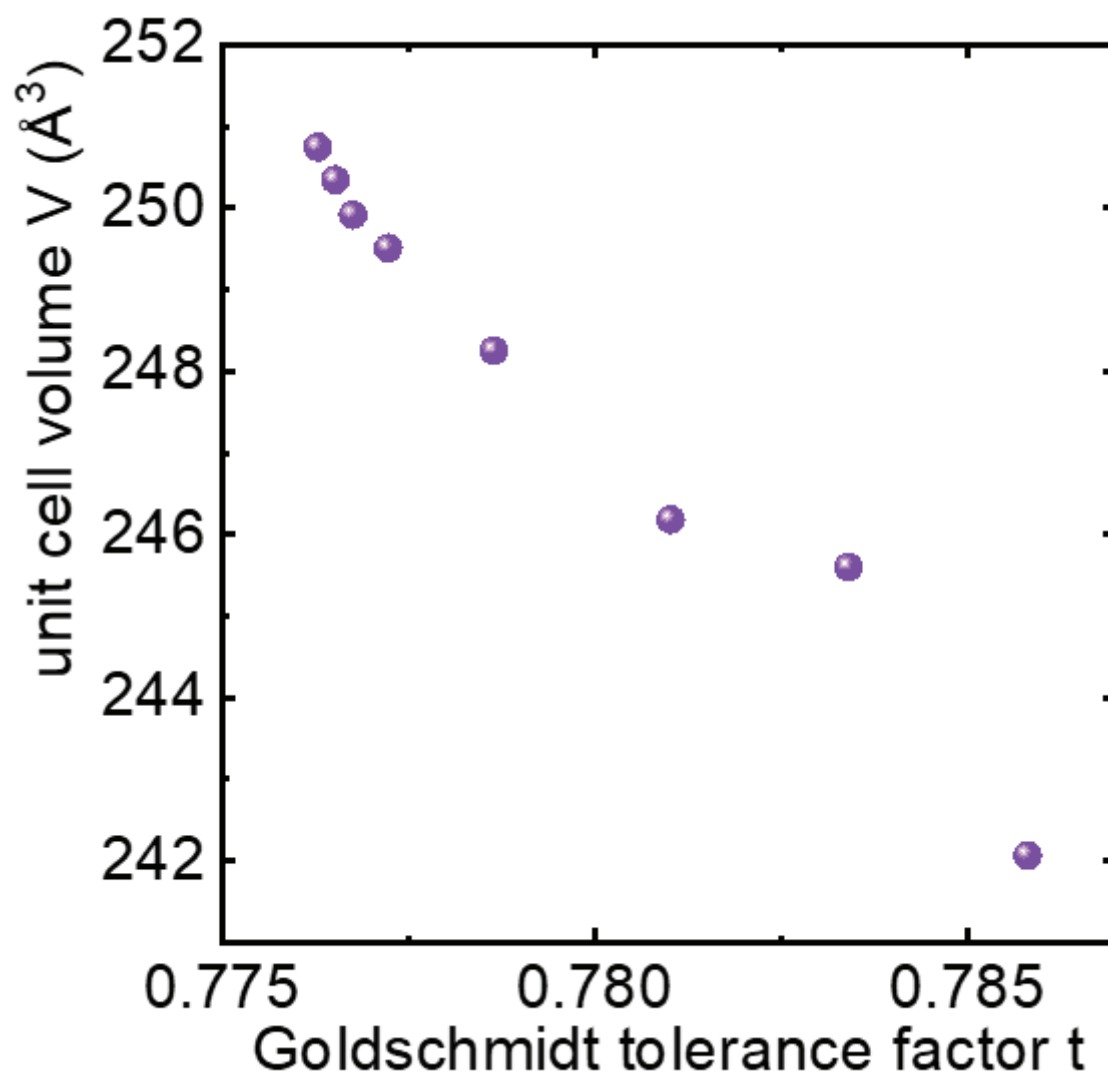
Figure S6. The influence of the Cr^{3+} concentration on the Er^{3+}/Nd^{3+} emission intensity ratio in the $GdScO_3$:Nd^{3+}, Er^{3+}, x% Cr^{3+} with different Cr^{3+} concentration.
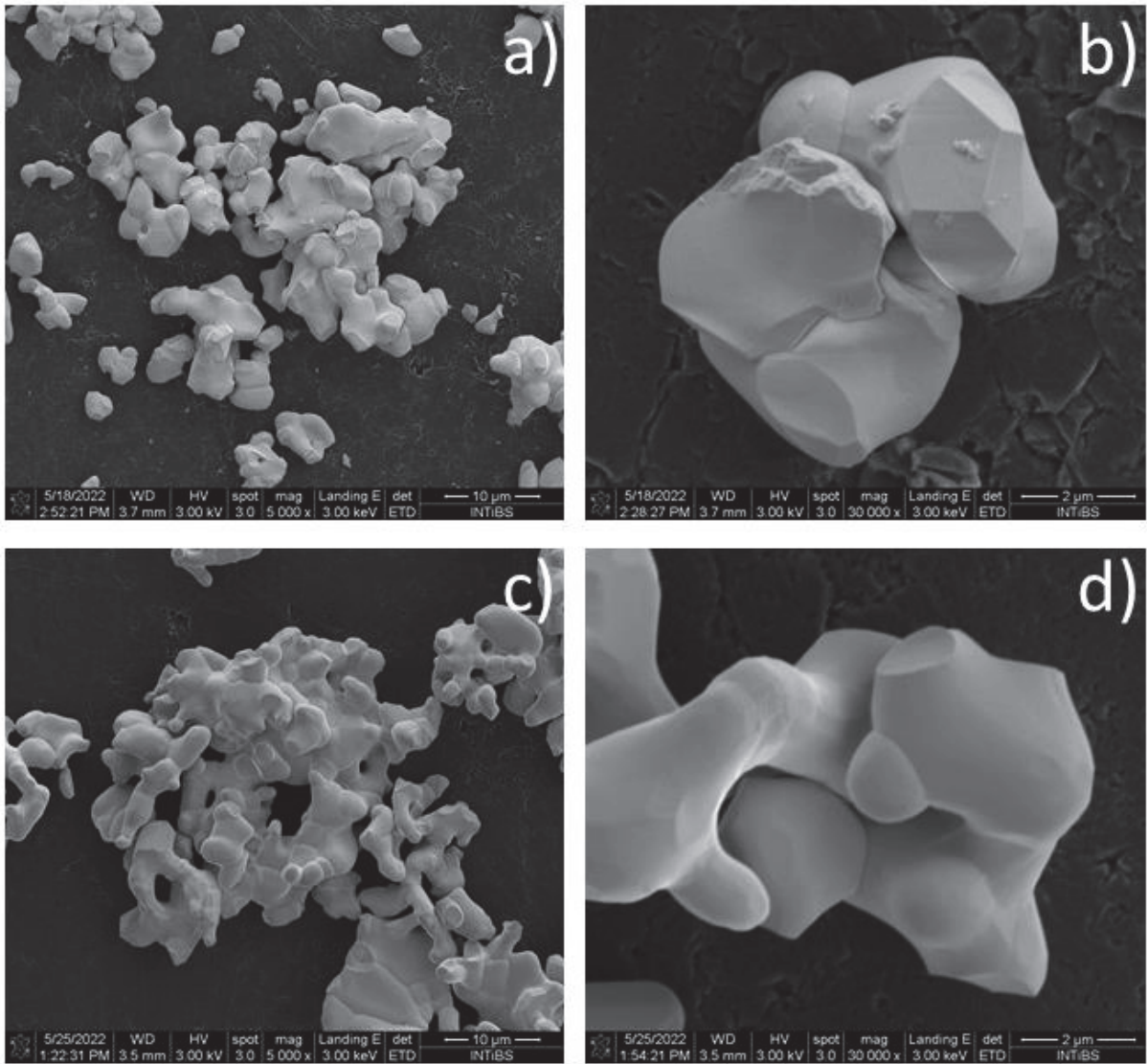
Figure S7. Representative SEM images of GdScO$_3$:1%Nd^{3+},Er^{3+}-a), -b) and
GdScO$_3$:1%Nd^{3+},Er^{3+},10%Cr^{3+}-c), -d).
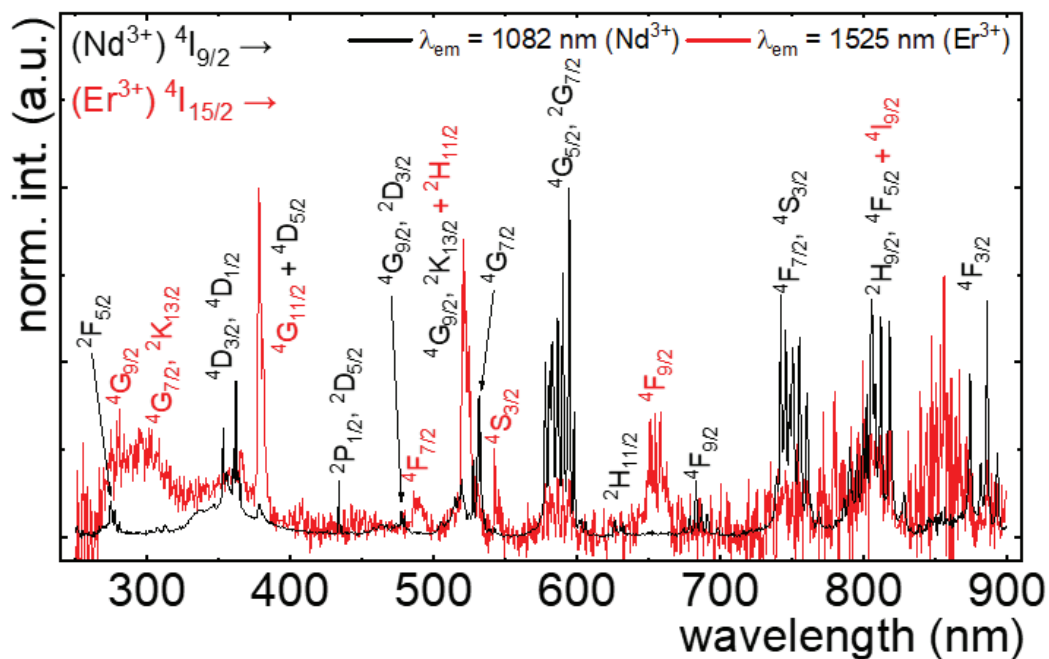
Figure S8. The excitation spectra of GdScO$_3$:Nd^{3+}, Er^{3+} unco-doped with Cr^{3+} measured for two different emission bands at 83 K.
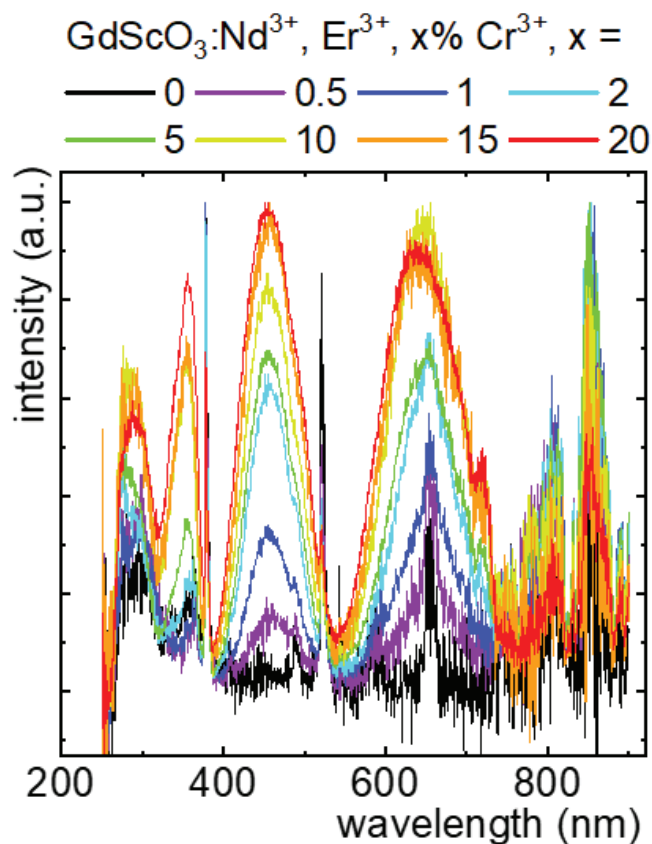
Figure S9. The influence of Cr^{3+} concentration on the excitation spectra of Er^{3+} ions (λ_{em} = 1525 nm) in GdScO$_3$:Nd^{3+}, Er^{3+}, x% Cr^{3+} samples.
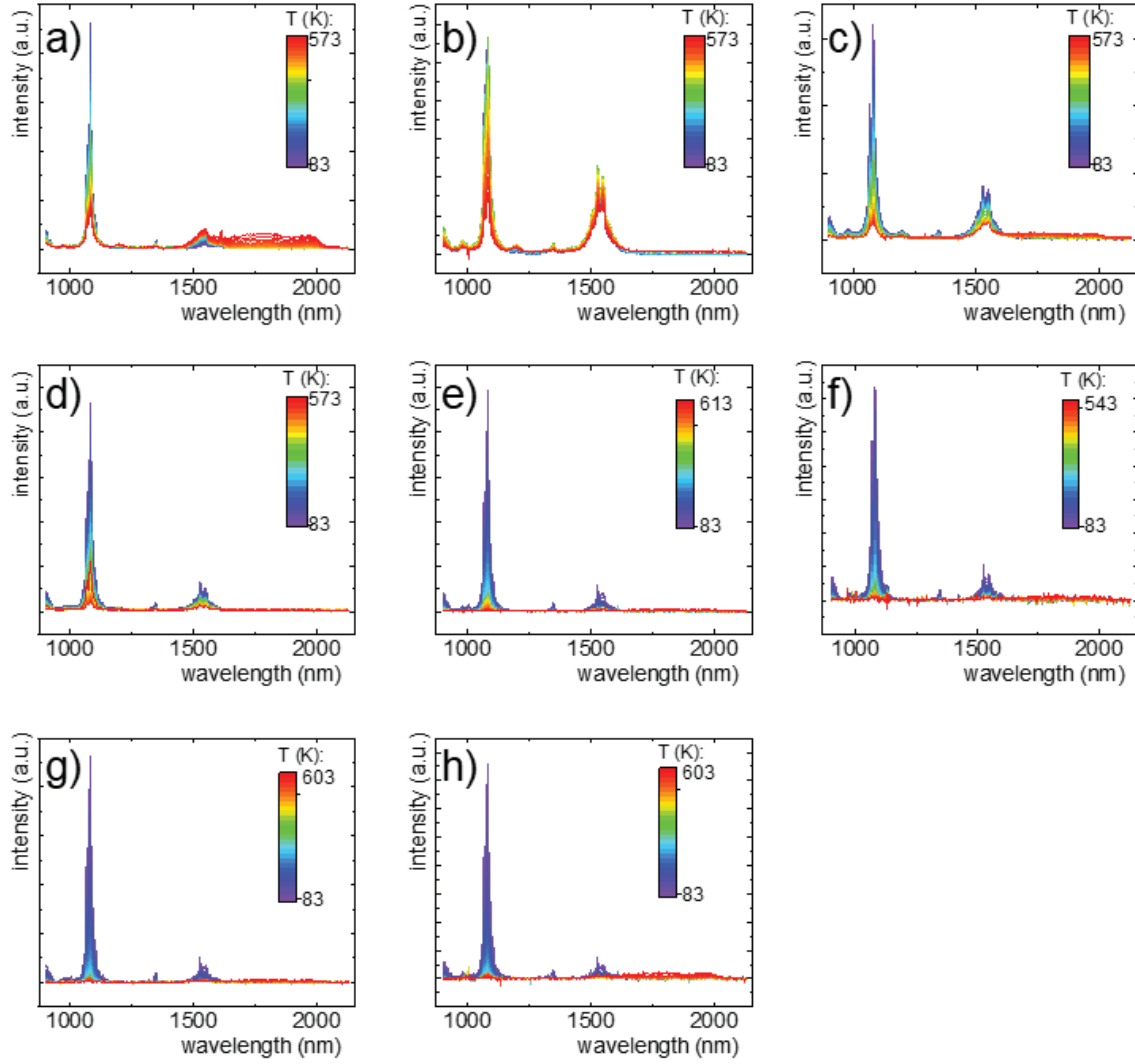
Figure S10. Thermal evolution of the emission spectra of GdScO$_3$:Nd^{3+}, Er^{3+}, x% Cr^{3+}, where x = 0 (λ_{exc} = 808 nm) – a); 0.5 (λ_{exc} = 445 nm) – b); 1 – c); 2 – d); 5 – e); 10 – f); 15 – g); 20 – h).

The integral intensities of the Nd^{3+} and Er^{3+} bands to calculate LIR values were fitted with Mott-Seitz equation (Eq. S2):

$$I = \frac{I_0}{C \cdot \exp(-\frac{W}{k \cdot T}) + 1} \tag{Eq. S2}$$

where: I – the intensity in temperature T, I$_0$ – the intensity in the initial temperature, W - the activation energy, k – Boltzmann constant, C – the dimensionless constant.

Temperature determination uncertainty was calculated using Eq. S3:

$$\delta T = \frac{1}{S_R} \cdot \frac{\delta LIR}{LIR} \qquad \text{(Eq. S3a)}$$

where: S_R is the relative sensitivity and $\delta LIR/LIR$ determines the uncertainty of the LIR determination where $\delta LIR/LIR$ was determined as follows:

$$\frac{\delta LIR}{LIR} = \sqrt{\left(\frac{\delta I_{Nd3+}}{I_{Nd3+}}\right)^2 + \left(\frac{\delta I_{Er3+}}{I_{Er3+}}\right)^2} \qquad \text{(Eq. S3b)}$$
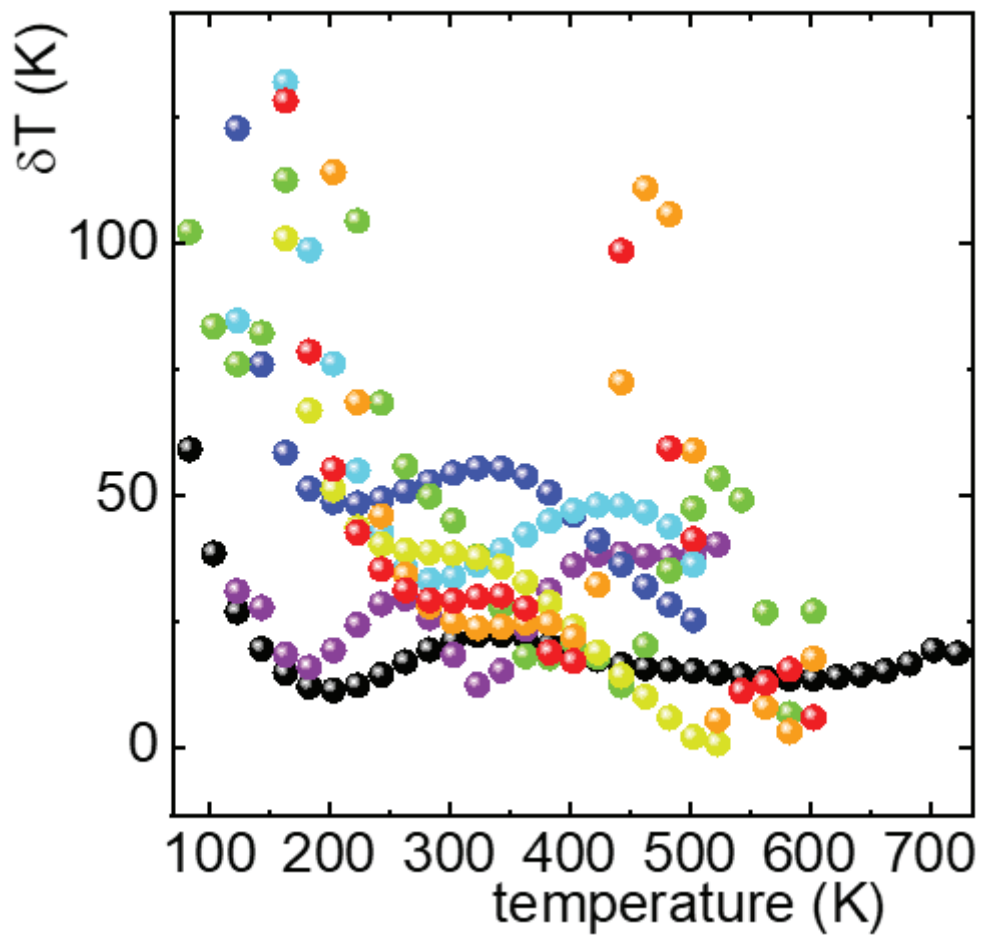
Figure S11. Thermal evolution of the temperature determination uncertainty for GdScO$_3$:Nd^{3+}, Er^{3+}, x% Cr^{3+} with different Cr^{3+} concentration.

The average lifetime of the excited states were calculated with the equation (Eq. S3):

$$\tau_{avr} = \frac{A_1\tau_1^2 + A_2\tau_2^2}{A_1\tau_1 + A_2\tau_2} \qquad \text{(Eq. S4a)}$$

where: τ_1, τ_2 – the average time, which is in accordance with the relation $\tau = t \cdot \ln(2)$ and A_1, A_2 – amplitude, which are the parameters of the doubleexponential function:

$$y = y_0 + A_1 \cdot \exp(-\frac{x}{t_1}) + A_2 \cdot \exp(-\frac{x}{t_2}) \qquad \text{(Eq. S4b)}$$
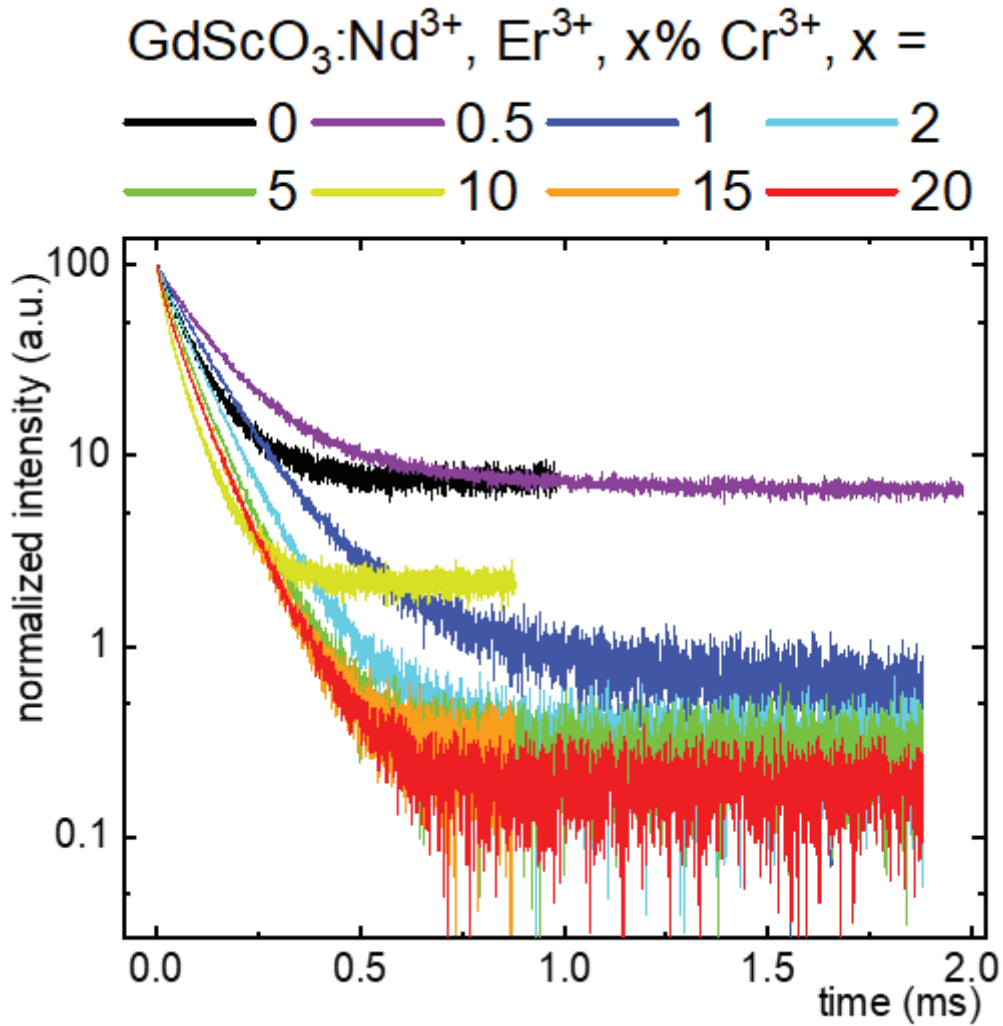
Figure S12. The luminescent decays of Nd^{3+} excited state ($\lambda_{em} = 1082$ nm) performed at 83 K in $GdScO_3$:Nd^{3+}, Er^{3+}, x% Cr^{3+} with different Cr^{3+} concentration.
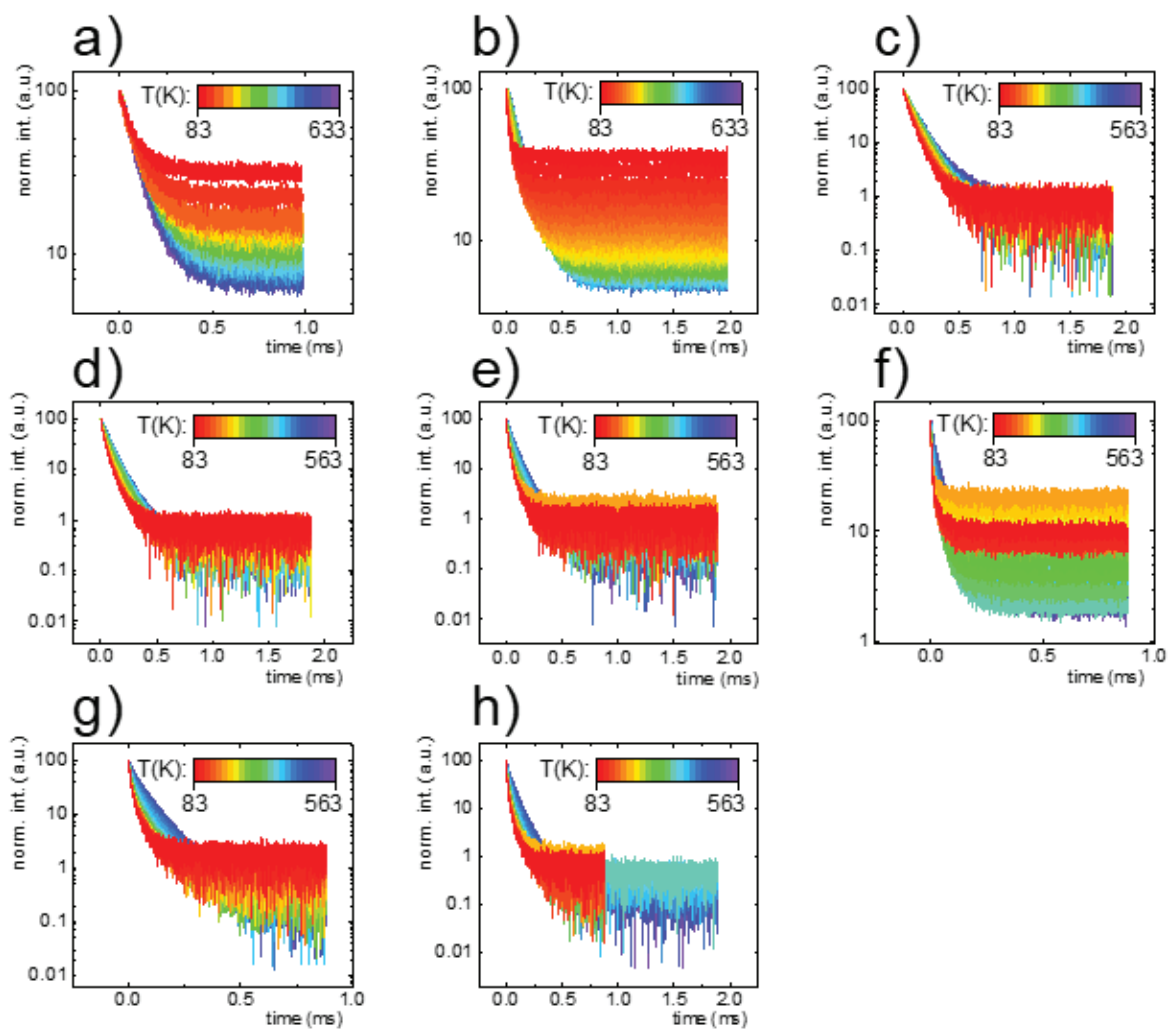
Figure S13. The thermal evolution of luminescent decays of Nd^{3+} excited state ($\lambda_{em} = 1082$ nm) in $GdScO_3$:Nd^{3+}, Er^{3+}, x% Cr^{3+}, where x = 0 – a); 0.5 – b); 1 – c); 2 – d); 5 – e); 10 – f); 15 – g); 20 – h).
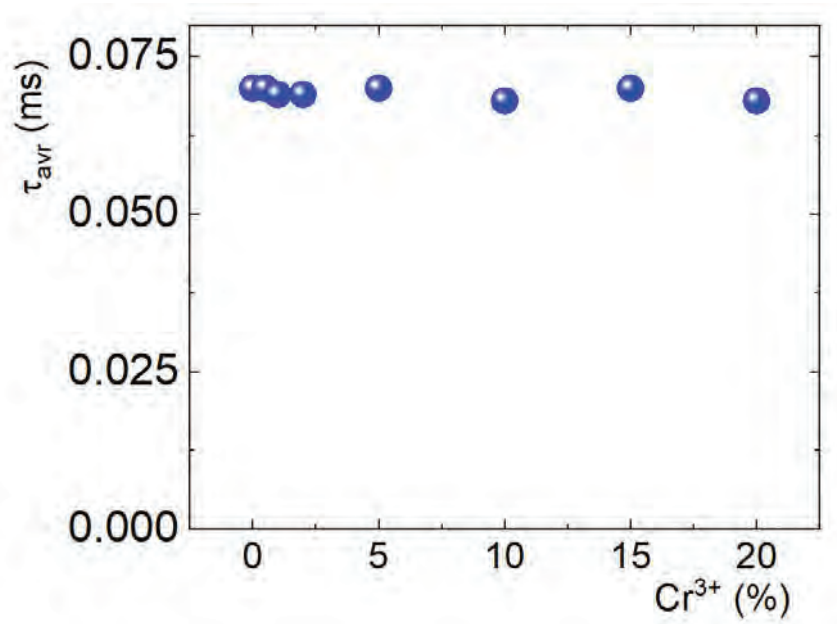
Figure S14. The τ_{avr} of the $^4F_{3/2}$ state of Nd^{3+} ions in $GdScO_3:Cr^{3+}$ measured at 77K upon λ_{exc}=808 nm.

Figure S15. The thermal evolution of the relative sensitivity of the luminescent decays of Nd^{3+} excited state (λ_{em} = 1082 nm) in $GdScO_3:Nd^{3+}, Er^{3+}, x\% Cr^{3+}$.
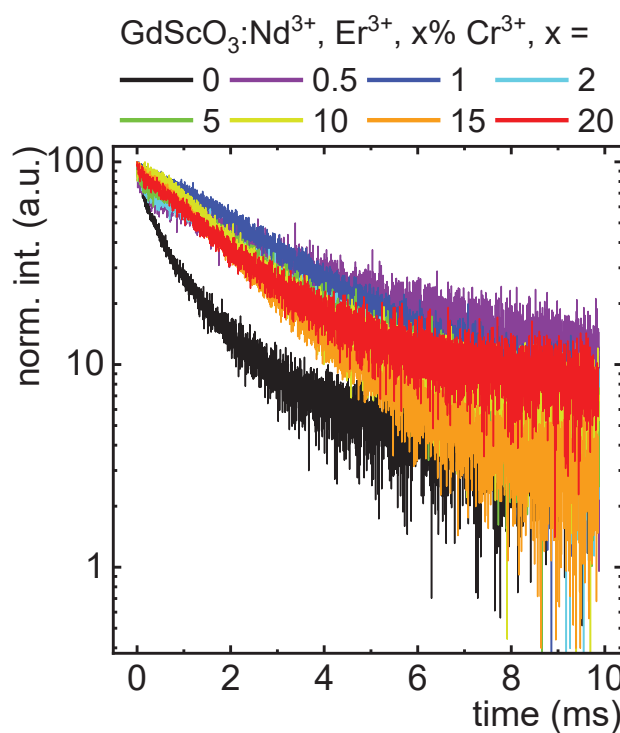
Figure S16. The luminescent decays of Er^{3+} excited state (λ_{em} = 1525 nm) performed at 83 K in GdScO$_3$:Nd^{3+}, Er^{3+}, x% Cr^{3+} with different Cr^{3+} concentration.
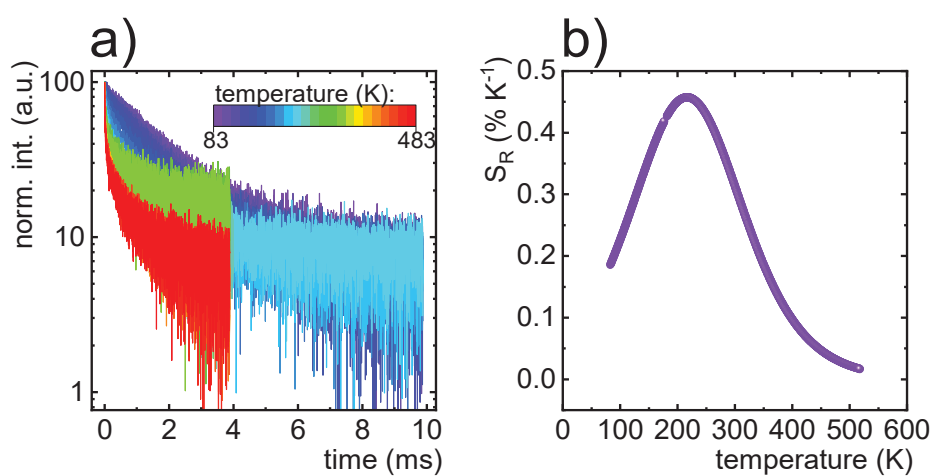
Figure S17. The thermal evolution of luminescent decays of Er^{3+} excited state (λ_{em} = 1525 nm) – a) and its relative sensitivity for GdScO$_3$:Nd^{3+}, Er^{3+}, 20% Cr^{3+} – b).

Boosting the thermometric performance of the Nd^{3+}, Er^{3+}-based luminescence thermometers by sensitization via Cr^{3+} ions: the role of the host material

W.M. Piotrowski, K. Maciejewska, L. Marciniak*

Institute of Low Temperature and Structure Research, Polish Academy of Sciences, Okólna 2, 50-422, Wroclaw, Poland

A B S T R A C T

The sensitization of the luminescence of lanthanide ions (Ln^{3+}) through codoping with Cr^{3+} ions enables an increase in the sensitivity of Ln^{3+}-based luminescent thermometers, as well as a significant enhancement of their luminescence intensity. However, achieving predictable thermometric performance in such thermometers necessitates an understanding of the correlation between the host material and thermometric parameters. In this study, we demonstrate the dependence of the relative sensitivity enhancement and thermal quenching temperature on the strength of the crystal field interacting with Cr^{3+} ions. The versatility of the presented research enables the development of a tool that allows the design of optical temperature sensors with predefined parameters.

© 2023 Elsevier Ltd. All rights reserved.

1. Introduction

Luminescence thermometry is a novel technique that has recently gained wide attention due to its potential use in remote temperature readout in numerous research and industrial fields [1–9]. Various approaches have been proposed based on the specific requirements of the application in question [9–12]. One of the most common of them is the ratiometric approach where the ratio of two emission bands of lanthanide ions (Ln^{3+}) is used as a thermometric parameter [6–8]. The advantage of this approach lies in the ease of spectral separation of the emission bands, which arises from the unique characteristics of the *4f-4f* electronic transitions of Ln^{3+} ions. However, the small absorption cross sections and narrow absorption bands of Ln^{3+} require careful selection of the excitation wavelength and high excitation source [13]. Additionally, the limited susceptibility of Ln^{3+} luminescence to temperature changes

restricts the thermometric performance of such thermometers. To overcome these limitations, various approaches have been proposed to enhance the thermometric performance of Ln^{3+}-based thermometers while maintaining the narrow and well-separated emission of Ln^{3+} ions [14,15]. One such approach relies on codoping Ln^{3+}-based thermometers with transition metal (TM) ions to play the role of a sensitizer of Ln^{3+} ions (the so-called antenna effect) [16–19]. As it was already proved the high absorption cross section and broad absorption bands of TM as well as the TM→Ln^{3+} energy transfer enable the boost of the luminescence brightness and the thermometric performance of such thermometers significantly. Among TM ions, Cr^{3+} ions appear to be the most promising candidates for sensitization, exhibiting the highest absorption cross section and susceptibility to crystal field strength, which significantly affects the position of the energy levels of Cr^{3+} ions and hence the probability of Cr^{3+} to Ln^{3+} energy transfer [16,17]. However, a lack of systematic studies on the correlation between the crystal field strength and the enhancement of the thermometric performance of the Ln^{3+}-based luminescent thermometer has limited the full potential of this approach and the design of on-

demand thermometers. Therefore, in order to create such an opportunity and fill this gap, this work aims to find a correlation between the structural properties of the host material and the thermometric properties of the luminescent thermometer. Since the position of $4f$ energy levels of Ln^{3+} is barely affected by the local ion's environment, the modification of the host material will modify the crystal field strength that affects the Cr^{3+} ions tunning the position of their energy levels. The probability of the phonon-assisted energy transfer between Cr^{3+} and Ln^{3+} depends on the energy mismatch between energy levels of interacting ions. Hence, the change in the energy of the Cr^{3+} states enables modification of the thermal quenching rate of the Ln^{3+} luminescence, which in consequence will affect the relative sensitivity and luminescence quenching temperature ($T_{1/2}$) of the temperature sensor. This hypothesis is examined here on the Nd^{3+}, Er^{3+}-based luminescent thermometers sensitized by the Cr^{3+} ions in five different host materials, that is, $Y_3Al_5O_{12}$, $Y_3Al_2Ga_3O_{12}$, $LaGaO_3$, $GdScO_3$, and $LaScO_3$. Their structural, spectroscopic, and thermometric properties were analyzed step by step in order to determine correlations that allow the understanding of the sensitization process and its capability to boost the thermometric properties of the Ln^{3+}-based luminescent thermometers.

2. Experimental

2.1. Synthesis of $YAl_2Ga_3O_{12}$, $LaScO_3$, $LaGaO_3$ codoped with Er^{3+}, Nd^{3+} and Cr^{3+}, Er^{3+}, Nd^{3+} ions

The following starting materials were used for the synthesis without further purification: yttrium oxide (Y_2O_3 with 99.995% purity from Stanford Materials Corporation), scandium oxide (Sc_2O_3 with 99.995% purity from Stanford Materials Corporation), lanthanum oxide (La_2O_3 with 99.995% purity from Stanford Materials Corporation), erbium oxide (Er_2O_3 with 99.995% purity from Stanford Materials Corporation), neodymium oxide (Nd_2O_3 with 99.998% purity from Stanford Materials Corporation), aluminium nitrate nonahydrate ($Al(NO_3)_3 \cdot 9H_2O$ Puratronic 99.999% purity from Alfa Aesar), gallium(III) nitrate nonahydrate ($Ga(NO_3)_3 \cdot 9H_2O$ Puratronic 99.999% purity from Alfa Aesar), chromium nitrate nonahydrate ($Cr(NO_3)_3 \cdot 9H_2O$, 99.99% purity from Alfa Aesar), citric acid ($C_6H_8O_7$ with 99.5+% purity from Alfa Aesar), and poly(-ethylene glycol) (PEG $C_2H_6O_2$ BioUltra 200 from Sigma).

The powders of $Y_3Al_2Ga_3O_{12}$, $LaScO_3$, $LaGaO_3$ doped with 15% Cr^{3+}, 1% Er^{3+}, 1% Nd^{3+}, and 1% Er^{3+}, 1% Nd^{3+} doped were synthesized via modified Pechini method. The concentration of lanthanide ions (Er^{3+}, Nd^{3+}) was calculated with respect to the molar amount of Y^{3+} or La^{3+} ions, whereas the Cr^{3+} in respect to the Al^{3+} or Ga^{3+} or Sc^{3+}. The Pechini synthesis has been carried out as follows: A stoichiometric amount of rare earth oxides was dissolved in distilled water and ultrapure nitric acid (96%). The formed rare earth nitrates were recrystallized three times using small quantities of distilled water. After this, stoichiometric quantities of desired salts $Ga(NO_3)_3 \cdot 9H_2O$, $Al(NO_3)_3 \cdot 9H_2O$, and $Cr(NO_3)_3 \cdot 9H_2O$ were diluted in distilled water and added to an aqueous solution of the obtained rare earth nitrates. The mixture was stirred with citric acid for 1 h in 363 K to form a clear solution of the metal complex. The molar ratio of citric acid to all metals was set to 6:1. Afterward, to the solution, the PEG-200 was added and maintained for 1 h and heated up to the temperature, which enables the initiation of the polymerization process. The molar ratio of PEG-200 to citric acid was 1:1. Then, the solution was dried for 1 week at 363 K. At this time, a resin was formed. Finally, the nanocrystals were obtained by annealing the resin in air for 12 h at 1273 K.

The $Y_3Al_5O_{12}$ and $GdScO_3$ codoped with 1% Nd^{3+}, 1% Er^{3+} and codoped with 1% Nd^{3+}, 1% Er^{3+}, 15% Cr^{3+} ions were prepared using the previously described in Refs. [16,17], respectively, procedures.

2.2. Characterization

All of the synthesized materials were examined by X-ray powder diffraction measurements carried out on PANalitycal X'Pert diffractometer, equipped with an Anton Paar TCU 1000 N temperature control unit, using Ni-filtered Cu-K$_\alpha$ radiation (V = 40 kV, I = 30 mA).

The emission spectra were measured using a FLS1000 Fluorescence spectrometer from Edinburgh Instruments with a R928P side window photomultiplier tube from Hamamatsu as a detector and the 445 nm and 808 nm laser diode as an excitation sources. The excitation spectra were also recorded using the FLS1000 Fluorescence spectrometer with a R928P side window photomultiplier tube from Hamamatsu as a detector with a 450 W halogen lamp. The temperature of the sample was controlled using a THMS 600 heating–cooling stage from Linkam (0.1 K temperature stability and 0.1 K set point resolution).

In order to obtain the results of relative sensitivity with lower uncertainty, all luminescent intensity ratio values were fitted according to the Mott-Seitz equation (Eq. S1).

3. Results and discussion

The investigated host materials belong to two families of crystal structures—garnets and perovskites. The garnets $Y_3Al_5O_{12}$ (hereinafter YAG) and $Y_3Al_2Ga_3O_{12}$ (hereinafter YAGG) crystalize in the cubic structure of $Ia\text{-}3d$ (No. 230) space group. In this case, in the general chemical formula of garnets of $C_3A_2D_3O_{12}$, the Y^{3+} ions occupy the dodecahedral 'C' sites and mixed Al^{3+}/Ga^{3+} ions occupy both the octahedral 'A' and tetrahedral 'D' sites. It is generally acknowledged that Cr^{3+} ions preferentially locate in the octahedral sites, while Ln^{3+} ions like Nd^{3+} and Er^{3+} will substitute Y^{3+} crystallographic sites (Fig. 1a). A summary of the parameters of crystallographic sites is presented in Table 1. It is worth noting that the included misfit factor (m_f), which, as a ratio of effective ionic radii (EIR) of dopant and substituted ions, assesses which of host material ions is more likely to be replaced with dopant ions. On the other hand, $LaGaO_3$, $GdScO_3$, and $LaScO_3$ are perovskites that belong to the same orthorhombic space group Pnma (no. 62) (for $LaGaO_3$ preferentially denoted as Pbnm) (Fig. 1b–d). According to Table 1, the coordination of RE^{3+} ions in these structures is different for each of the host materials, but their substitution by Nd^{3+} and Er^{3+} ions was confirmed by many reports. All these perovskites host materials possess octahedral sites (Ga^{3+} or Sc^{3+}), which are suitable for Cr^{3+} ions. An important structural parameter that has so far been used in the literature to determine correlations with spectroscopic properties is the distance between the ions whose crystallographic sites are preferentially substituted by luminescent centers and their ligands (O^{2-} ions in the case of oxides), denoted as $R(M\text{-}O^{2-})$ (Fig. 1f). The $R(M\text{-}O^{2-})$ distances were determined based on the adequate CIF files (ICSD 23848 — YAG, ICSD 280106- YAGG, ICSD 50388- LaGaO$_3$, ICSD 65513- GdScO$_3$, ICSD 242159- LaScO$_3$). It can be found that in this group of host materials, the $R(Cr^{3+}\text{-}O^{2-})$ ranges from 1.937 to 2.102 Å, for YAG and LaScO$_3$, respectively. Comparing the metal-oxygen distances with the data from Tables 1, it can be found that the EIR of the ions which are substituted by Cr^{3+} ions increases with increasing $R(M(Cr^{3+})\text{-}O^{2-})$, while for the same EIR values (i.e., occurring for the same ions), the ions in the second coordination sphere play a secondary role (compare Y^{3+}
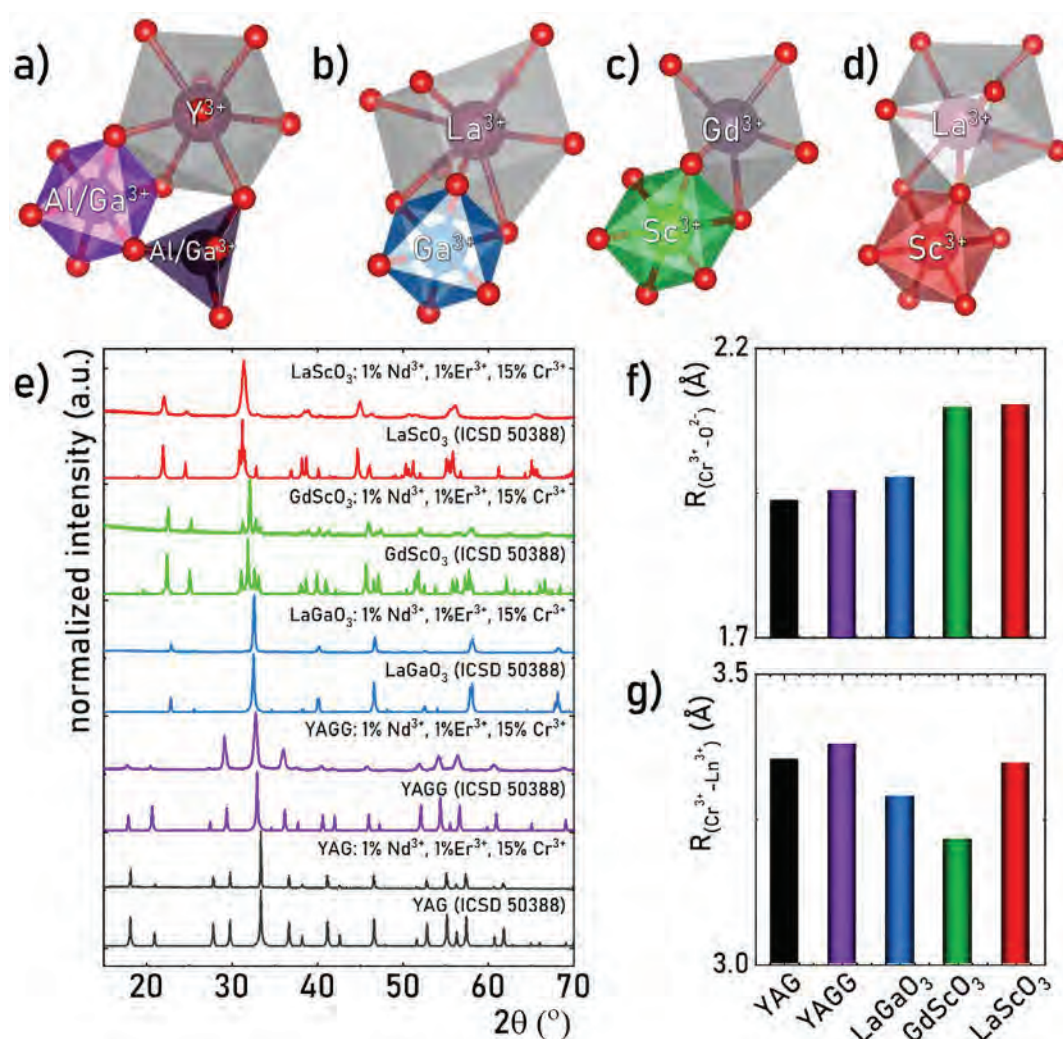
Fig. 1. The visualization of the polyhedra that can be replaced by the Cr^{3+} and Ln^{3+} ions in the YAG, YAGG − a) LaGaO3 − b), GdScO3 − c), LaScO3 − d); the comparison of the XRD pattern with the reference data of the synthesized powders − e); comparison of R(Cr^{3+}-O^{2-}) − f) and R(Cr^{3+}- Ln^{3+}) distance in investigated host materials − g).

Table 1
Summary of the structural parameters for the analyzed host materials.

host material	Crystallographic site preferred for Ln^{3+} dopants				Crystallographic site preferred for Cr^{3+} dopant		
	Ion and its coordination	EIR (pm)	m_f (Nd^{3+})	m_f (Er^{3+})	Ion and its coordination	EIR (pm)	m_f (Cr^{3+})
YAG	Y^{3+} (VIII)	101.9	108.8%	98.5%	Al^{3+} (VI)	53.5	115.0%
YAGG	Y^{3+} (VIII)	101.9	108.8%	98.5%	Al^{3+}/Ga^{3+} (VI)	53.5/62	115.0%/99.2%
LaGaO$_3$	La^{3+} (IX)	121.6	95.6%	87.3%	Ga^{3+} (VI)	62	99.2%
GdScO$_3$	Gd^{3+} (VI)	93.8	104.8%	94.9%	Sc^{3+} (VI)	74.5	82.6%
LaScO$_3$	La^{3+} (VIII)	116	95.6%	86.6%	Sc^{3+} (VI)	74.5	82.6%

and La^{3+} in YAGG and LaGaO$_3$, respectively, and Gd^{3+} and La^{3+} in GdScO$_3$ and LaScO$_3$, respectively). Nevertheless, it should be considered that $R(Cr^{3+}$-$O^{2-})$ is a more accurate and simpler structural parameter to implement. On the other hand, due to the energy transfer processes between Cr^{3+} and Ln^{3+} ions considered later in this work, the shortest Cr^{3+} and Ln^{3+} distance should be also considered (Fig. 1g). In this case, the largest distance was found for YAGG with the value of 3.380 Å and slightly lower for YAG and LaScO$_3$. In contrast, the replacement of La^{3+} ions by Gd^{3+} ions in GdScO$_3$ led to a significant decrease in $R(Cr^{3+}$-$Ln^{3+})$ from 3.347 Å to 3.215 Å.

The phase purity of the synthesized powders was verified with X-ray powder diffraction patterns (Fig. 1e, see also Figs. S1−S3). All of the observed crystallographic reflections correlate with the reference data confirming the phase purity of the obtained powders both in the case of Nd^{3+}, Er^{3+} and Nd^{3+},Er^{3+},Cr^{3+} codoped phosphors (YAGG - ICSD 280106, LaGaO$_3$ - ICSD 50388, LaScO$_3$ - ICSD 242159). It can be found that in the case of YAGG, codoping host material with 15% Cr^{3+} results in a slight shift of the reflection toward smaller 2Θ angles in respect to undoped counterpart, whereas for LaGaO$_3$ and LaScO$_3$, there is a slight shift toward bigger 2Θ angles. Both observations are related to the expansion or

contraction of the crystallographic unit cell, respectively, associated with the difference in the ionic radii between the Cr^{3+} and substituted host material ion.

The spectroscopic properties of the Nd^{3+}, Er^{3+}, Cr^{3+} ions can be explained based on the simplified configurational coordination diagram of Cr^{3+} ions and energy level diagrams of Nd^{3+}, Er^{3+} ions presented in Fig. 2a. Nd^{3+} ions are characterized by a very rich energy level scheme and their luminescence can be observed upon different excitation wavelengths. However, due to the very high absorption cross section of $^4I_{9/2} \rightarrow {}^4F_{5/2}$, $^4S_{3/2}$ band and the lack of its spectral overlap with Cr^{3+} absorption bands the $\lambda_{exc} = 808$ nm is used in this study. Upon this excitation, the $^4F_{5/2}$, $^4S_{3/2}$ state is populated followed by nonradiative transitions to the metastable $^4F_{3/2}$ state. Its radiative depopulation results in the occurrence of three emission bands at 880 nm, 1060 nm, and 1350 nm corresponding to the $^4F_{3/2} \rightarrow {}^4I_{9/2}$, $^4F_{3/2} \rightarrow {}^4I_{11/2}$, and $^4F_{3/2} \rightarrow {}^4I_{13/2}$ electronic transitions, respectively. Due to the fact that the $^4F_{3/2} \rightarrow {}^4I_{11/2}$ band is usually the most intensive further analysis will be limited to this transition. In the presence of the Er^{3+} codopant the $^4F_{3/2}$ level of Nd^{3+} ions can be also nonradiatively depopulated via $Nd^{3+} \rightarrow Er^{3+}$ energy transfer. Due to a small energy mismatch between the $^4F_{3/2}$ state of Nd^{3+} ions and the $^4I_{11/2}$ state of Er^{3+} ions the energy transfer occurs with the assistance of phonons. This process is followed by nonradiative depopulation to the $^4I_{13/2}$ state of Er^{3+} ions and results in the emission band at 1530 nm related to the $^4I_{13/2} \rightarrow {}^4I_{15/2}$ electronic transition. Indeed, Nd^{3+} and Er^{3+} emission bands were observed for different host materials upon excitation through ~808 nm wavelength [16,17,20,21]. Strong thermal dependence of the probability of phonon assisted energy transfer between those ions results in the thermally induced change of their emission intensities ratio, which can be exploited

for temperature sensing. However, when the Cr^{3+} codopant is introduced the Ln^{3+} luminescence can be obtained via the sensitization process. Cr^{3+} ions are characterized by broad absorption bands typically peaked at 450 nm and 650 nm associated with the $^4A_2 \rightarrow {}^4T_1$ and $^4A_2 \rightarrow {}^4T_2$ electronic transitions. As a result of nonradiative processes the metastable ^2E energy state is populated. Subsequently, interionic $Cr^{3+} \rightarrow Nd^{3+}$ and $Cr^{3+} \rightarrow Er^{3+}$ energy transfers are possible, which probably take place between the ^2E level of Cr^{3+} ions and $^4F_{7/2}$, $^4S_{3/2}$ of Nd^{3+} ions or $^4I_{9/2}$ of Er^{3+} ions. Nevertheless, it should be noted that the energy difference between ^2E and $^4F_{7/2}$, $4S_{3/2}$ is smaller, favoring the efficiency of $Cr^{3+} \rightarrow Nd^{3+}$ energy transfer over $Cr^{3+} \rightarrow Er^{3+}$. Since the crystal field strength affects the energy of the excited states of Cr^{3+} ions, the spectral position and energy mismatch between Cr^{3+} and Ln^{3+} states can be modified depending on the host material used. The occurrence of both $Cr^{3+} \rightarrow Nd^{3+}$ and $Cr^{3+} \rightarrow Er^{3+}$ energy transfers can be confirmed by the presence of broad excitation bands of Cr^{3+} ions in the excitation spectra of Cr^{3+}, Nd^{3+}, Er^{3+} codoped host materials performed for $\lambda_{em} = $ ~1060 nm (Nd^{3+}) as well as $\lambda_{em} = $ ~1530 nm (Er^{3+}) (wavelengths were adjusted to emission maxima depending on the host material) (Fig. 2c and Fig. S4). The bands whose maxima are located in the range from 418.5 to 461 nm (from ~23,895 to ~21,689 cm^{-1}) and from 560 to 648 nm (from ~17,865 to ~15,435 cm^{-1}) can be assigned to $^4A_2 \rightarrow {}^4T_1$ and $^4A_2 \rightarrow {}^4T_2$ electronic transitions, respectively. The gradual shift of the maxima of the $^4T_1$ and $^4T_2$ bands is shown in Fig. S5. On the other hand, the comparison of the excitation spectra of the analyzed phosphors with and without Cr^{3+} ions can be found here (Figs. S6 and S7) and the assignment of the energy of the absorption bands to the electronic transitions for five investigated host materials are presented as Table S1 and Table S2, respectively. Based on the energy of the
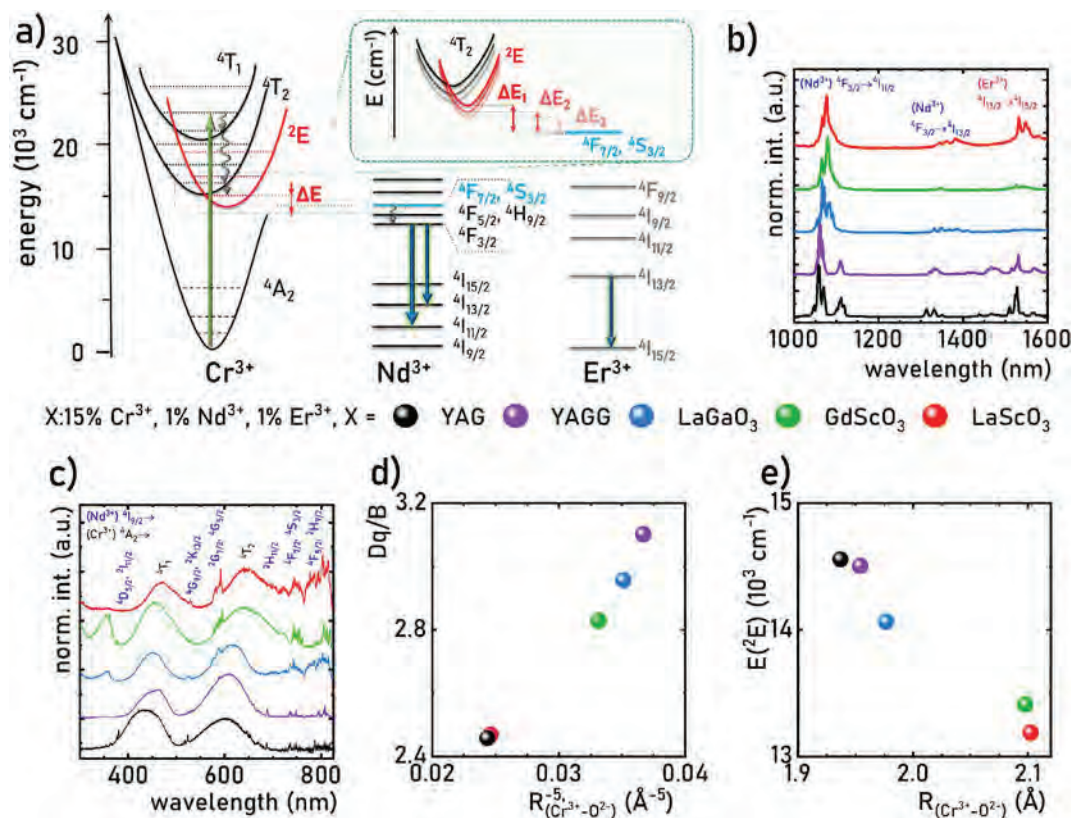
Fig. 2. Schematic configurational coordinate diagram for Cr^{3+}, Nd^{3+} and Er^{3+} ions − a); comparison of emission spectra ($\lambda_{exc} = 445$ nm) − b) and excitation spectra ($\lambda_{em} = $ ~1060 nm, Nd^{3+} emission) for five different host materials co-doped with Nd^{3+}, Er^{3+}, Cr^{3+} at 123 K − c); dependence of R(Cr^{3+}-O^{2-})$^{-5}$ on Dq/B − d); dependence of R(Cr^{3+}-O^{2-}) on energy of ^2E excited state of Cr^{3+} ions − e).

$^4A_2 \to {}^4T_1$ and $^4A_2 \to {}^4T_2$ bands, it is possible to estimate the parameters of the crystal field affecting Cr^{3+} ions using Eq. S2-4. The resulting parameters are summarized in Table S3. Fig. 2d compiles the crystal field strength parameter Dq/B with $1/R(Cr^{3+}-O^{2-})^n$ for n = 5 to show quasi-linear trend [22]. In addition, it is worth noting that Dq/B values above 2.4 classify into the intermediate or strong crystal field, which determines that the lowest excited level of the Cr^{3+} ions will be ^2E. Therefore, using the Tanabe-Sugano diagram for 3 d^3 electronic configuration, it can be seen that in addition to the significant influence of crystal field strength on the position of levels $^4T_1$ and $^4T_2$, the position of level ^2E slightly changes. Using the results presented so far in the literature, it is possible to compile the energies corresponding to the position of zero-phonon line (otherwise known as R-line) for the analyzed materials [23–27]. As it can be clearly seen, the energy of the ^2E level increases with increasing Dq/B values (Fig. S8). Therefore, $E(^2E)$ is expected to decrease with increasing $R(Cr^{3+}-O^{2-})$, which is confirmed in Fig. 2e.

3.1. Comparison of thermometric properties

To investigate the effect of the presence of Cr^{3+} ions on the thermometric properties of the luminescent thermometers based on Nd^{3+} and Er^{3+} emission, the thermal evolution of the emission spectra was investigated for five investigated phosphors undoped with Cr^{3+} ions and co-doped with 15% Cr^{3+} ions (please compare representative examples in Fig. 3a and b, other thermal evolution spectra can be found in Fig. S9). In the case of solely Nd^{3+}, Er^{3+} codoped phosphors, the Er^{3+} emission intensity increases with respect to the Nd^{3+} ones as described previously. However, observed changes are not spectacular over a wide temperature range from 123 K to ~593 K in materials doped with 1% Nd^{3+} and 1% Er^{3+} (Fig. 3a). However, with the introduction of Cr^{3+} ions imposes spectacular changes in the relative emission intensities. To analyze the influence of Cr^{3+} ions on the thermal evolution of

Ln^{3+} emission in detail, their integral intensities were analyzed. The representative results for YAGG are presented in Fig. 3c and d. The Nd^{3+} intensity in the case of the sample without Cr^{3+} ions decreases by around 3% in the considered temperature range, while the emission intensity of the same band decreases by 95% for the Cr^{3+} codoped system. A similar effect of the presence of Cr^{3+} ions on the quenching rate of Nd^{3+} emission was observed for other host materials (Fig. S10). The increased quenching rate of Nd^{3+} emission in Cr^{3+}-codoped systems may indicate the occurrence of two processes: (1) the dominant influence of $Cr^{3+} \to Nd^{3+}$ energy transfer or (2) the increasing probability of back $Nd^{3+} \to Cr^{3+}$ energy transfer. However, the fact that the emission intensity brightness of the Ln^{3+} emission intensities increases by over one order of magnitude for the Cr^{3+} codoped systems clearly confirms that the (1) is dominant. On the other hand, Er^{3+} emission intensity increases at elevated temperature due to the $Nd^{3+} \to Er^{3+}$ energy transfer for the sample without Cr^{3+}, whereas it remains temperature invariant up to 350 K followed by the quenching by 30% for the Cr^{3+} codoped system (Fig. S11). Similar thermal performance of Er^{3+} emission as YAGG:Nd^{3+}, Er^{3+} is presented by GdScO$_3$:Nd^{3+}, Er^{3+}, but at 523 K, it reaches 230% of the initial value and at 743 K even 350% of initial value. On the other hand, the presence of Cr^{3+} ions in GdScO$_3$ host material results in a much more drastic quenching rate, where the Er^{3+} emission signal at 403 K assumes a value of 12% of the value at 123 K. On the contrary, the thermal evolution of Er^{3+} emission for LaGaO$_3$ samples with and without Cr^{3+} ions is relatively similar, as evidenced by the temperature at which the signal reaches 50% of the initial value equal to 413 K and 293 K, respectively. Due to the multiple nonradiative processes occurring in Nd^{3+}, Er^{3+} and Nd^{3+}, Er^{3+}, Cr^{3+} doped systems, whose contribution to the thermal evolution of emission bands also varies depending on the considered host material, it was decided to determine the luminescent intensity ratio, defined as:
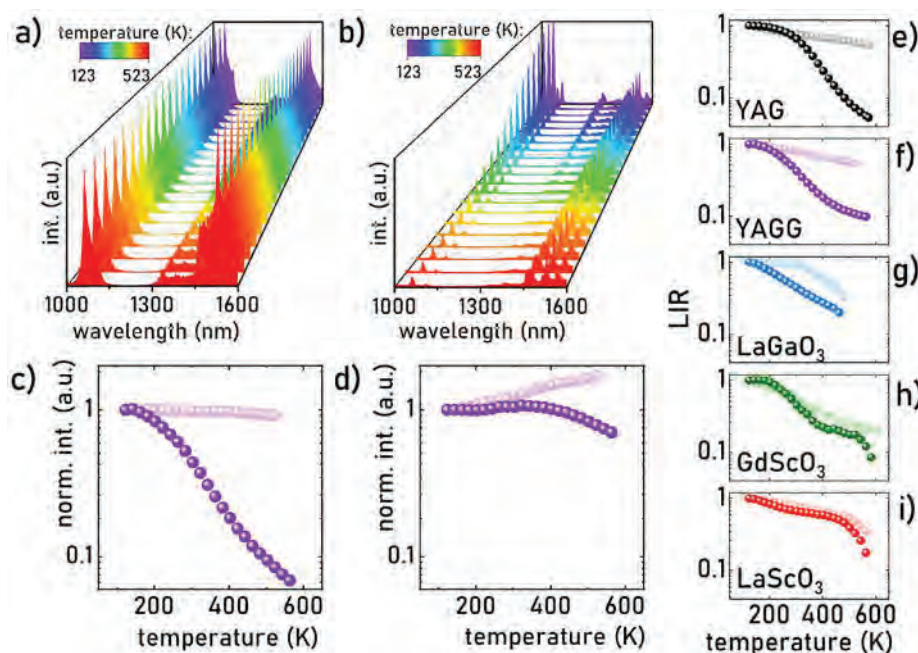
Fig. 3. Thermal evolution of emission spectra of YAGG:Nd^{3+}, Er^{3+} (λ_{exc} = 808 nm) − a) and YAGG:Nd^{3+}, Er^{3+}, Cr^{3+} phosphors (λ_{exc} = 445 nm) − b); comparison of thermal evolution of Nd^{3+} − c) and Er^{3+} emission intensity in YAGG co-doped with Nd^{3+}, Er^{3+} (bright violet dots) and Nd^{3+}, Er^{3+}, Cr^{3+} (dark violet dots) − d); comparison of thermal evolution of LIR for Nd^{3+}, Er^{3+} co-doped (brighter dots) and Nd^{3+}, Er^{3+}, Cr^{3+} co-doped (darker dots) phosphors: YAG − e); YAGG − f); LaGaO$_3$ − g); GdScO$_3$ − h); LaScO$_3$ − i).

$$LIR = \frac{\int\limits_{1063nm}^{1089nm} I\left({}^4F_{3/2} \rightarrow {}^4I_{11/2}\right) d\lambda \left[Nd^{3+}\right]}{\int\limits_{1514nm}^{1569nm} I\left({}^4I_{13/2} \rightarrow {}^4I_{15/2}\right) d\lambda \left[Er^{3+}\right]} \qquad (1)$$

As shown in Fig. 3(e)-(i), in the case of YAG:Nd^{3+},Er^{3+} 50% of initial value was noticed at 583 K, in respect to 333 K for the 15% Cr^{3+}-codoped counterpart, while the LIR value at 573 K reached only 5% of value at 123 K. For $LaGaO_3$, 50% of the initial value was reached at 433 K and 283 K for 0% and 15% Cr^{3+}, respectively. In comparison, in $GdScO_3$, such LIR values were noted at 313 K and 293 K. This suggests a lack of correlation between LIR values for Nd^{3+}, Er^{3+}-codoped host materials or Nd^{3+}, Er^{3+}, Cr^{3+}-codoped host materials.

In order to elucidate the difference in the thermal change of LIR for analyzed host materials after the introduction of Cr^{3+} ions, the phenomenological energy level scheme of dopant ions was analyzed (Fig. 4a, Figs. S12–S13). Literature data [23–27] were used to determine the energies of the lowest vibronic level of excited states of Cr^{3+} ions (indicated by a solid line in Figures), while the energies of the Stark levels of Nd^{3+} and Er^{3+} were determined from excitation spectra taken for Nd^{3+} and Er^{3+}-doped materials (indicated by a dashed line in Figures). It can be clearly seen that the

energies of both the ${}^2E$ and ${}^4T_2$ level parabola bottoms of the Cr^{3+} ions change depending on the structure, which stands in contrast to the almost constant energy positions of the bands of the Nd^{3+} and Er^{3+} ions. Comparing the position of the Nd^{3+} and Er^{3+} bands in respect to the lowest excitation band of the Cr^{3+} ions, that is, ${}^2E$, it can be seen that the Nd^{3+} ion bands are energetically closer to the Cr^{3+} ions. Therefore, it can be assumed that when energy transfer between Nd^{3+}/Er^{3+} ions and Cr^{3+} ions occurs, the vast majority of the energy will be transferred to or through Nd^{3+} ions. The first closest Nd^{3+} level underneath the ${}^2E$ level of Cr^{3+} ions is overlapping Stark components of the ${}^4F_{7/2}$, ${}^4S_{3/2}$ levels. In order to compare this quantitatively, it the energy difference ΔE between the ${}^2E$ level and the highest Stark component of the ${}^4F_{7/2}$, ${}^4S_{3/2}$ level shown graphically as arrows in Fig. 4a was calculated. It is noteworthy that due to the analysis of host materials belonging to two families of compounds, ΔE of ~850–950 cm^{-1} were obtained for garnets, ΔE = ~450 cm^{-1} for perovskite $LaGaO_3$, and only ΔE = ~40 cm^{-1} for scandate perovskites $GdScO_3$ and $LaScO_3$. Due to the multiplicity of nonradiative processes that occur between the three luminescent centers, it was assumed in this study that, using the temperature dependence of the LIR parameter based on the emission ratio of Nd^{3+} and Er^{3+} ions, it is possible to include all temperature-dependent processes that take place within the $Nd^{3+}+Er^{3+}$ system. In this way, the comparison of thermal decreases of LIR in materials undoped and codoped with Cr^{3+} ions should only take into account processes that are related to Cr^{3+}
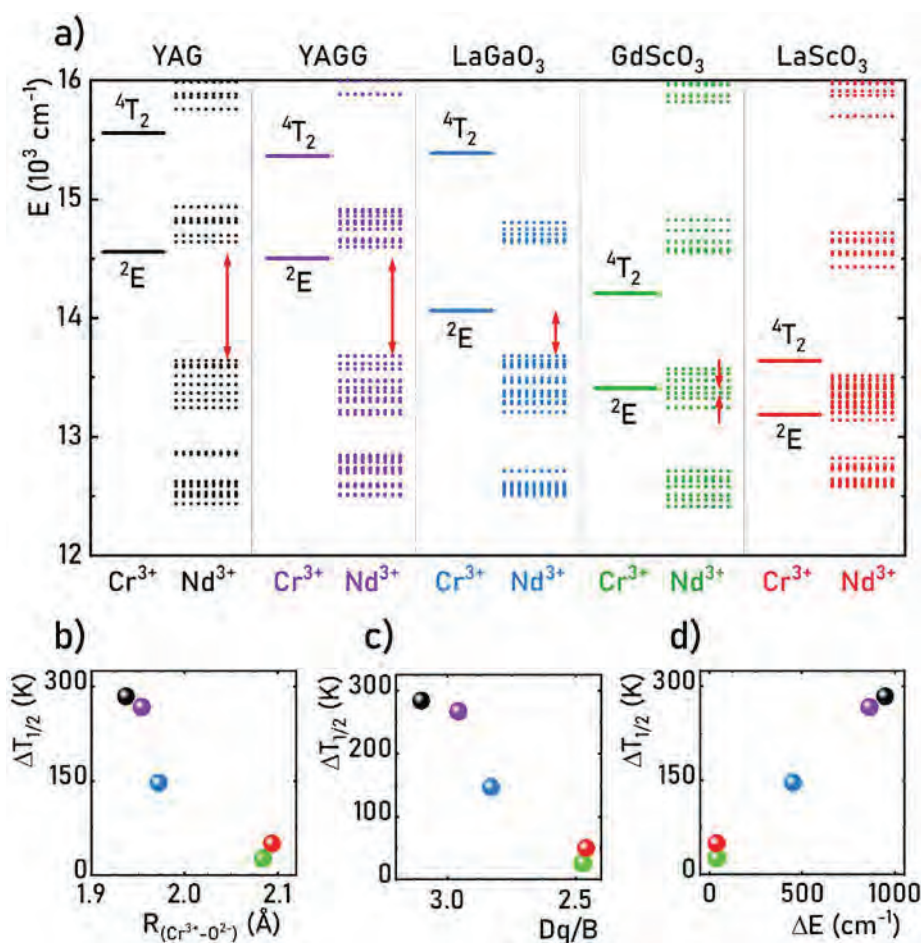
Fig. 4. The comparison of positions of energy levels of Cr^{3+} and Nd^{3+} ions in different host materials – a); the influence of R(Cr^{3+}-O^{2-}) distance – b) on $\Delta T_{1/2}$, the on $\Delta T_{1/2}$ as a function of Dq/B – c) and $\Delta T_{1/2}$ as a function of ΔE – d).
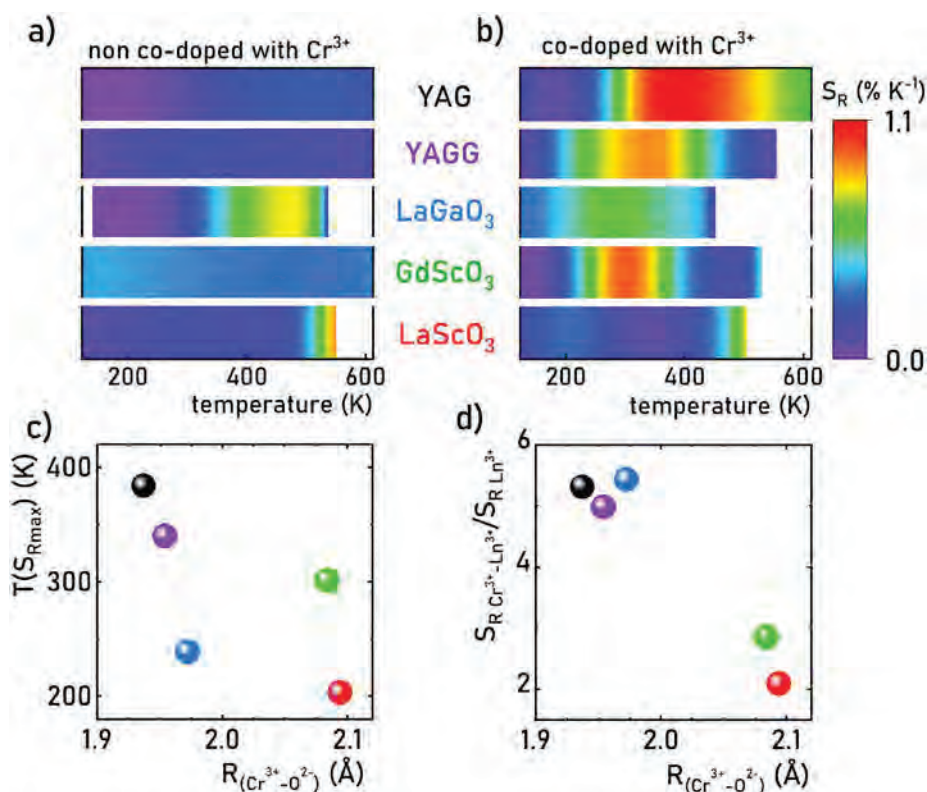
Fig. 5. The thermal evolution of the relative sensitivity in phosphors co-doped with Nd^{3+}, Er^{3+} — a) and Nd^{3+}, Er^{3+}, Cr^{3+} ions − b); comparison of $T(S_{Rmax})$ − c) and S_R enhancement factor for different host materials − d).

-Ln^{3+} interaction. On this basis, the parameter $\Delta T_{1/2}$ was used to evaluate an influence of the appearance of Cr^{3+} ions in the host material, defined as:

$$\Delta T_{1/2} = T_{1/2}(LIR)_{0\%Cr^{3+}} - T_{1/2}(LIR)_{15\%Cr^{3+}} \tag{2}$$

which represents the difference between the temperatures at which the LIR reaches 50% of its value of 123 K for phosphor undoped and codoped with Cr^{3+} ions. First, in line with the previous discussion, it is noted that $\Delta T_{1/2}$ decreases with increasing $R(Cr^{3+}-O^{2-})$ distance (Fig. 4b). These parameters have not been directly correlated so far, so attention was drawn to the comparison of the temperature dependent parameter $\Delta T_{1/2}$ with the position of the ^2E level (Fig. S14). It is expected that a similar trend would be obtained for the $^4T_2$ level (which can be seen in Fig. 4a), but, as previously mentioned, it is more likely to assume an influence of the lowest excited level of the Cr^{3+} ions on the temperature properties of the Ln^{3+} ions, and in all the host materials analyzed, the lowest energy level is ^2E. The correlation between the $\Delta T_{1/2}$ and the Dq/B parameter (Fig. 4c) confirms that the host material directly affects the thermal dynamics of LIR changes. Finally, the correlation between $\Delta T_{1/2}$ and ΔE from Fig. 4d) shown in Fig. 4a) reveal a more accurate correlation, due to the fact that ΔE includes not only the effect of the host material on Cr^{3+} ions but also on Ln^{3+} ions. Obtained results clearly indicate that the thermal dependence of Ln^{3+} emission intensity in the Cr^{3+},Ln^{3+} codoped system can be altered by the crystal field modification.

The clear correlation between the thermal quenching temperature and the crystal field strength affecting Cr^{3+} modified by the $R(Cr^{3+}-O^{2-})$ imposes the capability to alter the thermal stability of LIR by the selection of the host material. To verify how this technique affects the thermometric properties of the Cr^{3+} sensitized

Ln^{3+}-based luminescence thermometry the relative sensitivity was determined for Cr^{3+} undoped and codoped systems as follows:

$$S_R = \frac{1}{LIR} \frac{\Delta LIR}{\Delta T} \cdot 100\% \tag{3}$$

where ΔLIR represents the change of LIR for the ΔT change of temperature. A summary of results obtained for the five host materials shown in Fig. 5a and b (plots comparing S_R vs temperature within individual host materials are shown in Fig. S15) reveals a beneficial effect of Cr^{3+} ions on relative sensitivity values was observed in all cases. While the S_R for the Nd^{3+},Er^{3+}-based luminescent thermometer for most of the host materials under consideration does not exceed $S_R = 0.25\%$ K^{-1} value, significant enhancement of the sensitivity was found for the Cr^{3+} codoped systems. The highest S_{Rmax} value was obtained for YAG equal to 1.11% K^{-1} at 384 K. For the temperature at which the maximum S_R values were obtained for phosphors doped with 15% Cr^{3+} ions, no direct correlation was also observed (Fig. 5c). However, it is noteworthy that the obtained luminescent thermometers can operate in different temperature ranges, as confirmed by the wide range of $T(S_{Rmax})$ values from ~200 K to ~390 K. To quantify observed changes in sensitivity after Cr^{3+} codoping, the enhancement factor was calculated by the comparison of the S_{Rmax} for the Cr^{3+}-doped system with the corresponding S_R at the same temperature for luminescent thermometers without Cr^{3+} (Fig. 5d). In this case, the best value was obtained for $LaGaO_3$, close to a ~550% improvement in relative sensitivity (with $S_{Rmax} = 0.54\%$ K^{-1}). Noting the emergence of two separate groups of points, it is possible to propose a hypothesis suggesting that a more effective improvement in relative sensitivity (exceeding enhancement factor ~4.0) will be observed for materials for which ΔE is not close to zero, that is, ^2E and $^4F_{7/2}$, $^4S_{3/2}$ levels are not energy-matched. On the other hand, it

is worth noting that the relatively small enhancement factor = ~3 for $GdScO_3$ is not the only factor affecting the overall relative sensitivity of the luminescent thermometer, since the S_{Rmax} = 0.96% K^{-1} obtained for this material is the second best S_{Rmax} value, after YAG:Cr^{3+}, Nd^{3+}, Er^{3+}. Nevertheless, it should be emphasized that for all investigated phosphors, there was at least a 2-fold enhancement in relative sensitivity, which offers promising prospects for this method of increasing the sensitivity of thermometers. The results obtained allow stating that the thermometric parameters of these luminescent thermometers can be modulated by appropriate host material selection at least in the analyzed group of matrices. However, it is very likely that the described approach can be extrapolated to a much wider group of materials. In addition, it should be emphasized, what has been previously demonstrated, that the use of Cr^{3+} as a sensitizer not only leads to an increase in the relative sensitivity of luminescent thermometers based on Ln^{3+} emission but also enhances up to a 30-fold their luminescence intensity [17]. This is a key result that enables the reduction of uncertainty in temperature determination.

4. Conclusions

In the present work, the spectroscopic properties of five different phosphors codoped with Nd^{3+}, Er^{3+} and Cr^{3+}, Nd^{3+}, Er^{3+} ions were studied as a function of temperature in order to find a correlation between the material parameters of the host material and the potential to enhance the thermometric performance of thermometers based on Ln^{3+} emission by the sensitization with Cr^{3+} ions. As expected, the Cr^{3+}-O^{2-} distance differentiating the selected host materials directly affected the strength of the crystal field interacting with Cr^{3+} ions thereby modifying the energy of the excited levels of Cr^{3+} ions. In addition, a slight effect of the host material on the energy of the Stark components of the Nd^{3+} levels was observed. It was shown that codoping of the investigated luminescent thermometers does not cause significant structural changes while significantly affecting the rate of LIR thermal changes. As shown, this is directly related to the $Cr^{3+} \rightarrow Ln^{3+}$ energy transfer, the probability of which depends on the distance between the energy levels of the sensitizer (Cr^{3+}) and activator (Nd^{3+}) ΔE. As the ΔE increases, the effect of Cr^{3+} on lowering the $T_{1/2}$ temperature is strengthened in a sublinear manner. In addition, the enhancement of the relative sensitivity of the luminescent thermometer by introducing Cr^{3+} ions is directly dependent on the strength of the crystal field interacting with the Cr^{3+} ions. We believe that the proposed technique and presented results will contribute to the intentional design of Ln^{3+}-based luminescent thermometers with predefined thermometric parameters.

Credit author statement

Wojciech M. Piotrowski: Methodology, Investigations, Measurements, Visualization, Writing – Original Draft.

Kamila Maciejewska: Methodology, Investigations.

Lukasz Marciniak: Conceptualization, Writing – Original Draft.

Declaration of competing interest

The authors declare the following financial interests/personal relationships which may be considered as potential competing interests: Lukasz Marciniak reports was provided by National Science Centre Poland.

Data availability

Data will be made available on request.

Acknowledgements

Appendix A. Supplementary data

Supplementary data to this article can be found online at https://doi.org/10.1016/j.mtchem.2023.101591.

References

[1] S.W. Allison, G.T. Gillies, Remote thermometry with thermographic phosphors: instrumentation and applications, Rev. Sci. Instrum. 68 (1997) 2615–2650, https://doi.org/10.1063/1.1148174.

[2] A.H. Khalid, K. Kontis, Thermographic phosphors for high temperature measurements: principles, current state of the art and recent applications, Sensors 8 (2008) 5673–5744, https://doi.org/10.3390/s8095673.

[3] C.D.S. Brites, P.P. Lima, N.J.O. Silva, A. Millán, V.S. Amaral, F. Palacio, L.D. Carlos, Thermometry at the nanoscale, Nanoscale 4 (2012) 4799–4829, https://doi.org/10.1039/c2nr30663h.

[4] M.D. Dramićanin, Trends in luminescence thermometry, J. Appl. Phys. 128 (2020), 40902, https://doi.org/10.1063/5.0014825.

[5] M.D. Dramićanin, Sensing temperature via downshifting emissions of lanthanide-doped metal oxides and salts, A review, Methods Appl. Fluoresc. 4 (2016), 42001, https://doi.org/10.1088/2050-6120/4/4/042001.

[6] A. Bednarkiewicz, L. Marciniak, L.D. Carlos, D. Jaque, Standardizing luminescence nanothermometry for biomedical applications, Nanoscale 12 (2020) 14405–14421, https://doi.org/10.1039/d0nr03568h.

[7] J. Zhou, B. del Rosal, D. Jaque, S. Uchiyama, D. Jin, Advances and challenges for fluorescence nanothermometry, Nat. Methods 17 (2020) 967–980, https://doi.org/10.1038/s41592-020-0957-y.

[8] M. Suta, A. Meijerink, A theoretical framework for ratiometric single ion luminescent thermometers—thermodynamic and kinetic guidelines for optimized performance, Adv. Theory Simulations 3 (2020), 2000176, https://doi.org/10.1002/adts.202000176.

[9] L. Marciniak, K. Kniec, K. Elżbieciak-Piecka, K. Trejgis, J. Stefanska, M. Dramićanin, Luminescence thermometry with transition metal ions. A review, Coord. Chem. Rev. 469 (2022), 214671, https://doi.org/10.1016/j.ccr.2022.214671.

[10] A. Bednarkiewicz, J. Drabik, K. Trejgis, D. Jaque, E. Ximendes, L. Marciniak, Luminescence based temperature bio-imaging: status, challenges, and perspectives, Appl. Phys. Rev. 8 (2021), 11317, https://doi.org/10.1063/5.0030295.

[11] D. Jaque, F. Vetrone, Luminescence nanothermometry, Nanoscale 4 (2012) 4301–4326, https://doi.org/10.1039/c2nr30764b.

[12] Q. Wang, M. Liao, Q. Lin, M. Xiong, Z. Mu, F. Wu, A review on fluorescence intensity ratio thermometer based on rare-earth and transition metal ions doped inorganic luminescent materials, J. Alloys Compd. 850 (2021), 156744, https://doi.org/10.1016/j.jallcom.2020.156744.

[13] R. Renata, Optical properties of lanthanides in condensed phase, theory and applications, AIMS Mater. Sci. 2 (2015) 37–60, https://doi.org/10.3934/matersci.2015.2.37.

[14] H. Suo, C. Guo, J. Zheng, B. Zhou, C. Ma, X. Zhao, T. Li, P. Guo, E.M. Goldys, Sensitivity modulation of upconverting thermometry through engineering phonon energy of a matrix, ACS Appl. Mater. Interfaces 8 (2016) 30312–30319, https://doi.org/10.1021/acsami.6b12176.

[15] H. Suo, X. Zhao, Z. Zhang, Y. Wang, J. Sun, M. Jin, C. Guo, Rational design of ratiometric luminescence thermometry based on thermally coupled levels for bioapplications, Laser Photon. Rev. 15 (2021), 2000319, https://doi.org/10.1002/lpor.202000319.

[16] W.M. Piotrowski, K. Maciejewska, L. Dalipi, B. Fond, L. Marciniak, Cr3+ ions as an efficient antenna for the sensitization and brightness enhancement of Nd3+, Er3+-based ratiometric thermometer in GdScO3 perovskite lattice, J. Alloys Compd. 923 (2022), 166343, https://doi.org/10.1016/j.jallcom.2022.166343.

[17] W. Piotrowski, L. Dalipi, R. Szukiewicz, B. Fond, M. Dramicanin, L. Marciniak, The role of Cr3+ and Cr4+ in emission brightness enhancement and sensitivity improvement of NIR-emitting Nd3+/Er3+ ratiometric luminescent thermometers, J. Mater. Chem. C 9 (2021) 12671–12680, https://doi.org/10.1039/d1tc03046a.

[18] W. Piotrowski, L. Dalipi, K. Elzbieciak-Piecka, A. Bednarkiewicz, B. Fond, L. Marciniak, Self-referenced temperature imaging with dual light emitting diode excitation and single-band emission of AVO 4 :Eu 3+ (A=Y, La, Lu, Gd) nanophosphors, Adv. Photonics Res. 3 (2022), 2100139, https://doi.org/10.1002/adpr.202100139.

[19] W. Piotrowski, K. Kniec, L. Marciniak, Enhancement of the Ln3+ ratiometric nanothermometers by sensitization with transition metal ions, J. Alloys Compd. 870 (2021), 159386, https://doi.org/10.1016/j.jallcom.2021.159386.

[20] H.K. Dan, D. Zhou, Z. Yang, Z. Song, X. Yu, J. Qiu, Optimizing Nd/Er ratio for enhancement of broadband near-infrared emission and energy transfer in the Er3+−Nd3+ co-doped transparent silicate glass-ceramics, J. Non-Cryst. Solids 414 (2015) 21−26, https://doi.org/10.1016/j.jnoncrysol.2015.02.001.

[21] J. Rajagukguk, J.H. Panggabean, M. Djamal, C.S. Sarumaha, J. Kaewkhao, Energy transfer and broad-band luminescence of Nd3+-Er3+ co-doped Lithium Fluorophosphate (LFP) glasses, Opt. Mater. 125 (2022), 112007, https://doi.org/10.1016/j.optmat.2022.112007.

[22] D.S. McClure, Electronic structure of transition-metal complex ions, Radiat. Res. Suppl. 2 (1960) 218, https://doi.org/10.2307/3583598.

[23] A.P. Vink, A. Meijerink, Electron−phonon coupling of Cr3+ in YAG and YGG, J. Lumin. 87−89 (2000) 601−604, https://doi.org/10.1016/S0022-2313(99)00308-7.

[24] K. Elzbieciak, L. Marciniak, The impact of Cr3+ doping on temperature sensitivity modulation in Cr3+ doped and Cr3+, Nd3+ Co-doped Y3Al5O12, Y3Al2Ga3O12, and Y3Ga5O12 nanothermometers, Front. Chem. 6 (2018) 424, https://doi.org/10.3389/fchem.2018.00424.

[25] H. Hua, J. Ueda, J. Xu, M. Back, S. Tanabe, High-pressure photoluminescence properties of Cr3+-doped LaGaO3 perovskites modulated by pressure-induced phase transition, Inorg. Chem. 60 (2021) 19253−19262, https://doi.org/10.1021/acs.inorgchem.1c03074.

[26] D. Wang, W. Hou, N. Li, Y. Xue, Q. Wang, X. Xu, D. Li, H. Zhao, J. Xu, Growth, spectroscopic properties and crystal field analysis of Cr 3+ doped GdScO 3 crystal, Opt. Mater. Express 9 (2019) 4218, https://doi.org/10.1364/ome.9.004218.

[27] K. Elzbieciak-Piecka, M. Suta, L. Marciniak, Structurally induced tuning of the relative sensitivity of LaScO3:Cr3+ luminescent thermometers by co-doping lanthanide ions, Chem. Eng. J. 421 (2021), 129757, https://doi.org/10.1016/j.cej.2021.129757.

9

Supporting Information

Boosting the thermometric performance of the Nd^{3+}, Er^{3+} based luminescence thermometers by sensitization via Cr^{3+} ions: the role of the host material

W. M. Piotrowski[1], K. Maciejewska[1], L. Marciniak[1]*

[1]Institute of Low Temperature and Structure Research, Polish Academy of Sciences, Okólna 2, 50-422 Wroclaw, Poland

* corresponding author: l.marciniak@intibs.pl

KEYWORDS luminescent thermometry, transition metal ions, sensitization, sensitivity enhancement, lattice, Ln^{3+} ions, Y$_3$Al$_5$O$_{12}$, Y$_3$Al$_2$Ga$_3$O$_{12}$, LaGaO$_3$, GdScO$_3$, LaScO$_3$

The integral intensities of the Nd^{3+} and Er^{3+} bands to calculate LIR values were fitted with Mott-Seitz equation (Eq. S1):

$$I = \frac{I_0}{C \cdot \exp(-\frac{W}{k \cdot T}) + 1} \qquad \text{(Eq. S1)}$$

where: I – the intensity in temperature T, I$_0$ – the intensity in the initial temperature, W - the activation energy, k – Boltzmann constant, C – the dimensionless constant

S1
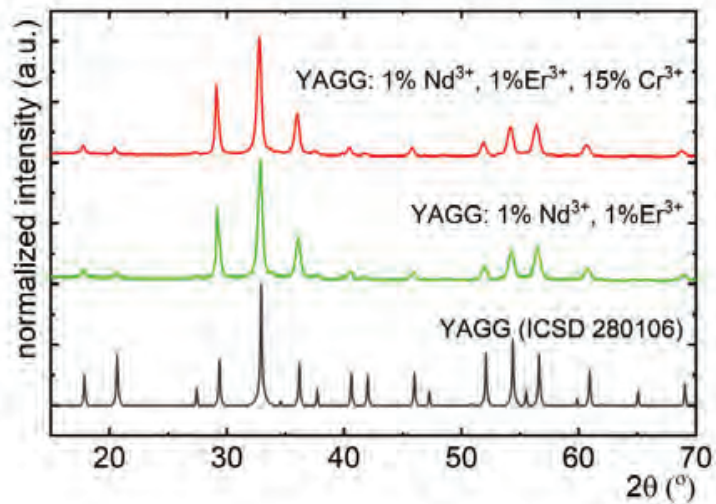
Figure S1. XRPD patterns of YAGG host doped with Nd^{3+}, Er^{3+} and Cr^{3+} ions.
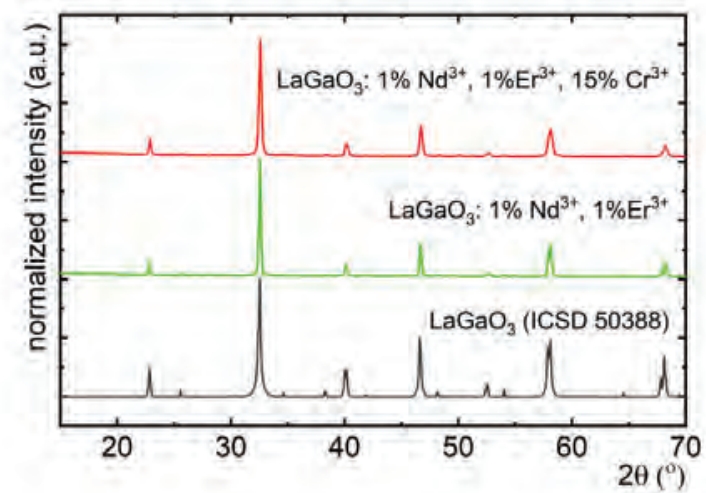
Figure S2. XRPD patterns of LaGaO$_3$ host doped with Nd^{3+}, Er^{3+} and Cr^{3+} ions.
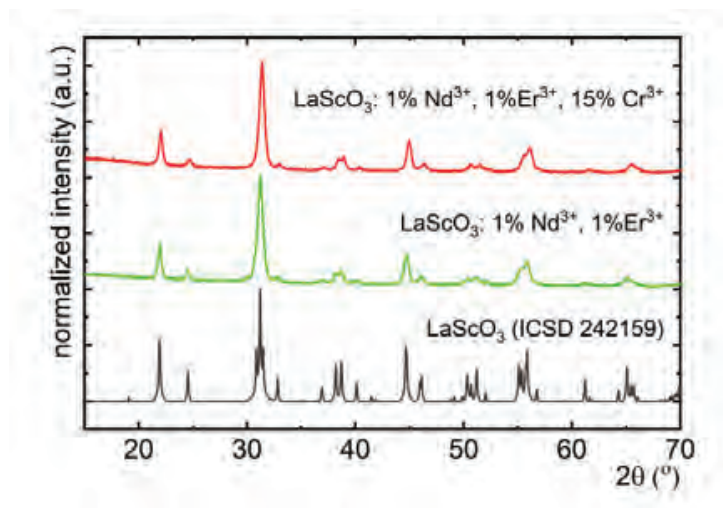
Figure S3. XRPD patterns of $LaScO_3$ host doped with Nd^{3+}, Er^{3+} and Cr^{3+} ions.
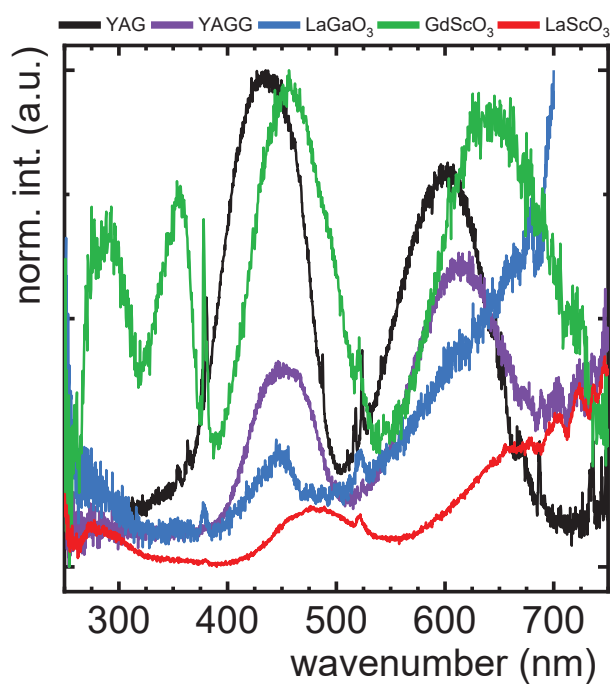
Figure S4. Excitation spectra of investigated phosphors monitored for λ_{exc} = ~1530 nm (Er^{3+} emission) for five different host materials co-doped with Nd^{3+}, Er^{3+}, Cr^{3+} at 123 K.

S3
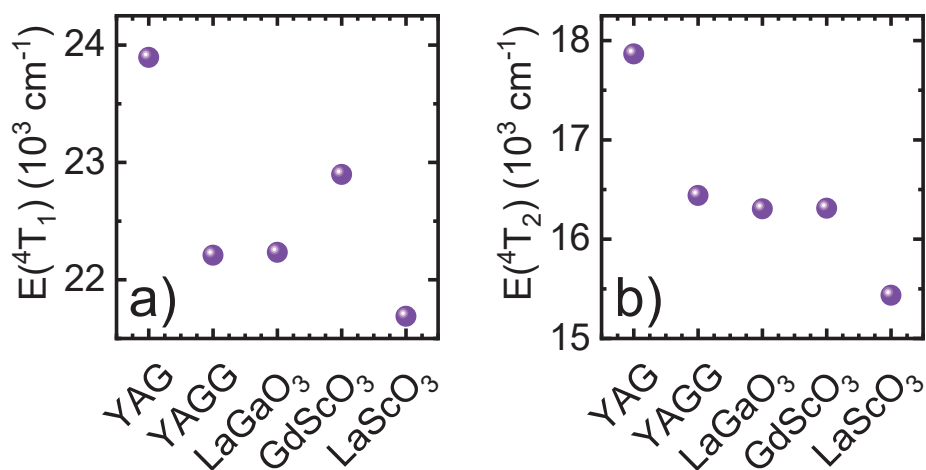
Figure S5. Comparison of position of $^4A_2 \rightarrow {}^4T_1$ – a) and $^4A_2 \rightarrow {}^4T_2$ bands – b) of Cr^{3+} ions noticed on the excitation spectra (λ_{em} = ~1060 nm, Nd^{3+} emission) for five different host materials co-doped with Nd^{3+}, Er^{3+}, Cr^{3+} at 123 K.
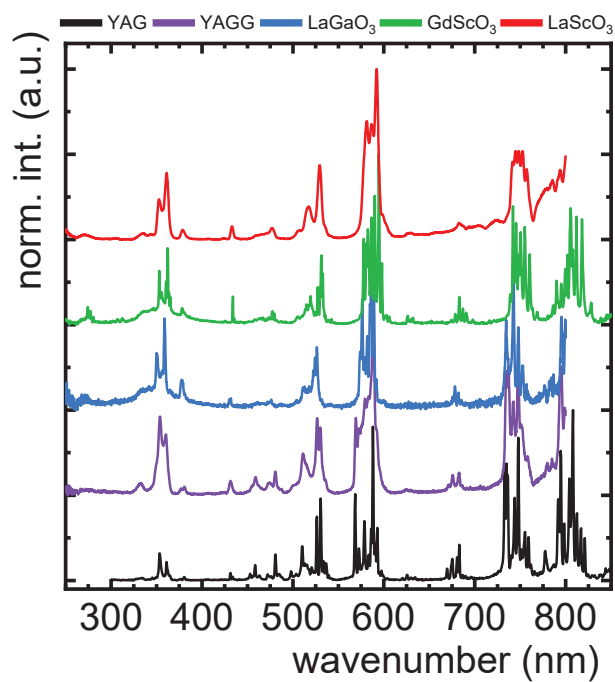
Figure S6. Excitation spectra (λ_{em} = ~1060 nm, Nd^{3+} emission) for five different host materials co-doped with Nd^{3+}, Er^{3+} at 123 K.

S4
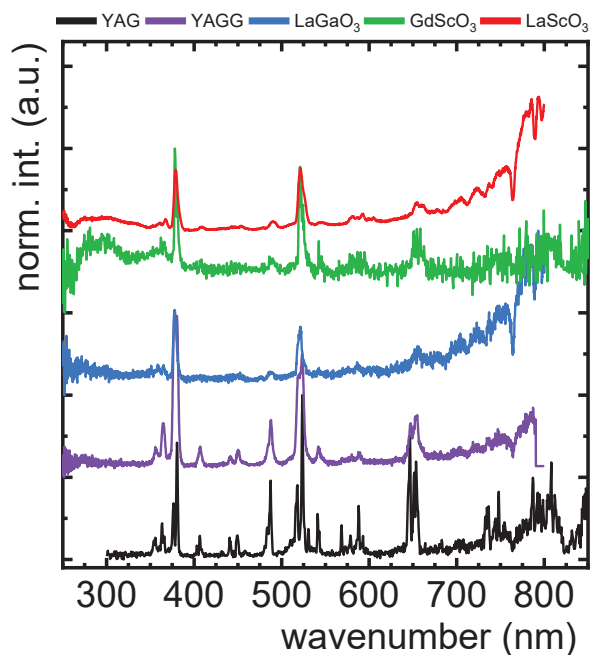
Figure S7. Excitation spectra (λ_{em} = ~1530 nm, Er^{3+} emission) for five different host materials co-doped with

Nd^{3+}, Er^{3+} at 123 K.

Table S1. Comparison of the position of the bands on the excitation spectrum at λ_{em} = ~1064 nm ($^4F_{3/2}\rightarrow{}^4I_{11/2}$ of Nd^{3+}) for different matrices doped with Nd^{3+}, Er^{3+} ions.

x excited state:	Maximum of $^4I_{9/2}\rightarrow$x excitation band in different host materials [cm^{-1}]:				
	YAG	YAGG	LaGaO$_3$	GdScO$_3$	LaScO$_3$
$^4F_{3/2}$	12026	-	-	11338	-
$^4F_{5/2}$ + $^2H_{9/2}$	12610	12698	12571	12626	12642
$^4F_{7/2}$ + $^4S_{3/2}$	13441	13414	13459	13414	13351
$^4F_{9/2}$	14695	14793	14706	14641	14556
$^2H_{11/2}$	15886	16000	-	15962	15911
$^4G_{5/2}$	16863	16992	17036	16821	16892
$^2G_{7/2}$	17467	17346	17361	17301	17271
$^4G_{7/2}$	18744	18868	18904	18815	18815
$^4G_{9/2}$	19399	19455	19417	19455	19342
$^2K_{13/2}$ + $^2G_{11/2}$	20619	20513	19841	20768	20921
$^2D_{3/2}$ + $^4G_{11/2}$ + $^2K_{15/2}$	21598	21786	21345	21413	21459
$^2D_{3/2}$ + $^2P_{1/2}$	23175	23557	23202	23041	23585
$^2P_{3/2}$	26316	26385	26455	26110	26316
$^4D_{3/2}$	27701	27739	27473	27510	27624
$^4D_{1/2}$ + $^4D_{5/2}$ + $^2I_{11/2}$	28289	28289	28209	28329	28409

S5

	30257	29806	29499	29851
$^2L_{15/2} + {}^4D_{7/2} + {}^2I_{13/2}$	30257	29806	29499	29851
$^2H_{9/2}$	-		32000	32787
$^2H_{11/2}$	-		34965	-
$^2F_{5/2} + {}^2F_{7/2}$	36900		36430	37244

Table S2. Comparison of the position of the bands on the excitation spectrum at λ_{em} = ~1530 nm ($^4I_{13/2}\rightarrow{}^4I_{15/2}$ of Er^{3+}) for different matrices doped with Nd^{3+}, Er^{3+} ions.

x excited state:	Maximum of $^4I_{15/2}\rightarrow$x excitation band in different host materials [cm^{-1}]:				
	YAG	YAGG	LaGaO$_3$	GdScO$_3$	LaScO$_3$
$^4I_{9/2}\rightarrow{}^4F_{3/2}$ - Nd^{3+}	12026			11765	
$^4I_{9/2}$	12438	12878	12438	12461	12446
$^4I_{9/2}\rightarrow{}^4F_{7/2} + {}^4S_{3/2}$ - Nd^{3+}	13369	13369	13459	13263	13342
$^4I_{9/2}\rightarrow{}^4F_{9/2}$ - Nd^{3+}			14225		14609
$^4I_{9/2}\rightarrow{}^4F_{9/2}$ - Nd^{3+}	15349	15361	15337	15198	15314
$^4G_{5/2}$	17286	17241	16992	17212	16878
$^4S_{3/2}$	18727	18416	18433	18399	18332
$^2H_{11/2}$	19361	19268	19175	19194	19268
$^4F_{7/2}$	20683	20619	20534	20513	20408
$^4F_{5/2}$	22247	22272	22271	22421	22173
$^4F_{5/2}$	22701	22676	22547	22598	22573
$^2G_{9/2}$	24600	24691	24630	24600	24510
$^4G_{11/2}$	26281	26490	26420	26281	26385
$^2K_{15/2} + {}^4G_{9/2}$	27510	27473	27778	27586	27624
$^2G_{7/2}$	28129	28129	28490	28329	28409
$^2K_{13/2} + {}^2P_{1/2} + {}^4G_{5/2}$				33223	
$^2H_{9/2}$			36832	36430	

The crystal field parameter Dq and Racah parameter B for Cr^{3+} ions were defined based on the energies of $^4A_2 \rightarrow {}^4T_1$ and $^4A_2 \rightarrow {}^4T_2$ bands obtained from excitation spectra. The empirical equations take the following form:

$$E({}^4A_2 \rightarrow {}^4T_2) = 10Dq \qquad \text{(Eq. S2)}$$

$$\frac{Dq}{B} = \frac{15\left(\frac{\Delta E}{Dq}-8\right)}{\left(\frac{\Delta E}{Dq}\right)^2 - 10\cdot\frac{\Delta E}{Dq}} \qquad \text{(Eq. S3)}$$

where ΔE was predefined as:

$$\Delta E = E(\,^4A_2 \rightarrow \,^4T_1) - E(\,^4A_2 \rightarrow \,^4T_2) \qquad\qquad \text{(Eq. S4)}$$

Table S3. Comparison of crystal field parameters for different host materials co-doped with Cr^{3+}.

Host	Dq [cm^{-1}]	B [cm^{-1}]	Dq/B [-]
YAG	1786.5	575.8	3.10
YAGG	1644.0	555.9	2.96
LaGaO$_3$	1630.6	576.4	2.83
GdScO$_3$	1631.2	660.6	2.47
LaScO$_3$	1543.5	628.0	2.46
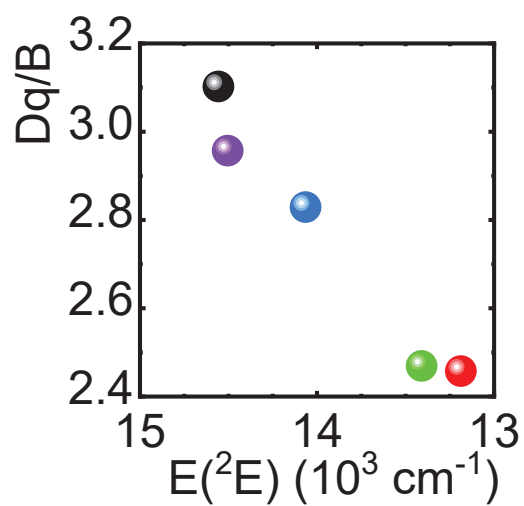
Figure S8. Dependance of Dq/B parameter on the position of ^2E excited state of Cr^{3+} ions in investigated host materials.

S7
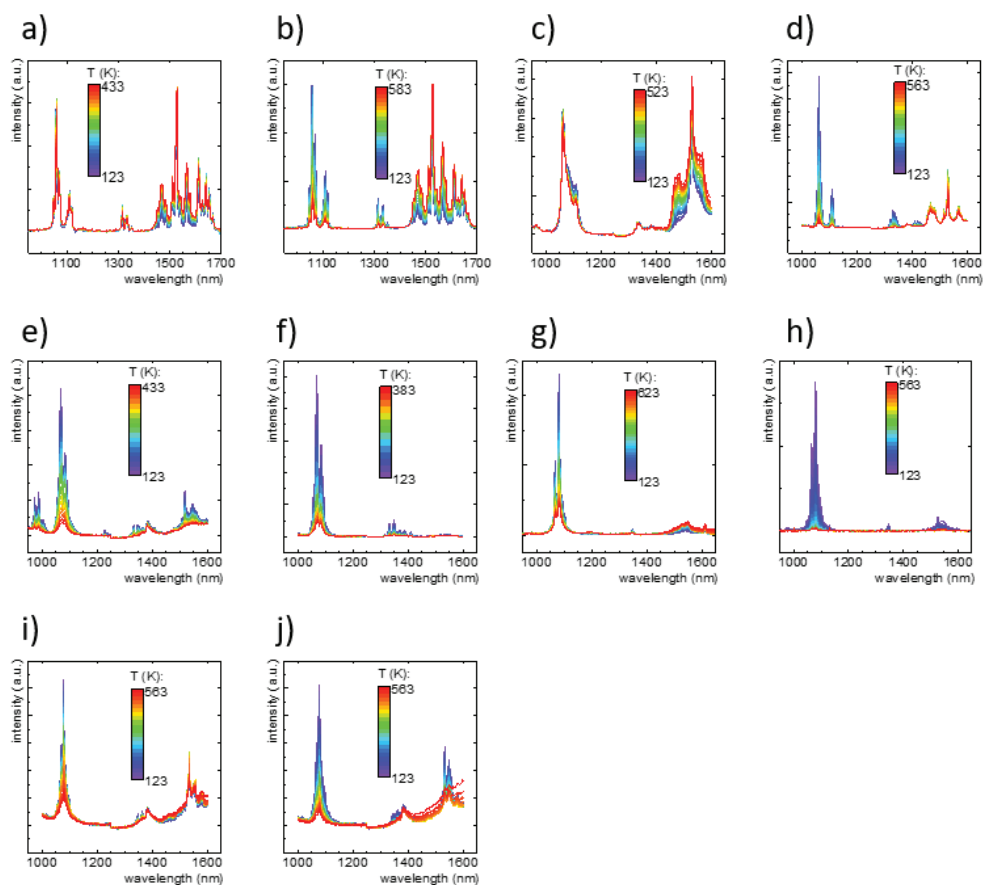
Figure S9. Thermal evolution of emission spectra performed for YAG (a, b), YAGG (c, d), LaGaO$_3$ (e, f), GdScO$_3$ (g, h) and LaScO$_3$ (i, j) co-doped with Nd^{3+}, Er^{3+} ions (a, c, e, g, i) and with Nd^{3+}, Er^{3+}, Cr^{3+} ions (b, d, f, h, j).
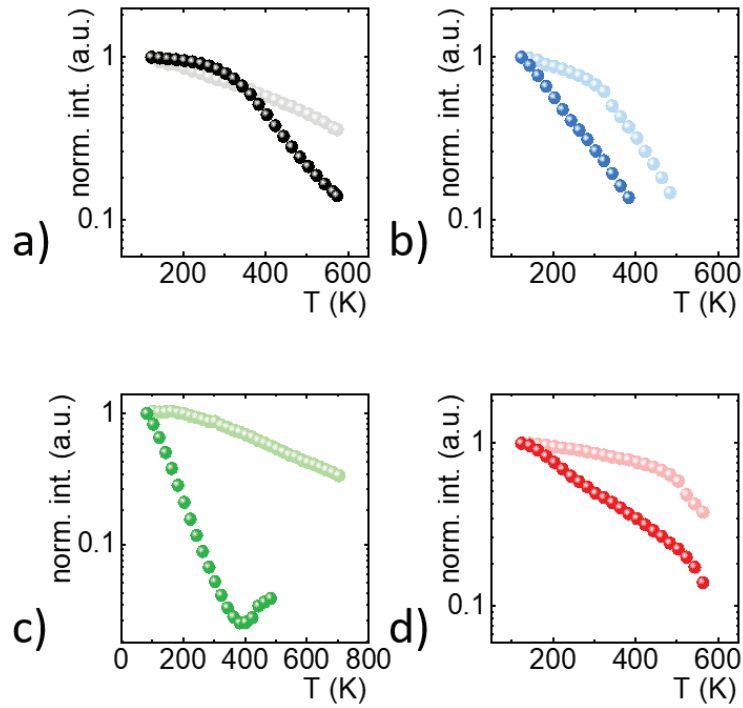
Figure S10. Thermal evolution of emission signal intensity of Nd^{3+} band ($^4F_{3/2} \rightarrow {}^4I_{11/2}$) for YAG – a), $LaGaO_3$ – b), $GdScO_3$ – c) and $LaScO_3$ – d) co-doped with Nd^{3+}, Er^{3+} ions (brighter dots) and with Nd^{3+}, Er^{3+}, Cr^{3+} ions (darker dots).
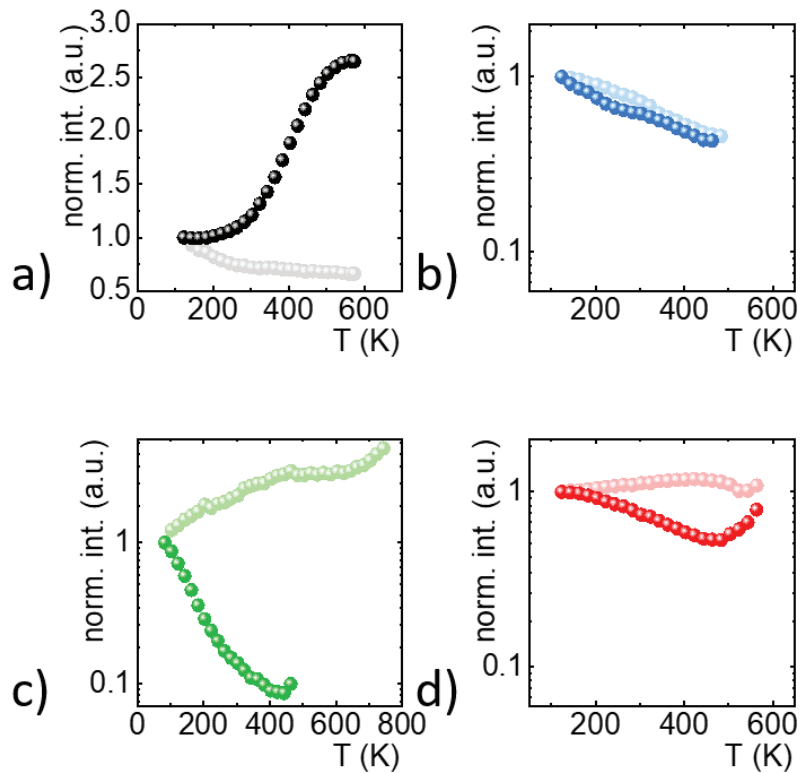
Figure S11. Thermal evolution of emission signal intensity of Er^{3+} band ($^4I_{13/2} \rightarrow {}^4I_{15/2}$) for YAG – a), $LaGaO_3$ – b), $GdScO_3$ – c) and $LaScO_3$ – d) co-doped with Nd^{3+}, Er^{3+} ions (brighter dots) and with Nd^{3+}, Er^{3+}, Cr^{3+} ions (darker dots).
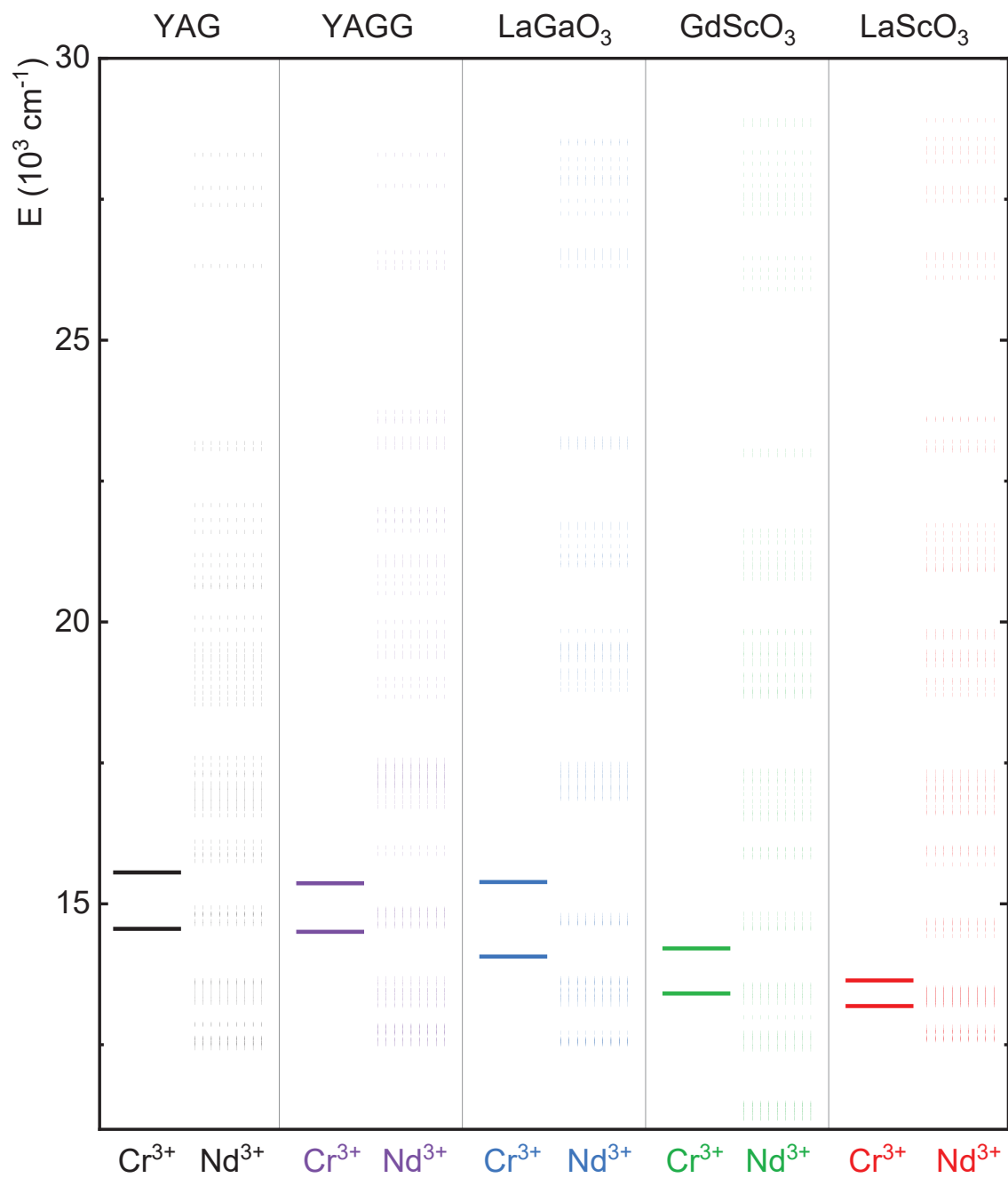
Figure S12. The comparison of positions of energy levels of Cr^{3+} and Nd^{3+} ions in different host materials.
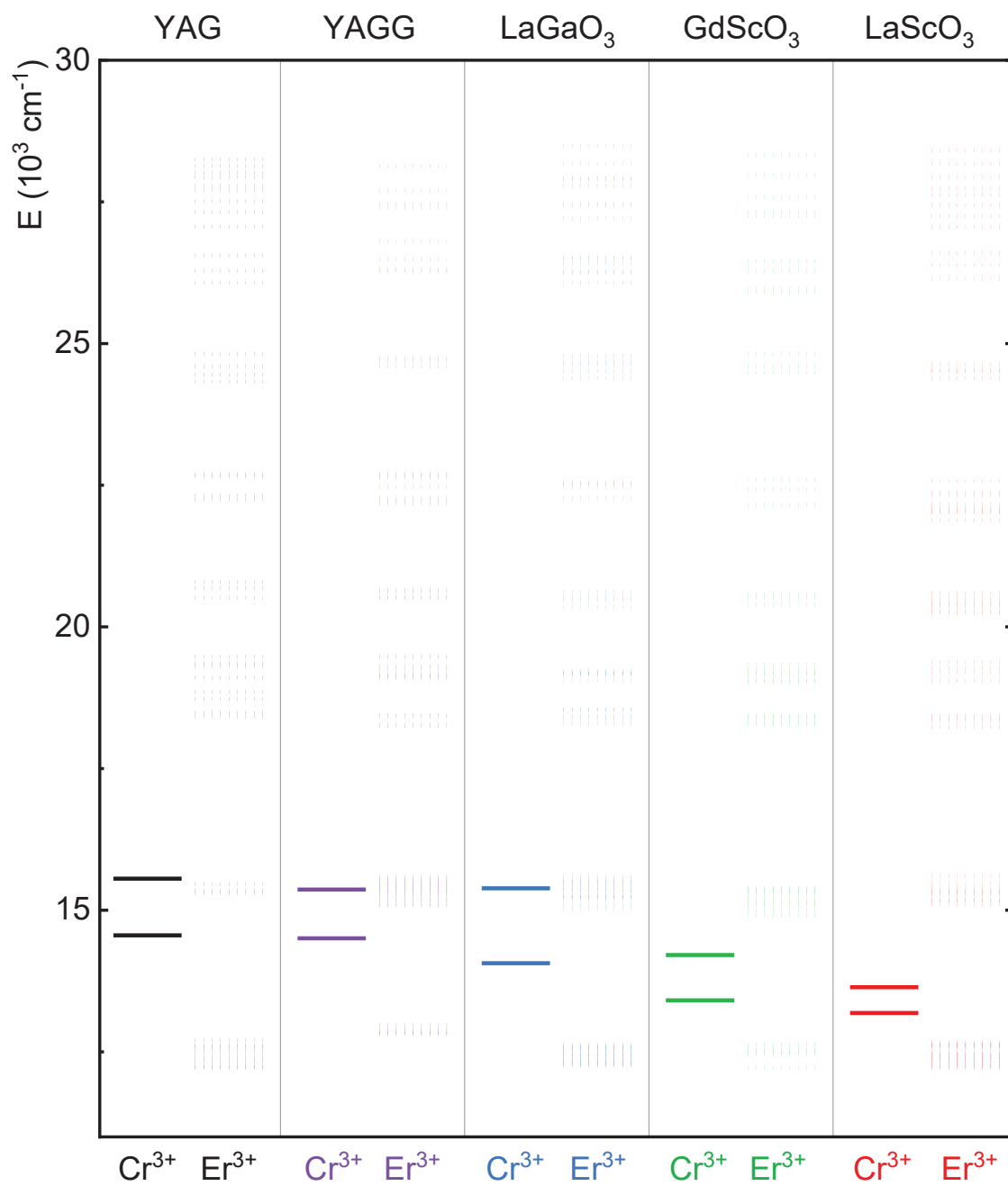
Figure S13. The comparison of positions of energy levels of Cr^{3+} and Er^{3+} ions in different host materials.
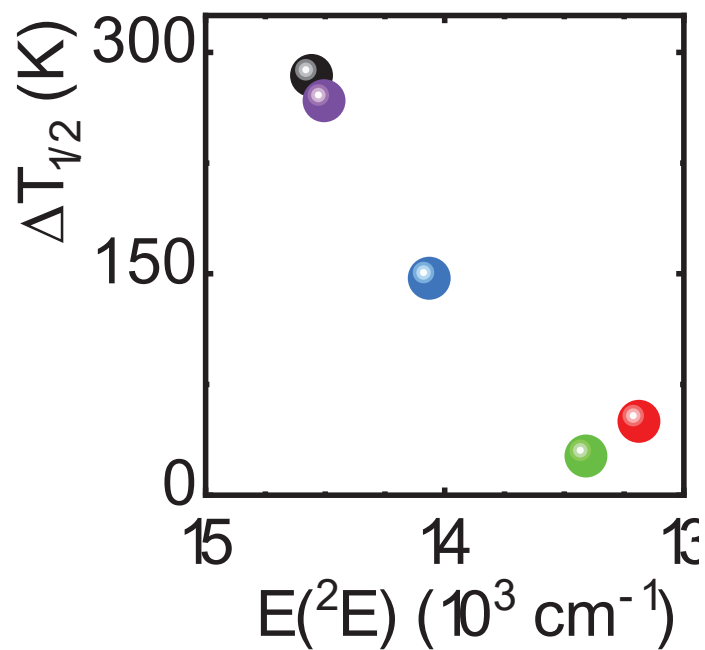
Figure S14. The influence of the energy of the energy of the ^2E state of Cr^{3+} ions on $\Delta T_{1/2}$ in the analyzed host materials.
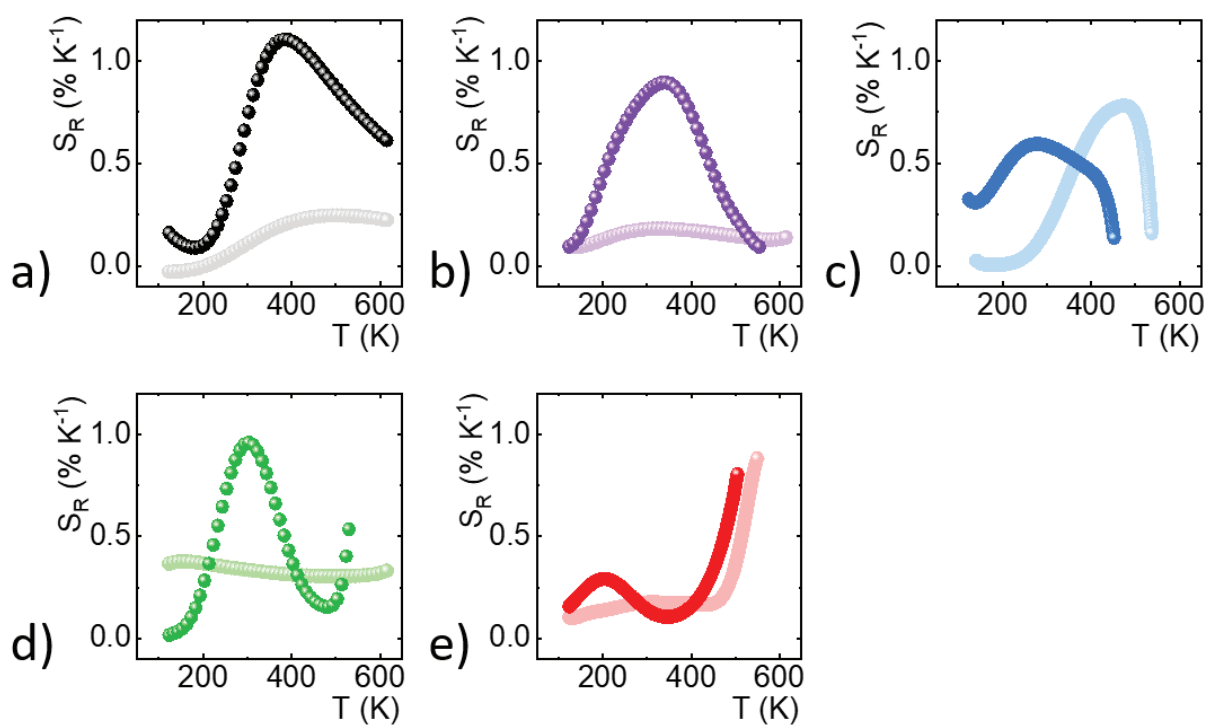
Figure S15. Thermal evolution of relative sensitivity for YAG – a), YAGG – b), $LaGaO_3$ – c), $GdScO_3$ – d) and $LaScO_3$ – e) co-doped with Nd^{3+}, Er^{3+} ions (brighter dots) and with Nd^{3+}, Er^{3+}, Cr^{3+} ions (darker dots).

S12

Positive luminescence thermal coefficient of Mn^{2+} ions for highly sensitive luminescence thermometry

W.M. Piotrowski [a], K. Kniec-Stec [a], M. Suta [c], B. Bogielski [b], B. Pozniak [b], L. Marciniak [a,*]

[a] *Institute of Low Temperature and Structure Research, Polish Academy of Sciences, Okólna 2, 50-422 Wroclaw, Poland*
[b] *Department of Pharmacology and Toxicology Faculty of Veterinary Medicine Wrocław University of Environmental and Life Sciences, ul. Norwida 25, 50-375 Wrocław, Poland*
[c] *Inorganic Photoactive Materials, Institute of Inorganic Chemistry & Structural Chemistry, Heinrich Heine University Düsseldorf, Universitätsstraße 1, 40225 Düsseldorf, Germany*

ABSTRACT

Luminescence thermal quenching phenomenon is a major limitation in the development of luminescent thermometers of high-resolution operating in the temperature range above 400 K. Therefore, in order to circumvent this limitation, in this work CaGa$_4$O$_7$:0.01 % Mn^{2+}, 0.05 % Cr^{3+} is proposed as a new biocompatible thermometer in which the luminescence intensity of the Mn^{2+} -based emission is thermally enhanced providing a high signal-to-noise ratio at temperatures even above 520 K. Therefore, as shown, the intensity ratio of Mn^{2+} and Cr^{3+} ions can be successfully used for ratiometric temperature readout not only for thermal sensing with a relative sensitivity of 2.08 % K^{-1} at 403 K and $\delta T = 0.1$ K and for 2-dimensional thermal imaging using a digital camera.

1. Introduction

Temperature is one of the most important physical parameters that affect our daily lives. It determines, among many other examples, the occurrence of inflammation in the human body [1], the correct operational work of machines and appliances or the proper transport and storage of food [2,3]. Therefore, the aim is to design multifunctional and correlated solutions which, in line with the principle of making people's lives safer, will continuously control the temperature of various objects. One of such solution is the idea of designing a so-called 'smart kitchen', which will be equipped with different kinds of sensors to control and regulate the humidity in the room [4], react to gas leaks [5], the weight applied to the kitchen worktop [6] or the temperature of the oven or pan placed on an induction cooker [7–9]. In the latter case, it would be particularly valuable to continuously monitor the temperature over the entire surface of the object in a remote manner. Of the currently used methods of temperature detection, the only one that meets all these requirements is luminescent thermometry. It is widely known that luminescence thermometry exploits the temperature dependence of the luminescence properties of the phosphor to allow a remote determination of the local temperature at a phosphor [10–23]. The most common and reliable of the thermometric parameters is the luminescence intensity ratio (LIR) of two separated spectral regions. In this case, the usually opposite temperature-dependent behavior of the two regarded emission bands results in a strong thermal response of the luminescence thermometer. Although one of the most commonly reported thermometric parameters of luminescence thermometers is its relative sensitivity, S_r, there is a gradual paradigm shift indicating that a more suited parameter than the relative sensitivity is the statistical temperature uncertainty δT, which becomes minimized for high relative sensitivity combined with a desirable high signal-to-noise ratio. Thus, optimally performing luminescent thermometers do not only show high thermally induced variability of the chosen thermometric parameter but also have high emission intensity. This is particularly critical in the temperature range above 100 °C because, due to temperature quenching of the luminescence, the signal-to-noise ratio for most luminescent thermometers usually drops significantly and therefore limits the temperature resolution of the reading [24]. A promising solution to this disadvantage are luminescent compounds that show an increasing luminescence intensity upon increasing temperatures. Three main mechanisms leading to such an effect can be recognized: i) thermally induced ion-ion or defect-ion energy transfer; ii) thermal broadening of the absorption bands and iii) thermally induced changes in the radiative decay of the excited state. The latter process is rarely reported and therefore deserves

special attention. It is mainly observed in materials doped with transition metal ions. The total spin of their energy levels can mix via exchange interaction thereby enabling transitions that were otherwise spin-forbidden [25]. This effect was reported for materials doped with Mn^{4+} and Cr^{3+} ions [26–30]. However, it is not often observed for materials doped with Mn^{2+} ions. Therefore, in this work, we use the positive thermal effect in Mn^{2+} doped $CaGa_4O_7$ to develop a sensitive and reliable ratiometric luminescence thermometer. The gradual enhancement of the luminescence intensity of the $^4T_{1(g)} \rightarrow {}^6A_{1(g)}$-based emission band of octahedrally coordinated Mn^{2+} ions in the 300 °C – 500 °C temperature range with simultaneous temperature quenching of the luminescence of co-doped Cr^{3+} allows the design of a luminescent thermometer with constantly high relative sensitivity ($S_r > 2\,\%\,K^{-1}$) and enhanced luminescence intensity at elevated temperatures. A detailed structural study and luminescence characterization of the $CaGa_4O_7$:Mn^{2+} phosphor is presented, focusing on understanding the origin of the thermal enhancement of the photoluminescence. Optimization of dopant concentrations was carried out to obtain a highly sensitive ratiometric luminescence thermometer with bright emission. In addition, the low cytotoxicity of this luminescent thermometer enables its safe potential application in food-related sectors.

2. Experimental

2.1. Synthesis of Mn^{2+}-doped crystals and Mn^{2+}, Cr^{3+} co-doped crystals

$CaGa_4O_7$ doped with xMn^{2+} ions and co-doped with xMn^{2+} and yCr^{3+} ions have been successfully synthesized by a modified Pechini method [31]. An appropriate amount of calcium nitrate tetrahydrate (Ca $(NO_3)_2 \cdot 4H_2O$ of 99.999 % purity from Alfa Aesar), gallium nitrate nonahydrate ($Ga(NO_3)_3 \cdot 9H_2O$ of 99.999 % purity from Alfa Aesar), manganese chloride tetrahydrate ($MnCl_2 \cdot 4H_2O$ of 99.999 % purity from Alfa Aesar) and chromium nitrate nonahydrate ($Cr(NO_3)_3 \cdot 9H_2O$ of 99.999 % purity from Alfa Aesar) were dissolved in distilled water and stirred until a clear solution was obtained. Then, citric acid (CA, $C_6H_8O_7$ of 99.5+% purity from Alfa Aesar) was added as a complexing agent to the mixture and stirring was continued for 2 h at 363 K. The CA was used in double excess with respect to the total molar amount of all metal cations. In order to avoid aggregation of the forming nanocrystals, an adequate volume of polyethylene glycol (PEG-200, from Alfa Aesar) was added dropwise to the aqueous solution of metal complexes and subsequently stirred at 363 K for 1 h, resulting in polyesterification process between the functional groups of the CA and PEG. PEG-200 and CA were used in the molar ratio of 1:1. Afterwards, the reaction mixture was dried at 363 K for one week. In a consequence the polymeric resin was formed and subjected to annealing process in air at 1123 K for 4 h resulting in powders of $CaGa_4O_7$:xMn^{2+} and $CaGa_4O_7$:xMn^{2+}, yCr^{3+}. For singly Mn^{2+}- doped $CaGa_4O_7$, the chosen representative concentrations of the Mn^{2+} ions were x = 0.01 mol%, 0.05 mol%, 0.2 mol%, 0.5 mol%, 1 mol%, 2 mol%, and 5 mol% with respect to Ca^{2+} ions. Considering the co-doped phosphors, the content of the Mn^{2+} ions was kept constant (0.01 mol%), whereas the Cr^{3+} concentration was varied between y = 0.01 mol%, 0.05 mol%, 0.1 mol%, and 0.5 mol% with respect to the Ca^{2+} ions.

2.2. Characterization

Powder diffraction studies were carried out on a PANalytical X'Pert Pro diffractometer equipped with Anton Paar TCU 1000 N Temperature Control Unit using Ni-filtered Cu Kα radiation ($\lambda = 1.5406\,Å$ $U = 40$ kV, $I = 30$ mA). Transmission electron microscopy images were obtained using a TEM Philips CM-20 SuperTwin with field emission gun operating at 160 kV accelerating voltage with an optical resolution of 0.25 nm.

The emission spectra were measured using the 266 nm excitation line from a laser diode of 20 mW/cm^2 excitation density (and a SilverNova Spectrometer from Stellarnet (1.5 nm spectral resolution). The

temperature of the sample was controlled using a THMS 600 heating–cooling stage from Linkam (0.1 K temperature stability and 0.1 K set point resolution). The excitation spectra and luminescence decay profiles were recorded using a FLS1000 Fluorescence spectrometer from Edinburgh Instruments with a 450 W Xe lamp and a μFlash lamp as excitation sources, double grating monochromators in excitation and emission compartment and a R928P side window photomultiplier tube from Hamamatsu as a detector.

The Raman spectra were recorded at room temperature using an InVia confocal microscope from Renishaw supplied with a silicon CCD camera as a detector, employing the 488 nm excitation line and under a 20 objective with a spatial resolution below 1 mm.

2.3. Cytotoxicity assessment of $CaGa_4O_7$:Mn^{2+}

Cytotoxicity tests were carried out on murine fibroblast (3 T3/Swiss Albino) and macrophage (J774.E) cell lines. The choice of the *in vitro* model relied on 3 T3 cells as a standard model to screen for cytotoxicity of biomaterials as fibroblasts are the main cellular component of connective tissues [32,33]. On the other hand, under *in vivo* conditions, macrophages form the primary line of defense to foreign bodies e.g. implants or biomaterials [34,35]. Thus, they are responsible for the distribution and clearance of nanoparticles and their agglomerates. Cells were cultured in RPMI-1640 medium (Institute of Immunology and Experimental Therapy, Wrocław, Poland) supplemented with 10 % fetal bovine serum (FBS, Sigma, USA), L-glutamine (Sigma, UK) and antibiotic (streptomycin and penicillin, Sigma, Germany). For the cytotoxicity assessment, cells were seeded in 96-well-plates (TTP, Switzerland) at a density of 6×10^3 (3 T3) or 8×10^3 (J774.E) cells per well and pre-incubated at 37 °C overnight in a humidified atmosphere of 5 % CO_2. After that, nanoparticle dispersions were added. Nanoparticles were suspended in 0.05 % BSA water solution and bath-sonicated at room temperature for up to 5 min. Next, the stock solutions were further diluted in 0.05 % BSA and dispersions in complete culture medium were prepared. In parallel, the highest nanoparticle concentrations were centrifuged at 30 000 *g* for 2 h and the particle-free supernatants were used as a diluent control (to exclude any possible particle-unrelated effects due to the presence of soluble compounds). Cells were exposed to the dispersions for 48 h (5 % CO_2, 37 °C). After that, the MTT assay was carried out. The test is based on the enzymatic reduction of the tetrazolium salt MTT [3-(4,5-dimethylthiazol-2-yl)-2,5-diphenyl-tetrazoliumbromide] in living, metabolically active cells. The metabolite, purple-coloured formazan is measured colourimetrically, using a multiwell plate reader. Preliminary experiment showed no interference of the nanoparticles with MTT or formazan in a cell-free system at concentrations used in this study. After 4 h of incubation, cells were lysed and optical density (OD) was measured after 24 h using a spectrophotometric microplate reader (Tecan Spark 10 M, Switzerland) at the wavelength of 570 nm (reference 630 nm). The OD of control cells was taken as 100 %. Cell viability was determined as follows: % viability = (mean OD in the test wells/mean OD for control wells) × 100. The results were obtained from at least 3 independent experiments.

2.4. Preparation procedure for $CaGa_4O_7$:Mn^{2+}, Cr^{3+}/silicone composite film

To prepare a flexible film with thermometric phosphor, the $CaGa_4O_7$ powder doped with 0.01 % Mn^{2+} and 0.1 % Cr^{3+} ions was selected. In the first step, 500.0 mg of crystalline powder was mixed with 5 ml of chloroform (pure P.A., POCH SA, Poland) and left for 15 min in an ultrasonic bath. Then, 10.000 g of colourless silicone (Ceresit CS 20, 100 % neutral, alkoxy type sanitary silicone) was added gradually under vigorous stirring of the solution. The solution was stirred for additional 30 min after complete addition of the silicone. Finally, the resulting mixture was poured into a gingerbread cookie-shaped mould attached to a glass surface and left to cure for 24 h at room temperature in air. After

2

this time, the composite film was separated from the glass surface using a bookbinding cutter and used for the proof-of-concept experiment without further processing. The resulting gingerbread cookie-shaped film had dimensions of 64 mm × 49 mm × 1 mm. The film was stored in air at room temperature and covered to prevent dust deposition.

2.5. Thermal imaging experiment with $CaGa_4O_7:Mn^{2+}$, Cr^{3+}/silicone composite film

In the thermal imaging experiment involving luminescence thermometry the film was placed on a heating plate with a centrally located single heater and excited with 254 nm excitation light of a Hg lamp. Digital images were taken with a Canon EOS 400D camera with an EFS 60 mm macro lens with an integration time of 20 s, a spatial resolution of 14.3 lp/mm. The pairs of colour images of the composite film were taken with one of two optical filters placed in front of macro lens of digital camera: 1) a long pass filter at 650 nm (Thorlabs FELH650); 2) a short pass filter at 650 nm (Thorlabs FESH650). In addition, a long pass filter at 550 nm (Thorlabs FELH650) was used in both cases to exclude the effect of excitation light scattering on the blue channel of the colour images. The RGB images were converted to 32-bit type emission maps in the ImageJ 1.8.0 software. Then, the resulting images were divided by each other using OriginLab 2022 software to obtain the LIR images ($LIR = \frac{FESH650}{FELH650}$). No smoothing was applied to the images. The 2-dimensional LIR maps were converted to temperature maps using a calibration curve. The calibration curve was obtained by placing a small 5x8 cm rectangle of 1 mm in thickness film in the centre of the heating plate and taking a series of optical images as a function of temperature. The image pairs were processed according to the procedure described above, while the temperature of the film was controlled by a FLIR T590 thermal camera. The emissivity of the composite film was evaluated by comparing the temperature of the powder placed on a fixed-temperature heating plate (313 K monitored by the IR camera) with that of a Scotch 130C tape with a standardised emissivity (0.95).

3. Results and discussion

3.1. Structural and morphological characterization

Grossite-type $CaGa_4O_7$ crystallizes in a monoclinic crystal system with the space group $C2/c$ (no. 15) [36]. In this structure, the Ga^{3+} ions are located in the two types of vertex-sharing tetrahedra, $[Ga_{(1)}O_4]^{5-}$ and $[Ga_{(2)}O_4]^{5-}$ and Ca^{2+} ions. Both crystallographically independent Ga sites have a C_1 site symmetry. According to conventional coordination chemistry, Ca^{2+} ions are 5-fold coordinated by O^{2-} ions in the form of a distorted trigonal bipyramid with C_2 (pseudo-C_{2v}) symmetry. However, Fukuda *et al.* discovered there is a one-dimensional Ca^{2+} ion conductivity along the ⟨101⟩ directions [37]. Based on this fact, they proposed a structural model of $CaGa_4O_7$ assuming that $[GaO_4]^{5-}$ tetrahedra form channels in one direction surrounded by six-membered $[Ga_6O_{18}]^{18-}$ rings. The Ca^{2+} ions are located within these channels in a zigzag fashion. According to the table presented by Shannon [38], the effective ionic radii (EIR) of Ga^{3+} located at the tetrahedral site is 47 pm. Since the value of EIR for 5-fold coordinated Ca^{2+} was not reported, it can be estimated (by extrapolation) that the EIR in this case is around 94 pm. When doping $CaGa_4O_7$ host material with Mn^{2+} ions, several scenarios are possible. Firstly, due to the occurrence of Ca^{2+} ions, the stabilization of Mn^{2+} ions should be considered, which is in fact confirmed by the analysis of spectroscopic properties presented later. On this basis, it can be assumed that the Mn^{2+} ions are surrounded by 5 O^{2-} ions, like Ca^{2+} ions, for which the three different metal–oxygen distance R(Ca-O) are equal: two 2.31 Å, two 2.37 Å and one 2.13 Å. In that case, their EIR is 75 pm and the misfit factor $EIR^V_{Mn2+}/EIR^V_{Ca2+} = 75$ pm /94 pm = ~ 0.80. On the other hand, due to the lack of a reported EIR value of Ca^{2+} ions at the 5-fold coordinated site and the closest distance to the next

sixth O^{2-} ion equaling 3.24 A, the occurrence of Mn^{2+} ions with 6-fold coordination can be considered. Then their EIR would be 83 pm, and the misfit factor with $EIR^{VI}_{Mn2+}/EIR^{VI}_{Ca2+} = 83$ pm /100 pm = 0.83 would be slightly higher in comparison to a value calculated for 5-fold coordinated site. It is worth mentioning for the subsequent analysis that the high-spin state of Mn^{2+} ions is considered in both cases. The determination of the surroundings of Mn^{2+} ions in $CaGa_4O_7$ is not completely clear. The consideration of the inclusion of an additional O^{2-} ion in the polyhedra is justified due to the spectroscopic results described below confirming the presence of Mn^{4+} ions in the $CaGa_4O_7$ structure. It is known that the strong covalent bonds of tetrahedra, like $[GaO_4]^{5-}$, are highly improper for Mn^{4+} ions due to their high oxidation state. Moreover, a strong deformation of $[GaO_4]^{5-}$ tetrahedra incorporating two additional O^{2-} ions are rather unlikely due to the stability of the $[Ga_6O_{18}]^{18-}$ ring structure. Therefore, it was assumed that, in addition to the predominantly Mn^{2+} ions, a small fraction of manganese ions (Mn^{4+}) substitutes in a 1:2 ratio with respect to Ca^{2+} ions to compensate for the electrical charge, and forms strongly deformed octahedra in the $CaGa_4O_7$ structure. Also in the case of co-doping with Cr^{3+} ions, whose luminescence can only be observed when they are located in octahedral sites, it should be assumed that they substitute the crystallographic positions of Ca^{2+} ions, which can be considered as filled holes between solidly structured rings of $[GaO_4]^{5-}$ tetrahedra. Comparing the misfit factor of $EIR^{VI}_{Mn4+}/EIR^{VI}_{Ca2+} = 53$ pm/100 pm = ~ 0.53 and $EIR^{VI}_{Cr3+}/EIR^{VI}_{Ca2+} = 61.5$ pm/100 pm = ~ 0.615, it can be assumed that the occurrence of Cr^{3+} octahedra leads to slightly smaller deformations of the structure of $CaGa_4O_7$. Nevertheless, it is expected that, due to the significant influence on the structure of host material, stable Mn^{4+} ions will constitute a minority of manganese ions (with a predominance for Mn^{2+}), while the successful incorporation of Cr^{3+} ions without precipitation of an additional phase will only be possible at low concentrations of Cr^{3+} as dopant.

The phase purity and impact of the doping concentration of microcrystalline $CaGa_4O_7$ was verified with X-ray diffraction (XRD) (Fig. 1b). The Bragg reflections obtained for samples doped with Mn^{2+} ions at concentrations from 0.01 % to 5 % agree with the reference pattern (ICSD 710351) based on single-crystal structural data confirming the phase purity of the synthesized phosphors. Even at a doping fraction of 5 % Mn^{2+}, no additional reflections suggesting the presence of an additional phase were observed. Also, when co-doping the $CaGa_4O_7$:0.01 % Mn^{2+} powder with Cr^{3+} ions at concentrations from 0.01 % to 0.5 % no additional phase was detectable by means of XRD (Figure S1). The transmission electron microscopy (TEM) studies of $CaGa_4O_7$: 0.01 % Mn^{2+} indicate that well-crystallized particles are prone to agglomeration (Fig. 1c-d). The analysis of the particle size distribution using Feret's method reveals that over 65 % of observed particles are between 200 and 300 nm in size and the average particle size is estimated to be 228 nm (Fig. 1e). In addition, to exclude the influence of structural changes on the spectroscopic properties of $CaGa_4O_7$:Mn^{2+} phosphor within the regarded temperature range, temperature-dependent Raman spectra were acquired (Figure S2). Over a wide temperature range of 123–573 K, neither significant shifts of the peaks nor changes in the appearance of the Raman spectra were observed.

3.2. Luminescent properties characterization

Mn^{2+} has a $3d^5$ valence electron configuration. Since the Mn^{2+} ions are assumed to substitute the fivefold coordinated Ca^{2+} ions, the ligand field is weak and consequently, the Mn^{2+} ions are in a high-spin (HS) electron configuration. Upon excitation at $\lambda_{exc} = 266$ nm, orange emission from the Mn^{2+} ions at $\lambda_{em} = 578$ nm is observable in $CaGa_4O_7$ (see Fig. 2a). The orange emission colour confirms the assumption of Mn^{2+} ions occupying the Ca sites with a weaker crystal field. Tetrahedrally coordinated Mn^{2+} usually emits in the green range as observed in e.g., $MgAl_2O_4$ or in selected halides [39,40], while octahedrally coordinated Mn^{2+} ions tend to emit in the red range [41,42] beyond 600 nm.

3
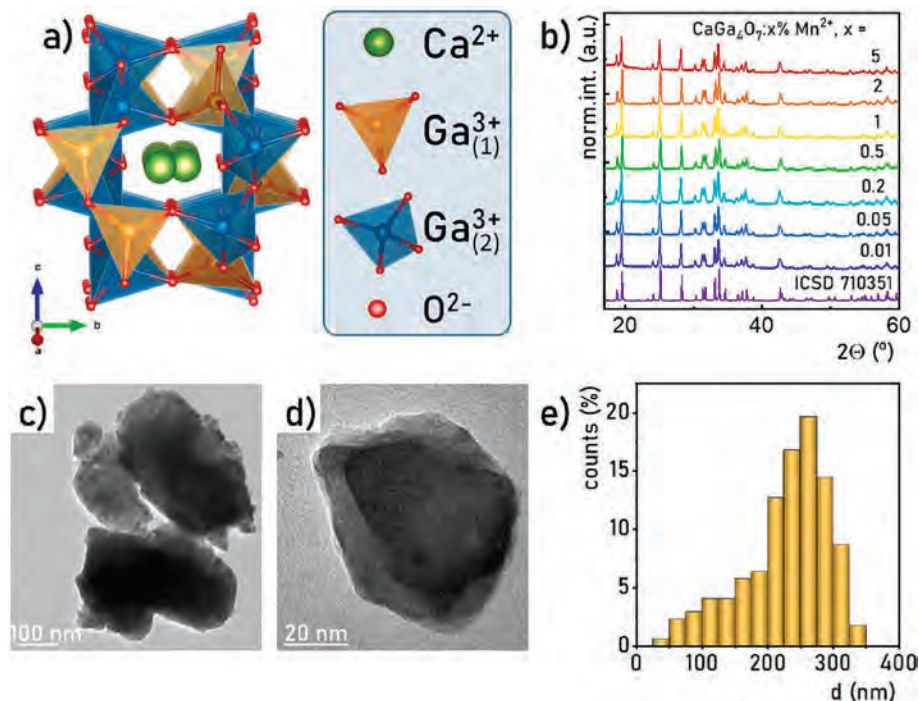
Fig. 1. Structural characterization of synthesized materials: perspective view of part of the crystal structure of $CaGa_4O_7$ - a); X-ray diffraction patterns of $CaGa_4O_7$ doped with different concentrations of Mn^{2+} ions - b); the representative TEM images – c), d) and particle size distributions of $CaGa_4O_7$:0.01 % Mn^{2+} - e).
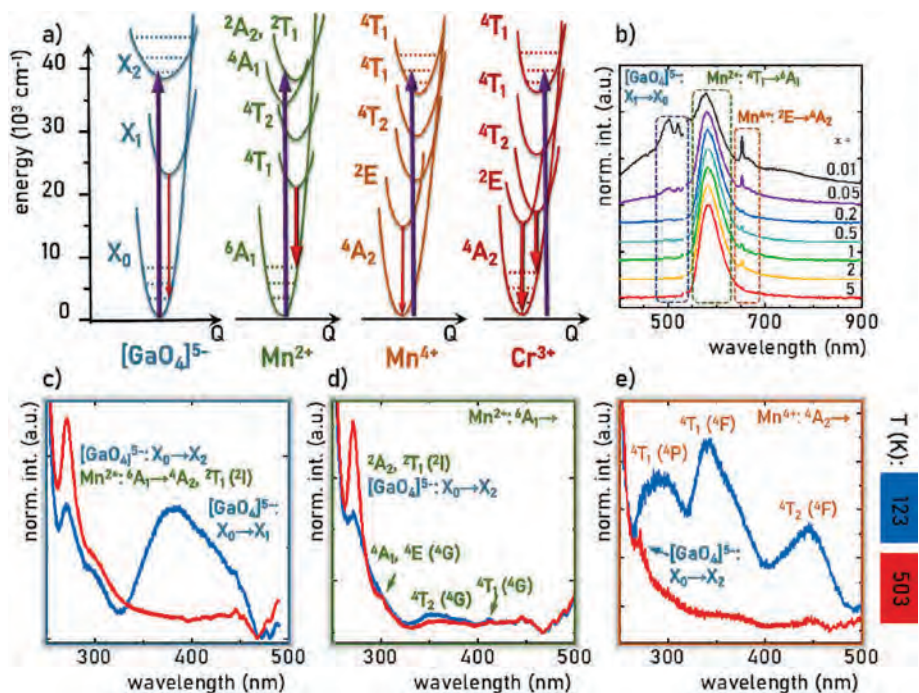
Fig. 2. Configurational coordinate diagram for Mn^{2+}, Mn^{4+} and Cr^{3+} and $[GaO_4]^{5-}$ group – a); the influence of Mn^{2+} concentration on the emission spectra ($\lambda_{exc} = 266$ nm) for $CaGa_4O_7$:Mn^{2+} crystals at 123 K – b); the comparison of low- (123 K) and high-temperature (503 K) excitation spectra of $CaGa_4O_7$:0.01 % Mn^{2+} detected at $\lambda_{em} = 545$ nm – c), $\lambda_{em} = 578$ nm – d) and $\lambda_{em} = 652$ nm – e).

It is noteworthy that both the Tanabe-Sugano diagram and the conventional labelling of the spectroscopically relevant states according to the irreducible representations of T_d/O_h symmetry are not applicable here anymore. Instead, the irreducible representations of an approximate D_{3h} or the actual C_2 site symmetry have to be used. The increase in the Mn^{2+} concentration results in the band centroid shift from 578 nm

for 0.01Mn^{2+} to 584 nm for 5 %Mn^{2+} (see Fig. 2b), which is associated with an increase in the crystal field strength resulting from the substitution of Ca^{2+} ions with smaller Mn^{2+} ions. On the other hand, such a high-energy excitation source as the 266 nm wavelength allows to excite other luminescent centres as well. Therefore, for materials with dopant concentrations below 0.05 % Mn^{2+}, an emission band with a maximum

4

of around 500 nm was observed, which can be attributed as host-related emission resulting from the presence of defects in the structure. This effect was previously observed by Puchalska *et al.* for $CaGa_4O_7$ nanocrystals upon 254 nm excitation [43]. Moreover, it is a known effect that host-related luminescence is already quenched at low concentrations of dopants. This is in agreement with our experimental data, for which the host emission is not observed anymore for doping concentrations of Mn^{2+} above 0.2 %. In addition, a narrow emission band with a maximum at 652 nm and a broad band at 665 nm were observed at low temperature for $CaGa_4O_7$ materials with Mn^{2+} concentrations in the range of 0.01 % to 2 %. This is most probably related to the presence of Mn^{4+} ions based on the small line width and emission wavelength. To confirm this hypothesis, excitation spectra were measured monitoring different emission wavelengths of $CaGa_4O_7$:0.01 % Mn^{2+} (Fig. 2c-e). In the low temperature (123 K) excitation spectra measured for $\lambda_{em} = 545$ nm, two broad excitation bands associated with the $[GaO_4]^{5-}$ entities are detectable, which have been assigned to electronic transition from the X_0 ground state to the X_1 (with a maximum located at 388 nm, 25,773 cm^{-1}) and X_2 (with a maximum at $\sim$ 271 nm, 36,900 cm^{-1}) levels of the $[GaO_4]^{5-}$ moieties in the host. At 503 K, the $X_0 \rightarrow X_1$ band is completely quenched. On the other hand, on the tail of the fundamental absorption band, a $X_0 \rightarrow X_2$ band is observed at 271 nm, whose intensity increases at 503 K. This unusual phenomenon, that will be discussed later in this work, can be attributed to the spectral overlap of this band with the excitation band related to the presence of Mn^{2+} ions, which in fact show an increasing luminescence intensity in $CaGa_4O_7$ upon increasing temperature. The intensity enhancement of this band is also observed in the excitation spectra taken for $\lambda_{em} = 578$ nm (Fig. 2d). Two additional excitation bands at 352 nm (28,409 cm^{-1}) and 411 nm (24,331 cm^{-1}) are observed at 123 K upon monitoring the emission at 578 nm. They do, however, vanish at 503 K. All discussed excitation bands related to the detected Mn^{2+}-based emission have very low intensity, which is a consequence of the spin-forbidden nature of the electronic transitions of Mn^{2+} in a HS electronic configuration [44]. This is also observed by comparing the excitation spectra of Mn^{2+} ions as a function of Mn^{2+} ion concentration (Figure S3). The intensity of the Mn^{2+}-related excitation bands decreases with respect to the fundamental host absorption at 266 nm for increasing doping concentrations. This indicates that quenching of the luminescence of Mn^{2+} in $CaGa_4O_7$ is effective at already low doping concentrations (>0.5 mol%). Occupation of Ca sites is not straightforward for Mn^{2+}. Indeed, usually Mn^{2+} ions particularly well occupy crystallographic positions of Zn^{2+} ions, which have a similar ionic radius compared to Mn^{2+} (EIR = 60 pm and 66 pm for 4-fold coordinated Zn^{2+} and Mn^{2+} ions, respectively) and generally prefer tetrahedral coordination based on their $3d^{10}$ configuration. Furthermore, the selection of host material for Mn^{2+} ions is significantly limited by the fact that Mn^{4+} can be stabilized if octahedral sites with isoelectronic ions are present in the host structure. Exceptions to this are $ZnGa_2O_4$:Mn^{2+} and Zn_2TiO_4:Mn^{2+}, for which the presence of both Mn^{2+} and Mn^{4+} ions was reported, and the degree of oxidation of the manganese ions is dependent on the chosen synthesis method [45,46]. Fig. 2e depicts the excitation spectrum obtained upon monitoring the narrow-line emission at $\lambda_{em} = 652$ nm. The three broad bands observed at 123 K with maxima at 448 nm (22,321 cm^{-1}), 345 nm (28,986 cm^{-1}) and 290 nm (34,483 cm^{-1}) are characteristic for ions with $3d^3$ configuration and can be therefore assigned to octahedrally coordinated Mn^{4+}. These bands correspond to the transitions from the $^4A_{2(g)}(^4F)$ ground state to the $^4T_2(^4F)$, $^4T_1(^4F)$ and $^4T_1(^4P)$ excited states, respectively. The Racah and crystal field parameters for Mn^{4+} based on Eq. S1-4 are derived as $B \approx 724$ cm^{-1}, $C \approx 3298$ cm^{-1} ($C/B = 4.55$) and $Dq/B \approx 2.97$ in this host compound.

3.3. The influence of temperature on the emission band of Mn^{2+} ions

The temperature-dependent emission spectra of $CaGa_4O_7$:Mn^{2+} upon excitation at $\lambda_{exc} = 266$ nm recorded between 123 K and 843 K are

depicted in Fig. 3a (see also Figure). In the case of $CaGa_4O_7$ doped with 0.01 mol% Mn^{2+}, an emission band originating from the host compound with a maximum at 500 nm is observed, which is gradually quenched at elevated temperatures up to 323 K above which its intensity cannot be recorded anymore. The increase of the dopant concentration results in reduction of its intensity relative to the intensity of the emission band of Mn^{2+} and is out of the scope of this work. A very intriguing feature of the orange Mn^{2+}-based luminescence in $CaGa_4O_7$ is the thermally induced enhancement of its intensity irrespective of the regarded doping fraction (see Fig. 3a and b). The enhancement of the luminescence intensity relative to the intensity at 123 K is reversible and most prominent for low doping fractions (0.05 mol%, 0.2 mol%). It leads to an increase in the luminescence intensity by a factor of 14 at 550 K, while it gradually decreases to a factor of 7.5 at a doping fraction of 5 mol% Mn^{2+}. Above 583 K, the Mn^{2+}-based luminescence is effectively quenched. The reduction in the thermal enhancement of the luminescence of Mn^{2+} indicates a counteracting effect based on energy migration between different Mn^{2+} ions. Due to the fact that above 713 K Mn^{2+} emission intensity is completely quenched such a strong thermal enhancement of the Mn^{2+} emission intensity for 0.05 % Mn^{2+} results in a very high luminescence quenching rate for this sample observed above 523 K (Figure S5).

For a better understanding of the excited state dynamics, temperature-dependent time-resolved luminescence was also analyzed (Figure S6). The luminescence decay traces show a biexponential decay behaviour over the whole regarded temperature range. In line with the temperature-dependent luminescence intensity evolution, the average decay times τ_{avr} remain constant between 123 K and 323 K ($\tau_{avr} = 7.35$ ms) and slightly increase to 8.00 ms at 363 K before decreasing to 3.67 ms at 543 K. The order of magnitude of the luminescence decay times clearly identifies the emission of Mn^{2+} in $CaGa_4O_7$ as a spin-forbidden transition and is similar to the reported values in e.g. $MgAl_2O_4$:Mn^{2+} ($\tau = 6.5$ ms)[40] or $BaZnAl_{10}O_{17}$:Mn^{2+} ($\tau = 5.2$ ms)[47], but shorter than luminescence decay times of octahedrally coordinated Mn^{2+} in e.g. $KMgF_3$ ($\tau \sim 100$ ms) at room temperature [48]. This clearly shows that
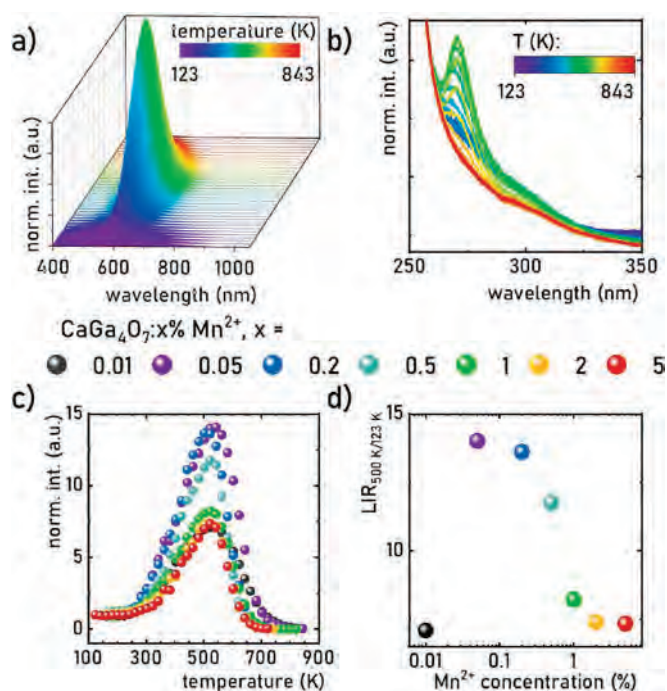
Fig. 3. Thermal evolution of emission spectra – a) and excitation spectra of $CaGa_4O_7$:0.01 % Mn^{2+} crystals – b); influence of Mn^{2+} concentration on the thermal evolution of integral intensities of Mn^{2+} emission band – c) and luminescence intensity ratio of Mn^{2+} emission band at 503 and 123 K – d).

the Mn^{2+} ions in $CaGa_4O_7$ occupy a non-centrosymmetric site, which leads to a loss of parity as an additional quantum number and supports the assignment of the substitution of the fivefold coordinated Ca^{2+} ions. The thermally induced increase in luminescence intensity accompanied by the decreasing decay time above 363 K could indicate a thermally activated population of a higher emissive state, from which the radiative transition becomes symmetry-allowed. Assuming approximate D_{3h} symmetry for a fivefold coordinated Mn^{2+} ion in form of a trigonal bipyramid, the ground term ^6S should transform as $^6A_1'$, while the first excited ^4G term is split into different states that transform as 2 $^4A_1' + $ $^4A_2' + 3$ $^4E'$. Out of these excited states, only transitions from E'-transforming states are orbitally electric-dipole allowed in D_{3h} symmetry, while those from A_2' are orbitally magnetic-dipole allowed. Transitions from the excited A_1'-transforming state are orbitally symmetry-forbidden. Based on this interpretation, the luminescence intensity enhancement could be explained by the following mechanism. At low temperatures, the lowest excited state must either transform as A_1' or A_2', which gives rise to a longer decay component of around 8 ms. This is line with known values from tetrahedrally coordinated Mn^{2+} ions, in which the $^4T_1(^4G) \rightarrow {}^6A_1(^6S)$ transition is also orbitally magnetic-dipolar in nature. In the case of $CaGa_4O_7:Mn^{2+}$, there must be a higher excited state transforming as E' with an energy separation of around 1000 cm^{-1} based on the onset of the thermal enhancement of the emission intensity at around 350 K since [10]

$$T_{on} \approx 0.2227 \frac{\Delta E}{k_B}$$

with k_B as Boltzmann's constant. At temperatures above 500 K, thermally induced crossover may take over, which leads to an overall quenching of the photoluminescence of Mn^{2+}. Advanced quantum chemical calculations or EPR studies could give additional insights whether our spectroscopic interpretation is justified.

3.4. The influence of Cr^{3+} co-doping concentration on the ratio of Mn^{2+} and Cr^{3+} band intensities

The thermal enhancement of the Mn^{2+} emission intensity is very beneficial for the performance as a luminescent thermometer since

emission intensity usually decreases with increasing temperature thus limiting the precision of the thermometer by a low signal-to-noise ratio. However, for a ratiometric readout concept, another emission band is required as an internal standard. Ideally, the intensity of that emission shows the opposite trend with increasing temperature for highest relative sensitivity. Since Cr^{3+} is well known for its susceptibility to thermal quenching the spectroscopic properties of $CaGa_4O_7: Mn^{2+}, Cr^{3+}$ were investigated as a function of temperature (see Fig. 4a, while emission spectra with other concentrations of Cr^{3+} ions are depicted in Figure S7). To the best of our knowledge, the spectroscopic properties of Cr^{3+} in in $CaGa_4O_7$ have so far not been reported. The emission spectra of $CaGa_4O_7:0.01\% Mn^{2+}, 0.01\% Cr^{3+}$ at 123 K and 403 K are depicted in Figure S8. At low temperatures, a broad band extending from 680 to 900 nm is detected, from which distinct local maxima at 691, 696.5, 706, and 712 nm can be distinguished. These transitions are associated with the emission of Cr^{3+} ions from both an $^2E_{(g)}(^2G)$ excited state (narrow lines) and the $^4T_{2(g)}(^4F)$ state (broad sideband) to the $^4A_{2(g)}(^4F)$ ground state. The co-existence of these two emission bands in the spectrum indicates that the Cr^{3+} ions are situated in an intermediate octahedral crystal field within $CaGa_4O_7$, however, the exact doping site is not readily evident given the strong thermodynamic tendency of Cr^{3+} ions for octahedral coordination. This can be confirmed by calculations of the crystal field parameters. Therefore, the excitation spectra were measured at 123 K monitoring the two emission wavelengths $\lambda_{em1} = 696$ nm and $\lambda_{em2} = 716$ nm (Figure S9). The spectra consist of three excitation bands, which can be assigned to the Cr^{3+} electronic transitions $^4A_{2(g)}(^4F) \rightarrow {}^4T_{1(g)}(^4P)$ (33003.3 cm^{-1}, 303 nm), $^4A_{2(g)}(^4F) \rightarrow {}^4T_{1(g)}(^4F)$ (22316.7 cm^{-1}, 448 nm) and $^4A_{2(g)} \rightarrow {}^4T_{2(g)}(^4F)$ (16715.4 cm^{-1}, 598 nm). Due to the $3d^3$ electron configuration of the Cr^{3+} ions, the same as that of the previously discussed Mn^{4+} ions, it is possible to estimate CFS parameters from Eq. S1-4. The resulting parameters for representative samples co-doped with 0.05 % and 0.5 % Cr^{3+} ions are summarized in Table S2. It can be found that the value of Dq/B decreases as the concentration of Cr^{3+} ions increases, and remain in the range of 2.06–2.11, characteristic for intermediate crystal fields at which the $^2E_{(g)}$ and $^4T_{2(g)}$ states cross. In addition, the effect of the presence of Cr^{3+} ions on the luminescence of Mn^{2+} ions was investigated. It is noted in Figure S10 that co-doping with Cr^{3+} ions leads to a general decrease in the intensity of Mn^{2+} excitation bands with respect to the fundamental
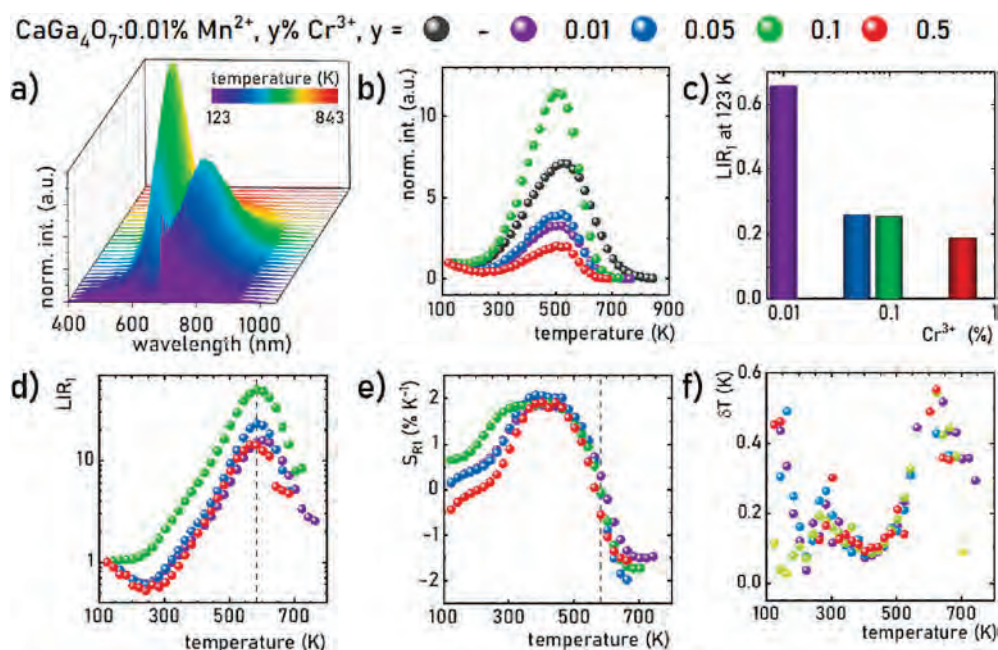
Fig. 4. Thermal evolution of the emission spectra of $CaGa_4O_7:0.01\% Mn^{2+}$, 0.01 % Cr^{3+} crystals – a); influence of Cr^{3+} concentration on the thermal evolution of integrated intensities of Mn^{2+}-based– b) and the influence of Cr^{3+} concentration on the LIR value at 123 K – c); thermal evolution of LIR – d) S_R value – e) and δT-f).

host absorption similar to the effect of increasing Mn^{2+} ion concentrations. In agreement with that result, the average decay time of the Mn^{2+} excited state is shortened from 7.33 ms to 6.22 ms when co-doped with Cr^{3+} ions (Figure S11) clearly indicating an energy transfer interaction between the Mn^{2+} and Cr^{3+} ions. From 123 K to 303 K, τ_{avr} increases from 6.22 ms to 7.48 ms in the sample co-doped with 0.1 % Cr^{3+} compared to the maintenance of 7.33–7.41 ms for the singly Mn^{2+}-doped sample. Consequently, the dynamic working range of the Mn^{2+}-based luminescent thermometer can be extended by the energy transfer interaction with the incorporated Cr^{3+} ions.

Figure S11 shows the effect of the presence of Cr^{3+} ions on the thermal evolution of integral intensities of the Mn^{2+} emission band in the orange spectral range. The integral signal intensity for 0.01 % and 0.05 % Cr^{3+} ions at 243 K reaches 57 % of the initial intensity, while for 0.5 % Cr^{3+}, this value is 41 %. Both the solely Mn^{2+}-doped and 0.1 % Cr^{3+} co-doped $CaGa_4O_7$ phosphors retain the luminescence intensity of the orange Mn^{2+}-based emission between 123 K and 303 K. Due to the opposite thermal evolution of the luminescence intensity of the Mn^{2+}- and Cr^{3+}-based emission, their luminescence intensity ratio can be used as a thermometric parameter:

$$LIR_1 = \frac{\int_{540nm}^{620nm} I(\ ^4T_1 \rightarrow\ ^6A_1)[Mn^{2+}]d\lambda}{\int_{690nm}^{710nm} I(\ ^2E \rightarrow\ ^4A_2)[Cr^{3+}]d\lambda} \tag{5}$$

$$LIR_2 = \frac{\int_{540nm}^{620nm} I(\ ^4T_1 \rightarrow\ ^6A_1)[Mn^{2+}]d\lambda}{\int_{730nm}^{800nm} I(\ ^4T_2 \rightarrow\ ^4A_2)[Cr^{3+}]d\lambda} \tag{6}$$

As shown in Fig. 4d, in the case of LIR_1 with increasing Cr^{3+} concentration LIR_1 at low temperatures tends to decrease, which is a cumulative effect of the increasing energy transfer probability from Mn^{2+} to Cr^{3+} and the increasing absorption of the Cr^{3+} ions given their increasing concentration.

To facilitate a comparison of the effect of Cr^{3+} ions concentration on the variation of LIR_1, the values have been normalised to the initial value at 123 K. Similar to the thermal evolution of Mn^{2+} emission, a decrease in LIR_1 for Cr^{3+} concentrations of 0.01 %, 0.05 % and 0.5 % can be observed at 243 K to about 52–56 % of initial LIR_1 value, which for crystals with 0.1 % Cr^{3+} is replaced by an almost constant value between 123 K and 223 K. Above 243 K an increase in intensity is observed reaching $LIR_1 = {\sim}15.7$, ${\sim}23.1$ and ${\sim}49.6$ at 583 K for samples co-doped with 0.01 %, 0.05 % and 0.1 % Cr^{3+}, respectively. The maximal LIR_1 value for 0.5 % Cr^{3+} is ${\sim}14.3$ and is reached at the slightly lower temperature of 563 K. Above this temperature, there is a gradual decrease in the LIR_1 value, which is related to the simultaneous thermal quenching of both the Mn^{2+} and Cr^{3+} luminescence. On the other hand, in the case of phosphors co-doped with 0.01, 0.05 and 0.5 % of Cr^{3+} ions LIR_2 initially decreases taking only 35 % of its initial value at 263 K (Figure S12). For 0.1 % Cr^{3+} the reduction in LIR_2 value is less rapid and the lowest value it adopts is 77 % of its initial value at 223 K. Above this temperature, the monotonicity of the tendency changes, the LIR value decreases. It is clearly seen that maximal values of LIR_2 are lower than LIR_1. This is due to a slight shift of the highest signal intensity originating from the $^4T_{2(g)} \rightarrow\ ^4A_{2(g)}$ transition towards higher temperatures to about 583–603 K in respect to 563 K observed for $^2E_{(g)} \rightarrow\ ^4A_{2(g)}$ emissions. In this temperature range the most significant enhancement of Mn^{2+} ions emission can be found. Therefore, LIR_1 was selected for further analysis as a potential temperature-dependent parameter. Nevertheless, when considering $CaGa_4O_7{:}Mn^{2+}$, Cr^{3+} as potential luminescent thermometer with high temperature readout precision, it is necessary to analyze not only the values of the temperature-dependent parameter, but also its change as a function of temperature. Therefore, to verify the influence of Cr^{3+} concentration on thermal changes of LIR_1 values in a quantitative way, the relative sensitivity S_R was calculated according to the following formula (Eq. 7):

$$S_R = \frac{1}{LIR}\frac{\Delta LIR}{\Delta T}100\% \tag{7}$$

where ΔLIR represents the change of LIR within a temperature interval ΔT. It was found that for materials doped with Cr^{3+} ions in the range of 0.01 % to 0.5 %, S_R values above 1 % were obtained in the range from 283 K to 523 K (see Fig. 4e). Maximum S_R values, $S_{Rmax} = 1.85$, 2.08, 1.89 and 1.92 % K^{-1} for $CaGa_4O_7{:}Mn^{2+}$ crystals co-doped with 0.01 %, 0.05 %, 0.1 % and 0.5 % of Cr^{3+} ions, respectively, are obtained at 403 K. This demonstrates that the $CaGa_4O_7{:}0.01\ \%\ Mn^{2+}$, 0.05 % Cr^{3+} phosphor performs slightly better with respect to other Cr^{3+} concentrations as a luminescent thermometer. The previously analysed intensity ratio of the emission signal from both ions also confirms the selection of these doping fractions as the most promising ones for applications of $CaGa_4O_7{:}Mn^{2+}$, Cr^{3+} in luminescence thermometry. Due to the opposite temperature evolution of the Mn^{2+}- and Cr^{3+}-based luminescence, S_R for LIR_1 becomes negative above 583 K. Therefore, a useful temperature range for $CaGa_4O_7{:}0.01\ \%\ Mn^{2+}$, 0.05 % Cr^{3+} is limited to 263–543 K.

Another important parameter is the statistical temperature uncertainty δT which was calculated according to Eq. (S8-9) and is shown in Fig. 4f. The δT is a parameter that more accurately depicts the true application potential of the tested thermometer than the S_R values, as it takes into account both the S_R and the emission intensity value. It is common that the largest changes in the LIR values and thus the highest S_R are obtained for intensity values that decrease rapidly leading to a decrease of the signal-to-noise ratio. Consequently, the temperature uncertainty increases then. However, for Mn^{2+} co-doped phosphors that show thermal enhancement of the luminescence intensity profit from an equal increase in S_R and decreasing δT. This is in agreement with the δT values obtained for $CaGa_4O_7{:}0.01\ \%\ Mn^{2+}$, y% Cr^{3+} phosphors. For the four compounds co-doped with Cr^{3+} ions, $\delta T < 0.16$ K was obtained in the range 303–503 K, which is in line with the strongest variation of LIR values achieved in this temperature range. The lowest δT values were reached with ${\sim}\ 0.08$ K for 0.01 % and 0.05 % Cr^{3+}. Additionally, the repeatability of the temperature determination using $CaGa_4O_7{:}0.01\ \%\ Mn^{2+}$, 0.05 % Cr^{3+} calculated using eq. S10 at 520 K was as high as 99.92 %.

4. Cytotoxicity assessment

The effects of the $CaGa_4O_7$ Mn^{2+} nanoparticles on cell viability are summarized in Fig. 5a. No significant cytotoxicity is detectable up to the concentration of 50 μg/ml. In both cell lines the viability drops slightly to 80 % as cells are exposed to the highest concentration of 100 μg/ml. It should be noted that the prepared dispersion showed relatively low stability, especially at higher concentrations. Lower stability translates into higher dose delivered directly to cells over time and the actual exposure is quite complicated to predict [49]. It is, however, reasonable to estimate that the actual concentration of particles and their agglomerates in the immediate proximity of cells was much higher than the nominally expected 100 μg/ml. Despite this lack of stability, the investigated particles are non-toxic in both cellular models. Fig. 5b shows the effects on cell morphology and some degree of cellular uptake of nanoparticle agglomerates by both cell types as determined by light microscopy. For the 3 T3 fibroblasts the main route of particle internalisation are different types of endocytosis [50], whereas for J774.E cells are known to be efficient in phagocytosis – a route targeting much larger, micron-sized agglomerates [51]. Since the uptake of nanoparticles was clear in both cell lines it seems that the crystallites could reach the cellular compartment by both endocytosis (free particles and small agglomerates) and phagocytosis (larger agglomerates). Interestingly, the internalised material tended to accumulate in the perinuclear region (particularly visible in more flat fibroblast cells, Fig. 5 c).

In conclusion, the nanoparticles under investigation were found to be biocompatible in the applied *in vitro* model and may be considered for
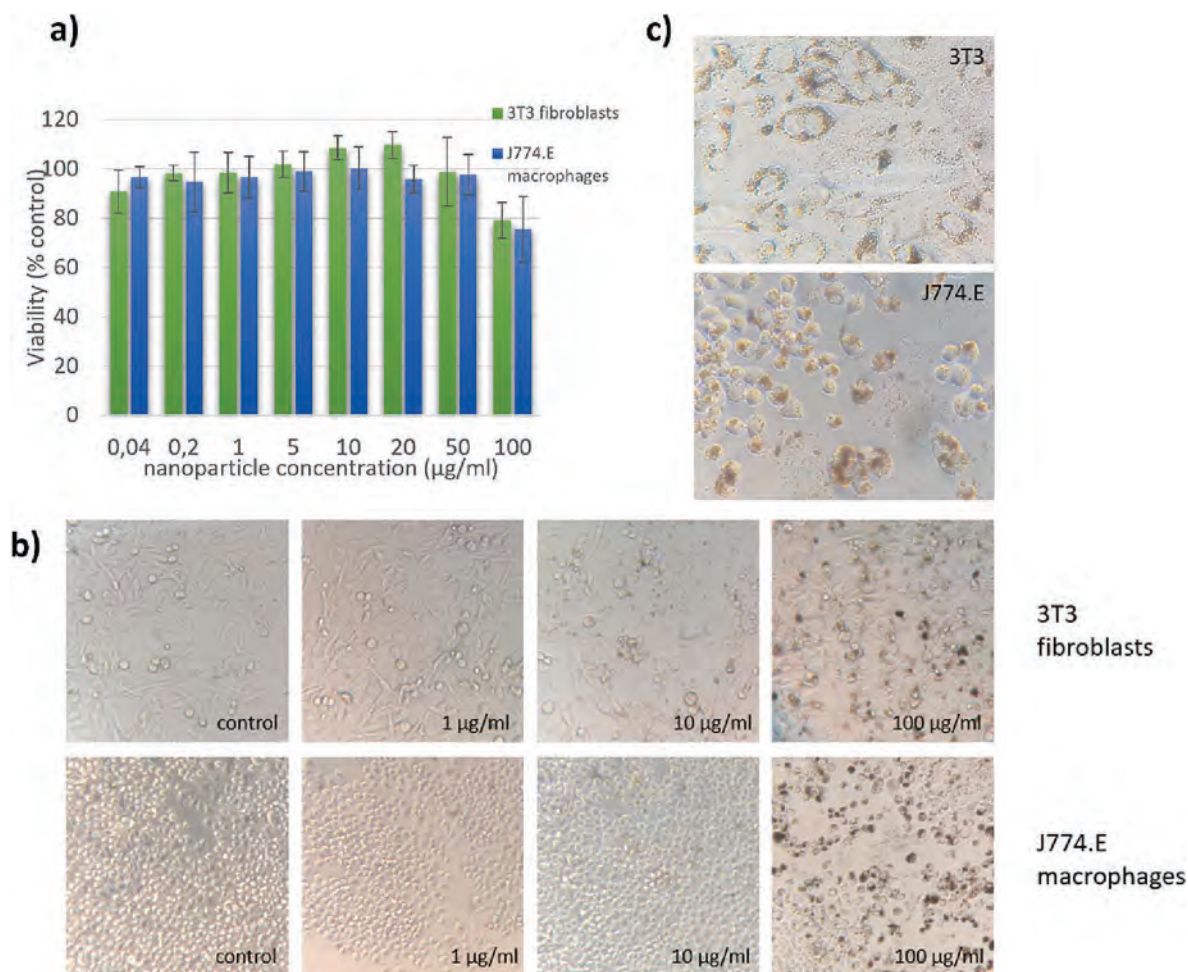
Fig. 5. Mean (±SD) viability of J774.E macrophages and 3 T3 fibroblasts exposed for 48 h to different concentrations of $CaGa_4O_7$ Mn^{2+} nanoparticles. Viability determined by MTT assay and expressed as the percent of control – a); 3 T3 (upper panel) and J774.E (lower panel) cells exposed to the $CaGa_4O_7$ Mn^{2+} nanoparticles in concentration 1, 10 and 100 μg/ml and their corresponding controls (magnification 200 ×) – b); 3 T3 (upper panel) and J774.E (lower panel) cells exposed to the $CaGa_4O_7$ Mn^{2+} nanoparticles at the concentration of 100 μg/ml (magnification 400 ×) – c).

further biological investigation. However, the identification of the route of particle internalisation as well as the consequences for cell physiology require further studies.

5. Proof-of-concept temperature imaging experiment

Due to the exceptional thermometric performance of $CaGa_4O_7$: Mn^{2+}, Cr^{3+}, a thermal imaging experiment has been employed to verify its applicative potential for remote temperature readout (Fig. 6, Figure S13). For this purpose, a 1 mm thick film containing $CaGa_4O_7$: Mn^{2+}, Cr^{3+} powder and colourless sanitary silicone was prepared (please find details in the Experimental section). Such a composite material can be cut and shaped into any shape, which is a gingerbread man-like temperature sensitive material in our case. This gingerbread man was placed on a heating plate to induce a temperature gradient along its length (Fig. 6a). The gradient was independently controlled using a thermal camera, which showed that, for a representative example, a temperature gradient between ∼ 310 to 500 K could be achieved along 64 mm of the film (Fig. 6b). Simultaneously, the film was excited using 254 nm excitation light. Luminescence images of the Mn^{2+} and Cr^{3+} emission intensities were takes separately. It is noteworthy that the signal changes uniformly in both cases, indicating a homogeneous distribution of luminescent powder in the film volume. The spectral ranges of 550–650 nm and above 650 nm were chosen to allow the signal coming from the Mn^{2+} and Cr^{3+} bands to be separated in the two

images and determining the temperature-dependent LIR parameter. Dividing the two images by each other resulted in an LIR that ranged from ∼ 2.9 to ∼ 5.5. However, due to the use of different spectral ranges relative to the previously determined LIR_1 and LIR_2 obtained from the emission spectra, as well as the use of the digital camera instead of the spectrometer, it was necessary to determine the calibration curve of LIR vs temperature to verify if the prepared composite film is useful for temperature imaging (Fig. 6c). It was found that its shape was equal to the temperature evolution of LIR_1 in the range 300–500 K. Subsequently, it was possible to determine the thermal map of the composite film (Fig. 6d). Comparison between the obtained 2-D thermal maps using the luminescence thermometer and IR camera indicates a noticeable selectivity of luminescence thermometry technique. Thermal sensing in this case is only limited to the spatial area in which phosphor is distributed. In order to quantitatively compare the obtained results, a thermal profile was selected that covers the entire temperature range in which the phosphor-containing film was located (Fig. 6e). Both profiles have a similar shape, covering the range from ∼ 500 to 310 K. The apparent noise of the temperature readout in the case of the LIR profile is mostly related to the much higher resolution offered by the digital camera compared to the IR camera (3888 × 2592 px and 640 × 480 px for digital and thermal camera, respectively), as well as the limited thermal resolution of IR camera, which for the mode operating in the range 298–923 K is 1.0 K. Moreover, no signal smoothing procedure was involved in the thermal images generated from luminescence
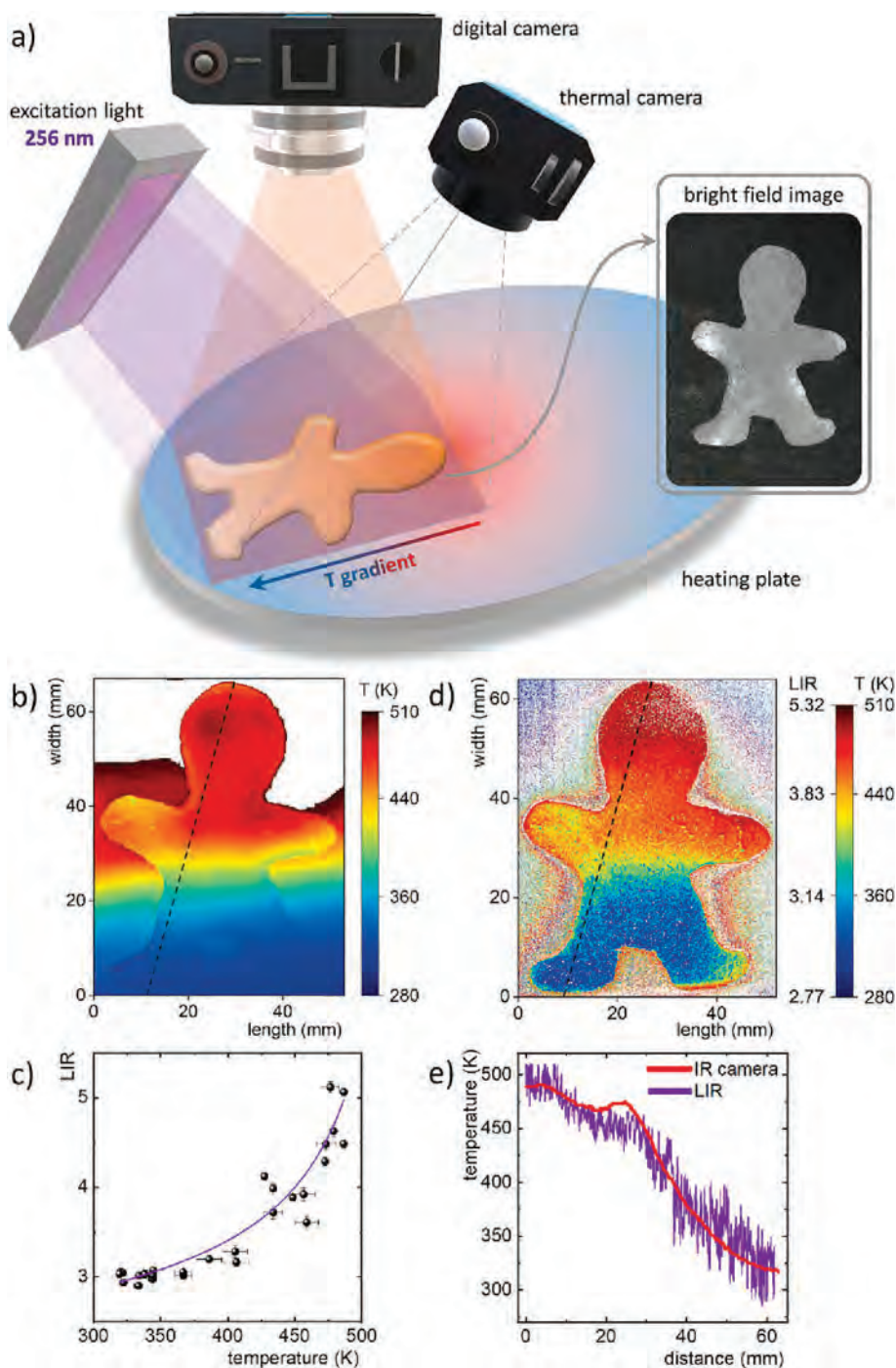
Fig. 6. Schematic visualization of the proof-of-concept experiment of thermal imaging with CaGa$_4$O$_7$:Mn^{2+}, Cr^{3+}/silicone composite film – a); thermal image of composite film obtained with IR camera – b); the calibration curve of temperature vs ratio of two images performed with different optical filters (LIR) for the composite film – c); corresponding temperature map obtained with LIR – d); the comparison of the thermal profiles across the black dashed lines in b) and d) obtained using thermal camera and luminescence thermometry – e).

thermometry in contrast to the images from the thermal IR camera. The obtained results confirm the high applicative potential of the CaGa$_4$O$_7$: Mn^{2+}, Cr^{3+} for temperature sensing and imaging.

6. Conclusions

Luminescent thermometers with increasing luminescence intensity at elevated temperatures are promising candidates to combine high relative sensitivity with high signal-to-noise ratio for minimized temperature uncertainties, which is usually a limitation at high temperatures. In this work, we present CaGa$_4$O$_7$: Mn^{2+}, Cr^{3+} as a new ratiometric thermometer exploiting this concept, in which the intensity of the broad-band emission of Mn^{2+} in the orange range increases with increasing temperature up to 523 K. The effect is reversible and reproducible. We ascribe this unusual behaviour to the special coordination of the Mn^{2+} ions substituting the fivefold coordinated Ca^{2+} in CaGa$_4$O$_7$. This would lead to an unusual splitting pattern of the excited ^{4}G term into ligand field states. While the lowest emissive state is considered to give rise to only an orbitally magnetic dipolar transition, a thermally accessible higher excited state could give rise to an orbitally electric-dipole allowed transition thereby leading to an enhancement of the luminescence intensity. By co-doping with Cr^{3+}, it is possible to exploit this sensitive temperature response of the Mn^{2+}-based luminescence in a ratiometric temperature readout concept with high (relative) sensitivity $S_{Rmax} = 2.08 \% \, K^{-1}$. Cytotoxicity assessments clearly showed no toxicity issues with CaGa$_4$O$_7$:Mn^{2+}, Cr^{3+}. It was explicitly demonstrated that

$CaGa_4O_7$:Mn^{2+}, Cr^{3+} allows thermal imaging in a similar manner to a thermal camera.

Declaration of Competing Interest

Data availability

Data will be made available on request.

Acknowledgements

Appendix A. Supplementary data

Supplementary data to this article can be found online at https://doi.org/10.1016/j.cej.2023.142492.

References

[1] A. Anselmi, A. Abbate, F. Girola, G. Nasso, G.G.L. Biondi-Zoccai, G. Possati, M. Gaudino, Myocardial ischemia, stunning, inflammation, and apoptosis during cardiac surgery: a review of evidence, Eur. J. Cardio-Thoracic Surg. 25 (2004) 304–311.

[2] M.J. Terpstra, L.P.A. Steenbekkers, N.C.M. de Maertelaere, S. Nijhuis, Food storage and disposal: consumer practices and knowledge, Br. Food J. 107 (2005) 526–533.

[3] Y. Yang, W.J. Khoo, Q. Zheng, H.-J. Chung, H.-G. Yuk, Growth temperature alters Salmonella Enteritidis heat/acid resistance, membrane lipid composition and stress/virulence related gene expression, Int. J. Food Microbiol. 172 (2014) 102–109.

[4] M. Ralevski, B.R. Stojkoska, IoT based system for detection of gas leakage and house fire in smart kitchen environments, in: 2019 27th Telecommun. Forum, 2019: pp. 1–4.

[5] W.-L. Hsu, J.-Y. Jhuang, C.-S. Huang, C.-K. Liang, Y.-C. Shiau, Application of Internet of Things in a Kitchen Fire Prevention System, Appl. Sci. 9 (17) (2019) 3520.

[6] S. Sasirekha, I.J.L. Paul, S. Swamynathan, An API Centric Smart Kitchen Application, in: 2018 Int. Conf. Comput. Commun. Signal Process., 2018: pp. 1–6.

[7] F. Nugroho, A.B. Pantjawati, Automation and Monitoring Smart Kitchen Based on Internet of Things (IoT), IOP Conf. Ser. Mater. Sci. Eng. 384 (2018) 12007.

[8] A. Ghelli, H. Hagras, G. Aldabbagh, A Fuzzy Logic-Based Retrofit System for Enabling Smart Energy-Efficient Electric Cookers, IEEE Trans. Fuzzy Syst. 23 (6) (2015) 1984–1997.

[9] R. Yared, B. Abdulrazak, T. Tessier, P. Mabilleau, Cooking Risk Analysis to Enhance Safety of Elderly People in Smart Kitchen. Proc. 8th ACM Int. Conf. PErvasive Technol. Relat. to Assist, Environ., Association for Computing Machinery, New York, NY, USA, 2015.

[10] M. Suta, A. Meijerink, A Theoretical Framework for Ratiometric Single Ion Luminescent Thermometers—Thermodynamic and Kinetic Guidelines for Optimized Performance, Adv. Theory Simulations. 3 (2020) 2000176.

[11] L. Marciniak, K. Kniec, K. Elżbieciak-Piecka, K. Trejgis, J. Stefanska, M. Dramićanin, Luminescence thermometry with transition metal ions. A review, Coord. Chem. Rev. 469 (2022), 214671.

[12] A. Bednarkiewicz, L. Marciniak, L.D. Carlos, D. Jaque, Standardizing luminescence nanothermometry for biomedical applications, Nanoscale 12 (27) (2020) 14405–14421.

[13] D. Jaque, F. Vetrone, Luminescence nanothermometry, Nanoscale 4 (2012) 4301–4326.

[14] K. Okabe, N. Inada, C. Gota, Y. Harada, T. Funatsu, S. Uchiyama, Intracellular temperature mapping with a fluorescent polymeric thermometer and fluorescence lifetime imaging microscopy, Nat. Commun. 3 (2012) 705.

[15] M.D. Dramićanin, Trends in luminescence thermometry, J. Appl. Phys. 128 (2020) 40902.

[16] X.D. Wang, O.S. Wolfbeis, R.J. Meier, Luminescent probes and sensors for temperature, Chem. Soc. Rev. 42 (2013) 7834–7869.

[17] G. Kucsko, P.C. Maurer, N.Y. Yao, M. Kubo, H.J. Noh, P.K. Lo, H. Park, M.D. Lukin, Nanometre-scale thermometry in a living cell, Nature 500 (7460) (2013) 54–58.

[18] B. del Rosal, D. Ruiz, I. Chaves-Coira, B.H. Juárez, L. Monge, G. Hong, N. Fernández, D. Jaque, In Vivo Contactless Brain Nanothermometry, Adv. Funct. Mater. 28 (2018) 1806088.

[19] Y.H. Kim, P. Arunkumar, B.Y. Kim, S. Unithrattil, E. Kim, S.-H. Moon, J.Y. Hyun, K. H. Kim, D. Lee, J.-S. Lee, W.B. Im, A zero-thermal-quenching phosphor, Nat. Mater. 16 (5) (2017) 543–550.

[20] J. Qiao, L. Ning, M.S. Molokeev, Y.-C. Chuang, Q. Liu, Z. Xia, Eu^{2+} Site Preferences in the Mixed Cation $K_2BaCa(PO_4)_2$ and Thermally Stable Luminescence, J. Am. Chem. Soc. 140 (30) (2018) 9730–9736.

[21] R. Shi, L. Ning, Z. Wang, J. Chen, T.-K. Sham, Y. Huang, Z. Qi, C. Li, Q. Tang, H. Liang, Zero-Thermal Quenching of Mn^{2+} Red Luminescence via Efficient Energy Transfer from Eu^{2+} in $BaMgP_2O_7$, Adv. Opt. Mater. 7 (2019) 1901187.

[22] H. Lv, P. Du, W. Li, L. Luo, Tailoring of Upconversion Emission in Tm^{3+}/Yb^{3+}-Codoped $Y_2Mo_3O_{12}$ Submicron Particles Via Thermal Stimulation Engineering for Non-invasive Thermometry, ACS Sustain. Chem. Eng. 10 (7) (2022) 2450–2460.

[23] P. Du, J. Tang, W. Li, L. Luo, Exploiting the diverse photoluminescence behaviors of $NaLuF_4$:xEu^{3+} nanoparticles and g-C_3N_4 to realize versatile applications in white light-emitting diode and optical thermometer, Chem. Eng. J. 406 (2021), 127165.

[24] T.P. van Swieten, A. Meijerink, F.T. Rabouw, Impact of Noise and Background on Measurement Uncertainties in Luminescence Thermometry, ACS Photonics 9 (4) (2022) 1366–1374.

[25] A.P. Vink, M.A. de Bruin, S. Roke, P.S. Peijzel, A. Meijerink, Luminescence of Exchange Coupled Pairs of Transition Metal Ions, J. Electrochem. Soc. 148 (7) (2001) E313.

[26] T. Senden, R.J.A. Van DIjk-Moes, A. Meijerink, Quenching of the red Mn^{4+} luminescence in Mn^{4+}-doped fluoride LED phosphors, Light Sci. Appl. 7 (2018) 8.

[27] B. Malysa, A. Meijerink, T. Jüstel, Temperature dependent luminescence Cr3+-doped $GdAl_3(BO_3)_4$ and $YAl_3(BO_3)_4$, J. Lumin. 171 (2016) 246–253.

[28] M. Grinberg, $^2E \rightarrow ^4A_2$ fluorescence of Cr^{3+} in high and intermediate field garnets, J. Lumin. 54 (6) (1993) 369–382.

[29] Z. Zhang, K.T.V. Grattan, A.W. Palmer, Temperature dependences of fluorescence lifetimes in Cr^{3+}-doped insulating crystals, Phys. Rev. B 48 (1993) 7772–7778.

[30] K. Elzbieciak-Piecka, M. Suta, L. Marciniak, Structurally induced tuning of the relative sensitivity of $LaScO_3$:Cr^{3+} luminescent thermometers by co-doping lanthanide ions, Chem. Eng. J. 421 (2021), 129757.

[31] M.P. Pechini, Method of preparing lead and alkaline earth titanates and niobates and coating method using the same to form a capacitor, 1967.

[32] W. Geurtsen, F. Lehmann, W. Spahl, G. Leyhausen, Cytotoxicity of 35 dental resin composite monomers/additives in permanent 3T3 and three human primary fibroblast cultures, J. Biomed. Mater. Res. 41 (3) (1998) 474–480.

[33] S.K. Bhatia, A.B. Yetter, Correlation of visual in vitro cytotoxicity ratings of biomaterials with quantitative in vitro cell viability measurements, Cell Biol. Toxicol. 24 (4) (2008) 315–319.

[34] H.C. Fischer, T.S. Hauck, A. Gómez-Aristizábal, W.C.W. Chan, Exploring primary liver macrophages for studying quantum dot interactions with biological systems, Adv. Mater. 22 (23) (2010) 2520–2524.

[35] R. Miyata, S.F. van Eeden, The innate and adaptive immune response induced by alveolar macrophages exposed to ambient particulate matter, Toxicol. Appl. Pharmacol. 257 (2) (2011) 209–226.

[36] H.-J. Deiseroth, H. Müller-Buschbaum, Ü. Erdalkalimetall-Oxogallate, I. Zur Kenntnis von $CaGa_4O_7$, ZAAC -, J. Inorg. Gen. Chem. 382 (1971) 149–156.

[37] K. Fukuda, R. Harada, H. Banno, D. Urushihara, T. Asaka, Discovery of Fast Calcium-Ion Conduction in Grossite-Type Compounds $CaAl_4O_7$ and $CaGa_4O_7$ by Bond Valence Screening Method, ACS Appl. Energy Mater. 5 (3) (2022) 3227–3234.

[38] R.D. Shannon, Revised effective ionic radii and systematic studies of interatomic distances in halides and chalcogenides, Acta Crystallographica Section A 32 (5) (1976) 751–767.

[39] V. Morad, I. Cherniukh, L. Pöttschacher, Y. Shynkarenko, S. Yakunin, M. V. Kovalenko, Manganese(II) in Tetrahedral Halide Environment: Factors Governing Bright Green Luminescence, Chem. Mater. 31 (2019) 10161–10169.

[40] E.H. Song, Y.Y. Zhou, Y. Wei, X.X. Han, Z.R. Tao, R.L. Qiu, Z.G. Xia, Q.Y. Zhang, A thermally stable narrow-band green-emitting phosphor $MgAl_2O_4$:Mn^{2+} for wide color gamut backlight display application, J. Mater. Chem. C 7 (2019) 8192–8198.

[41] Y. Fu, C. Li, F. Zhang, S. Huang, Z. Wu, Y. Wang, Z. Zhang, Site preference and the optical thermometry strategy by different temperature response from two sites environment of Mn^{2+} in $K_7ZnSc_2B_{15}O_{30}$, Chem. Eng. J. 409 (2021), 128190.

[42] S. Li, W. Hu, M.G. Brik, S. Lian, Z. Qiu, Achieving highly thermostable red emission in singly Mn^{2+}-doped $BaXP_2O_7$ (X = Mg/Zn) via self-reduction, Inorg. Chem. Front. 9 (13) (2022) 3224–3232.

[43] M. Puchalska, E. Zych, Effect of Na co-dopant and activator concentration on luminescent properties of $CaGa_4O_7$: Eu 3, J. Lumin. 132 (11) (2012) 2879–2884.

[44] M.G. Brik, N.M. Avram, C.N. Avram, Exchange charge model of crystal field for 3d ions, in: N.M. Avram, M.G. Brik (Eds.), Opt. Prop. 3d-Ions Cryst. Spectrosc. Cryst. F, Anal., Springer, Berlin Heidelberg, Berlin, Heidelberg, 2013, pp. 29–94.

[45] S. Lv, B. Shanmugavelu, Y. Wang, Q. Mao, Y. Zhao, Y. Yu, J. Hao, Q. Zhang, J. Qiu, S. Zhou, Transition Metal Doped Smart Glass with Pressure and Temperature Sensitive Luminescence, Adv. Opt. Mater. 6 (2018) 1800881.

[46] L.P. Sosman, A. López, A.R. Camara, S.S. Pedro, I.C.S. Carvalho, N. Cella, Optical and Structural Properties of Zn_2TiO_4:Mn^{2+}, J. Electron. Mater. 46 (12) (2017) 6848–6855.

[47] H. Li, Y. Liang, S. Liu, W. Zhang, Y. Bi, Y. Gong, W. Lei, Highly Efficient Green-Emitting Phosphor $BaZnAl_{10}O_{17}$:Mn^{2+} with Ultra-Narrow Band and Extremely Low

Thermal Quenching for Wide Color Gamut LCD Backlights, Adv. Opt. Mater. 9 (2021) 2100799.

[48] F. Rodríguez, H. Riesen, H.U. Güdel, Luminescence properties of Mn^{2+} in $KMgF_3$ and $KZnF_3$ perovskite crystals. Evidence of a dynamical Jahn-Teller effect, J. Lumin. 50 (2) (1991) 101–110.

[49] J.G. Teeguarden, P.M. Hinderliter, G. Orr, B.D. Thrall, J.G. Pounds, Particokinetics in vitro: Dosimetry considerations for in vitro nanoparticle toxicity assessments, Toxicol. Sci. 95 (2007) 300–312.

[50] D. Drescher, G. Orts-Gil, G. Laube, K. Natte, R.W. Veh, W. Österle, J. Kneipp, Toxicity of amorphous silica nanoparticles on eukaryotic cell model is determined by particle agglomeration and serum protein adsorption effects, Anal. Bioanal. Chem. 400 (5) (2011) 1367–1373.

[51] K. Tejle, K.E. Magnusson, B. Rasmusson, Phagocytosis and phagosome maturation are regulated by calcium in J774 macrophages interacting with unopsonized prey, Biosci. Rep. 22 (2002) 529–540.

255

Supporting Information

Positive luminescence thermal coefficient of Mn^{2+} ions for highly sensitive luminescence thermometry

W. M. Piotrowski[1], K. Kniec-Stec[1], M. Suta[3], B. Bogielski[2], B. Pozniak[2], L. Marciniak[1]*

[1]Institute of Low Temperature and Structure Research, Polish Academy of Sciences, Okólna 2, 50-422 Wroclaw, Poland

[2] Department of Pharmacology and Toxicology Faculty of Veterinary Medicine Wrocław University of Environmental and Life Sciences, ul. Norwida 25, 50-375 Wrocław, Poland

3 Inorganic Photoactive Materials, Institute of Inorganic Chemistry & Structural Chemistry, Heinrich Heine University Düsseldorf, Universitätsstraße 1, 40225 Düsseldorf, Germany

* corresponding author: l.marciniak@intibs.pl
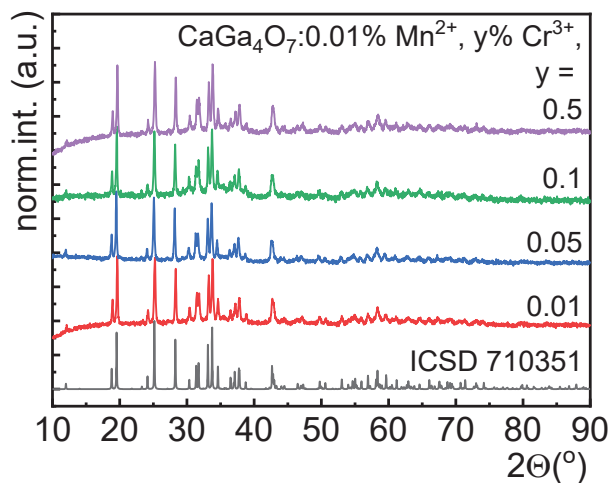
Figure S1. X-ray diffraction patterns of CaGa$_4$O$_7$:0.01% Mn^{2+} co-doped with different concentrations of Cr^{3+} ions.
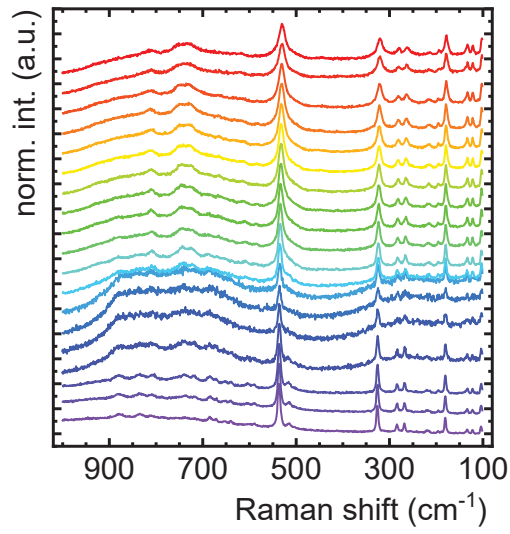
Figure S2. Thermal evolution of the Raman spectra of the $CaGa_4O_7$:0.01% Mn^{2+} phosphor.
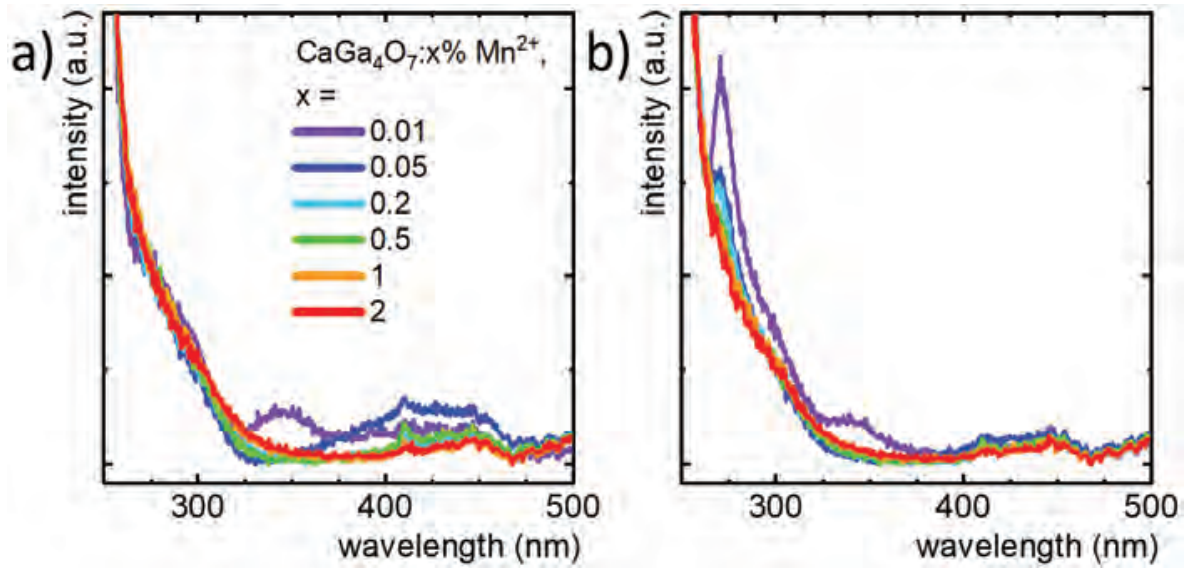
Figure S3. Influence of the Mn^{2+} concentration on the excitation spectra for $\lambda_{em} = 578$ nm in $CaGa_4O_7$:x% Mn^{2+}

phosphors measured at 293 K – a) and 473 K – b).

Table S1. Comparison of crystal field parameters for representative phosphors based on luminescence of Mn^{2+} ions.

Compound	B [cm^{-1}]	C [cm^{-1}]	Dq [cm^{-1}]	Dq/B	Ref.
CaF$_2$:Mn^{2+}	770	3449.6	425	0.55	[1]
ZnO:Mn^{2+}	715	-	450	0.63	[2]
CdF$_2$:Mn^{2+}	770	3449.6	500	0.65	[1]
ZnWO$_4$:Mn^{2+}	688	3440	505	0.73	[3]
KCl:Mn^{2+}	760	2955	590	0.78	[4]
Zn$_2$SiO$_4$:Mn^{2+}	622	3504	562	0.90	[5]
ZnS:Mn^{2+}	546	3181	516	0.95	[6]
ZnS:Mn^{2+}	500	-	510	1.02	[7]
Na$_2$CaP$_2$O$_7$:Mn^{2+}	740	-	712	1.04	[8]
ZnS:Mn^{2+}	551	3246	600	1.09	[9]
ZnS:Mn^{2+}	520	3308	583	1.12	[10]
ZnGa$_2$O$_4$:Mn^{2+}	740	-	861	1.16	[11]
Zn$_2$TiO$_4$:Mn^{2+}	756	3227	887	1.17	[12]
MgGa$_2$O$_4$ (tetragonal site)	665	-	784	1.18	[13]
KHSO$_4$:Mn^{2+}	627	2580	790	1.26	[14]
SrB$_4$O$_7$:Mn^{2+} glass	700	2975	880	1.26	[15]
KPb$_2$Cl$_5$:Mn^{2+}	618	3549	790	1.28	[16]
CaGa$_4$O$_7$:Mn^{2+}	739	5167	1281	1.73	This work

The crystal field parameter Dq and Racah parameters for Mn^{4+} and Cr^{3+} ions with 3d^3 electron configuration were defined based on experimental excitation and emission spectra data. For this purpose, the energies of $^4A_2 \rightarrow {^4T_1}$ and $^4A_2 \rightarrow {^4T_2}$ bands obtained from excitation spectra and zero phonon line (R-line) of $^2E \rightarrow {^4A_2}$ band from emission spectra. The empirical equations take the following form:

$$E(\,^4A_2 \rightarrow {^4T_2}) = 10Dq \tag{Eq. S1}$$

$$\frac{Dq}{B} = \frac{15\left(\frac{\Delta E}{Dq}-8\right)}{\left(\frac{\Delta E}{Dq}\right)^2 - 10\cdot\frac{\Delta E}{Dq}} \tag{Eq. S2}$$

$$\frac{E(\,^2E \rightarrow {^4A_2})}{B} = \frac{3.05\cdot C}{B} + 7.90 - \frac{1.80\cdot B}{Dq} \tag{Eq. S3}$$

where ΔE was predefined as:

$$\Delta E = E(\,^4A_2 \rightarrow {^4T_1}) - E(\,^4A_2 \rightarrow {^4T_2}) \tag{Eq. S4}$$
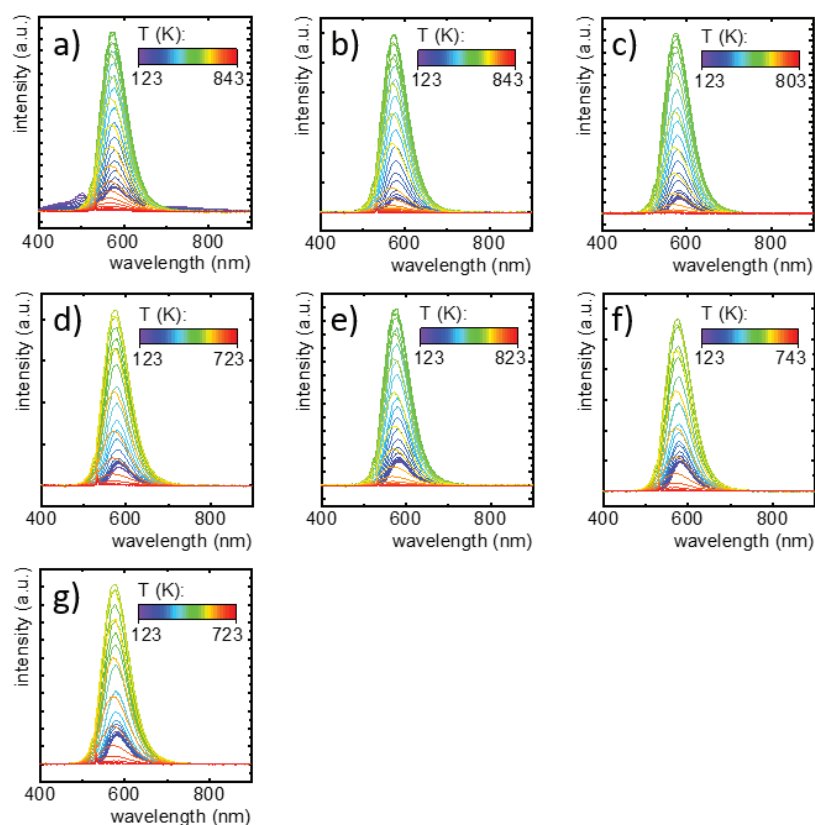
Figure S4. Thermal evolution of emission spectra for $CaGa_4O_7:x\%$ Mn^{2+} phosphors with different Mn^{2+} concentration: x = 0.01 – a); 0.05 – b); 0.2 – c); 0.5 – d); 1 – e); 2 – f); 5 – g).
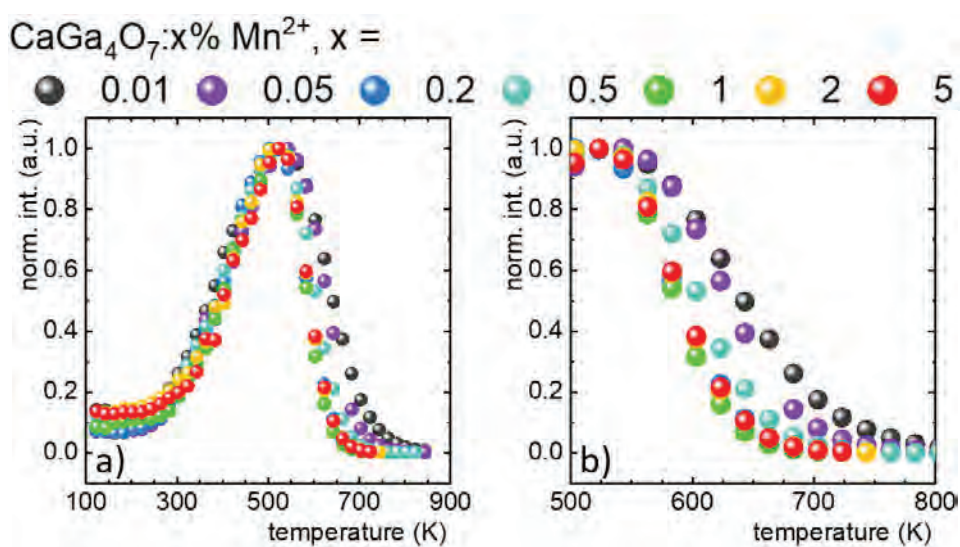
Figure S5. Influence of Mn^{2+} concentration on the thermal evolution of integral intensities of Mn^{2+} emission band normalized to the maximal intensity value at 503 K in the range of 123-873 K – a) and 500-800 K – b).

The average lifetime of the excited states were calculated with the equation Eq. S5:

$$\tau_{avr} = \frac{A_1\tau_1{}^2 + A_2\tau_2{}^2}{A_1\tau_1 + A_2\tau_2}$$

(Eq. S5)

where: τ_1, τ_2 are the decay parameters and A_1, A_2 are amplitudes of the bi-exponential function:

$$I(t) = I_0 + A_1 \cdot \exp\left(-\frac{t}{\tau_1}\right) + A_2 \cdot \exp\left(-\frac{t}{\tau_2}\right)$$

(Eq. S6)
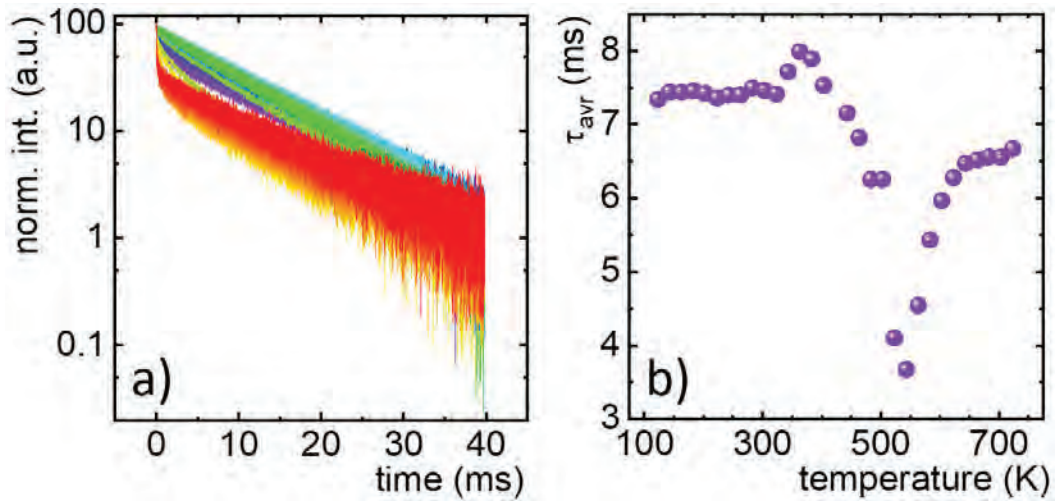
Figure S6. Thermal evolution of the luminescent decays of $^4T_1$ excited state of Mn^{2+} ions for $CaGa_4O_7$:0.2%

Mn^{2+} sample – a) and the average decays τ_{avr} of Mn^{2+} excited state – b).
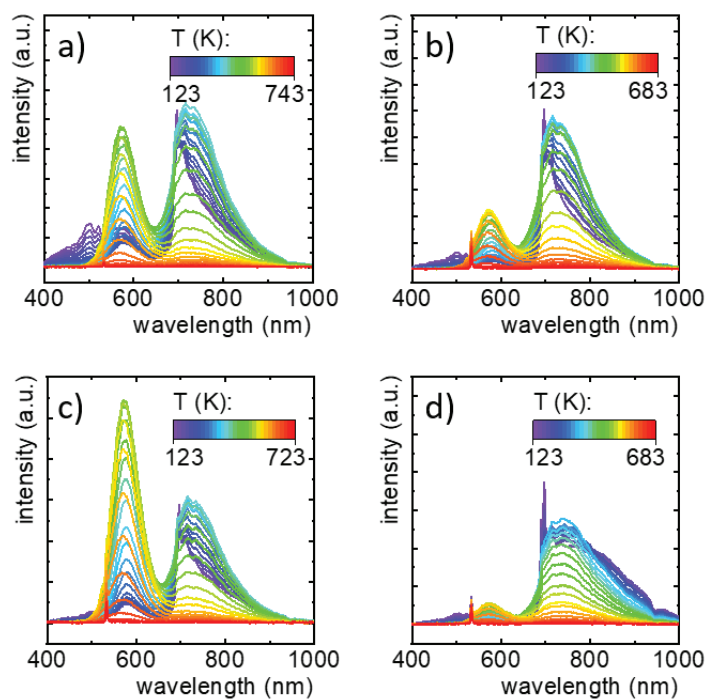
Figure S7. Thermal evolution of emission spectra for $CaGa_4O_7$:0.01% Mn^{2+}, y% Cr^{3+} phosphors with different Cr^{3+} concentration: y = 0.01 - a), 0.05 - b), 0.1 - c), 0.5 - d).
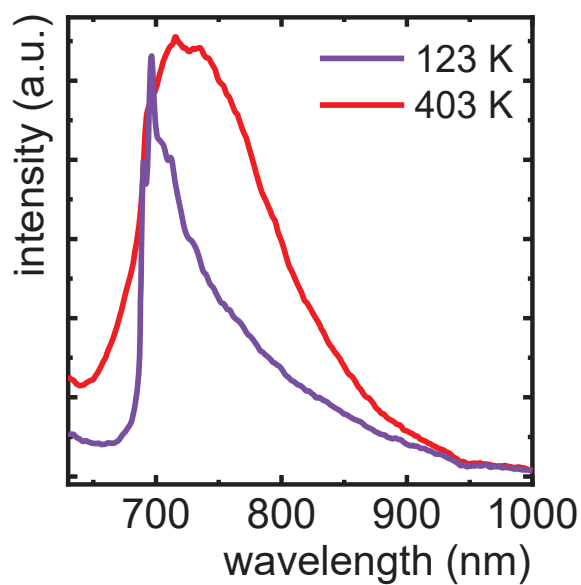
Figure S8. Comparison of emission spectra performed at 123 K and 403 K for representative $CaGa_4O_7$:0.01% Mn^{2+}, 0.01% Cr^{3+} phosphor.
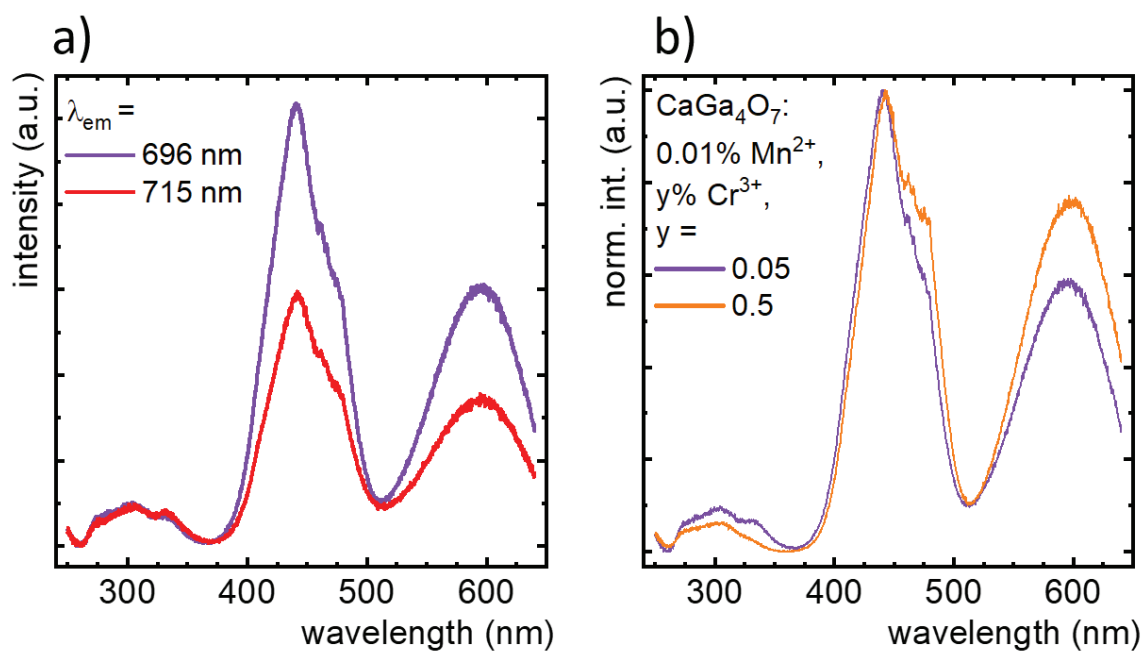
Figure S9. Comparison of excitation spectra performed for λ_{em1} = 696 nm and λ_{em2} = 716 nm for

CaGa$_4$O$_7$:0.01% Mn^{2+}, 0,01% Cr^{3+} phosphor – a) and comparison of excitation spectra performed for λ_{em1} = 696

nm for CaGa$_4$O$_7$:0.01% Mn^{2+} co-doped with 0.05% and 0.5% of Cr^{3+} ions – b).

Table S2. The influence of Cr^{3+} concentration in CaGa$_4$O$_7$:0.01% Mn^{2+}, y% Cr^{3+} phosphors on the crystal field parameters.

Co-dopants of CaGa$_4$O$_7$ compound	Dq [cm^{-1}]	B [cm^{-1}]	C [cm^{-1}]	C/B	Dq/B
0.01% Mn^{2+}, 0.05% Cr^{3+}	1541.395	731.3	3058	4.184	2.11
0.01% Mn^{2+}, 0.5% Cr^{3+}	1543.49	750.9	3017	4.019	2.06
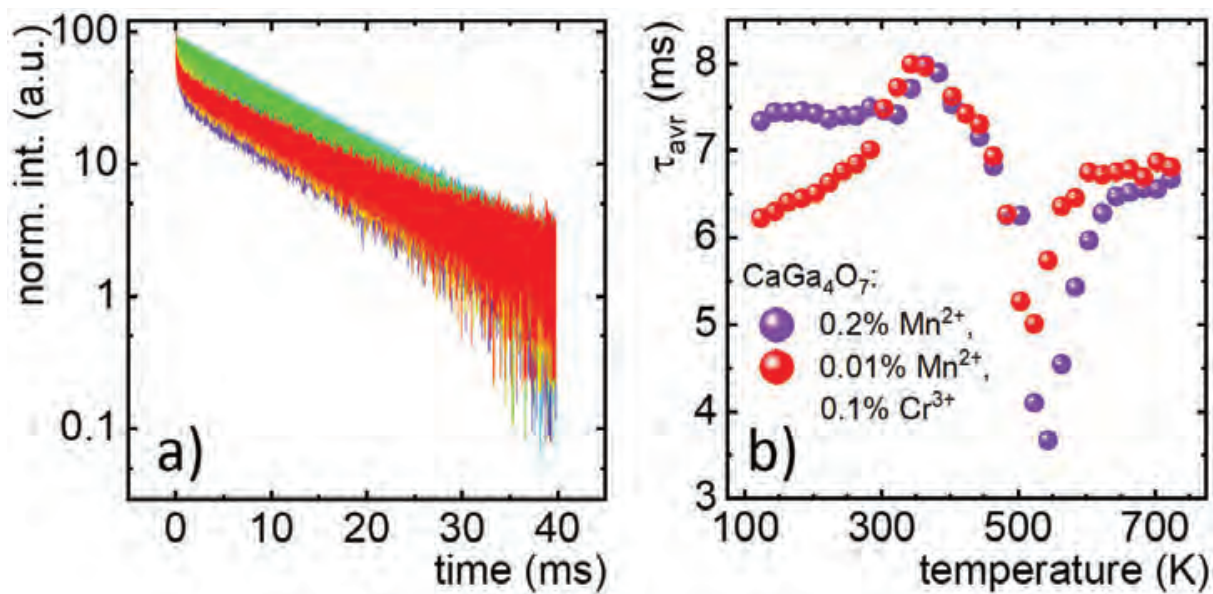
Figure S10. Thermal evolution of the luminescent decays of $^4T_1$ excited state of Mn^{2+} ions for $CaGa_4O_7$:0.01% Mn^{2+}, 0.1% Cr^{3+} sample – a) and comparison of the average decays τ_{avr} of Mn^{2+} excited state for Cr^{3+}-co-doped and un-coped $CaGa_4O_7$ phosphor – b).
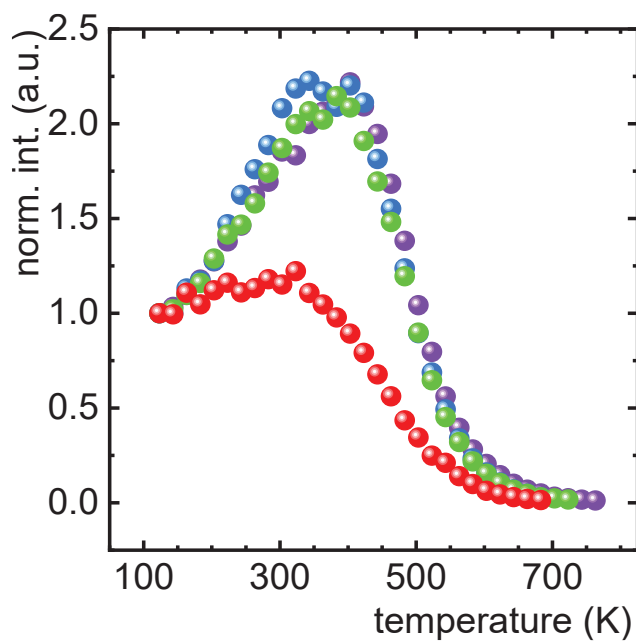
Figure S11. Thermal evolution of integral intensities of $^4T_2 \rightarrow {}^4A_2$ emission band of Cr^{3+} for $CaGa_4O_7$:0.01% Mn^{2+}, y% Cr^{3+} phosphors with different Cr^{3+} concentration.
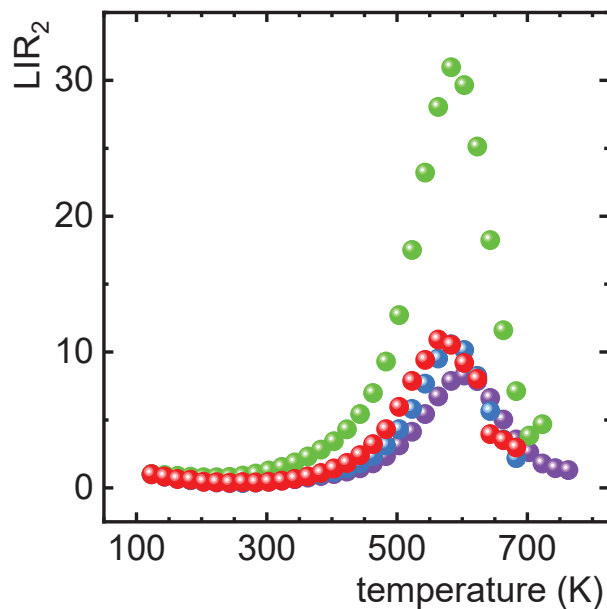
Figure S12. Thermal evolution of LIR_2 for $CaGa_4O_7$:0.01% Mn^{2+}, y% Cr^{3+} phosphors with different Cr^{3+} concentration.

The integral intensities of the Mn^{3+} and Cr^{3+} bands to calculate LIR values were fitted with Mott-Seitz equation (Eq. S7):

$$I = \frac{I_0}{C \cdot \exp(-\frac{W}{k \cdot T}) + 1}$$

(Eq. S7)

where: I – the intensity in temperature T, I_0 – the intensity in the initial temperature, W - the activation energy, k – Boltzmann constant, C – the dimensionless constant

Temperature determination uncertainty was calculated using Eq. S8:

$$\delta T = \left| \frac{1}{S_R} \cdot \frac{\delta LIR}{LIR} \right|$$

(Eq. S8)

where: S_R is the relative sensitivity and δLIR/LIR determines the uncertainty of the LIR determination

where δLIR/LIR was determined as follows:

$$\frac{\delta LIR}{LIR} = \sqrt{\left(\frac{\delta I_{Mn2+}}{I_{Mn2+}}\right)^2 + \left(\frac{\delta I_{Cr3+}}{I_{Cr3+}}\right)^2}$$

(Eq. S9)

Repeatability of the luminescent thermometer was determined as follows:

$$R = \left(1 - \frac{\max\left| LIR_{avr} - LIR_i \right|}{LIR_{avr}} \right) \cdot 100\%$$

(Eq. S10)

where LIR_{avr} is the average value of the LIR at given temperature determined based on i measurements of LIR and LIR_i I the value of LIR for *i-th* measurement.
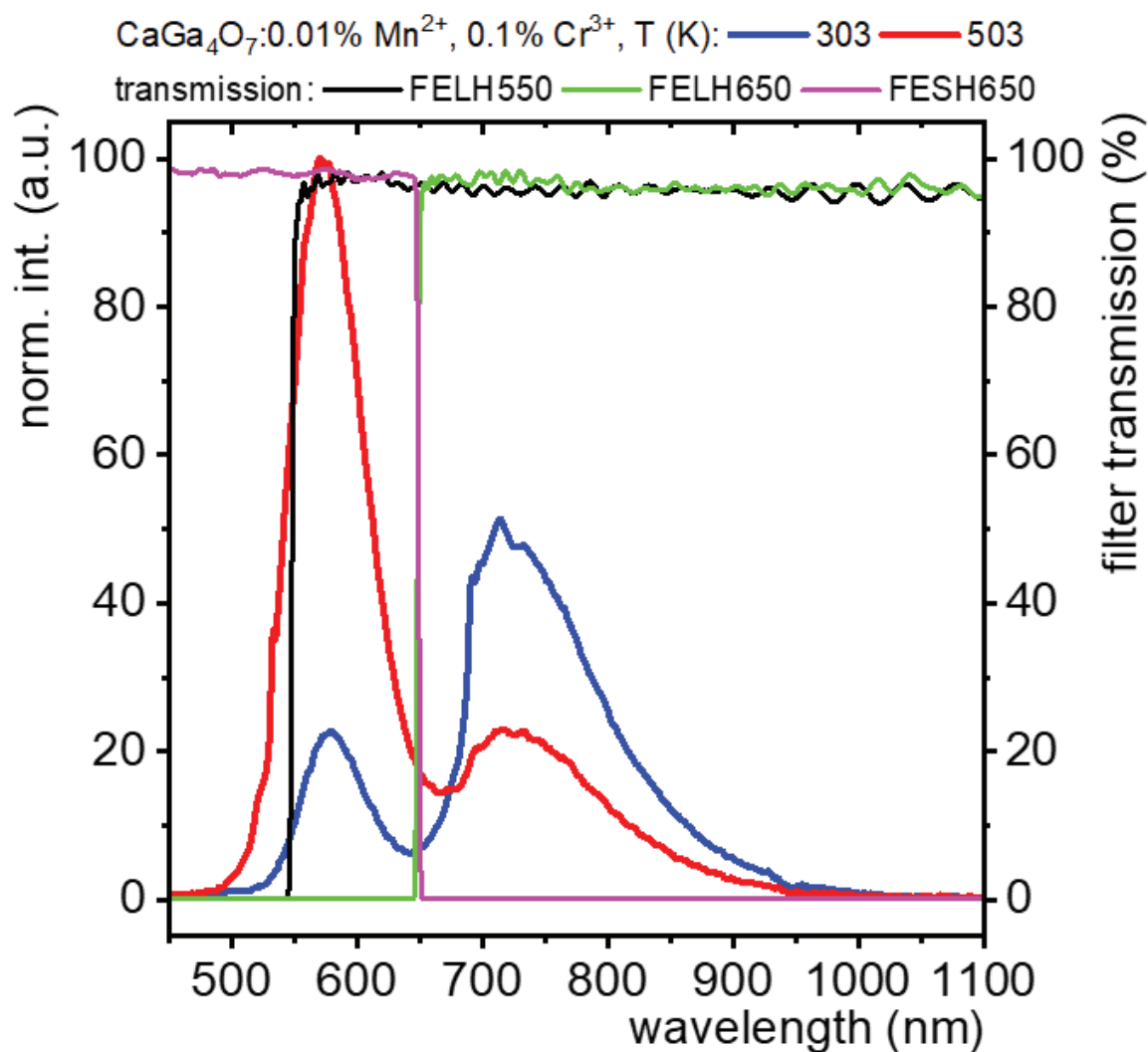
Figure 13. The comparison of the emission spectra of $CaGa_4O_5$:0.01%Mn^{2+}, 0.1%Cr^{3+} measured at 303 K and 503 K with the spectral characteristic of FELH550, FELH650 and FESH650 optical filters.

References

[1]   P.J. Alonso, R. Alcalá, Excitation spectra and fluorescent lifetime measurements of Mn2+ in CaF2 and CdF2, J Lumin. 22 (1981) 321–333. https://doi.org/10.1016/0022-2313(81)90027-2.

[2]   J.F. Suyver, J.J. Kelly, A. Meijerink, Temperature-induced line broadening, line narrowing and line shift in the luminescence of nanocrystalline ZnS:Mn2+, J Lumin. 104 (2003) 187–196. https://doi.org/10.1016/S0022-2313(03)00015-2.

[3]   H. Ren, F. Yang, Influence of Mn2+ on the up-conversion emission performance of Mn2+, Yb3+, Er3+: ZnWO4 green phosphors, Journal of Materials Science: Materials in Electronics. 29 (2018) 15396–15403. https://doi.org/10.1007/s10854-018-9053-9.

[4]   A. Mehra, P. Venkateswarlu, Absorption Spectrum of Mn 2+ in KCl, J Chem Phys. 45 (1966) 3381–3383. https://doi.org/10.1063/1.1728118.

[5]   M. Czaja, R. Lisiecki, R. Juroszek, T. Krzykawski, Luminescence Properties of Tetrahedral Coordinated Mn2+; Genthelvite and Willemite Examples, Minerals. 11 (2021) 1215. https://doi.org/10.3390/min11111215.

[6]   D. van Thai, P. van Ben, T.M. Thi, N. van Truong, H.H. Thu, The photoluminescence enhancement of Mn2+ ions and the crystal field in ZnS:Mn nanoparticles covered by polyvinyl alcohol, Opt Quantum Electron. 48 (2016) 362. https://doi.org/10.1007/s11082-016-0622-y.

[7]   P.J. Alonso, R. Alcalá, Excitation spectra and fluorescent lifetime measurements of Mn2+ in CaF2 and CdF2, J Lumin. 22 (1981) 321–333. https://doi.org/10.1016/0022-2313(81)90027-2.

[8]   F. Xiao, E.H. Song, Q.Y. Zhang, A yellow-emitting phosphor of Mn2+-doped Na2CaP2O7, Spectrochim Acta A Mol Biomol Spectrosc. 122 (2014) 343–347. https://doi.org/10.1016/j.saa.2013.10.078.

[9]   W. Chen, G. Li, J.-O. Malm, Y. Huang, R. Wallenberg, H. Han, Z. Wang, J.-O. Bovin, Pressure dependence of Mn2+ fluorescence in ZnS:Mn2+ nanoparticles, J Lumin. 91 (2000) 139–145. https://doi.org/10.1016/S0022-2313(00)00222-2.

[10]   W. Chen, R. Sammynaiken, Y. Huang, J.-O. Malm, R. Wallenberg, J.-O. Bovin, V. Zwiller, N.A. Kotov, Crystal field, phonon coupling and emission shift of Mn2+ in ZnS:Mn nanoparticles, J Appl Phys. 89 (2001) 1120–1129. https://doi.org/10.1063/1.1332795.

[11]   S. Lv, B. Shanmugavelu, Y. Wang, Q. Mao, Y. Zhao, Y. Yu, J. Hao, Q. Zhang, J. Qiu, S. Zhou, Transition Metal Doped Smart Glass with Pressure and Temperature Sensitive Luminescence, Adv Opt Mater. 6 (2018) 1800881. https://doi.org/10.1002/adom.201800881.

[12]   L.P. Sosman, A. López, A.R. Camara, S.S. Pedro, I.C.S. Carvalho, N. Cella, Optical and Structural Properties of Zn2TiO4:Mn2+, J Electron Mater. 46 (2017) 6848–6855. https://doi.org/10.1007/s11664-017-5742-z.

[13]   G.K.B. Costa, S.S. Pedro, I.C.S. Carvalho, L.P. Sosman, Preparation, structure analysis and photoluminescence properties of MgGa2O4:Mn2+, Opt Mater (Amst). 31 (2009) 1620–1627. https://doi.org/10.1016/j.optmat.2009.03.011.

[14]   R. Kripal, V. Mishra, ESR and optical study of Mn2+ doped potassium hydrogen sulphate, Solid State Commun. 133 (2005) 23–28. https://doi.org/10.1016/j.ssc.2004.09.056.

[15]   C.H. Bates, W.B. White, R. Roy, The solubility of transition metal oxides in zinc oxide and the reflectance spectra of Mn2+ and Fe2+ in tetrahedral fields, Journal of Inorganic and Nuclear Chemistry. 28 (1966) 397–405. https://doi.org/10.1016/0022-1902(66)80318-4.

[16]   G. Jia, H. Wang, C. Wang, S. Zhao, D. Deng, L. Huang, Y. Hua, C. Li, S. Xu, Growth and optical spectroscopy of KPb2Cl5 crystal containing Mn2+, J Alloys Compd. 509 (2011) 8365–8369. https://doi.org/10.1016/j.jallcom.2011.05.010.

ACS APPLIED MATERIALS & INTERFACES

Research Article

Thermochromic Luminescent Nanomaterials Based on Mn^{4+}/Tb^{3+} Codoping for Temperature Imaging with Digital Cameras

Wojciech Piotrowski, Karolina Trejgis, Kamila Maciejewska, Karolina Ledwa, Benoit Fond, and Lukasz Marciniak*

Cite This: *ACS Appl. Mater. Interfaces* 2020, 12, 44039−44048

Read Online

ACCESS | Metrics & More | Article Recommendations | Supporting Information

ABSTRACT: A new thermographic nanocrystalline $Sr_4Al_{14}O_{25}$:Mn^{4+},Tb^{3+} phosphor was developed, and the concentrations of both dopants and the synthesis conditions were optimized. The combination of the thermally quenched luminescence from the Mn^{4+} ions to the almost temperature-independent emission from Tb^{3+} provides a sensitive luminescent thermometer (S_R = 2.8%/°C at 150 °C) with strong emission color variability. In addition, a figure of merit for this luminescence thermochromism was proposed, as the relative sensitivities of the x and y CIE coordinates, which for this phosphor reaches at 150 °C $S_R(x)$ = 0.6%/°C and $S_R(y)$ = 0.4%/°C, respectively. Noncontact thermal imaging was demonstrated with this phosphor using a single consumer digital camera and exploiting the ratio of red (R) and green (G) channels of the RGB images, thereby confirming the high application potential of $Sr_4Al_{14}O_{25}$:Mn^{4+},Tb^{3+} nanocrystals for thermal sensing and mapping.

KEYWORDS: manganese, terbium, $Sr_4Al_{14}O_{25}$ nanocrystals, luminescent thermometer, thermal imaging, thermochromicity, chromatic coordinates, relative sensitivity
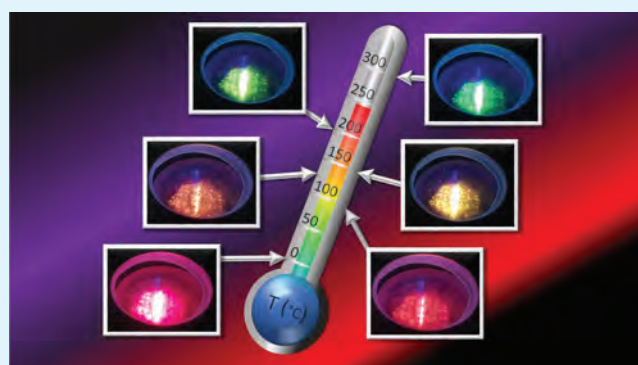
INTRODUCTION

Luminescence thermometry (LT) is a class of optical techniques exploiting the temperature dependence of luminescence processes of tracers introduced in transparent fluids or solids or coated onto surfaces to measure their temperature remotely.[1−6] By allowing spatial, temporal, and spectral discrimination in both laser excitation and luminescence detection processes, luminescence thermometry allows remote sensing with high spatial and temporal resolution and can be applied in environments with high luminosity, which are significant advantages against intrusive probes and infrared thermography.[7−10] These lends LT a large application potential, in particular for nanothermometry, for example, on microelectronics,[11] lab-on-a-chip systems,[12] and in biomedicine;[9,13] for the study of rapidly varying phenomena, for example, in fluid flows[14] or on rotating parts;[15] and for robust thermometry in harsh environments with significant luminosity, for example, on burning materials[16] or in internal combustion engines.[16] Among luminescence thermometers, inorganic phosphors doped with transition metals (TM) and lanthanides ions are particularly attractive because of their high thermochemical and photo stability.[17]

Lanthanide (Ln)-doped thermographic phosphors are some of the most commonly used materials for this type of applications. However, it is well-known that for f−f electronic transitions occurring in Ln^{3+} ions, multiphonon relaxation is usually responsible for thermal quenching of the whole luminescence emission, which occurs only at elevated temperature. This has the advantage of a detectable emission over wide temperature ranges, with measurements reported up to 1400 K,[18] but it also results in the limited temperature sensitivity of this response around ambient temperature when the goal is to detect smaller temperature variations. On the other hand, TM ions are well-known for their strong susceptibility to thermal quenching, which has the additional advantage that it can be tuned by the strong susceptibility of the energy levels positions on the choice of host. However, for robust temperature measurements, monitoring only the absolute intensity of the quenched luminescence emission is not adequate because this signal is also linked to the local excitation intensity, the concentration of the luminescence tracer and losses in the detection systems. Instead, the decrease in the luminescence lifetime as a result of this quenching is
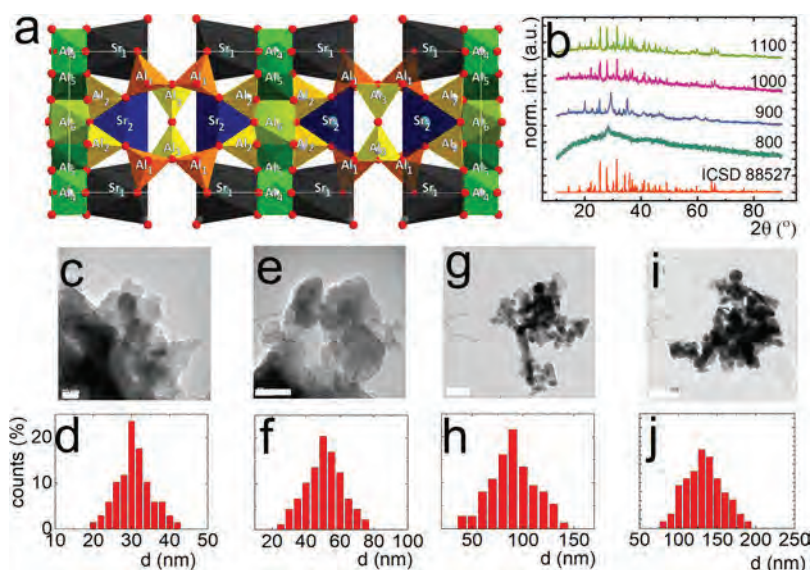
Figure 1. Crystal structure of the SAO unit cell (view from the *z*-axis; red balls represent O^{2-} ions) (a). X-ray diffraction patterns of SAO:0.1% Mn^{4+} powders annealed at different temperatures (b). Representative TEM images (c) (scale bar: 20 nm),(e) (50 nm), (g) (200 nm), (i) (500 nm), particle size distributions for SAO:Mn^{4+} powders (d,f,h,j) annealed at different temperatures (800, 900, 1000, and 1100 °C, respectively).

often preferred as it uses temporal separation to achieve self-reference measurement but this requires using pulsed excitation and multiple detection gates.[19,20] Another approach is to simultaneously detect the luminescence emission from another independent radiative transition, which is temperature insensitive and therefore acts as a reference to extract a temperature dependent ratio of intensities. In the approach presented here, this role is assumed by a codoped trivalent lanthanide ion because Ln^{3+} ions exhibit high quenching temperatures.

Among all TM ions, the Mn^{4+} ion is one of the most promising ones because of its bright red emission. Mn^{4+} ions, which prefer to occupy octahedral sites are characterized by a strong crystal field strength (CFS) caused by their high positive effective charge. This crystal field does not affect the location of the emission band, but it determines the rate of its thermal quenching.

When selecting the lanthanide dopant to act as the reference emitter, it is important to choose one with emission lines that do not spectrally overlap with the temperature probe band. Additionally, Mn^{4+} emission being in the red region, choosing a reference emission located in the blue or green region would lead to a high variability in the emission color output with temperature, which can then be monitored by a single color sensor array, greatly simplifying the verification of the temperature change. Therefore, in this particular case, the Tb^{3+} ion with its intense green emission was used for this purpose.[21] Finally, the selection of the host material is also very important in the design of luminescence thermometers. This choice should be oriented toward high thermal and mechanical stability and an appropriate local symmetry around the ionic sites, which will be occupied by the dopant ions. The SrO−Al_2O_3 system seems to be a proper host for TM and Ln^{3+} dopant because the small difference in the ionic radii between strontium (132 and 140 pm for 6- and 8-coordinated Sr^{2+}, respectively) and aluminum ions (53 and 67.5 pm for Al^{3+} in tetrahedral and octahedral coordination, respectively). Among six different structures, $SrAl_2O_4$ and $Sr_4Al_{14}O_{25}$ arouse big interest as bright luminescence emissions from trivalent Ln

ions (especially Eu^{3+},[22−25] Ce^{3+},[25] and Dy^{3+}[23,24]) were reported in that matrix. However, when those structures are doped with Mn^{4+} ions, the difference in optical response is noticeable, that is, no emission of manganese in $SrAl_2O_4$:Mn^{4+} was observed[22] while for $Sr_4Al_{14}O_{25}$:Mn^{4+} intense red luminescence was reported. It indicates that in $SrAl_2O_4$ nanocrystals, Al^{3+} ions are substituted by Mn^{3+} ions whose emission is seldom observed rather than by Mn^{4+} ions whose emission is clearly visible in the $Sr_4Al_{14}O_{25}$ (hereinafter SAO) host. In the SAO structure, two Sr^{2+} sites that can be substituted by Ln^{3+} ions and six inequivalent Al^{3+} sites of two different coordination which can be occupied by TM ions can be found. This great number of possible crystallographic positions enable the significant modification of their spectroscopic properties and makes SAO an especially interesting host for LT applications.

In this work, a detailed structural and luminescence characterization study is presented, which is aimed at optimizing the synthesis conditions and dopant concentrations to obtain a highly sensitive ratiometric LT. The conducted research is devoted to obtain a thermometric phosphor with a high variability of the emission color with temperature. A proof of concept experiment is then presented, which exploits the luminescence thermochromism of SAO:Mn^{4+}, Tb^{3+} nanocrystals with a consumer digital camera to image transient temperature gradient in a powder stud placed in contact with a hotter body.

■ RESULTS AND DISCUSSION

Structural and Morphological Characterization. The SAO host crystallizes in an orthorhombic system of centrosymmetric *Pmma* space group (*a* = 24.785, *b* = 8.487, and *c* = 4.866 Å). According to the bond valence theory, the crystal lattice is composed of two double layers made up of $(AlO_4)^{5-}$ tetrahedra, which are similar to a $SrAl_2O_4$ unit cell separated by an $(AlO_6)^{9-}$ octahedral layer (Figure 1a). In a single unit cell that is composed of two formula units, there are three inequivalent tetrahedral Al^{3+} sites (Al_1, Al_2, and Al_3) and three octahedral ones (Al_4, Al_5, and Al_6). Strontium ions are
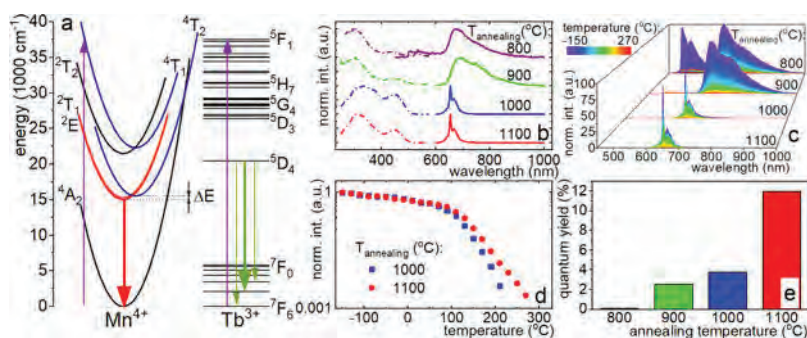
Figure 2. Configurational coordinate diagram for Mn^{4+} and Tb^{3+} ions (a). Room temperature excitation (dashed line) and emission (solid line) spectra of SAO:0.1% Mn^{4+} powders (b). Thermal evolution of emission spectra for $Sr_4Al_{14}O_{25}$:0.1% Mn^{4+} powders annealed at different temperatures (c). Thermal evolution of band integral intensities in 650−658 nm range for SAO:Mn^{4+} samples annealed at 1000 and 1100 °C, respectively (d). QY of SAO:0.1% Mn^{4+} powders as a function of annealing temperature (e).

located in two different sites, that is, the Sr_1 and the Sr_2, with 7- and 10-fold coordination to oxygen ions, respectively.[22,26,27] Because of the similar ionic radii, the Mn^{4+} ions occupy the Al^{3+} sites in this structure (Shannon ionic radius equals 67.5 pm for both Al^{3+} and Mn^{4+} in octahedral coordination). However, strong covalent bonds make $(AlO_4)^{5-}$ tetrahedra highly improper for Mn^{4+}. Therefore, the most likely possibility is that Mn^{4+} ions incorporate into the $(AlO_6)^{9-}$ octahedron. Moreover, according to Peng et al.,[28] Mn^{4+} ions occupy the more covalent Al_4 and Al_5 sites after doping, rather than the Al_6 site.

The 0.1% Mn^{4+} dopant concentration was based on the research of Peng et al.[28] who showed that the most intense emission of SAO:Mn^{4+} can be obtained for this concentration. To optimize the synthesis conditions and understand the influence of annealing temperature on the phase purity, the X-ray powder diffraction (XRPD) patterns of SAO/0.1%Mn^{4+} samples annealed at 800, 900, 1000, and 1100 °C were measured (Figure 1b). At 800 °C, a wide band, which indicates a highly amorphous phase and only one diffraction peak matched to the ICSD 24249 pattern, which probably corresponds to SrO_2 presence, can be found. When the annealing temperature increases to 900 °C the amount of amorphous phase seems to decrease and XRPD peaks corresponding to Al_2O_3 (ICSD 9770), SrO (ICSD 163625), and SrO_2 appear. Finally, for annealing temperatures above 1000 °C patterns corresponding to a phase pure SAO structure are obtained (ICSD 88527). The broadening of the diffraction peaks in respect to the reference pattern is related to the small size of the SAO particles (Figure S1). For an annealing temperature of 1100 °C, no evidence of phase change or additional peaks were found. However, the significantly narrower diffraction peaks indicate an enlargement of the SAO particles. Therefore, for further analysis, the 1000 °C temperature was chosen as an optimal one for crystallization of SAO nanoparticles. The ICP-OES (inductively coupled plasma optical emission spectrometry) measurements conducted for 0.1% Mn^{4+} and x % Tb^{3+} (x = 1, 5, 10, 20) codoped SAO powders annealed at 1000 °C confirm close to expected Tb^{3+} concentrations in those samples (Table S1). XRPD studies conducted for 0.1% Mn^{4+} and x % Tb^{3+} (x = 1, 5, 10, 20, 50) codoped SAO powders annealed at 1000 °C indicate that the samples with 1 and 5% Tb^{3+} concentration are characterized by pure SAO structure, while for 10 and 20% Tb^{3+} concentration, single peaks originating from SrO_2 (2θ = 51.5°) can be seen (Figure S2). The observed shift of the peak positions by

around 0.03−0.08° toward higher angles in comparison to the reference pattern comes from the contraction of the cell size associated with the difference in the ionic radii between the Sr^{2+} ions and the smaller Tb^{3+} activator ions. In the case of the 0.1% Mn^{4+}, 50% Tb^{3+} codoped powder, additional peaks which correspond to terbium, strontium, and aluminum oxides phases can be found indicating the dephasing of the SAO structure. The transmission electron microscopy (TEM) studies of SAO:Mn^{4+} nanocrystals annealed at 800, 900, 1000 and 1100 °C indicate well-crystallized and mostly agglomerated grains which are formed as two-dimensional sheet-like structures, similar to the SEM images obtained by Peng et al.[28] (Figure 1c,e,g,i; additional TEM and selected-area electron diffraction (SAED) images for SAO:Mn^{4+} annealed at 800, 900, 1000, and 1100 °C can be seen in Figures S3−S6, respectively). The crystallization process that has already begun in samples annealed at 800 and 900 °C is confirmed by the presence of crystals in Figure 1c,e and afterward by reflection spots observed on SAED patterns in Figures S3b and S4b. Diffuse rings noticed for nanoparticles annealed at 800 and 900 °C correspond to the presence of an amorphous phase, meanwhile the absence of those rings for nanocrystals annealed at 1000 and 1100 °C (Figures S5b and S6b) assures entire crystallization. The analysis of reflection spots shown in Figure S2b allows to confirm several crystallographic planes with the strongest intensities (Figure S7). The shape of the nanocrystal resembling flat sheets makes the obtention of a high contrast difficult. For annealing temperatures above 800 °C, the attribution of planes is unclear because of superimposed reflections and a significant amount of theoretical values with similar interatomic spacing d_{hkl} and intensities. It is worth noting that the pattern observed on the 1100 °C sample (Figure S6b) affirms that the created crystal system is orthorhombic.[29] The representative TEM images for SAO codoped with Mn^{4+} and Tb^{3+} ions annealed at 1000 °C are shown in Figure S8. The histograms for SAO:Mn^{4+} (Figure 1d,f,h,j for 800, 900, 1000, 1100 °C, respectively) indicate that the average grain size increases with the annealing temperatures from 800 to 1100 °C as follows: 32, 45, 90, and 140 nm, respectively.

Luminescent Properties Characterization. In order to understand the spectroscopic properties of Mn^{4+} ions of d^3 electron configuration, a schematic configurational coordinate diagram is performed in Figure 2a. The violet arrows represent λ_{exc} = 266 nm, used here, which enables the transition of the electrons from the $^4A_2$ ground state to the $^4T_1$ excited state.

271

Subsequently, nonradiative relaxation processes lead to the population of the ^2E state which radiative depopulation leads to the generation of a red emission (the red arrow). The lack of distortion of the ^2E state in respect to the $^4A_2$ one results in the occurrence of the narrow emission line at around 650 nm. That emission line, as well as the broad band centred at 664 nm, are ^2E Stokes-like phonon sidebands which originate from electric dipole vibronic transitions induced by lattice vibrations.[30,31] Meanwhile, in accordance with the magnetic dipole nature, the zero-phonon line emission intensity is very weak and observed only in emission spectra measured below 40 K.[30,32] However, for the samples annealed at 800 and 900 °C, inhomogeneously broadened emission bands are observed, which results from the fact that emission from Mn^{4+} ions localized in different crystallographic sites contribute to the emission. This indicates a high fraction of amorphous phase and the presence of additional oxide phases. The two broad excitation bands, observed for SAO annealed at 1000 and 1100 °C (Figure 2b), are related to $^4A_2 \rightarrow {}^4T_2$ (centred in 449−460 nm range) and $^4A_2 \rightarrow {}^4T_1$ (312−338 nm) spin-allowed transitions. The spectroscopic properties of SAO powders were examined in a wide temperature range from −150 to 270 °C (Figure 2c) in which, as a consequence of the presence of an intersection point between the ^2E and $^4T_2$ parabolas, a luminescence thermal quenching process occurs. At elevated temperatures, the electronic population of higher vibronic levels of ^2E state gradually increases. When the provided thermal energy is sufficient to overcome the intersection point (higher than ΔE_a) the $^4T_2$ state becomes populated which is followed by its rapid nonradiative depopulation to the ground state.[33,34] Therefore, ΔE_a is a crucial parameter from the thermometric point of view. Its value can be directly determined from the emission intensity versus temperature plot (Figure S9) according to the eq 1

$$-\frac{\Delta E_a}{k} \cdot \frac{1}{T} = \ln\left(\frac{I_0}{I_{em}} - 1\right)$$
(1)

where I_0 is the initial emission intensity (in this case at $T =$ −150 °C) and k is Boltzmann constant. At low temperatures $\Delta E_a \approx 0.31$ eV (2466 cm^{-1}) was found.

The activation energy ΔE_a depends on the relative positions of the $^4T_2$ and ^2E parabolas. However, since the spectral position of the $^2E \rightarrow {}^4A_2$ emission band does not change, the location of the $^4T_2$ state determines ΔE_a which in turn is associated with the CFS. Empirical equations for Dq, local CFS and the Racah parameter B (eqs 2−4) were applied[35−37] and compiled in Table 1.

$$Dq = \frac{E_a(^4A_2 \rightarrow {}^4T_2)}{10}$$
(2)

$$x = \frac{E_a(^4A_2 \rightarrow {}^4T_1) - E_a(^4A_2 \rightarrow {}^4T_2)}{Dq}$$
(3)

$$CFS \equiv \frac{Dq}{B} = \frac{15(x-8)}{x^2 - 10x}$$
(4)

The spectral positions of particular bands were determined based on the excitation spectra (Figure 2b) obtained for $\lambda_{em} =$ 652 and 664 nm for SAO:Mn^{4+} annealed at 1000 and 1100 °C, respectively. The broadening of the excitation bands related with $^4A_2 \rightarrow {}^4T_2$ and $^4A_2 \rightarrow {}^4T_1$ electronic transitions results from the fact that they are superpositions of those bands for

Table 1. Comparison of Crystal Field Parameters for SAO:Mn^{4+}

annealing temperature [°C]	λ_{em} [nm]	band maximum	Dq	CFS	B
1000	652	lower energy	2205	3.24	680
		higher energy	2281	2.34	977
	664	lower energy	1968	1.71	1154
		higher energy	2199	1.73	1273
1100	652	lower energy	2204	3.01	732
		higher energy	2491	3.23	772
	664	lower energy	2193	2.89	759
		higher energy	2459	3.06	804

different Al^{3+} sites (octahedral Al_4, Al_5 and Al_6) occupied by Mn^{4+} ions.[28] To examine that, the CFS values for both samples are compared as a function of R_{av}^{-5} and R_{min}^{-5} (where R_{av} and R_{min} are average and minimum metal−oxygen distance, respectively) for Al_4, Al_5 and Al_6 sites (Figure S10). According to the band assignment theory of Peng et al., the correlation observed for the 1000 °C sample would indicate that the excitation bands at 19683 cm^{-1} (~508 nm) and at 29842 cm^{-1} (335 nm) can be ascribed to the Mn^{4+} ion in the Al_4 position and those at 22049 cm^{-1} (453.5 nm) and at 29226 cm^{-1} (342 nm) to the Al_6 site. In accordance with the Tanabe−Sugano diagram for d^3 configuration, the minimum of $^4T_1$ is localized beyond the ^2E parabola [16] [25] in the case of strong CFS approximation (namely, above 1.7), due to the fact that ^2E is t_2^3 electronic orbital derivative whereas $^4T_1$ originates from t_2^2e.

The thermal evolution of the integral emission intensities of Mn^{4+} ions for SAO annealed at 1000 and 1100 °C presented in Figure 2d (see also Figure S11) indicates that up to 90 °C no significant difference in the luminescence thermal stability between these two samples can be found. However, above 90 °C, faster thermal quenching was noticed for the sample annealed at 1000 °C. In this case at 210 °C, the emission is totally quenched, while for the sample annealed at 1100 °C, the emission can still be observed until 290 °C. Because of the fact that sidebands at 654 nm are quenched faster than the sideband at 670 nm, the integral intensity of the whole Mn^{4+} emission intensity was considered in further studies. The difference in the thermal dependence between these two signals can be explained by their thermal coupling, which was confirmed by the fitting procedure using the Boltzmann equation (see Figure S12).

Additionally, for a better understanding of de-excitation processes, the impact of the annealing temperature on the quantum yield (QY) was measured (Figure 2e) and an evident enhancement of the QY value with the increase in annealing temperature was noted. The values of QY were $QY_{800} = 0.11\%$, $QY_{900} = 2.56\%$, $QY_{1000} = 3.81\%$, $QY_{1100} = 11.95\%$, respectively. It can clearly be seen that the reduction of the nonradiative losses associated with the high fraction of surface effects results in an enhancement of the QY by about one order of magnitude.

Optimization of the Co-dopant Concentration. If another emission presenting a different thermal quenching behavior than that from the Mn^{4+} ions could be probed simultaneously, then the ratio of the intensities of the two emissions could be used as a robust temperature readout.

Here, Tb^{3+} ions, which emission typically only quenches at high temperatures, were selected to provide the reference emission. In order to optimize the Tb^{3+} concentration, spectroscopic properties of a series of SAO:0.1% Mn^{4+},x % Tb^{3+} powders (x = 1; 5; 10; 20) annealed at 1000 °C were examined in a wide temperature range. The emission spectra of the obtained nanocrystals exhibit beside the previously described Mn^{4+} emission bands, three additional bands at 490 nm, 545 nm, and 587 nm associated with the $^5D_4 \rightarrow {}^7F_6$, $^5D_4 \rightarrow {}^7F_5$, and $^5D_4 \rightarrow {}^7F_4$ electronic transitions of Tb^{3+} ions (Figure 3a). Excitation spectra were also measured for Tb^{3+}
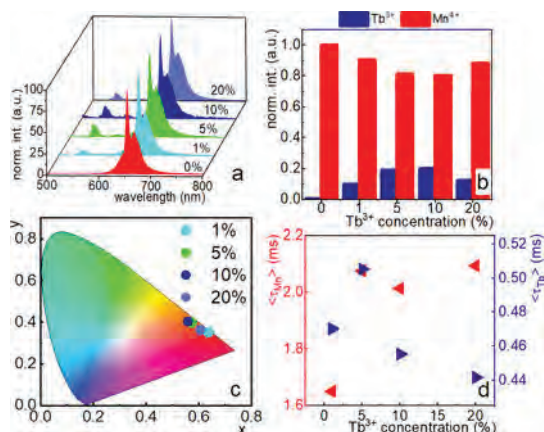
Figure 3. Emission spectra (a) and CIE 1931 chromaticity diagram for SAO:0.1% Mn^{4+},x % Tb^{3+} (x = 1, 5, 10, 20) powder at room temperature (b). Integral intensities (c). and average lifetime of Mn^{4+} and Tb^{3+} excited states as a function of Tb^{3+} concentration (d).

ions, by monitoring at 545 nm (Figure S13a). Among others, the peaks correspond to transitions between the ground state $^7F_6$ and subsequent levels $^5H_5$ (301 nm), $^5H_7$ (318 nm), $^5L_6$ (340 nm), $^5G_4$ (350 nm), $^5D_2$ (355 nm), $^5G_5$ (362 nm), and $^5L_{10}$ (370 nm) states. A broad excitation band with maximum intensity (centerd in the range 373−378 nm) originates from the $^7F_6 \rightarrow {}^5D_3$ electronic transition of Tb^{3+} ions. Interestingly, the Mn^{4+} excitation bands previously described are absent in the excitation spectra for Tb^{3+} λ_{em} = 545 nm, which indicates

that there is no $Mn^{4+} \rightarrow Tb^{3+}$ energy transfer (Figure S13a). Analogously, excitation spectra measured for λ_{em} = 654 nm (Mn^{4+} emission) consist only of Mn^{4+} absorption bands (Figure S13b). The lack of interionic energy transfer reveals that the f states of Tb^{3+} ions are directly excited confirming their high performance as a luminescent reference.

It is noteworthy that the contribution of the Tb^{3+} luminescence in the emission spectra of SAO:Mn^{4+},Tb^{3+} depends on the Tb^{3+} concentration. The room temperature emission spectra clearly indicate that with the increase of the Tb^{3+} amount up to 10% of Tb^{3+} ions, an enhancement of the Tb^{3+} emission intensity in respect to the Mn^{4+} one can be observed (Figure 3b). In the case of SAO:Mn^{4+},20% Tb^{3+}, a slight lowering of the Tb^{3+} emission intensity can be found, which can be explained in terms of either structural changes for this sample or by the energy migration among the excited states of Tb^{3+} ions toward the surface quenchers. This concentration effect has natural implications in the change of the emission color. Chromatic coordinates (CIE 1931) for all samples are located in the red region, wherein the impact of the Tb^{3+} concentration is substantial. The enhancement of the Tb^{3+} concentration causes a shift of the emission color toward the orange region (Figure 3c).

The analysis of the kinetics of the excited states of Mn^{4+} and Tb^{3+} ions provides additional insight into the process of light generation in the SAO:Mn^{4+},Tb^{3+} nanocrystals (Figures 3d and S14). Surprisingly the lifetime of the ^2E state of Mn^{4+} increases from 1.65 ms for SAO:Mn^{4+},1% Tb^{3+} to 2.08 ms for SAO:Mn^{4+},5% Tb^{3+}. The origin of this effect is not clear but is probably related to the modification of the Mn^{4+} local ions symmetry by the introduction of the Tb^{3+} ions causing a lowering of the probability of radiative depopulation of the ^2E state. As seen, above 5%, increasing the Tb^{3+} concentration does not affect the decay constant of the ^2E excited state of Mn^{4+}, which would agree with the lack of the interionic energy transfer between Mn^{4+} and Tb^{3+} ions previously discussed basing on the excitation spectra analysis.

The thermal evolution of the emission spectrum of the SAO:0.1% Mn^{4+},5% Tb^{3+} phosphor, representative of the behavior, is shown in Figure 4a (the thermal evolution of the emission spectrum for all Tb^{3+} concentration can be found in Figure S15). Similarly to outcomes observed in SAO:Mn^{4+}
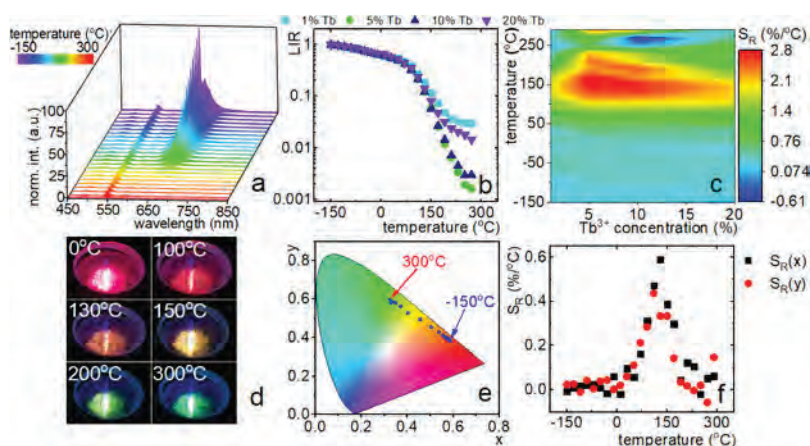
Figure 4. Thermal evolution of the emission spectra for SAO:0.1% Mn^{4+},5% Tb^{3+} powder annealed at 1000 °C (a). LIR of SAO:0.1% Mn^{4+},x % Tb^{3+} (x = 1, 5, 10, 20) powders (b). Influence of Tb^{3+} ions concentration on the thermal evolution of relative sensitivity S_R in SAO:0.1% Mn^{4+},x % Tb^{3+} powder (c). Photographs of the SAO:0.1% Mn^{4+},5% Tb^{3+} powder under 266 nm laser light illumination at different temperatures (d). CIE 1931 chromacity diagram for SAO:0.1% Mn^{4+},5% Tb^{3+} powder (e). Thermal evolution of S_R of chromacity coordinates x and y (f).

273

powders, in codoped nanoparticles, the intensity of the manganese emission is also gradually quenched up to about 210 °C, which guarantees a high temperature sensitivity. On the other hand, the Tb^{3+} emission intensity is temperature independent, which results from the high energy gap between emitting $^5D_4$ and the next lower laying $^7F_0$ state (above 14,000 cm^{-1}). This sufficiently prevents the $^5D_4$ state depopulation via the multiphonon processes and thus thermal quenching of Tb^{3+} luminescence. Surprisingly, a high Tb^{3+} dopant concentration increases the rate of thermal quenching of the $^2E \rightarrow {}^4A_2$ electronic transition at temperatures above 150 °C. The most significant changes of the Mn^{4+} luminescence were found in the case of SAO:Mn^{4+},5% Tb^{3+} ions, for which a decrease by three orders of magnitude was noted. On the other hand, the emission intensity of Tb^{3+} at 545 nm becomes almost temperature-independent in a wide range, namely, from −150 to 300 °C, which facilitates the ratiometric temperature readout. To verify this thesis, the luminescence intensity ratio (LIR) defined as follows

$$\text{LIR} = \frac{{}^2E \rightarrow {}^4A_2(Mn^{4+})}{{}^5D_4 \rightarrow {}^7F_5(Tb^{3+})} \quad (5)$$

was used as a thermometric parameter (Figure 4b). Below 50 °C only a slight change of LIR can be found independently of the Tb^{3+} concentration. However, above 50 °C, a drastic decrease of the LIR by over two orders of magnitude can be observed, which results from the significant quenching of Mn^{4+} emission intensity. To quantify the observed thermally induced changes, the relative sensitivity of SAO:Mn^{4+},Tb^{3+} nanopowders to temperature changes was calculated as follows

$$S_R = \frac{1}{\text{LIR}} \cdot \frac{\Delta \text{LIR}}{\Delta T} \times 100\% \quad (6)$$

where ΔLIR represents change of LIR corresponding to ΔT change of temperature (Figure 4c). Independently on Tb^{3+} concentration, at temperatures below 50 °C the $S_R \sim 0.5\%/°C$ was found. Above this critical temperature the enhancement of S_R up to 2.8%/°C at 150 °C was noticed. For a Tb^{3+} concentration of 5%, a relative sensitivity over 2%/°C was maintained over a temperature range as wide as 150 °C (80−230 °C). The further increase of the Tb^{3+} amount to 20% results in the gradual narrowing of the temperature range, in which this high relative sensitivity was obtained to only 90 °C (the range from 80 to 170 °C). Excitation spectra measured over the −150 to 300 °C temperature range for the representative SAO:0.1% Mn^{4+},5% $MnTb^{3+}$ powder when monitoring the Tb^{3+} (Figure S16a) and Mn^{4+} (Figure S16b) emissions do not show any thermally induced change in the band position and shape. This indicates the CFS does not change with temperature. Moreover the thermometry performance of SAO:Mn^{4+},Tb^{3+} powder in terms of stability was confirmed by measurements of the LIR readout within 10 heating-cooling cycles (Figure S17), which showed excellent repeatability (maximum deviation of 1.9%). In order to determine the useful temperature range, the signal to noise ratio-based LIR uncertainty at each temperature was converted using the relative temperature sensitivity into a temperature uncertainty (Figure S18). A value of $\delta T = 0.5$ °C within the 50−210 °C temperature range promises a high performance in that range. An additional advantage of the SAO:Mn^{4+},Tb^{3+} thermographic phosphor is the great variability of its emission color with temperature (Figure 4d). The emission color shifts

from bright red at 0 °C to green at 300 °C. These changes, visible to the naked eye, are confirmed by the strong shift of the chromatic CIE coordinates from red to green shown in Figure 4e. Thermographic phosphors with a high variability in their emission colors are of great importance as their temperature can be measured with a single color array, which makes for an easy to use and inexpensible temperature sensor, which can be used, for example, for the early detection of overheating spots on different surfaces. Several studies have reported using a CIE diagram a strong color response of some luminescent compounds for thermometry.[38−42] In order to, in the future, compare the thermochromic performance of these materials, we, for the first time, suggest to consider the relative sensitivity of the emission color CIE coordinate as figure of merit parameters [$S_R(x)$, $S_R(y)$ calculated using eq 6]. These parameters would be the chromatic counterpart of the relative sensitivity, which is an accepted figure of merit for the ratio of intensities between transitions from thermalized levels. In the case of SAO:0.1% Mn^{4+},5% Tb^{3+} nanocrystals, chromatic relative sensitivities as high as $S_R(x) = 0.6\%/°C$ and $S_R(y) = 0.4\%/°C$ were found at 150 °C. In addition, as shown in Figure S19, the Mn^{4+} and Tb^{3+} emission are located in regions where there is very little overlap between the color filter curves of consumer digital cameras, so that the two emission can be almost completely separated between the red and the green channel.

Proof-of-Concept Temperature Imaging Experiment. The applicative potential of SAO:0.1% Mn^{4+},5% Tb^{3+} nanocrystals for noncontact temperature sensing was verified by a proof-of-concept experiment (Figure 5). A quartz tube (5 mm in diameter) was filled with the SAO:0.1% Mn^{4+},5% Tb^{3+} powder and placed on a heating plate at a temperature of 25 °C. At $t = 0$ the set point temperature of the heating plate was increased up to 250 °C and from there on, every 5 s, digital color camera images (Figure 5a) and infrared thermography
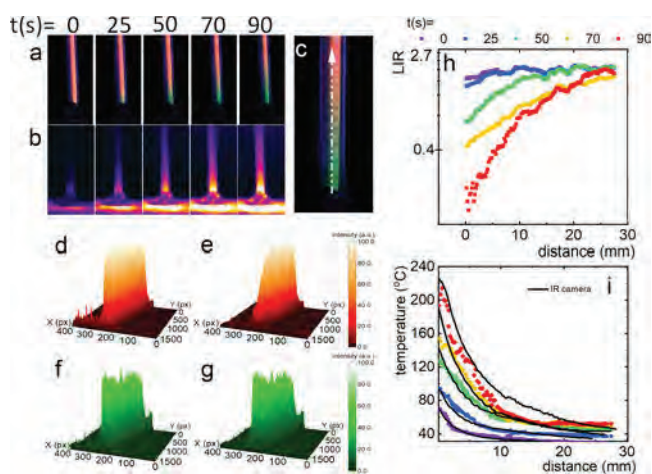
Figure 5. Photographs from digital color camera (a) and thermovision camera (b) of quartz tube with SAO:0.1% Mn^{4+},5% Tb^{3+} powder under UV light excitation recorded at different times of heating exposition; zoom in of the photography with the line along which the thermal gradient was analyzed (c); maps presenting the emission intensity in red (d,e) and green (f,g) channels at time $t = 0$ s (d,f) and $t = 70$ s (e,g); LIR of green to red channels as a function of distance from the heating plates at different measurement moments (h) and thermal profile obtained at different moments using SAO: 0.1% Mn^{4+},5% Tb^{3+} nanocrystals and thermovision camera (i).

274

camera images (Figure 5b) were recorded. It can clearly be seen that upon 256 nm excitation light, the emission of the powder, which is intense red at the start of the experiment gradually changes with time into green, as heat diffuses from the plate into the power. The profile of the color change along the line shown in Figure 5c was analyzed (see also Figure S20). Because of the fact that CIE coordinates of SAO Mn^{4+}, Tb^{3+} nanocrystals changes from red to green in the analyzed temperature range, the noncontact temperature readout using a digital camera may be simplified to the analysis of the intensity of red (R) and green (G) channels of RGB color images (Figure 5d−g). This allows to obtain two-dimensional LIR images, from which a profile as a function of the distance from the heating plate was plotted at different t (Figure 5h). This profile is then converted to temperature using a calibration curve obtained by measuring the LIR at different controlled temperatures (monitored by the thermal imager) under steady state conditions (Figure S21), and is shown in Figure 5h. As shown, with time, the maximum thermal gradient decreases while its spatial extent increases, which is a textbook illustration of the one-dimensional time-dependent heat equation. To assess the measurement uncertainty, the temperature profile obtained from the luminescence and from the IR imager were compared. Until $t = 70$ s, the maximum deviation between the profiles is about 5 °C, which demonstrates excellent accuracy in the range 25−150 °C (Figure S22). At $t = 90$ s, larger deviations are observed, which may be explained by two factors. As the plate temperature increases, the amount of thermal radiation emitted from the plate and reflected by the tube, which has a reflectivity of $(1 - \varepsilon)$, where ε is the emissivity, grows with the fourth power of the plate temperature. This can lead to an overestimation of the tube temperature. Reflection radiation interference is a well-known issue of IR thermography, which is also discussed in ref 46. The emissivity of quartz, which is measured as 0.93 at 40 °C, decreases with temperature. It is also worth noticing that the thermal imager measures mainly the tube temperature while luminescence thermometry measures the powder temperature, which thermal profiles may differ. In addition, above 200 °C, the signal in the red channel approaches the noise floor so that nonlinearity and signal interference may alter the temperature reading of the luminescence thermometry. However, as reported in ref 49, the camera includes an IR blocking filter, which may be lead to a 75% signal loss in the red channel. Removing this filter should allow to increase the temperature range of this thermal imaging concept. Finally, using an RGB image of the powder on the heated plate under steady state conditions, the deviation from a uniform temperature field was used to estimate the random uncertainty or precision of the technique for single exposures, which was found to be better than 1.6 °C at 150 °C and for a resolution of 14 line pairs per mm.

This experiment clearly confirms the high application potential of SAO:Mn^{4+},Tb^{3+} nanocrystals for temperature imaging using a simple and cheap digital camera. Additionally, it is worth noticing that in contrary to the thermovision camera, no information concerning the emissivity of the object is required.

◼ CONCLUSIONS

In this work, step-by-step optimization of the synthesis condition and Tb^{3+} dopant concentration of SAO:Mn^{4+},Tb^{3+} nanocrystals was presented in order to obtain a highly sensitive

ratiometric luminescent thermometer. It was found that above 100 °C the intense red emission of SAO:Mn^{4+},Tb^{3+} nanocrystals associated with the $^2E \rightarrow {}^4A_2$ electronic transition of Mn^{4+} ions was drastically quenched while the $^5D_4 \rightarrow {}^7F_5$ emission of Tb^{3+} stayed almost thermally independent. The SAO:0.1% Mn^{4+},5% Tb^{3+} nanocrystals displayed a thermal sensitivity above 2%/°C over the range 80−250 °C with a maximum of $S_R = 2.8\%$/°C at 150 °C. Because of the distinct spectral location of the emissions from the two ions, the thermal quenching of the Mn^{4+} emission was associated with a pronounced change in emission color, which can be captured by a consumer digital camera, as shown in the proof-of-concept experiment. For future comparison, a chromatic temperature sensitivity was quantified as a figure of merit on the basis of the x and y coordinates.

The developed nanophosphors were demonstrated to provide sensitive temperature measurements in the range of 25−150 °C, which includes the boiling point of liquids used for spray cooling[43] and the glass transition temperature of polymers used in 3D printing,[44] and which is also relevant to the thermal management of batteries, fuel cells, and electric motors.[45] Those applications demand the observation of complex thermal phenomena which impacts the process performance but the implementation of IR thermography is not possible because of the opacity of liquids and polymers, and to reflections of thermal radiation by inner surfaces of battery, fuel cell, and motor assemblies.[46] This combined to the flexibility of the ratiometric approach and the simplicity of detection of color change with consumer cameras holds great promises for widespread use as a temperature imaging sensors in key industrial processes.

◼ MATERIALS AND METHODS

The SAO powders can be obtained using various synthesis procedures such as combustion,[22] solid state reaction,[23,47] or ceramic methods;[24] however, a modified Pechini method[48] was applied in this case because of its simplicity and the lower annealing temperatures in respect to other methods.[47] $Sr(NO_3)_2$ (99.9965% purity, Puratronic), $Al(NO_3)_3 \cdot x H_2O$ ($x \approx 9$, 99.999% purity, Alfa Aesar), $Mn(NO_3)_2 \cdot 4H_2O$ (99.99% purity, Sigma-Aldrich), Tb_4O_7 (99.999% purity, Stanford Materials Corporation), $C_6H_8O_7$ (>99.5% purity, Alfa Aesar), and $H(OCH_2CH_2)_nOH$, (PEG-200, Alfa Aesar) were used as starting materials. Stoichiometric amounts of aluminum, strontium, and manganese nitrates were dissolved in deionized water in separate glasses and then mixed together. Terbium oxide was dissolved in deionized water with the addition of a small amount of HNO_3 (65% purity, Avantor), then recrystallized three times to remove the excess nitrogen and added to the water solution of nitrates. After that, an anhydrous citric acid and polyglycol were added to the mixture of nitrates. The molar ratios of citric acid to all metals, and that of PEG-200 to citric acid were set to 6:1 and 1:1, respectively. Subsequently, the obtained solution was dried for 24 h at 100 °C until a resin was formed. The produced resin of the sample with 0.1% molar Mn^{4+} concentration in respect to Al^{3+} ions was annealed in porcelain crucibles for 12 h in air at 800, 900, 1000, and 1100 °C. The samples with 0.1% Mn^{4+} and x % Tb^{3+} ($x = 1, 5, 10, 20$) concentration in respect to the number of Sr^{2+} moles ions were annealed for 12 h in air at a temperature of 1000 °C. All of the synthesized materials were examined by XRPD measurements carried out on a PANalitycal X'Pert diffractometer, equipped with an Anton Paar TCU 1000 N temperature control unit, using Ni-filtered Cu Kα radiation ($V = 40$ kV, $I = 30$ mA). The ICP-EOS measurements were taken using a Thermo Scientific ICAP 7000 spectrometer with a charge injection device detector.

Transmission electron microscope (TEM) images were taken using a Philips CM-20 SuperTwin TEM microscope. The samples were

dispersed in methanol, and a droplet of such suspension was put on a microscope copper grid. Next, the samples were dried and purified in a plasma cleaner. Studies were performed in a conventional TEM procedure with 160 kV parallel beam electron energy.

The sizes were determined manually using ImageJ software by measuring the longest linear size (Feret diameter) of each particle.

The emission spectra were measured using the 266 nm excitation line from a laser diode (20 mW) and a Silver-Nova Super Range TEC spectrometer from StellarNet (1 nm spectral resolution) as a detector. The temperature of the sample was controlled using a THMS 600 heating-cooling stage from Linkam (0.1 °C temperature stability and 0.1 °C set point resolution).

The excitation spectra and luminescence decay profiles were recorded using a FLS980 Fluorescence spectrometer from Edinburgh Instruments with a 450 W xenon lamp and μFlash lamp as an excitation sources and a R928P side window photomultiplier tube from Hamamatsu as a detector. The luminescence QY of the synthesized nanocrystalline powders was measured using the above-mentioned system equipped with an integrating sphere and Al_2O_3 powder as a reference. Average decay constant of the excited states was calculated as follows

$$\langle \tau \rangle = \frac{\int I(t) \cdot t \, \mathrm{d}t}{\int I(t) \, \mathrm{d}t} \tag{M1}$$

where $I(t)$ represents the emission intensity at time t. Thermovision images were collected using a T540 camera from FLIR.

The digital images were taken using a Canon EOS 400D camera with a EFS 60 mm macro lens using a 1 s integration time, 14.3 lp/mm spatial resolution. After capturing color images of the quartz cuvette filled with $SAO:Mn^{4+},Tb^{3+}$ powder the emission maps for red and green channels (RGB) were extracted using IrfanView 64 4.51 software. After that obtained pictures were divided by each other using OriginLab 2019 Software in order to obtain LIR profiles along the quartz tube. No smoothing was applied to the image. LIR profiles were converted into temperature profiles using the calibration curve. To obtain this calibration curve, the $SAO:Mn^{4+},Tb^{3+}$ powder was placed on the heating plate and LIR was calculated using the above-described procedure as a function of temperature. The temperature of the powder was controlled by the thermovision camera. The emissivity of the $SAO:Mn^{4+},Tb^{3+}$ powder was estimated by the comparison of the temperature of the powder placed on the heating plate of constant temperature (40 °C monitored by IR camera) with the temperature of the Scotch 130C tape of standardized emissivity (0.95). The emissivity of the quartz tube has been estimated using the same procedure.

■ ASSOCIATED CONTENT

Ⓢ Supporting Information

The Supporting Information is available free of charge at https://pubs.acs.org/doi/10.1021/acsami.0c11730.

> Results of ICP-EOS, XRPD, TEM, and SAED measurements for different samples, graphs of CFS versus metal−oxide bond, emission intensity versus $1/T$, thermal evolution of band integral intensities, graphical representation of the Boltzmann distribution through $1/T$, excitation spectra in function of Tb^{3+} concentration and temperature, luminescent decays for Tb^{3+} concentration, comparison of the emission spectra with the color filter curves of consumer digital camera, photographs from digital and thermovision camera, and calibration curve as the LIR versus temperature(PDF)

■ AUTHOR INFORMATION

Corresponding Author

Lukasz Marciniak − *Institute of Low Temperature and Structure Research, Polish Academy of Sciences, 50-422 Wroclaw,*

Poland; ⓞ orcid.org/0000-0001-5181-5865; Email: l.marciniak@intibs.pl

Authors

Wojciech Piotrowski − *Institute of Low Temperature and Structure Research, Polish Academy of Sciences, 50-422 Wroclaw, Poland*

Karolina Trejgis − *Institute of Low Temperature and Structure Research, Polish Academy of Sciences, 50-422 Wroclaw, Poland;* ⓞ orcid.org/0000-0002-9399-9399

Kamila Maciejewska − *Institute of Low Temperature and Structure Research, Polish Academy of Sciences, 50-422 Wroclaw, Poland;* ⓞ orcid.org/0000-0002-8411-3234

Karolina Ledwa − *Institute of Low Temperature and Structure Research, Polish Academy of Sciences, 50-422 Wroclaw, Poland;* ⓞ orcid.org/0000-0003-2826-7623

Benoit Fond − *Institute of Fluid Mechanics and Thermodynamics, Otto-von-Guericke Universität Magdeburg, 39106 Magdeburg, Germany;* ⓞ orcid.org/0000-0002-8152-4126

Complete contact information is available at:
https://pubs.acs.org/10.1021/acsami.0c11730

Notes

The authors declare no competing financial interest.

■ ACKNOWLEDGMENTS

■ REFERENCES

(1) Carlos, L. D.; Palacio, F. *Thermometry at the Nanoscale*; Nanoscience & Nanotechnology Series; The Royal Society of Chemistry, 2016.

(2) Jaque, D.; Vetrone, F. Luminescence Nanothermometry. *Nanoscale* 2012, 4, 4301.

(3) Qiu, X.; Zhou, Q.; Zhu, X.; Wu, Z.; Feng, W.; Li, F. Ratiometric Upconversion Nanothermometry with Dual Emission at the Same Wavelength Decoded via a Time-Resolved Technique. *Nat. Commun.* 2020, 11, 4.

(4) Xu, M.; Zou, X.; Su, Q.; Yuan, W.; Cao, C.; Wang, Q.; Zhu, X.; Feng, W.; Li, F. Ratiometric Nanothermometer in Vivo Based on Triplet Sensitized Upconversion. *Nat. Commun.* 2018, 9, 2698.

(5) Bao, G.; Wong, K.-L.; Jin, D.; Tanner, P. A. A Stoichiometric Terbium-Europium Dyad Molecular Thermometer: Energy Transfer Properties. *Light: Sci. Appl.* 2018, 7, 96.

(6) Runowski, M.; Woźny, P.; Lis, S.; Lavín, V.; Martín, I. R. Optical Vacuum Sensor Based on Lanthanide Upconversion—Luminescence Thermometry as a Tool for Ultralow Pressure Sensing. *Adv. Mater. Technol.* 2020, 5, 1901091.

(7) Pickel, A. D.; Teitelboim, A.; Chan, E. M.; Borys, N. J.; Schuck, P. J.; Dames, C. Apparent Self-Heating of Individual Upconverting Nanoparticle Thermometers. *Nat. Commun.* 2018, 9, 4907.

(8) Yakunin, S.; Benin, B. M.; Shynkarenko, Y.; Nazarenko, O.; Bodnarchuk, M. I.; Dirin, D. N.; Hofer, C.; Cattaneo, S.; Kovalenko, M. V. High-Resolution Remote Thermometry and Thermography Using Luminescent Low-Dimensional Tin-Halide Perovskites. *Nat. Mater.* 2019, 18, 846−852.

(9) Zhu, X.; Feng, W.; Chang, J.; Tan, Y.-W.; Li, J.; Chen, M.; Sun, Y.; Li, F. Temperature-Feedback Upconversion Nanocomposite for Accurate Photothermal Therapy at Facile Temperature. *Nat. Commun.* 2016, 7, 10437.

(10) Brites, C. D. S.; Xie, X.; Debasu, M. L.; Qin, X.; Chen, R.; Huang, W.; Rocha, J.; Liu, X.; Carlos, L. D. Instantaneous Ballistic

Velocity of Suspended Brownian Nanocrystals Measured by Upconversion Nanothermometry. *Nat. Nanotechnol.* **2016**, *11*, 851−856.

(11) Löw, P.; Kim, B.; Takama, N.; Bergaud, C. High-Spatial-Resolution Surface-Temperature Mapping Using Fluorescent Thermometry. *Small* **2008**, *4*, 908−914.

(12) Geitenbeek, R. G.; Vollenbroek, J. C.; Weijgertze, H. M. H.; Tregouet, C. B. M.; Nieuwelink, A.-E.; Kennedy, C. L.; Weckhuysen, B. M.; Lohse, D.; van Blaaderen, A.; van den Berg, A.; et al. Luminescence Thermometry for in Situ Temperature Measurements in Microfluidic Devices. *Lab Chip* **2019**, *19*, 1236−1246.

(13) Okabe, K.; Inada, N.; Gota, C.; Harada, Y.; Funatsu, T.; Uchiyama, S. Intracellular Temperature Mapping with a Fluorescent Polymeric Thermometer and Fluorescence Lifetime Imaging Microscopy. *Nat. Commun.* **2012**, *3*, 705−709.

(14) Abram, C.; Fond, B.; Beyrau, F. Temperature Measurement Techniques for Gas and Liquid Flows Using Thermographic Phosphor Tracer Particles. *Prog. Energy Combust. Sci.* **2018**, *64*, 93−156.

(15) Tobin, K. W.; Allison, S. W.; Gates, M. R.; Capps, G. J.; Beshears, D. L.; Cyr, M.; Noel, B. W. High-Temperature Phosphor Thermometry of Rotating Turbine Blades. *AIAA J.* **1990**, *28*, 1485−1490.

(16) Omrane, A.; Ossler, F.; Aldén, M. Two-Dimensional Surface Temperature Measurements of Burning Materials. *Proc. Combust. Inst.* **2002**, *29*, 2653−2659.

(17) Allison, S. W.; Gillies, G. T. Remote Thermometry with Thermographic Phosphors: Instrumentation and Applications. *Rev. Sci. Instrum.* **1997**, *68*, 2615−2650.

(18) Aldén, M.; Omrane, A.; Richter, M.; Särner, G. Thermographic Phosphors for Thermometry: A Survey of Combustion Applications. *Prog. Energy Combust. Sci.* **2011**, *37*, 422−461.

(19) Fuhrmann, N.; Schneider, M.; Ding, C.-P.; Brübach, J.; Dreizler, A. Two-Dimensional Surface Temperature Diagnostics in a Full-Metal Engine Using Thermographic Phosphors. *Meas. Sci. Technol.* **2013**, *24*, 095203.

(20) Liebsch, G.; Klimant, I.; Frank, B.; Holst, G.; Wolfbeis, O. S. Luminescence Lifetime Imaging of Oxygen, PH, and Carbon Dioxide Distribution Using Optical Sensors. *Appl. Spectrosc.* **2000**, *54*, 548−559.

(21) Bünzli, J. C. G.; Piguet, C. Taking Advantage of Luminescent Lanthanide Ions. *Chem. Soc. Rev.* **2005**, *34*, 1048.

(22) Zand, S. K.; Baghshahi, S.; Rajabi, M. Synthesis of Sr4Al14O25:Eu2+ Green Emitting Luminescent Nano-Pigment by Solution Combustion Method. *J. Mater. Sci.: Mater. Electron.* **2014**, *25*, 4412.

(23) Li, F.; Li, Z.; Wang, X.; Zhang, M.; Shen, Y.; Cai, P.; He, X. Crystal Structure and Luminescent Property of Flaky-Shaped Sr4Al14O25:Eu2+, Dy3+phosphor Doped with Er3+ions. *J. Alloys Compd.* **2017**, *692*, 10.

(24) Luitel, H. N.; Watari, T.; Chand, R.; Torikai, T.; Yada, M. Giant Improvement on the Afterglow of Sr 4 Al 14 O 25 :Eu 2+ ,Dy 3+ Phosphor by Systematic Investigation on Various Parameters. *J. Mater.* **2013**, *2013*, 613090.

(25) Han, S. H.; Kim, Y. J. Luminescent Properties of Ce and Eu Doped Sr4Al 14O25 Phosphors. *Opt. Mater.* **2006**, *28*, 626.

(26) Chen, L.; Xue, S.; Chen, X.; Bahader, A.; Deng, X.; Zhao, E.; Jiang, Y.; Chen, S.; Chan, T. S.; Zhao, Z.; et al. The Site Occupation and Valence of Mn Ions in the Crystal Lattice of Sr 4 Al 14 O 25 and Its Deep Red Emission for High Color-Rendering White Light-Emitting Diodes. *Mater. Res. Bull.* **2014**, *60*, 604.

(27) Long, J.; Yuan, X.; Ma, C.; Du, M.; Ma, X.; Wen, Z.; Ma, R.; Wang, Y.; Cao, Y. Strongly Enhanced Luminescence of Sr4Al14O25:Mn4+ Phosphor by Co-Doping B3+ and Na+ Ions with Red Emission for Plant Growth LEDs. *RSC Adv.* **2018**, *8*, 1469.

(28) Peng, M.; Yin, X.; Tanner, P. A.; Brik, M. G.; Li, P. Site Occupancy Preference, Enhancement Mechanism, and Thermal Resistance of Mn4+ Red Luminescence in Sr4Al14O25: Mn4+ for Warm WLEDs. *Chem. Mater.* **2015**, *27*, 2938.

(29) Zhang, N.; Tsai, Y. T.; Fang, M. H.; Ma, C. G.; Lazarowska, A.; Mahlik, S.; Grinberg, M.; Chiang, C. Y.; Zhou, W.; Lin, J. G.; et al. Aluminate Red Phosphor in Light-Emitting Diodes: Theoretical Calculations, Charge Varieties, and High-Pressure Luminescence Analysis. *ACS Appl. Mater. Interfaces* **2017**, *9*, 28.

(30) Zhu, H.; Lin, C. C.; Luo, W.; Shu, S.; Liu, Z.; Liu, Y.; Kong, J.; Ma, E.; Cao, Y.; Liu, R. S.; et al. Highly Efficient Non-Rare-Earth Red Emitting Phosphor for Warm White Light-Emitting Diodes. *Nat. Commun.* **2014**, *5*, 4312.

(31) Jansen, T.; Gorobez, J.; Kirm, M.; Brik, M. G.; Vielhauer, S.; Oja, M.; Khaidukov, N. M.; Makhov, V. N.; Jüstel, T. Narrow Band Deep Red Photoluminescence of Y 2 Mg 3 Ge 3 O 12 :Mn 4+ ,Li + Inverse Garnet for High Power Phosphor Converted LEDs. *ECS J. Solid State Sci. Technol.* **2018**, *7*, R3086.

(32) Ji, H.; Ueda, J.; Brik, M. G.; Du, M. H.; Chen, D.; Tanabe, S. Intense Deep-Red Zero Phonon Line Emission of Mn4+ in Double Perovskite La4Ti3O12. *Phys. Chem. Chem. Phys.* **2019**, *21*, 25108.

(33) Matuszewska, C.; Elzbieciak-Piecka, K.; Marciniak, L. Transition Metal Ion-Based Nanocrystalline Luminescent Thermometry in SrTiO3:Ni2+,Er3+ Nanocrystals Operating in the Second Optical Window of Biological Tissues. *J. Phys. Chem. C* **2019**, *123*, 18646−18653.

(34) Senden, T.; van Dijk-Moes, R. J. A.; Meijerink, A. Quenching of the Red Mn4+ Luminescence in Mn4+-Doped Fluoride LED Phosphors. *Light: Sci. Appl.* **2018**, *7*, 8.

(35) Chen, D.; Zhou, Y.; Xu, W.; Zhong, J.; Ji, Z.; Xiang, W. Enhanced Luminescence of Mn4+:Y3Al5O12 Red Phosphor via Impurity Doping. *J. Phys. Chem. C* **2016**, *4*, 1704.

(36) Xu, J.; Ueda, J.; Tanabe, S. Toward Tunable and Bright Deep-Red Persistent Luminescence of Cr3+ in Garnets. *J. Am. Ceram. Soc.* **2017**, *100*, 4033.

(37) Elzbieciak, K.; Bednarkiewicz, A.; Marciniak, L. Sensors and Actuators B : Chemical Temperature Sensitivity Modulation through Crystal Field Engineering in Ga3+ Co-Doped Gd3Al5-XGaxO12: Cr3+, Nd3+ Nanothermometers. *Sens. Actuators, B* **2018**, *269*, 96−102.

(38) Ramalho, J. F. C. B.; Correia, S. F. H.; Fu, L.; António, L. L. F.; Brites, C. D. S.; André, P. S.; Ferreira, R. A. S.; Carlos, L. D. Luminescence Thermometry on the Route of the Mobile-Based Internet of Things (IoT): How Smart QR Codes Make It Real. *Adv. Sci.* **2019**, *6*, 1900950.

(39) Wang, Z.; Yu, S.; Zhang, H.; Duan, H. Thermochromic Luminescence and Dielectric Response of Copper(I) Iodide Based MOFs as Luminescent Thermometer. *Synth. Met.* **2019**, *255*, 116104.

(40) Wu, Y.; Zhang, X.; Zhang, Y.-Q.; Yang, M.; Chen, Z.-N. Achievement of Ligand-Field Induced Thermochromic Luminescence via Two-Step Single-Crystal to Single-Crystal Transformations. *Chem. Commun.* **2018**, *54*, 13961−13964.

(41) Du, P.; Cai, P.; Li, W.; Luo, L.; Hou, Y.; Liu, Z. Ratiometric Optical Thermometer Based on the Use of Manganese(II)-Doped Cs3Cu2I5 Thermochromic and Fluorescent Halides. *Microchim. Acta* **2019**, *186*, 730.

(42) Zhang, X.; Zhu, Z.; Guo, Z.; Sun, Z.; Chen, Y. A Ratiometric Optical Thermometer with High Sensitivity and Superior Signal Discriminability Based on Na3Sc2P3O12: Eu2+, Mn2+ Thermochromic Phosphor. *Chem. Eng. J.* **2019**, *356*, 413−422.

(43) Dragomirov, P.; Mendieta, A.; Abram, C.; Fond, B.; Beyrau, F. Planar Measurements of Spray-Induced Wall Cooling Using Phosphor Thermometry. *Exp. Fluid* **2018**, *59*, 42.

(44) Huanxiong, X.; Jiacai, L.; Gretar, T. Fully Resolved Numerical Simulations of Fused Deposition Modeling. Part II − Solidification, Residual Stresses and Modeling of the Nozzle. *Rapid Prototyp. J.* **2018**, *24*, 973−987.

(45) Duan, X.; Naterer, G. F. Heat Transfer in Phase Change Materials for Thermal Management of Electric Vehicle Battery Modules. *Int. J. Heat Mass Transfer* **2010**, *53*, 5176−5182.

(46) Datcu, S.; Ibos, L.; Candau, Y.; Matteï, S. Improvement of Building Wall Surface Temperature Measurements by Infrared Thermography. *Infrared Phys. Technol.* **2005**, *46*, 451−467.

(47) Wang, D.; Wang, M.; Lü, G. Synthesis, Crystal Structure and X-Ray Powder Diffraction Data of the Phosphor Matrix 4SrO·7Al2O3. *J. Mater. Sci.* **1999**, *34*, 4959.

(48) Danks, A. E.; Hall, S. R.; Schnepp, Z. The Evolution of "sol-Gel" Chemistry as a Technique for Materials Synthesis. *Mater. Horiz.* **2016**, *3*, 91.

(49) Lebourgeois, V.; Bégué, A.; Labbé, S.; Mallavan, B.; Prévot, L.; Roux, B. Can Commercial Digital Cameras Be Used as Multispectral Sensors? A Crop Monitoring Test. *Sensors* **2008**, *8*, 7300−7322.

Supporting Information

Thermochromic luminescent nanomaterials based on Mn^{4+}/Tb^{3+} codoping

for temperature imaging with digital cameras

Wojciech Piotrowski[1], Karolina Trejgis[1], Kamila Maciejewska[1], Karolina Ledwa[1],

Benoit Fond[2], Lukasz Marciniak[1]*

[1]Institute of Low Temperature and Structure Research, Polish Academy of Sciences,

Okólna 2, 50-422 Wroclaw, Poland

2 Institute of Fluid Mechanics and Thermodynamics, Otto-von-Guericke Universität
Magdeburg, Universitätsplatz 2, Magdeburg Germany

* corresponding author: *l.marciniak@intibs.pl*

KEYWORDS manganese, terbium, $Sr_4Al_{14}O_{25}$ nanocrystals, luminescent thermometry

Table S1. Results of ICP-EOS measurements for samples co-doped with Mn^{4+} and Tb^{3+} ions.

Sample	Concentration (in respect to the Al^{3+})			
	Mn^{4+} (%)	+/-	Tb^{3+} (%)	+/-
SAO 0.1% Mn^{4+},1% Tb^{3+}	0.1000	0.0051	1.000	0.053
SAO 0.1% Mn^{4+},5% Tb^{3+}	0.1015	0.0051	5.000	0.267
SAO 0.1% Mn^{4+},10% Tb^{3+}	0.1000	0.0051	9.609	0.534
SAO 0.1% Mn^{4+},20% Tb^{3+}	0.0956	0.0051	19.47	0.890
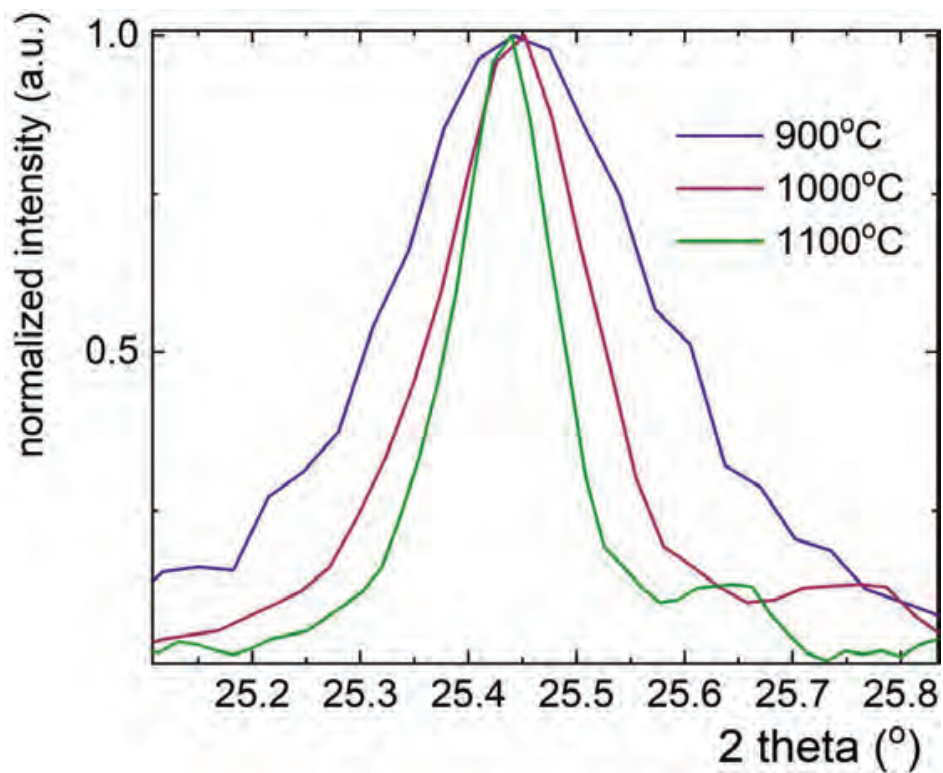
Figure S1. The narrowing of the X-ray diffraction peak of SAO:0.1%Mn^{4+} powders annealed at different temperatures.
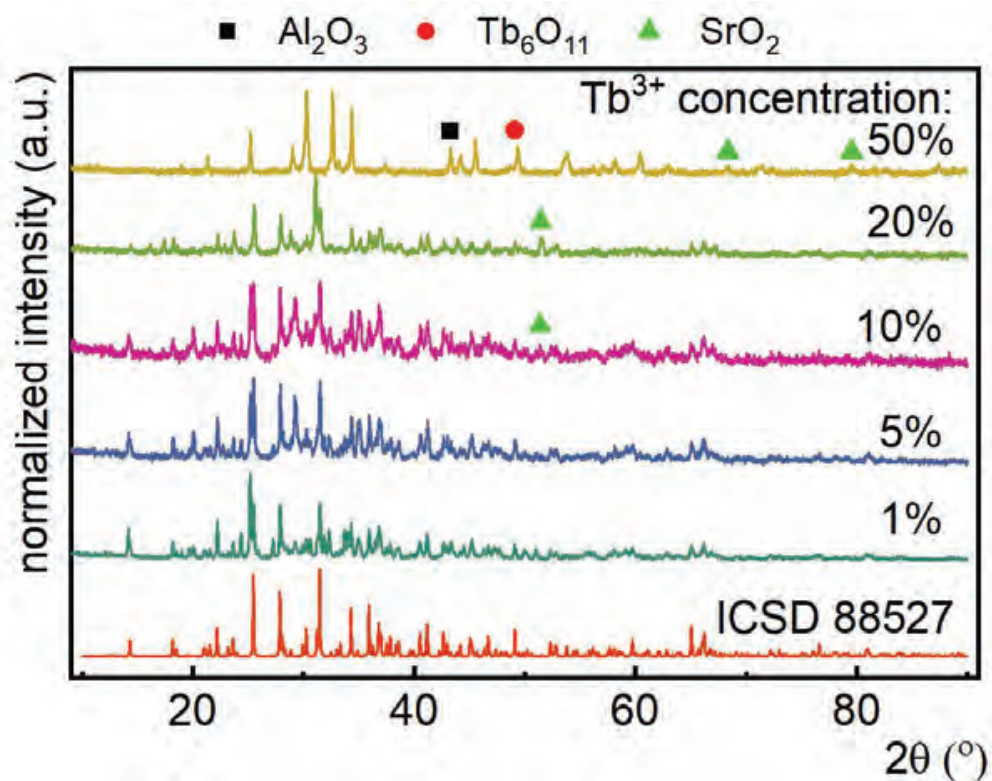
Figure S2. X-ray diffraction patterns of SAO:0.1% Mn^{4+}, x% Tb^{3+} powders annealed at 1000 °C.
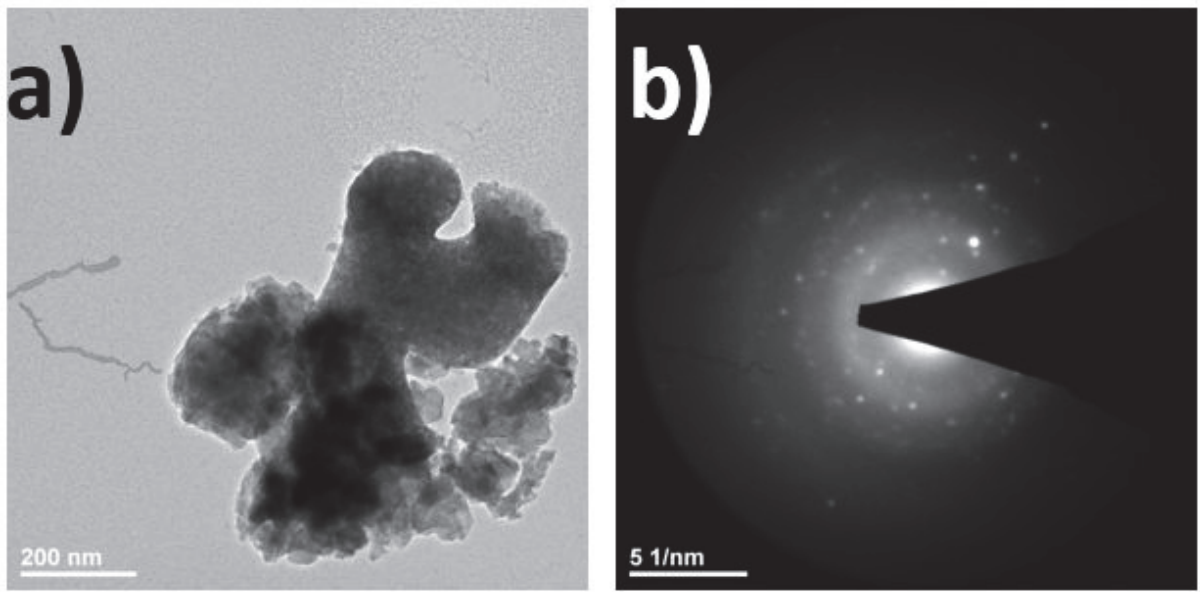
Figure S3. The representative TEM image –a and SAED reflection spots for SAO:Mn^{4+} powder –b annealed at 800 °C.
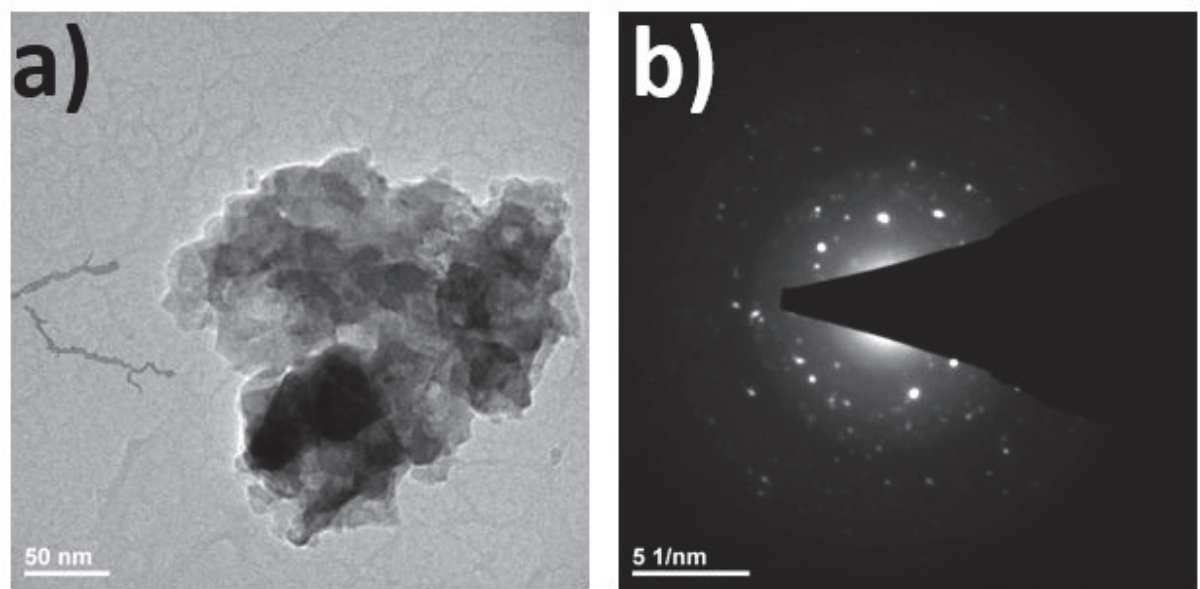
Figure S4. The representative TEM image –a and SAED reflection spots for SAO:Mn^{4+} powder –b annealed at 900 °C.
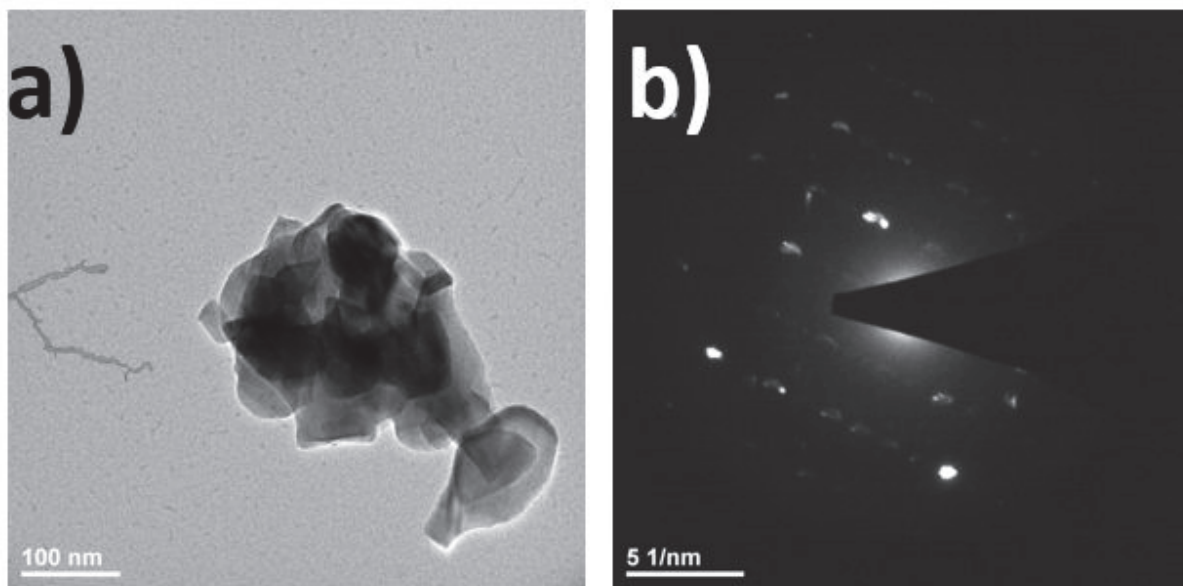
Figure S5. The representative TEM image –a and SAED reflection spots for SAO:Mn^{4+} powder –b annealed at 1000 °C.
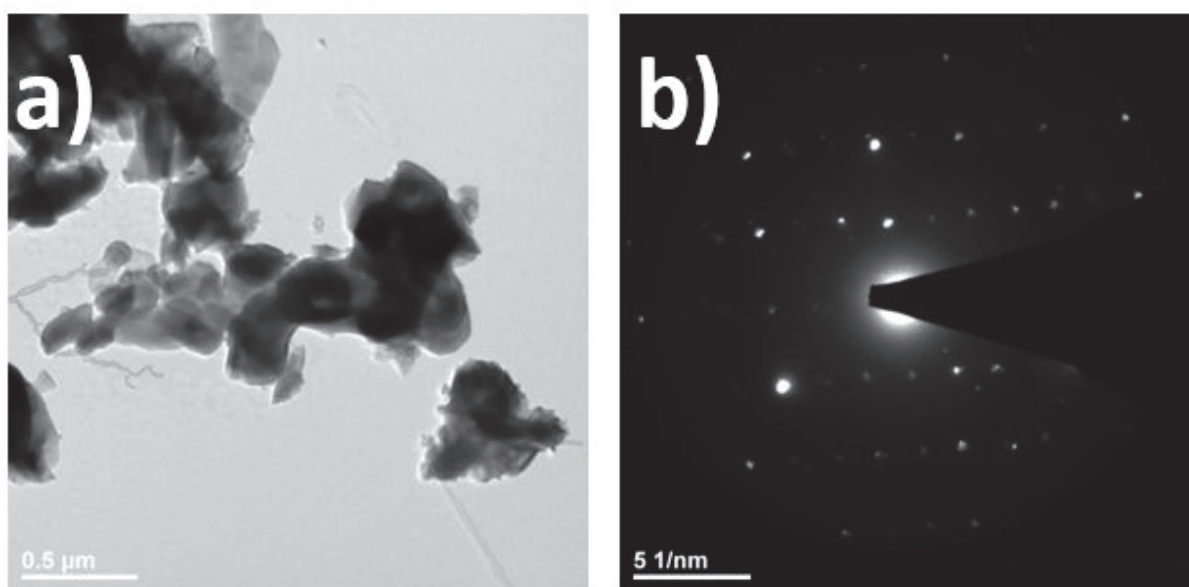
Figure S6. The representative TEM image –a and SAED reflection spots for SAO:Mn^{4+} powder –b annealed at 1100 °C.
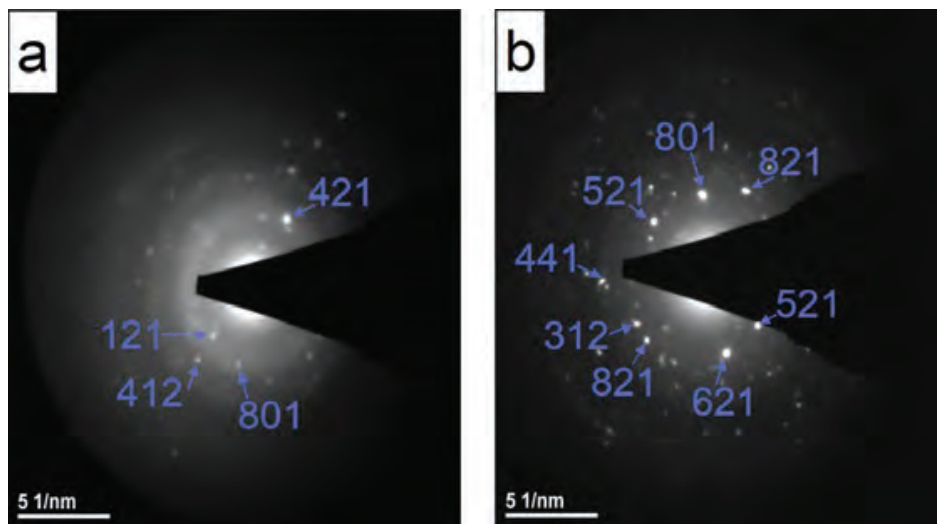
Figure S7. Analysis of SAED reflection spots for SAO:Mn^{4+} powder annealed at 800 °C – a and 900 °C - b.
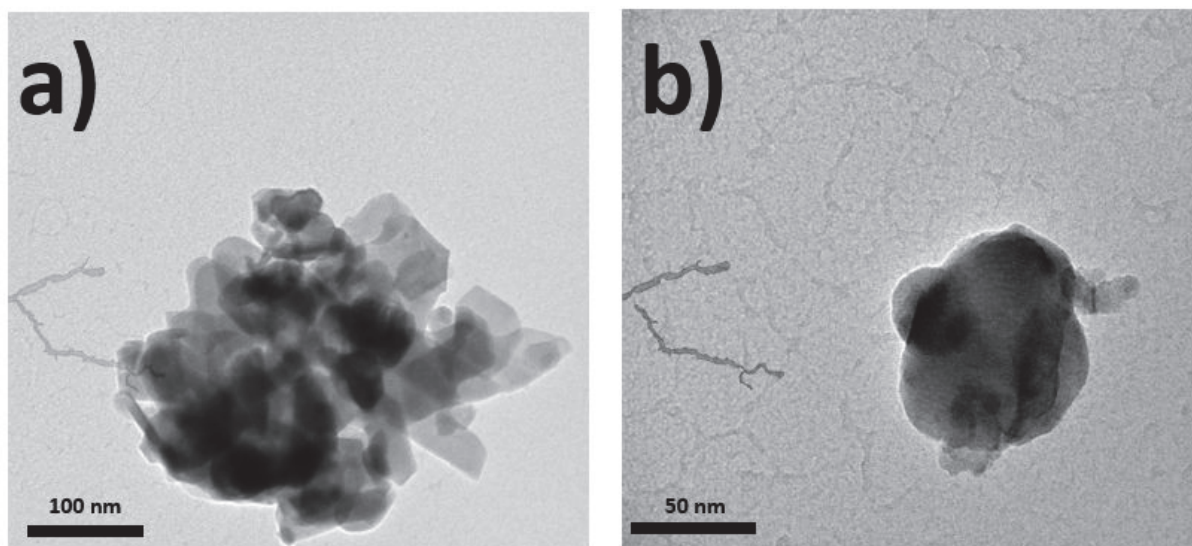
Figure S8. The representative TEM images –a,b for SAO:0.1%Mn^{4+}, 5%Tb^{3+} powder annealed at 1000 °C.
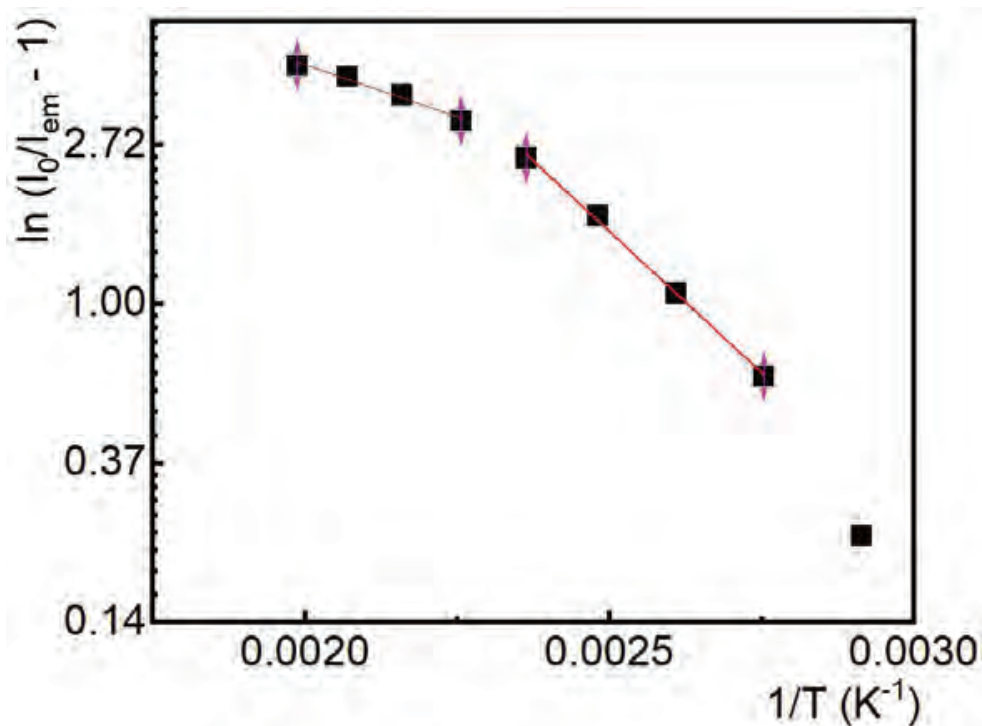
Figure S9. Integral emission intensity in function of 1/T for 650-658 nm range in SAO:Mn^{4+} annealed at 1000 °C.
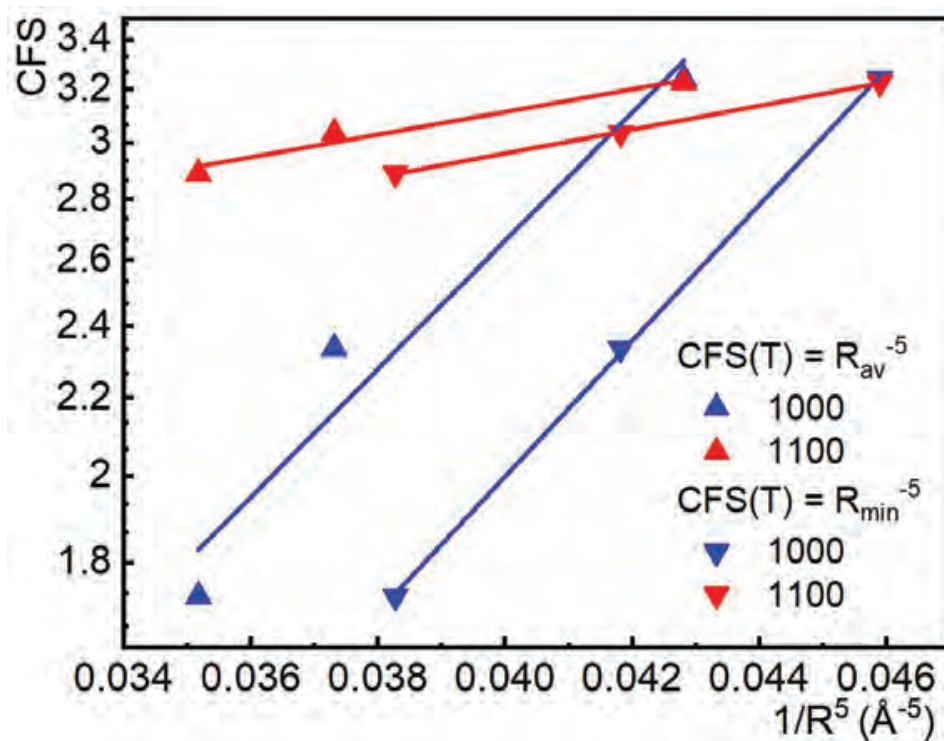
Figure S10. CFS as function of average (R_{av}) and minimum metal-oxide bond (R_{min}) for Mn^{4+} ions in different Al^{3+} sites in SAO:Mn^{4+} annealed at different temperatures.

S-6

284
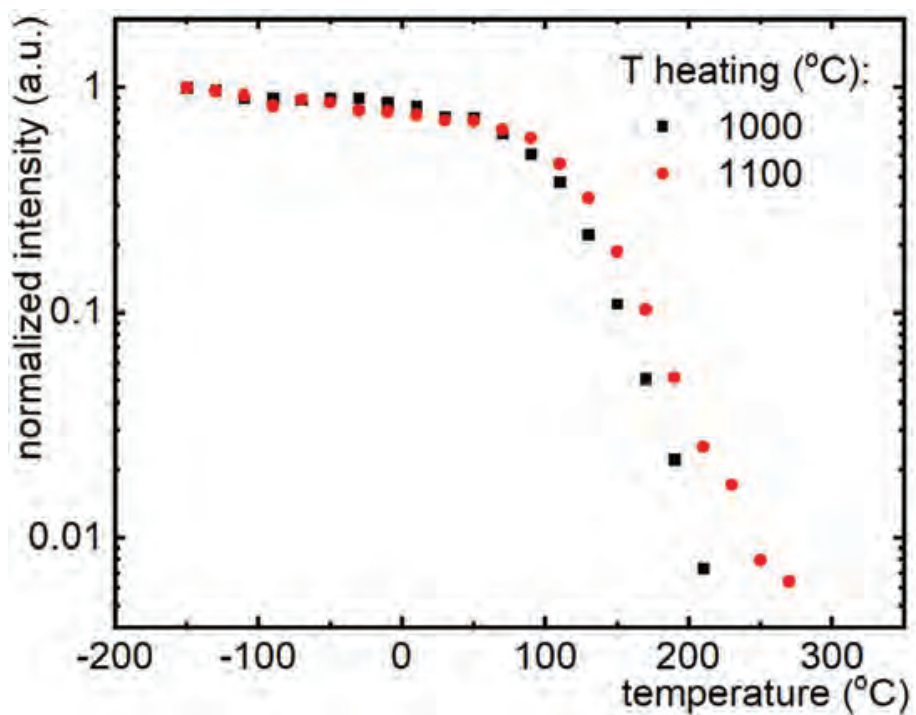
Figure S11. Thermal evolution of band integral intensities in 660-677 nm range for SAO:Mn^{4+} samples annealed at 1000 and 1100 °C respectively.
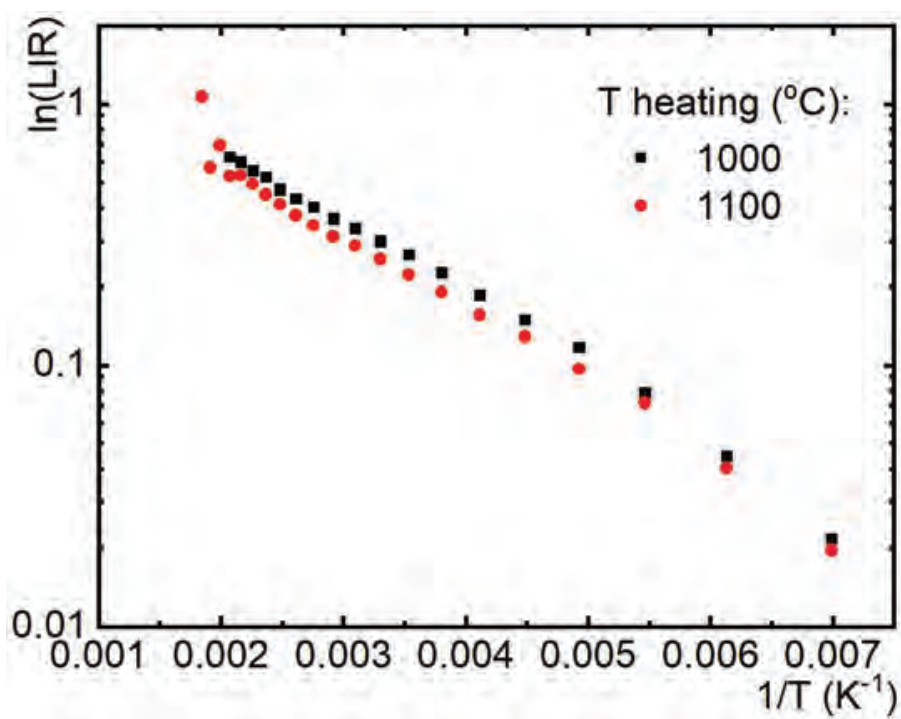
Figure S12. Graphic rerepresentation of the Boltzmann distribution through the ratio of the the bands in the 650-658 and 660-677 nm range in SAO:Mn^{4+} annealed at different temperatures.

S-7
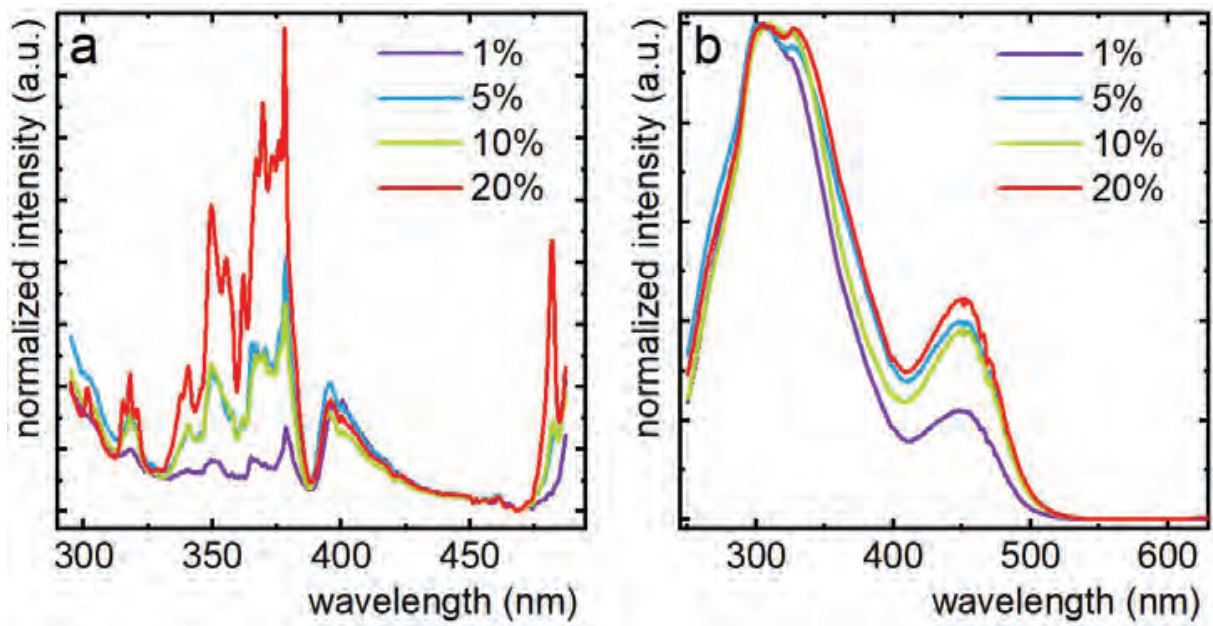
Figure S13. The influence of Tb^{3+} ions concentration on excitation spectra in SAO:Mn^{4+}, Tb^{3+} for 545 nm – a and 654 nm - b.
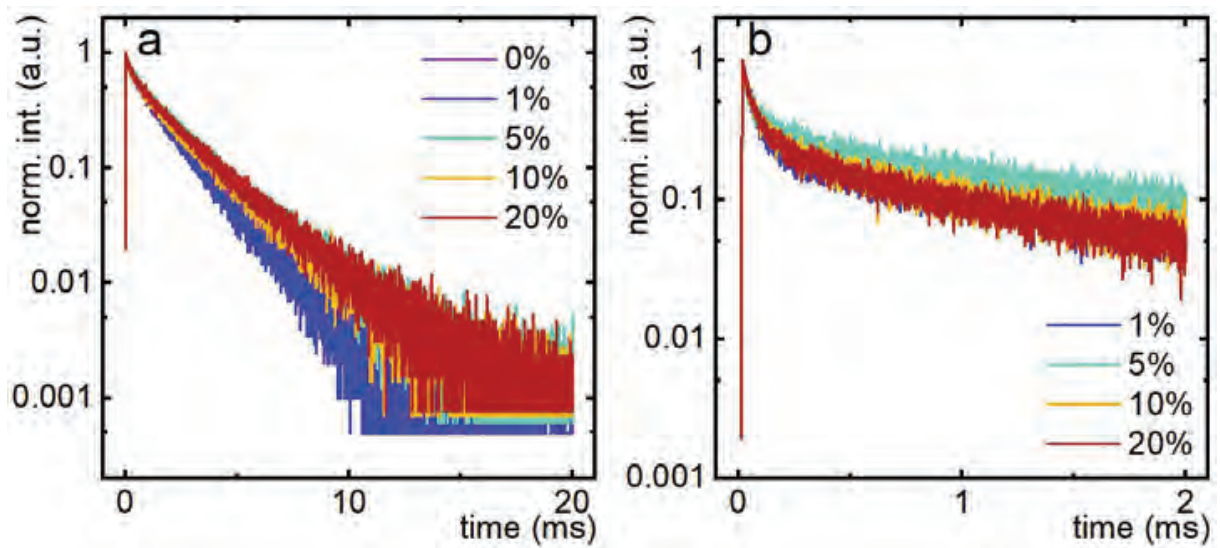
Figure S14. The influence of Tb^{3+} ions concentration on luminescent decays in SAO:Mn^{4+}, Tb^{3+} for λ_{em} = 654 nm – a and 545 nm - b.

286
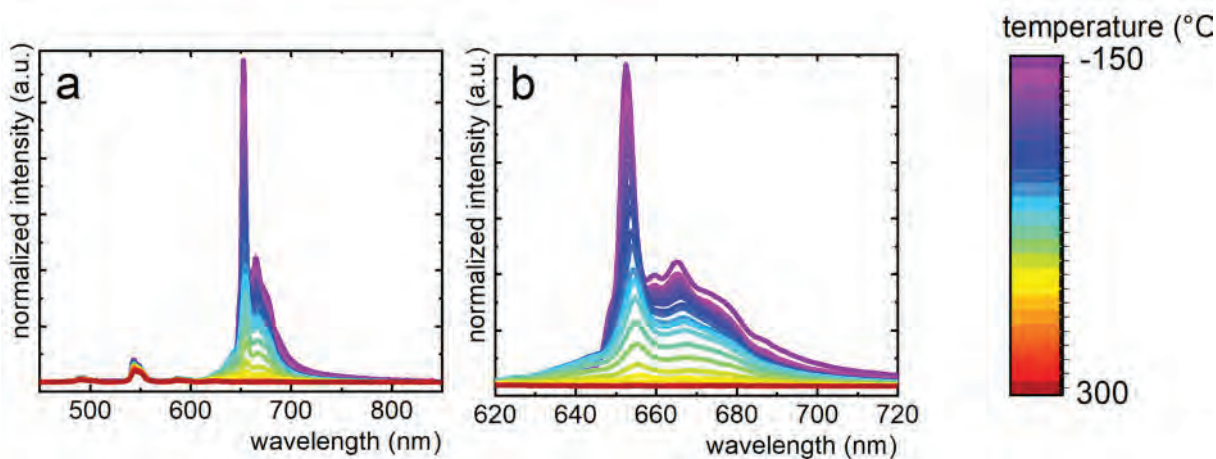
Figure S15. Thermal evolution of emission spectra for SAO:0.1%Mn^{4+}, 5%Tb^{3+}-a; and the zoom of the same spectra in the 620-720 nm spectral range-b.
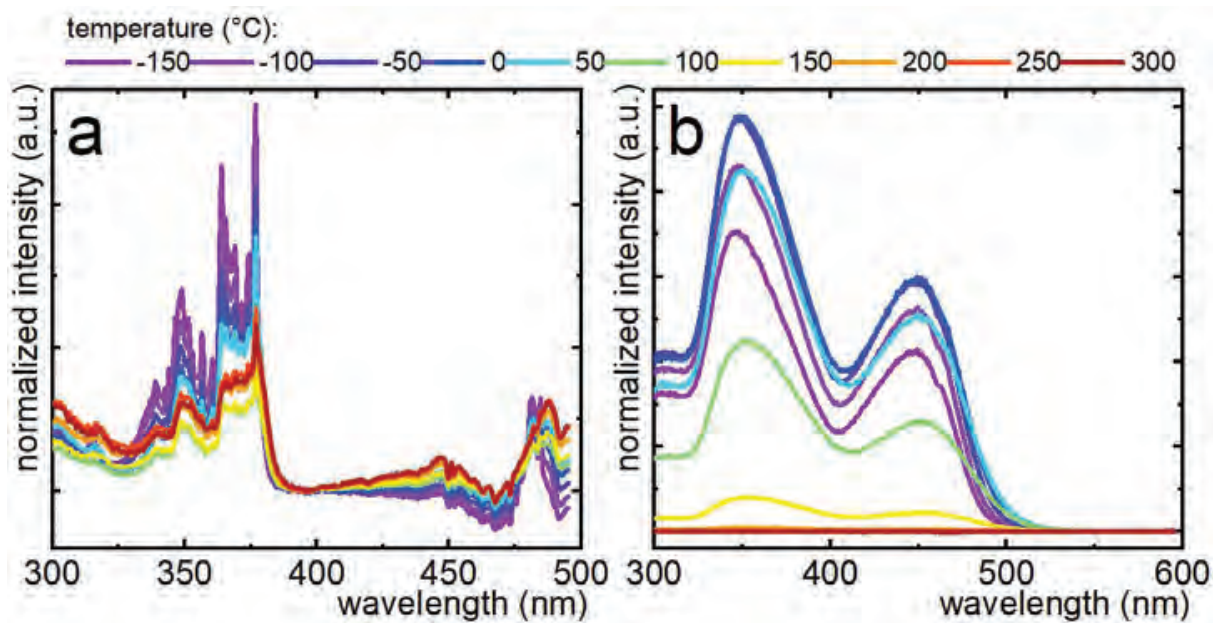
Figure S16. The influence of temperature on excitation spectra in SAO:0.1%Mn^{4+}, 5%Tb^{3+} for 545 nm – a and 654 nm – b.

S-9
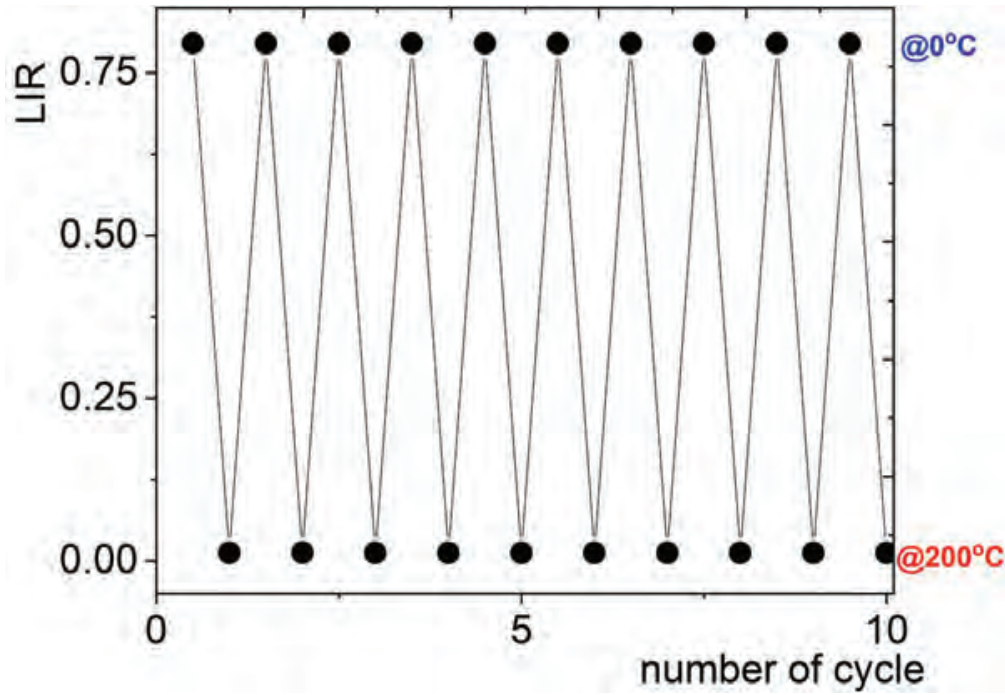
Figure 17 The heating-cooling cycle of the LIR for the representative sample of SAO:0.1%Mn^{4+}, 5%Tb^{3+}.

Temperature determination uncertainty was calculated using eq.S1:

$$\delta T = \frac{1}{S_R} \frac{\delta LIR}{LIR} \qquad \text{(eq. S1)}$$

S$_R$ is the relative sensitivity and δLIR/LIR determines the uncertainty of the LIR determination.

where δLIR/LIR was determined as follows:

$$\frac{\delta LIR}{LIR} = \sqrt{\left(\frac{\delta I_{Tb}}{I_{Tb}}\right)^2 + \left(\frac{\delta I_{Mn}}{I_{Mn}}\right)^2} \qquad \text{(eq. S2)}$$
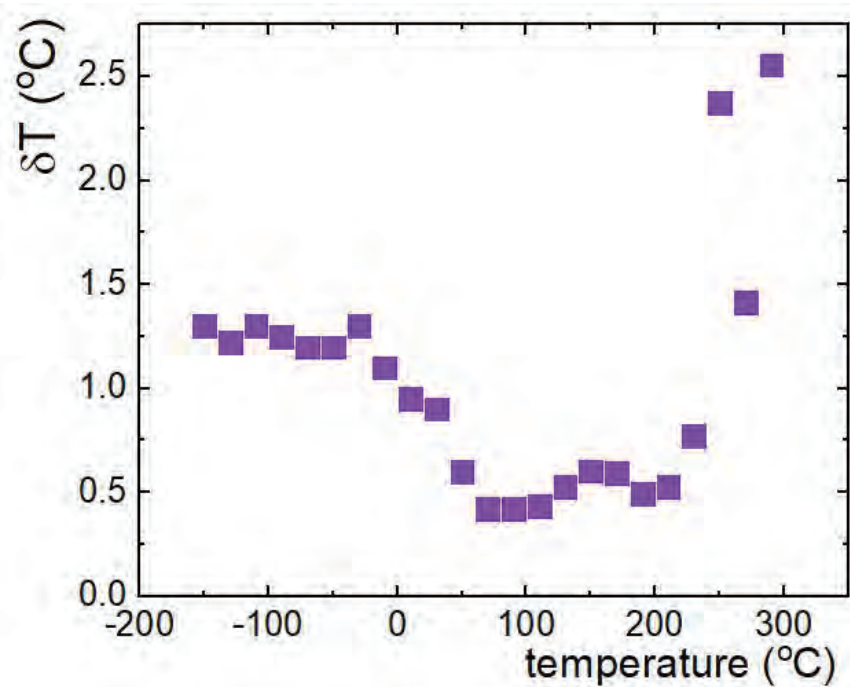
Figure S18. Thermal dependence of temperature estimation uncertainty for SAO:0.1%Mn^{4+}, 5%Tb^{3+}.
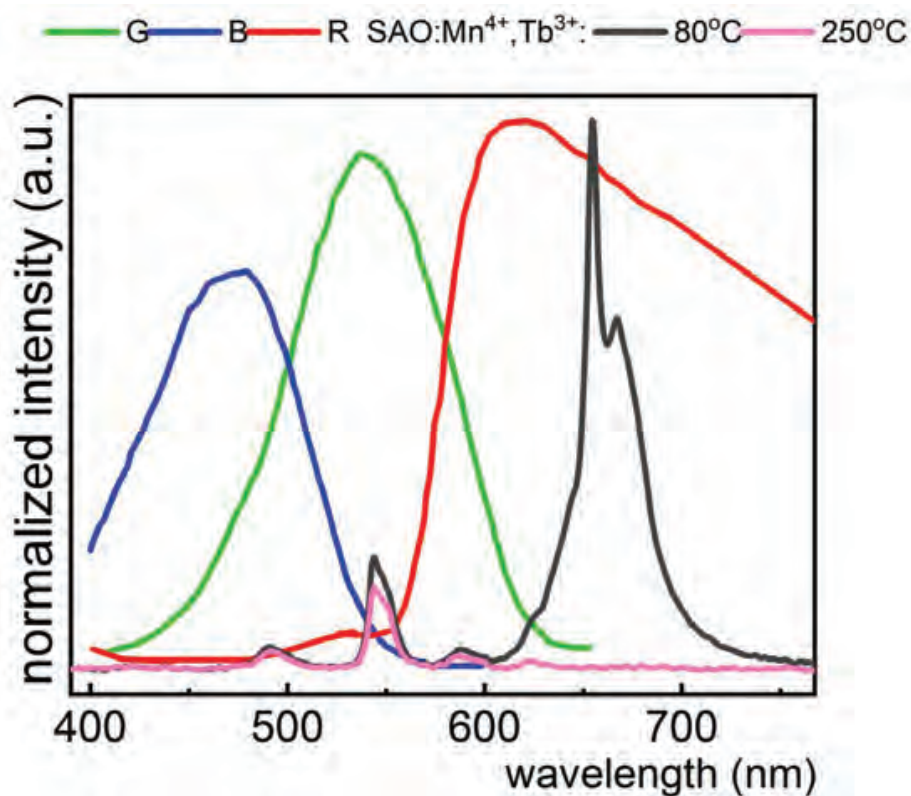
Figure S19. The comparison of the normalized emission spectra of SAO:Mn^{4+},Tb^{3+} nanocrystals measured at 80°C and 250°C with the colour filter curves of consumer digital cameras

S-11

t(s)= 0 5 10 15 20 25 30 35 40 45 50 55 60 65 70 75 80 85 90
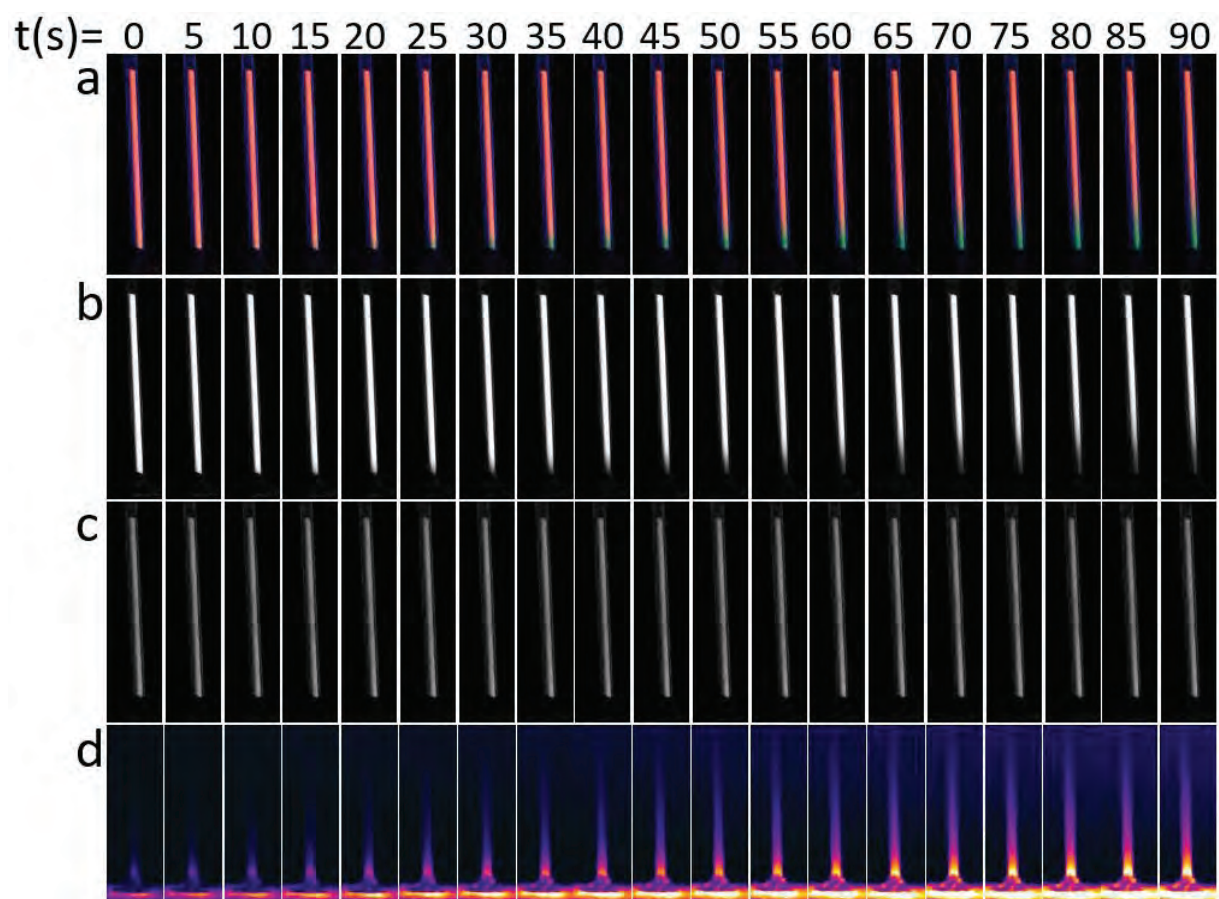
Figure S20. Photographs from digital camera – a, red – b and green channels of RGB colour images – c and photographs from thermovision camera of quartz tube with SAO:0.1%Mn^{4+}, 5%Tb^{3+} powder under UV light excitation recorded at different times of heating exposition – d.
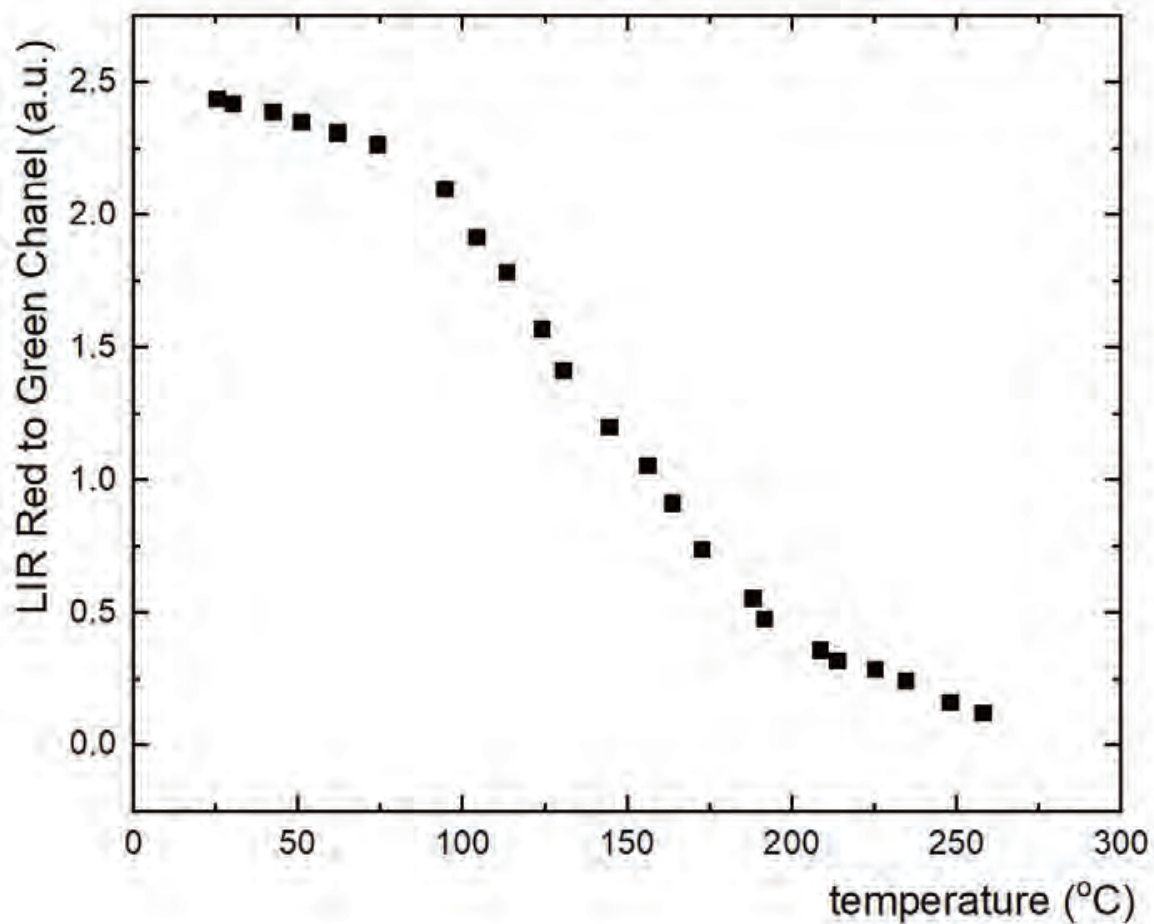
Figure S21. The calibration curve obtained by measuring the LIR as a emission intensity of Red to Green channels vs temperature controlled using thermovising camera.
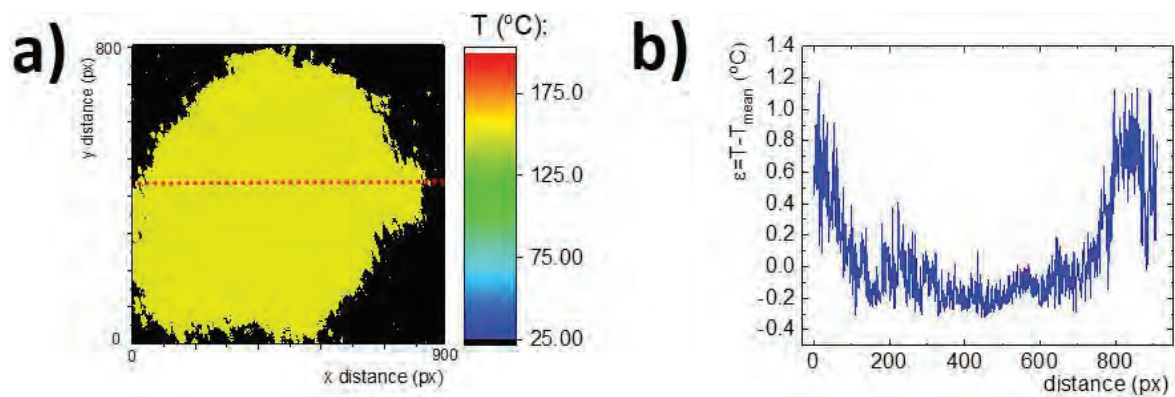
Figure S22. Thermal map of SAO:Mn^{4+},Tb^{3+} powder placed on the heating plate at 150°C –a and ε calculated across the doted red line presented in a- b.

Frontiers of Deep-Red Emission of Mn^{4+} Ions with Ruddlesden−Popper Perovskites

Wojciech M. Piotrowski,* Paulina Bolek, Mikhail G. Brik, Eugeniusz Zych, and Lukasz Marciniak*

Cite This: https://doi.org/10.1021/acs.inorgchem.3c03113

Read Online

ACCESS | 📊 Metrics & More | 📖 Article Recommendations | 🆘 Supporting Information

ABSTRACT: It is well-known that the chemical composition of the host material significantly affects the spectroscopic performance of transition metal ions. However, it is worth noting that also the structure and symmetry of crystallographic sites play significant roles in transition metal ion luminescence. In this study, we demonstrate three perovskite structures of strontium titanate forming so-called Ruddlesden−Popper phases doped with Mn^{4+} ions. The observed reduction in the average Ti^{4+}−O$^{2−}$ distance in the series SrTiO$_3$–Sr$_2$TiO$_4$–Sr$_3$Ti$_2$O$_7$ allowed for a record-breaking shift in the spectral position of Mn^{4+} emission band with a maximum of around 734 nm and led to an improvement of the already impressive thermometric performance of SrTiO$_3$:Mn^{4+} in ratiometric and lifetime-based approaches. This research encourages a further search for structures that, with the help of the developed correlations between structural and optical properties, could lead to the discovery of phosphors beyond the limits established so far.
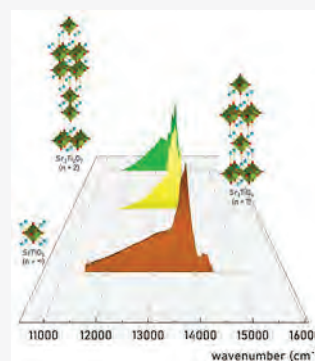
INTRODUCTION

Tetravalent manganese (Mn^{4+}) ions are some of the most intensively investigated transition metal ions as luminescent centers for inorganic phosphors.[1−3] The main reason for this is their unique characteristics, including the high absorption cross-section in a wide spectral range of excitability from ultraviolet (UV) up to even 600 nm and bright red/near-infrared (NIR) emission, which lead to the selection of Mn^{4+} luminescence as suitable for many specific applications.[4−6] It is known from previous studies that the spectroscopic properties of Mn^{4+} ions, as well as their susceptibility to temperature changes, are strongly dependent on the host material in which they are embedded. Several reviews have presented the correlations between the structure of Mn^{4+}-doped phosphors and their luminescence and thermometric properties.[6−8] It should be noted that even small differences in the crystallographic structure of the host material in, for example, polytypes can result in a significant modification of the luminescence range and its thermal quenching rate.[9]

Among the materials investigated to date, it has been determined that the Mn^{4+} emission band maximum ranges between 620 and 725 nm associated with the ^{2}E → ^{4}A$_2$ electronic transition. The fact that the ^{2}E level is the first excited state of Mn^{4+} ions is the result of the high positive effective charge of the Mn^{4+} ions, which ensures that the crystal field strength (CFS) is limited to be strong (roughly $Dq/B >$ 2.2).[10] To date, the lowest CFS affecting the Mn^{4+} ions (parameter $Dq/B \approx 2.47$) has been reported for SrTiO$_3$ with an emission maximum located at ∼725 nm.[11] In addition, it is worth noting that the great susceptibility of the spectroscopic properties of Mn^{4+} in SrTiO$_3$ to temperature changes makes it

a promising material for use in luminescence thermometry. The strontium titanate SrTiO$_3$ owes the aforementioned parameters to the regular distribution of well-ordered Ti^{4+} octahedra and less ordered Sr^{2+} cations.[11,12] However, the other strontium titanate perovskite structures present different configurations for a similar group of atoms known as Ruddlesden−Popper (R-P) phases. Similar to SrTiO$_3$, other R-P phases contain Ti^{4+} octahedral sites, suitable for Mn^{4+} ions, but differences in the surroundings of the dopant ions will affect their luminescence and temperature dependence. In this way, it is possible to shift the position of the Mn^{4+} emission maximum above the so far defined limit of 725 nm and enhance thermometric performance with respect to the SrTiO$_3$:Mn^{4+} phosphor.

In this work, the influence of a structure of three representatives of the R-P group of perovskite strontium titanates, e.g. SrTiO$_3$, Sr$_2$TiO$_4$, and Sr$_3$Ti$_2$O$_7$, on the luminescence of Mn^{4+} ions was investigated. The theoretically calculated positions of the energy levels of Mn^{4+} ions were compared with experimentally determined excitation and emission spectra. Also included in the discussion is the influence of the charge transfer transition between Ti^{4+} and the O$^{2−}$ ions, as well as the Ti^{3+} luminescence observed in Sr$_3$Ti$_2$O$_7$:Mn^{4+}. Thermal evolution of emission spectra and

A

luminescent decay profiles were analyzed and therefore three temperature-sensitive parameters were developed, which complement each other to achieve high sensitivity in the temperature range of 13−300 K.

■ EXPERIMENTAL SECTION

The SrTiO$_3$:0.1% Mn^{4+}, Sr$_2$TiO$_4$:0.1% Mn^{4+}, and Sr$_3$Ti$_2$O$_7$:0.1% Mn^{4+} phosphors were synthesized using a modified Pechini method.[13] The following starting materials were used as reagents without further purification: Sr(NO$_3$)$_2$ (99.9965% purity, Alfa Aesar), Ti(OC$_4$H$_9$)$_4$ (99+% purity, Alfa Aesar), 2,4-pentanedione (C$_5$H$_8$O$_2$, 99% purity, Alfa Aesar), MnCl$_2$·4H$_2$O (>99.0% purity, Sigma-Aldrich), and citric acid (C$_6$H$_8$O$_7$, >99.5% purity, Alfa Aesar). First, stoichiometric amounts of Sr(NO$_3$)$_2$ and MnCl$_2$·4H$_2$O were dissolved in deionized water and mixed together. In a separate beaker, an appropriate amount of Ti(OC$_4$H$_9$)$_4$ was mixed with 2,4-pentanedione in a 1:1 molar ratio in order to stabilize the Ti(OC$_4$H$_9$)$_4$ solution. The contents of the beaker were gently stirred until a transparent, yellowish solution was obtained, which was then combined with the stabilized nitrate solution. Immediately after that, anhydrous citric acid was added to the mixture with the molar ratio of citric acid to all metals set to 6:1. Finally, PEG-200 was added to the mixture in a 1:1 molar ratio with respect to citric acid. The resulting solutions were then dried for 7 days at 363 K until resins were formed. Next, the samples with 0.1% Mn^{4+} with respect to the Ti^{4+} ions were calcined in an air atmosphere. SrTiO$_3$:0.1% Mn^{4+} and Sr$_2$TiO$_4$:0.1% Mn^{4+} were annealed at 1173 K for 3 h. In the case of Sr$_3$Ti$_2$O$_7$:0.1% Mn^{4+}, a series of materials were made under different annealing conditions to optimize them (at a temperature in the range of 1173−1773 K, for 3 or 12 h). Finally, the obtained powders were ground in an agate mortar.

No uncommon hazards were noted.

Characterization. All of the synthesized materials were examined by powder X-ray diffraction (XRPD) measurements carried out on a PANalitycal X'Pert diffractometer equipped with an Anton Paar TCU 1000 N temperature control unit using Ni-filtered Cu Kα_1 radiation (1.54056 Å, V = 40 kV, I = 30 mA).

The excitation and emission spectra were measured using a double-grating FLS1000 spectrometer from Edinburg Instruments Ltd. equipped with a 450 W xenon lamp and a 60 W xenon flash lamp as excitation sources for continuous and pulse excitation, respectively, and a Hamamatsu R928P high-gain photomultiplier detector cooled to 253 K with a Peltier plate. The sample was mounted on the copper holder of a closed-cycle helium cryostat (Lake Shore Cryotronics, Inc.) using Silver Adhesive 503 glue from Electron Microscopy Sciences.

Thermal dependences of the luminescence intensity ratio (LIR) were fitted using the Mott−Seitz model (eq S1). The average lifetimes of the excited states were calculated with the use of a double-exponential function according to the procedure described in eqs S2 and S3 in the Supporting Information.

■ RESULTS AND DISCUSSION

Structural and Morphological Characterization. Ruddlesden−Popper (R-P) phases are a group of materials that belongs to the perovskite family which, in the case of strontium titanates, may be expressed with the chemical formula: Sr$_{n+1}$Ti$_n$O$_{3n+1}$. Their structure can be described in terms of n layers with structures of the perovskite type (SrTiO$_3$) separated by unit cells with the rock-salt-type structure (SrO) (Figure 1a). The repeat unit of each R-P structure is defined by the n number from its general formula; i.e. for Sr$_3$Ti$_2$O$_7$ when n = 2, there are two layers of SrTiO$_3$ surrounded by single SrO layers. However, for the most common SrTiO$_3$ host material, n = ∞ is due to the lack of SrO type layers. This kind of structural change results in the reduction of symmetry from the cubic system of the $Pm\bar{3}m$
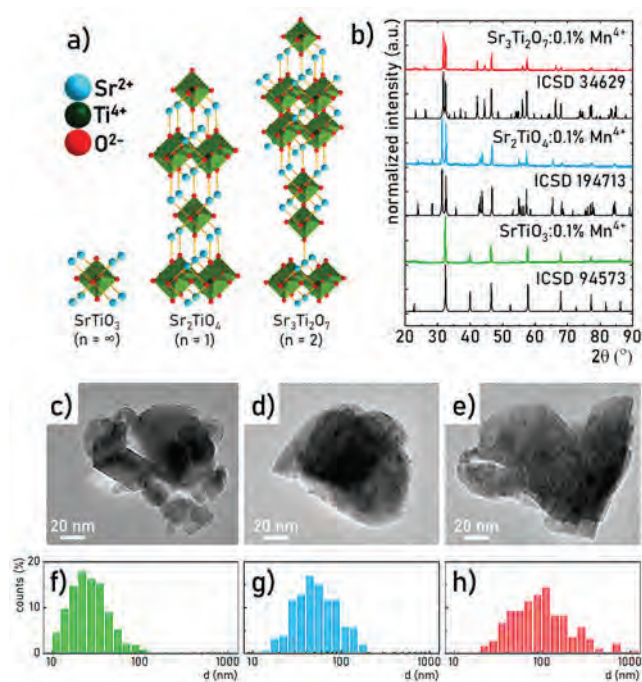
Figure 1. (a) Schematic comparison of structures of R-P phases. (b) XRPD patterns of SrTiO$_3$, Sr$_2$TiO$_4$, and Sr$_3$Ti$_2$O$_7$ doped with 0.1% Mn^{4+} ions. (c−e) Representative TEM images and (f−h) particle size distributions of (c, f) SrTiO$_3$, (d, g) Sr$_2$TiO$_4$, and (e, h) Sr$_3$Ti$_2$O$_7$ doped with 0.1% Mn^{4+} ions.

space group for SrTiO$_3$ to the tetragonal system of the $I4/mmm$ space group for other R-P phases. Moreover, it can be noted that Sr^{2+} ions are located in 12-fold and 9-fold coordinated sites in SrTiO$_3$ and Sr$_2$TiO$_4$, respectively, while in Sr$_3$Ti$_2$O$_7$ a combination of 12-fold and 9-fold coordination of Sr^{2+} occurs. However, regardless of the host material, the structure contains 6-fold-coordinated Ti^{4+} octahedral sites.

When considering the doping of R-P phases with Mn^{4+} ions, due to the preferred 6-fold coordination and the same electronic charge, Mn^{4+} will mostly be located in Ti^{4+} sites. For the octahedral Ti^{4+} site in the SrTiO$_3$ structure, six equal bonds with R = 1.9517 Å are reported. Therefore, a Ti^{4+} site is characterized by the O_h point group. In the case of Sr$_2$TiO$_4$, the distortion of the octahedra with stretching along the c axis (parallel to the distribution of the SrTiO$_3$ planes) results in the contraction of the four bonds with R = 1.9433 Å at the expense of two longer Ti^{4+}−O^{2-} distances with R = 1.9803 Å. Moreover, the replacement of the SrTiO$_3$-like single layer with the double layer in Sr$_3$Ti$_2$O$_7$ leads to further modifications of the Ti^{4+} sites. The contraction of the Ti^{4+} octahedra along the c-axis to R = 1.9157 Å and the expansion of two different pairs of bonds with R = 1.9500 Å can be observed. Therefore, for Sr$_2$TiO$_4$ and Sr$_3$Ti$_2$O$_7$ the point group of the Ti^{4+} site is reduced to D_{4h} with respect to SrTiO$_3$. Comparing the average Ti^{4+}−O^{2-} distances for n = 1, 2 and ∞, it can be found that the highest R_{av} = 1.9556 Å was achieved for Sr$_2$TiO$_4$ and the lowest R_{av} = 1.9271 Å for Sr$_3$Ti$_2$O$_7$ with respect to 1.9517 Å for SrTiO$_3$.

XRPD patterns of three R-P materials were compared with reference data (ICSD 94573, 194713, and 34629 for SrTiO$_3$, Sr$_2$TiO$_4$, and Sr$_3$Ti$_2$O$_7$, respectively) to verify their phase purity (Figure 1b). In the case of SrTiO$_3$ and Sr$_2$TiO$_4$ materials doped with 0.1% Mn^{4+} ions, the XRPD patterns

294

correspond well with the ICSD standard patterns. In the case of $Sr_3Ti_2O_7$, optimization of the annealing conditions was performed (Figure S1). For samples annealed at 1173−1473 K, additional reflections originating from the $SrTiO_3$ and Sr_2TiO_4 phases were observed. Above 1673 K, the presence of Sr_2TiO_4 was reduced, but still reflections associated with $SrTiO_3$ were found. Finally, a pure phase was achieved after annealing at 1773 K. This is consistent with the lattice energy calculations reported by Haeni et al., who confirm that it is possible to obtain nanocrystalline $Sr_3Ti_2O_7$ at a temperature higher than that for the other two R-P phases.[14] A more detailed analysis of the structure was carried out using Rietveld refinement (Figure S2). It was observed that the unit cell parameter a (which equals b) decreases in the following order: $SrTiO_3 > Sr_3Ti_2O_7 > Sr_2TiO_4$ (Table S1). This suggests that when the number of the SrO layers increases with respect to perovskite layers (from 0:1 for $SrTiO_3$ to 1:1 for Sr_2TiO_4), the $a-b$ plane area decreases. On the other hand, the c parameter increases with n with the order $n = \infty$, 1, 2, which is expected due to the decrease in symmetry and the need to include more atoms in the unit cell.

For $SrTiO_3$ and Sr_2TiO_4 annealed at 1173 K and $Sr_3Ti_2O_7$ annealed at 1773 K, TEM images were performed (Figure 1c− e and Figures S3−S5). The obtained images reveal that the materials under investigation consist of well-crystallized particles with a tendency to agglomerate, which is a typical feature of materials prepared with the Pechini method. For $SrTiO_3$, particles with a more rounded shape were obtained compared to Sr_2TiO_4 prepared under the same annealing conditions, which corresponds well with a reduction in symmetry from a cubic to a tetragonal system. On the contrary, $Sr_3Ti_2O_7$ tends to form elongated needle-shaped particles, which can be related to the significantly elongated unit cell in the z-direction. Such a modified shape of the unit cell of $Sr_3Ti_2O_7$ and a much higher annealing temperature are reflected in the particle size distribution (Figure 1f−h). Despite the presence of small (<50 nm) particles in all R-P materials, it can be clearly seen that the smallest particles were obtained for $SrTiO_3$ and the largest for $Sr_3Ti_2O_7$. This is in agreement with the average particle sizes, which equal 29, 62, and 133 nm for $SrTiO_3$, Sr_2TiO_4, and $Sr_3Ti_2O_7$, respectively.

Characterization of Luminescent Properties. The simplified form of a well-known configurational coordinate diagram for TM ions with a $3d^3$ electronic configuration (like Mn^{4+}) is presented in Figure 2a. Using an appropriate excitation wavelength, it is possible to efficiently excite electrons of Mn^{4+} ions from the $^4A_2$ ground state to the $^4T_1$ or $^4T_2$ excited state, followed by the nonradiative depopulation to the lowest ^2E excited state. As a result of its radiative depopulation, the emission in the red spectral range associated with the $^2E \rightarrow {}^4A_2$ electronic transition can be observed. At first, based on crystal field theory, local site symmetry is considered to determine the degeneracy of both the orbital triplet and doublet states, which affects the width of the excitation bands. The exchange charge model of crystal field[15] was used to calculate the Mn^{4+} energy levels in all studied materials. For R-P materials, the O_h point group in $SrTiO_3$ and the D_{4h} point group in Sr_2TiO_4 and $Sr_3Ti_2O_7$ can be considered as the relatively high symmetry of Mn^{4+} sites. For this reason, the number of non-zero crystal field parameters is only 2 for $SrTiO_3$ whereas it is 3 for Sr_2TiO_4 and $Sr_3Ti_2O_7$ structures (Table 1). Moreover, it should be mentioned that due to the reduction of the octahedral symmetry from O_h to
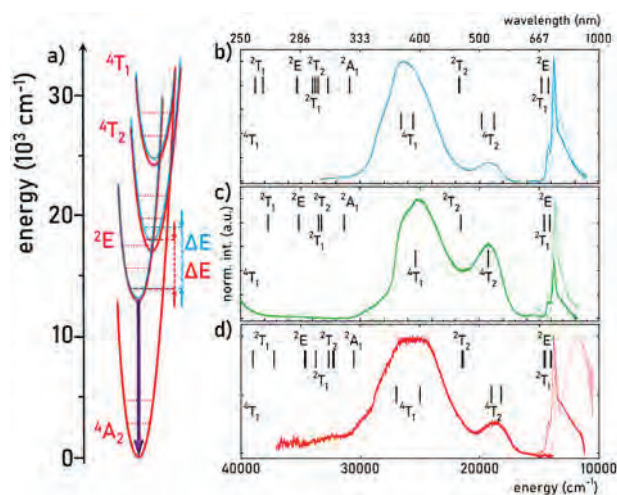
Figure 2. (a) Simplified configurational coordinate diagram for Mn^{4+} ions. Comparison of the calculated Mn^{4+} energy levels (vertical lines) with experimental excitation (measured at 13 K) and emission spectra (measured at 13 K in light color and at 220 K in deep color) in (b) Sr_2TiO_4, (c) $SrTiO_3$, and (d) $Sr_3Ti_2O_7$.

Table 1. Non-Zero Parameters of Crystal Field B_p^k and Racah parameters B and C (all in cm^{-1}) for Mn^{4+} in $SrTiO_3$, Sr_2TiO_4, and $Sr_3Ti_2O_7$

	$SrTiO_3$	Sr_2TiO_4	$Sr_3Ti_2O_7$
B_2^0	0	−706	1464
B_4^0	5064	4895	5073
B_4^4	25320	25994	23887
B	570	690	650
C	3254	3030	3053

D_{4h}, the irreducible representation of the excited states should be changed; however, to keep the nomenclature and labeling simple and comparable among all three host materials, the designations of the excited states corresponding to the O_h symmetry are used in the manuscript. Therefore, no degeneracy removal of the orbital triplet and doublet states in $SrTiO_3$ is expected, while in the two other host materials, $^4T_2$ and $^4T_1$ triplets and ^2E doublets will be split.

To verify this, Figure 2b−d compares the experimental excitation spectra measured at 13 K and the emission spectra taken at 13 and 220 K with the values of the calculated energy levels (obtained by the diagonalization of the corresponding crystal field Hamiltonians with the crystal field parameters from Table 1) for Sr_2TiO_4 (Figure 2b), $SrTiO_3$ (Figure 2c), and $Sr_3Ti_2O_7$ (Figure 2d) doped with Mn^{4+} ions. The exact values of the theoretical data are listed in Table S2. It can be seen that the calculated energies of $^4T_1$, $^4T_2$, and ^2E levels correspond well with the experimental data. Comparing the maxima of both $^4A_2 \rightarrow {}^4T_1$ and $^4A_2 \rightarrow {}^4T_2$ excitation bands and $^2E \rightarrow {}^4A_2$ emission bands, it can be seen that their energies decrease in the order $Sr_2TiO_4 > SrTiO_3 > Sr_3Ti_2O_7$, in agreement with the average metal−oxygen distance R_{av} (Figures S6 and S7).

Another well-detectable band in the emission spectrum of $SrTiO_3:Mn^{4+}$ is a broad band centered at 500 nm, which has been attributed to a charge transfer (CT) transition from Ti^{4+} to O^{2-} ions. Figure S8 shows the effect of the excitation wavelength on the ratio of CT and Mn^{4+} emission bands in $SrTiO_3:Mn^{4+}$. Although the use of $\lambda_{exc} = 365$ nm would excite
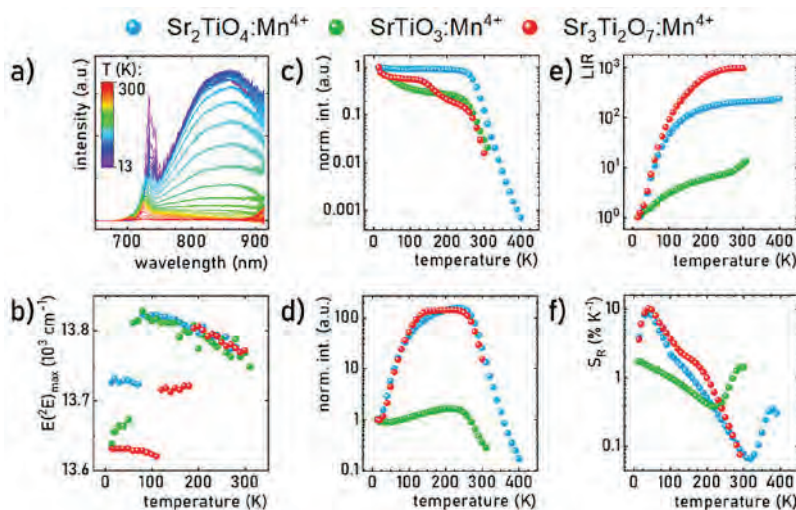
Figure 3. (a) Thermal evolution of emission spectra of $Sr_3Ti_2O_7$ doped with 0.1% Mn^{4+} (λ_{exc} = 387 nm). (b) Thermal evolution of the spectral position of $^2E \rightarrow {}^4T_2$ emission band maximum for Mn^{4+} doped R-P materials. Influence of the host material composition on the thermal evolution of emission intensity of (c) 730−745 nm spectral range and (d) 690−705 nm spectral range and (e) their LIR and (f) relative sensitivity.

the Mn^{4+} emission so that CT luminescence would be virtually impossible to detect, λ_{exc} = 380 nm that allows the most intense emission of Mn^{4+} ions, which are the focus of the work, was selected for further measurements (Figure S9). In addition, it should be mentioned that the CT emission band was also detectable for $Sr_2TiO_4:Mn^{4+}$ and $Sr_3Ti_2O_7:Mn^{4+}$, even though its intensity was much lower with respect to the Mn^{4+} band (Figure S10). It should be mentioned that the position of the observed CT bands in Sr_2TiO_4 and $Sr_3Ti_2O_7$ stays in agreement with the previously reported results in the literature.[16,17] Comparing the position of both the emission and excitation bands of the CT transition, it was noted that their energy decreases in the same order as the bands of Mn^{4+} ions (Sr_2TiO_4 > $SrTiO_3$ > $Sr_3Ti_2O_7$), confirming that they are also affected by the decrease in R_{av} value.

In the case of the emission spectra of $Sr_3Ti_{i2}O_7$, a broad band with a maximum at ∼850 nm with intensity similar to or even higher than that of the Mn^{4+} emission band is observed. Comparing the quenching rate of the excitation band for λ_{em} = 850 nm, it can be seen that it is faster than for the maximum of Mn^{4+} emission, namely λ_{em} = 733.5 nm (Figure S11). Considering the possibilities of the electronic transitions that may occur in $Sr_3Ti_2O_7$ solely doped with Mn^{4+} ions, it may be suggested that the emission band at 850 nm is related with the $^2E \rightarrow {}^2T_2$ transition of Ti^{3+} ions. To confirm this, the emission spectrum for the undoped $Sr_3Ti_2O_7$ material was verified (Figure S12). It was found that there is a broad band with a maximum at 804 nm with a weak intensity with respect to the Mn^{4+}-doped counterpart. Furthermore, using the strategy of stabilizing Ti^{3+} ions with La^{3+} ions presented so far in the $Sr^{2+}Ti^{4+}O_3$ host material,[18,19] emission and excitation spectra were performed for $Sr_3Ti_2O_7:1\%$ La^{3+} (Figure S13). In this case, a broad emission band centered at about 780 nm was also observed. The shift in the position of this band for $Sr_3Ti_2O_7:1\%$ La^{3+} with respect to 850 nm in $Sr_3Ti_2O_7:1\%$ Mn^{4+} may be the result of a change in local symmetry with the assumption that the most intense emission comes from Ti^{3+} ions stabilized with La^{3+} ions with respect to Ti^{3+} ions formed with the presence of oxygen vacancies, which at the same time should play the role of suppressing the emission of luminescent centers. In addition, a broad band with a maximum at 350 nm

was noted in the excitation spectrum, which did not overlap with the excitation bands of Mn^{4+} ions.

Nevertheless, it is important to mention that the spectral location of the Mn^{4+} emission band maximum in the investigated R-P materials is among the most red-shifted $^2E(Mn^{4+})$ positions reported so far. Based on the Racah parameters from Table 1 the nephelauxetic parameter β_1 was calculated, which is known to have a good quasi-linear correlation with the energy of the ^2E state (eq S4). The results obtained for the R-P materials are compared with those for other representative host materials in Table S3 and Figure S14.[20,21,30−39,22,40,41,23−29] Indeed, the proposed materials present both the lowest ^2E energies as well as some of the lowest β_1 values. Furthermore, it should be noted that the obtained results fit into a linear trend that has been reported so far in several reviews.[7]

Influence of Temperature on Mn^{4+} Emission in R-P Materials. Due to the relatively low energy of the ^2E and $^4T_2$ levels, the luminescence of Mn^{4+} ions in R-P materials is expected to be strongly temperature dependent. Therefore, the thermal evolution of their emission spectra was carried out (Figure 3a and Figures S15 and S16). In fact, it was observed that the emission of the three analyzed phosphors is barely detectable already at about 300−400 K. However, performing thermal evolution from 13 K made it possible to observe a dynamic change in the spectral position of the band maximum (Figure 3b). First, in the case of the $SrTiO_3:Mn^{4+}$ phosphor, the emission band maximum occurs at 13640 cm^{-1} (733.1 nm) at 13 K and shifts rapidly toward 13670 cm^{-1} at 50 K, implying a mixed influence of ν_3 and ν_4 vibronic states in this temperature range. This information complements previous scientific works, which reported a band maximum for $SrTiO_3:Mn^{4+}$ at ∼13800 cm^{-1} (∼724.6 nm) at 80 K.[5,11,42] It stays in agreement with a significant jump in the position of the band maximum to 13810 cm^{-1} (ν_6, 724.1 nm) at 60 K, which gradually decreased above this temperature until 13750 cm^{-1} (727.3 nm) at 310 K.

A similarly low value of the emission band maximum was also reached in $Sr_3Ti_2O_7:Mn^{4+}$: i.e., 13630 cm^{-1} (733.7 nm) at 13 K. However, in this case, this maximum remained at a similar energy up to 110 K with an observed slight shift to

D

13620 cm^{-1} (734.2 nm). Thereafter, the maximum was covered by the vibronic ν_4 state in the 120−180 K range with an energy of ~13720 cm^{-1} (728.9 nm), and finally above 190 K the maximum occurred at 13800 cm^{-1} (724.6 nm) corresponding to the dominant influence of the ν_6 vibronic state. In the case of Sr$_2$TiO$_4$, the least spectral changes were obtained: i.e., in the 13−70 K range the main impact on the emission band shape was made by the ν_4 state with 13720 cm^{-1} (728.9 nm), and at 70−290 K it was the ν_6 state, which maximum gradually shifted from 13820 cm^{-1} (723.6 nm) to 13760 cm^{-1} (726.7 nm) due to the thermal promotion of the higher vibronic levels of the ^{4}A$_2$ state.

Interesting changes were observed also in the thermal evolution of emission band intensity (Figure S17). By considering a broad spectral range (670−760 nm) covering the entire band originating from the ^{2}E → ^{4}T$_2$ transition of Mn^{4+} ions (Figure S17a) it can be noted that in Sr$_2$TiO$_4$ the emission increases slightly to maximally 115% of its initial value in the range of 13−250 K. Above 250 K, there is a sharp decrease in intensity, and above 300 K the intensity does not interfere with 10% of the initial value. On the other hand, Mn^{4+} emission in SrTiO$_3$ is quenched rapidly in the range 13−100 K to reach 60% of the initial intensity, after which the thermal quenching slows down considerably so that at 230 K the signal remains at 57%. Above 230 K there is a significant drop in intensity again, and only 13% of the signal from 13 K remains at 300 K. In the case of Sr$_3$Ti$_2$O$_7$:Mn^{4+}, the signal intensity is 77% of the initial value at 50 K, followed by a slight increase in intensity to 85% at 120 K. This is probably due to the Ti^{3+} → Mn^{4+} energy transfer, as well as the quenching of the Ti^{3+} band which is spectrally overlapped with the Mn^{4+} emission band in Sr$_3$Ti$_2$O$_7$. Above 120 K, thermal quenching occurs, as evidenced by 10% of the initial value noted at 280 K. Although the interpretation of the thermal evolution of the Mn^{4+} band in Sr$_3$Ti$_2$O$_7$ is hampered by the presence of the broad Ti^{3+} emission band, it can be noted that the rate of thermal quenching increases in the following order: Sr$_2$TiO$_4$ > SrTiO$_3$ > Sr$_3$Ti$_2$O$_7$. This corresponds with the average metal−oxygen distances R_{av}. To explain this, it is necessary to take into account the energy difference between the ^{2}E parabola and its intersection with the ^{4}T$_2$ parabola, the so-called activation energy ΔE (see Figure 1a), which determines the energy to be supplied for effective thermal quenching to occur. The activation energy was determined from eq 1

$$\frac{-\Delta E}{k} \cdot \frac{1}{T} = \ln\left(\frac{I_0}{I_{em}} - 1\right) \tag{1}$$

where I_{em} is the emission intensity at temperature T, I_0 is the initial emission intensity at T = 13 K, and k is the Boltzmann constant ($k \approx 0.6950$ cm^{-1}/K). Thus, values of ΔE = 2362, 2041, and 1867 cm^{-1} were obtained for Sr$_2$TiO$_4$, SrTiO$_3$, and Sr$_3$Ti$_2$O$_7$, respectively. Therefore, it is expected that thermal quenching of Mn^{4+} emission will be most effective in the Sr$_3$Ti$_2$O$_7$:Mn^{4+} phosphor. Additionally, although the intense CT band is only observed on the emission spectra of SrTiO$_3$:Mn^{4+}, it is also detectable for Sr$_2$TiO$_4$:Mn^{4+} and Sr$_3$Ti$_2$O$_7$:Mn^{4+} and its thermal evolution is compared in Figure S17b. In all three materials, the rate of thermal quenching of the CT band is uniform over the whole measurement range, while a quenching rate is arranged in the order Sr$_2$TiO$_4$ > Sr$_3$Ti$_2$O$_7$ > SrTiO$_3$. It may suggest that the thermal quenching of the CT band in Sr$_3$Ti$_2$O$_7$ is hampered by the Ti^{3+} → CT

and Mn^{4+} → CT energy transfers, as thermal quenching was expected to be the fastest of the three host materials.

As mentioned in the case of changes in the Mn^{4+} luminescence band maximum position as a function of temperature in R-P materials, significant differences can be observed between the thermal evolution of different spectral regions within the Mn^{4+} band on the emission spectra. Therefore, it was proposed to evaluate which spectral regions are characterized by inverse behavior with a change in temperature (Figure S18). It was observed that, in all investigated R-P phosphors, the Mn^{4+} band quenched most rapidly in the 730−745 nm spectral range, while the most impressive increase in intensity with respect to the initial value (at 13 K) was noticed in the 690−705 nm range. The resulting thermal evolution of integrals in the given ranges is shown in Figure 3c,d, respectively. Therefore, in the 730−745 nm range, the Mn^{4+} emission intensity follows a curve similar to that of the whole band shown previously in Figure S17a, but it is devoid of any intensity increase. On the other hand, in the 690−705 nm spectral range in Mn^{4+}-doped R-P materials, a band located energetically above the zero phonon lines (ZPL) of Mn^{4+} emission was noted, the intensity of which increases with increasing temperature.[42] Therefore, the intensity of this band increases between 13 and 240 K. Due to the near-zero intensity of the signal coming from this spectral range at 13 K, the relative values take on impressive quantities: i.e., more than 155 times the 13 K intensity at 240 K and 133 times the intensity at 150 K for Sr$_2$TiO$_4$ and Sr$_3$Ti$_2$O$_7$, respectively. Surprisingly, in the case of SrTiO$_3$, this increase is 2 orders of magnitude lower, reaching only 1.65 at 220 K of the initial value. Additionally, the thermal evolution of emission spectra of Sr$_3$Ti$_2$O$_7$:Mn^{4+} under excitation λ_{exc} = 387 nm and λ_{exc} = 415 nm was compared (Figure S19). It was observed that the intensity of the Mn^{4+}, Ti^{3+}, and CT bands varied depending on the excitation used. Therefore, also for λ_{exc} = 415 nm, a faster thermal quenching in the 730−745 nm range was obtained, but also a smaller intensity increase in the 690−705 nm range when comparing to λ_{exc} = 387 nm (Figures S20 and S21). Considering the encouraging intensity vs temperature plots with different monotonicities, a luminescence intensity ratio (LIR) calculation was proposed as follows:

$$\text{LIR} = \frac{\int_{690nm}^{705nm} I(^2\text{E} \rightarrow {}^4\text{A}_2)[\text{Mn}^{4+}] \, d\lambda}{\int_{730nm}^{745nm} I(^2\text{E} \rightarrow {}^4\text{A}_2)[\text{Mn}^{4+}] \, d\lambda} \tag{2}$$

The values obtained for SrTiO$_3$, Sr$_2$TiO$_4$, and Sr$_3$Ti$_2$O$_7$ doped with Mn^{4+} are shown in Figure 3e. For SrTiO$_3$:Mn^{4+} due to the small increase in intensity in the range 690−705 nm, the LIR values increased almost linearly in the range of 13−310 K, reaching a maximum value of 13.4 at 310 K. The Sr$_2$TiO$_4$:Mn^{4+} phosphor presented more variability, reaching a ~48 times increase at 100 K with respect to its initial value, followed by the slowdown of its rate and finally reaching 242.1 at 400 K. However, the most impressive result was determined for Sr$_3$Ti$_2$O$_7$:Mn^{4+}, for which the LIR = 92.7 at 100 K, while the maximum reached LIR = 976.8 at 300 K. Interestingly, regardless of the excitation used (λ_{exc} = 387 nm or λ_{exc} = 415 nm), the LIR parameter as a function of temperature had a similar course for Sr$_3$Ti$_2$O$_7$:Mn^{4+}, so it was decided to preserve the results obtained upon λ_{exc} = 387 nm in the main analysis (Figure S22). The intense increase of the LIR in the low-temperature range was encouraging to treat the LIR as a
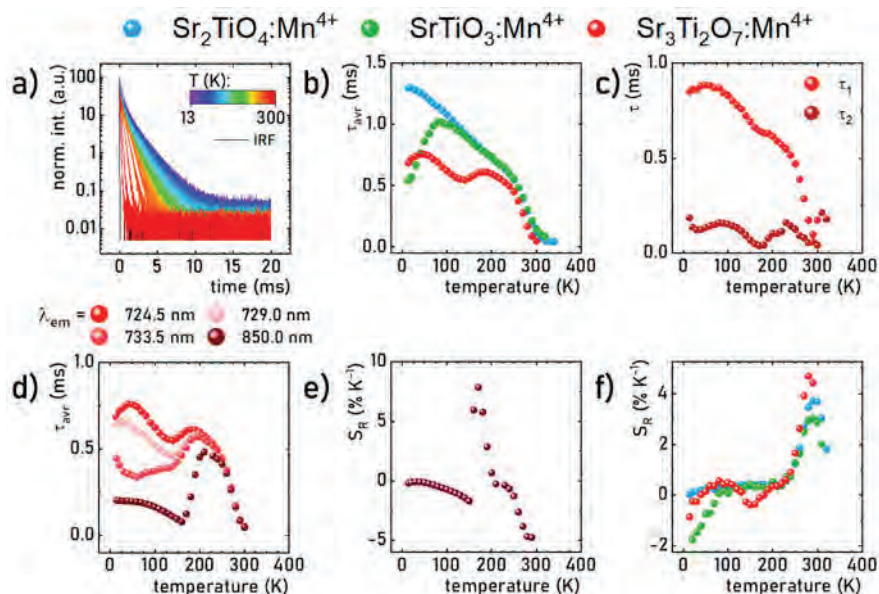
Figure 4. (a) Thermal evolution of luminescent decay profiles of emission from ^{2}E excited state in $Sr_3Ti_2O_7$:Mn^{4+}. (b) Influence of host material composition on the thermal evolution of Mn^{4+} average lifetimes. (c) Thermal evolution of components of τ_{av}: τ_1 and τ_2 for $Sr_3Ti_2O_7$:Mn^{4+} phosphor. (d) Comparison of the thermal evolution of average lifetimes in $Sr_3Ti_2O_7$:Mn^{4+} for different λ_{em}. Thermal evolution of S_R value of thermometer based on (e) the Mn^{4+}/Ti^{3+} lifetime in $Sr_3Ti_2O_7$ (f) the Mn^{4+} lifetime in R-P materials.

temperature-dependent parameter and to verify the relative sensitivities of the potential optical thermometers, according to eq 3

$$S_R = \frac{1}{\text{LIR}} \frac{\Delta \text{LIR}}{\Delta T} \times 100\% \qquad (3)$$

where ΔLIR represents the change of LIR for the change of temperature ΔT. The obtained S_R values are summarized in Figure 3f. In the case of the $SrTiO_3$:Mn^{4+} host material, $S_{Rmax} = 1.75\%$ K^{-1} at 13 K was obtained, which gradually decreased with increasing temperature, reaching 0.39% K^{-1} at 210 K and then increasing slightly up to 300 K, reaching 1.45% K^{-1}. However, much more impressive results were obtained for Sr_2TiO_4 and $Sr_3Ti_2O_7$ doped with Mn^{4+} in the temperature range below 100 K. Maximum sensitivity values of $S_{Rmax} = 8.99\%$ K^{-1} and $S_{Rmax} = 10.37\%$ K^{-1} were obtained at 40 K for Sr_2TiO_4:Mn^{4+} and $Sr_3Ti_2O_7$:Mn^{4+}, respectively. However, it is also worth noting that the S_R value was not lower than 2.20% K^{-1} and 3.73% K^{-1} in the 13−100 K range for these materials. Above 40 K, there was a gradual decrease in S_R value in both cases, associated with a flattening of the LIR vs temperature plot curvature, resulting in values lower than $S_R = 0.1\%$ K^{-1} at 290 K. In addition, it was proposed to consider the temperature determination uncertainty, denoted as δT, which describes the potential utility of the luminescence thermometer more accurately than S_R (eqs S5 and S6). The values of δT as a function of temperature are shown in Figure S23. It can be found that from 13 to 200 K, δT is within the range of 0.05−0.12 K for all three R-P materials. It is worth noting, despite the reduction in S_R values above 40 K, the increase in signal intensity coming from the spectral bands selected for the LIR calculation also has a positive effect on the accuracy of the temperature readout. With a sharp decrease in S_R value above 200 K, δT increased, reaching values on the order of 8.0 K for Sr_2TiO_4 and $Sr_3Ti_2O_7$. Therefore, the useful range of a thermometer based on the LIR parameter should be limited to the 13−200 K range. Despite achieving a relatively high value

of $S_R = 10.37\%$ K^{-1}, it should be emphasized that similar results obtained in the cryogenic temperature range have already been reported in the literature.[43−45] This is the result of thermal activation of many nonradiative processes in this temperature range in the host material. Moreover, temperature readout in the realistic application may be hampered since such a high increase of LIR value and such a high increase in LIR by as much as 3 orders of magnitude mean that the intensities of the spectral ranges under consideration are significantly different. It may prevent the precise detection of the two signals necessary for temperature determination. Therefore, it was decided to evaluate the lifetime potential of Mn^{4+} ions as a temperature-dependent parameter for applications in luminescence thermometry.

Temperature-Dependent Performance of Lifetimes in Mn^{4+}-Doped R-P Materials. The thermal depopulation of the emitting ^{2}E state of Mn^{4+} in the R-P materials should affect the kinetics of the Mn^{4+} ions as well (Figure 4a and Figure S24). By fitting the luminescence decay profiles with the biexponential curve, average lifetimes of τ_{av} were determined (eqs S2 and S3 and Figure 4b). It was found that $\tau_{avr} = 1.30$ ms at 13 K for Sr_2TiO_4:Mn^{4+} is significantly longer than $\tau_{avr} = 0.54$ ms and $\tau_{avr} = 0.69$ ms in the cases of $SrTiO_3$ and $Sr_3Ti_2O_7$, respectively. In Sr_2TiO_4, a gradual shortening of lifetimes was observed in the 13−340 K range, which was close to linear up to 240 K followed by an increase in the quenching rate at higher temperatures.

Surprisingly, the Mn^{4+} lifetime in $SrTiO_3$ in the range 13−80 K is almost doubled, reaching $\tau_{av} = 1.02$ ms. Then it undergoes a gradual quenching and above 140 K reaches values similar to that of the Sr_2TiO_4:Mn^{4+} phosphor. On the other hand, in the case of $Sr_3Ti_2O_7$, a slight elongation of lifetimes to 0.75 ms from 13 to 40 K was observed, which then shortened to 0.54 ms at 140 K. Surprisingly, there is a renewed elongation to ~180 K, above which there is a gradual shortening of lifetimes up to 300 K, similar to the other two R-P materials. To understand the abnormal thermal evolution of τ_{av} in $Sr_3Ti_2O_7$,

F

298

the thermal evolution of two components derived from the biexponential fitting, namely τ_1 and τ_2, was analyzed (Figure 4c). It was observed that the thermal evolution of τ_1 for $Sr_3Ti_2O_7$:Mn^{4+} presents a shape similar to that found for Sr_2TiO_4:Mn^{4+}, but with a different shortening rate, which is the expected effect due to the difference in the activation energy described above. Meanwhile, τ_2 reflects the occurrence of a significant shortening of τ_{av} to 180 K. This may be indicative of the contribution of the ^2E level of Ti^{3+} ions to the lifetimes observed at λ_{exc} = 387 nm and λ_{em} = 724.5 nm in the range 13−180 K, which subsequently quenches and leaves a dominant contribution of the ^2E level of Mn^{4+} ions above 180 K.

To confirm this hypothesis, we analyzed the thermal evolution of τ_{av} for different excitation and emission wavelengths (Figures S25 and S26 and Figure 4d). Comparing the thermal evolution of τ_{av} for different λ_{em} at fixed λ_{exc}, it can be seen that the lifetime observed in the range of 13−180 K decreases with increasing λ_{em}, which is also related to the increasing contribution of Ti^{3+} luminescence to the received τ_{av}. Thus, for λ_{em} = 733.5 nm and λ_{exc} = 415 nm a 3-fold shorter τ_{av} value, i.e. 0.25 ms, was achieved at 60 K than for λ_{em} = 724.5 nm and λ_{exc} = 387 nm. This suggests that Ti^{3+} ions lead to a shortening of the lifetimes recorded for λ_{em} = 724.5 nm in the range 13−180 K, and then, its effect is significantly reduced. On the other hand, the choice of λ_{exc} also determines the contribution of the lifetimes of the ^2E states of Mn^{4+} and Ti^{3+} ions in the average lifetime value. This also manifests itself as a clear difference in lifetimes in the range 13−180 K.

Comparing the thermal evolution of the excitation spectra of Ti^{3+} and Mn^{4+} ions in $Sr_3Ti_2O_7$, it is expected that λ_{exc2} = 415 nm should excite Mn^{4+} more effectively than Ti^{3+} ions with respect to λ_{exc1} = 387 nm. Figure S27 shows that the contribution of τ_2 to τ_{av} is similar for all combinations of λ_{em} and λ_{exc}. This interpretation is consistent with the obtained thermal evolution of τ_{av} for the emission wavelength falling at the Ti^{3+} band maximum, i.e. λ_{em} = 850 nm, where the greatest influence of Ti^{3+} lifetimes was obtained at low temperatures (below 180 K) and Mn^{4+} in the higher temperature range (Figure S28 and Figure 4d). The value of τ_{av} at 13 K is 0.20 ms and then it gradually decreases to reach 0.089 ms at 150 K. Above this value, there is a sharp increase in τ_{av} up to 0.48 ms at 210 K, which, however, should be interpreted as the lifetime of Mn^{4+} ions. The strong thermal variability of τ_{av} suggests its high potential for optical thermometry. Hence, its S_R value was determined (Figure 4e). In the 13−150 K range, it adopts relatively small S_R values, reaching a maximum of −1.70% K^{-1} at 150 K. However, the rapid elongation in lifetimes provided that a relatively impressive S_{Rmax} = 7.86% K^{-1} at 170 K was achieved. However, it is also worth noting the S_R values at around room temperature, where a sharp shortening in lifetimes ensured the achievement of $|S_R|$ > 4.5% K^{-1} in the range 280−290 K. The sharp increase in τ_{av} in the temperature domain associated with a shortening of the lifetime of one luminescent center while maintaining the lifetime value of the other luminescent center taking over the dominant role on the luminescent decay profile can be considered as a novel strategy to design highly sensitive thermometers.

In a similar manner, S_R values were calculated for $SrTiO_3$, Sr_2TiO_4, and $Sr_3Ti_2O_7$ (Figure 4f). In contrast to the LIR-based approach in the range 13−200 K the S_R values for the luminescence kinetics are not high and do not exceed ∼0.50% K^{-1}. The exceptionx zfd the negative S_R valuex for $SrTiO_3$:Mn^{4+}, which reach a maximum of S_R = −1.73% K^{-1} at 20 K. The negative sign is due to the elongation of the lifetimes observed in this temperature range. On the other hand, the more pronounced S_R values of all three materials can be found above 230 K, as a result of a sharp reduction in lifetimes up to 300−320 K. Consequently, the maximum S_R values are 3.04% K^{-1}, 3.70% K^{-1} and 4.68% K^{-1} obtained in the range 280−290 K for $SrTiO_3$, Sr_2TiO_4, and $Sr_3Ti_2O_7$, respectively. Nevertheless, it should be emphasized that temperature determination above 320 K with these materials is not further possible due to both the rapid shortening of lifetimes and the almost complete quenching of Mn^{4+} luminescence around these temperature. In order to take both of these aspects into account in assessing the application potential of lifetime-based thermometers, the temperature determination uncertainty δT was calculated (eq S7 and Figure S29). Therefore, due to the small S_R values, in the range 13−200 K the δT value varies between 0.3 and 1.0 K. However, above 200 K δT decreases to $\delta T \approx 0.10$ at 270−280 K for $SrTiO_3$:Mn^{4+} and Sr_2TiO_4:Mn^{4+}. For $Sr_3Ti_2O_7$:Mn^{4+}, the decrease in δT is more pronounced and even reaches δT = 0.013 at 280 K. This demonstrates the high application potential of thermometers based on the lifetimes of Mn^{4+} ions.

■ CONCLUSIONS

In this work, the spectroscopic and thermometric parameters of Mn^{4+} luminescence in three Ruddlesden−Popper strontium titanate structures were compared. It was observed for the first time that the emission band maximum of Mn^{4+} in $SrTiO_3$ reaches 733.2 nm (13640 cm^{-1}) at 13 K and shifts to the previously reported 723.75 nm (13820 cm^{-1}) at 110 K. On the other hand, in $Sr_3Ti_2O_7$ the emission band maximum falls at 733.6 nm (13630 cm^{-1}) at 13 K, which even shifts to 734.2 nm (13620 cm^{-1}) at 110 K, meaning that it is the most red-shifted emission band maximum for Mn^{4+} ions among those reported so far. The shapes of excitation and emission spectra were compared with theoretical calculations. Among the three materials, a correlation was observed between the average metal−oxygen R_{av} distance and spectroscopic properties such as the position of excitation and emission bands β_1, activation energy ΔE, and thermal quenching rate. Finally, the thermal performance of the $^2E \rightarrow {}^4A_2$ emission band and lifetime of ^2E excited state were compared for the three structures and verified for thermometric applications. By determination of the two temperature-dependent parameters, thermometers capable of operating over a wide range from cryogenic to room temperatures were obtained. The proposed new $Sr_3Ti_2O_7$:Mn^{4+} phosphor allowed an improvement in the relative sensitivity of the LIR-based thermometer from 1.50% K^{-1} to 10.37% K^{-1} at 40 K, as well as in the lifetime-based strategy from 3.04% K^{-1} to 4.68% K^{-1} at 280 K in the $SrTiO_3$:Mn^{4+} material. Taking also into account S_{Rmax} = 7.86% K^{-1} at 170 K obtained for the novel Mn^{4+}/Ti^{3+} mixed lifetime approach, $Sr_3Ti_2O_7$:Mn^{4+} can be considered as a multi-parameter thermometer, achieving high sensitivities in the range of 13−300 K.

■ ASSOCIATED CONTENT

Ⓢ Supporting Information

The Supporting Information is available free of charge at https://pubs.acs.org/doi/10.1021/acs.inorgchem.3c03113.

Additional XRD of the synthesized materials, results of Rietveld refinement, TEM images of the synthesized materials, excitation and emission spectra of synthesized materials, thermal dependence of emission intensities of synthesized materials, comparison of the crystal field parameters of different phosphors doped with Mn^{4+} ions, and temperature determination uncertainty of obtained luminescence manometers (PDF)

■ AUTHOR INFORMATION

Corresponding Authors

Wojciech M. Piotrowski − *Institute of Low Temperature and Structure Research, Polish Academy of Sciences, 50-422 Wrocław, Poland;* ⊙ orcid.org/0000-0002-8155-2688; Email: w.piotrowski@intibs.pl

Lukasz Marciniak − *Institute of Low Temperature and Structure Research, Polish Academy of Sciences, 50-422 Wrocław, Poland;* ⊙ orcid.org/0000-0001-5181-5865; Email: l.marciniak@intibs.pl

Authors

Paulina Bolek − *Faculty of Chemistry, University of Wrocław, PL-50383 Wrocław, Poland*

Mikhail G. Brik − *School of Optoelectronic Engineering & CQUPT-BUL Innovation Institute, Chongqing University of Posts and Telecommunications, 400065 Chongqing, People's Republic of China; Centre of Excellence for Photoconversion, Vinča Institute of Nuclear Sciences - National Institute of the Republic of Serbia, University of Belgrade, 110000 Belgrade, Serbia; Institute of Physics, University of Tartu, Tartu 50411, Estonia; Faculty of Science and Technology, Jan Długosz University, 42 200 Częstochowa, Poland; Academy of Romanian Scientists, 010719 Bucharest, Romania*

Eugeniusz Zych − *Faculty of Chemistry, University of Wrocław, PL-50383 Wrocław, Poland*

Complete contact information is available at:
https://pubs.acs.org/10.1021/acs.inorgchem.3c03113

Notes

The authors declare no competing financial interest.

■ ACKNOWLEDGMENTS

■ REFERENCES

(1) Adachi, S. Review—Mn^{4+}-Activated Red and Deep Red-Emitting Phosphors. *ECS J. Solid State Sci. Technol.* **2020**, *9* (1), 016001.

(2) Adachi, S. Photoluminescence Properties of Mn^{4+}-Activated Oxide Phosphors for Use in White-LED Applications: A Review. *J. Lumin.* **2018**, *202*, 263−281.

(3) Zhou, Z.; Zhou, N.; Xia, M.; Yokoyama, M.; Hintzen, H. T. B. Research Progress and Application Prospects of Transition Metal $Mn4+$-Activated Luminescent Materials. *J. Mater. Chem. C* **2016**, *4* (39), 9143−9161.

(4) Jansen, T.; Funke, L. M.; Gorobez, J.; Böhnisch, D.; Hoffmann, R.-D.; Heletta, L.; Pöttgen, R.; Hansen, M. R.; Jüstel, T.; Eckert, H. Red-Emitting $K_3HF_2WO_2F_4:Mn^{4+}$ for Application in Warm-White Phosphor-Converted LEDs − Optical Properties and Magnetic Resonance Characterization. *Dalt. Trans.* **2019**, *48* (16), 5361−5371.

(5) Bryknar, Z; Trepakov, V; Potucek, Z; Jastrabık, L Luminescence Spectra of SrTiO3:Mn4+. *J. Lumin.* **2000**, *87−89*, 605−607.

(6) Grinberg, M.; Lesniewski, T. Non-Radiative Processes and Luminescence Quenching in Mn^{4+} Doped Phosphors. *J. Lumin.* **2019**, *214*, 116574.

(7) Brik, M. G.; Ma, C. G.; Srivastava, A. M.; Piasecki, M. Mn^{4+} Ions for Solid State Lighting. *Faguang Xuebao/Chin. J. Lumin.* **2020**, *41* (9), 1011−1029.

(8) Senden, T.; Van DIjk-Moes, R. J. A.; Meijerink, A. Quenching of the Red Mn^{4+} Luminescence in Mn^{4+}-Doped Fluoride LED Phosphors. *Light Sci. Appl.* **2018**, *7* (1), 8.

(9) Šturm, S.; Rečnik, A.; Scheu, C.; Čeh, M. Formation of Ruddlesden−Popper Faults and Polytype Phases in SrO-Doped SrTiO3. *J. Mater. Res.* **2000**, *15* (10), 2131−2139.

(10) Brik, M. G.; Camardello, S. J.; Srivastava, A. M. Influence of Covalency on the $Mn^{4+2}E_g \rightarrow {}^4A_{2g}$ Emission Energy in Crystals. *ECS J. Solid State Sci. Technol.* **2015**, *4* (3), R39.

(11) Trejgis, K.; Dramićanin, M. D.; Marciniak, L. Highly Sensitive Multiparametric Luminescent Thermometer for Biologically-Relevant Temperatures Based on Mn^{4+}, Ln^{3+} Co-Doped $SrTiO_3$ Nanocrystals. *J. Alloys Compd.* **2021**, *875*, 159973.

(12) Kubo, T.; Nozoye, H. Surface Structure of SrTiO3(1 0 0). *Surf. Sci.* **2003**, *542* (3), 177−191.

(13) Pechini, M. P. Method of Preparing Lead and Alkaline Earth Titanates and Niobates and Coating Method Using the Same to Form a Capacitor. U.S. Patent US3330697A, 1967.

(14) Haeni, J. H.; Theis, C. D.; Schlom, D. G.; Tian, W.; Pan, X. Q.; Chang, H.; Takeuchi, I.; Xiang, X.-D. Epitaxial Growth of the First Five Members of the $Sr_{n+1}Ti_nO_{3n+1}$ Ruddlesden−Popper Homologous Series. *Appl. Phys. Lett.* **2001**, *78* (21), 3292−3294.

(15) Malkin, B. Z. Crystal Field and Electron−Phonon Interaction in Rare-Earth Ionic Paramagnets. In *Spectroscopy of Solids Containing Rare Earth Ions*; Kaplyanskii, A. A., Macfarlane, R. M. B., Eds.; Elsevier: 1987; Vol. 21, Chapter 2, pp 13−50.

(16) Lu, Z.; Zhang, L.; Wang, L.; Zhang, Q. Concentration Dependence of Luminescent Properties for Sr_2TiO_4: Eu^{3+} Red Phosphor and Its Charge Compensation. *J. Nanomater.* **2012**, *2012*, 698434.

(17) Zhang, L.; Sun, B.; Liu, Q.; Ding, N.; Yang, H.; Wang, L.; Zhang, Q. Novel Layered Perovskite $Sr_3Ti_2O_7:Eu^{3+}$ Phosphor with High-Efficiency Luminescence Enhanced by Charge Compensation. *J. Alloys Compd.* **2016**, *657*, 27−31.

(18) Piotrowski, W.; Kuchowicz, M.; Dramićanin, M.; Marciniak, L. Lanthanide Dopant Stabilized Ti^{3+} State and Supersensitive Ti^{3+}-Based Multiparametric Luminescent Thermometer in $SrTiO_3:Ln^{3+}$ (Ln^{3+} = Lu^{3+}, La^{3+}, Tb^{3+}) Nanocrystals. *Chem. Eng. J.* **2022**, *428*, 131165.

(19) Piotrowski, W. M.; Ristic, Z.; Dramićanin, M. D.; Marciniak. Modification of the Thermometric Performance of the Lifetime-Based Luminescent Thermometer Exploiting Ti^{3+} Emission in $SrTiO_3$ and $CaTiO_3$ by Doping with Lanthanide Ions. *J. Alloys Compd.* **2022**, *906*, 164398.

(20) Brik, M. G.; Srivastava, A. M.; Avram, N. M. Comparative Analysis of Crystal Field Effects and Optical Spectroscopy of Six-Coordinated Mn^{4+} Ion in the $Y_2Ti_2O_7$ and $Y_2Sn_2O_7$ Pyrochlores. *Opt. Mater. (Amst).* **2011**, *33* (11), 1671−1676.

(21) Peng, M.; Yin, X.; Tanner, P. A.; Brik, M. G.; Li, P. Site Occupancy Preference, Enhancement Mechanism, and Thermal Resistance of Mn^{4+} Red Luminescence in $Sr_4Al_{14}O_{25}$: Mn^{4+} for Warm WLEDs. *Chem. Mater.* **2015**, *27* (8), 2938−2945.

(22) Piotrowski, W.; Trejgis, K.; Maciejewska, K.; Ledwa, K.; Fond, B.; Marciniak, L. Thermochromic Luminescent Nanomaterials Based

on Mn^{4+}/Tb^{3+} Codoping for Temperature Imaging with Digital Cameras. *ACS Appl. Mater. Interfaces* **2020**, *12* (39), 44039−44048.

(23) Riseberg, L. A.; Weber, M. J. Spectrum and Anomalous Temperature Dependence of the $^2E \rightarrow {}^4A_2$ Emission of Y$_3$Al$_5$O$_{12}$: Mn^{4+}. *Solid State Commun.* **1971**, *9* (11), 791−794.

(24) Wang, B.; Lin, H.; Xu, J.; Chen, H.; Wang, Y. CaMg$_2$Al$_{16}$O$_{27}$:Mn^{4+}-Based Red Phosphor: A Potential Color Converter for High-Powered Warm W-LED. *ACS Appl. Mater. Interfaces* **2014**, *6* (24), 22905−22913.

(25) Zou, W.; Nie, W.; Wu, D.; Wu, S.; Wang, W.; Peng, J.; Ye, X. Synthesis, Luminescence Properties and Potential Applications for Plant Growth: A Novel Mn^{4+}-Activated SrLa$_2$Al$_2$O$_7$ Phosphor with Far-Red Emission. *J. Lumin.* **2023**, *257*, 119759.

(26) Srivastava, A. M.; Brik, M. G. Crystal Field Studies of the Mn^{4+} Energy Levels in the Perovskite, LaAlO$_3$. *Opt. Mater. (Amst).* **2013**, *35* (8), 1544−1548.

(27) Wu, X.-X.; Zheng, W.-C.; Fang, W. Theoretical Investigations of the EPR Parameters for Cr^{3+} and Mn^{4+} Ions in PbTiO$_3$ Crystals. *Spectrochim. Acta Part A Mol. Biomol. Spectrosc.* **2008**, *69* (2), 498− 502.

(28) Cao, Y.; Fang, Y.; Zhang, G.; Zhao, G.; Liu, Y.; Zou, J.; Vainos, N.; Hou, J. High Quantum Yield Red-Emission Phosphor Li$_2$Ge$_4$O$_9$:Mn^{4+} for WLEDs Application. *Opt. Mater. (Amst).* **2019**, *98*, 109442.

(29) Brik, M. G.; Sildos, I.; Berkowski, M.; Suchocki, A. Spectroscopic and Crystal Field Studies of YAlO$_3$ Single Crystals Doped with Mn Ions. *J. Phys.: Condens. Matter* **2009**, *21* (2), 025404.

(30) Takeda, Y.; Kato, H.; Kobayashi, M.; Kobayashi, H.; Kakihana, M. Photoluminescence Properties of Mn^{4+}-Activated Perovskite-Type Titanates, La$_2$MTiO$_6$:Mn^{4+} (M = Mg and Zn). *Chem. Lett.* **2015**, *44* (11), 1541−1543.

(31) Srivastava, A. M.; Brik, M. G. Ab Initio and Crystal Field Studies of the Mn^{4+}-Doped Ba$_2$LaNbO$_6$ Double-Perovskite. *J. Lumin.* **2012**, *132* (3), 579−584.

(32) Talewar, R. A.; Mahamuda, S.; Rao, A. S.; Moharil, S. V. Novel Mn^{4+}-Activated NaLiTi$_3$O$_7$ Far-Red Emitting Phosphors. *J. Lumin.* **2023**, *255*, 119591.

(33) Zhang, S.; Hu, Y.; Duan, H.; Fu, Y.; He, M. An Efficient, Broad-Band Red-Emitting Li$_2$MgTi$_3$O$_8$:Mn^{4+} Phosphor for Blue-Converted White LEDs. *J. Alloys Compd.* **2017**, *693*, 315−325.

(34) Chen, H.; Sun, A.; Fang, D.; Xu, S.; Zhang, M.; Wang, A.; Mi, B.; Gao, Z. Structure and Luminescent Properties of Mn^{4+}-Activated Li$_2$Mg$_2$TiO$_5$ with Broadband Deep-Red Emission. *J. Mater. Sci. Mater. Electron.* **2022**, *33* (19), 15879−15893.

(35) Da Fonseca, R. J. M.; Abritta, T. Radiative and Nonradiative Processes in LiGa$_5$O$_8$: Mn^{4+}. *Phys. B Condens. Matter* **1993**, *190* (4), 327−332.

(36) Brik, M. G.; Srivastava, A. M. Electronic Energy Levels of the Mn^{4+} Ion in the Perovskite, CaZrO$_3$. *ECS J. Solid State Sci. Technol.* **2013**, *2* (7), R148.

(37) Wang, S.; Sun, Q.; Liang, J.; Sun, L.; Devakumar, B.; Huang, X. Preparation and Photoluminescence Properties of Novel Mn^{4+} Doped Li$_3$Mg$_2$TaO$_6$ Red-Emitting Phosphors. *Inorg. Chem. Commun.* **2020**, *116*, 107903.

(38) Meng, L.; Liang, L.; Wen, Y. Deep Red Phosphors SrMgAl$_{10}$O$_{17}$:Mn^{4+}, M (M = Li$^+$, Na$^+$, K$^+$, Cl$^-$) for Warm White Light Emitting Diodes. *J. Mater. Sci. Mater. Electron.* **2014**, *25* (6), 2676−2681.

(39) Wang, X.; Li, P.; Brik, M. G.; Li, X.; Li, L.; Peng, M. Thermal Quenching of Mn^{4+} Luminescence in SrAl$_{12}$O$_{19}$:Mn^{4+}. *J. Lumin.* **2019**, *206*, 84−90.

(40) Medić, M. M.; Brik, M. G.; Dražić, G.; Antić, Ž. M.; Lojpur, V. M.; Dramićanin, M. D. Deep-Red Emitting Mn^{4+} Doped Mg$_2$TiO$_4$ Nanoparticles. *J. Phys. Chem. C* **2015**, *119* (1), 724−730.

(41) Cao, R.; Zhang, F.; Cao, C.; Yu, X.; Liang, A.; Guo, S.; Xue, H. Synthesis and Luminescence Properties of CaAl$_2$O$_4$:Mn^{4+} Phosphor. *Opt. Mater. (Amst).* **2014**, *38*, 53−56.

(42) Srivastava, A. M.; Brik, M.; Beers, W. W.; Cohen, W. On the Mn^{4+} R-Line Intensity and Energy in the Perovskite Layer of SrLaAlO$_4$ and Sr$_2$TiO$_4$: A Comparative Study with LaAlO$_3$ and SrTiO$_3$. *Opt. Mater. (Amst).* **2020**, *109*, 110372.

(43) Li, R.; Wei, G.; Wang, Z.; Wang, Y.; Li, J.; He, S.; Li, L.; Suo, H.; Ding, W.; Li, P. Cr^{3+}-Facilitated Ultra-Sensitive Luminescence Ratiometric Thermometry at Cryogenic Temperature. *Laser Photon. Rev.* **2023**, *17* (3), 2200589.

(44) Mykhaylyk, V. B.; Kraus, H.; Zhydachevskyy, Y.; Tsiumra, V.; Luchechko, A.; Wagner, A.; Suchocki, A. Multimodal Non-Contact Luminescence Thermometry with Cr-Doped Oxides. *Sensors (Switzerland).* **2020**, *20*, 5259.

(45) Kalinichev, A. A.; Afanaseva, E. V.; Kolesnikov, E. Y.; Kolesnikov, I. E. Boltzmann-Type Cryogenic Ratiometric Thermometry Based on Nd^{3+}-Doped LuVO$_4$ Phosphors. *J. Mater. Chem. C* **2023**, *11* (36), 12234−12242.

Supporting Information

Frontiers of deep-red emission of Mn^{4+} ions with Ruddlesden-Popper perovskites

Wojciech M. Piotrowski[1]*, Paulina Bolek[2], Mikhail G. Brik[3,4,5,6,7],

Eugeniusz Zych[2], Lukasz Marciniak[1]*

[1]Institute of Low Temperature and Structure Research, Polish Academy of Sciences, Okólna 2, 50-422 Wroclaw, Poland

[2]Faculty of Chemistry, University of Wrocław, 14.p F. Joliot-Curie Street, PL-50383, Wrocław, Poland

[3] School of Optoelectronic Engineering & CQUPT-BUL Innovation Institute, Chongqing University of Posts and Telecommunications, Chongqing, PR China

[4] Centre of Excellence for Photoconversion, Vinča Institute of Nuclear Sciences - National Institute of the Republic of Serbia, University of Belgrade, Belgrade, Serbia

[5] Institute of Physics, University of Tartu, W. Ostwald Str 1, Tartu 50411, Estonia

[6] Faculty of Science and Technology, Jan Długosz University, Armii Krajowej 13/15, Częstochowa, Poland

[7] Academy of Romanian Scientists, Ilfov Str. No. 3, Bucharest, Romania

* corresponding author: w.piotrowski@intibs.pl, l.marciniak@intibs.pl

KEYWORDS luminescence thermometry, manganese, $SrTiO_3$, Sr_2TiO_4, $Sr_3Ti_2O_7$

The integral intensities of the emission bands were fitted with Mott-Seitz equation (Eq. S1):

$$I = \frac{I_0}{C \cdot \exp(-\frac{W}{k \cdot T}) + 1} \qquad \text{(Eq. S1)}$$

where: I – the intensity in temperature T, I_0 – the intensity in the initial temperature, W - the activation energy, k – Boltzmann constant, C – the dimensionless constant

The average lifetime of the Mn^{4+} excited states were calculated with the equation Eq. S2:

$$\tau_{avr} = \frac{A_1\tau_1^2 + A_2\tau_2^2}{A_1\tau_1 + A_2\tau_2} \qquad \text{(Eq. S2)}$$

where: τ_1, τ_2 are the decay parameters and A_1, A_2 are amplitudes of the bi-exponential function:

$$I(t) = I_0 + A_1 \cdot \exp\left(-\frac{t}{\tau_1}\right) + A_2 \cdot \exp\left(-\frac{t}{\tau_2}\right) \qquad \text{(Eq. S3)}$$
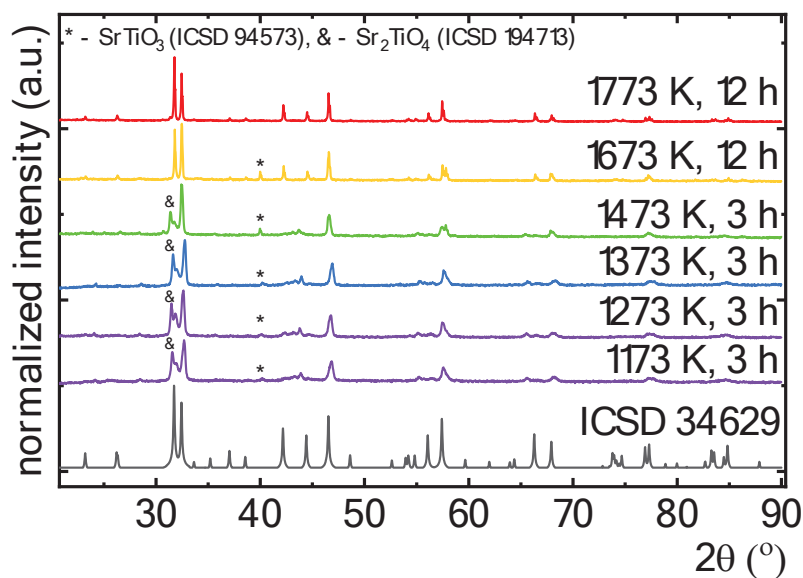
Figure S1. Influence of annealing parameters on XRPD patterns of $Sr_3Ti_2O_7$:0.1% Mn^{4+} powder.
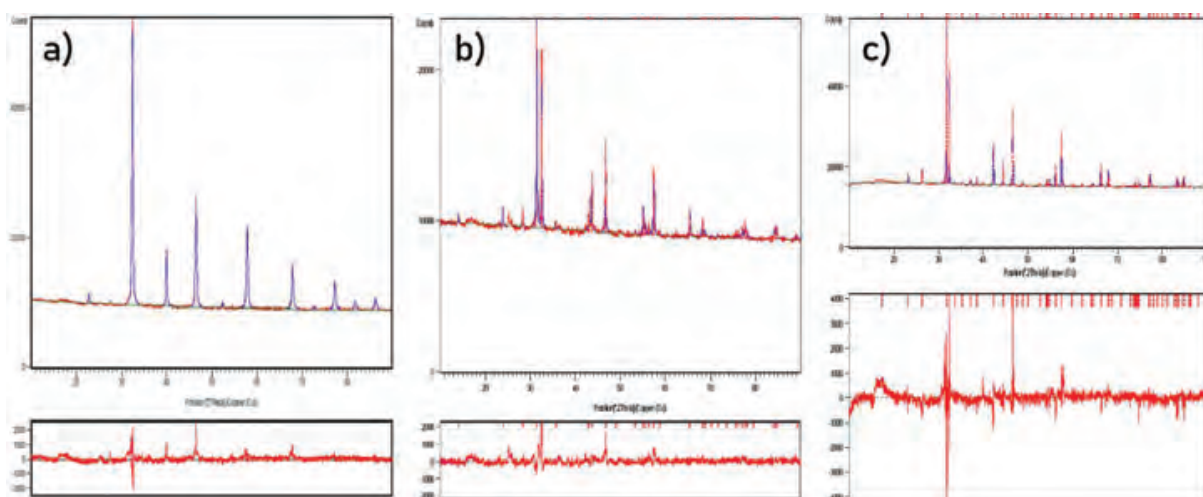
Figure S2. Rietveld refinement of R-P materials doped with 0.1% Mn^{4+} Sr_2TiO_4 – (a), $SrTiO_3$ – (b), $Sr_3Ti_2O_7$ – (c).

Table S1. Unit cell parameters calculated with Rietveld refinement for R-P materials doped with 0.1% Mn^{4+}.

host	a (Å)	c (Å)	V (Å^3)	R profile (%)	weighted R profile (%)	goodness of fit
$SrTiO_3$:0.1% Mn^{4+}	3.906	-//-	59.59	1.309	1.843	3.358
Sr_2TiO_4:0.1% Mn^{4+}	3.885	12.582	189.95	1.243	1.764	2.946
$Sr_3Ti_2O_7$:0.1% Mn^{4+}	3.898	20.346	309.08	1.067	1.610	4.079
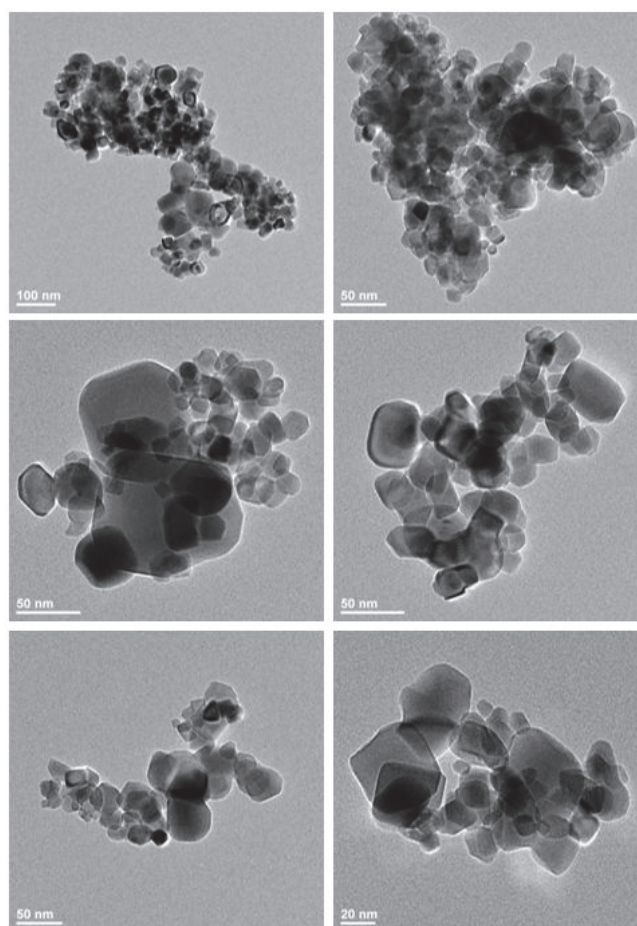
Figure S3. Representative TEM images of $SrTiO_3$ powder doped with 0.1% Mn^{4+}.
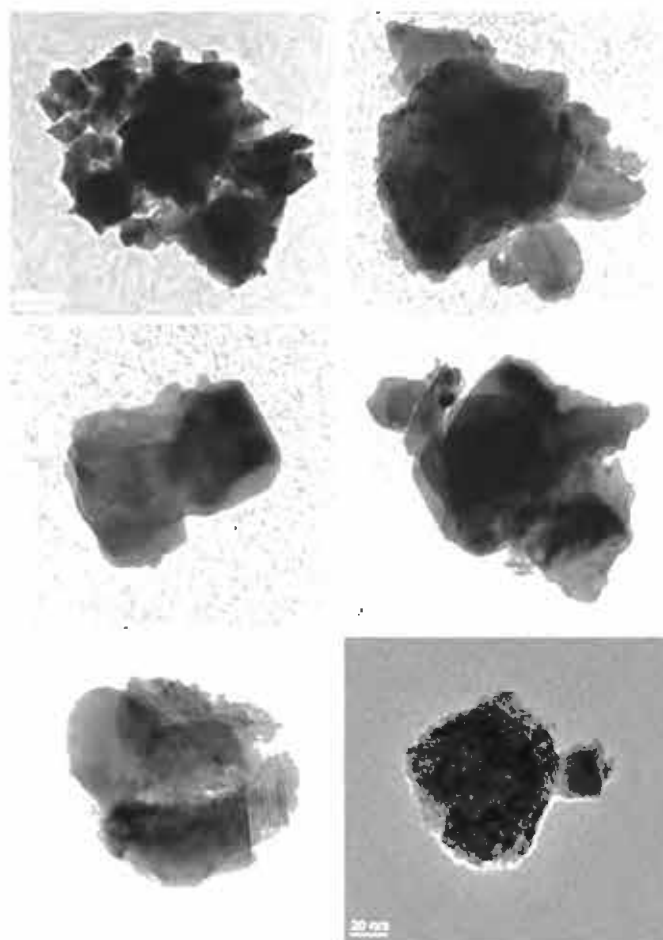
Figure S4. Representative TEM images of Sr_2TiO_4 powder doped with 0.1% Mn^{4+}.
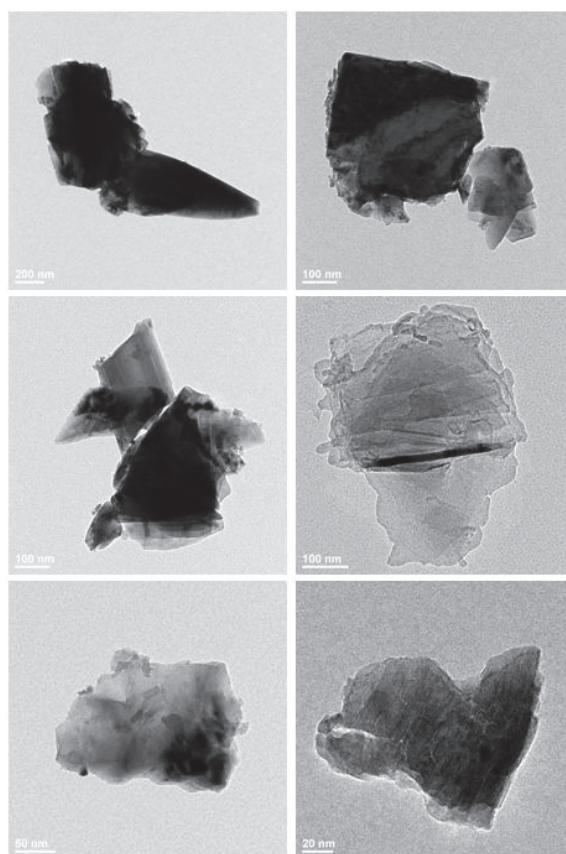
Figure S5. Representative TEM images of $Sr_3Ti_2O_7$ powder doped with 0.1% Mn^{4+}.

Table S2. Calculated spin-quartet energy levels (in cm^{-1}) for Mn^{4+} in $SrTiO_3$, Sr_2TiO_4, $Sr_3Ti_2O_7$.
The orbital doublet states are denoted with an asterisk.

	$SrTiO_3$	Sr_2TiO_4	$Sr_3Ti_2O_7$
$^4A_2$	0	0	0
^2E	14126	14221, 14247	14005, 14064
$^2T_1$	14564	14831*, 14835	14528*, 14585
$^4T_2$	19291	18750*, 19805	18199, 19031*
$^2T_2$	21569	21661, 21701*	21394*, 21451
$^4T_1$	25349	25543, 26566*	25005*, 26990
$^2A_1$	31333	30889	30549
$^2T_2$	33240	32691*, 33751	32210, 32286*
$^2T_1$	33476	33522*, 33977	32650, 33715*
^2E	35116	35241, 35273	34586, 34676
$^2T_1$	37704	38099, 38774*	37212*, 38992
$^4T_1\,(^4P)$	41075	41507, 41566*	40446, 40907*
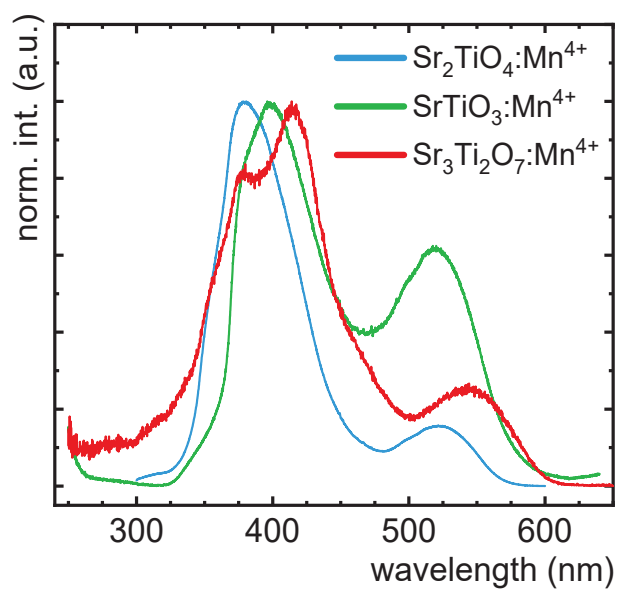
Figure S6. Comparison of excitation spectra performed at 13 K for R-P materials doped with 0.1% Mn^{4+}.
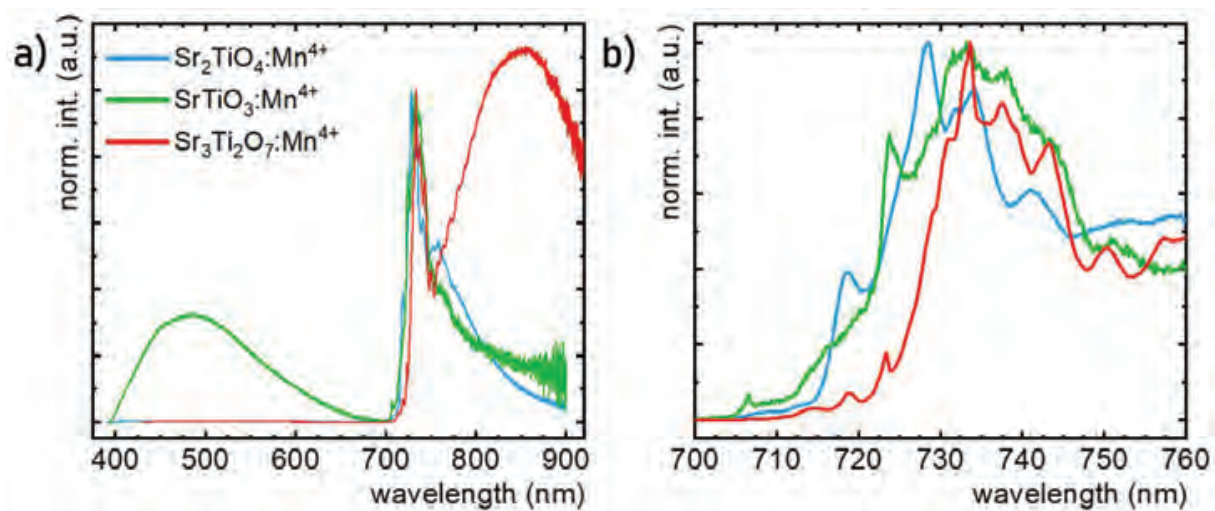
Figure S7. Comparison of emission spectra performed at 13 K and normalized to $^2E \rightarrow {}^4T_2$ band maximum for R-P materials doped with 0.1% Mn^{4+}-(a) and the zoom of the spectra in the 700-760 nm spectral range-(b).
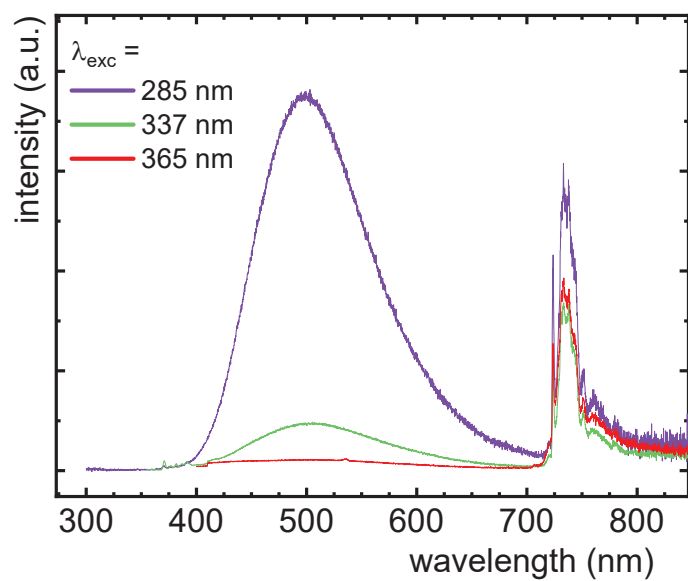
Figure S8. Comparison of emission spectra of SrTiO$_3$ doped with 0.1% Mn^{4+} performed with different excitation wavelength.
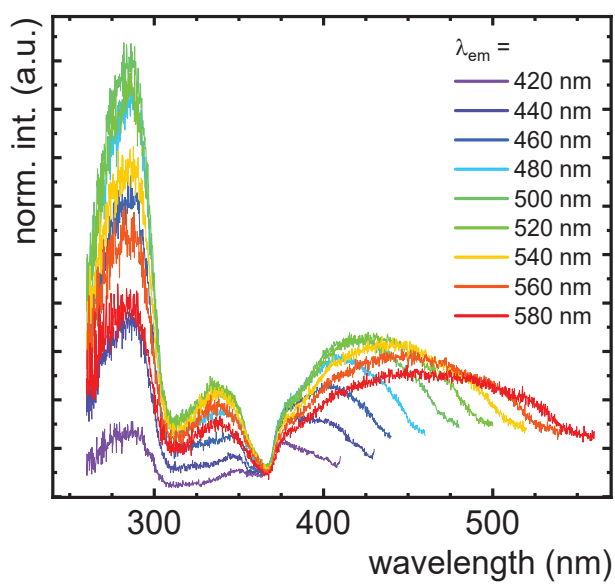
Figure S9. Comparison of excitation spectra of SrTiO$_3$ doped with 0.1% Mn^{4+} for different emission wavelength.
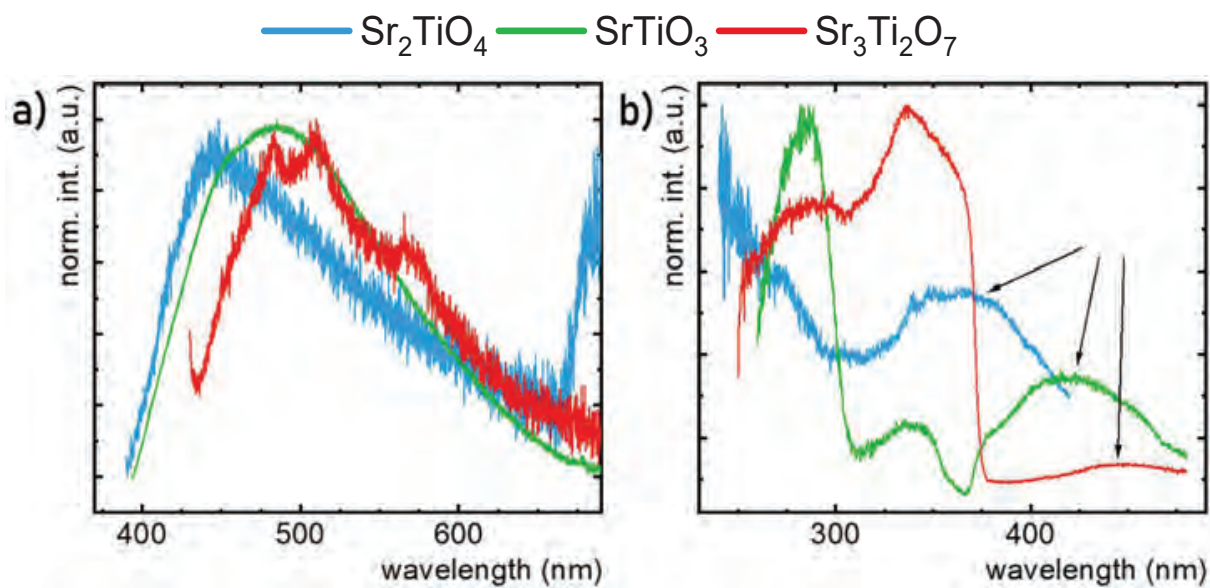
Figure S10. Comparison of CT emission bands – (a) and their excitation spectra – (b) performed at 13 K for R-P materials doped with 0.1% Mn^{4+}.
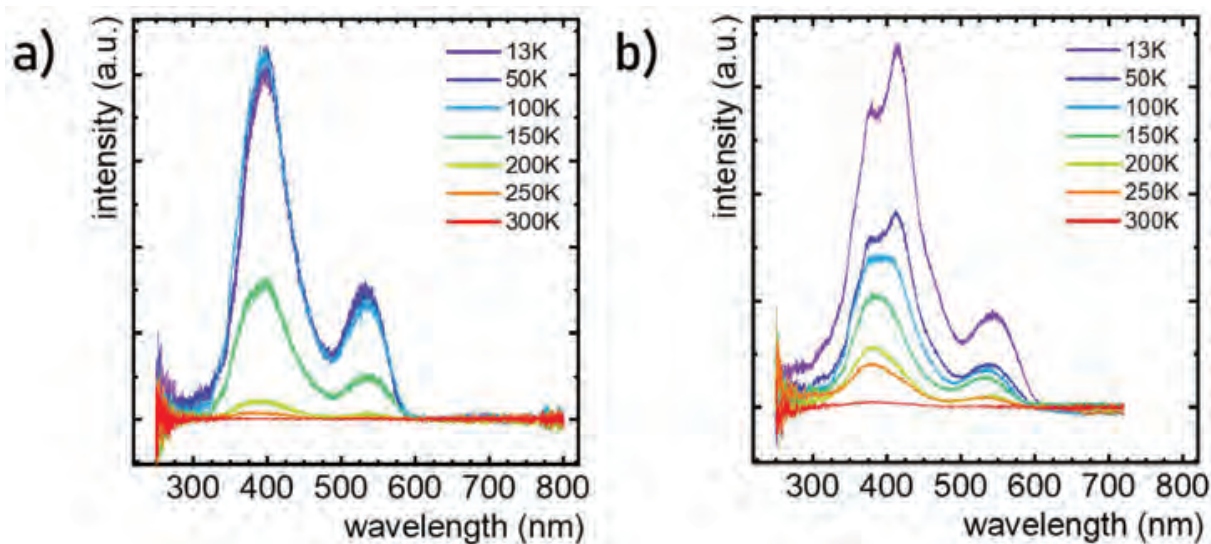
Figure S11. Thermal evolution of the excitation spectra of $Sr_3Ti_2O_7$ doped with 0.1% Mn^{4+} for $\lambda_{em} = 850$ nm ($^2E \rightarrow {}^2T_2$ of Ti^{3+}) – (a) and $\lambda_{em} = 733.5$ nm ($^2E \rightarrow {}^4T_2$ of Mn^{4+}) – (b).
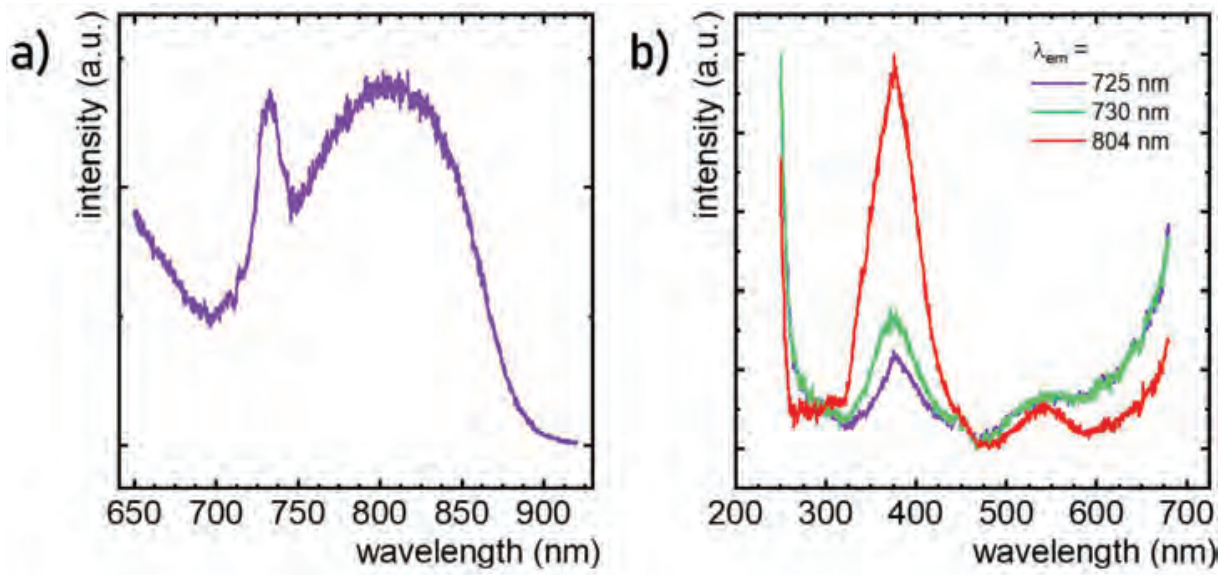
Figure S12. The emission spectra ($\lambda_{\text{exc}} = 400$ nm) – (a) and the excitation spectra performed for different emission wavelength – (b) of undoped $Sr_3Ti_2O_7$ powder.
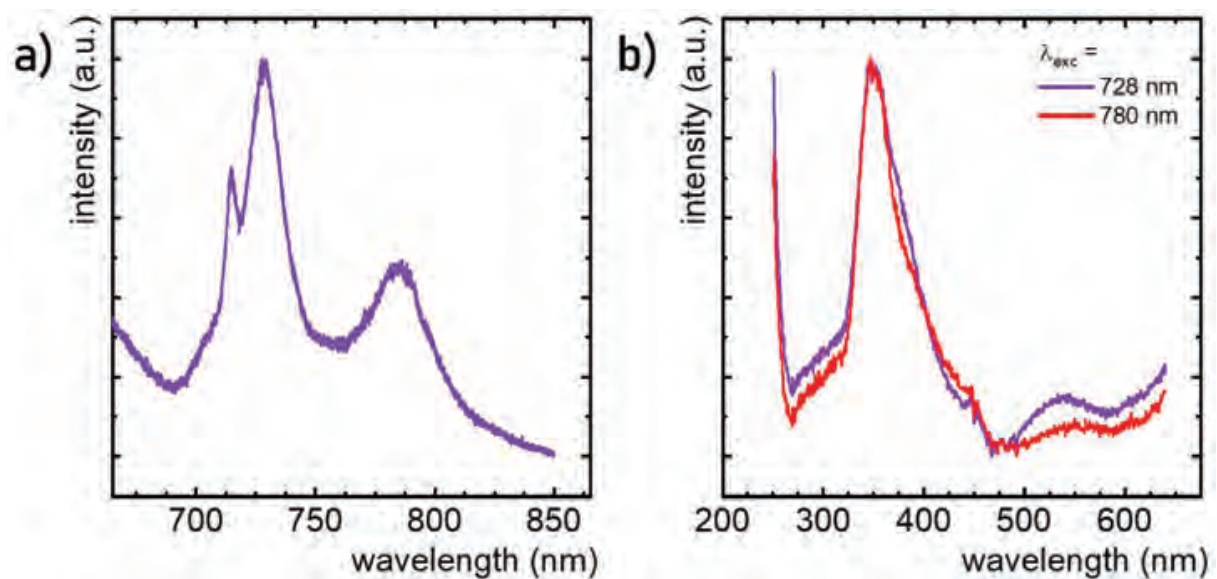
Figure S13. The emission spectra ($\lambda_{\text{exc}} = 400$ nm) – (a) and the excitation spectra performed for different emission wavelength – (b) of $Sr_3Ti_2O_7$ doped with 1% La^{3+}.

The nephelauxetic parameter β_1 was calculated with the following equation (Eq. S4):

$$\beta_1 = \sqrt{\left(\frac{B}{B_0}\right)^2 + \left(\frac{C}{C_0}\right)^2} \qquad \text{(Eq. S4)}$$

where (B, C) and (B_0, C_0) are related to the values of the Racah parameters in a crystal field and in a free state, respectively.

Table S3. Comparison of the Racah parameters, β_1 and the energy of $^2E \rightarrow {}^4T_2$ maximum of Mn^{4+} ions in representative host materials from literature and this work.

host material	B (cm^{-1})	C (cm^{-1})	β_1	E(^{2}E) maximum (cm^{-1})	Ref.
$Y_2Sn_2O_7$	700	3515	1.016	15563	[1]
$Sr_4Al_{14}O_{25}$	790	3172	1.004	15361	[2]
$Sr_4Al_{14}O_{25}$	680	3397	0.983	15361	[3]
$Y_3Al_5O_{12}$	525	3728	0.977	15271	[4]
$CaMg_2Al_{16}O_{27}$	737	3247	0.986	15267	[5]
$CaAl_2O_4$	520	3700	0.970	15198	[6]
Mg_2TiO_4	790	3172	1.004	15193	[7]
$SrAl_{12}O_{19}$	949	2766	1.040	15162	[8]
$SrMgAl_{10}O_{17}$	802	3069	0.993	15151	[9]
$Li_3Mg_2TaO_6$	757	3163	0.983	15129	[10]
$CaZrO_3$	754	3173	0.983	15054	[11]
$LiGa_5O_8$	660	2640	0.837	14959	[12]
$Y_2Ti_2O_7$	600	3500	0.964	14956	[1]
$Li_2Mg_2TiO_5$	756	3038	0.961	14749	[13]
$Li_2MgTi_3O_8$	765	3004	0.960	14706	[14]
$NaLiTi_3O_7$	772	2988	0.962	14684	[15]
Ba_2LaNbO_6	670	3290	0.958	14679	[16]
La_2MgTiO_6	700	3136	0.946	14492	[17]
$YAlO_3$	720	3025	0.938	14450	[18]
$Li_2Ge_4O_9$	588	3253	0.910	14286	[19]
$PbTiO_3$	780	2890	0.950	14236	[20]
$LaAlO_3$	695	2941	0.909	14034	[21]
$SrLa_2Al_2O_7$	645	3032	0.898	13966	[22]
Sr_2TiO_4	690	3030	0.922	13726	This work
$SrTiO_3$	570	3254	0.902	13639	This work
$Sr_3Ti_2O_7$	650	3053	0.904	13631	This work
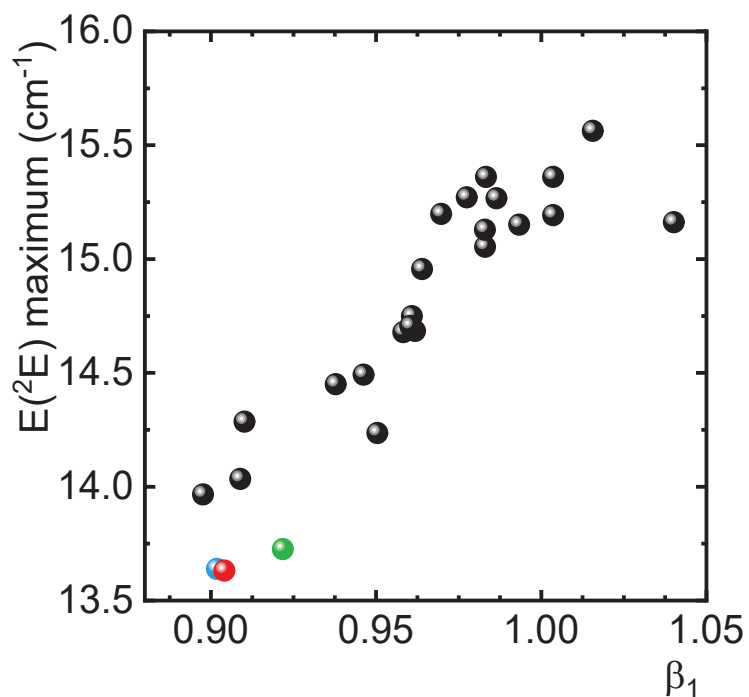
Figure S14. Representative correlation between the β_1 parameter with the energy of $^2E \rightarrow {}^4T_2$ maximum of Mn^{4+} ions in host materials from literature and this work (blue, green and red dot represent Sr_2TiO_4, $SrTiO_3$ and $Sr_3Ti_2O_7$, respectively).
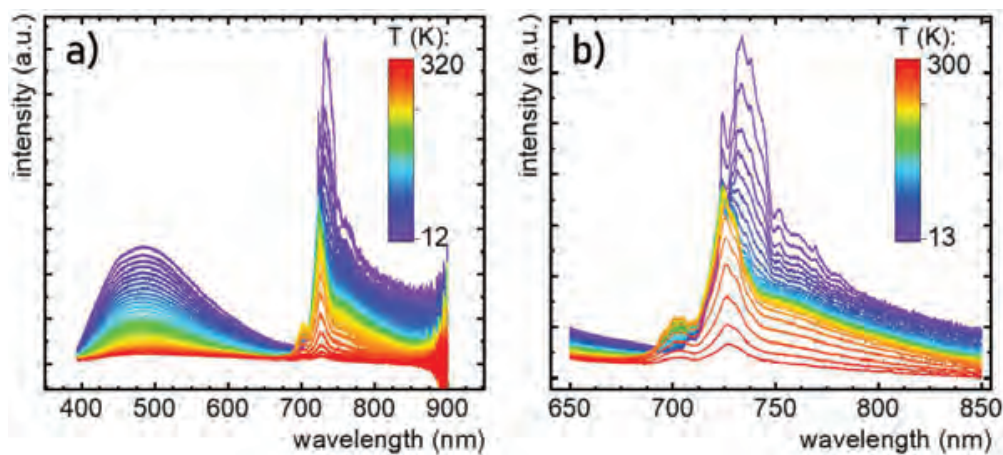
Figure S15. Thermal evolution of emission spectra ($\lambda_{exc} = 380$ nm) of $SrTiO_3$ doped with 0.1% Mn^{4+} presented in a full-(a) and the short spectral range –(b).

Figure S16. Thermal evolution of emission spectra (λ_{exc} = 380 nm) of Sr_2TiO_4 doped with 0.1% Mn^{4+} in a full- (a) and the short spectral range –(b).
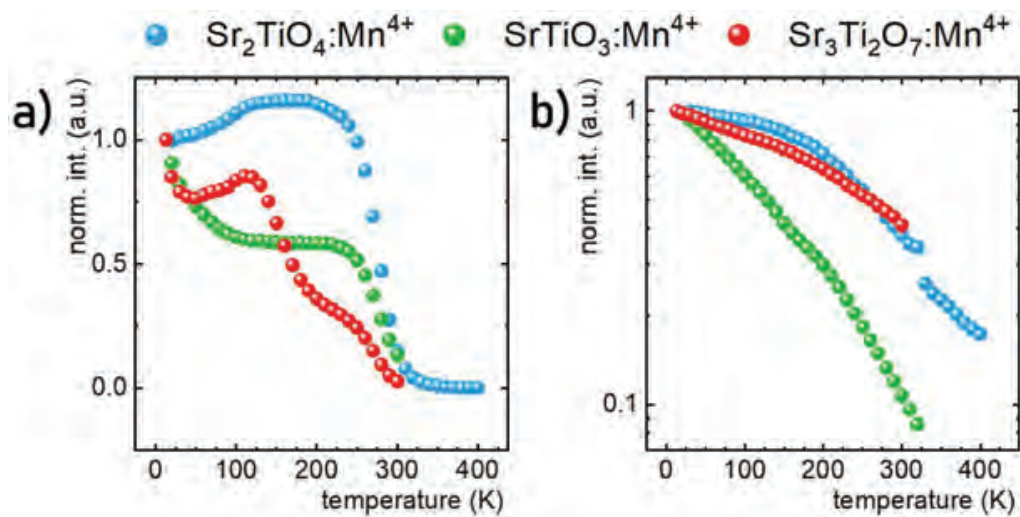
Figure S17. Thermal evolution of $^2E\rightarrow^4T_2$ emission band of Mn^{4+} ions – (a) and charge transfer band – (b) of R-P materials doped with 0.1% Mn^{4+}.
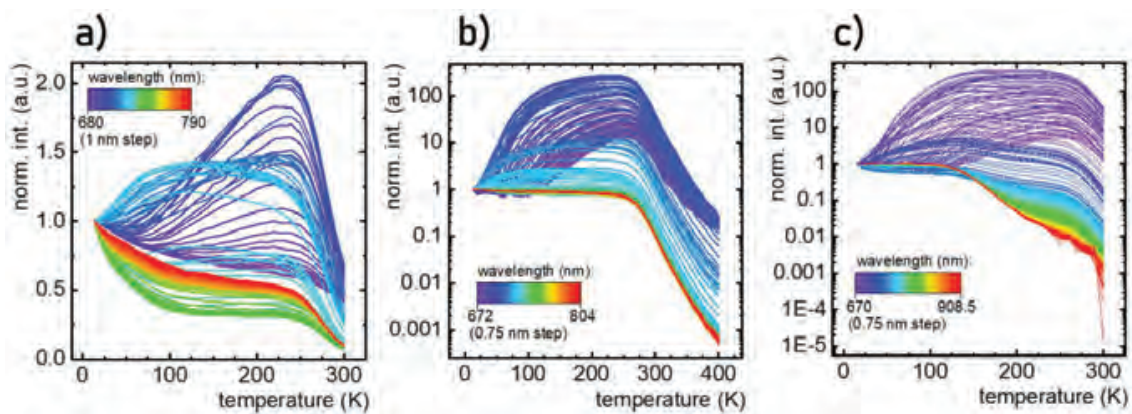
Figure S18. The thermal evolution of integral subtotal for 1 nm and 0.75 nm steps of $SrTiO_3$ (λ_{exc} = 380 nm) – (a), Sr_2TiO_4 (λ_{exc} = 380 nm) – (b) and $Sr_3Ti_2O_7$ (λ_{exc} = 387 nm) – (c) doped with 0.1% Mn^{4+}.
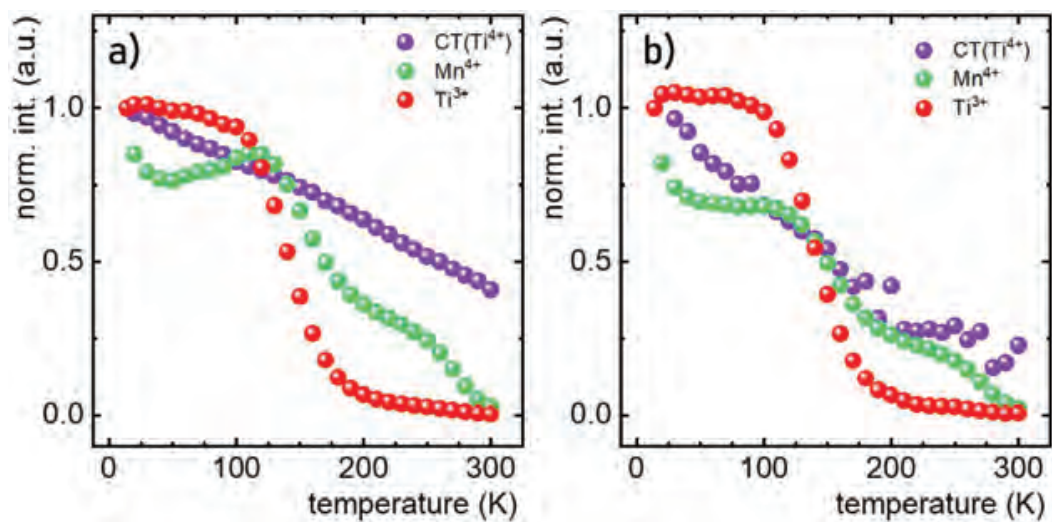
Figure S19. Thermal evolution of different emission band in $Sr_3Ti_2O_7$ doped with 0.1% Mn^{4+} when excited by λ_{exc} = 387 nm – (a) and λ_{exc} = 415 nm – (b).
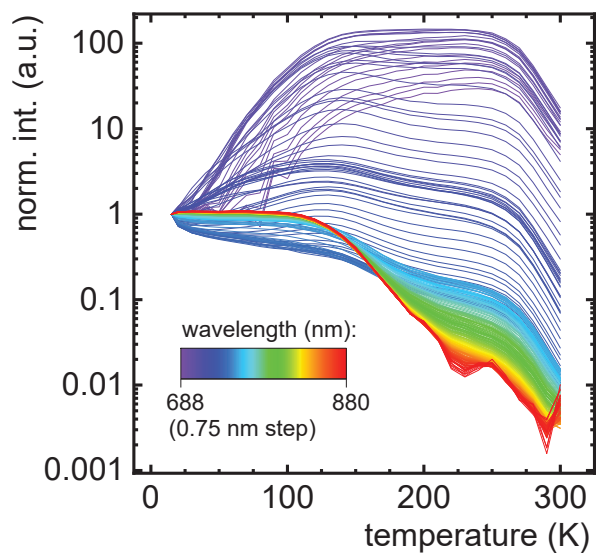
Figure S20. The thermal evolution of integral subtotal for 0.75 nm steps on the emission spectra (λ_{exc} = 415 nm) of $Sr_3Ti_2O_7$ doped with 0.1% Mn^{4+}.
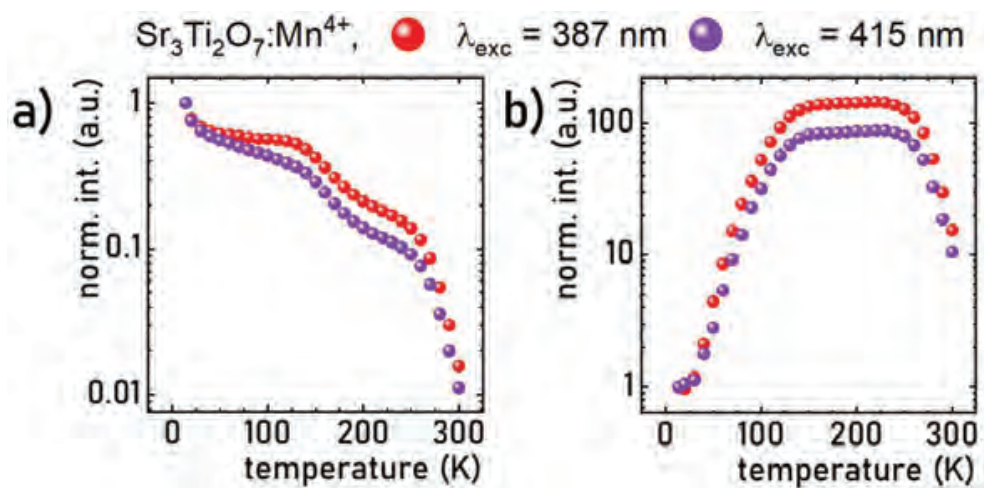
Figure S21. Comparison of thermal evolution of emission intensity of 730-745 nm spectral range – (a) and 690-705 nm spectral range – (b) for different excitation wavelength for $Sr_3Ti_2O_7$ powder doped with 0.1% Mn^{4+}.
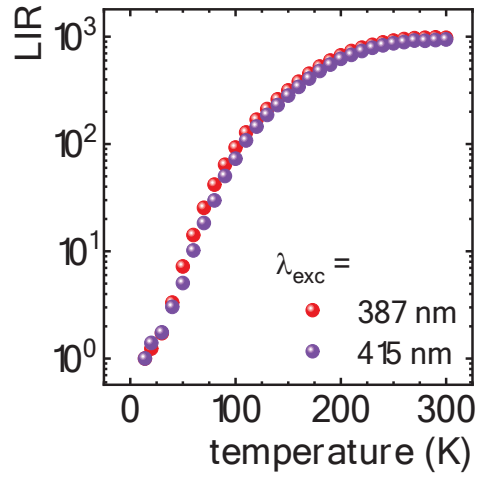
Figure S22. Comparison of thermal evolution of LIR for different excitation wavelength for $Sr_3Ti_2O_7$ powder doped with 0.1% Mn^{4+}.

Temperature determination uncertainty for ratiometric approach was calculated using Eq. S5:

$$\delta T = \frac{1}{S_R} \cdot \frac{\delta LIR}{LIR} \quad \text{(Eq. S5)}$$

where: S_R is the relative sensitivity and $\delta LIR/LIR$ determines the uncertainty of the LIR determination where $\delta LIR/LIR$ was determined as follows:

$$\frac{\delta LIR}{LIR} = \sqrt{\left(\frac{\delta I_1}{I_1}\right)^2 + \left(\frac{\delta I_2}{I_2}\right)^2} \quad \text{(Eq. S6)}$$
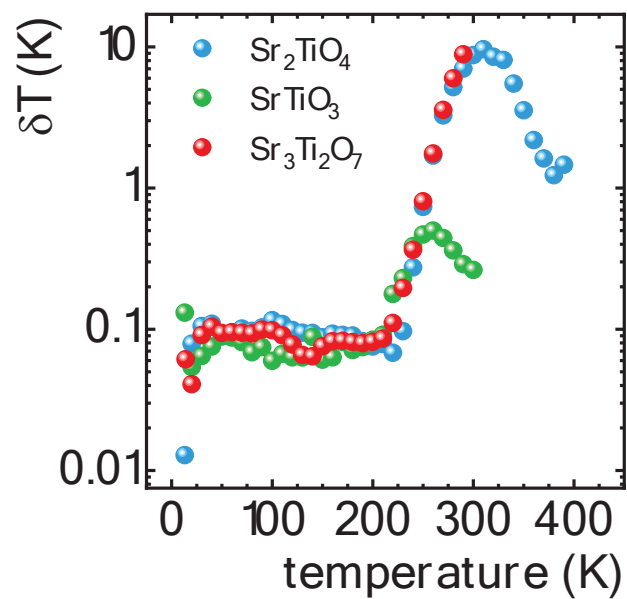
Figure S23. Thermal evolution of temperature determination uncertainty for LIR approach of R-P materials doped with 0.1% Mn^{4+}.
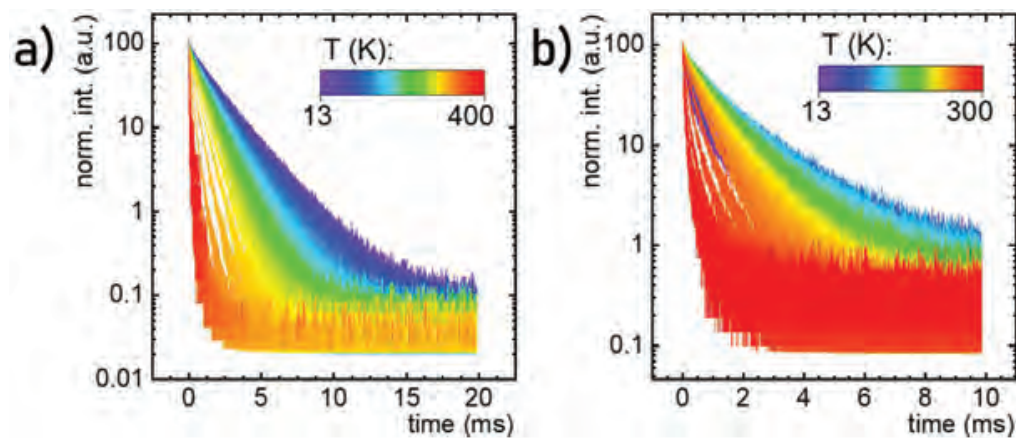
Figure S24. Thermal evolution of luminescent decay profiles of emission from ^2E excited state in Sr_2TiO_4 – (a) and $SrTiO_3$ – (b) doped with 0.1% Mn^{4+}.
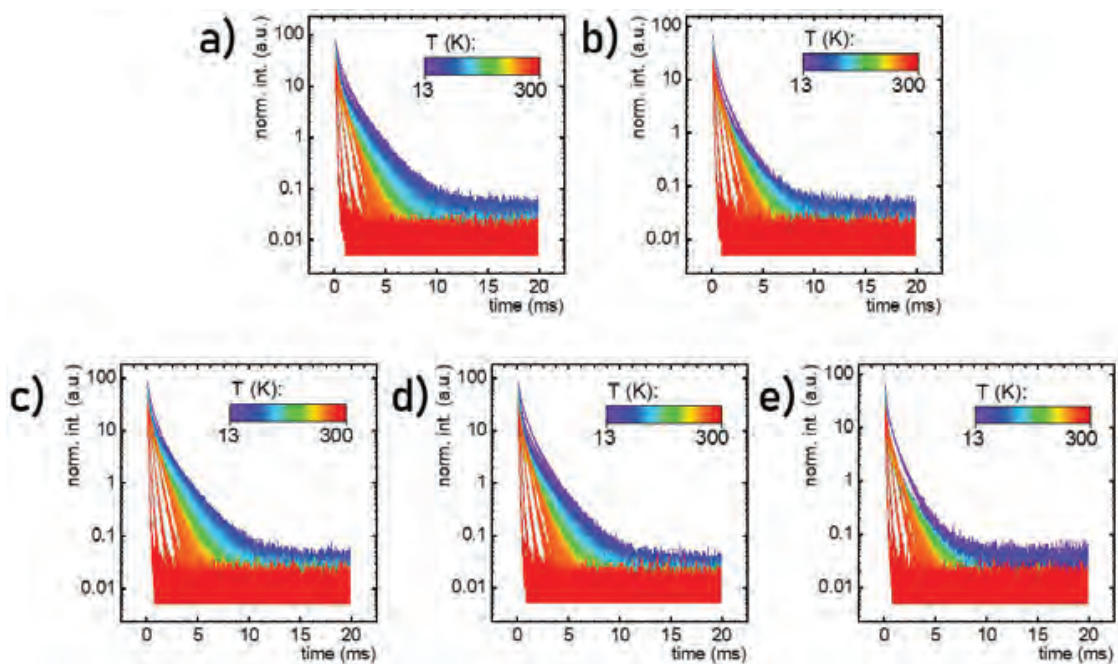
Figure S25. Thermal evolution of luminescent decay profiles of emission from ^2E excited state in $Sr_3Ti_2O_7$ doped with 0.1% Mn^{4+} with $\lambda_{exc} = 380$ nm, $\lambda_{em} = 729.0$ nm – (a), $\lambda_{exc} = 380$ nm, $\lambda_{em} = 733.5$ nm – (b) or $\lambda_{exc} = 415$ nm, $\lambda_{em} = 724.5$ nm – (c), $\lambda_{exc} = 415$ nm, $\lambda_{em} = 729.0$ nm – (d), $\lambda_{exc} = 415$ nm, $\lambda_{em} = 733.5$ nm – (e).
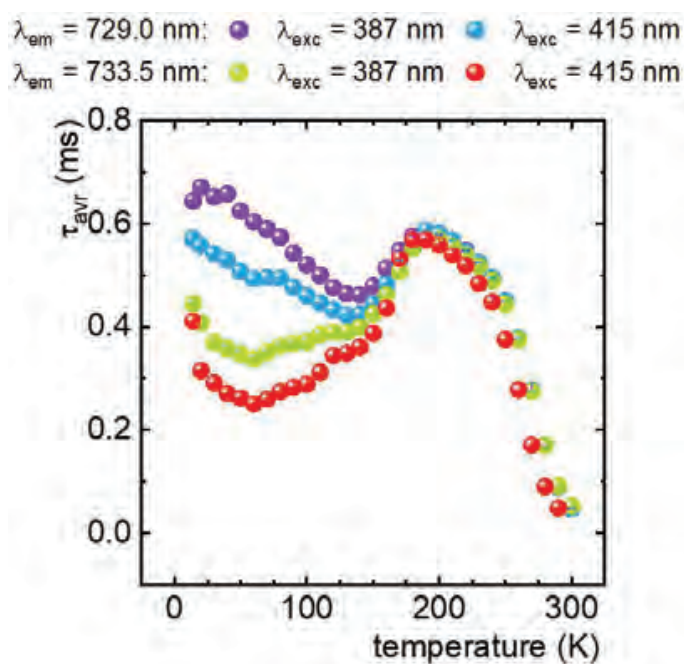
Figure S26. Thermal evolution of the average lifetimes in $Sr_3Ti_2O_7$ doped with 0.1% Mn^{4+} with different excitation and emission wavelengths.
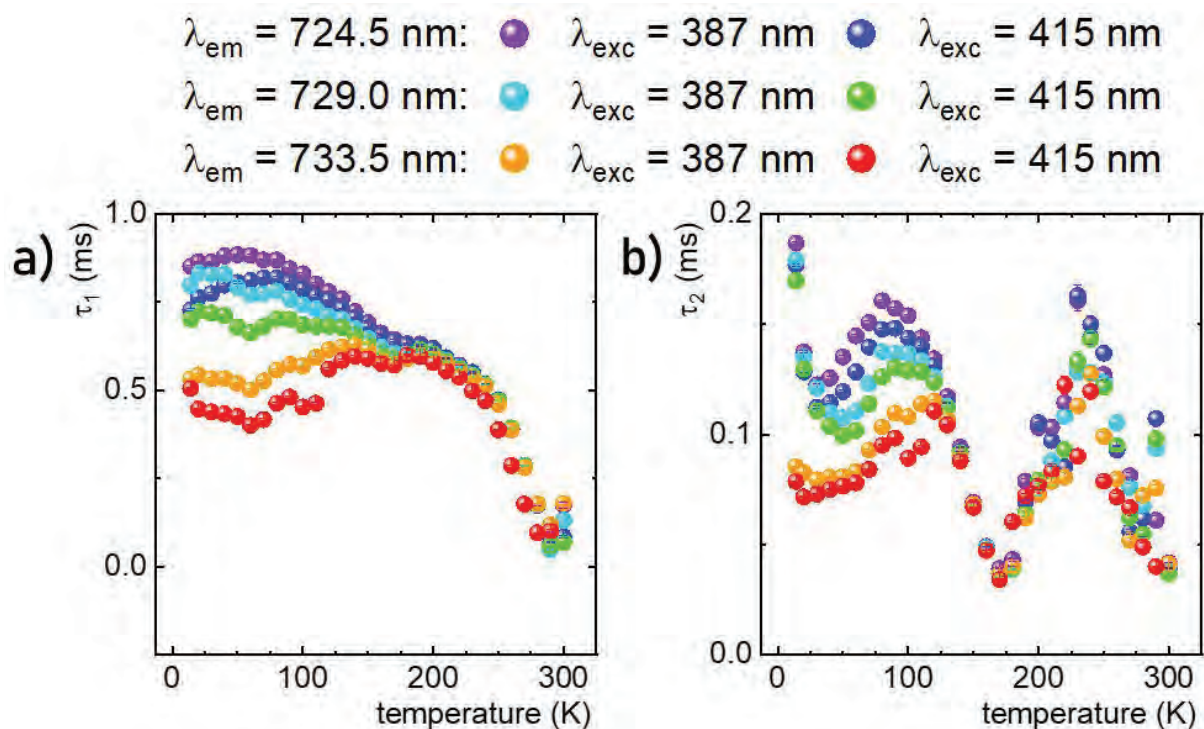
Figure S27. Thermal evolution of τ_1 –(a) and τ_2 –(b) parameters from the double-exponential fit in $Sr_3Ti_2O_7$ doped with 0.1% Mn^{4+} with different excitation and emission wavelengths.
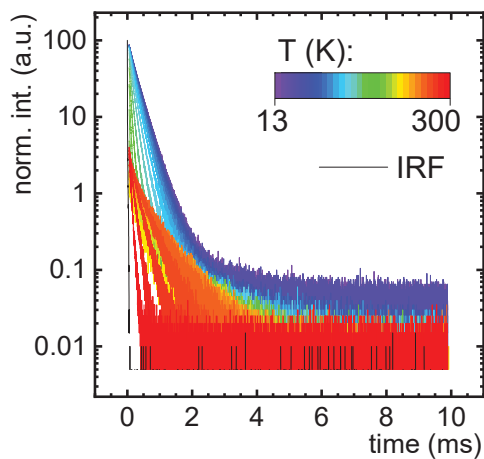
Figure S28. Thermal evolution of luminescent decay profiles of emission from ^2E excited state of Ti^{3+} ions in $Sr_3Ti_2O_7$ doped with 0.1% Mn^{4+} (λ_{exc} = 400, λ_{em} = 850 nm).

Temperature determination uncertainty for lifetime based approach was calculated using Eq. S7:

$$\delta T = \frac{1}{S_R} \cdot \frac{\delta\tau_{avr}}{\tau_{avr}} \qquad \text{(Eq. S7)}$$
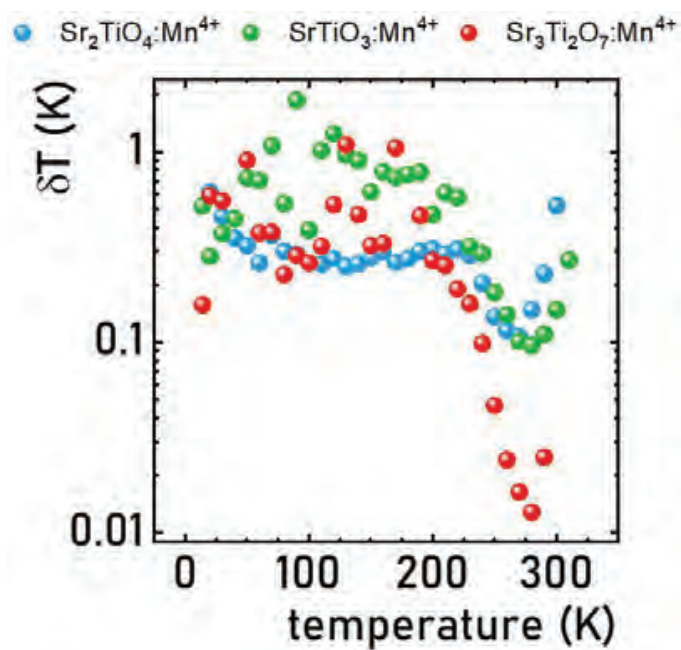
Figure S29. Thermal evolution of temperature determination uncertainty for lifetime approach of R-P materials doped with 0.1% Mn^{4+}.
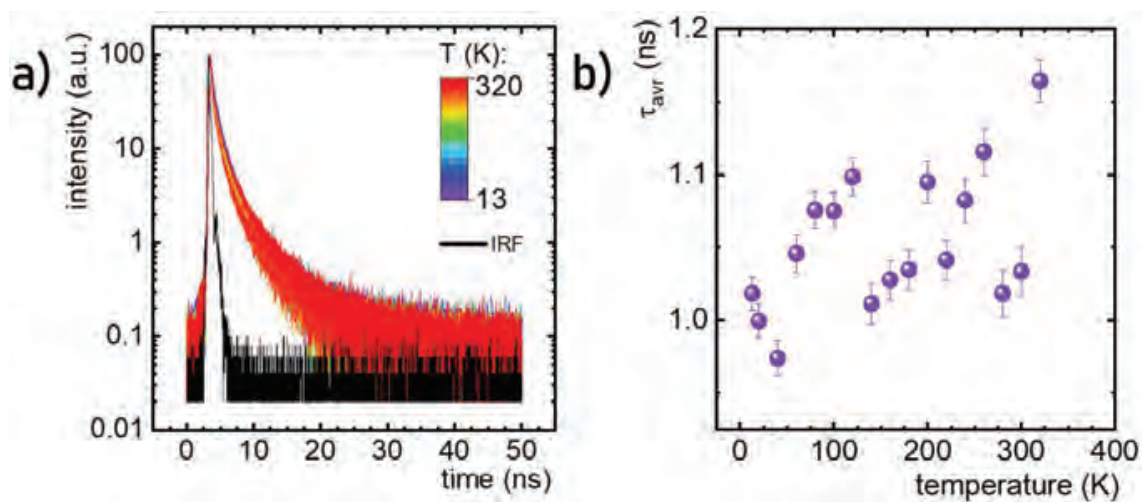
Figure S30. Thermal evolution of luminescent decay profiles of CT emission – (a) and average lifetimes – (b) in $SrTiO_3$ doped with 0.1% Mn^{4+}.
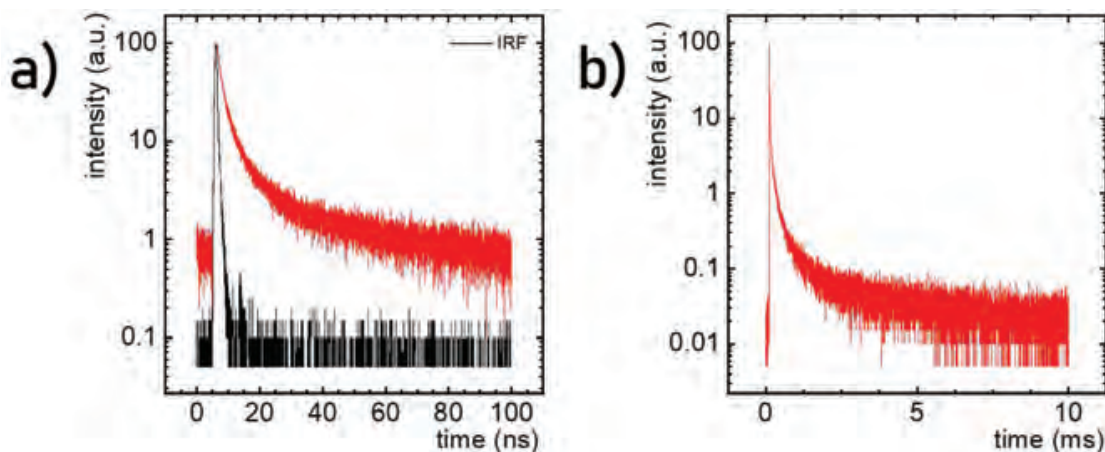
Figure S31. Luminescent decay profiles of CT emission at 13 K for Sr_2TiO_4 (λ_{exc} = 360 nm, λ_{em} = 440 nm) – (a) and $Sr_3Ti_2O_7$ (λ_{exc} = 350 nm, λ_{em} = 485 nm) – (b) doped with 0.1% Mn^{4+}.

Table S4. Comparison of average lifetimes of CT emission at 13 K obtained for R-P materials doped with 0.1% Mn^{4+}.

host	τ_{avr} of CT band
$SrTiO_3$	1.018±0.012 ns
Sr_2TiO_4	1.239±0.005 ns
$Sr_3Ti_2O_7$	0.125±0.001 ms

References:

(1)   Brik, M. G.; Srivastava, A. M.; Avram, N. M. Comparative Analysis of Crystal Field Effects and Optical Spectroscopy of Six-Coordinated Mn^{4+} Ion in the $Y_2Ti_2O_7$ and $Y_2Sn_2O_7$ Pyrochlores. *Opt Mater (Amst)* **2011**, *33* (11), 1671–1676.

(2)   Peng, M.; Yin, X.; Tanner, P. A.; Brik, M. G.; Li, P. Site Occupancy Preference, Enhancement Mechanism, and Thermal Resistance of Mn^{4+} Red Luminescence in $Sr_4Al_{14}O_{25}$:Mn^{4+} for Warm WLEDs. *Chemistry of Materials* **2015**, *27* (8), 2938–2945.

(3)   Piotrowski, W.; Trejgis, K.; Maciejewska, K.; Ledwa, K.; Fond, B.; Marciniak, L. Thermochromic Luminescent Nanomaterials Based on Mn^{4+}/Tb^{3+} Codoping for Temperature Imaging with Digital Cameras. *ACS Appl Mater Interfaces* **2020**, *12* (39), 44039–44048.

(4)   Riseberg, L. A.; Weber, M. J. Spectrum and Anomalous Temperature Dependence of the $^2E \rightarrow {}^4A_2$ Emission of $Y_3Al_5O_{12}$:Mn^{4+}. *Solid State Commun* **1971**, *9* (11), 791–794.

(5)   Wang, B.; Lin, H.; Xu, J.; Chen, H.; Wang, Y. $CaMg_2Al_{16}O_{27}$:Mn^{4+} -Based Red Phosphor: A Potential Color Converter for High-Powered Warm W-LED. *ACS Appl Mater Interfaces* **2014**, *6* (24), 22905–22913.

(6)   Cao, R.; Zhang, F.; Cao, C.; Yu, X.; Liang, A.; Guo, S.; Xue, H. Synthesis and Luminescence Properties of $CaAl_2O_4$:Mn^{4+} Phosphor. *Opt Mater (Amst)* **2014**, *38*, 53–56.

(7)   Medić, M. M.; Brik, M. G.; Dražić, G.; Antić, Ž. M.; Lojpur, V. M.; Dramićanin, M. D. Deep-Red Emitting Mn^{4+} Doped Mg_2TiO_4 Nanoparticles. *The Journal of Physical Chemistry C* **2015**, *119* (1), 724–730.

(8)   Wang, X.; Li, P.; Brik, M. G.; Li, X.; Li, L.; Peng, M. Thermal Quenching of Mn^{4+} Luminescence in $SrAl_{12}O_{19}$:Mn^{4+}. *J Lumin* **2019**, *206*, 84–90.

(9)   Meng, L.; Liang, L.; Wen, Y. Deep Red Phosphors $SrMgAl_{10}O_{17}$:Mn^{4+}, M (M = Li^+, Na^+, K^+, Cl^-) for Warm White Light Emitting Diodes. *Journal of Materials Science: Materials in Electronics* **2014**, *25* (6), 2676–2681.

(10)   Wang, S.; Sun, Q.; Liang, J.; Sun, L.; Devakumar, B.; Huang, X. Preparation and Photoluminescence Properties of Novel Mn^{4+} Doped $Li_3Mg_2TaO_6$ Red-Emitting Phosphors. *Inorg Chem Commun* **2020**, *116*, 107903.

(11)   Brik, M. G.; Srivastava, A. M. Electronic Energy Levels of the Mn^{4+} Ion in the Perovskite, $CaZrO_3$. *ECS Journal of Solid State Science and Technology* **2013**, *2* (7), R148–R152.

(12)   Da Fonseca, R. J. M.; Abritta, T. Radiative and Nonradiative Processes in $LiGa_5O_8$:Mn^{4+}. *Physica B Condens Matter* **1993**, *190* (4), 327–332.

(13)   Chen, H.; Sun, A.; Fang, D.; Xu, S.; Zhang, M.; Wang, A.; Mi, B.; Gao, Z. Structure and Luminescent Properties of Mn^{4+}-Activated $Li_2Mg_2TiO_5$ with Broadband Deep-Red Emission. *Journal of Materials Science: Materials in Electronics* **2022**, *33* (19), 15879–15893.

(14)   Zhang, S.; Hu, Y.; Duan, H.; Fu, Y.; He, M. An Efficient, Broad-Band Red-Emitting $Li_2MgTi_3O_8$:Mn^{4+} Phosphor for Blue-Converted White LEDs. *J Alloys Compd* **2017**, *693*, 315–325.

(15)   Talewar, R. A.; Mahamuda, Sk.; Rao, A. S.; Moharil, S. V. Novel Mn^{4+}-Activated $NaLiTi_3O_7$ Far-Red Emitting Phosphors. *J Lumin* **2023**, *255*, 119591.

(16)   Srivastava, A. M.; Brik, M. G. Ab Initio and Crystal Field Studies of the Mn^{4+}-Doped Ba_2LaNbO_6 Double-Perovskite. *J Lumin* **2012**, *132* (3), 579–584.

(17)   Takeda, Y.; Kato, H.; Kobayashi, M.; Kobayashi, H.; Kakihana, M. Photoluminescence Properties of Mn^{4+} -Activated Perovskite-Type Titanates, La_2MTiO_6:Mn^{4+} (M = Mg and Zn). *Chem Lett* **2015**, *44* (11), 1541–1543.

(18)   Brik, M. G.; Sildos, I.; Berkowski, M.; Suchocki, A. Spectroscopic and Crystal Field Studies of $YAlO_3$ Single Crystals Doped with Mn Ions. *Journal of Physics: Condensed Matter* **2009**, *21* (2), 025404.

(19) Cao, Y.; Fang, Y.; Zhang, G.; Zhao, G.; Liu, Y.; Zou, J.; Vainos, N.; Hou, J. High Quantum Yield Red-Emission Phosphor $Li_2Ge_4O_9$:Mn^{4+} for WLEDs Application. *Opt Mater (Amst)* **2019**, *98*, 109442.

(20) Wu, X.-X.; Zheng, W.-C.; Fang, W. Theoretical Investigations of the EPR Parameters for Cr^{3+} and Mn^{4+} Ions in $PbTiO_3$ Crystals. *Spectrochim Acta A Mol Biomol Spectrosc* **2008**, *69* (2), 498–502.

(21) Srivastava, A. M.; Brik, M. G. Crystal Field Studies of the Mn^{4+} Energy Levels in the Perovskite, $LaAlO_3$. *Opt Mater (Amst)* **2013**, *35* (8), 1544–1548.

(22) Zou, W.; Nie, W.; Wu, D.; Wu, S.; Wang, W.; Peng, J.; Ye, X. Synthesis, Luminescence Properties and Potential Applications for Plant Growth: A Novel Mn^{4+}-Activated $SrLa_2Al_2O_7$ Phosphor with Far-Red Emission. *J Lumin* **2023**, *257*, 119759.

This information is available free of charge at the website: http://pubs.acs.org/

PAPER

Check for updates

Strong sensitivity enhancement in lifetime-based luminescence thermometry by co-doping of SrTiO$_3$:Mn^{4+} nanocrystals with trivalent lanthanide ions†

W. M. Piotrowski, [ID] [a] K. Trejgis, [a] M. Dramicanin [ID] [b] and L. Marciniak [ID] *[a]

The co-doping of SrTiO$_3$:Mn^{4+} luminescent nanocrystals with trivalent lanthanide ions (Ln^{3+} = Lu^{3+}, Tm^{3+}, Er^{3+}, Ho^{3+}, Dy^{3+}, Eu^{3+}, and La^{3+}) is demonstrated as a new strategy for significant sensitivity improvement of lifetime-based luminescent thermometers. SrTiO$_3$:Mn^{4+}:Ln^{3+} nanocrystals of about 25 nm diameter were prepared by the modified Pechini method and characterized using X-ray powder diffraction and electron microscopy techniques. The temperature dependence of Mn^{4+} emission in SrTiO$_3$ was considerably altered by the co-doping of Ln^{3+} due to the cooperating effects of Mn^{4+} → Ti^{3+} and Mn^{4+} → Ln^{3+} energy transfers. A substantial enhancement of the relative sensitivity of lifetime-based thermometry as high as 145% with respect to the unco-doped nanocrystals reveals the success of the approach. The obtained values of maximal relative sensitivity for different Ln^{3+} co-dopants are 5.10% K^{-1} at 290 K for Er^{3+}, 5.00% K^{-1} at 301 K for Eu^{3+}, 4.84% K^{-1} at 303 K for Dy^{3+}, 4.71% K^{-1} at 289 K for Ho^{3+}, and 3.87% K^{-1} at 290.7 K for Lu^{3+}.

Introduction

Luminescence thermometry (LT) enables the remote temperature measurements from changes in the luminescence properties of the phosphor.[1–8] These days, the general trend in LT aims to improve the reliability of the temperature readouts and simplify measurement methodology.[5,7] LT is mainly focused on two techniques for temperature readout from luminescence where the temperature is determined based on the (i) intensity ratio of two emission bands (the steady-state technique, the luminescence intensity ratio method – LIR) and (ii) the kinetics of the emission (the time-resolved technique, the lifetime method).[9–19] Both approaches provide self-referencing temperature readouts and present some advantages over one another. The LIR technique is faster to operate, simpler, and requires less sophisticated instrumentation than the lifetime method.[20–27] However, one of the major LIR shortcomings is related to the effect of spectral heterogeneity of the transmittance of the measuring medium which may lead to a change in the shape of the luminescence spectrum and thus an erroneous temperature readout.[28–30] This effect does not occur in luminescent thermometers based on the lifetime of the excited level.[5] Unfortunately, in this case, the commonly obtained thermometer sensitivities to temperature changes are much lower than in the case of the luminescence intensity ratio counterparts.[5,16–18,31,32] Therefore, extensive research is ongoing to develop new phosphors and/or to thermally activate different physical processes taking place in them to improve the sensitivity of lifetime-based luminescent thermometers. Recently, it has been shown that the SrTiO$_3$:Mn^{4+} nanocrystals show favourable thermometric properties not only in the LIR approach but also in the lifetime-based approach.[33] The position of the Mn^{4+} emission in SrTiO$_3$:Mn^{4+} at 725 nm results from the location of the ^{2}E emitting state of the Mn^{4+} ions at relatively low energy compared to other Mn^{4+} doped phosphors. This is related to both the relatively long Ti–O bond lengths (1.95 A) compared to other Mn^{4+} doped phosphors which slightly decrease in energy with decreasing crystal field strength according to the Tanabe–Sugano diagram and with the covalency and the corresponding nephelauxetic effect. According to the calculation performed by Brik *et al.* in order to enhance the relative sensitivity of LT based on the Mn^{4+} luminescence, the host material should have the lowest possible β_1 value and low energies of the ^{4}T$_2$ and ^{2}E levels. Versatile analysis revealed that among all oxide and fluoride host materials reported so far, SrTiO$_3$ showed the lowest β_1 value of 0.9102, and the lowest energies of ^{2}E level of 13 795 cm^{-1} and ^{4}T$_2$ level of 18 201 cm^{-1},[34] thus being the most promising host for Mn^{4+} for thermometric applications. The maximum relative sensitivity of this kind of luminescent thermometer has been

[a] *Institute of Low Temperature and Structure Research, Polish Academy of Sciences, Okólna 2, 50-422 Wroclaw, Poland. E-mail: l.marciniak@intibs.pl*

[b] *Vinča Institute of Nuclear Sciences – National Institute of the Republic of Serbia, University of Belgrade, P.O. Box 522, Belgrade 11001, Serbia*
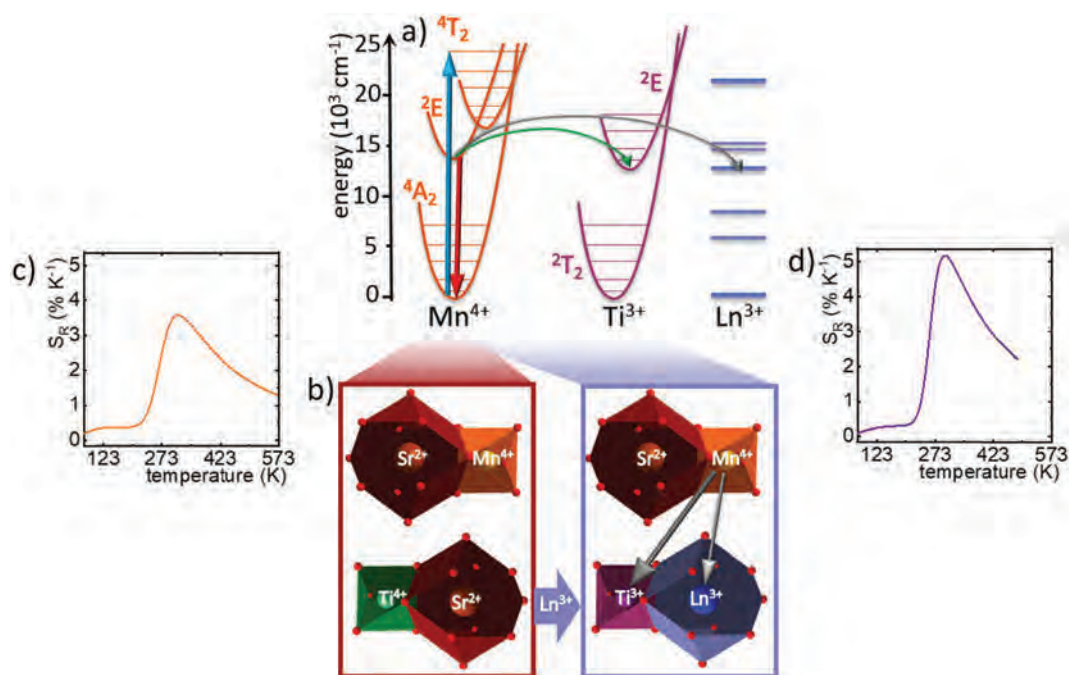
Fig. 1 The visualization of the concept of the proposed approach: simplified energy diagram of Mn^{4+}, Ti^{3+} and Ln^{3+} ions – (a); the polyhedral visualization of the substitution of the octahedral Ti^{4+} sites with Mn^{4+} ions and cuboctahedrally coordinated Sr^{2+} sites with Ln^{3+} ions in the $SrTiO_3$:Mn^{4+} structure – (b); thermal evolution of relative sensitivity $S_R(\tau_{avr})$ of $SrTiO_3$:Mn^{4+} – (c) and $SrTiO_3$:Mn^{4+},Tm^{3+} – (d) nanocrystals.

reported as $S_R = 3.57\%$ K^{-1} at 318 K. Our recent findings indicate that the co-doping of the $SrTiO_3$ nanocrystals with lanthanide (Ln^{3+}) ions leads to the reduction of the Ti^{4+} to the Ti^{3+} ions.[35] Since Ti^{3+} is optically active and the position of its energy levels is located in the close vicinity of the ^2E state of Mn^{4+}, co-doping with Ln^{3+} is presented in this paper as a novel strategy for the improvement of the relative sensitivity of the lifetime-based $SrTiO_3$:Mn^{4+},Ln^{3+} luminescent thermometer. The main conception of the manuscript is presented in Fig. 1. According to the previously reported results[35] the introduction of Ln^{3+} ions to the Sr^{2+} sites in the $SrTiO_3$ structure induces charge compensation by the local reduction of titanium from Ti^{4+} to Ti^{3+}. Therefore, the doping of the $SrTiO_3$ lattice with Mn^{4+} and any of Ln^{3+} ions shall contain also the optically active Ti^{3+} centers. Moreover, the excited state of Ti^{3+} ions is energetically located slightly below the ^2E level of Mn^{4+} ions (around 1100 cm^{-1}) and thus extremely efficient energy transfer $Mn^{4+} \rightarrow Ti^{3+}$ should be expected. Additionally, the 4f states of the Ln^{3+} ions may lead to the $Mn^{4+} \rightarrow Ln^{3+}$ energy transfer which may further enhance the sensitivity of luminescent thermometer.

Experimental

$SrTiO_3$:0.1%Mn^{4+} and $SrTiO_3$:0.1%Mn^{4+}, 1%Ln^{3+} (Ln^{3+} = Lu^{3+}, Tm^{3+}, Er^{3+}, Ho^{3+}, Dy^{3+}, Eu^{3+}, La^{3+}) nanopowders were synthesized using the modified Pechini method.[36] Strontium nitrate ($Sr(NO_3)_2$ of 99.9965% purity from Alfa Aesar), titanium(IV) n-butoxide ($Ti(OC_4H_9)_4$ with 99+% purity from Alfa Aesar), 2,4-pentanedione ($C_5H_8O_2$ with 99% purity from Alfa Aesar), citric acid ($C_6H_8O_7$ of 99% purity from Sigma Aldrich) and different lanthanide oxides: lutetium oxide (Lu_2O_3 with

99.995% purity from Stanford Materials Corporation), thulium oxide (Tm_2O_3 of 99.99% purity from Alfa Aesar), erbium oxide (Er_2O_3 of 99.999% purity from Sigma Aldrich), holmium oxide (Ho_2O_3 of 99.997% purity from Stanford Materials Corporation), dysprosium oxide (Dy_2O_3 of 99.999% purity from Stanford Materials Corporation), europium oxide (Eu_2O_3 of 99.99% purity from Stanford Materials Corporation) and lanthanum oxide (La_2O_3 of 99.99% purity from Stanford Materials Corporation) were used as the starting compounds. An appropriate amount of nitrates was dissolved in deionized water. In the case of Ln^{3+} co-doped nanocrystals, to obtain nitrates from oxides, their stoichiometric amounts were diluted in an aqueous solution of ultrapure nitric acid. Then, all aqueous solutions of nitrates were mixed together. Subsequently, an appropriate amount of $Ti(OC_4H_9)_4$ was measured out into a small laboratory beaker; then, a solution of 2,4-pentanedione in a stoichiometric ratio of 1:1 was added to stabilize $Ti(OC_4H_9)_4$ solution. The contents of the beaker were gently stirred to obtain a transparent, yellowish solution, which then was combined with the nitrate solution. After this, the solution was mixed with anhydrous citric acid. Subsequently, the obtained solution was dried for 1 week at 363.15 K until a resin was formed and annealed at 1173.15 K for 3 hours in air atmosphere.

All materials were examined by X-ray powder diffraction (XRPD) measurements carried out using a PANalytical X'Pert diffractometer, equipped with an Anton Paar TCU 1000 N temperature control unit, using Ni-filtered Cu-K$_\alpha$ radiation ($V = 40$ kV, $I = 30$ mA).

Transmission electron microscope (TEM) images were taken using a Philips CM-20 SuperTwin TEM microscope. The samples

were dispersed in methanol, and a droplet of this suspension was put on a microscope copper grid. Next, the samples were dried and purified in a plasma cleaner. Studies were performed using a conventional TEM procedure with 160 kV parallel beam electron energy.

The emission spectra were measured using the 400 nm excitation lines from a laser diode and a Silver-Nova Super Range TEC spectrometer from Stellarnet (1 nm spectral resolution) as the detector. The temperature of the sample was controlled using a THMS 600 heating–cooling stage from Linkam (0.1 K temperature stability and 0.1 K set point resolution).

The excitation spectra and luminescence decay profiles were recorded using a FLS1000 Fluorescence spectrometer from Edinburgh Instruments with a 450 W xenon lamp and µFlash lamp as the excitation sources and a R928P side window photomultiplier tube from Hamamatsu as the detector. The average lifetimes of the excited states were calculated with the use of double exponential function using eqn (S1), ESI.†

Results and discussion

Structural and morphological characterization

$SrTiO_3$ is one of the most widely investigated compounds from the family of perovskite oxides with a general chemical formula of ABO_3.[37–42] In the case of strontium titanate, the 'B' sites occupied by Ti^{4+} ions are octahedrally coordinated to six O^{2-} anions while the Sr^{2+} cations are cuboctahedrally coordinated to the 'A' sites between the Ti^{4+} octahedrons. Since manganese ions may exist in both the Mn^{2+} and Mn^{4+} oxidation states; theoretically, manganese ions may occupy both the Sr^{2+} and Ti^{4+} sites. In this case, the occupation of the octahedral Ti^{4+} sites with Mn^{4+} (effective ionic radii (EIR) = 53 pm) is clear and may be highly probable: $EIR_{Mn^{4+}}/EIR_{Ti^{4+}} = 53$ pm$/60.5$ pm ≈ 0.87. Therefore, due to the difference in the effective ionic radii and in the coordination number mainly the Mn^{4+} ions in the Ti^{4+} position are observed in the $SrTiO_3$ structure.[33,43–46] Additionally Mn^{4+} as a $3d^3$ ion is thermodynamically extremely

stabilized in the octahedral fields. On the other hand, the presence of Mn^{2+} in the Sr^{2+} sites in $SrTiO_3$ was reported by e.g. Tkach et al. in ceramics[47] and Yang et al. in the nanocrystals[48] when these materials were synthesized under favourable conditions, i.e. with the stoichiometric deficit of Sr^{2+} ions. There are no ionic radii reported by Shannon for the Mn^{2+} ions with coordination number (CN) above 8 (EIR = 96 pm for 8-fold coordinated Mn^{2+} ions).[43] However, Trepokov et al.[49] and Tkach et al.[47] suggest the extrapolation to CN = 12 from the EIR values of Mn^{2+} for lower CN with the EIR = 127 pm as a result. In this case, the misfit factor would equal $EIR_{Mn^{2+}}^{XII}/EIR_{Sr^{2+}}^{XII} = 127$ pm$/144$ pm ≈ 0.88 instead of $EIR_{Mn^{2+}}^{VIII}/EIR_{Sr^{2+}}^{XII} = 96$ pm$/144$ pm ≈ 0.67. However, the EIR vs. CN dependence is not clearly described and Shannon[43] intentionally did not present the ionic radius for Mn^{2+} with CN = 12. Nevertheless, the results from the mentioned papers lead to the conclusion that both Mn^{2+} and Mn^{4+} ions may be successfully located in the $SrTiO_3$ lattice depending on the deficit of Sr^{2+} or Ti^{4+}, respectively, and for the synthesis of $SrTi_{1-x}Mn_xO_3$ compound, the only Mn^{4+} substituting Ti^{4+} ions should be expected. To validate the phase purity of the synthesized phosphors, the X-ray powder diffraction (XRPD) patterns were analysed (Fig. 2a). Regardless of the dopant, the $SrTiO_3$ structure was obtained with no additional phases. In the case of the sample doped with 0.1% Mn^{4+}, the observed shift of peak positions by $\sim 0.03°$ toward higher angles in comparison to the reference pattern (ICSD 187296) is a consequence of the contraction of the unit cell corresponding to the Ti^{4+} with smaller Mn^{4+} ions (Fig. S1, ESI†). This result clearly confirms that the Ti^{4+} site cannot be substituted by Mn^{3+} or Mn^{2+} ions which would extend the cell size (EIR = 64.5 and 83 pm for high spin with CN = 6, respectively). On the other hand, the XRPD patterns of $SrTiO_3$ doped with Mn^{4+} and different Ln^{3+} ions (Table S1, ESI†) are shifted toward lower angles. The Ln^{3+} preferably occupy the Sr^{2+} sites and all of them are characterized by lower EIR than Sr^{2+} which should cause even deeper contraction. However, as shown recently, due to the difference in the ionic charge, the introduction of the Ln^{3+} ions in the Sr^{2+} site of the $SrTiO_3:Ln^{3+}$ structure leads to
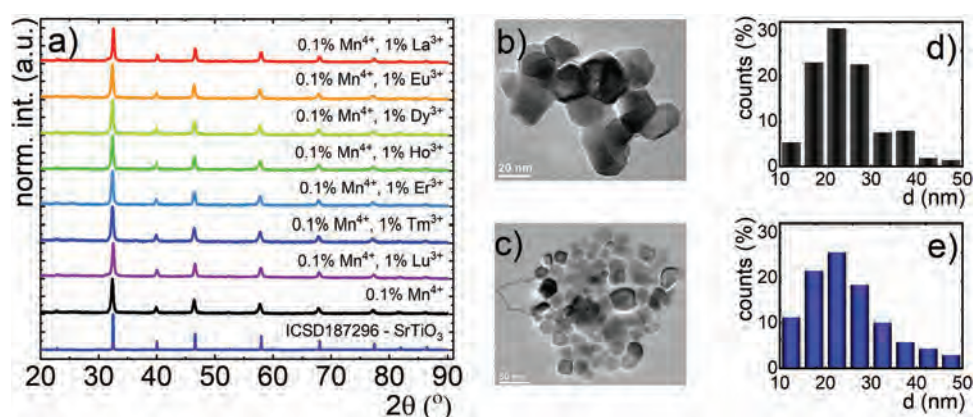
Fig. 2 Structural characterization of the synthesized materials: the X-ray diffraction patterns of $SrTiO_3:Mn^{4+}$ with different Ln^{3+} dopants – (a); the representative TEM images of $SrTiO_3:Mn^{4+}$ – (b) and $SrTiO_3:Mn^{4+},Tm^{3+}$ powders – (c); and the particle size distributions for $SrTiO_3:Mn^{4+}$ powder – (d) and $SrTiO_3:Mn^{4+},Tm^{3+}$ nanocrystals – (e).

the reduction of Ti^{4+} to Ti^{3+}. In this case, the Ti^{3+} with EIR = 67 pm in the octahedral coordination (CN = 6), which has a greater impact on the local symmetry in comparison to the dodecahedral Sr^{2+}/Ln^{3+} site, generates the enlargement of the cell size which is in the agreement with the presented results. Additionally, the analysis of the transmission electron microscopy (TEM) images is presented for the representative powders of $SrTiO_3$ doped with Mn^{4+} and co-doped with Mn^{4+} and Tm^{3+} (Fig. 2b and c). The analysis indicated that the nanocrystals formed well-crystalized and mostly agglomerated particles. For both phosphors, the average grain size achieved similar magnitudes, namely average Feret diameters were D_f = 27.0 nm and 24.6 nm for $SrTiO_3$:Mn^{4+} and $SrTiO_3$:Mn^{4+},Tm^3, respectively (Fig. 2d and e).

In the case of the $SrTiO_3$:Mn^{4+} nanocrystals, the mechanism responsible for the luminescence of Mn^{4+} ions is depicted in Fig. 3a. The λ_{exc} = 400 nm laser diode (25 000 cm^{-1}, blue arrow in Fig. 3a) excites electrons from the ground $^4A_2$ state of Mn^{4+} to its $^4T_1$ state. After this, because of the nonradiative processes, the ^2E state is populated and its radiative depopulation leads to the occurrence of the emission band centered at 725 nm ($^2E \rightarrow {}^4A_2$ electronic transition). At elevated temperatures, the Mn^{4+} emission starts quenching since the higher vibrational state of the ^2E parabola starts to be gradually occupied, and,

when the provided thermal energy exceeds the energy at which the ^2E and $^4T_2$ parabola intersects each other, the nonradiative processes becomes more pronounced. However, when the Ln^{3+} ions are introduced to the structure as the co-dopant, two additional processes are activated. First of them is the $Mn^{4+} \rightarrow Ln^{3+}$ energy transfer, which due to the energy mismatch of the ^2E state and the 4f states of the Ln^{3+} should occur with the assistance of the phonon. Therefore, the presence of these additional nonradiatively depopulating channels of the ^2E state will lead to both shortening of the lifetime of the ^2E state and its thermal quenching rate. However, as shown recently,[35] the difference in the ionic charge between the dopant and the Sr^{2+} ions leads to the reduction of Ti^{4+} to Ti^{3+}, which is an optically active ion. Therefore, the Ti^{3+} ^2E excited state which is localized below the ^2E state of Mn^{4+} becomes the acceptor in the $Mn^{4+} \rightarrow Ti^{3+}$ energy transfer. This effect was confirmed by the observation of the change in the emission thermal quenching rate of the nanocrystals co-doped with optically inactive ions $SrTiO_3$:Mn^{4+},La^{3+} and $SrTiO_3$:Mn^{4+},Lu^{3+}. The co-dopant does not affect the spectral position of the $^2E \rightarrow {}^4A_2$ emission bands which means that any significant changes in the crystal field strength after Ln^{3+} co-doping are not observed (Fig. 3b). Except the Tm^{3+}, the emission band of the Ln^{3+} ions cannot be observed in the spectral range which overlaps with
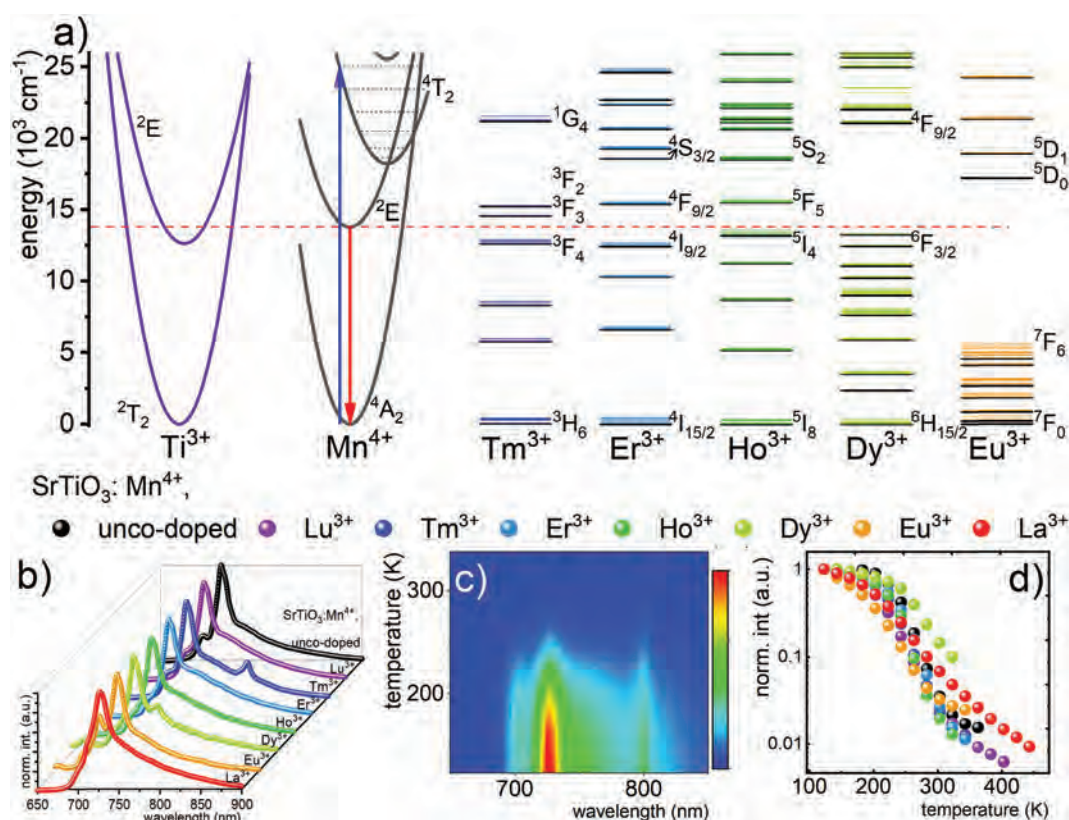
Fig. 3 Configurational coordinate diagrams for Ti^{3+}, Mn^{4+} and different Ln^{3+} ions (Tm^{3+}, Er^{3+}, Ho^{3+}, Dy^{3+}, and Eu^{3+}) – (a); the emission spectra of Mn^{4+} ions measured at 123 K for $SrTiO_3$ powders doped with Mn^{4+} and different Ln^{3+} ions – (b); the emission map as a function of temperature for representative $SrTiO_3$:Mn^{4+},Tm^{3+} sample – (c); and thermal evolution of the integral band intensities of the $^2E \rightarrow {}^4A_2$ transition of Mn^{4+} ion for different Ln^{3+} ions in $SrTiO_3$:Mn^{4+},Ln^{3+} nanocrystals – (d).

the $^2E \rightarrow ^4A_2$ band of Mn^{4+} ions. To analyze the possible $Mn^{4+} \rightarrow Ln^{3+}$ energy transfer, the position of the 4f energy levels localized in the closest energetical vicinity of the ^2E state of Mn^{4+} should be considered (Table 1). In this study, the exact energy of the ^2E energy level used for the calculation was based on the Brik's and Avram's calculations.[50] The small energy difference between the ^2E and 4f states of Ln^{3+} facilitates the interionic energy transfer. From this perspective, it can be clearly seen that the most beneficial energy level configuration has Tm^{3+} with both the $^3F_3$ and $^3F_4$ levels located with the energetic distance below 1000 cm^{-1} from the Mn^{4+} emitting state. The $^5I_4$ level of Ho^{3+} ions is the closest to the ^2E level ($\sim$300 cm^{-1}) in contrast to its upper level $^5F_5$ (above 1600 cm^{-1}). A similar situation is observed for Dy^{3+}; however, both states are in the slightly larger energy distance from the ^2E of Mn^{4+}. The largest energy separation was observed for Eu^{3+} ions where the $^5D_0$ state is localized 3460 cm^{-1} above the ^2E state.

Independent of the use of Ln^{3+} co-dopant, the excitation spectra for Mn^{4+} emission ($\lambda_{em} = 725$ nm) consist of two broad bands related to the $^4A_2 \rightarrow ^4T_1$ (with the maximum at 400 nm) and $^4A_2 \rightarrow ^4T_2$ (centered at around 530 nm) transitions (Fig. S2, ESI†). Therefore, the use of a 400 nm laser diode as the pumping source provides the efficient excitation of Mn^{4+} ions and its emission at $\sim$725 nm corresponding to the $^2E \rightarrow ^4A_2$ transition (Fig. 3b and Fig. S3, ESI†). $SrTiO_3$ is found to be a host material of one of the lowest crystal field strength among all Mn^{4+} doped phosphors ($D_q/B = 2.47$).[50] Moreover, the relatively low value of the activation energy between the ^2E and $^4T_2$ states found for the $SrTiO_3$:Mn^{4+} nanocrystals ($\Delta E_a \approx 2950$ cm^{-1}) makes this phosphor especially attractive from the luminescence thermometry perspective.[33] Therefore, to evaluate the luminescence thermal quenching in the $SrTiO_3$:Mn^{4+},Ln^{3+} nanocrystals, their emission intensity ratio was analyzed in a wide temperature range (Fig. 3c, and Fig. S4, ESI†). To avoid the spectral overlapping of the Mn^{4+} and Ln^{3+} emission bands which may affect the accuracy of the performed readout (which is especially problematic for the $^4F_{9/2} \rightarrow ^6H_{9/2}$ transition of Dy^{3+} at $\sim$751 nm or $^5D_0 \rightarrow ^7F_4$ of Eu^{3+} at $\sim$700 nm), the Mn^{4+} emission signal was integrated in the 720–740 nm spectral range (Fig. 3d). The Mn^{4+} emission intensity for $SrTiO_3$:Mn^{4+} nanocrystals remains unchanged up to around 203 K above which drastic quenching of intensity by almost two orders of magnitude can be observed. However, the thermal dependence of Mn^{4+} emission intensity changes when the nanocrystals are co-doped with the Ln^{3+} ions. In the case of

the La^{3+} and Lu^{3+} co-doped systems, the quenching process starts around 143 K due to the $Mn^{4+} \rightarrow Ti^{3+}$ energy transfer. The Mn^{4+} emission intensity of the $SrTiO_3$:Mn^{4+},La^{3+} nanocrystals decreases with a smaller and almost constant slope in the analyzed temperature range when compared to the intensity of the Lu^{3+} co-doped counterpart. On the other hand, in the case of the Lu^{3+} doped nanocrystals, an increase in the luminescence thermal quenching rate above 180 K can be observed. Due to the lack of the 4f energy state and the similarities in the electronic charge, the observed differences in the Mn^{4+} thermal quenching rates can be explained in terms of the differences in the ionic radii of the co-dopants. The difference in the size of the ions localized in the second coordination sphere of the Ti^{3+} ions may modify its crystal field strength and thus change the position of the ^2E state of Ti^{3+}. As a consequence, the probability of thermally dependent $Mn^{4+} \rightarrow Ti^{3+}$ energy transfer will be modified. The analysis starts to be more complex when the optically active Ln^{3+} ions are introduced to the $SrTiO_3$ structure due to the additional $Mn^{4+} \rightarrow Ln^{3+}$ energy transfer routes. The fastest thermal quenching of the $^2E \rightarrow ^4A_2$ emission intensity was observed for $SrTiO_3$:Mn^{4+},Tm^{3+} while the slowest was observed in the case of $SrTiO_3$:Mn^{4+},Dy^{3+} nanocrystals.

An increase in the luminescence thermal quenching rate associated with Ln^{3+} co-doping may suggest the beneficial influence of the co-doping process on the thermometric properties of lifetime based luminescent thermometers in $SrTiO_3$:Mn^{4+},Ln^{3+} nanocrystals. Indeed, an increase in temperature results in the shortening of the luminescence decay profile of the ^2E state of Mn^{4+} ions and the gradual deviation from their exponential shape (Fig. 4a and Fig. S5, ESI†). Therefore, to perform a comparative analysis on the influence of temperature on the decay kinetics, the average lifetimes were (τ_{avr}) calculated according to the procedure described in the ESI† (eqn (S1) and (S2)). The initial analysis indicates that at low temperature (at 123 K) τ_{avr} undergoes the shortening from the $\tau_{avr} = 1.72$ ms for $SrTiO_3$:Mn^{4+} to 0.53 ms for $SrTiO_3$:Mn^{4+},Tm^{3+} nanocrystals. Above 200 K, the thermal shortening of the τ_{avr} can be observed for all the nanocrystals, however, with different thermal quenching rates. The thermal dependence of the τ_{avr} of Mn^{4+} can be very well fitted by the theoretical dependence (eqn (1) and Fig. 4b):

$$\tau(T) = \frac{\tau_R(0) \cdot \tanh(h\nu/2k_BT)}{1 + (\tau_R(0) \cdot \tanh(h\nu/2k_BT)/\tau_{NR}) \cdot \exp(-\Delta E/k_BT)},$$

(1)

where $\tau_R(0)$ is the radiative lifetime at $T = 0$ K, $k_B = 0.69503476$ cm^{-1} K^{-1} is the Boltzmann constant, $h\nu$ is the average energy of phonons coupled to the $^2E \rightarrow ^4A_2$ transition, $1/\tau_{NR}$ is the non-radiative decay rate, and ΔE is the activation energy of the process. To quantify the observed thermally-induced variation of τ_{avr}, the absolute (S_A) relative sensitivity (S_R) of luminescent thermometers was calculated using the following equations:

$$S_A = \frac{\Delta \tau_{avr}}{\Delta T},$$

(2)

Table 1 The differences between the ^2E level of Mn^{4+} and Ln^{3+} states located above and below it

Co-dopant ion	Tm^{3+}	Er^{3+}	Ho^{3+}	Dy^{3+}	Eu^{3+}
Excited state above ^2E	$^3F_3$	$^4F_{9/2}$	$^5F_5$	$^4F_{9/2}$	$^5D_0$
Energy (cm^{-1})	689	1591	1658	7228	3436
Excited state below ^2E	$^3F_4$	$^4I_{9/2}$	$^5I_4$	$^6F_{3/2}$	$^7F_6$
Energy (cm^{-1})	940	1107	299	560	8144
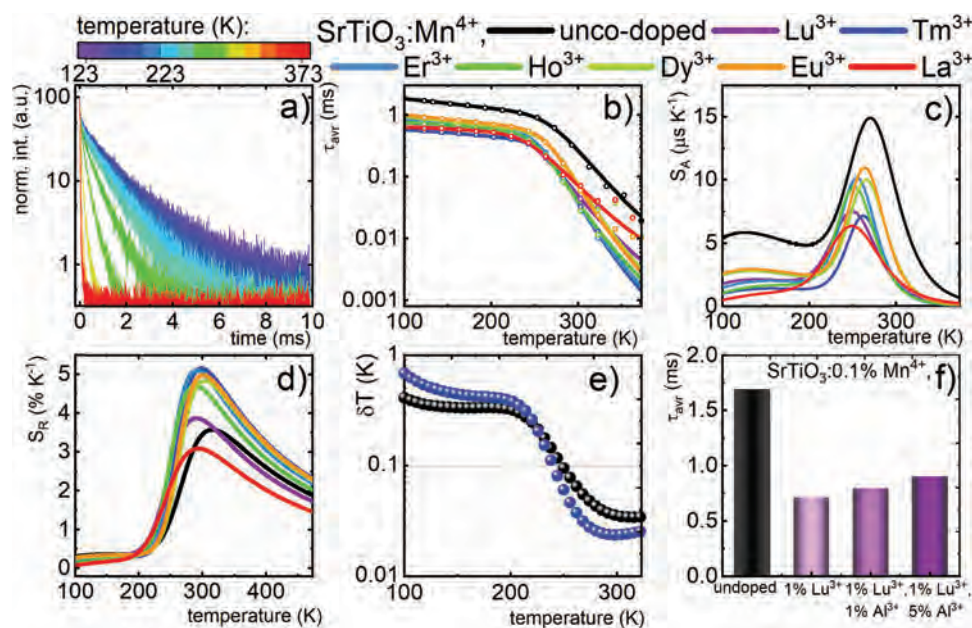
Fig. 4 Thermal evolution of luminescence decays of the ^{2}E excited state of Mn^{4+} for the representative $SrTiO_3$:Mn^{4+},Eu^{3+} nanocrystals – (a); thermal evolution of average lifetime τ_{avr} of the ^{2}E excited state of Mn^{4+} ions – (b), absolute sensitivities S_A – (c) and relative sensitivities S_R – (d) of $SrTiO_3$:Mn^{4+},Ln^{3+}; thermal dependence of temperature estimation uncertainty for $SrTiO_3$:Mn^{4+} and $SrTiO_3$:Mn^{4+},Tm^{3+} (e); and the influence of charge compensator concentration (Al^{3+}) on τ_{avr} at 123 K for $SrTiO_3$:Mn^{4+},Lu^{3+},Al^{3+} – (f).

$$S_R = \frac{1}{\tau_{avr}} \cdot \frac{\Delta\tau_{avr}}{\Delta T} \times 100\%, \qquad (3)$$

where $\Delta\tau_{avr}$ is the change in the lifetime of the ^{2}E excited state corresponding to the change of temperature ΔT. The highest values of S_A were found for $SrTiO_3$:Mn^{4+} nanocrystals with the maximum at $S_{Amax} = 14.93$ µs K^{-1} at 273 K (Fig. 4c). The smaller values of S_A observed for Ln^{3+} co-doped nanocrystals result from the shorter τ_{avr} values in those cases. However, when S_R is considered the favorable influence of the Ln^{3+} ions on the thermometric properties of these nanocrystals can be clearly confirmed (Fig. 4d). The maximal value of $S_R = 3.57\%$ K^{-1} at 318 K was found. The introduction of Ln^{3+} ions increases the S_R up to 5.19% K^{-1} for $SrTiO_3$:Mn^{4+},Tm^{3+} at 298 K. This significant enhancement of the relative sensitivity by around 145% with respect to the unco-doped nanocrystals reveals the beneficial role of the Ln^{3+} ions. The maximum values of relative sensitivity in the case of the nanocrystals with other co-dopant were as follows: 5.10% K^{-1} at 290 K for Er^{3+} ions, 5.00% K^{-1} at 301 K for Eu^{3+} ions, 4.84% K^{-1} at 303 K for Dy^{3+} ions 4.71% K^{-1} at 289 K for Ho^{3+} ions, and 3.87% K^{-1} at 290.7 K for Lu^{3+}. Only in the case of the La^{3+} co-doped nanocrystal a lower S_R with respect to that of the un-co doped counterparts was observed which results from the lower slope of the $\tau_{avr}(T)$ dependence. As discussed above, the quenching of the Mn^{4+} emission intensity starts at lower temperatures in this case which results in the continuous quenching of the ^{2}E $\rightarrow$ ^{4}A$_2$ luminescence in the considered temperature range. This causes the broadening of the usable temperature range of this luminescent thermometer since the $S_R > 1\%$ K^{-1} can be observed already above 325 K for $SrTiO_3$:Mn^{4+},La^{3+}. It is noteworthy that it the case of thermal

imaging using the lifetime approach usually two intensity frames are divided by each other to receive a 2D thermal map. Therefore, the acquisition time in this case is limited by the value of τ_{avr}. Therefore, although the shortening of τ_{avr} observed after the introduction of the Ln^{3+} co-dopants is beneficial from the relative sensitivity perspective it may affect the quality of thermal imaging by the limitation of the maximal available acquisition time. Nevertheless, for thermal imaging of the fast processes, the short τ_{avr} is favorable. Additional parameter which enables the verification of the quality of temperature readout using the luminescent thermometer is the temperature determination uncertainty calculated as follows:

$$\delta T = \frac{1}{S_R} \frac{\delta\tau_{avr}}{\tau_{avr}} \qquad (4)$$

where $\delta\tau_{avr}/\tau_{avr}$ is the uncertainty in the determination of τ_{avr} (determined as a standard deviation in 30 measurements of τ_{avr}) (Fig. S6, ESI†). Due to the introduction of the Ln^{3+} co-dopants the temperature determination uncertainty decreases from $\delta T = 0.034$ K at 310 K for $SrTiO_3$:Mn^{4+} to $\delta T = 0.020$ K for $SrTiO_3$:Mn^{4+},Tm^{3+} nanocrystals (Fig. 4e). Even the presence of Lu^{3+} ions enables the reduction of δT with respect to the unco-doped counterpart. In order to confirm that the reduction of the titanium ions to the Ti^{3+} oxidation state is responsible for the changes in the spectroscopic properties of the $SrTiO_3$:Mn^{4+},Lu^{3+} nanocrystals, the charge compensation has been used by the introduction of ions which (i) prefer the (3+) oxidation state, (ii) are optically inactive and (iii) may substitute the octahedral site of the Ti^{4+}. All these requirements are met by the Al^{3+} ions (Fig. S7, ESI†). The charge compensation can be written as follows:

$$SrTiO_3 \rightarrow Ti(4+) \rightarrow Sr(2+) \rightarrow Ti(4+) \rightarrow (10+) \quad (5)$$

$$SrTiO_3:Mn^{4+} \rightarrow Mn(4+) \rightarrow Sr(2+) \rightarrow Ti(4+) \rightarrow (10+) \quad (6)$$

$$SrTiO_3:Mn^{4+},Ln^{3+} \rightarrow Mn(4+) \rightarrow Ln(3+) \rightarrow Ti(3+) \rightarrow (10+) \quad (7)$$

$$SrTiO_3:Mn^{4+},Ln^{3+},Al^{3+} \rightarrow Mn(4+) \rightarrow Ln(3+) \rightarrow Al(3+) \rightarrow (10+) \quad (8)$$
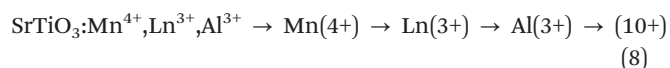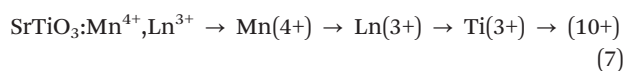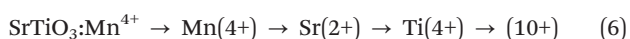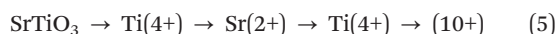
The presence of the Al^{3+} ions lessens the probability of the $Ti^{4+} \rightarrow Ti^{3+}$ reduction and, thus, should reduce the quenching rate of the ^2E state of the Mn^{4+} ions. Since this process is possible when the Al^{3+} and Ln^{3+} ions are in the close vicinity, excess of Al^{3+} with respect to the Lu^{3+} should be used. As shown in Fig. 4f, the τ_{avr} of ^2E which has been shortened after Lu^{3+} introduction starts to gradually elongate when the concentration of Al^{3+} ions increases from 0.7 ms to 0.9 ms for 5% Al^{3+} ions (Fig. S8, ESI†). However, the further increase in the Al^{3+} amount leads to structural decomposition and the occurrence of additional reflections in the XRD patterns. The obtained results confirm that quenching of the ^2E state in the Lu^{3+} co-doped nanocrystals is caused by energy transfer to the Ti^{3+} ions. Although presented in this manuscript experimental results may confirm the hypothesis that the presence of the Ti^{3+} ions in the $SrTiO_3:Mn^{4+},Ln^{3+}$ nanocrystals are responsible for the enhancement of the relative sensitivity of the luminescent thermometer based on the lifetime of the ^2E state of the Mn^{4+} ions, further, more specific experiments such as concentration-dependent photoluminescence studies or magnetic measurements will follow to elaborate on the hypothesis of Ti^{3+} in future and enable to verify if other processes or nonintentional dopants could also be responsible for the discussed effect. Presented data confirm the highly favorable influence of Ln^{3+} co-doping on the thermometric properties of the lifetime based luminescent thermometers in $SrTiO_3:Mn^{4+},Ln^{3+}$ nanocrystals.

Conclusions

In this work, a strategy for the improvement of a lifetime-based luminescent thermometer in $SrTiO_3:Mn^{4+}$ nanocrystals by the introduction of Ln^{3+} ions is proposed and investigated in detail. It was found that the introduction of the Ln^{3+} ions leads to the quenching of the lifetime of the ^2E state and increases the thermal quenching rate. This effect was discussed in terms of the cooperation of two effects, $Mn^{4+} \rightarrow Ti^{3+}$ energy transfer and $Mn^{4+} \rightarrow Ln^{3+}$ energy transfer. In the case of the former, it was proved that the difference in the ionic charge between Sr^{2+} and the co-dopant Ln^{3+} ions leads to the reduction of Ti^{4+} to Ti^{3+} which efficiently quenches the Mn^{4+} luminescence. This effect can be compromised to some extent by the introduction of Al^{3+} ions as charge compensators. When the optically active Ln^{3+} ions are introduced to the nanocrystals, the cooperation of both the effects occurs leading to the enhancement of the relative sensitivity of the lifetime based luminescent thermometer by as much as 145% for $SrTiO_3:Mn^{4+},Tm^{3+}$ ($S_R = 5.19\%/K$ at 298 K)

with respect to its unco-doped counterpart $SrTiO_3:Mn^{4+}$ ($S_R = 3.57\%$ K^{-1} at 318 K). Additionally, the presence of Ln^{3+} decreases the temperature determination uncertainty to $\delta T = 0.020$ K for $SrTiO_3:Mn^{4+},Tm^{3+}$ nanocrystals. These results clearly indicate that the proposed strategy enables the improvement of the thermometric properties of the lifetime based luminescent thermometry in strontium titanites and allows the development of highly sensitive lifetime based luminescent thermometers operating in biologically relevant temperatures.

Conflicts of interest

There are no conflicts to declare.

Acknowledgements

References

1 X. D. Wang, O. S. Wolfbeis and R. J. Meier, *Chem. Soc. Rev.*, 2013, **42**, 7834–7869.

2 D. Jaque and F. Vetrone, *Nanoscale*, 2012, **4**, 4301–4326.

3 C. D. S. Brites, P. P. Lima, N. J. O. Silva, A. Millán, V. S. Amaral, F. Palacio and L. D. Carlos, *Thermometry at the nanoscale*, The Royal Society of Chemistry, 2012, vol. 4.

4 C. D. S. Brites, S. Balabhadra and L. D. Carlos, *Adv. Opt. Mater.*, 2019, **7**, 1801239.

5 A. Bednarkiewicz, L. Marciniak, L. D. Carlos and D. Jaque, *Nanoscale*, 2020, **12**, 14405–14421.

6 M. Dramićanin, in *Luminescence Thermometry*, ed. M. B. T.-L. T. Dramićanin, Woodhead Publishing, 2018, pp. 251–263.

7 M. D. Dramićanin, *J. Appl. Phys.*, 2020, **128**, 40902.

8 M. Suta and A. Meijerink, *Adv. Theory Simul.*, 2020, **3**, 2000176.

9 A. M. Kaczmarek, M. Suta, H. Rijckaert, T. P. van Swieten, I. Van Driessche, M. K. Kaczmarek and A. Meijerink, *J. Mater. Chem. C*, 2021, **9**, 3589–3600.

10 M. Runowski, P. Woźny and I. R. Martín, *J. Mater. Chem. C*, 2021, **9**, 4643–4651.

11 P. Bolek, J. Zeler, C. D. S. Brites, J. Trojan-Piegza, L. D. Carlos and E. Zych, *Chem. Eng. J.*, 2021, **421**, 129764.

12 M. Runowski, P. Wozny, N. Stopikowska, I. R. Martín, V. Lavín and S. Lis, *ACS Appl. Mater. Interfaces*, 2020, **12**, 43933–43941.

13 M. Runowski, A. Shyichuk, A. Tymiński, T. Grzyb, V. Lavín and S. Lis, *ACS Appl. Mater. Interfaces*, 2018, **10**, 17269–17279.

14 Y. Gao, Y. Cheng, T. Hu, Z. Ji, H. Lin, J. Xu and Y. Wang, *J. Mater. Chem. C*, 2018, **6**, 11178–11183.

15 L. Marciniak, A. Bednarkiewicz, D. Kowalska and W. Strek, *J. Mater. Chem. C*, 2016, **4**, 5559–5563.

16 L. Marciniak and K. Trejgis, *J. Mater. Chem. C*, 2018, **6**, 7092–7100.

17 M. Wu, D. Deng, F. Ruan, B. Chen and S. Xu, *Chem. Eng. J.*, 2020, **396**, 125178.

18 L. Marciniak, K. Elzbieciak-Piecka, K. Kniec and A. Bednarkiewicz, *Chem. Eng. J.*, 2020, **388**, 124347.

19 X. Chen, S. Liu, K. Huang, J. Nie, R. Kang, X. Tian, S. Zhang, Y. Li and J. Qiu, *Chem. Eng. J.*, 2020, **396**, 125201.

20 F. Vetrone, R. Naccache, A. Zamarrón, A. J. De La Fuente, F. Sanz-Rodríguez, L. M. Maestro, E. M. Rodriguez, D. Jaque, J. G. Sole and J. A. Capobianco, *ACS Nano*, 2010, **4**, 3254–3258.

21 C. D. S. Brites, S. Balabhadra and L. D. Carlos, *Adv. Opt. Mater.*, 2019, **7**, 1801239.

22 Y. Cheng, Y. Gao, H. Lin, F. Huang and Y. Wang, *J. Mater. Chem. C*, 2018, **6**, 7462–7478.

23 E. Casagrande, M. Back, D. Cristofori, J. Ueda, S. Tanabe, S. Palazzolo, F. Rizzolio, V. Canzonieri, E. Trave and P. Riello, *J. Mater. Chem. C*, 2020, **8**, 7828–7836.

24 J. Trojan-Piegza, C. D. S. Brites, J. F. C. B. Ramalho, Z. Wang, G. Zhou, S. Wang, L. D. Carlos and E. Zych, *J. Mater. Chem. C*, 2020, **8**, 7005–7011.

25 M. Łukaszewicz, R. Tomala and R. Lisiecki, *J. Mater. Chem. C*, 2020, **8**, 1072–1082.

26 G. H. Pan, L. L. Zhang, H. H. Wu, X. Qu, H. H. Wu, Z. Hao, L. L. Zhang, X. Zhang and J. Zhang, *J. Mater. Chem. C*, 2020, **8**, 4518–4533.

27 H. Suo, X. Zhao, Z. Zhang and C. Guo, *Chem. Eng. J.*, 2020, **389**, 124506.

28 K. T. V. Grattan, Z. Y. Zhang, T. Sun, Y. Shen, L. Tong and Z. Ding, *Meas. Sci. Technol.*, 2001, **12**, 981–986.

29 L. Labrador-Páez, M. Pedroni, A. Speghini, J. García-Solé, P. Haro-González and D. Jaque, *Nanoscale*, 2018, **10**, 22319–22328.

30 Y. Shen, J. Lifante, N. Fernández, D. Jaque and E. Ximendes, *ACS Nano*, 2020, **14**, 4122–4133.

31 L. Yao, Y. Li, D. Xu, H. Lin, Y. Peng, S. Yang and Y. Zhang, *New J. Chem.*, 2019, **43**, 3848–3855.

32 N. Katumo, G. Gao, F. Laufer, B. S. Richards and I. A. Howard, *Adv. Opt. Mater.*, 2020, **8**, 2000507.

33 K. Trejgis, M. D. Dramićanin and L. Marciniak, *J. Alloys Compd.*, 2021, **875**, 159973.

34 M. G. Brik, S. J. Camardello and A. M. Srivastava, *ECS J. Solid State Sci. Technol.*, 2014, **4**, R39–R43.

35 L. M. W. Piotrowski, M. Kuchowicz and M. Dramićanin, *Chem. Eng. J.*, 2021, 131165.

36 M. P. Pechini, *US Pat.*, 3330697, 1967, p. 2.

37 L. F. Mattheiss, *Phys. Rev. B: Solid State*, 1972, **6**, 4740–4753.

38 T. S. Chang, *J. Appl. Phys.*, 1972, **43**, 3591–3595.

39 C. P. Enz, *Phys. Rev. B: Solid State*, 1972, **6**, 4695–4702.

40 M. Cardona, *Phys. Rev.*, 1965, **140**, A651–A655.

41 R. Pazik, M. Maczka, M. Malecka, L. Marciniak, A. Ekner-Grzyb, L. Mrowczynska and R. J. Wiglusz, *Dalton Trans.*, 2015, **44**, 10267–10280.

42 C. Matuszewska, K. Elzbieciak-Piecka and L. Marciniak, *J. Phys. Chem. C*, 2019, **123**, 18646–18653.

43 R. D. Shannon, *Acta Crystallogr., Sect. A: Cryst. Phys., Diffr., Theor. Gen. Crystallogr.*, 1976, **32**, 751–767.

44 Z. Bryknar, V. Trepakov, Z. Potůček and L. Jastrabík, *J. Lumin.*, 2000, **87-89**, 605–607.

45 M. G. Brik, *J. Phys. Chem. Solids*, 2006, **67**, 856–861.

46 H. Kato, Y. Takeda, M. Kobayashi, H. Kobayashi and M. Kakihana, *Front. Chem.*, 2018, **6**, 467.

47 A. Tkach, P. M. Vilarinho and A. L. Kholkin, *Acta Mater.*, 2005, **53**, 5061–5069.

48 H. Yang, K. Kan, J. Ouyang and Y. Li, *J. Alloys Compd.*, 2009, **485**, 351–355.

49 V. Trepakov, M. Makarova, O. Stupakov, E. A. Tereshina, J. Drahokoupil, M. Čerňanský, Z. Potůček, F. Borodavka, V. Valvoda, A. Lynnyk, A. Jäger, L. Jastrabik and A. Dejneka, *Mater. Chem. Phys.*, 2014, **143**, 570–577.

50 M. G. Brik and N. M. Avram, *J. Phys.: Condens. Matter*, 2009, **21**, 155502.

Supporting Information

Strong sensitivity enhancement in lifetime-based luminescence thermometry by co-doping of SrTiO$_3$:Mn^{4+} nanocrystals with trivalent lanthanide ions

W. M. Piotrowski[1], K. Trejgis[1], M. Dramicanin[2], L. Marciniak[1]*

[1]Institute of Low Temperature and Structure Research, Polish Academy of Sciences, Okólna 2, 50-422 Wroclaw,

Poland

[2]Vinča Institute of Nuclear Sciences - National Institute of the Republic of Serbia, University of Belgrade, P.O. Box 522, Belgrade 11001, Serbia

* corresponding author: *l.marciniak@intibs.pl*

KEYWORDS luminescent thermometry, emission decays, lanthanides, SrTiO$_3$, luminescence

The average lifetime of the excited states were calculated with the equation Eq. S1:

$$\tau_{avr} = \frac{A_1 \tau_1^2 + A_2 \tau_2^2}{A_1 \tau_1 + A_2 \tau_2} \tag{Eq. S1}$$

where: τ_1, τ_2 – the average time, which is in accordance with the relation $\tau = t \cdot \ln(2)$ and A_1, A_2 – amplitude, which are the parameters of the doubleexponential function:

$$y = y_0 + A_1 \cdot \exp(-\frac{x}{t_1}) + A_2 \cdot \exp(-\frac{x}{t_2}) \tag{Eq. S2}$$
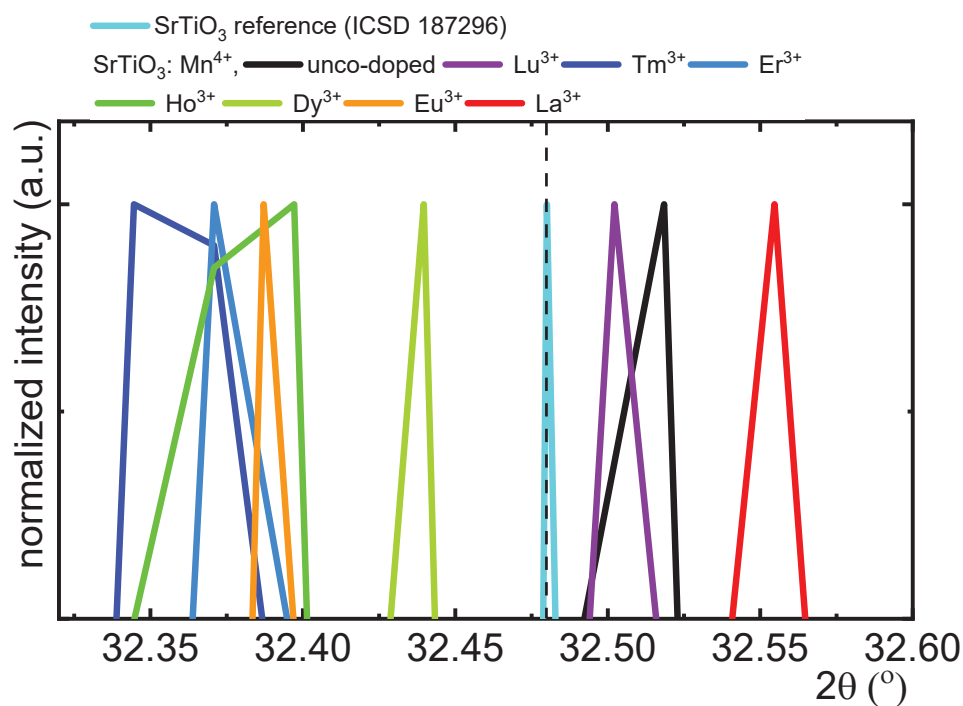
Figure S1. The zoom of the maximum of X-ray diffraction patterns of $SrTiO_3$:Mn^{4+} with different Ln^{3+} dopants.

Table S1. Shannon effective ionic radii of $SrTiO_3$ lattice and dopant ions.

Site	Coordination number (CN)	Shannon effective ionic radii (EIR) (pm)							
		Ti^{4+}		Mn^{4+}			Ti^{3+}		
octahedral	VI (6-fold)	60.5		53			67		
		Sr^{2+}	Lu^{3+}	Tm^{3+}	Er^{3+}	Ho^{3+}	Dy^{3+}	Eu^{3+}	La^{3+}
preferred	VIII/X (8-/10-fold)	-	97.7 (VIII)	99.4 (VIII)	100.4 (VIII)	101.5 (VIII)	102.7 (VIII)	106.6 (VIII)	127 (X)
cuboctahedral	XII (12-fold)	144	120.4 [e]	122.4 [e]	123.4 [e]	123.4 [e]	125.5 [e]	129.5 [e]	136

e – extrapolated linearly (in the all cases $R^2 > 0.9987$)
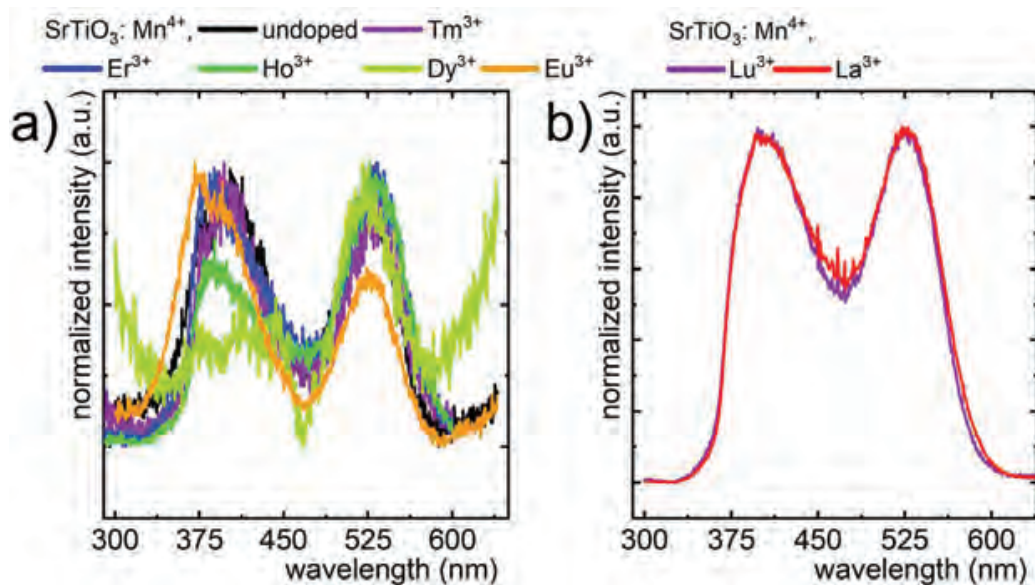
Figure S2. Excitation spectra of SrTiO$_3$:Mn^{4+}, Ln^{3+} with different optically active-a) and passive -b) Ln^{3+} ions measured at 123 K for emission of Mn^{4+} (λ_{em} = 725 nm).
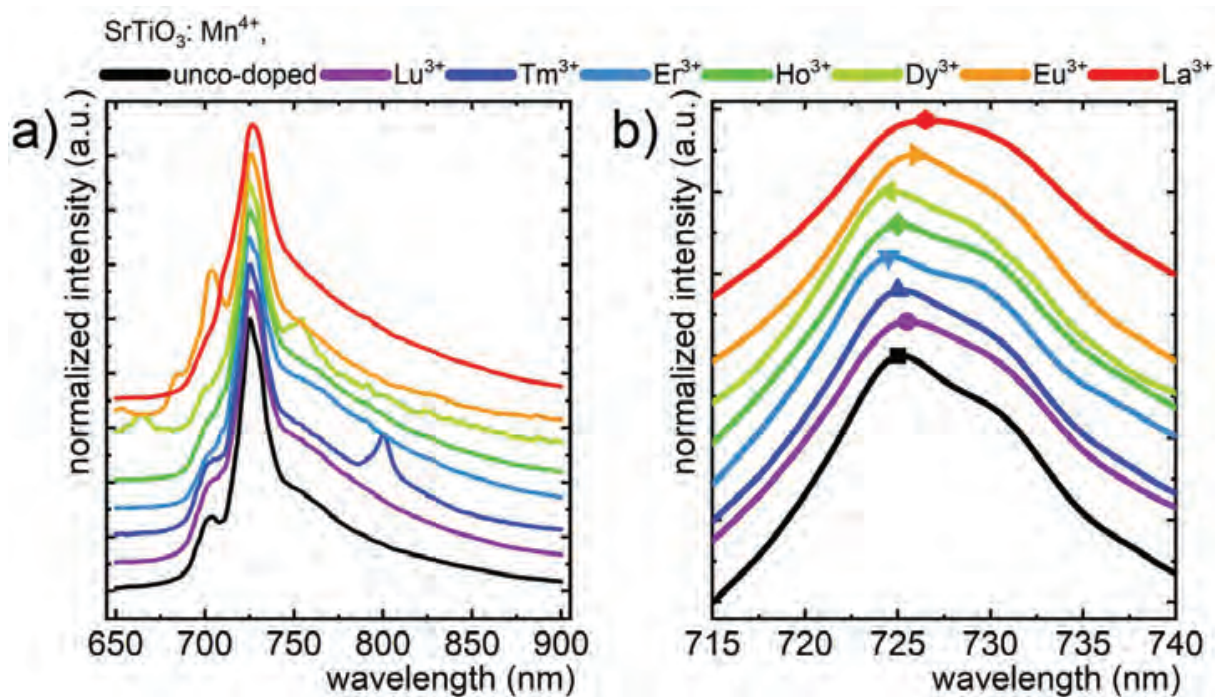
Figure S3. Emission spectra of SrTiO$_3$:Mn^{4+}, Ln^{3+} with different Ln^{3+} ions measured with λ_{exc} = 400 nm at 123 K – a) with the zoom of the same spectra in the 715-740 nm spectral range – b).
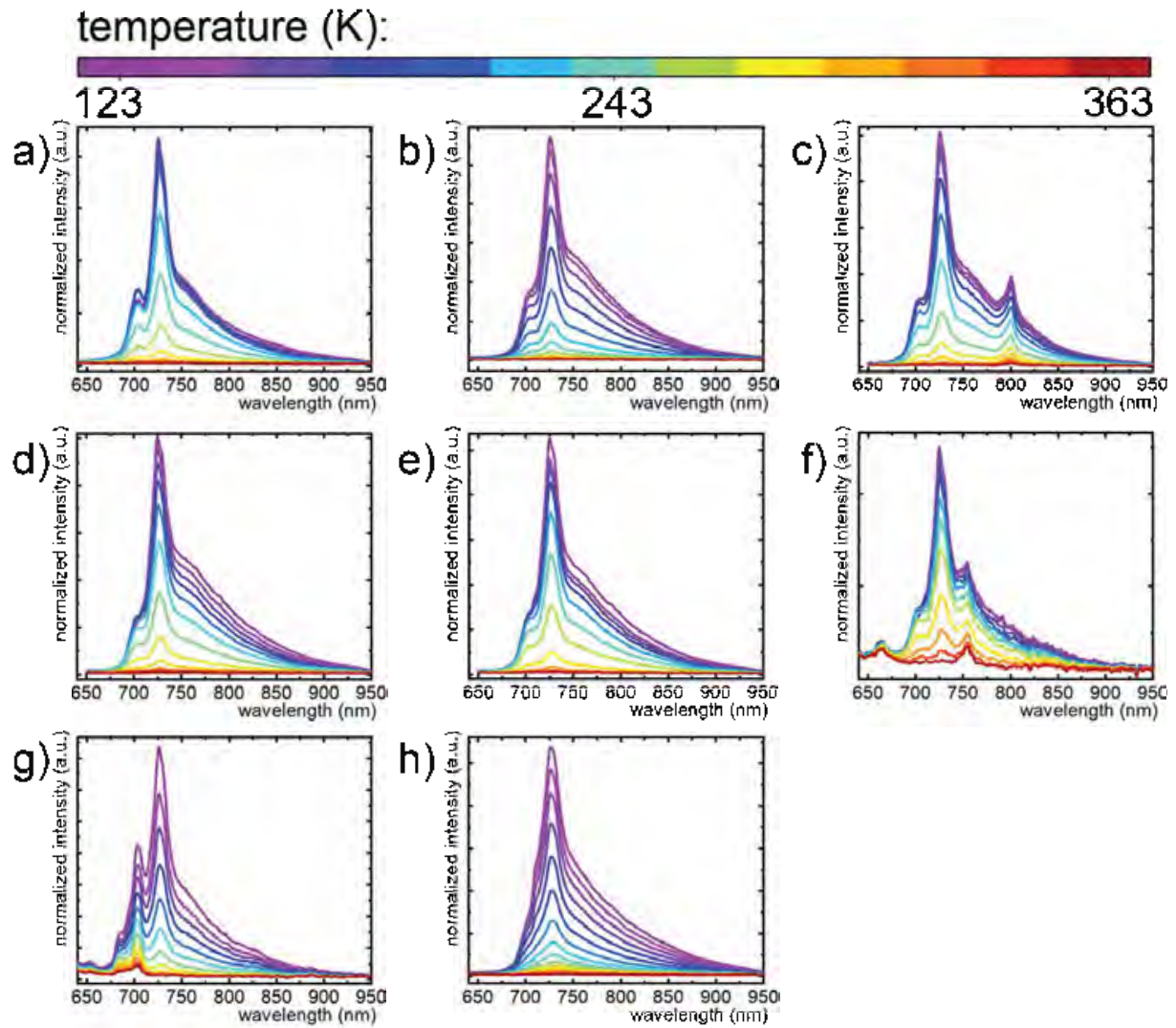
Figure S4. Thermal evolution of emission spectra excited by $\lambda_{exc} = 400$ nm for the SrTiO$_3$:0.1% Mn^{4+} – a) and SrTiO$_3$:0.1% Mn^{4+}, Ln^{3+}, where Ln^{3+} = Lu^{3+} – b), Tm^{3+} – c), Er^{3+} – d), Ho^{3+} – e), Dy^{3+} – f), Eu^{3+} – g), La^{3+} – h).
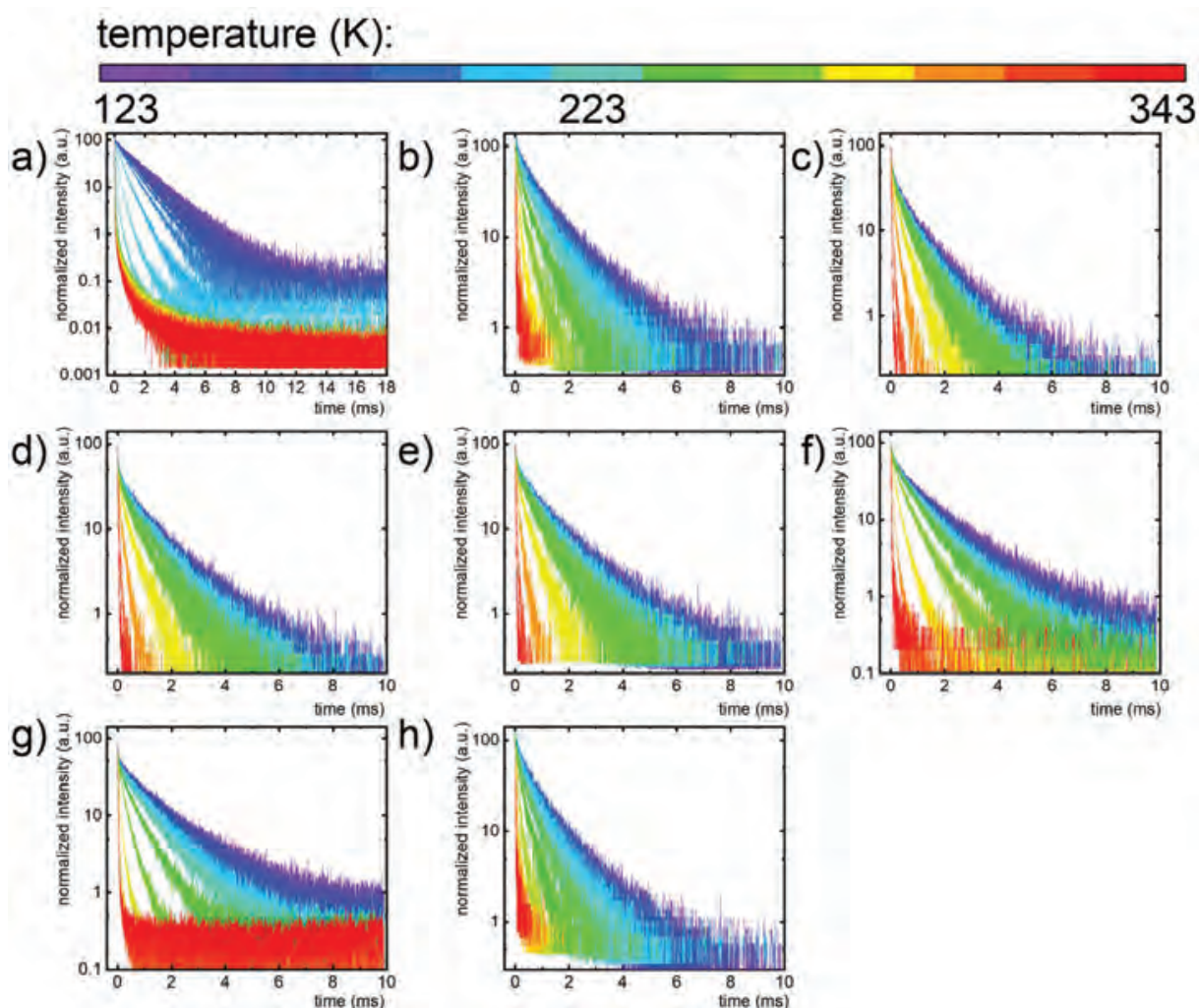
Figure S5. Thermal evolution of luminescent decays of ^2E excited state of Mn^{4+} for the $SrTiO_3$:0.1% Mn^{4+} – a) and $SrTiO_3$:0.1% Mn^{4+}, Ln^{3+}, where Ln^{3+} = Lu^{3+} – b), Tm^{3+} – c), Er^{3+} – d), Ho^{3+} – e), Dy^{3+} – f), Eu^{3+} – g), La^{3+} – h).

Table S2. The comparison of energy distances of Ln^{3+} excited states from ^2E of Mn^{4+} ions and thermometric parameters.

co-dopant ion	Eu^{3+}	Dy^{3+}	Er^{3+}	Ho^{3+}	Lu^{3+}	La^{3+}	Tm^{3+}
energy distance of excited state above ^2E (cm^{-1})	3436	7228	1591	1658	-	-	689
energy distance of excited state below ^2E (cm^{-1})	8144	560	1107	299	-	-	940
mean energy distance of excited state from ^2E (cm^{-1})	5790	3894	1349	978.5	--	--	814.5
τ_{avr} at 123 K (ms)	0.90	0.86	0.78	0.71	0.71	0.61	0.54
local minimum value of S_A	2.5331	2.3892	1.9774	1.6879	2.066	~0.8894	~1.373

(μs K^{-1})							
temperature of $S_{A\,min}$ (K)	196.9	199.8	182.4	164.9	173.15	~131.4	~190.05
maximum value of S_A (μs K^{-1})	10.959	10.003	10.155	9.4355	7.5298	6.3693	7.1677
temperature of $S_{A\,max}$ (K)	263.5	265.2	254.7	251.9	249.15	248.9	261.9
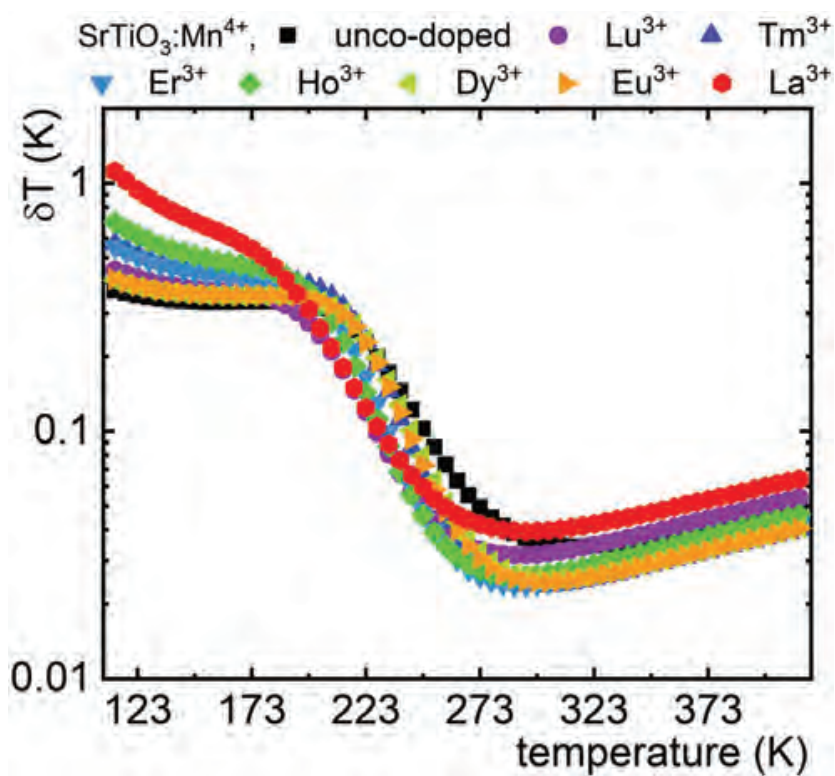
Figure S6. Thermal dependence of temperature estimation uncertainty for different Ln^{3+} in SrTiO$_3$:Mn^{4+}, Ln^{3+} samples.
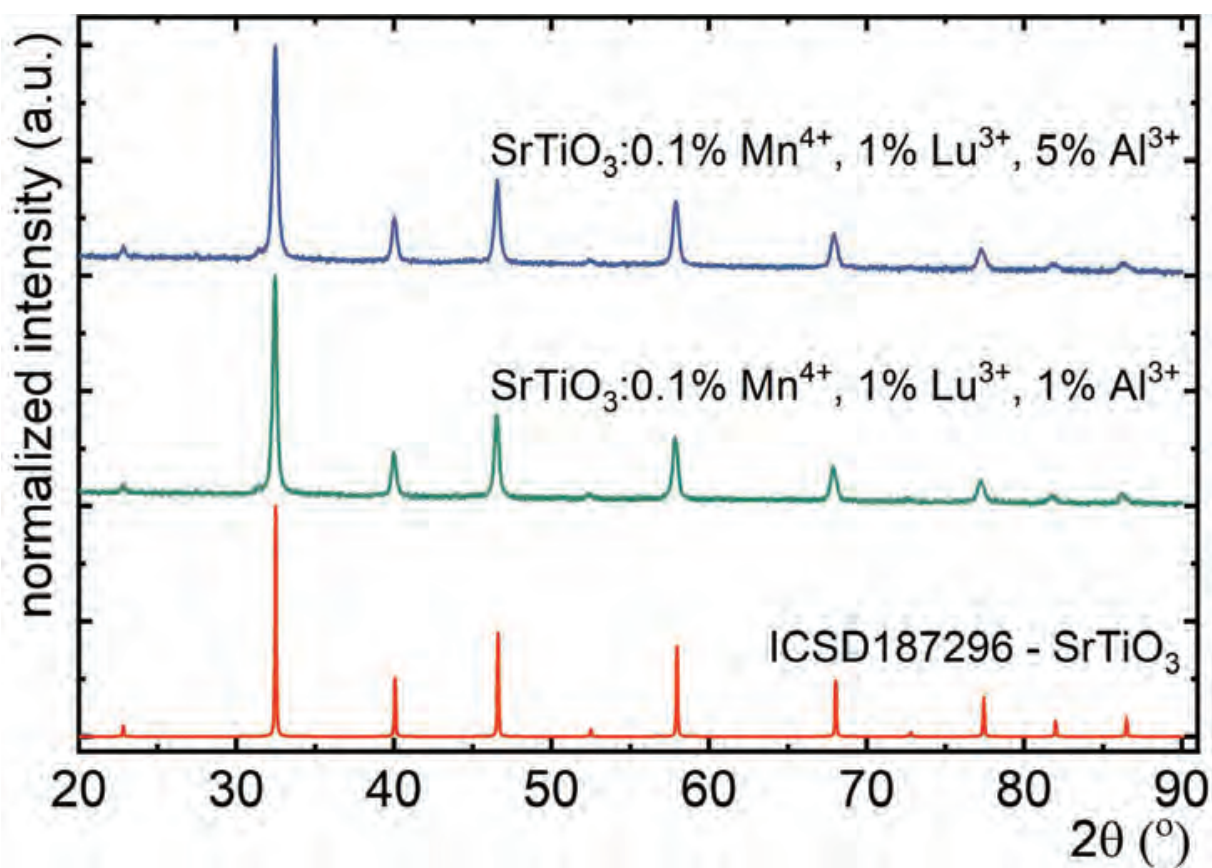
Figure S7. X-ray diffraction patterns of SrTiO$_3$:Mn^{4+}, Lu^{3+} co-doped with 1% and 5% of Al^{3+} ions.
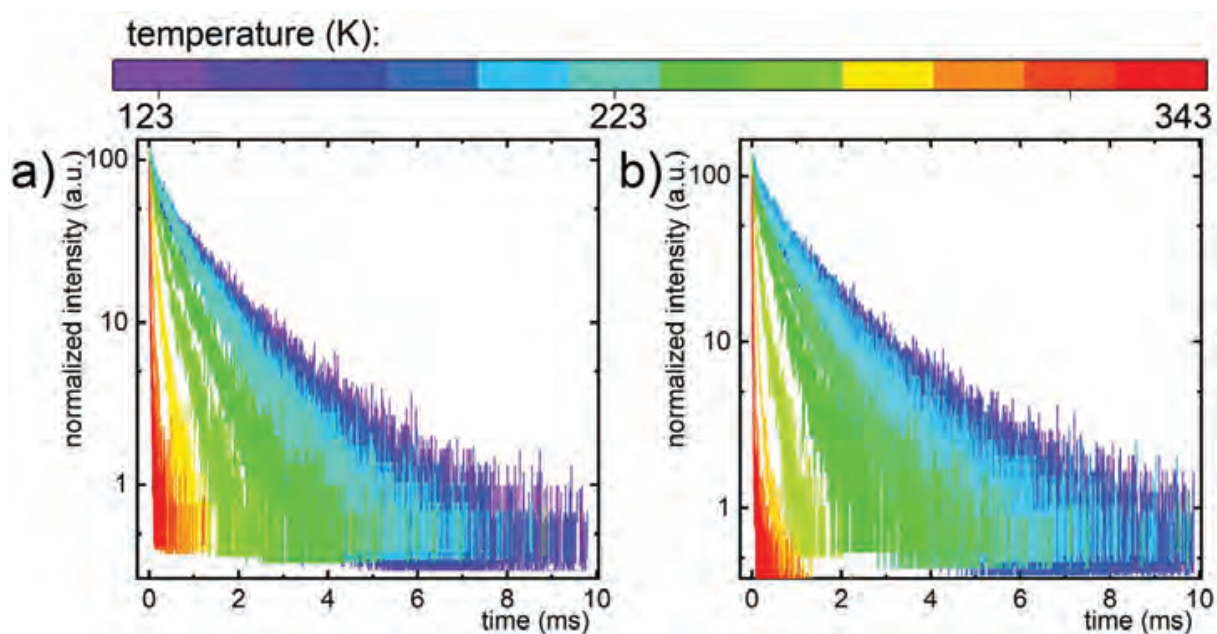
Figure S8. Thermal evolution of luminescent decays of ^{2}E excited state of Mn^{4+} for the SrTiO$_3$:0.1% Mn^{4+}, 1% Lu^{3+}, 1% Al^{3+} - a and SrTiO$_3$:0.1% Mn^{4+}, 1% Lu^{3+}, 5% Al^{3+} - b.

11. Copies of the co-authors' statements

Dr Vasyl Kinzhybalo

Institute of Low Temperature and Structure Research

Polish Academy of Sciences

Declaration of the co-authorship of the publication

I confirm my participation in the following publication:

W. M. Piotrowski, V. Kinzhybalo, L. Marciniak, Revisiting $Y_3Al_{5-x}Ga_xO_{12}$ Solid Solutions Doped with Chromium Ions: Effect of Local Symmetry on Thermal Quenching of Cr^{3+} and Cr^{4+} Ions. *ECS J Solid State Sci Technol*, 12, **(2023)**, 066003.

My contribution to this publication was conduction of (X-ray diffraction) XRD measurements and detailed Rietveld refinement with site occupancy calculations.

I confirm that MSc Eng. Wojciech Piotrowski was the lead co-author of this publication.

Dr Vasyl Kinzhybalo

MSc Maja Szymczak

Institute of Low Temperature and Structure Research

Polish Academy of Sciences

Declaration of the co-authorship of the publication

I confirm my participation in the following publication:

W.M. Piotrowski, <u>M. Szymczak</u>, E. Martín Rodríguez, R. Marin, M. Henklewska, B. Poźniak, M. Dramićanin, L. Marciniak, Step by step optimization of luminescence thermometry in $MgTiO_3:Cr^{3+}$, $Nd^{3+}@SiO_2$ nanoparticles towards bioapplications, Mater. Chem. Phys., (2023), 128623.

My contribution to this publication was conduction and optimization of coating of $MgTiO_3:Cr^{3+}$, Nd^{3+} nanoparticles with silica.

I confirm that MSc Eng. Wojciech Piotrowski was the lead co-author of this publication.

Maja Szymczak

MSc Maja Szymczak

Instytut Niskich Temperatur I Badań Strukturalnych Institute of Low Temperature and Structure Research
im. Włodzimierza Trzebiatowskiego Polskiej Akademii Nauk Polish Academy of Sciences

344

• ul. Okólna 2, 50-422 Wrocław Poland   • tel. +48 71 343 5021   • intibs@intibs.pl   • www.intibs.pl
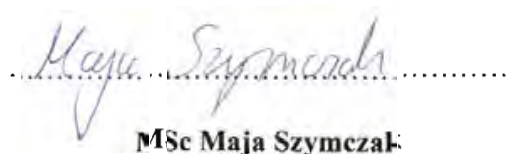
Declaration of coauthorship of publication

I hereby confirm my participation in the publication indicated below:

W.M. Piotrowski, M. Szymczak, E. Martín Rodríguez, R. Marin, M. Henklewska, B. Poźniak, M. Dramićanin, L. Marciniak, *Step by step optimization of luminescence thermometry in MgTiO$_3$:Cr^{3+}, Nd^{3+}@SiO$_2$ nanoparticles towards bioapplications*, **Mater. Chem. Phys**., (2023), 128623.

My contribution to this publication was the review and editing of the final version of the manuscript.

I also confirm that MSc Eng. Wojciech Piotrowski was the lead co-author of this publication.

Emma Martín Rodríguez, PhD
Dpto. de Física Aplicada
Universidad Autónoma de Madrid • Campus de Cantoblanco
C/Francisco Tomás y Valiente n° 7, 28049, Madrid
Facultad de Ciencias, módulo 12, despacho 506
Tel.: 91 497 6889 – emma.martin@uam.es – www.uam.es

Madrid, 31/10/2023

OBJECT: Declaration of co-authorship of the publication

I, Dr. Riccardo Marin, hereby I confirm my participation in the following publication:

W.M. Piotrowski, M. Szymczak, E. Martín Rodríguez, R. Marin, M. Henklewska, B. Poźniak, M. Dramićanin, L. Marciniak, Step by step optimization of luminescence thermometry in MgTiO$_3$:Cr^{3+}, Nd^{3+}@SiO$_2$ nanoparticles towards bioapplications, Mater. Chem. Phys., **(2023)**, 128623.

My contribution to this publication was the review and editing of final version of the manuscript. I confirm that MSc Eng. Wojciech Piotrowski was the lead co-author of this publication.

Sincerely,
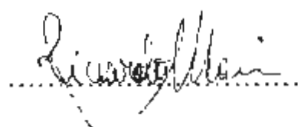
Riccardo Marin
Ramón y Cajal Fellow
Nanomaterials for Bioimaging Group (nanoBIG)
Institute for Advanced Research in Chemical Sciences (IAdChem)
Universidad Autónoma de Madrid (UAM), Spain

Dr Marta Henklewska   Wrocław, 31.10.2023

Department of Pharmacology and Toxicology

Wrocław University of Environmental and Life Sciences

Declaration of the co-authorship of the publication

I confirm my participation in the following publication:

W.M. Piotrowski, M. Szymczak, E. Martín Rodríguez, R. Marin, M. Henklewska, B. Poźniak, M. Dramićanin, L. Marciniak, Step by step optimization of luminescence thermometry in MgTiO$_3$:Cr^{3+}, Nd^{3+}@SiO$_2$ nanoparticles towards bioapplications, Mater. Chem. Phys., **(2023)**, 128623.

My contribution to this publication was the conduction and interpretation of cytotoxicity assessment of nanocrystalline phosphors noncoated and coated with silica.

I confirm that MSc Eng. Wojciech Piotrowski was the lead co-author of this publication.

Dr Marta Henklewska

Prof. Miroslav Dramićanin   Belgrade, 31.10.2023

Vinča Institute of Nuclear Sciences

University of Belgrade

Declaration of the co-authorship of the publications

I confirm my participation in the following publications:

1) W. Piotrowski, L. Dalipi, R. Szukiewicz, B. Fond, <u>M. Dramićanin</u>, L. Marciniak, The role of Cr^{3+} and Cr^{4+} in emission brightness enhancement and sensitivity improvements of NIR-emitting Nd^{3+}/Er^{3+} ratiometric luminescence thermometers, J. Mater. Chem. C, **(2021)**, 9, 12671-12680.

    My contribution to this publication was the review and editing of final version of the manuscript.

2) W. M. Piotrowski, K. Trejgis, <u>M. Dramićanin</u>, L. Marciniak, Strong sensitivity enhancement in lifetime-based luminescence thermometry by co-doping of $SrTiO_3{:}Mn^{4+}$ nanocrystals with trivalent lanthanide ions, J. Mater. Chem. C, **(2021)**, 10309-10316.

    My contribution to this publication was the modelling of thermal dependence of the average lifetimes and the review and editing of final version of the manuscript.

3) W.M. Piotrowski, M. Szymczak, E. Martín Rodríguez, R. Marin, M. Henklewska, B. Poźniak, <u>M. Dramićanin</u>, L. Marciniak, Step by step optimization of luminescence thermometry in $MgTiO_3{:}Cr^{3+}$, $Nd^{3+}@SiO_2$ nanoparticles towards bioapplications, Mater. Chem. Phys., **(2023)**, 128623.

    My contribution to this publication was the review and editing of final version of the manuscript.

I confirm that MSc Eng. Wojciech Piotrowski was the lead co-author of this publications.

……………………………………….

Prof. Miroslav Dramićanin

WROCŁAW UNIVERSITY OF ENVIRONMENTAL AND LIFE SCIENCES

FACULTY OF VETERINARY MEDICINE
DEPARTMENT OF PHARMACOLOGY AND TOXICOLOGY
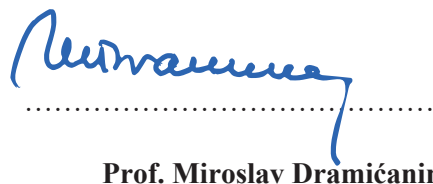
dr hab. Błażej Poźniak, prof. uczelni   Wrocław, 31.10.2023

Declaration of the co-authorship of the publications

I confirm my participation in the following publications:

1) W. M. Piotrowski, K. Kniec-Stec, M. Suta, B. Bogielski, B. Poźniak, L. Marciniak, Positive luminescence thermal coefficient of Mn^2 ions for highly sensitive luminescence thermometry, Chem. Eng. J. 464, **(2023)**, 142492.

2) W.M. Piotrowski, M. Szymczak, E. Martin Rodriguez, R. Marin, M. Henklewska, B. Poźniak, M. Dramićanin, L. Marciniak, Step by step optimization of luminescence thermometry in $MgTiO_3{:}Cr^{3+}$, $Nd^{3+}@SiO_2$ nanoparticles towards bioapplications, Mater. Chem. Phys., **(2023)**, 128623.

My contribution to this publications was the conduction and interpretation of cytotoxicity assessment of nanocrystalline phosphors.

I confirm that MSc Eng. Wojciech Piotrowski was the lead co-author of this publications.

dr hab. Błażej Poźniak, prof. uczelni

Dr Eng. Karolina Knieć-Stec   Winterthur, 05.09.2023
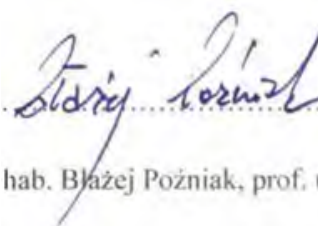
Declaration of the co-authorship of the publications

I confirm my participation in the following publications:

W. Piotrowski, <u>K. Kniec</u>, L. Marciniak, Enhancement of the Ln^{3+} ratiometric nanothermometers by sensitization with transition metal ions, J. Alloys Compd., 870, (2021), 159386.

My contribution to this publication was support in the synthesis of nanocrystalline phosphors.

I also confirm my participation in the following publication:

W. M. Piotrowski, <u>K. Kniec-Stec</u>, M. Suta, B. Bogielski, B. Pozniak, L. Marciniak, Positive luminescence thermal coefficient of Mn^{2+} ions for highly sensitive luminescence thermometry, Chem. Eng. J. 464, (2023), 142492.

My contribution to this publication was synthesis of microcrystalline phosphors used for structural and spectroscopic characterization and conduction of spectroscopic measurements: the excitation spectra, thermal evolution of the emission spectra, Raman spectra.

I confirm that MSc Eng. Wojciech Piotrowski was the lead co-author of above-mentioned publications.

Dr Eng. Karolina Knieć-Stec

MSc. Linda Dalipi   Magdeburg, 14.08.2023

Institute of Fluid Dynamics and Thermodynamics

Otto-von-Guericke University Magdeburg

Declaration of the co-authorship of the publications

I confirm my participation in the following publications:

W. Piotrowski, L. Dalipi, R. Szukiewicz, B. Fond, M. Dramićanin, L. Marciniak, The role of Cr^{3+} and Cr^{4+} in emission brightness enhancement and sensitivity improvements of NIR-emitting Nd^{3+}/Er^{3+} ratiometric luminescence thermometers, J. Mater. Chem. C, (2021), 9, 12671-12680

&

W.M. Piotrowski, K. Maciejewska, L. Dalipi, B. Fond, L. Marciniak, Cr^{3+} ions as an efficient antenna for the sensitization and brightness enhancement of Nd^{3+}, Er^{3+}-based ratiometric thermometer in $GdScO_3$ perovskite lattice, J. Alloys Compd., (2022), 923, 166343.

My contribution to these publications was conduction of absolute emission intensity measurements and brightness enhancement calculations.

I confirm that MSc Eng. **Wojciech Piotrowski** was the lead co-author of these publications.

....

MSc. Linda Dalipi

Dr Rafał Szukiewicz   Wroclaw, 14.08 2023

Institute of Experimental Physics

Faculty of Physics and Astronomy, University of Wroclaw

Declaration of the co-authorship of the publication

I confirm my participation in the following publication:

W. Piotrowski, L. Dalipi, R. Szukiewicz, B. Fond, M Dramićanin, L. Marciniak, The role of Cr^{3} and Cr^{4+} in emission brightness enhancement and sensitivity improvements of NIR-emitting Nd^{3+}/Er^{3+} ratiometric luminescence thermometers, *J. Mater. Chem. C*, (2021), 9, 12671-12680.

My contribution to this publication was conduction and interpretation of X-ray photoelectron spectroscopy (XPS) measurements.

I confirm that MSc Eng. Wojciech Piotrowski was the lead co-author of this publication
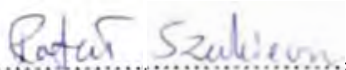
Rafał Szukiewicz

Dr Rafal Szukiewicz

Dr. Benoit Fond   Paris, 14.08.2023

Department of Aerodynamics

ONERA, the French Aerospace Laboratory

Declaration of the co-authorship of the publications

I confirm my participation in the following publications:

W. Piotrowski, L. Dalipi, R. Szukiewicz, <u>B. Fond</u>, M. Dramićanin, L. Marciniak, The role of Cr^{3+} and Cr^{4+} in emission brightness enhancement and sensitivity improvements of NIR-emitting Nd^{3+}/Er^{3+} ratiometric luminescence thermometers, J. Mater. Chem. C, (2021), 9, 12671-12680

&

W.M. Piotrowski, K. Maciejewska, L. Dalipi, <u>B. Fond</u>, L. Marciniak, Cr^{3+} ions as an efficient antenna for the sensitization and brightness enhancement of Nd^{3+}, Er^{3+}-based ratiometric thermometer in $GdScO_3$ perovskite lattice, *J. Alloys Compd.*, (2022), 923, 166343.

My contribution to these publications was the methodology, and supervision of the absolute emission intensity measurements and brightness enhancement calculations as well as the review and editing of the manuscript.

I also confirm my participation in the following publication:

W. Piotrowski, K. Trejgis, K. Maciejewska, K. Ledwa, <u>B. Fond</u>, L. Marciniak, Thermochromic luminescent nanomaterials based on Mn^{4+}/Tb^{3+} codoping for temperature imaging with digital cameras, *ACS Appl. Mater. Interfaces*, 12, 39, (**2020**), 44039-44048.

My contribution to this publication was the review and editing of the manuscript.

I confirm that MSc Eng. Wojciech Piotrowski was the lead co-author of this publications.

………………………………….

Prof. Benoit Fond

Dr Kamila Maciejewska
Institute of Low Temperature and Structure Research
Polish Academy of Sciences

Declaration of the co-authorship of the publication

I confirm my participation in the following publication:

W.M. Piotrowski, K. Maciejewska, L. Dalipi, B. Fond, L. Marciniak, Cr^{3+} ions as an efficient antenna for the sensitization and brightness enhancement of Nd^{3+}, Er^{3+}-based ratiometric thermometer in $GdScO_3$ perovskite lattice, *J. Alloys Compd.*, (2022), 923, 166343.

My contribution to this publications was the synthesis of microcrystalline phosphors.

I confirm my participation in the following publication:

W. M. Piotrowski, K. Maciejewska, L. Marciniak, Boosting the thermometric performance of the Nd^{3+}, Er^{3+} based luminescence thermometers by sensitization via Cr^{3+} ions: the role of the host material, Mater. Today Chem. 30, (2023), 101591.

My contribution to this publications was the synthesis of micro-/nano-crystalline phosphors and conduction of spectroscopic measurements: the excitation spectra, thermal evolution of the emission spectra and thermal evolution of luminescent decay profiles.

I also confirm my participation in the following publication:

W. Piotrowski, K. Trejgis, K. Maciejewska, K. Ledwa, B. Fond, L. Marciniak, Thermochromic luminescent nanomaterials based on Mn^{4+}/Tb^{3+} codoping for temperature imaging with digital cameras, *ACS Appl. Mater. Interfaces*, 12, 39, (2020), 44039-44048.

My contribution to this publication was conduction of (X-ray diffraction) XRD measurements.

I confirm that MSc Eng. Wojciech Piotrowski was the lead co-author of this publications.

Dr Kamila Maciejewska

Faculty of Mathematics and Natural Sciences

Institute of Inorganic Chemistry & Structural Chemistry II

Inorganic Photoactive Materials

Jun.-Prof. Dr. Markus Suta

Phone +49 211 81 13147
Mobile +49 176 701 623 32
E-mail markus.suta@hhu.de
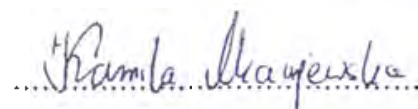
Declaration of the co-authorship of a publication

Düsseldorf, 18.08.2023

Heinrich Heine University Düsseldorf
Universitätsstraße 1
40225 Düsseldorf
Building 26.42
Level 01 Room 21

www.hhu.de

I hereby confirm the participation in the following publications:

W. M. Piotrowski, K. Kniec-Stec, M. Suta, B. Bogielski, B. Pozniak, L. Marciniak, *Positive luminescence thermal coefficient of Mn^{2+} ions for highly sensitive luminescence thermometry, Chem. Eng. J.* 464, **(2023)**, 142492. My contribution to this publication was a discussion of data and review and editing of the final version of the manuscript.

I confirm that MSc Eng. Wojciech Piotrowski was the leading author of this publication.

Institut für Anorganische Chemie
Photoaktive Materialien
Heinrich-Heine-Universität Düsseldorf
Universitätsstr. 1
40225 Düsseldorf

Jun.-Prof. Dr. Markus Suta

Dr Bartosz Bogielski

Department of Physiology

Medical University of Silesia in Katowice

Wrocław, 31.10.2023

Declaration of the co-authorship of the publication

I confirm my participation in the following publication:

W. M. Piotrowski, K. Kniec-Stec, M. Suta, B. Bogielski, B. Pozniak, L. Marciniak, Positive luminescence thermal coefficient of Mn^{2+} ions for highly sensitive luminescence thermometry, Chem. Eng. J. 464, (2023), 142492.

My contribution to this publication was the conduction and interpretation of cytotoxicity assessment of nanocrystalline phosphors.

I confirm that MSc Eng. Wojciech Piotrowski was the lead co-author of this publication.

Dr Bartosz Bogielski

Dr Eng. Karolina Kaczmarczyk (Trejgis)   Wrocław, 17.08.2023

Declaration of the co-authorship of the publications

I confirm my participation in the following publications:

1) W. Piotrowski, <u>K. Trejgis</u>, K. Maciejewska, K. Ledwa, B. Fond, L. Marciniak, Thermochromic luminescent nanomaterials based on Mn^{4+}/Tb^{3+} codoping for temperature imaging with digital cameras, ACS Appl. Mater. Interfaces, 12, 39, (2020), 44039-44048.

My contribution to this publication was the synthesis of the majority of nanocrystalline phosphors.

2) W. M. Piotrowski, <u>K. Trejgis</u>, M. Dramićanin, L. Marciniak, Strong sensitivity enhancement in lifetime-based luminescence thermometry by co-doping of $SrTiO_3:Mn^{4+}$ nanocrystals with trivalent lanthanide ions, J. Mater. Chem. C, (2021), 10309-10316.

My contribution to this publication was the synthesis of part of nanocrystalline phosphors.

I confirm that MSc Eng. Wojciech Piotrowski was the lead co-author of this publications.

Karolina Kaczmarczyk

Dr Eng. Karolina Kaczmarczyk (Trejgis)

357

Dr Karolina Ledwa

Institute of Low Temperature and Structure Research

Polish Academy of Sciences

Declaration of the co-authorship of the publication

I confirm my participation in the following publication:

W. Piotrowski, K. Trejgis, K. Maciejewska, K. Ledwa, B. Fond, L. Marciniak, Thermochromic luminescent nanomaterials based on Mn^{4+}/Tb^{3+} codoping for temperature imaging with digital cameras, *ACS Appl. Mater. Interfaces*, 12, 39, (2020), 44039-44048.

My contribution to this publication was conduction of transmission electron microscopy (TEM) and selected-area electron diffraction (SAED) images.

I confirm that MSc Eng. Wojciech Piotrowski was the lead co-author of this publication.

..........Karolina Ledwa..........

Dr Karolina Ledwa

Dr. Paulina Bolek
Luminescent Materials Group
14 F. Joliot-Curie Street
50-383 Wrocław
Tel. +48 71 3757644
paulina.bolek@uwr.edu.pl

December 15, 2023.

Declaration of the co-authorship of the publication

I confirm my participation in the following publication:

W. M. Piotrowski, P. Bolek, M. G. Brik, E. Zych, L. Marciniak, Frontiers of Deep-Red Emission of Mn^{4+} Ions with Ruddlesden–Popper Perovskites, Inorg. Chem. **(2024)**, accepted, DOI: https://doi.org/10.1021/acs.inorgchem.3c03113

My contribution to this publication was the conduction of spectroscopic measurements: thermal evolution of the emission spectra and luminescent decay profiles of the investigated phosphors.

I confirm that MSc Eng. Wojciech Piotrowski was the lead co-author of this publication.

Dr. Paulina Bolek

Prof. Mikhail G. Brik   Tartu, 14.12.2023

Institute of Physics,

University of Tartu, Estonia

Declaration of the co-authorship of the publication

I confirm my participation in the following publication:

W. M. Piotrowski, P. Bolek, M. G. Brik, E. Zych, L. Marciniak, Frontiers of Deep-Red Emission of Mn^{4+} Ions with Ruddlesden−Popper Perovskites, Inorg. Chem. **(2024)**, accepted, DOI: https://doi.org/10.1021/acs.inorgchem.3c03113

My contribution to this publication was the theoretical calculations of crystal field and Racah parameters for Mn^{4+} ions.

I confirm that MSc Eng. Wojciech Piotrowski was the lead co-author of this publication.

Prof. Mikhail G. Brik

Prof. Eugeniusz Zych   Wrocław, 14.12.2023

Faculty of Chemistry

University of Wrocław

Declaration of the co-authorship of the publication

I confirm my participation in the following publication:

W. M. Piotrowski, P. Bolek, M. G. Brik, <u>E. Zych</u>, L. Marciniak, Frontiers of Deep-Red Emission of Mn^{4+} Ions with Ruddlesden−Popper Perovskites, Inorg. Chem. **(2024)**, accepted, DOI: https://doi.org/10.1021/acs.inorgchem.3c03113

My contribution to this publication was the review and editing of the final version of the manuscript.

I confirm that MSc Eng. Wojciech Piotrowski was the lead co-author of this publication.

………………………………………
Prof. Eugeniusz Zych

Wrocław, 15.12.2023

Prof. Łukasz Marciniak

Institute of Low Temperature and Structure Research

Polish Academy of Sciences

Declaration of the co-authorship of the publications

I confirm my participation in the following publications:

P1) W. M. Piotrowski, V. Kinzhybalo, <u>L. Marciniak</u>, Revisiting $Y_3Al_{5-x}Ga_xO_{12}$ Solid Solutions Doped with Chromium Ions: Effect of Local Symmetry on Thermal Quenching of Cr^{3+} and Cr^{4+} Ions, *ECS J Solid State Sci Technol*, 12, **(2023)**, 066003.

P2) W. M. Piotrowski, M. Szymczak, E. Martin Rodríguez, R. Marin, M. Henklewska, B. Poźniak, M. Dramićanin, <u>L. Marciniak</u>, Step by step optimization of luminescence thermometry in $MgTiO_3:Cr^{3+}$, $Nd^{3+}@SiO_2$ nanoparticles towards bioapplications, *Mater. Chem. Phys.*, **(2023)**, 128623.

P3) W. Piotrowski, K. Kniec, <u>L. Marciniak</u>, Enhancement of the Ln^{3+} ratiometric nanothermometers by sensitization with transition metal ions, *J. Alloys Compd.*, 870, **(2021)**, 159386.

P4) W. Piotrowski, L. Dalipi, R. Szukiewicz, B. Fond, M. Dramićanin, <u>L. Marciniak</u>, The role of Cr^{3+} and Cr^{4+} in emission brightness enhancement and sensitivity improvements of NIR-emitting Nd^{3+}/Er^{3+} ratiometric luminescence thermometers, *J. Mater. Chem. C*, **(2021)**, 9, 12671-12680.

P5) W.M. Piotrowski, K. Maciejewska, L. Dalipi, B. Fond, <u>L. Marciniak</u>, Cr^{3+} ions as an efficient antenna for the sensitization and brightness enhancement of Nd^{3+}, Er^{3+}-based ratiometric thermometer in $GdScO_3$ perovskite lattice, *J. Alloys Compd.*, **(2022)**, 923, 166343.

P6) W. M. Piotrowski, K. Maciejewska, <u>L. Marciniak</u>, Boosting the thermometric performance of the Nd^{3+}, Er^{3+} based luminescence thermometers by sensitization via Cr^{3+} ions: the role of the host material, *Mater. Today Chem.* 30, **(2023)**, 101591.

P7) W. M. Piotrowski, K. Kniec-Stec, M. Suta, B. Bogielski, B. Pozniak, <u>L. Marciniak</u>, Positive luminescence thermal coefficient of Mn^{2+} ions for highly sensitive luminescence thermometry, *Chem. Eng. J.* 464, **(2023)**, 142492.

P8) W. Piotrowski, K. Trejgis, K. Maciejewska, K. Ledwa, B. Fond, L. Marciniak, Thermochromic luminescent nanomaterials based on Mn^{4+}/Tb^{3+} codoping for temperature imaging with digital cameras, *ACS Appl. Mater. Interfaces*, 12, 39, **(2020)**, 44039-44048.

P9) W. M. Piotrowski, P. Bolek, M. G. Brik, E. Zych, L. Marciniak, Frontiers of Deep-Red Emission of Mn^{4+} Ions with Ruddlesden–Popper Perovskites, *Inorg. Chem.* **(2024)**, accepted, DOI: https://doi.org/10.1021/acs.inorgchem.3c03113

P10) W. M. Piotrowski, K. Trejgis, M. Dramićanin, L. Marciniak, Strong sensitivity enhancement in lifetime-based luminescence thermometry by co-doping of $SrTiO_3{:}Mn^{4+}$ nanocrystals with trivalent lanthanide ions, *J. Mater. Chem. C*, **(2021)**, 10309-10316.

As the Supervisor of doctoral dissertation, I was responsible for conceptualization and I carried out the review and editing of all above mentioned papers [P1-P10] to prepare their final version and submitted them to the journals.

I confirm that MSc Eng. Wojciech Piotrowski was the lead co-author of this publication.
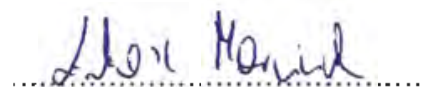
Prof. Łukasz Marciniak

12. References

[1] A. McNaught, A. Wilkinson, The IUPAC Compendium of Chemical Terminology, International Union of Pure and Applied Chemistry (IUPAC), Research Triangle Park, NC, 2019. https://doi.org/10.1351/goldbook.

[2] G. Blasse, B.C. Grabmaier, Luminescent Materials, Springer Berlin Heidelberg, Berlin, Heidelberg, 1994. https://doi.org/10.1007/978-3-642-79017-1.

[3] P. Atkins, T. Overton, J. Rourke, M. Weller, F. Armstrong, Shriver and Atkins' Inorganic Chemistry, 5th ed., Oxford University Press, 2010.

[4] L. Marciniak, K. Kniec, K. Elżbieciak-Piecka, K. Trejgis, J. Stefanska, M. Dramićanin, Luminescence thermometry with transition metal ions. A review, Coord Chem Rev. 469 (2022) 214671. https://doi.org/10.1016/j.ccr.2022.214671.

[5] C.D.S. Brites, S. Balabhadra, L.D. Carlos, Lanthanide-Based Thermometers: At the Cutting-Edge of Luminescence Thermometry, Adv Opt Mater. 7 (2019) 1801239. https://doi.org/10.1002/adom.201801239.

[6] C.D.S. Brites, A. Millán, L.D. Carlos, Lanthanides in Luminescent Thermometry, in: Handbook on the Physics and Chemistry of Rare Earths, 2016: pp. 339–427. https://doi.org/10.1016/bs.hpcre.2016.03.005.

[7] J.G. Solé, L.E. Bausá, D. Jaque, An Introduction to the Optical Spectroscopy of Inorganic Solids, 2005. https://doi.org/10.1002/0470016043.

[8] M.G. Brik, N.M. Avram, C.N. Avram, Advances of crystal field theory and exchange charge model, Magnetic Resonance in Solids. 21 (2019). https://doi.org/10.26907/mrsej-19405.

[9] M. Dramićanin, Luminescence: The Basics, Methods, and Instrumentation, Luminescence Thermometry. (2018) 33–61. https://doi.org/10.1016/B978-0-08-102029-6.00003-8.

[10] A.A. Ansari, M.R. Muthumareeswaran, R. Lv, Coordination chemistry of the host matrices with dopant luminescent Ln^{3+} ion and their impact on luminescent properties, Coord Chem Rev. 466 (2022) 214584. https://doi.org/10.1016/j.ccr.2022.214584.

[11] G. Liu, Z. Xia, Modulation of Thermally Stable Photoluminescence in Cr^{3+}-Based Near-Infrared Phosphors, J Phys Chem Lett. 13 (2022) 5001–5008. https://doi.org/10.1021/acs.jpclett.2c01143.

[12] C. Matuszewska, L. Marciniak, The influence of host material on NIR II and NIR III emitting Ni^{2+}-based luminescent thermometers in $ATiO_3:Ni^{2+}$ (A = Sr, Ca, Mg, Ba) nanocrystals, J Lumin. 223 (2020) 117221. https://doi.org/10.1016/j.jlumin.2020.117221.

[13] S. Adachi, Review—Mn^{4+}-Activated Red and Deep Red-Emitting Phosphors, ECS Journal of Solid State Science and Technology. 9 (2020) 016001. https://doi.org/10.1149/2.0022001JSS.

[14] G. Dantelle, M. Matulionyte, D. Testemale, A. Cantarano, A. Ibanez, F. Vetrone, Nd^{3+} doped $Gd_3Sc_2Al_3O_{12}$ nanoparticles: towards efficient nanoprobes for temperature sensing, Physical Chemistry Chemical Physics. 21 (2019) 11132–11141. https://doi.org/10.1039/C9CP01808E.

[15] A. Benayas, B. del Rosal, A. Pérez-Delgado, K. Santacruz-Gómez, D. Jaque, G.A. Hirata, F. Vetrone, Nd:YAG Near-Infrared Luminescent Nanothermometers, Adv Opt Mater. 3 (2015) 687–694. https://doi.org/10.1002/adom.201400484.

[16] R.S. Pugina, E.G. Hilário, E.G. da Rocha, M.L. da Silva-Neto, A. Das, J.M.A. Caiut, A.S.L. Gomes, Nd^{3+}:YAG microspheres powders prepared by spray pyrolysis: Synthesis, characterization and random laser application, Mater Chem Phys. 269 (2021) 124764. https://doi.org/10.1016/j.matchemphys.2021.124764.

[17] C. Sun, D. Xue, Chemical bonding theory of single crystal growth and its application to φ 3″ YAG bulk crystal, CrystEngComm. 16 (2014) 2129. https://doi.org/10.1039/c3ce42292e.

[18] M.G. Brik, C.-G. Ma, Theoretical Spectroscopy of Transition Metal and Rare Earth Ions, Jenny Stanford Publishing, 2019. https://doi.org/10.1201/9780429278754.

[19] B. Henderson, R.H. Bartram, Crystal-Field Engineering of Solid-State Laser Materials, Cambridge University Press, 2000. https://doi.org/10.1017/CBO9780511524165.

[20] O. Svelto, Principles of Lasers, Springer US, Boston, MA, 1982. https://doi.org/10.1007/978-1-4615-7667-9.

[21] S.A. Wade, S.F. Collins, G.W. Baxter, Fluorescence intensity ratio technique for optical fiber point temperature sensing, J Appl Phys. 94 (2003) 4743. https://doi.org/10.1063/1.1606526.

[22] N.M. Avram, M.G. Brik, Optical properties of 3d-ions in crystals, Beijing, 2013. https://doi.org/10.1007/978-3-642-30838-3.

[23] M. de Jong, L. Seijo, A. Meijerink, F.T. Rabouw, Resolving the ambiguity in the relation between Stokes shift and Huang–Rhys parameter, Physical Chemistry Chemical Physics. 17 (2015) 16959–16969. https://doi.org/10.1039/C5CP02093J.

[24] P.A. Tanner, Some misconceptions concerning the electronic spectra of tri-positive europium and cerium, Chem Soc Rev. 42 (2013) 5090. https://doi.org/10.1039/c3cs60033e.

[25] M. Grinberg, T. Lesniewski, Non-radiative processes and luminescence quenching in Mn^{4+} doped phosphors, J Lumin. (2019). https://doi.org/10.1016/j.jlumin.2019.116574.

[26] K.-L. Wong, J.-C.G. Bünzli, P.A. Tanner, Quantum yield and brightness, J Lumin. 224 (2020) 117256. https://doi.org/10.1016/j.jlumin.2020.117256.

[27] H. Kusama, O.J. Sovers, T. Yoshioka, Line Shift Method for Phosphor Temperature Measurements, Jpn J Appl Phys. 15 (1976) 2349–2358. https://doi.org/10.1143/JJAP.15.2349.

[28] S.F. Collins, G.W. Baxter, S.A. Wade, T. Sun, K.T. V. Grattan, Z.Y. Zhang, A.W. Palmer, Comparison of fluorescence-based temperature sensor schemes: Theoretical analysis and experimental validation, J Appl Phys. 84 (1998) 4649–4654. https://doi.org/10.1063/1.368705.

[29] N.F. Mott, On the absorption of light by crystals, Proc R Soc Lond A Math Phys Sci. 167 (1938) 384–391. https://doi.org/10.1098/rspa.1938.0137.

[30] F. Seitz, An interpretation of crystal luminescence, Transactions of the Faraday Society. 35 (1939) 74. https://doi.org/10.1039/tf9393500074.

[31] V. Pagonis, C. Ankjærgaard, A.S. Murray, M. Jain, R. Chen, J. Lawless, S. Greilich, Modelling the thermal quenching mechanism in quartz based on time-resolved optically stimulated luminescence, J Lumin. 130 (2010) 902–909. https://doi.org/10.1016/j.jlumin.2009.12.032.

[32] M. Stalder, M. Bass, B.H.T. Chai, Thermal quenching of fluorescence in chromium-doped fluoride laser crystals, Journal of the Optical Society of America B. 9 (1992) 2271. https://doi.org/10.1364/JOSAB.9.002271.

[33] M. Duarte, E. Martins, S.L. Baldochi, N.D. Vieira, M.M.F. Vieira, De-excitation mechanisms of $BaLiF_3:Co^{2+}$ crystals, Opt Commun. 159 (1999) 221–224. https://doi.org/10.1016/S0030-4018(98)00616-6.

[34] S.W. Allison, G.T. Gillies, Remote thermometry with thermographic phosphors: Instrumentation and applications, Review of Scientific Instruments. 68 (1997) 2615–2650. https://doi.org/10.1063/1.1148174.

[35] Z. Zeng, Y. Xu, Z. Zhang, Z. Gao, M. Luo, Z. Yin, C. Zhang, J. Xu, B. Huang, F. Luo, Y. Du, C. Yan, Rare-earth-containing perovskite nanomaterials: design, synthesis, properties and applications, Chem Soc Rev. 49 (2020) 1109–1143. https://doi.org/10.1039/C9CS00330D.

[36] P. Dang, Y. Wei, D. Liu, G. Li, J. Lin, Recent Advances in Chromium-Doped Near-Infrared Luminescent Materials: Fundamentals, Optimization Strategies, and Applications, Adv Opt Mater. 11 (2023) 2201739. https://doi.org/10.1002/adom.202201739.

[37] M.G. Brik, Fully relativistic analysis of the covalence effects for the isoelectronic $3d^3$ ions (Cr^{3+}, Mn^{4+}, Fe^{5+}) in $SrTiO_3$, Journal of Physics and Chemistry of Solids. (2006). https://doi.org/10.1016/j.jpcs.2005.12.006.

[38] M.G. Brik, N.M. Avram, Microscopic analysis of the crystal field strength and electron-vibrational interaction in cubic $SrTiO_3$ doped with Cr^{3+}, Mn^{4+} and Fe^{5+} ions, Journal of Physics Condensed Matter. (2009). https://doi.org/10.1088/0953-8984/21/15/155502.

[39] S. Adachi, Luminescence spectroscopy of Cr^{3+} in an oxide: A strong or weak crystal-field phosphor?, J Lumin. 234 (2021) 117965. https://doi.org/10.1016/j.jlumin.2021.117965.

[40] M.G. Brik, N.M. Avram, C.N. Avram, Exchange charge model of crystal field for 3d ions, in: Optical Properties of 3d-Ions in Crystals: Spectroscopy and Crystal Field Analysis, Springer Berlin Heidelberg, Berlin, Heidelberg, 2013: pp. 29–94. https://doi.org/10.1007/978-3-642-30838-3_2.

[41] M.G. Brik, A.M. Srivastava, Critical Review—A Review of the Electronic Structure and Optical Properties of Ions with d^3 Electron Configuration (V^{2+}, Cr^{3+}, Mn^{4+}, Fe^{5+}) and Main Related Misconceptions, ECS Journal of Solid State Science and Technology. 7 (2018) R3079–R3085. https://doi.org/10.1149/2.0041801jss.

[42] F. Zhao, Z. Song, Q. Liu, Advances in Chromium-Activated Phosphors for Near-Infrared Light Sources, Laser Photon Rev. 16 (2022) 2200380. https://doi.org/10.1002/lpor.202200380.

[43] T. Senden, R.J.A. van Dijk-Moes, A. Meijerink, Quenching of the red Mn^{4+} luminescence in Mn^{4+}-doped fluoride LED phosphors, Light Sci Appl. 7 (2018) 8. https://doi.org/10.1038/s41377-018-0013-1.

[44] K. Kniec, L. Marciniak, A ratiometric luminescence pH sensor based on YAG:V^{3+},V^{5+} nanoparticles, New Journal of Chemistry. 46 (2022) 11562–11569. https://doi.org/10.1039/D2NJ01595A.

[45] K. Kniec, K. Ledwa, L. Marciniak, Enhancing the Relative Sensitivity of V^{5+}, V^{4+} and V^{3+} Based Luminescent Thermometer by the Optimization of the Stoichiometry of $Y_3Al_{5-x}Ga_xO_{12}$ Nanocrystals, Nanomaterials. 9 (2019) 1375. https://doi.org/10.3390/nano9101375.

[46] K. Kniec, L. Marciniak, Spectroscopic properties of LaGaO$_3$:V, Nd^{3+} nanocrystals as a potential luminescent thermometer, Physical Chemistry Chemical Physics. 20 (2018) 21598–21606. https://doi.org/10.1039/C8CP04080J.

[47] K. Kniec, L. Marciniak, The influence of grain size and vanadium concentration on the spectroscopic properties of YAG:V^{3+},V^{5+} and YAG: V, Ln^{3+} (Ln^{3+} = Eu^{3+}, Dy^{3+}, Nd^{3+}) nanocrystalline luminescent thermometers, Sens Actuators B Chem. 264 (2018) 382–390. https://doi.org/10.1016/j.snb.2018.02.189.

[48] K. Kniec, M. Tikhomirov, B. Pozniak, K. Ledwa, L. Marciniak, LiAl$_5$O$_8$:Fe^{3+} and LiAl$_5$O$_8$:Fe^{3+}, Nd^{3+} as a New Luminescent Nanothermometer Operating in 1st Biological Optical Window, Nanomaterials. 10 (2020) 189. https://doi.org/10.3390/nano10020189.

[49]   K. Kniec, W. Piotrowski, K. Ledwa, M. Suta, L.D. Carlos, L. Marciniak, From quencher to potent activator – Multimodal luminescence thermometry with Fe^{3+} in the oxides MAl_4O_7 (M = Ca, Sr, Ba), J Mater Chem C Mater. 9 (2021) 6268–6276. https://doi.org/10.1039/D1TC01272J.

[50]   K. Kniec, K. Ledwa, K. Maciejewska, L. Marciniak, Intentional modification of the optical spectral response and relative sensitivity of luminescent thermometers based on Fe^{3+}, Cr^{3+}, Nd^{3+} co-doped garnet nanocrystals by crystal field strength optimization, Mater Chem Front. 4 (2020) 1697–1705. https://doi.org/10.1039/D0QM00097C.

[51]   K. Schmetzer, H.H. Eysel, Absorptions- und Emissionsspektrum von V^{2+}/V^{3+} in Beryllen, Zeitschrift Für Naturforschung A. 29 (1974) 1458–1460. https://doi.org/10.1515/zna-1974-1011.

[52]   M.J.L. Sangster, C.W. McCombie, Calculation of phonon sidebands in emission spectra of V^{2+} and Ni^{2+} in MgO, Journal of Physics C: Solid State Physics. 3 (1970) 1498–1512. https://doi.org/10.1088/0022-3719/3/7/007.

[53]   L.F. Johnson, H.J. Guggenheim, Phonon-Terminated Coherent Emission from V^{2+} Ions in MgF_2, J Appl Phys. 38 (1967) 4837–4839. https://doi.org/10.1063/1.1709230.

[54]   A. Hauser, H.U. Güdel, Single-crystal absorption and emission spectra of $CsVCl_3$ and $CsMgCl_3$:V^{2+}, J Lumin. 27 (1982) 249–256. https://doi.org/10.1016/0022-2313(82)90002-3.

[55]   U. Brauch, U. Dürr, Vibronic laser action of V^{2+}:$CsCaF_3$, Opt Commun. 55 (1985) 35–40. https://doi.org/10.1016/0030-4018(85)90080-X.

[56]   M.G. Brik, C. Ma, A.M. Srivastava, M. Piasecki, Mn^{4+} Ions for Solid State Lighting, Chinese Journal of Luminescence. 41 (2020) 1011–1029. https://doi.org/10.37188/fgxb20204109.1011.

[57]   M. Grinberg, T. Lesniewski, S. Mahlik, R.S. Liu, $3d^3$ system – Comparison of Mn^{4+} and Cr^{3+} in different lattices, Opt Mater (Amst). (2017). https://doi.org/10.1016/j.optmat.2017.03.057.

[58]   G. Huber, C. Kränkel, K. Petermann, Solid-state lasers: status and future, Journal of the Optical Society of America B. 27 (2010) B93. https://doi.org/10.1364/JOSAB.27.000B93.

[59]   S. Kück, Laser-related spectroscopy of ion-doped crystals for tunable solid-state lasers, Applied Physics B. 72 (2001) 515–562. https://doi.org/10.1007/s003400100540.

[60]   Y. Zhydachevskii, D. Galanciak, S. Kobyakov, M. Berkowski, A. Kamińska, A. Suchocki, Y. Zakharko, A. Durygin, Photoluminescence studies of Mn^{4+} ions in $YAlO_3$ crystals at ambient and high pressure, Journal of Physics: Condensed Matter. 18 (2006) 11385–11396. https://doi.org/10.1088/0953-8984/18/49/028.

[61]   T. Cai, Y. Park, S. Mohammadshahi, K.C. Kim, Rise time-based phosphor thermometry using Mg_4FGeO_6:Mn^{4+}, Meas Sci Technol. 32 (2021) 015201. https://doi.org/10.1088/1361-6501/abac8a.

[62]   D.K. Amarasinghe, F.A. Rabuffetti, Ratiometric Thermometry Using Thermochromic Tb^{3+}:Mn^4:$Na_4Mg(WO_4)_3$ Phosphors, Inorg Chem. 60 (2021) 3165–3171. https://doi.org/10.1021/acs.inorgchem.0c03513.

[63]   Y. Fang, Y. Zhang, Y. Zhang, J. Hu, Achieving high thermal sensitivity from ratiometric $CaGdAlO_4$:Mn^{4+}, Tb^{3+} thermometers, Dalton Transactions. 50 (2021) 13447–13458. https://doi.org/10.1039/D1DT02185K.

[64]   Z. Li, X. Yu, T. Wang, S. Wang, L. Guo, Z. Cui, G. Yan, W. Feng, F. Zhao, J. Chen, X. Xu, J. Qiu, Highly sensitive optical thermometer of Sm^{3+}, Mn^{4+} activated $LaGaO_3$ phosphor

for the regulated thermal behavior, Journal of the American Ceramic Society. 105 (2022) 2804–2812. https://doi.org/10.1111/jace.18286.

[65] K. Syassen, Ruby under pressure, High Press Res. 28 (2008) 75–126. https://doi.org/10.1080/08957950802235640.

[66] G. Shen, Y. Wang, A. Dewaele, C. Wu, D.E. Fratanduono, J. Eggert, S. Klotz, K.F. Dziubek, P. Loubeyre, O. V. Fat'yanov, P.D. Asimow, T. Mashimo, R.M.M. Wentzcovitch, Toward an international practical pressure scale: A proposal for an IPPS ruby gauge (IPPS-Ruby2020), High Press Res. 40 (2020) 299–314. https://doi.org/10.1080/08957959.2020.1791107.

[67] M. Pieprz, M. Runowski, K. Ledwa, J.J. Carvajal, A. Bednarkiewicz, L. Marciniak, Improving Accuracy and Sensitivity of Lanthanide-Based Luminescent Manometers by Augmented Spectral Shift Method, ACS Applied Optical Materials. (2023). https://doi.org/10.1021/acsaom.2c00198.

[68] M. Szymczak, P. Woźny, M. Runowski, M. Pieprz, V. Lavín, L. Marciniak, Temperature invariant ratiometric luminescence manometer based on Cr^{3+} ions emission, Chemical Engineering Journal. 453 (2023) 139632. https://doi.org/10.1016/j.cej.2022.139632.

[69] A.M. Ruiz, G. Sakai, A. Cornet, K. Shimanoe, J.R. Morante, N. Yamazoe, Cr-doped TiO_2 gas sensor for exhaust NO_2 monitoring, Sens Actuators B Chem. 93 (2003) 509–518. https://doi.org/10.1016/S0925-4005(03)00183-7.

[70] F. Ahmed, N. Arshi, M.S. Anwar, R. Danish, B.H. Koo, Mn-doped ZnO nanorod gas sensor for oxygen detection, Current Applied Physics. 13 (2013) S64–S68. https://doi.org/10.1016/j.cap.2012.12.029.

[71] T. Ai, J. Li, S. Nie, Y. Yin, J. Lu, S. Bao, L. Yan, High-performance H_2 gas sensor based on Mn-doped α-Fe_2O_3 polyhedrons from N, N-dimethylformamide assisted hydrothermal synthesis, Int J Hydrogen Energy. 47 (2022) 20561–20571. https://doi.org/10.1016/j.ijhydene.2022.04.168.

[72] N.D. Tho, D. Van Huong, H.T. Giang, P.Q. Ngan, G.H. Thai, D.T.A. Thu, D.T. Thu, N.T.M. Tuoi, N.N. Toan, P.D. Thang, H.N. Nhat, High temperature calcination for analyzing influence of 3d transition metals on gas sensing performance of mixed potential sensor $Pt/YSZ/LaMO_3$ (M = Mn, Fe, Co, Ni), Electrochim Acta. 190 (2016) 215–220. https://doi.org/10.1016/j.electacta.2015.12.205.

[73] A. Ferreira, J.P. Silva, D.M. Correia, N. Pereira, M.A. Correa, S. Lanceros-Mendez, F. Vaz, Nanostructured Cr(N,O) based thin films for relative humidity sensing, Vacuum. 191 (2021) 110333. https://doi.org/10.1016/j.vacuum.2021.110333.

[74] C.H. Kim, Y. Myung, Y.J. Cho, H.S. Kim, S.-H. Park, J. Park, J.-Y. Kim, B. Kim, Electronic Structure of Vertically Aligned Mn-Doped $CoFe_2O_4$ Nanowires and Their Application as Humidity Sensors and Photodetectors, The Journal of Physical Chemistry C. 113 (2009) 7085–7090. https://doi.org/10.1021/jp900165c.

[75] S. Pokhrel, K.S. Nagaraja, Electrical and humidity sensing properties of Chromium(III) oxide–tungsten(VI) oxide composites, Sens Actuators B Chem. 92 (2003) 144–150. https://doi.org/10.1016/S0925-4005(03)00251-X.

[76] S.M. Borisov, K. Gatterer, I. Klimant, Red light-excitable dual lifetime referenced optical pH sensors with intrinsic temperature compensation, Analyst. 135 (2010) 1711. https://doi.org/10.1039/c0an00180e.

[77] M. Strobl, T. Mayr, I. Klimant, S.M. Borisov, Photostable upconverting and downconverting pH sensors based on combination of a colorimetric NIR indicator and stable inorganic phosphors as secondary emitters, Sens Actuators B Chem. 245 (2017) 972–979. https://doi.org/10.1016/j.snb.2017.01.189.

[78] S.M. Borisov, R. Seifner, I. Klimant, A novel planar optical sensor for simultaneous monitoring of oxygen, carbon dioxide, pH and temperature, Anal Bioanal Chem. 400 (2011) 2463–2474. https://doi.org/10.1007/s00216-010-4617-4.

[79] S.M. Borisov, I. Klimant, A versatile approach for ratiometric time-resolved read-out of colorimetric chemosensors using broadband phosphors as secondary emitters, Anal Chim Acta. 787 (2013) 219–225. https://doi.org/10.1016/j.aca.2013.05.032.

[80] M. Nakayama, A. Sato, R. Yamaguchi, Decomposition and Detection of Hydrogen Peroxide Using δ-MnO_2 Thin Film Electrode with Self-Healing Property, Electroanalysis. (2013). https://doi.org/10.1002/elan.201300285.

[81] P. Zuo, X. Lu, Z. Sun, Y. Guo, H. He, A review on syntheses, properties, characterization and bioanalytical applications of fluorescent carbon dots, Microchimica Acta. 183 (2016) 519–542. https://doi.org/10.1007/s00604-015-1705-3.

[82] H. Ma, X. Liu, X. Wang, X. Li, C. Yang, A. Iqbal, W. Liu, J. Li, W. Qin, Sensitive fluorescent light-up probe for enzymatic determination of glucose using carbon dots modified with MnO_2 nanosheets, Microchimica Acta. 184 (2017) 177–185. https://doi.org/10.1007/s00604-016-2004-3.

[83] Y. Zhang, R. Huang, H. Li, Z. Lin, D. Hou, Y. Guo, J. Song, C. Song, Z. Lin, W. Zhang, J. Wang, P.K. Chu, C. Zhu, Triple-Mode Emissions with Invisible Near-Infrared After-Glow from Cr^{3+}-Doped Zinc Aluminum Germanium Nanoparticles for Advanced Anti-Counterfeiting Applications, Small. 16 (2020) 2003121. https://doi.org/10.1002/smll.202003121.

[84] Y. Wang, Y. Zhou, H. Ming, Y. Zhao, E. Song, Q. Zhang, Luminescence Enhancement of Mn^{4+}-Activated Fluorides via a Heterovalent Co-Doping Strategy for Monochromatic Multiplexing, ACS Appl Mater Interfaces. 13 (2021) 51255–51265. https://doi.org/10.1021/acsami.1c17135.

[85] J. Xiahou, Q. Zhu, L. Zhu, S. Huang, T. Zhang, X. Sun, J.-G. Li, Lattice-site engineering in $ZnGa_2O_4$:Cr^{3+} through Li^+ doping for dynamic luminescence and advanced optical anti-counterfeiting, J Mater Chem C Mater. 10 (2022) 7935–7948. https://doi.org/10.1039/D2TC00627H.

[86] J.Y. Park, K.W. Jang, H.K. Yang, Development of red-emitting Ba_2LaSbO_6:Mn^{4+} phosphors for latent fingerprint detection, Ceram Int. 47 (2021) 19496–19504. https://doi.org/10.1016/j.ceramint.2021.03.287.

[87] D. Peng, S. He, Y. Zhang, L. Yao, W. Nie, Z. Liao, W. Cai, X. Ye, Blue light-induced rare-earth free phosphors for the highly sensitive and selective imaging of latent fingerprints based on enhanced hydrophobic interaction, Journal of Materiomics. 8 (2022) 229–238. https://doi.org/10.1016/j.jmat.2021.03.005.

[88] S. Zheng, J. Shi, X. Wang, X. Fu, H. Fan, H. Zhang, Flexible thermosensitive films based on shallow-trap persistent luminescence for high-resolution texture imaging of fingerprints even through latex gloves, J Mater Chem C Mater. 9 (2021) 9619–9626. https://doi.org/10.1039/D1TC01888D.

[89] H. Liu, F. Ren, H. Zhang, Y. Han, H. Qin, J. Zeng, Y. Wang, Q. Sun, Z. Li, M. Gao, Oral administration of highly bright Cr^{3+} doped $ZnGa_2O_4$ nanocrystals for *in vivo* targeted imaging of orthotopic breast cancer, J Mater Chem B. 6 (2018) 1508–1518. https://doi.org/10.1039/C7TB03148C.

[90] Y. Liu, J.-M. Liu, D. Zhang, K. Ge, P. Wang, H. Liu, G. Fang, S. Wang, Persistent Luminescence Nanophosphor Involved Near-Infrared Optical Bioimaging for Investigation of Foodborne Probiotics Biodistribution in Vivo: A Proof-of-Concept Study, J Agric Food Chem. 65 (2017) 8229–8240. https://doi.org/10.1021/acs.jafc.7b02870.

[91] M. Pellerin, E. Glais, T. Lecuyer, J. Xu, J. Seguin, S. Tanabe, C. Chanéac, B. Viana, C. Richard, $LaAlO_3:Cr^{3+}$, Sm^{3+}: Nano-perovskite with persistent luminescence for in vivo optical imaging, J Lumin. 202 (2018) 83–88. https://doi.org/10.1016/j.jlumin.2018.05.024.

[92] K. Elzbieciak-Piecka, L. Marciniak, Optical heating and luminescence thermometry combined in a Cr^{3+}-doped $YAl_3(BO_3)_4$, Sci Rep. 12 (2022) 16364. https://doi.org/10.1038/s41598-022-20821-4.

[93] K. Elzbieciak-Piecka, K. Ledwa, L. Marciniak, A novel approach in light-to-heat conversion: Cr^{3+}-based photothermal agent, Mater Today Chem. 26 (2022) 101039. https://doi.org/10.1016/j.mtchem.2022.101039.

[94] K. Maciejewska, A. Paściak, M. Szalkowski, M. Ptak, A. Bednarkiewicz, L. Marciniak, Two-dimentional photo-thermo-polimerisation of MMA with Cr^{3+} doped nanoheaters, Mater Res Bull. 160 (2023) 112119. https://doi.org/10.1016/j.materresbull.2022.112119.

[95] G. Wei, P. Li, R. Li, J. Li, Y. Shi, Y. Wang, S. He, Y. Yang, H. Suo, Z. Wang, Chromium(III)-Doped Phosphors of High-Efficiency Two-Site Occupation Broadband Infrared Emission for Vessel Visualization Applications, Inorg Chem. 61 (2022) 5665–5671. https://doi.org/10.1021/acs.inorgchem.2c00451.

[96] Y. Zhou, C. Li, Y. Wang, Crystal-Field Engineering Control of an Ultraviolet–Visible-Responsive Near-Infrared-Emitting Phosphor and Its Applications in Plant Growth, Night Vision, and NIR Spectroscopy Detection, Adv Opt Mater. 10 (2022) 2102246. https://doi.org/10.1002/adom.202102246.

[97] H. Yu, J. Chen, R. Mi, J. Yang, Y. Liu, Broadband near-infrared emission of $K_3ScF_6:Cr^{3+}$ phosphors for night vision imaging system sources, Chemical Engineering Journal. 417 (2021) 129271. https://doi.org/10.1016/j.cej.2021.129271.

[98] E.V. Radkov, S.A. McCollister, E. Fay, F. Minnich, US Patent 2006/0169998 A1, 2005.

[99] T. Deng, E. Song, Y. Zhou, J. Yuan, Implementation of high color quality, high luminous warm WLED using efficient and thermally stable $Rb_3AlF_6:Mn^{4+}$ as red color converter, J Alloys Compd. 795 (2019) 453–461. https://doi.org/10.1016/j.jallcom.2019.04.305.

[100] J.Y. Park, J.S. Joo, H.K. Yang, M. Kwak, Deep red-emitting $Ca_{14}Al_{10}Zn_6O_{35}:Mn^{4+}$ phosphors for WLED applications, J Alloys Compd. 714 (2017) 390–396. https://doi.org/10.1016/j.jallcom.2017.04.247.

[101] T.E. Peters, R.G. Pappalardo, R.B. Hunt, Lamp phosphors, in: Solid State Luminescence, Springer Netherlands, Dordrecht, 1993: pp. 313–348. https://doi.org/10.1007/978-94-011-1522-3_10.

[102] K. Li, H. Lian, R. Van Deun, M.G. Brik, A far-red-emitting $NaMgLaTeO_6:Mn^{4+}$ phosphor with perovskite structure for indoor plant growth, Dyes and Pigments. 162 (2019) 214–221. https://doi.org/10.1016/j.dyepig.2018.09.084.

[103] S. Gu, M. Xia, C. Zhou, Z. Kong, M.S. Molokeev, L. Liu, W.-Y. Wong, Z. Zhou, Red shift properties, crystal field theory and nephelauxetic effect on Mn^{4+}-doped $SrMgAl_{10-y}Ga_yO_{17}$ red phosphor for plant growth LED light, Chemical Engineering Journal. 396 (2020) 125208. https://doi.org/10.1016/j.cej.2020.125208.

[104] R. Cao, Z. Shi, G. Quan, T. Chen, S. Guo, Z. Hu, P. Liu, Preparation and luminescence properties of $Li_2MgZrO_4:Mn^{4+}$ red phosphor for plant growth, J Lumin. 188 (2017) 577–581. https://doi.org/10.1016/j.jlumin.2017.05.002.

[105] M.A. Noginov, N. Noginova, M. Curley, N. Kukhtarev, H.J. Caulfield, P. Venkateswarlu, G.B. Loutts, Optical characterization of $Mn:YAlO_3$: material for holographic recording and data storage, Journal of the Optical Society of America B. 15 (1998) 1463. https://doi.org/10.1364/JOSAB.15.001463.

[106] Y. Zhydachevskii, A. Suchocki, D. Sugak, A. Luchechko, M. Berkowski, S. Warchol, R. Jakieła, Optical observation of the recharging processes of manganese ions in $YAlO_3$:Mn crystals under radiation and thermal treatment, Journal of Physics: Condensed Matter. 18 (2006) 5389–5403. https://doi.org/10.1088/0953-8984/18/23/011.

[107] Ya. Zhydachevskii, A. Durygin, A. Suchocki, A. Matkovskii, D. Sugak, P. Bilski, S. Warchol, Mn-doped $YAlO_3$ crystal: a new potential TLD phosphor, Nucl Instrum Methods Phys Res B. 227 (2005) 545–550. https://doi.org/10.1016/j.nimb.2004.09.013.

[108] H. Bethe, Theorie der Beugung von Elektronen an Kristallen, Ann Phys. 392 (1928) 55–129. https://doi.org/10.1002/andp.19283921704.

[109] J.H. Van Vleck, Theory of the Variations in Paramagnetic Anisotropy Among Different Salts of the Iron Group, Physical Review. 41 (1932) 208–215. https://doi.org/10.1103/PhysRev.41.208.

[110] M.T. Cieślak-Golonka, J. Starosta, M. Wasielewski, Wstęp do chemii koordynacyjnej, Wydawnictwo Naukowe PWN, Warszawa, 2010.

[111] G.N.A. De Guzman, S.F. Hu, R.S. Liu, Enticing applications of near-infrared phosphors: Review and future perspectives, Journal of the Chinese Chemical Society. 68 (2021) 206–215. https://doi.org/10.1002/jccs.202000287.

[112] M. Voda, J. García Solé, F. Jaque, I. Vergara, A. Kaminskii, B. Mill, A. Butashin, Fano antiresonances in the optical-absorption spectra of Cr^{3+}-doped $La_3Ga_{5.5}Nb_{0.5}O_{14}$ and $La_3Ga_{5.5}Ta_{0.5}O_{14}$ crystals, Phys Rev B. 49 (1994) 3755–3759. https://doi.org/10.1103/PhysRevB.49.3755.

[113] M. Casalboni, A. Luci, U.M. Grassano, B. V. Mill, A.A. Kaminskii, Optical spectroscopy of $La_3Ga_5SiO_{14}$:Cr^{3+} crystals, Phys Rev B. 49 (1994) 3781–3790. https://doi.org/10.1103/PhysRevB.49.3781.

[114] V. Rajendran, T. Lesniewski, S. Mahlik, M. Grinberg, G. Leniec, S.M. Kaczmarek, W.-K. Pang, Y.-S. Lin, K.-M. Lu, C.-M. Lin, H. Chang, S.-F. Hu, R.-S. Liu, Ultra-Broadband Phosphors Converted Near-Infrared Light Emitting Diode with Efficient Radiant Power for Spectroscopy Applications, ACS Photonics. 6 (2019) 3215–3224. https://doi.org/10.1021/acsphotonics.9b01086.

[115] M.M. Medić, M.G. Brik, G. Dražić, Ž.M. Antić, V.M. Lojpur, M.D. Dramićanin, Deep-Red Emitting Mn^{4+} Doped Mg_2TiO_4 Nanoparticles, The Journal of Physical Chemistry C. 119 (2015) 724–730. https://doi.org/10.1021/jp5095646.

[116] J.E. Lennard-Jones, The electronic structure of some diatomic molecules, Transactions of the Faraday Society. 25 (1929) 668. https://doi.org/10.1039/tf9292500668.

[117] Linus. Pauling, The nature of the chemical bond. II. The one-electron bond and the three-electron bond, J Am Chem Soc. 53 (1931) 3225–3237. https://doi.org/10.1021/ja01360a004.

[118] R.S. Mulliken, Electronic Population Analysis on LCAO–MO Molecular Wave Functions, J Chem Phys. 23 (1955) 1833–1840. https://doi.org/10.1063/1.1740588.

[119] G. Racah, Group theory and spectroscopy, 1965. https://doi.org/10.1007/BFb0045770.

[120] J.C. Slater, W.F. Meggers, Quantum theory of atomic structure, Phys Today. 14 (1961) 48–50. https://doi.org/10.1063/1.3057555.

[121] E.U. Condon, G.H. Shortley, C.W. Ufford, The Theory of Atomic Spectra, Am J Phys. 20 (1952) 383–383. https://doi.org/10.1119/1.1933256.

[122] M. Grinberg, P.I. Macfarlane, B. Henderson, K. Holliday, Inhomogeneous broadening of optical transitions dominated by low-symmetry crystal-field components in Cr^{3+}-doped gallogermanates, Phys Rev B. 52 (1995) 3917–3929. https://doi.org/10.1103/PhysRevB.52.3917.

[123] C.K. Jørgensen, The Nephelauxetic Series, in: Progress in Inorganic Chemistry, 2007: pp. 73–124. https://doi.org/10.1002/9780470166055.ch2.

[124] C.E. Schäffer, C. Klixbüll Jørgensen, The nephelauxetic series of ligands corresponding to increasing tendency of partly covalent bonding, Journal of Inorganic and Nuclear Chemistry. 8 (1958) 143–148. https://doi.org/10.1016/0022-1902(58)80176-1.

[125] M.G. Brik, A.M. Srivastava, Electronic Energy Levels of the Mn^{4+} Ion in the Perovskite, $CaZrO_3$, ECS Journal of Solid State Science and Technology. 2 (2013) 148–152. https://doi.org/10.1149/2.020307jss.

[126] M.G. Brik, A.M. Srivastava, N.M. Avram, A. Suchocki, Empirical relation between covalence and the energy position of the Ni^{2+} ^1E state in octahedral complexes, J Lumin. 148 (2014) 338–341. https://doi.org/10.1016/j.jlumin.2013.12.052.

[127] R. Tsuchida, Absorption Spectra of Co-ordination Compounds. I, Bull Chem Soc Jpn. 13 (1938) 388–400. https://doi.org/10.1246/bcsj.13.388.

[128] W. Piotrowski, M. Kuchowicz, M. Dramićanin, L. Marciniak, Lanthanide dopant stabilized Ti^{3+} state and supersensitive Ti^{3+}-based multiparametric luminescent thermometer in $SrTiO_3:Ln^{3+}$ ($Ln^{3+} = Lu^{3+}, La^{3+}, Tb^{3+}$) nanocrystals, Chemical Engineering Journal. 428 (2022) 131165. https://doi.org/https://doi.org/10.1016/j.cej.2021.131165.

[129] Y. Tanabe, S. Sugano, On the Absorption Spectra of Complex Ions II, J Physical Soc Japan. 9 (1954) 766–779. https://doi.org/10.1143/JPSJ.9.766.

[130] Y. Wei, P. Dang, Z. Dai, G. Li, J. Lin, Advances in Near-Infrared Luminescent Materials without Cr^{3+}: Crystal Structure Design, Luminescence Properties, and Applications, Chemistry of Materials. 33 (2021). https://doi.org/10.1021/acs.chemmater.1c01325.

[131] D. Wang, W. Hou, N. Li, Y. Xue, Q. Wang, Q. Wang, X. Xu, D. Li, H. Zhao, H. Zhao, J. Xu, Growth, spectroscopic properties and crystal field analysis of Cr^{3+} doped $GdScO_3$ crystal, Optical Materials Express, Vol. 9, Issue 11, Pp. 4218-4227. 9 (2019) 4218–4227. https://doi.org/10.1364/OME.9.004218.

[132] K. Elzbieciak-Piecka, C. Matuszewska, L. Marciniak, Step by step designing of sensitive luminescent nanothermometers based on Cr^{3+}, Nd^{3+} co-doped $La_{3-x}Lu_xAl_{5-y}Ga_yO_{12}$ nanocrystals, New Journal of Chemistry. 43 (2019) 12614–12622. https://doi.org/10.1039/C9NJ03167G.

[133] K. Elzbieciak, A. Bednarkiewicz, L. Marciniak, Temperature sensitivity modulation through crystal field engineering in Ga^{3+} co-doped $Gd_3Al_{5-x}Ga_xO_{12}:Cr^{3+}$, Nd^{3+} nanothermometers, Sens Actuators B Chem. 269 (2018) 96–102. https://doi.org/10.1016/j.snb.2018.04.157.

[134] S. Adachi, Review—Mn^{4+} vs Cr^{3+}: A Comparative Study as Activator Ions in Red and Deep Red-Emitting Phosphors, ECS Journal of Solid State Science and Technology. (2020). https://doi.org/10.1149/2162-8777/ab6ea6.

[135] A. Van Die, G. Blasse, W.F. Van Der Weg, Luminescence properties of Cr^{3+} doped borate glasses: Influence of crystal field strength and microcrystallite formation, Mater Chem Phys. 14 (1986) 513–523. https://doi.org/10.1016/0254-0584(86)90095-7.

[136] S. Adachi, Review—Photoluminescence Properties of Cr^{3+} -Activated Oxide Phosphors, ECS Journal of Solid State Science and Technology. 10 (2021) 026001. https://doi.org/10.1149/2162-8777/abdc01.

[137] R.D. Shannon, Revised effective ionic radii and systematic studies of interatomic distances in halides and chalcogenides, Acta Crystallogr. Sect. A. 32 (1976) 751–767. https://doi.org/10.1107/S0567739476001551.

[138] M.G. Brik, A.M. Srivastava, On the optical properties of the Mn^{4+} ion in solids, J Lumin. (2013). https://doi.org/10.1016/j.jlumin.2011.08.047.

[139] C. Park, A Dictionary of Environment and Conservation, Oxford University Press, 2007. https://doi.org/10.1093/acref/9780198609957.001.0001.

[140] A. Paściak, R. Marin, L. Abiven, A. Pilch-Wróbel, M. Misiak, W. Xu, K. Prorok, O. Bezkrovnyi, Ł. Marciniak, C. Chanéac, F. Gazeau, R. Bazzi, S. Roux, B. Viana, V.-P. Lehto, D. Jaque, A. Bednarkiewicz, Quantitative Comparison of the Light-to-Heat Conversion Efficiency in Nanomaterials Suitable for Photothermal Therapy, ACS Appl Mater Interfaces. 14 (2022) 33555–33566. https://doi.org/10.1021/acsami.2c08013.

[141] B. del Rosal, E. Ximendes, U. Rocha, D. Jaque, In Vivo Luminescence Nanothermometry: from Materials to Applications, Adv Opt Mater. 5 (2017) 1600508. https://doi.org/10.1002/adom.201600508.

[142] J. Zhou, B. del Rosal, D. Jaque, S. Uchiyama, D. Jin, Advances and challenges for fluorescence nanothermometry, Nat Methods. 17 (2020) 967–980. https://doi.org/10.1038/s41592-020-0957-y.

[143] B. Fond, C. Abram, A.L. Heyes, A.M. Kempf, F. Beyrau, Simultaneous temperature, mixture fraction and velocity imaging in turbulent flows using thermographic phosphor tracer particles, Opt Express. 20 (2012) 22118. https://doi.org/10.1364/OE.20.022118.

[144] C. Abram, B. Fond, F. Beyrau, Temperature measurement techniques for gas and liquid flows using thermographic phosphor tracer particles, Prog Energy Combust Sci. 64 (2018) 93–156. https://doi.org/10.1016/j.pecs.2017.09.001.

[145] J. Jordan, D.A. Rothamer, Pr:YAG temperature imaging in gas-phase flows, Applied Physics B. 110 (2013) 285–291. https://doi.org/10.1007/s00340-012-5274-4.

[146] M.D. Dramićanin, Trends in luminescence thermometry, J Appl Phys. 128 (2020) 040902. https://doi.org/10.1063/5.0014825.

[147] L. Marciniak, W.M. Piotrowski, M. Szymczak, M. Pieprz, K. Trejgis, New Strategies to Improve Thermal Sensitivity and Temperature Resolution in Lanthanide-Doped Luminescent Thermometers, in: J.J. Carvajal Marti, M.C. Pujol Baiges (Eds.), Luminescent Thermometry. Applications and Uses, Springer Science and Business Media LLC, 2023: pp. 69–105. https://doi.org/10.1007/978-3-031-28516-5_2.

[148] J.C. Martins, C.D.S. Brites, A.N. Carneiro Neto, R.A.S. Ferreira, L.D. Carlos, An Overview of Luminescent Primary Thermometers, in: J.J. Carvajal Martí, M.C. Pujol Baiges (Eds.), Luminescent Thermometry, Springer Science and Business Media LLC, 2023: pp. 105–153. https://doi.org/10.1007/978-3-031-28516-5_3.

[149] Z. Jia, C. Yuan, Y. Liu, X.J. Wang, P. Sun, L. Wang, H. Jiang, J. Jiang, Strategies to approach high performance in Cr^{3+}-doped phosphors for high-power NIR-LED light sources, Light: Science & Applications 2020 9:1. 9 (2020) 1–9. https://doi.org/10.1038/s41377-020-0326-8.

[150] P. Dorenbos, Charge transfer bands in optical materials and related defect level location, Opt Mater (Amst). 69 (2017) 8–22. https://doi.org/10.1016/j.optmat.2017.03.061.

[151] T. Senden, F.T.H. Broers, A. Meijerink, Comparative study of the Mn^{4+} $^2E \rightarrow ^4A_2$ luminescence in isostructural $RE_2Sn_2O_7:Mn^{4+}$ pyrochlores ($RE^{3+} = Y^{3+}$, Lu^{3+} or Gd^{3+}), Opt Mater (Amst). 60 (2016) 431–437. https://doi.org/10.1016/j.optmat.2016.08.024.

[152] G. Blasse, P.H.M. de Korte, The luminescence of tetravalent manganese in $CaZrO_3$:Mn, Journal of Inorganic and Nuclear Chemistry. 43 (1981) 1505–1506. https://doi.org/10.1016/0022-1902(81)80325-9.

[153] G. Blasse, B.C. Grabmaier, Energy Transfer, Luminescent Materials. (1994) 91–107. https://doi.org/10.1007/978-3-642-79017-1_5.

[154] N. Yamada, S. Shionoya, T. Kushida, Phonon-Assisted Energy Transfer between Trivalent Rare Earth Ions, J Physical Soc Japan. 32 (1972) 1577–1586. https://doi.org/10.1143/JPSJ.32.1577.

[155] T. Miyakawa, D.L. Dexter, Phonon Sidebands, Multiphonon Relaxation of Excited States, and Phonon-Assisted Energy Transfer between Ions in Solids, Phys Rev B. 1 (1970) 2961–2969. https://doi.org/10.1103/PhysRevB.1.2961.

[156] W.M. Piotrowski, Z. Ristic, M.D. Dramićanin, Ł. Marciniak, Modification of the thermometric performance of the lifetime-based luminescent thermometer exploiting Ti^{3+} emission in $SrTiO_3$ and $CaTiO_3$ by doping with lanthanide ions, J Alloys Compd. 906 (2022) 164398. https://doi.org/10.1016/J.JALLCOM.2022.164398.

[157] J. Drabik, L. Marciniak, The influence of Eu^{3+} concentration on the spectroscopic properties of YAG:Ti, Eu^{3+} nanocrystalline luminescent thermometer, J Lumin. (2019). https://doi.org/10.1016/j.jlumin.2018.12.054.

[158] L. Marciniak, W. Piotrowski, M. Szalkowski, V. Kinzhybalo, M. Drozd, M. Dramicanin, A. Bednarkiewicz, Highly sensitive luminescence nanothermometry and thermal imaging facilitated by phase transition, Chemical Engineering Journal. 427 (2022) 131941. https://doi.org/10.1016/j.cej.2021.131941.

[159] T. Gavrilović, J. Periša, Z. Ristić, K. Elzbieciak-Piecka, Ł. Marciniak, C.-G. Ma, Ž. Antić, M.D. Dramićanin, Thermal history forensics using the emission intensity ratio of $YVO_4:Eu^{3+}$ phosphor, Measurement. 202 (2022) 111942. https://doi.org/10.1016/j.measurement.2022.111942.

[160] K. Maciejewska, P. Szklarz, A. Bednarkiewicz, M.D. Dramićanin, L. Marciniak, Thermally-induced structural phase transition in rare earth orthophosphate nanocrystals for highly sensitive thermal history paints, J Alloys Compd. 935 (2023) 168064. https://doi.org/10.1016/j.jallcom.2022.168064.

[161] M. Back, J. Ueda, M. G. Brik, T. Lesniewski, M. Grinberg, S. Tanabe, Revisiting Cr^{3+}-Doped $Bi_2Ga_4O_9$ Spectroscopy: Crystal Field Effect and Optical Thermometric Behavior of Near-Infrared-Emitting Singly-Activated Phosphors, ACS Appl Mater Interfaces. 10 (2018) 41512–41524. https://doi.org/10.1021/acsami.8b15607.

[162] M. Grinberg, J. Barzowska, Y.R. Shen, K.L. Bray, J. Hanuza, P.J. Dereń, The effect of pressure on luminescence properties of Cr^{3+} ions in $LiSc(WO_4)_2$ crystals— Part II: Pressure- and temperature-dependent luminescence kinetics, J Lumin. 116 (2006) 15–27. https://doi.org/10.1016/J.JLUMIN.2005.02.011.

[163] K. Trejgis, K. Ledwa, A. Bednarkiewicz, L. Marciniak, Impact of host composition and dopant ion concentration on the thermometric properties of a Eu^{3+} activated fluoride-based single-band ratiometric luminescent thermometer, J Alloys Compd. 898 (2022) 162839. https://doi.org/10.1016/j.jallcom.2021.162839.

[164] J. Drabik, L. Marciniak, $KLaP_4O_{12}:Tb^{3+}$ Nanocrystals for Luminescent Thermometry in a Single-Band-Ratiometric Approach, ACS Appl Nano Mater. 3 (2020) 3798–3806. https://doi.org/10.1021/acsanm.0c00485.

[165] K. Trejgis, K. Maciejewska, A. Bednarkiewicz, L. Marciniak, Near-Infrared-to-Near-Infrared Excited-State Absorption in $LaPO_4:Nd^{3+}$ Nanoparticles for Luminescent Nanothermometry, ACS Appl Nano Mater. 3 (2020) 4818–4825. https://doi.org/10.1021/acsanm.0c00853.

[166] J. Stefanska, L. Marciniak, Single-Band Ratiometric Luminescent Thermometry Using Pr^{3+} Ions Emitting in Yellow and Red Spectral Ranges, Adv Photonics Res. 2 (2021) 2100070. https://doi.org/10.1002/adpr.202100070.

[167] D.J. Fisher, Negative Thermal Expansion Materials, Materials Research Forum LLC, 2018. https://doi.org/10.21741/9781945291494.

[168] H. Cui, Y. Cao, Y. Zhang, T. Peng, L. Cao, S. Ran, Y. Wang, D. Wu, X. Li, X. Zhang, B. Chen, Thermal enhancement of up-conversion luminescence in $Lu_2W_{2.5}Mo_{0.5}O_{12}$: Er^{3+}, Yb^{3+} phosphors, Ceram Int. 47 (2021) 21271–21275. https://doi.org/10.1016/j.ceramint.2021.04.132.

[169] H. Lv, P. Du, W. Li, L. Luo, Tailoring of Upconversion Emission in Tm^{3+}/Yb^{3+}-Codoped $Y_2Mo_3O_{12}$ Submicron Particles Via Thermal Stimulation Engineering for Non-invasive Thermometry, ACS Sustain Chem Eng. 10 (2022) 2450–2460. https://doi.org/10.1021/acssuschemeng.1c07323.

[170] H. Zou, B. Chen, Y. Hu, Q. Zhang, X. Wang, F. Wang, Simultaneous Enhancement and Modulation of Upconversion by Thermal Stimulation in $Sc_2Mo_3O_{12}$ Crystals, J Phys Chem Lett. 11 (2020) 3020–3024. https://doi.org/10.1021/acs.jpclett.0c00628.

[171] K.C.B. Lee, J. Siegel, S.E.D. Webb, S. Lévêque-Fort, M.J. Cole, R. Jones, K. Dowling, M.J. Lever, P.M.W. French, Application of the Stretched Exponential Function to Fluorescence Lifetime Imaging, Biophys J. 81 (2001) 1265–1274. https://doi.org/10.1016/S0006-3495(01)75784-0.

[172] E.N. Bodunov, V. V. Danilov, A.S. Panfutova, A.L. Simões Gamboa, Room-temperature luminescence decay of colloidal semiconductor quantum dots: Nonexponentiality revisited, Ann Phys. 528 (2016) 272–277. https://doi.org/10.1002/andp.201500350.

[173] J. Yao, G. López-Peña, J. Lifante, M.C. Iglesias-de la Cruz, R. Marin, E. Martín Rodríguez, D. Jaque, D.H. Ortgies, Adjustable near-infrared fluorescence lifetime emission of biocompatible rare-earth-doped nanoparticles for in vivo multiplexing, Optical Materials: X. 17 (2023) 100225. https://doi.org/10.1016/j.omx.2022.100225.

[174] E. Ximendes, E. Martín Rodríguez, D.H. Ortgies, M. Tan, G. Chen, B. del Rosal, Nanoparticles for In Vivo Lifetime Multiplexed Imaging, in: Multiplexed Imaging, 2021: pp. 239–251. https://doi.org/10.1007/978-1-0716-1593-5_15.

[175] M. Dramićanin, Luminescence thermometry, 2018. https://doi.org/10.1016/C2016-0-01905-8.

[176] A. Bednarkiewicz, L. Marciniak, L.D. Carlos, D. Jaque, Standardizing luminescence nanothermometry for biomedical applications, Nanoscale. (2020). https://doi.org/10.1039/d0nr03568h.

[177] Ł. Marciniak, A. Bednarkiewicz, M. Stefanski, R. Tomala, D. Hreniak, W. Strek, Near infrared absorbing near infrared emitting highly-sensitive luminescent nanothermometer based on Nd^{3+} to Yb^{3+} energy transfer, Physical Chemistry Chemical Physics. 17 (2015) 24315–24321. https://doi.org/10.1039/C5CP03861H.

[178] T.P. van Swieten, A. Meijerink, F.T. Rabouw, Impact of Noise and Background on Measurement Uncertainties in Luminescence Thermometry, ACS Photonics. 9 (2022) 1366–1374. https://doi.org/10.1021/acsphotonics.2c00039.

[179] C.D.S. Brites, P.P. Lima, N.J.O. Silva, A. Millán, V.S. Amaral, F. Palacio, L.D. Carlos, Organic–Inorganic Eu^{3+}/Tb^{3+} codoped hybrid films for temperature mapping in integrated circuits, Front Chem. 1 (2013). https://doi.org/10.3389/fchem.2013.00009.

[180] B.A. Weinstein, Ruby thermometer for cryobaric diamond-anvil cell, Review of Scientific Instruments. 57 (1986) 910–913. https://doi.org/10.1063/1.1138833.

[181] V.C. Fernicola, L. Rosso, R. Galleano, T. Sun, Z.Y. Zhang, K.T. V. Grattan, Investigations on exponential lifetime measurements for fluorescence thermometry, Review of Scientific Instruments. 71 (2000) 2938–2943. https://doi.org/10.1063/1.1150714.

[182] S.M. Borisov, K. Gatterer, B. Bitschnau, I. Klimant, Preparation and Characterization of Chromium(III)-Activated Yttrium Aluminum Borate: A New Thermographic Phosphor for Optical Sensing and Imaging at Ambient Temperatures, The Journal of Physical Chemistry C. 114 (2010) 9118–9124. https://doi.org/10.1021/jp1016467.

[183] J.F.C.B. Ramalho, L.D. Carlos, P.S. André, R.A.S. Ferreira, mOptical Sensing for the Internet of Things: A Smartphone-Controlled Platform for Temperature Monitoring, Adv Photonics Res. 2 (2021) 2000211. https://doi.org/10.1002/adpr.202000211.

[184] F. Fei, Z. Gao, H. Wu, W. Wurendaodi, S. Zhao, S. Asuha, Facile solid-state synthesis of Fe_3O_4/kaolinite nanocomposites for enhanced dye adsorption, J Solid State Chem. 291 (2020) 121655. https://doi.org/10.1016/j.jssc.2020.121655.

[185] P.J. Kumar, K. Nishimura, M. Senna, A. Düvel, P. Heitjans, T. Kawaguchi, N. Sakamoto, N. Wakiya, H. Suzuki, A novel low-temperature solid-state route for nanostructured cubic garnet $Li_7La_3Zr_2O_{12}$ and its application to Li-ion battery, RSC Adv. 6 (2016) 62656–62667. https://doi.org/10.1039/C6RA09695F.

[186] M.P. Pechini, Method of preparing lead and alkaline earth titanates and niobates and coating method using the same to form a capacitor, 1967.

[187] L. Dimesso, Pechini Processes: An Alternate Approach of the Sol-Gel Method, Preparation, Properties, and Applications, in: Handbook of Sol-Gel Science and Technology, Springer International Publishing, Cham, 2018: pp. 1067–1088. https://doi.org/10.1007/978-3-319-32101-1_123.

[188] W. Wu, S. Zuo, X. Zhang, X. Feng, Two-Step Solid State Synthesis of Medium Entropy $LiNi_{0.5}Mn_{1.5}O_4$ Cathode with Enhanced Electrochemical Performance, Batteries. 9 (2023) 91. https://doi.org/10.3390/batteries9020091.

[189] D.V. Mamonova, I.E. Kolesnikov, A.A. Manshina, M.D. Mikhailov, V.M. Smirnov, Modified Pechini method for the synthesis of weakly-agglomerated nanocrystalline yttrium aluminum garnet (YAG) powders, Mater Chem Phys. 189 (2017) 245–251. https://doi.org/10.1016/j.matchemphys.2016.12.025.

[190] X. Tao, X. Chen, Y. Xia, H. Huang, Y. Gan, R. Wu, F. Chen, W. Zhang, Highly mesoporous carbon foams synthesized by a facile, cost-effective and template-free Pechini method for advanced lithium–sulfur batteries, J Mater Chem A Mater. 1 (2013) 3295. https://doi.org/10.1039/c2ta01213h.

[191] W. Stöber, A. Fink, E. Bohn, Controlled growth of monodisperse silica spheres in the micron size range, J Colloid Interface Sci. 26 (1968) 62–69. https://doi.org/10.1016/0021-9797(68)90272-5.

[192] K. Kniec, K.A. Ledwa, L. Marciniak, Role of SiO_2 Coating on YAG:V^{3+}, Nd^{3+} Nanoparticles in Luminescence Thermometry, ACS Appl Nano Mater. 5 (2022) 8271–8278. https://doi.org/10.1021/acsanm.2c01180.

[193] B. Fond, C. Abram, M. Pougin, F. Beyrau, Characterisation of dispersed phosphor particles for quantitative photoluminescence measurements, Opt Mater (Amst). 89 (2019) 615–622. https://doi.org/10.1016/J.OPTMAT.2019.01.011.

[194] W. Geurtsen, F. Lehmann, W. Spahl, G. Leyhausen, Cytotoxicity of 35 dental resin composite monomers/additives in permanent 3T3 and three human primary fibroblast cultures, J Biomed Mater Res. 41 (1998) 474–480. https://doi.org/10.1002/(sici)1097-4636(19980905)41:3%3C474::aid-jbm18%3E3.0.co;2-i.

[195] S.K. Bhatia, A.B. Yetter, Correlation of visual in vitro cytotoxicity ratings of biomaterials with quantitative in vitro cell viability measurements, Cell Biol Toxicol. 24 (2008) 315–319. https://doi.org/10.1007/s10565-007-9040-z.

[196] H.C. Fischer, T.S. Hauck, A. Gómez-Aristizábal, W.C.W. Chan, Exploring Primary Liver Macrophages for Studying Quantum Dot Interactions with Biological Systems, Advanced Materials. 22 (2010) 2520–2524. https://doi.org/10.1002/adma.200904231.

[197] R. Miyata, S.F. van Eeden, The innate and adaptive immune response induced by alveolar macrophages exposed to ambient particulate matter, Toxicol Appl Pharmacol. 257 (2011) 209–226. https://doi.org/10.1016/j.taap.2011.09.007.